An investigation into the use of cavitation for the optimisation of high intensity focused ultrasound (HIFU) treatments

Thesis submitted to the

University of London

for the

Degree of Doctor of Philosophy in Physics

by

James Ross McLaughlan

Joint Department of Physics
Institute of Cancer Research and Royal Marsden NHS Trust
Downs Road, Sutton, SM2 5PT

September 2008

ABSTRACT

High intensity focused ultrasound (HIFU) is an emerging treatment for soft tissue tumours, but long treatment times (3-4 hours for tumour volumes ≤4 cm^3) remain a significant problem. Cavitation can increase the local energy deposition in tissue, which may result in faster, more efficient treatments. There is, however, a lack of understanding of HIFU generated cavitation activity in tissue. This thesis investigates the role that cavitation could play in the optimisation of HIFU treatments, with a view to incorporation of the findings into a clinical HIFU system.

An extensive study of cavitation activity in ex-vivo bovine liver tissue has been undertaken. Passive and active cavitation detection techniques have been combined to give a system for use in HIFU fields. This has been used to investigate cavitation activity over a range of intensities, and to determine appropriate methods for cavitation detection during clinical use. Cavitation activity in tissues exposed to HIFU falls into two categories: micron sized bubbles generated by the peak negative acoustic pressures (acoustic cavitation) and millimetre sized bubbles generated by thermal ex-solution of gas vapour ('boiling'). Acoustic cavitation itself can be split into two types of behaviour, non-inertial (stable) cavitation and inertial (transient) cavitation. Thresholds for these different categories were investigated for clinically relevant exposure times (2-5 s) for degassed water, ex-vivo and perfused liver and ex-vivo kidney. A sonochemical study was also undertaken in water, to further elucidate cavitation behaviour.

Two methods of using cavitation to increase HIFU energy deposition by "pre-conditioning" tissue prior to an ablative exposure, were investigated. Firstly, the ability to 'seed' acoustic cavitation in a controlled and repeatable way was studied. Secondly, the use of 'boiling' bubbles as reflectors post-focally was tested. Both techniques are implementable in the new clinical system under construction at the Institute of Cancer Research (ICR).

ACKNOWLEDGEMENTS

Thank you first and foremost to my supervisors, Drs. Gail ter Haar and Ian Rivens, I would have not been able to complete this PhD without their guidance and support. I would especially like to thank Gail for her mentorship (and cookies) over the years and Ian for providing unwavering support (and tea) despite my relentless pestering.

I would especially like to thank Professors Timothy Leighton and Victor Humphrey for their advice and assistance throughout this thesis.

This project would not have been possible without the technical support from Yixin Ma, who designed and implemented the 3-D automated gantry and FPGA card. I extend my gratitude to Craig Cummings for building the sample holders and Perspex tanks and making any repairs with speed and efficiency and also to Richard Symonds-Taylor for the loan of electrical test equipment. Thank you to Hugh Morris for performing the thermocouple measurements described in Chapter 7 and to Chaturika Jayadewa who processed all of the perfused liver tissue samples for histology. I would also like to thank Victoria Bull whose help with the experimental work in Chapter 11 was invaluable.

The work described in chapter 8 would not have been possible without the collaboration of Boston University and I would especially like to thank Professor Ron Roy and Dr Caleb Farny for their involvement in this study. I also express my gratitude to Professor Peter Friend's surgery unit at Oxford and in particular Dr. Constantin Coussios who set up the perfused liver experiments and Dr Jeff Bamber and his team for allowing me to use the Zonare diagnostic ultrasound scanner for this thesis.

I would like to thank my family for their encouragement and understanding during this time. Finally like to thank my partner, Eleanor Peacey, for her love and encouragement throughout the years, as without it I would not have been able to come this far.

This PhD was funded by a grant from the Engineering and Physical Sciences Research Council (EPSRC).

Table of Contents

List of Figures

List of Tables

Symbols and Abbreviations

Symbols

$\widetilde{\beta}$	Perturbation in the compressibility of an inhomogeneous volume
$\widetilde{\vartheta}$	Perturbation in the density of an inhomogeneous volume
$\dot{Q}$	Rate of heat deposition per unit volume
$\langle \dot{W} \rangle$	Time-averaged power loss per bubble
Ω_b^{ext}	Extinction cross-section of a bubble
Ω_b^{abs}	Absorption cross-section of a bubble
Ω_b^{th}	Thermal dissipation cross-section of a bubble
Ω_b^{vis}	Viscous dissipation cross-section of a bubble
δ_{tot}	Total damping constant for a resonant bubble
$\dot{R}$	Radial velocity of a spherical symmetric bubble
$\ddot{R}$	Radial acceleration of a spherical symmetric bubble
p_∞	Liquid pressure at infinity
$\in_n$	Coefficient of the n^{th} term
$\zeta_d(t)$	A driving force
$\Phi(t)$	Amplitude response of a bubble to a driving force
λ	Wavelength
θ	Phase
ε	Particle displacement
ω	Angular frequency
ρ	Density
α	Amplitude attenuation constant
μ	Attenuation coefficient
γ	Attenuation coefficient in units of Np/cm/MHz
σ	Surface tension
κ	Polytropic index

μ_a	Absorption coefficient
α_A	Advancing contact angle
β_c	Half angle of a crevice
θ_I	Angle of incidence
ω_o	Angular resonant frequency
θ_p	Phase lag
α_R	Receding contact angle
μ_s	Scattering coefficient
θ_T	Angle of transmission
ρ_t	Tissue density
ξ_t	Oscillatory amplitude of the transducer face
§	Section
A	The state of a liquid that has been superheated
A_l	A liquid at a specific temperature and pressure
A_d	Displacement amplitude
B/A	Non-linear parameter for a medium
c	Speed of sound
C	Velocity of sound at a bubble wall
C_b	Specific heat capacity of blood
C_t	Specific heat capacity of tissue
dBm	Decibel with reference to 1 mW
d_{rad}	Off-resonance damping coefficients for radiation loss mechanisms
d_{th}	Off-resonance damping coefficients for thermal loss mechanisms
d_{vis}	Off-resonance damping coefficients for viscous loss mechanisms
E	Energy Density
f	Frequency
F	Total force on a target
f_0	HIFU drive frequency/Fundamental frequency
F_{rad}	Radiation force
g	Acceleration due to gravity
h	Collision geometry constant
H	Difference in the liquid enthalpy between a bubble wall and infinity

h_e	Electromechanical constant
I	Acoustic Intensity
i	Drive current
I_2	Molecular iodine
I_b	Acoustic Intensity emitted from a bubble
I_{sal}	Spatially averaged acoustic intensity
I_{scatt}	Acoustic Intensity scattered from a bubble
I_{sp}	Spatial peak intensity
k	Wavenumber
KI	Potassium Iodide
k_t	Thermal conductivity of the tissue
M	Mach number
m	Mass
n	Number of samples
N	Number of cycles
N_b	Number of resonant bubbles
n_f	Frequency dependence of the attenuation coefficient
n_i	Positive integer
OH^+	Free radical
p	Pressure
P	Drive power
p_0	Hydrostatic liquid pressure away from a bubble
P_A	Acoustic pressure amplitude
P_B	Blake threshold pressure
$P_b(r,t)$	Radiated pressure from a bubble
p_g	Gas pressure inside a bubble
p_L	Liquid pressure immediately outside a bubble
p_{pp}	In-situ peak to peak pressure
p_v	Vapour pressure inside a bubble
Q	Quality factor
R_l	Reflection coefficient
$\underline{r}$	Position vector
R	Bubble radius

R_0	Equilibrium radius of a bubble
R_c	Critical radius of a bubble
t	Time
T	Transmission coefficient
t_{43}	Equivalent minutes at 43^{o}C
T_b	Temperature of blood
u	Particle velocity
V	Drive voltage
$V_C(f)$	Frequency-dependent spectral magnitude of voltage
V_{OB}	Off balance voltage
V_{rms}	Root mean squared voltage
W	Acoustic Power
W_b	Dissipation due to perfusion of blood
W_{vis}	Power dissipated by a bubble
x, y, or z	Cartesian co-ordinate or direction
Z	Acoustic impedance
Z_0	Clamped electrical impedance
Z_{mot}	Motional impedance
τ	Time period

Abbreviations

ABS	Absorbance
BIE	Broadband Integrated Energy
BP	Band Pass
BSA	Bovine Serum Albumin
CA	Microbubble Echo Contrast Agent
CCD	Charged Coupled Device
CW	Continuous Wave
dB	Decibel
DCS	Decompression Sickness
FFT	Fast Fourier Transform
FIFO	First In First Out

FPGA	Field-Programmable Gate Array
fps	Frames Per Second
FWT	Fine Wire Thermocouple
GPIB	General Purpose Interface Bus
HIFU	High Intensity Focused Ultrasound
HP	High Pass
I/Q	In-phase and Quadrature Sinusoidal Components
LED	Light Emitting Diode
LP	Low Pass
MRI	Magnetic Resonance Imaging
NF	Notch Filter
NPL	National Physical Laboratory
NT	Needle Thermocouple
PM	Photomultiplier
PVDF	Polyvinylidene Difluoride
PZT	Lead Zirconate Titanate
RAM	Random Access Memory
RF	Radiofrequency
RPE	Rayleigh-Plesset Equation
SLR	Single-Lens Reflex
TURP	Trans-Urethral Resection of the Prostate
US	Diagnostic Ultrasound

1 – Introduction

1.1 Thesis aim

The broad aim of this thesis was to investigate whether cavitation can be used to improve clinical High Intensity Focused Ultrasound treatments. This task was undertaken using three different approaches: detection, understanding, and enhancement of lesion size. Cavitation detection techniques that might be implemented in a clinical environment were investigated. Cavitation activity was studied in both perfused and unperfused ex-vivo tissue in an effort to understand better the biological effects this could have during clinical HIFU exposures. The final aspect of study was enhancement. The use of cavitation during HIFU exposures was investigated to ascertain whether it could result in larger areas of tissue damage than those obtained with heating alone from the same exposure duration.

1.2 High intensity focused ultrasound (HIFU)

1.2.1 History

High intensity focused ultrasound (HIFU) has been used for scientific research since the early 1940s (Lynn *et al*, 1942; Lynn and Putnam, 1944). Lynn *et al* (1942) described the first HIFU system, which was used to generate thermal damage at depth in ex-vivo bovine liver tissue while sparing the intervening tissue. The early investigations into HIFU were for its use as a tool for neurosurgical research. Fry *et al* (1950; 1951) performed research into the effect high intensity ultrasound had on living systems. These studies showed that it was possible to make irreversible changes to nerve and brain tissue *in vivo* with high intensity ultrasound. At this early stage, temperature was recognised as the primary cause of damage, however cavitation (§2.4) was also believed to play a role. Fry and Fry (1953) were the first to measure temperature changes *in vivo*, due to high intensity ultrasound exposures using implanted thermocouples. This technique used ultrasound with a frequency of 0.98 MHz over the intensity range 60-80 W/cm^2 to determine the acoustic absorption coefficient of spinal cord tissue. Neurological research *in vivo* by Fry *et al* (1955) demonstrated that white brain matter was more susceptible to damage from high intensity ultrasound than grey matter. The groundbreaking studies by the Fry brothers were the early catalyst for developments in

focusing high intensity ultrasound beams to provide an extra-corporeal device for generating localised trackless damage *in vivo*, i.e. no damage to the surrounding area. This early work has been summarised in a book chapter written by Fry (1958). This system was first reported to have been used to expose human patients by Fry and Fry (1960), where the aim was to treat patients suffering from Parkinson's disease and other hyperkinetic disorders. Even though they reported that the symptoms of Parkinsonism disease were eliminated in 48 patients, the technique was not pursued further. A possible cause of this could have been that, in order to provide an acoustic window for HIFU to propagate successfully through to the brain, a section of the skull needed to be removed, and also that this technique was competing with the newly developed drug L-DOPA (Hill *et al*, 2004).

Despite this and some success with ophthalmological treatments (Lizzi *et al*, 1981), HIFU was not reconsidered for clinical applications until the 1990's (ter Haar, 1995; ter Haar and Coussios, 2007). The main reasons for this were that the early equipment was not practical for widespread clinical use, and diagnostic imaging was insufficient for treatment planning purposes (ter Haar and Coussios, 2007). The feasibility of HIFU treatment of soft tissue tumours has been demonstrated in organs such as the bladder (Vallancien *et al* 1993; Vallancien *et al*, 1996), kidney (Watkin *et al*, 1997), prostate (Foster *et al*, 1993; Bihrle *et al*, 1994) and the liver (ter Haar *et al* 1998).

1.2.2 Clinical uses of HIFU

A number of centres, mainly located in China, have treated over a thousand tumours (Wu *et al* 2004). The main targets have included tumours of the liver, bone, breast, kidney, bladder and pancreas. Phase I clinical trials of liver and kidney HIFU treatments have been carried out at the Royal Marsden Hospital, in Sutton, to test safety aspects of treatment (Visioli *et al* 1999), while at the Churchill Hospital, in Oxford, clinical trials have been carried out using the JC HIFU system (HAIFU Technology Company, Chongqing, PR China) (Illing *et al* 2005). Other targets for extra-corporeal HIFU include uterine fibroids (Hindley *et al* 2004). Clinical HIFU treatments have also been delivered using trans-rectal probes for the treatment of prostate cancer (Chaussy *et al*, 2005). Long term studies for the treatment of benign prostate hyperplasia (BHP) using transrectal HIFU were not as successful as the standard trans-urethral resection of the prostate (TURP) (Madesbacher *et al*, 2000). However, HIFU has been shown to be a

promising treatment option for cancer patients with recurrence after external beam radiotherapy (Gelet *et al*, 2004). A review article by Illing and Chapman (2007) discusses the potential uses of trans-rectal HIFU for prostate cancer, highlighting the fact that it is the only currently available treatment which is non-invasive and does not utilise the effects of ionising radiation on tissue.

The basic principle behind the use of HIFU for the minimally invasive treatment of soft tissue tumours is the generation of a continuous wave (CW) ultrasound field, which is focused to a relatively small volume at which the intensity is sufficient to cause irreversible tissue damage. The focal volumes of HIFU beams are typically ellipsoidal, 1-2 mm in diameter and 15-20 mm in length (axial direction) at 1.5 MHz (Watkin *et al*, 1996*)*. In order to treat a tumour larger than the focus, the HIFU beam's focal volume must be scanned, or stepped across the required volume. Figure 1.1 shows a schematic diagram of the concept of extra-corporeal HIFU treatment of a soft tissue tumour located in the liver.

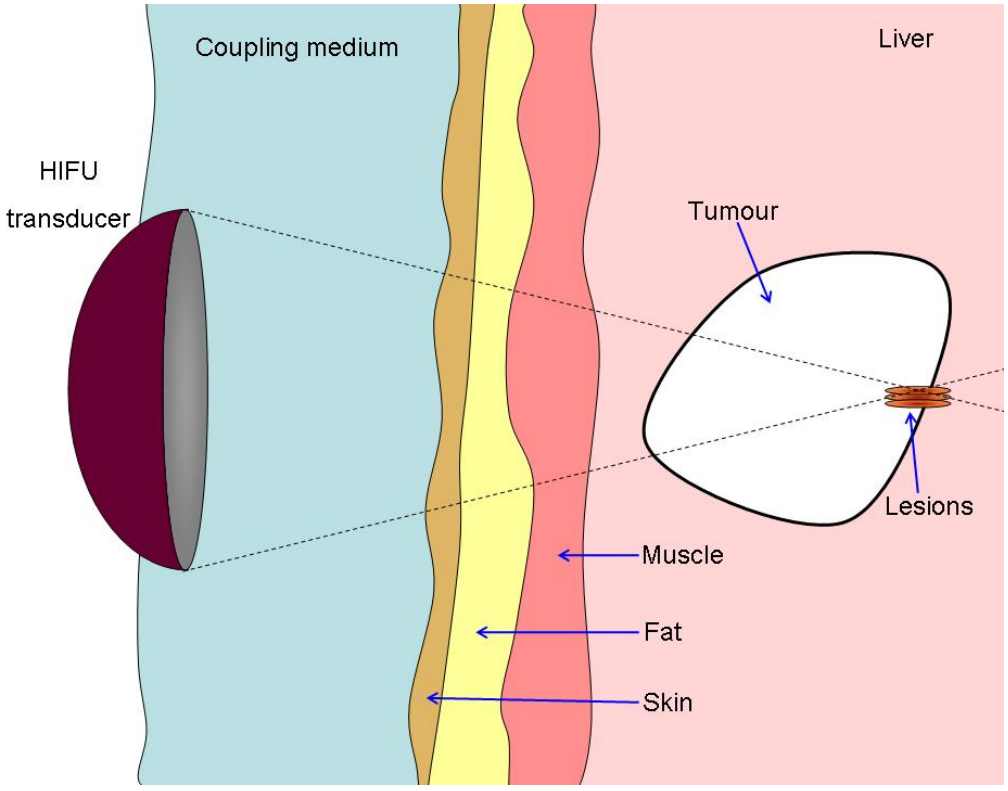

Figure 1.1. A schematic diagram showing the basic principle of extra-corporeal HIFU for treatment of a soft tissue tumour in the liver. The focal region can be placed at depth within a tumour, where a series of adjacent 'lesions' known as a lesion array can be formed as shown.

HIFU-induced thermal damage may be achieved by raising tissue to a temperature in excess of 56^{o}C for 1s (Hill, 2004). This heating causes coagulative necrosis of the tissue, where this damaged volume is referred to as a lesion. Lesions from a single fixed position HIFU exposure, like the focal region used, are usually ellipsoidal, and thus, in order to ensure that all target tissue is ablated, lesions must overlap in order to generate what is referred to as an array. The combination of a small focal zone (compared to the treatment volume), with the associated need to overlap lesions and to wait between exposures to allow cooling of surrounding tissues (Malcolm and ter Haar, 1996), means that treatment times are long (Wu, 2006).

The greater the path length through an absorbing/scattering medium (such as tissue) the greater the ultrasound exposure needed to form a lesion. This increases the likelihood of skin burns and other clinical side effects (Kennedy *et al*, 2004), due to an increase in the pre-focal HIFU intensity to levels at which tissue damage could occur. The current evidence suggests that HIFU is a safe and feasible technique for treatment of liver and kidney tumours. However the rate of tumour volume ablation currently restricts the widespread use of this treatment modality. An alternative to lesion arrays (Figure 1.1) is to produce a 'track' lesion, for which the active HIFU source is scanned over a region in order to ablate a larger volume of tissue more time efficiently. Further complications with the clinical application of HIFU can arise from tissue movement caused by cardiac and respiratory motion, and the presence of air or bone in the HIFU path. These pose particular problems for liver treatments where the organ moves significantly and tumours may be shielded by the rib cage. Bringing the interest in HIFU a full cycle, back to the early studies in the 1950s, research has also been carried out to overcome the barrier presented by the skull to HIFU treatments of brain tumours (Clement *et al*, 2000; Tanter *et al*, 2007). Meanwhile, an alternative to complete thermal ablation of tumours is to use HIFU as a means of occluding the major blood vessels which feed tumours (Rivens *et al*, 1999; Ishikawa *et al* 2003).

Diagnostic ultrasound (US) and magnetic resonance imaging (MRI) are usually used for HIFU treatment guidance. Both imaging techniques have associated benefits and drawbacks as a treatment guidance modality. While MRI offers 3-D topographical information, excellent ability to distinguish between different tissues, can be used for non-invasive thermometry during treatment and is not affected by the HIFU acoustic field, it is expensive to set-up and maintain, and also requires the HIFU equipment to be MRI compatible. US currently does not offer the same ability to distinguish between

different tissues, or temperature imaging, but is cheaper and more portable. While ordinary B-mode ultrasound imaging offers a rather limited ability to target and monitor HIFU treatment, since it is not possible to image while the HIFU beam is on, research into different imaging techniques, for example elastography (Ophir *et al*, 1991) or interleaving of imaging and the HIFU exposures (Rabkin *et al*, 2005) may show further promise.

1.3 The basics of ultrasound

This section introduces some of the basics of ultrasound that are applicable to diagnostic and therapeutic ultrasound. The concepts described in this section are discussed in more detail in these references, Gooberman (1968), Leighton (1994) and Hill (2004).

1.3.1 *The ultrasonic wave*

Ultrasound can be described as a periodic pressure wave that has a frequency which is greater than the upper limit of human hearing (~20 kHz). Acoustic waves are longitudinal waves, so the particles in the medium, which may be a liquid, solid or gas, oscillate in the direction of propagation. It is worth stressing that the particles only oscillate about their equilibrium points and it is only the acoustic wave that propagates through the medium. While the majority of the energy of an acoustic wave propagates longitudinally, if the medium has a shear modulus some of the energy can be dispersed through shear or transverse waves. The propagation of ultrasound in air is limited to much lower frequencies than those used in medical ultrasound imaging. As biological tissue is predominantly water, for medical imaging it is often convenient to make the assumption that the ultrasound is propagating through a liquid medium.

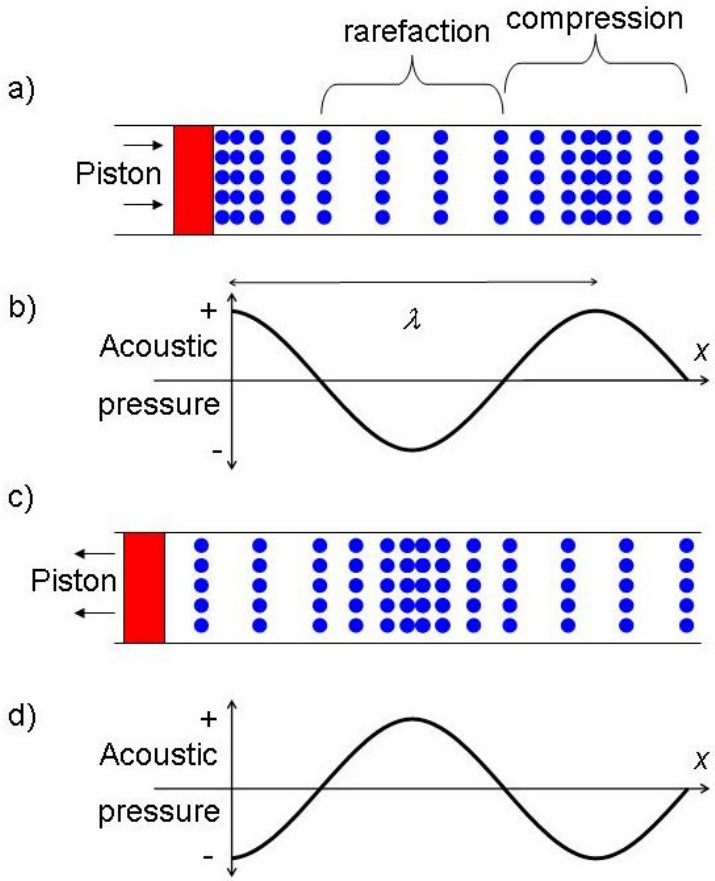

Figure 1.2. Schematic diagram showing the generation of an ultrasound wave with an oscillating piston ((a) and (c)) and the resulting acoustic pressure field ((b) and (d)). The blue circles represent the particles in a medium, which are perturbed by the piston.

Figure 1.2 shows a schematic diagram of the generation of an ultrasonic wave by an oscillating piston. The oscillatory motion of the piston exerts a force on the adjacent particles which causes a longitudinal ultrasound wave to propagate away from it. Figure 1.2(b) and (d) show the acoustic pressure fluctuation caused by the propagation of the ultrasound wave. The regions of high pressure (compression) correspond to the points at which the particles have a high population density (Figure 1.2(b)). Conversely, low pressure regions (rarefaction) occur at points with a low population density (Figure 1.2(d)). For an infinitely long sinusoidal longitudinal wave propagating in one direction, it is possible to determine the frequency (f) of the wave from the speed of sound in the medium (c) and the wavelength (λ). This is given by the relationship:

$$f = \frac{c}{\lambda} \tag{1.1}$$

An equation for wave motion can be rewritten for a longitudinal acoustic wave propagating in the x direction with infinitesimally small amplitude. This gives the second order rate of change of pressure (p) with respect to space (x) and time (t), with the speed of sound in the material:

$$\frac{1}{c^2}\frac{\partial^2 p}{\partial t^2} - \frac{\partial^2 p}{\partial x^2} = 0 \tag{1.2}$$

A general solution for equation 1.2, for a sinusoidal pressure wave, can be written as,

$$p = P_{A1}\sin(\omega t - \beta x + \theta) + P_{A2}\sin(\omega t + \beta x) \tag{1.3}$$

where $\beta = \frac{\omega}{c} = \frac{2\pi}{\lambda}$, and ω denotes the angular frequency ($2\pi f$). P_{A1} and P_{A2} are the pressure amplitude of the wave travelling in the positive and negative x directions, respectively and θ is the phase between the two waves.

1.3.2 *Non-linearity*

The general solution to the wave equation (equation 1.3) is only valid for longitudinal waves that have infinitesimally small pressure amplitude. If the pressure amplitude is finite then the wave is no longer sinusoidal and tends towards a 'saw-tooth' shape. This non-linear effect can be caused by two mechanisms. Firstly the 'convection' effect, if the ratio of the particle velocity (u) to the speed of the pressure wave (c) is not negligible then, the positive parts of the wave tend to propagate as $c + u$. The particle velocity, due to exposure to an acoustic wave, will depend on the particle's location with respect to the acoustic cycle (Figure 1.2), e.g. if the acoustic pressure is 0 MPa the particle velocity will be 0 ms^{-1} and its displacement (ε) will be 0 m. The particle velocity varies as the wave propagates through the medium. It is at a maximum for the peak positive pressure (assuming the particle velocity is in the same direction as the wave velocity), i.e. compression (Figure 1.2) and a minimum at the rarefaction (Figure 1.2). Thus the pressure peaks will travel at the highest speed and the pressure minima will travel at the lowest.

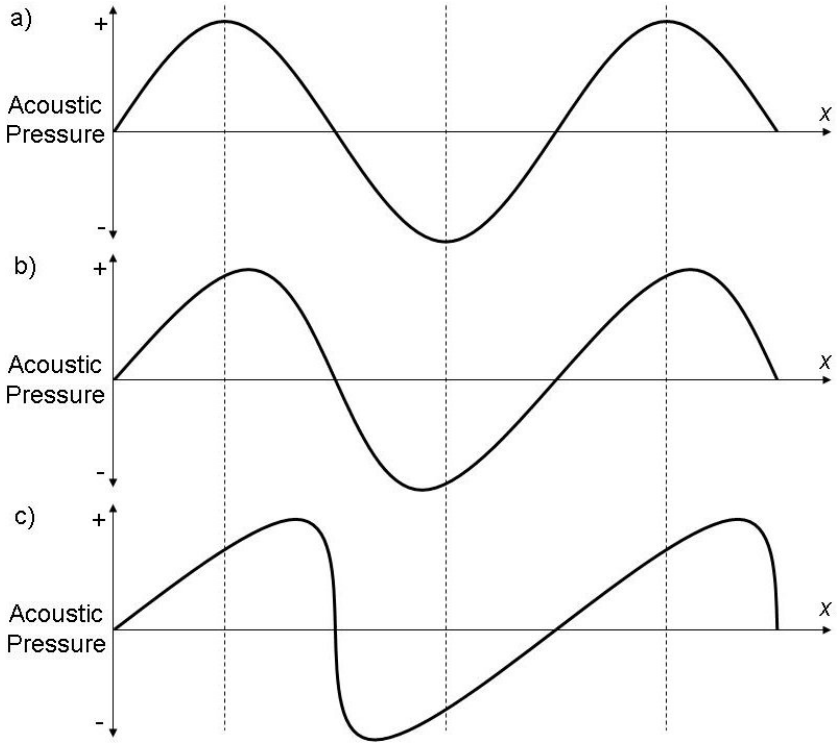

Figure 1.3. A schematic diagram of the development of a 'saw-tooth' from an initially sinusoidal waveform. The waveforms (a), (b) and (c) show the distortion of the wave as it propagates in a medium at increasing distances from the acoustic source.

The second effect, a 'medium' effect, is due to the compression of the propagation medium from the acoustic pressure. When, for example, a liquid is compressed, its bulk modulus and stiffness increase, leading to an increase in the sound speed (c). This too causes the pressure peaks to travel faster than the pressure minima. Since a pressure peak is unable to overtake the pressure minimum, a discontinuous (or 'shocked') waveform develops, as shown in Figure 1.3. This figure shows a waveform that is initially sinusoidal (Figure 1.3(a)). As it progresses through the medium each compressive region catches up with the preceding rarefaction region half cycle and the waveform becomes increasingly steep (Figure 1.3(b)). Once the wave has propagated a sufficient distance (the 'discontinuity length') the waveform becomes 'saw-tooth' (Figure 1.3(c)). A saw-tooth has high frequency components which are attenuated more rapidly than the fundamental and therefore further propagation leads to dissipation of these higher frequency components causing a reduction in amplitude that eventually leads to the wave being unable to maintain the shocked waveform, and returning to a lower amplitude sinusoidal wave.

The wave equation shown in equation 1.3 is a first order approximation which neglects non-linear effects. A first order approximation refers to the first order terms in a Taylor power series of the acoustic variables. For example, the total pressure (p) at a given point in space and time can be written as the Taylor expansion,

$$p = \varepsilon p_1 + \varepsilon^2 p_2 + \ldots\ldots \tag{1.4}$$

where ε a dimensionless parameter that is << 1. This means that the magnitude of each term is approximately a factor of ε smaller than the preceding term. An equivalent series can be written for the density (ρ) and the particle velocity (u) of the medium. Equation 1.4 includes the first and second order approximations for the acoustic pressure. The second order approximation for the wave equation is,

$$\frac{1}{c^2}\frac{\partial^2 p_2}{\partial t^2} - \frac{\partial^2 p_2}{\partial x^2} = \frac{1}{2}\frac{\beta_N}{c^2}\frac{\partial^2 \rho_1}{\partial t^2} + \rho_0 \frac{\partial^2 u_1}{\partial x^2} \tag{1.5}$$

where $\beta_N \equiv \frac{c^2}{\rho_0}\frac{B}{A}$, and ρ_0 the undisturbed density of the medium. The constants A and B are proportional to $\rho_0 c^2$ and $\rho_0{}^2\left(\frac{\partial^2 p}{\partial \rho^2}\right)_{\rho=0}$. These coefficients depend only on the properties of the medium. The second order wave equation has non-linear components which are shown on the right hand side of the equation, the two terms show the separate 'medium' and 'convective' non-linear components that were discussed earlier. With the addition of the second order terms, the solution to the wave equation for a positive x propagating wave reduces to the linear case with a wave propagating at twice the fundamental frequency ($2f_0$). Assuming the boundary condition at $x = 0$ is such that the wave is purely sinusoidal, the second order component of the acoustic pressure shown in equation 1.5 can be described by:

$$p_2 = \frac{1}{2}\frac{P_0^2}{\rho_0 c^2}\left(1 + \frac{1}{2}\frac{B}{A}\right) kx \sin\left\{2\left(\omega t - kx - \frac{\pi}{4}\right)\right\} \tag{1.6}$$

where P_0 the original pressure amplitude at the source and $\frac{B}{A}$ is a parameter which describes the non-linear propagation of sound in the medium. Equation 1.6 shows that the amplitude of this wave increases linearly with propagation distance (x) and with frequency (f), and quadratically with respect to the initial pressure amplitude. Both the medium and convective non-linear effects contribute, but the medium effects dominate in a typical liquid medium such as water.

Non-linear propagation is an important effect when using HIFU, where large pressure amplitudes (> 2 MPa) are often generated. As a HIFU wave propagates, energy is transferred to higher harmonics, each of which will contribute to heating (from absorption) and will also be attenuated in the tissue at different rates. This may generate 'hotspots', causing inhomogeneous tissue ablation and increasing the risk of damage to overlying tissues. The effects of non-linear propagation in HIFU are therefore complex, especially in those situations where large path lengths (up to 15 cm), focusing and multiple tissue layers with different properties are also encountered.

1.3.3 *Acoustic impedance and intensity*

The term impedance generally refers to the ratio of a general driving force to the velocity response. For an ultrasound wave, the driving force is the acoustic pressure amplitude (P_A)**,** and the velocity response is the particle velocity (u) in the medium. This gives the acoustic impedance (Z)

$$Z = \frac{P_A}{u} \tag{1.7}$$

Since the acoustic pressure (P_A**)** equals the change in local pressure from equilibrium pressure and assuming harmonic motion for the particle displacement it is possible to rewrite equation 1.7 in terms of the speed of sound (c) and density (ρ) of the medium

$$Z = \rho c \tag{1.8}$$

An ultrasound wave carries energy in the form of kinetic energy (particle movement) as it propagates. This energy can be quantified in terms of total energy density (E), defined as the amount of energy in a unit volume. By considering a sinusoidal longitudinal plane wave over a single acoustic cycle it is possible to write the total energy density as:

$$E = \frac{1}{2}\rho |u|^2_{\max} \tag{1.9}$$

Acoustic intensity (I) is the rate at which energy in a wave crosses a unit area perpendicular to the direction of propagation. The relationship between energy density (E) and acoustic intensity is thus given by:

$$I = Ec \tag{1.10}$$

From equations, 1.7 to 1.10 it is possible to write the time averaged acoustic intensity (I) over one cycle as

$$I = \frac{P_A^{\,2}}{2Z} \tag{1.11}$$

The acoustic intensity (I) in an acoustic field is often characterised by measuring the radiation force that is incident on an absorbing or reflecting target. The radiation force effect is due to a net transfer of momentum that arises when the target is placed in the field. The total force exerted on a target of finite size which is placed into the field is given by the relationship

$$F = \frac{hIA}{c} \tag{1.12}$$

where F is the total force on the target, A is the surface area of the target and h is a constant dependent on the collision geometry. $h = 1$ for total absorption of the beam, $h = 2$ for total normal reflection, and $0 < h < 2$ for partial absorption and/or non-normal reflection.

Momentum absorbed by a liquid from an acoustic wave propagating through it can cause a flow in the direction of propagation, this is called acoustic streaming. Acoustic streaming generated by B-mode imaging has been measured in water flowing at speeds of 1 cm/s (Starritt *et al*, 1989). This definition of acoustic streaming refers to the bulk movement of liquid. However, it is possible to observe similar effects near small obstacles located in the acoustic field. It arises from the frictional interaction between these small boundaries and the pressure fluctuations from an acoustic field in the liquid, and is referred to as microstreaming.

1.3.4 *Ultrasound attenuation*

In biological tissues, refraction, reflection, scattering and absorption contribute to the total attenuation of an acoustic wave propagating through the tissue. Refraction of an acoustic wave is caused by the wave propagating through a region in which there is a sound speed gradient. An acoustic wave can be reflected between two interfaces that have different values of acoustic impedance (Z). At any such interface, a proportion of the energy in the incident acoustic wave will be reflected. If a wave propagating through a medium with characteristic impedance Z_1 propagates normally towards, and through, a second material with characteristic impedance Z_2, it can be shown that

$$T = \frac{2Z_2}{(Z_1 + Z_2)} \tag{1.13}$$

$$R_I = \frac{(Z_2 - Z_1)}{(Z_1 + Z_2)} \tag{1.14}$$

where T is the pressure amplitude transmission coefficient, and equals the ratio of the amplitude of the transmitted to the incident pressure wave. R_I is the corresponding reflection coefficient and is the ratio of the pressure amplitude of the reflected and incident pressure waves. It is possible to see that from equations 1.13 and 1.14 that if $Z_1 = Z_2$ then $R_I = 0$ and $T = 1$ and no reflection occurs. When the wave is incident on a boundary not at normal incidence, partial transmission of a wave can occur, provided that it is not at, or greater than, the critical angle (i.e. the angle above which total internal reflection occurs). For this case, it is possible to rewrite equations 1.13 and 1.14 as,

$$T_\varepsilon = \frac{2Z_1 \cos\theta_I}{(Z_1 \cos\theta_T + Z_2 \cos\theta_I)} \tag{1.15}$$

$$R_\varepsilon = \frac{Z_1 \cos\theta_T - Z_2 \cos\theta_I}{(Z_1 \cos\theta_T + Z_2 \cos\theta_I)} \tag{1.16}$$

where T_ε is the displacement amplitude transmission coefficient, and R_ε is the corresponding reflection coefficient. The transmitted wave will also be refracted. Equation 1.16 shows that at normal incidence $R = -R_\varepsilon$ such that at the plane rigid boundary the particle velocity (u), wave velocity (c) and particle displacement (ε) is reversed. However at a free interface (i.e. tissue boundary) the reflection causes the reversal of the wave velocity and pressure, where the particle velocity and displacement are unchanged. Reflections from interfaces between tissue boundaries that have different densities and/or sound speeds can therefore arise. This is the basis of pulse-echo diagnostic ultrasound imaging. Scattering is a general term that describes an effect of an acoustic wave propagating through an inhomogeneous medium. In biological tissue, scattering specifically refers to part of the acoustic wave that is reflected and/or refracted from interfaces between different tissues, which is due to inhomogeneities in the tissue density or compressibility. The interaction of an acoustic wave with an inhomogeneous medium can be described by the following wave equation (Morse and Ingard, 1968)

$$\nabla^2 p(\underline{r},\underline{t}) - \frac{1}{c^2}\frac{\partial^2 p(\underline{r},t)}{\partial t^2} = \frac{1}{c^2}\frac{\partial^2 p(\underline{r},t)}{\partial t^2}\tilde{\beta}(\underline{r}) + \nabla \cdot \left[\tilde{g}(\underline{r})\nabla p(\underline{r},t)\right] \tag{1.17}$$

where $\tilde{\beta}$ and $\tilde{\vartheta}$ describe the small fluctuations in the compressibility and density inside an inhomogeneous volume, respectively and $\underline{r}$ is a position vector.

An acoustic wave propagating in the x direction through a lossy medium can be described (in complex notation) as:

$$p = p_0 e^{i(\omega t - kx)} e^{-\alpha x} \tag{1.18}$$

The term α is the amplitude attenuation constant which is typically quoted in nepers per centimetre (Np/cm). Equation 1.18 shows that an acoustic wave propagating in x dirceetion decays at an exponential rate that is determined by the value of α. There are a number of mechanisms by which energy can be lost from the acoustic wave. The most significant of these is the transformation of mechanical energy into heat, as the acoustic wave does work against the viscous forces that oppose the internal motion within the medium. Energy dissipation can occur due to a heat flow between the compressions and rarefactions causing an increase in the entropy of the system and a loss of energy. Dissipation can also occur as heat is radiated from compression to rarefactions through intermolecular energy exchange. If the medium is inhomogeneous (as for tissue) it is possible to lose energy through scattering and from frictional heating from the relative motions between, for example, different tissue layers. As the intensity is proportional to the square of pressure it is possible to write an attenuation coefficient (μ) which is equal to 2α. This coefficient has units of decibels per centimetre (dB/cm) which is equivalent to $10\log_{10}\left(\frac{Np}{cm}\right)$. Since both absorption and scattering contribute to the total loss of energy from an acoustic wave it is possible to write μ as a sum of the absorption (μ_a) and scattering (μ_s) coefficients,

$$\mu = \mu_a + \mu_s \tag{1.19}$$

As the frequency of the acoustic wave increases, the timescale and physical distance between the compression and rarefaction distances decrease, which means that the attenuation of the acoustic wave increases. The frequency dependence of the attenuation coefficients can be described using a power law:

$$\mu(f) = \gamma f^{n_f} \tag{1.20}$$

where γ is the attenuation coefficient in units of Np/cm/MHz and f is the frequency in MHz. The factor n_f describes the frequency dependence of the attenuation coefficient, for example n_f = 1.2 for ex-vivo bovine liver at room temperature (Duck, 1990).

Absorption of an acoustic wave in tissue causes heat generation through visco-elastic interaction with the molecules of the medium. If it is assumed that all energy lost from the acoustic wave causes heating then it is possible to describe the rate of heat deposition per unit volume ($\dot{Q}$) as,

$$\dot{Q} = \mu I \tag{1.21}$$

It is possible to estimate the temperature rise in a biological system when a heat source (i.e. HIFU) and sink (i.e. convective blood flow) are present. This is given by the transient heat transfer equation (Pennes, 1948).

$$\rho_t C_t \frac{\partial T}{\partial t} = k_t \nabla^2 T - W_b C_b (T - T_b) - \left[G((T - T_b)^2 f(t) \right] + \dot{Q} \tag{1.22}$$

where ρ_t, C_t and k_t are the density, specific heat and thermal conductivity of the tissue. W_b, $C_{b,}$ and T_b are the perfusion, specific heat and temperature of the blood, respectively, and G is a constant. Equation 1.22 can be solved numerically using either finite difference or finite element methods (Meaney *et al*, 1998). A solution to this equation, using appropriate parameters, can give an estimation of the thermal effects and possible damage that can be caused from exposure of tissue to HIFU. However, in its current form, it neglects any mechanical effects on the tissue that may be generated during a HIFU exposure. These mechanical effects, or cavitation, are introduced and discussed in the next chapter.

2 – Introduction to cavitation

This chapter serves as an introduction to the basics of cavitation discussed in this thesis, and predominantly focuses on reviewing the state of knowledge about cavitation activity that can occur during ultrasound exposures.

2.1 Cavitation

The term 'cavitation' was first used in literature to describe a phenomenon that was observed when the negative pressure, generated from the motion of propellers in water, exceeded a pressure threshold (Barnaby and Thornycroft, 1895) of 6.75 pounds per square inch (~ 0.05 MPa) giving rise to cavities behind the blades. Cavitation may be defined as the formation and activity of bubbles (or cavities) in a liquid (Neppiras, 1980). The term formation can refer to the creation of a new cavity or to the growth of a pre-existing cavity to a size at which macroscopic effects can be observed (Young, 1989). These cavities can be suspended in a liquid, or trapped in tiny cracks either at a liquid/solid boundary or on an impurity within the liquid. The growth of a cavity can be affected by increasing/reducing the ambient pressure of the liquid, by static or dynamic methods.

Young (1989) suggests that there are four physical processes in which it is possible to cause the growth of a bubble. Firstly, for a gas-filled bubble, its growth is caused by the application of a negative pressure or a temperature increase. Secondly, a gas-filled bubble can be caused to grow through a reduction in the ambient pressure. Thirdly, a gas filled bubble can grow by diffusion (called degassing), as gas comes out of the liquid. Finally, a vapour-filled bubble can grow when there is a sufficient temperature rise, commonly referred to as boiling. These four growth mechanisms assume that the bubble contains only gas or vapour. Young (1989) suggested that it would be better to distinguish between four different types of cavitation relating them to how the cavities were produced. Firstly, hydrodynamic cavitation can be generated through pressure variations in a flowing liquid (e.g. close to a propeller). Secondly, acoustic cavitation can be caused by the pressure variations in an oscillating acoustic wave. Thirdly, optic cavitation can be produced by the deposition of high energy photons in a liquid and, finally, particle cavitation can result from energy deposition by an elementary particle in a liquid.

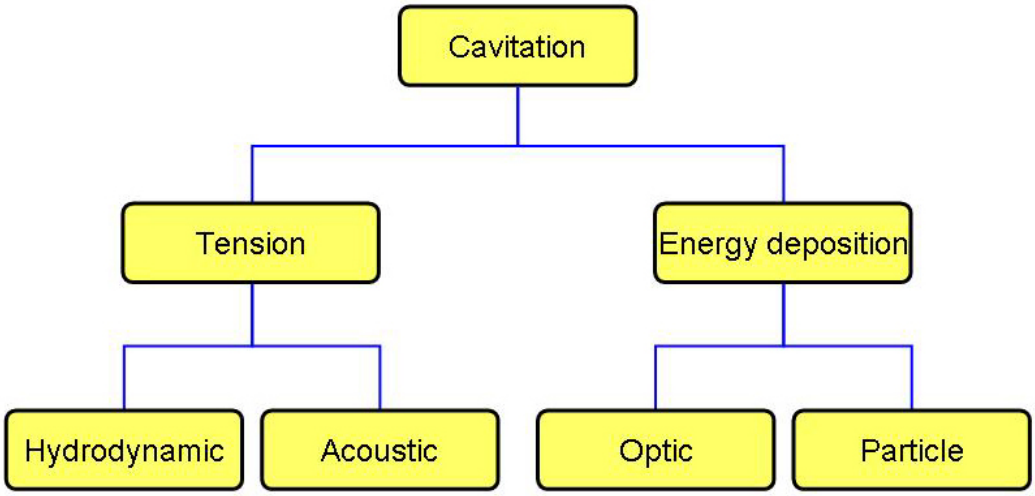

Figure 2.1. A classification scheme for different types of cavitation (Lauterborn, 1980).

Figure 2.1 depicts an alternative scheme for classification of cavitation (Lauterborn, 1980), based on the inception process by which cavities form. This distinguishes cavitation generated by tension from that caused by local deposition of energy in the liquid. It is important to note that HIFU can generate cavitation through both of these mechanisms in an attenuating medium.

2.1.1 Acoustic cavitation

The large negative pressures (up to 5 MPa) generated in the rarefaction portion of the pressure cycle of a HIFU field can cause tension in the medium through which it is propagating, which can lead to the formation and/or activity of gas and/or vapour filled bubbles (Leighton, 1994). As described above, this is acoustic cavitation, and is a threshold effect (Neppiras, 1984). Since the compressibility of bubbles is much higher than that of the surrounding medium, they react to the HIFU field.

The temperature rise in tissue exposed to HIFU can be dependent on for example, the acoustic absorption coefficient μ_a, acoustic intensity and exposure time. As the tissue temperature rises, the threshold for acoustic cavitation falls, since the partial pressures of the vapour and/or gas dissolved in the tissue increase. Therefore, less tension (or force acting to separate the particles in the medium) in the tissue is needed for the inception of cavitation at elevated temperatures. The forms of acoustic cavitation which are relevant to this thesis fall into two categories. A bubble can oscillate stably about its equilibrium radius; this is referred to as non-inertial (stable) cavitation. Alternatively, a

bubble can grow to many times its equilibrium radius, and then collapse violently. This is referred to as inertial (or transient or collapse) cavitation, so called as the inertial forces of the bubble motion dominate in the collapse (Leighton, 1994). Section 2.4 discusses some of the effects of acoustic cavitation from HIFU exposures. Section 4.1 discusses further the relationship between these types of acoustic cavitation and an ultrasound field, specifically the generation of acoustic emissions.

2.1.2 Thermal exsolution of vapour

A second mechanism for cavitation formation within a HIFU field comes from the focal deposition of energy which heats the tissue. As discussed above, this type of cavitation will only occur when the temperature rise is sufficient to cause exsolution, thus this phenomenon cannot arise in non-absorbing media such as degassed water. When the tissue temperature is sufficiently high, the interstitial liquid can change into a vapour, which may result in bubble formation. This is sometimes referred to as superheating (Crum and Law, 1995). Superheating occurs when a liquid, at constant pressure, is heated at to a point at which it would normally be a vapour.

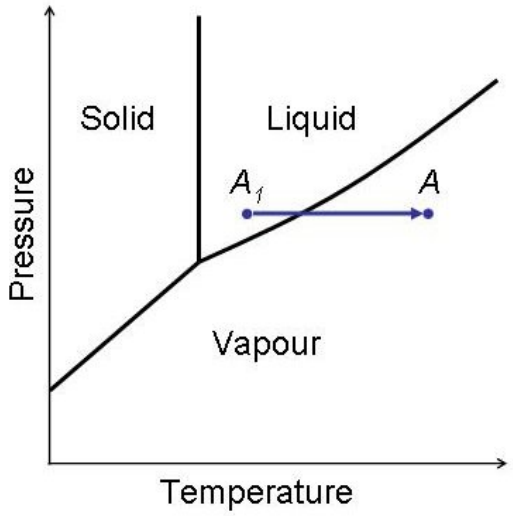

Figure 2.2. A simple phase diagram for a substance (Young, 1989). A_1 relates to a liquid at a particular temperature and pressure, where A is a state of a liquid that is said to be superheated.

Figure 2.2 shows a simple phase diagram for a substance. At point A it would normally be considered to be a vapour. However, by starting at A_1 and heating slowly, while keeping the pressure constant, the substance can remain liquid. Such a liquid in the state

represented by *A* is "superheated" and is therefore in a metastable state. A metastable state can be considered to be a temporary high-energy state that is not changing with time, but can fall into a lower energy state following a small interaction. For example, it is possible to heat water that is free of impurities at atmospheric pressure (0.1 MPa) to 180°C above the boiling point, i.e. 280°C (Young, 1989), however the addition of impurities would result in the vaporisation of this liquid. However, at the limit of super-heating, the tensile stress of the liquid is reduced to zero and the liquid spontaneously vaporises. This effect was particularly of interest when it was found that liquid sodium, the coolant used in fast-breeder nuclear reactors, can superheat to hundred of degrees above its boiling point (Winterton, 1977) which could pose a significant safety hazard. This effect, is thought to occur in tissue, and is generally referred to as "boiling". It has been suggested that in ex-vivo tissue, this effect can generate audible (1-20 kHz) emissions during HIFU exposures (Khokhlova *et al*, 2006; Rabkin *et al*, 2006). Boiling bubbles in tissue/gel typically have a radius a few orders of magnitude larger (~ mm) than those of resonant cavitation bubbles (~ 2.5 μm at 1.69 MHz) and are consequently not resonant in the HIFU field. The interaction of these types of bubbles and a HIFU field is discussed in Section 7.2.3.

2.2 Cavitation activity and nucleation

This section gives a basic introduction to the dynamics of a single pre-existing bubble where the pressure changes but there is no heat flow (i.e. semi-static condition), and to the main mechanisms for cavitation inception in water and biological tissue. Both topics are important in the investigation of the cavitation activity generated by HIFU exposures.

Firstly, consider the dynamics of a single, static bubble, of radius R, located inside a liquid medium that has an internal pressure (p_i), which is the sum of the gas (p_g) and vapour (p_v) pressures inside the bubble. This internal pressure is greater than the liquid pressure immediately outside the bubble (p_L) because of the surface tension of the wall (Leighton, 1994). The excess pressure inside the bubble, p_σ, which results from surface tension, (σ), is given by:

$$p_\sigma = \frac{2\sigma}{R}. \tag{2.1}$$

For a spherical bubble at equilibrium, where $R = R_0$, and the pressure of the liquid immediately outside the bubble wall (p_L) is equal to the pressure of the liquid away from the bubble (p_0), it is possible to write the internal pressure as (Prosperetti, 1984):

$$p_i = p_0 + \frac{2\sigma}{R_0} \tag{2.2}$$

By rearranging equation 2.2 it is possible to define the critical radius (R_c) of R that is needed for the bubble to be stable

$$R_c = \frac{2\sigma}{p_i - p_0} \tag{2.3}$$

Equation 2.3 demonstrates that if the radius of the bubble is smaller than the critical radius ($R < R_c$) then the surface tension will dominate, causing the bubble to contract. For the reverse situation, if the internal pressure of the bubble dominates it will cause the bubble to grow ($R > R_c$). In general there are four processes by which a bubble is prevented from being stable (Young, 1989). A bubble can rise in the liquid due to buoyancy. It may also dissolve due to diffusion of gas out of the bubble. As discussed above, it can contract due to surface tension or grow due to the internal gas pressure. If the pressure of the liquid is reduced during the rarefaction cycle of an ultrasonic wave, it may be assumed that the effects of buoyancy and diffusion would be negligible, since they occur over a much longer time scale than the oscillations of an ultrasonic wave. It is therefore possible to find the minimum value of acoustic pressure amplitude (P_A) that could cause the growth of a bubble of radius R_B. For a decrease in the local pressure, due to application of an acoustic field, the equilibrium condition for the bubble becomes:

$$\left(p_0 + \frac{2\sigma}{R_B}\right)\left(\frac{R_B}{R}\right)^3 = p_0 - P_A + \frac{2\sigma}{R} \tag{2.4}$$

The left hand side of equation 2.4 gives the gas pressure in the bubble from an isothermal expansion, while the right hand P_A is the peak negative acoustic pressure (Apfel, 1984) needed for equilibrium. Evaluating P_A in terms of initial bubble size gives the Blake threshold pressure (P_B) (Blake, 1949; Prosperetti, 1984; Apfel, 1984):

$$P_B = p_0 + \frac{8\sigma}{9}\left[\frac{3\sigma}{2\left(p_0 + \frac{2\sigma}{R_B}\right)R_B^3}\right]^{\frac{1}{2}} \tag{2.5}$$

where R_B is the minimum bubble radius that will allow growth. This model neglects inertial and viscous effects on the bubble and is therefore applicable only where the thermodynamic process occurs infinitely slowly (i.e. quasi-static). For a 1 μm radius bubble in water at 20^{o}C, equation 2.5 shows that it would take a minimum of 0.14 MPa to cause the bubble to grow.

The following section will briefly discuss the mechanisms for formation of cavitation. The concepts introduced here provide a useful context in which it is possible to discuss cavitation nucleation in later chapters. Leighton (1994) describes the process of initiation of acoustic cavitation in a pure homogeneous liquid, in the simplest case, as tearing the liquid apart. The cavity formed would then fill with liquid vapour and/or gas dissolved in the liquid. The tensile strength of a liquid is the maximum tension that a liquid can support before cavitating. Cavitation inception occurs where the pressure amplitude was sufficient to generate a tension in the liquid that is equal to, or greater than, the tensile strength of the liquid. In order to cause tension in a liquid with an acoustic wave, the peak negative pressure must exceed the static pressure of the fluid. For a HIFU field, the peak negative pressures can be an order of magnitude greater than the static ambient pressure of 0.1 MPa. The theoretical values of the tensile strength of water at 10^{o}C are of the order of 1000 MPa (Kwak and Panton, 1985). This was calculated on the basis of overcoming of the interaction of the forces between the molecules in a face centred cubic lattice structure. It would thus not be expected that a HIFU field would be able to generate cavitation in water. It has, however, been shown that it is possible to cavitate water at 10 kHz with negative pressures of 0.1 MPa (Leighton, 1994). This several order of magnitude discrepancy suggests that additional weaknesses or cavitation nuclei must exist in the water. Young (1989) suggests that there are three possible causes for the occurrence of cavitation when a suitable nucleus is subjected to negative pressure (or elevated temperature). Firstly, in water, there is evidence of spherical gas bubbles, which have been stabilised against gaseous diffusion by the formation of a skin of organic impurity (Fox and Herzfeld, 1954). Leighton (1994) discusses this in detail, suggesting that the formation of a variably permeable skin can stop a bubble from dissolving while leaving it free to grow from an influx of a gas previously dissolved in the liquid. The second and third reasons derive from the same mechanism, namely the trapping of gas on solid particles (‘motes’) either within the liquid, or in the crevices on the surfaces of the vessel containing the liquid. For

example, unfiltered tap water may have a concentration of solid particle ('motes') of the order 5-10*10^4 cm^{-3} (Apfel, 1984). Each one could act as a possible nucleation site for cavitation activity. These two mechanisms suggest that cavitation will form at specific locations containing trapped gas.

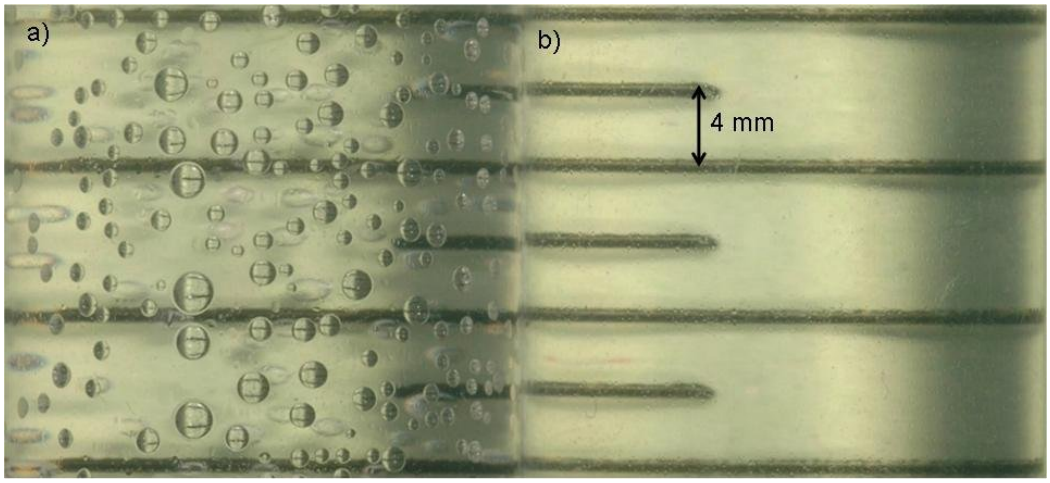

Figure 2.3. A photograph of two syringes containing tap (a) and degassed (b) water that has been kept at room temperature (20°C) for 24 h from a starting temperature of 16°C.

Figure 2.3(a) shows the formation of bubbles that have been stabilised against the effects of buoyancy by attachment to crevices (imperfections) in a plastic syringe. These bubbles can be seen attached to the internal surface of the syringe. There is a clear difference between these two samples, as no bubbles have formed in the syringe containing degassed water (the degassing procedure is described in §5.2). This suggests that the partial gas pressure in the degassed water sample is sufficiently low that, even in the presence of crevices, no bubbles will form. Leighton (1994) discusses the common observation of the formation of bubbles on the side of a container due to the decrease in solubility of air in water with increasing temperature. As demonstrated by Figure 2.3(a), gas will come out of tap water as its temperature increases to room temperature. This is one of the main reasons why the coupling medium used for the HIFU and cavitation studies discussed in this study is degassed, since even in the absence of an acoustic field, bubbles form in water kept at room temperature.

Gas may also be trapped in a crevice, which may be approximated to a conical pit, in the surface of a solid that is either an impurity in the liquid, or a defect in the side of the liquid container. If a liquid is exposed to a sufficiently large negative (acoustic)

pressure, the liquid gas interface will be drawn out of the conical pit and become bowed which leads to the formation of a bubble as shown in Figure 2.4 (Apfel, 1984).

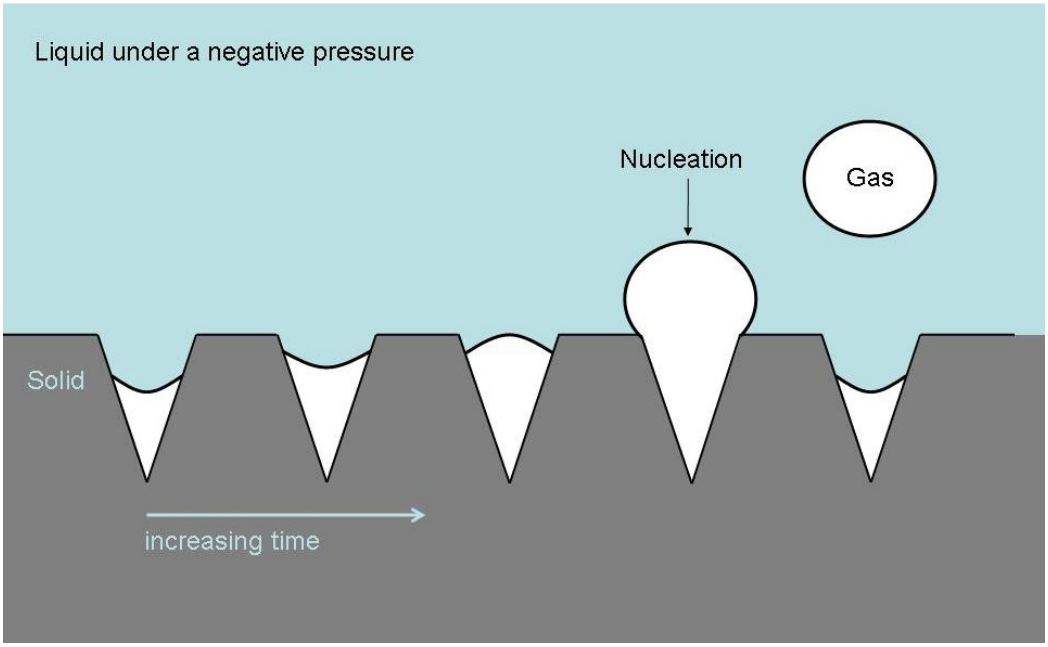

Figure 2.4. A schematic diagram showing the formation of a bubble from gas trapped in a crevice (shown as a conical pit).

Using this simple model it is possible to see how bubbles are nucleated at specific locations. The term nucleation here refers to the formation of a bubble from gas trapped in a conical pit. However, it is a simplification of the physical process since it does not incorporate the change in gas pressure as the gas pocket expands, or the effect of unstable growth (i.e. a bubble that has a radius greater or less than the critical radius in equation 2.3) which may lead to nucleation (Atchley and Prosperetti, 1989). Apfel (1970) derived a low frequency threshold (<100 kHz) for the acoustic pressure amplitude required to nucleate a vapour cavity from a submerged crevice approximated to a conical pit:

$$P_A \geq \left(p_0 - p_v - \gamma_c p_g\right) + \left(p_0 - p_v - p_g\right)\left|\frac{\cos(\alpha_R - \beta_c)}{\cos(\alpha_A - \beta_c)}\right| \tag{2.6}$$

where α_A and α_R are the advancing and receding contact angles of the liquid-gas interface in the crevice, respectively. β_c is the half angle of the crevice. γ_c is a constant with a value between 0 and 1, related to the rate at which nucleation process is occurring compared with the diffusion of gas into the crevice. For example, γ_c is equal

to one for the static case. Equation 2.6 is only valid for crevices that have an angle between the receding contact angles that is greater than the half angle of the crevice. This model is limited due to the difficulty in determining the advancing and receding contact angles for a crevice in either an impurity or imperfection. Crum (1979) compared this relationship with experimental values for the cavitation inception threshold in distilled water. Unfortunately this relationship is only valid for low frequencies (<100 kHz) since at higher frequencies the dynamics of the vapour cavity after nucleation are more significant in determining the threshold (Apfel, 1970). Thus, it is not possible to apply this relationship at the HIFU frequencies used in this study (1.7 MHz). This model has been discussed here, since no equivalent formulation exists for the frequencies of interest in HIFU applications. Nevertheless, the concept of conical pits nucleating cavitation is still applicable for HIFU studies.

The previous section discussed the sources of cavitation nuclei that can exist in water that are exposed to an acoustic field. However, the majority of this study was undertaken in either perfused or unperfused ex-vivo biological tissue. Therefore, the following section discusses the basic mechanics behind bubble formation in biological tissue.

One of the commonly known instances of bubble formation in biological tissue is decompression sickness (DCS), which occurs in underwater divers who surface from depth too rapidly. The cause of this is thought to be the formation of gas bubbles in the body (Chappell and Payne, 2006a). These bubbles can form when the dissolved gases, held in solution within human tissue, are released during too rapid decompression. This occurs when a diver returns to the surface (i.e. atmospheric pressure) from a deep-sea dive in which they have been exposed to increased pressure (0.1 MPa increase for every 10 m in depth). This decrease in the pressure may be thought of as analogous to the exposure from the negative pressure portion of an acoustic cycle, but over a larger volume.

The availability of cavitation nucleation sites within the body is of particular interest for the study of cavitation activity from HIFU exposures in tissue. A simplistic description of a mammalian cell is that most contain a (~5 μm diameter) nucleus (i.e. it is eukaryotic), cytoskeleton, and cytoplasmic organelles which are surrounded by a plasma membrane (Cooper, 2000). There are many different types (and therefore sizes and shapes) of cells, and whilst a description of them is outside the scope of this thesis,

it is informative to note that these cells usually also contain organelles such as mitochondria, chloroplasts and Golgi bodies and have typical diameters between 10-100 μm. Water is the predominant constituent of a cell, typically making up ≥70% of its molecular mass. Since a cell is largely water it might be expected that the generation of acoustic cavitation in biological tissue would occur throughout the targeted region. However, as discussed above, the generation of bubbles in water typically requires the pre-existence of nuclei, either in the form of bubbles or gas trapped in crevices or on motes. The finding that the bubbles formed from DCS are unlikely to be homogeneously generated in the body, but tend to grow from pre-formed micro-bubbles or nuclei supports this hypothesis (Chappell and Payne, 2006a). It has been suggested (Harvey *et al*, 1944a; Harvey *et al*, 1944b) that a number of potential nucleation sites (such as, for example, mitochondrial membranes), that have a suitably 'rough' surface to trap gas held in solution in the body tissues (Chappell and Payne, 2006a). In blood, it has been suggested that there may be "crevices" in the walls lining blood vessels (Chappell and Payne, 2006b). The existence of cavitation nuclei in the blood and tissue would suggest that the application of an acoustic field might be able to generate acoustic cavitation.

It is also possible to introduce cavitation nuclei through the insertion of a foreign object, for example a fine wire thermocouple. Such a thermocouple has been used for the measurement of temperature rise in ultrasound applications (§7.4.1).

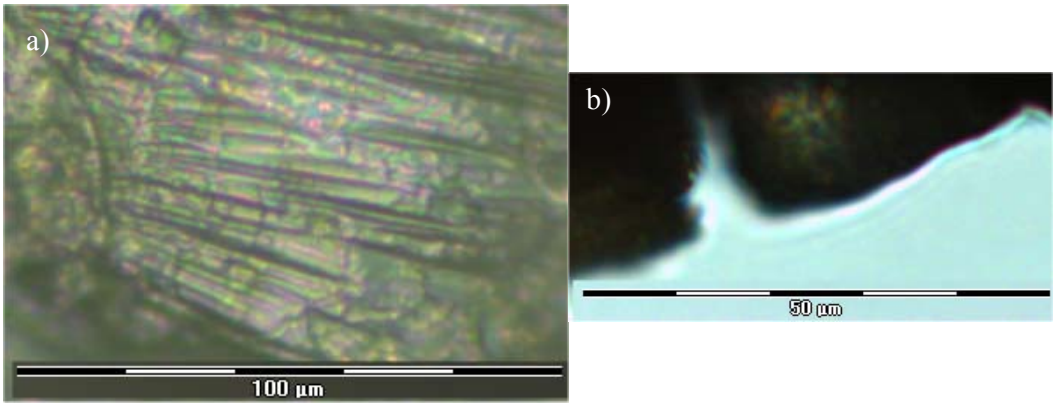

Figure 2.5. Two photographs of the junction of a fine wire thermocouple that showing crevices on the surface (a) and the side (b).

Figure 2.5 shows a microscopic view of a fine wire thermocouple (see §7.4 for details). It shows that its surface might be able to trap cavitation nuclei.

2.3 Models for single pre-existing bubbles

A mass on a spring can be analogous to a linearly oscillating bubble (Leighton, 1994). For a driven oscillator (i.e. a bubble in an acoustic field) the displacement of the mass is analogous to the motion of the bubble wall and the spring constant is the restoring force analogous to the changes in the internal gas pressure of the bubble. The driving force provided by an acoustic field is analogous to the periodic displacement of the point of attachment of the spring to the other end of the spring (Leighton, 1994). By incorporating damping into this model, it is possible to write the displacement amplitude (A_d) and phase ($\tan\theta_p$) as (Leighton, 1994):

$$\left|A_d\right| = \frac{F_o}{m\omega_0^2}\frac{\frac{\omega_o}{\omega}}{\sqrt{\left(\frac{\omega_o}{\omega}-\frac{\omega}{\omega_o}\right)^2+\frac{1}{Q^2}}} \tag{2.7}$$

$$\tan\theta_p = \frac{\frac{1}{Q}}{\left(\frac{\omega_o}{\omega}-\frac{\omega}{\omega_o}\right)} \tag{2.8}$$

where m is the mass of the bob, F_o is the amplitude of the driving force, ω is the driving frequency and ω_o is the resonant frequency. Q is the 'quality factor', which in this case is the response of the oscillator to being driven at frequencies away from resonance and θ_p is the phase lag between the driving force and the displacement amplitude. Figure 2.6 shows a plot of the displacement amplitude and phase lag for this simple linear oscillator system for a number of different Q values. As would be expected, Figure 2.6(a) shows that as Q increases, the peak normalised displacement amplitude increases. Figure 2.6(b) shows that as the drive frequency increases, from well below the resonant frequency, the displacement starts to lag behind the driving force and as it increases well past resonance the displacement becomes 180^o out of phase with the driving force (antiphase). These two regions are referred to as stiffness-controlled (well below resonance) and inertia controlled (well above resonance). This suggests that for a bubble driven at a frequency well above its resonant frequency, the inertia in the surrounding medium would be more significant than the driving force (in this case an acoustic field) and vice versa for the stiffness controlled regime. This suggests that inertial cavitation would be more likely when the frequency of a HIFU exposure is above the resonant frequency for the bubble population exposed. If the frequency dependence of damping

in this model can be ignored then the response curves shown in Figure 2.6 are representative of a bubble undergoing small-amplitude oscillations in response to an acoustic field.

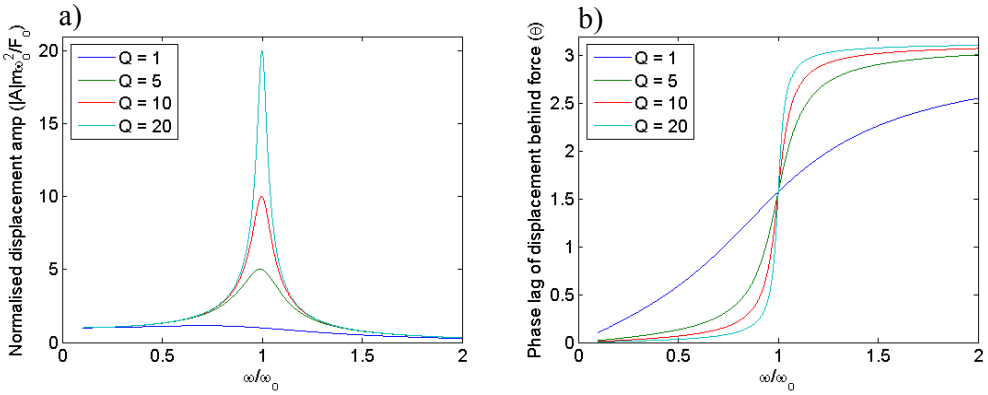

Figure 2.6. The amplitude (a) and the phase response (b) of a damped linear oscillator as a function of the drive frequency (Leighton, 1994).

The following section discusses the damping experienced by a bubble exposed to an ultrasound field and the effect this has on the surrounding medium An acoustic field propagating through a region containing a bubble can experience a loss of energy, causing the bubble to undergo oscillations. These bubble oscillations can transfer energy from the acoustic field into the medium through thermal and viscous dissipation. Thermal dissipation arises from thermal conduction between the gas within the bubble and the surrounding medium. Viscous dissipation comes from the work required for the bubble to overcome the viscous forces due to the medium surrounding the bubble wall. An oscillating bubble leads to further attenuation of the acoustic field from scattering or radiated pressure waves (§4.1) from the bubble. The loss of energy from the acoustic field due to the presence of a bubble can be expressed as the ratio of the time-averaged power loss per bubble ($\langle \dot{W} \rangle$) to the acoustic field intensity, which gives a dimensionless quantity called the extinction cross-section (Ω_b^{ext}) of the bubble (Leighton, 1994):

$$\Omega_b^{ext} = \frac{\langle \dot{W} \rangle}{I} \tag{2.9}$$

The extinction cross-section can be described in terms of the absorption cross-section (Ω_b^{abs}) due the effects of thermal and viscous dissipation, and the scattering cross-

section (Ω_b^{scat}). For bubble oscillations that are approximately linear, the scattering cross-section can be written as (Leighton, 1994):

$$\Omega_b^{scat} = \frac{4\pi {R_0}^2}{((\omega_0/\omega)^2 - 1)^2 + (2\beta_{tot}/\omega)^2} \tag{2.10}$$

where $\omega_0 = \frac{1}{R_0}\sqrt{\frac{3\kappa p_0}{\rho}}$ and the total resistive constant leading to damping is, $\beta_{tot} = \frac{\omega_0}{2Q}$, the angular frequency, $\omega = 2\pi f_0$, and R_0 is the equilibrium radius of the bubble. Equation 2.10 can be used to calculated the acoustic scattering cross-section for a range of bubble sizes in water at 20°C, giving a density (ρ) of 1000 kg/m^3, hydrostatic pressure of 0.1 MPa and the polytropic index (κ) of 4/3 (adiabatic conditions).

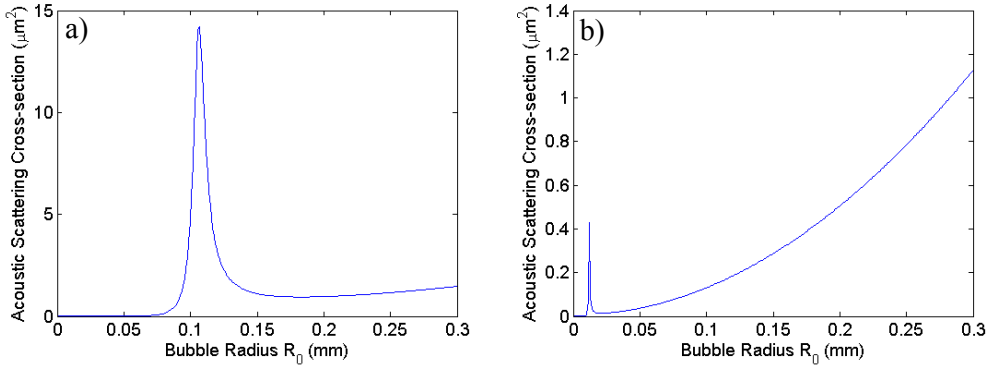

Figure 2.7. The scattering cross-section for a bubble, where the damping has been assumed to be independent of frequency, in an acoustic field with frequency (a) 30 and (b) 248 kHz (Leighton, 1994).

Figure 2.7 shows that there is a peak in the scattering cross-section when a bubble is at resonance. Below resonance, the cross-section tends towards zero. Figure 2.7(b) shows that as the bubble size increases the scattering-cross section can be much larger than that for a bubble driven at resonance. This suggests that as well as resonant bubbles, bubbles that are significantly larger than the resonant size would scatter acoustic waves effectively. Resonant bubbles couple strongly with the acoustic field, causing large radial oscillations. However, bubbles, which are larger than the acoustic wavelength, will be unresponsive to the acoustic field and have negligible oscillations, and any scattering from these bubbles would be related to the geometric size of the bubble (Leighton, 1994). For example, this suggests that the resonant acoustic cavitation bubbles generated in a HIFU field could have a smaller scattering-cross sections than

bubbles generated from thermal mechanisms which are a few orders of magnitude larger, this is discussed in section 7.2.3.

The absorption cross-section can be written as the sum of the thermal dissipation (Ω_b^{th}) and the viscous dissipation cross-sections (Ω_b^{vis}), which can be expressed in terms of the scattering cross-section and dimensionless damping constants (Leighton, 1994):

$$\Omega_b^{abs} = \Omega_b^{th} + \Omega_b^{vis} = \left(\frac{d_{th}}{d_{rad}} + \frac{d_{vis}}{d_{rad}} \right) \Omega_b^{scat} \tag{2.11}$$

where d_{th}, d_{vis} and d_{rad} are the off-resonance damping coefficients for thermal, viscous and radiation loss mechanisms. These coefficients can be calculated from the work of Eller (1970). Figure 2.8 shows the damping coefficients for a range of bubble sizes exposed to 10 kHz and 1.69 MHz acoustic fields. Figure 2.8(a) shows that for the low acoustic frequency, thermal damping is dominant below resonance, but above it radiation damping is the dominant effect. Near resonance, there is a transition between dominant mechanisms from thermal to radiation damping (Eller, 1970). At the higher acoustic frequency (1.69 MHz) Figure 2.8(b) show, that viscous damping is the dominant source below resonant size, but above this radiation damping dominates. This would suggest, assuming only small amplitude oscillations occur, that in a HIFU field at this frequency heating from viscous effects would be the dominant effect for bubbles smaller than 2.5 μm, while scattering would dominate for larger bubbles. Leighton (1994) provides an in depth discussion of the Eller (1970) and Prosperetti (1997) formulation of these damping coefficients.

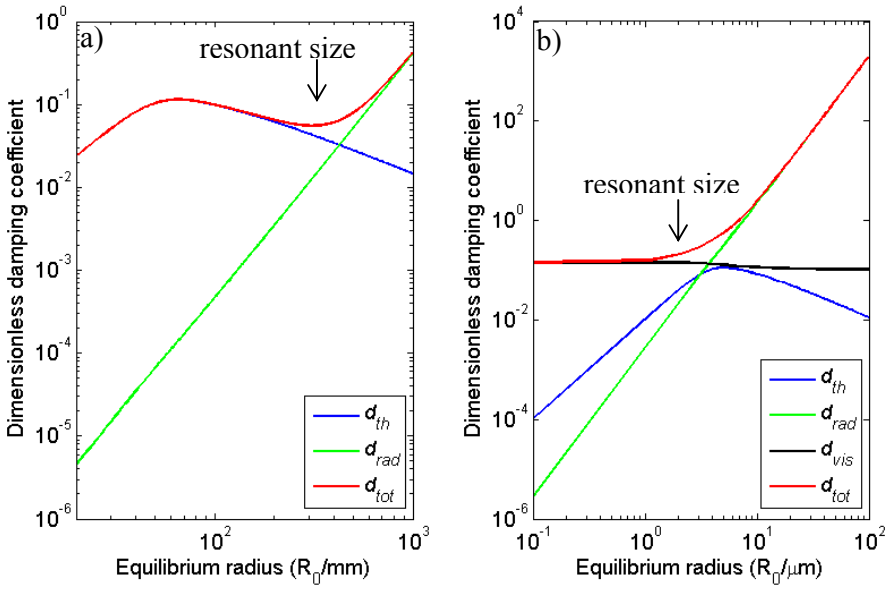

Figure 2.8. The damping coefficients for a range of bubble sizes for an acoustic frequency of (a) 10 kHz (Eller, 1970) and (b) 1.69 MHz. The d_{vis} is not shown in (a) as it is much smaller than values on the axis shown. The arrows indicate the resonant sizes for a bubble at these acoustic frequencies.

The extinction cross-section is the sum of the scattering and absorption cross-sections and can be written (Leighton, 1994):

$$\Omega_b^{ext} = \Omega_b^{scat} + \Omega_b^{abs} = \frac{d_{tot}}{d_{rad}}\Omega_b^{scat} \tag{2.12}$$

Equation 2.12 gives the proportion of incident energy from an acoustic field that is dissipated by all mechanisms through the small amplitude oscillations of a bubble. Inspection of equation 2.10 shows that these cross-sections have a maximum at resonance (ω_0), which can be reduced to:

$$\Omega_b^{scat} = \frac{4\pi R_0^{\,2}}{\delta_{tot}^2} \qquad (\text{for } kR_0 << 1) \tag{2.13}$$

where the total damping constant for oscillations at the bubbles resonant frequency $\delta_{tot} \approx \frac{2\beta_{tot}}{\omega_0}$ (Leighton, 1994). Equation 2.13 shows that, at resonance, the scattering cross-section is δ_{tot}^{-2} times greater than the geometrical cross-section ($4\pi R_0^2$) (since $\delta_{tot} = 1/Q$, where Q is the quality factor of the bubble, hence $\delta_{tot} < 1$). This relationship is only valid when the product of the wave number and equilibrium radius

is much less than one, limiting the maximum range of bubble sizes and/or frequencies for which this model is applicable. The extinction cross-section can be simplified to:

$$\Omega_b^{ext} = \frac{4\pi R_0 c}{\delta_{tot}\omega_0} \qquad \text{(for } kR_0 << 1\text{)} \tag{2.14}$$

Equations 2.13 and 2.14 demonstrate that gas bubbles readily interact with an acoustic field via scattering and absorption of the acoustic energy. This shows why they are of such importance to the investigation and development of HIFU research.

So far, this section has discussed the basic mechanisms behind a linearly oscillating bubble. However, a bubble is a non-linear oscillator, and hence the amplitude of the bubble oscillation is not directly proportional to the driving force. The remainder of this section will introduce, and briefly discuss, some of the more commonly used non-linear equations for the modelling of bubble dynamics.

The simplest of these models is called the RPNNP-bubble model (Lauterborn, 1976), named after the authors who contributed to its formulation (Rayleigh, 1917; Plesset, 1949; Noltingk and Neppiras, 1950; Neppiras and Noltingk, 1951; Poritsky, 1952). However, it is more commonly referred to as the Rayleigh-Plesset equation (RPE). Lord Rayleigh (1917) considered the kinetic energy in an incompressible liquid during the collapse of a spherical empty cavity (i.e. containing no vapour or gas pressure). This model was expanded by Plesset in 1949 who derived the following relationship for a vapour filled bubble in a changing pressure field (Young, 1989):

$$\frac{p_L - p_\infty}{\rho} = R\ddot{R} + \frac{3}{2}\dot{R}^2 \tag{2.15}$$

where $\dot{R}$ and $\ddot{R}$ are the radial velocity and acceleration of a spherically symmetric bubble wall. p_∞ is the pressure in the liquid at infinity. The next addition to the model, provided by the two papers from Noltingk and Neppiras (1950; 1951), considered gas filling the bubble. Gas acts as a cushion for the collapse, and as a driving force for the subsequent expansion of the bubble. The liquid pressure (p_L) is determined for the bubble in equilibrium. Since the internal pressure of a bubble is the sum of the gas (p_g) and vapour (p_v) pressures it is possible to rewrite equation 2.2 as:

$$p_g = p_0 + \frac{2\sigma}{R_0} - p_v \text{ (at equilibrium)} \tag{2.16}$$

If the pressure of the liquid changes from equilibrium causing the pressure just outside the bubble to be equal to p_L. This change from equilibrium pressure will cause the

bubble radius to change from its equilibrium value to *R*. Assuming the gas can be approximated to an ideal gas and considering the effects of surface tension (equation 2.1), it is possible to write the pressure immediately outside the bubble wall as (Leighton, 1994):

$$p_L = \left(p_0 + \frac{2\sigma}{R_0} - p_v \right) \left(\frac{R_0}{R} \right)^{3\kappa} + p_v - \frac{2\sigma}{R} \tag{2.17}$$

where κ, the polytropic index, equals 1 for isothermal conditions, or varies with the ratio of the specific heat capacity of the ideal gas, C_P / C_V, which corresponds to adiabatic behaviour. Combining equation 2.17 with equation 2.15, and substituting the relationship for $p_\infty = p_0 + P(t)$, gives

$$R\ddot{R} + \frac{3}{2}\dot{R}^2 = \frac{1}{\rho}\left[\left(p_0 + \frac{2\sigma}{R_0} - p_v \right) \left(\frac{R_0}{R} \right)^{3\kappa} + p_v - \frac{2\sigma}{R} - p_0 - P(t) \right] \tag{2.18}$$

where $P(t)$ is a time varying pressure (e.g. an acoustic field). The incorporation of the effect of viscosity by Poritsky (1952) into equation 2.18 gives the common form (Leighton, 1994) of the 'Rayleigh-Plesset equation':

$$R\ddot{R} + \frac{3}{2}\dot{R}^2 = \frac{1}{\rho}\left[\left(p_0 + \frac{2\sigma}{R_0} - p_v \right) \left(\frac{R_0}{R} \right)^{3\kappa} + p_v - \frac{2\sigma}{R} - \frac{4\eta\dot{R}}{R} - p_0 - P(t) \right] \tag{2.19}$$

where η is the shear viscosity of the liquid. Authors commonly point out the limitations of this equation (Young, 1989; Leighton, 1994), which are as follows. (1) It only considers a single bubble in an infinite medium, (2) at all times the bubble remains spherical, (3) spatially uniform conditions exist within the bubble, (4) the bubble radius is small compared to the acoustic wavelength, (5) no body forces (such as gravity) are present, (6) the density of the liquid is large and of infinitely small compressibility compared with that of the gas within the bubble, (7) the gas content of the bubble is constant and (8) the vapour pressure is negligible. The assumption that the bubble remains spherically symmetric is probably the least valid assumption when trying to model the physical process, since it is known that bubbles undergo shape distortions during oscillations (Leighton, 1994).

It is possible to model equation 2.19 by rewriting it as two coupled, first order differential equations, which was modelled in this study using a fourth order Runge-Kutta (Birchenhall, 1994) routine with a adaptive time step, written in the C programming language. Figure 2.9 shows the oscillations of a single bubble in water

exposed to an (10 kHz) acoustic field. The acoustic field is defined by, $P(t) = P_A \sin(\omega t)$.

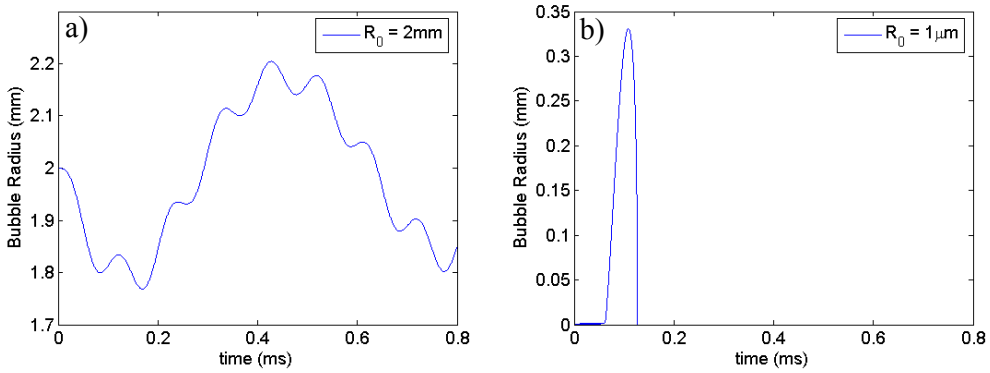

Figure 2.9. Radial bubble oscillations in water at 20°C, calculated from equation 2.19, for (a) a bubble with an equilibrium radius of 2 mm exposed to a 10 kHz and P_A = 0.27 MPa acoustic field (b) a bubble with a 1 μm equilibrium radius exposed to a P_A = 0.24 MPa, 10 kHz acoustic field. These plots reproduce data shown in Leighton (1994).

The numerical solutions to the RPE shown in Figure 2.9 show general examples of the bubble behaviour categorised as non-inertial (Figure 2.9(a)) and inertial (Figure 2.9(b)) activity.

The most common improvement to the approximations of the RPE equation is to improve on the incompressible liquid assumption. This assumption breaks down when the bubble wall velocities approach the sound speed of the liquid. The Herring-Trilling equation allows the modelling of cavitation in a compressible medium.

$$R\dot{R}\frac{\partial \dot{R}}{\partial R}(1-2M)+\frac{3\dot{R}^2}{2}(1-4M)=\frac{R\dot{R}}{\rho_0 c}\frac{dp_L}{dR}+\frac{p_\infty - p_L}{\rho_0} \tag{2.20}$$

where M is the acoustic Mach number ($M = \dot{R}/c$). This model assumes that there is a finite, constant speed of sound in the liquid. It is limited to describing bubble collapse from a small expansion i.e. the maximum radius achieved during expansions is only a few times greater than the equilibrium radius (Leighton, 1994). The Gilmore equation improves further on this by applying a further approximation, addressing the formation of shockwaves when the bubble wall velocity approaches the velocity of sound in the medium. The shockwave velocity is the sum of the sound and fluid velocity (Young, 1989). This gives:

$$\left(1-\frac{\dot{R}}{C}\right)R\ddot{R}+\frac{3}{2}\left(1-\frac{\dot{R}}{3C}\right)\dot{R}^2=\left(1+\frac{\dot{R}}{C}\right)H+\frac{R}{C}\left(1-\frac{\dot{R}}{C}\right)\frac{dH}{dt} \tag{2.21}$$

where H is the difference in the liquid enthalpy between the bubble wall and infinity, and C is velocity of sound at the bubble wall. These terms are both functions of the motion of the bubble, making this a much more involved, but accurate, solution for radius oscillations (Young, 1989). Work by Keller and Miksis (1980) provided a radial equation which was suitable for describing large-amplitude forced oscillations, incorporating the effects of acoustic radiation on the bubble and using the approximation of a linear polytropic index (Leighton, 1994). The Keller-Miksis equation can be written as (Parlitz *et al*, 1990):

$$\left(1-\frac{\dot{R}}{c}\right)R\ddot{R}+\frac{3}{2}\left(1-\frac{\dot{R}}{3c}\right)\dot{R}^2=\left(1+\frac{\dot{R}}{c}\right)\frac{P(\dot{R},R,t)}{\rho}+\frac{R}{\rho c}\frac{\partial P(\dot{R},R,t)}{\partial t} \tag{2.22}$$

where

$$P(\dot{R},R,t)=\left(p_\infty-p_v+\frac{2\sigma}{R_0}\right)\left(\frac{R_0}{R}\right)^{3\kappa}-\frac{2\sigma}{R_0}-\frac{4\sigma\dot{R}}{R}-p_\infty+p_v-P(t) \tag{2.23}$$

Prosperetti *et al* (1988) further modified the work of Keller and Miksis (1980) allowing for a non-uniform temperature distribution inside the bubble and including the effects of the convection and conduction of heat. This model allows the study of the effects of a temperature change in the surrounding medium. This is an important factor when considering the generation of bubbles during HIFU exposures in tissues (or phantoms). These models, if they were to be used for HIFU exposures, would need to incorporate a non-linear acoustic field model into the *P(t)* term, which is non trivial. This section has discussed some of the available models for describing cavitation activity. The RPE is used later in this study (§7.2.3) to investigate scattering effects seen during HIFU exposures in tissue. It was believed that this model was sufficient for this task. Since this study had an experimental focus the other models have not been pursued.

2.4 Cavitation effects in HIFU studies

The previous section discussed some of the linear and non-linear models used in the description of the complex field of cavitation. This discussion was predominantly concerned with a single bubble that was exposed to a general acoustic field in a liquid medium. The following section will discuss some key publications which report cavitation in HIFU studies in tissue and phantoms. These discussions predominantly focus on the effects of cavitation on the temperature rise or tissue damage associated

with HIFU exposures. A detailed discussion of detection systems will be presented in the next chapter.

Hynynen (1991) reported one of the first studies which looked specifically at the effect of cavitation on the enhancement of HIFU lesions *in vivo*. In this study, the thigh muscles of 13 dogs were exposed to a range of frequencies from 0.246 to 1.68 MHz. A focused hydrophone was used to monitor acoustic signals (§4.1) in the frequency range 0.2–1.0 MHz. Temperature was measured using a fine-wire thermocouple (FWT) that was inserted using a catheter filled with degassed saline. The data presented were the simultaneous (focused) hydrophone and temperature measurements at different locations in the muscle. They showed that as the HIFU intensity was increased, temperature rises were recorded that exceeded the expected linear relationship, based on temperatures seen at lower intensities. This data was compared with the acoustic emission data and there was a correlation between the sudden increases in the rate of rise of the temperature and the detection of wide band noise was found. This led the authors to suggest that cavitation activity caused the increased heating. This was a reasonable assumption based on their experimental technique. Since it is possible that the FWT seeded the cavitation, it would have been useful to compare the signals detected with and without a thermocouple, at some of the intensity levels. However, the temperature increase reported could have just been a localised measurement that directly resulted from the introduction of a thermocouple, rather than an observation of a general increase in the temperature of the tissue from the cavitation activity. It was also noted, that the temperature rise, for some exposures above the cavitation threshold, reached the boiling point of water. This suggests that both thermally and acoustically generated bubbles could have been created during the in-vivo exposures. The paper states that it is inertial cavitation that caused the "enhanced" temperature rise, but a half harmonic was clearly present in the acoustic emissions when increased temperature rise was seen. This suggests that non-inertial cavitation could also have occurred, since half harmonic emissions can be generated by both types of bubble behaviour (§2.1). Considering this, and the fact that it is quite possible that thermally generated bubbles could have formed, the paper's conclusion that the temperature rise was caused by inertial cavitation may be incomplete. The author did not attempt to describe the physical causes for cavitation enhancement of the heating *in vivo*.

Watkin *et al* (1996) investigated the relationship between the spatial peak intensity (I_{sp}) and the position of a lesion generated from a 1.69 MHz HIFU transducer in in-vitro

tissue models. Ex-vivo bladder and liver tissue was exposed to a range of I_{sp} values between 1220-4660 W/cm^2 for durations of either 2 or 4 s. The aim of this was to find suitable HIFU exposure conditions that produced predictable lesion sizes and shapes, which could be used clinically. They found that for 2 s exposures at a free field I_{sp} range of 2500-4200 W/cm^2 the position of the lesion shifted towards the HIFU transducer. They also found that these types of lesions had a characteristic 'tadpole' shape. A possible cause for this was suggested to be due to the formation of bubbles, either from boiling or acoustic cavitation, which caused an increase in absorption within this region. However, no secondary evidence for this hypothesis was investigated and these assumptions were based on previous authors' observations, for example Hynynen (1991). Another hypothesis investigated was that non-linear propagation of the HIFU field generated superharmonics that were absorbed more readily in the tissue. However, the authors state that this would be unlikely to cause the shape distortion, as this effect would be maximal at the HIFU focus. For these reasons, the authors suggest that a clinical HIFU exposure should be for a longer duration at a lower intensity in order to generate predictable lesion geometry and positions. This publication recommended that cavitation should be avoided for clinical applications.

Clarke and ter Haar (1997) studied the temperature rise created in ex-vivo liver caused by various levels of 1.7 MHz HIFU exposures. Temperature change was measured using an implanted needle thermocouple. The aim of this work was predominantly to demonstrate the ability of HIFU to denature proteins ex-vivo establishing whether the temperature rise would cause this effect. However, the authors noticed that at the higher range of their exposure parameters, the measured temperatures were lower than those expected from comparison with the lower exposure levels. They hypothesise that the formation of bubbles in the pre-focal region caused these effects. The bubble type is not specified, other than the suggestion that it was "cavitation and/or boiling". This lack of differentiation between acoustic cavitation and boiling, when describing the mechanism by which the bubble is formed (§3.1), is a common problem in the HIFU literature. The formation of boiling bubbles in the pre-focal region is the more likely explanation for the shielding effects seen based on the rate of heating before shielding occurs. However, in one example, a "temperature runaway" was shown which was followed by a reduction in the measured temperature rise, presumably caused by shielding. 'Temperature runaway' was defined as the measurement of a faster rate of heating than would have been expected from the absorption of acoustic energy. A

possible alternative explanation, not considered by the authors, is that this reduced heating could be due to non-linear propagation causing superharmonics which were attenuated more rapidly in the tissue. This study, from the perspective of cavitation studies, showed that the possible formation of bubbles during HIFU exposures could have a detrimental effect on the temperature change in the tissue at the focus.

Meaney *et al* (2000) used a non-linear acoustic field model to investigate the intensity dependence of the lesion position during HIFU exposures. Incorporated into this model was an approximation for the occurrence of acoustic cavitation and/or boiling. It was assumed that due to the rapid heating at the modelled HIFU intensities that these two types of cavitation could be assumed, for the purposes of the model, to have occurred almost instantaneously and be indistinguishable. The cavitation effects were incorporated into the model by assuming that when the tissue temperature exceeded 100^{o}C that all of the incident energy would be summed and deposited uniformly in over a 0.5 cm diameter spherical volume around the point which first reached this temperature. This technique was able to provide qualitative information about how a boiling region in the focal field would effect lesion growth. The results obtained simulated the shape distortion of those seen in earlier experimental investigations (Watkin *et al*, 1996; ter Haar and Daniels 1997). Unfortunately, this technique for the estimation of the effects of cavitation does not rely on any bubble dynamics, rather it relies on empirical observations. Thus you would expect the model to agree with the empirical observations on which the approximations were based. However, a full realisation of the bubble activity in an large volume would require a significant research effort and the assumptions made for example for bubble populations or nucleation probability may prove no more valid than those made in this model.

Holt and Roy (2001) presented an experimental and theoretical investigation into the effect of "bubble enhanced heating". The authors referred to the possibility that enhanced heating from acoustic cavitation could be caused during HIFU exposures in an effort to explain the phenomena observed in the two publications discussed previously. The experimental aspect of the paper discussed bubble activity and heating in agar gel phantoms measured independently. An array of wire thermocouples (type E, Omega Engineering) was embedded into the gel phantoms and a needle hydrophone (embedded in the gel at the HIFU focus) was used to measure the HIFU field, and to detect acoustic emissions. The results are similar to those of the Hynynen (1991) study. However, the hydrophone was not in place (since it was located at the HIFU focal peak) for the

temperature measurements. This could suggest a potential problem because the needle hydrophone may have seeded cavitation, thus throwing doubt on the threshold pressures for the detection of acoustic emissions quoted in the paper. "Enhanced" temperatures are shown as temperature increases that deviate from the linear heating model outlined in the paper. For example, for a 10.2 s HIFU exposure the measured temperature was 15^{o}C higher than that predicted from the linear model at an in-situ peak negative pressure of 1.5 MPa ±10%. The theoretical section of this publication discusses two possible bubble mechanisms that may lead to the "enhanced" temperatures seen. Their analysis was based on the solution of the Keller-Miksis equation (Keller and Miksis, 1980), as discussed in the previous section. A number of steps from this analysis has been reproduced here in order to identify the key ideas involved in the hypothesis that 'enhanced' heating could originate from acoustic cavitation activity in a HIFU field. The power dissipated by a bubble, W_{vis} can then be given by (Prosperetti, 1977):

$$W_{vis} = 16\pi\mu R\dot{R}^{2} \tag{2.24}$$

where R is the instantaneous radius of the bubble and $\dot{R}$ is the velocity of the bubble wall. If it is assumed that the energy is dissipated solely as heat then equation 2.24 gives the viscous component of the heat contribution for a single bubble. For example, they calculated for a HIFU field of 2 MPa with a frequency of 1 MHz that the maximum energy dissipated from this process is approximately 32 mW which was suggested as being increased by about 5% due to a HIFU exposure alone. This theoretical prediction suggests that even a single bubble can have a significant effect on the absorbed energy. The second mechanism is acoustic absorption. This can be either from bubble radiated acoustic radiation or from scattering of the acoustic field from the bubble. The radiated sound energy that is converted into heat energy may be calculated by assuming that the far field pressure, $P_b(r,t)$ radiated by an oscillating bubble is:

$$P_b(r,t) = \frac{\rho R}{r}(2\dot{R}^{2} + R\ddot{R}) \tag{2.25}$$

where ρ was the density of the medium. $\ddot{R}$ gives the acceleration of the bubble wall and r is the distance away from the bubble at which the pressure was calculated. It is assumed that the pressure is that of the far field, and thus that the acoustic pressure and velocity are in phase and that the pressure propagates as a plane wave. This allows the acoustic intensity to be written as $I_b = P_b^2/2\rho c$, where c is the speed of sound in the

medium. The power dissipated to heat from bubble radiation or absorption is thus estimated to be:

$$W_{rad} = (\frac{4}{3}\pi R_0^3)2\alpha I_b \quad (2.26)$$

where R_0 is the equilibrium radius of the bubble and α is the attenuation of the medium. Equation 2.26 can be modified to give the power dissipated from scattered radiation if I_b is evaluated for $r = R_0$. I_b becomes I_{scatt}, related to the circumference of the bubble, incident HIFU intensity and the bubble scattering cross-section (section 2.3; Leighton, 1994). The authors point out that since the bubbles are treated as linear oscillators, their calculations are only estimates of the contribution of the heating enhancement from this non-linear bubble behaviour. To extend these calculations for non-linear oscillations is a non-trivial task since the assumptions for the absorption coefficient (Devin, 1959; Eller, 1970) are for linear oscillations. The estimates for heat deposition from acoustic cavitation activity provided by the modelling in this publication suggests that a population of 100 bubbles active in the focal region could account for the 'enhanced' heating observed from the HIFU exposures in a tissue mimicking material. They suggest that the dominant mechanisms for this enhancement are the viscous component and absorption of the acoustic emission. This publication thus provides a useful reference for the possible mechanisms for 'enhanced' heating from acoustic cavitation during a HIFU exposure.

A study by Sokka *et al* (2003) of gas-bubble enhancement of ultrasound heating *in vivo*, showed the use of a single high intensity exposure (1.1 or 1.7 MHz, 300 W acoustic power, 0.5 s exposure) followed by a lower intensity, longer exposure to create 'larger regions' of tissue damage. Larger regions were assessed through comparison with equivalent duration and acoustic power exposures without the high intensity exposure. This work was carried out using a HIFU transducer driven at two frequencies, and was guided by MRI. The use of MRI allowed monitoring of the temperature rise during the HIFU exposure. Unfortunately, accuracy was limited as a measurement could only be acquired every 4 s. At both drive frequencies, the tissue damage from a range of 20 s HIFU exposures over a range of acoustic powers was compared with that generated by exposures of 0.5 s at 60 W acoustic power followed by single 19.5 s HIFU exposures at increasing acoustic power levels. Subharmonic emissions were monitored with focused PZT elements, which were co-focally aligned with the HIFU focus to

provide evidence of acoustic cavitation activity. However, the MR temperature imaging acquisition sequence generated noise that interfered with the cavitation measurements, thus subharmonic emissions could only be measured between temperature imaging acquisitions. The use of the high power (300 W) 0.5 s exposure caused a higher temperature rise in these measurements, particularly in the first measurement at 4 s. For example in muscle tissue the average temperature at 4 s for the 28 W, 20 s exposure was 5.1 ±0.7^{o}C (measured from Figure 3(e) and (f) in the publication), compared with 15 ±3.7^{o}C for a 0.5 s 300 W and 30 W 19.5 s exposures. However, the peak temperature at the end (20 s) for these exposures was 30.6 ±7^{o}C and 32.5 ±6^{o}C, respectively. The authors suggest that the range of peak temperature rises for both exposure types is due to targeting at different depths, which could be why this averaging was not done. The difference in lesion sizes was quantified by taking the ratio of the mean lesion width/height, for a 14 W acoustic power exposure. This gave ratios of 0.55±0.21 and 0.96±0.23 for exposures with and without the 300 W 0.5 s exposure. This does not strictly demonstrate that the lesion volumes were larger as they could be more 'tadpole' in shape. Thus, it is difficult to establish that this was definitely caused by acoustic cavitation activity, as the authors claim since there is no data showing the temperature rise caused by the high power exposure alone, which could have been the cause of the initially large temperature rise seen. For example, the total energy deposited from the 20 s exposure at 14 W is 280 J where the 0.5 s at 300 W and 19.5 at 14 W is 423 J, which represents a more than 60% increase in the energy deposited that would mainly be converted into heating. This is further complicated by the fact that is it not possible to resolve the heating from this 0.5s exposure using the 4 s MRI temperature imaging. The suggestion that the presence of subharmonic emissions is evidence for the increased temperature rise and damage being caused by inertial cavitation is also misleading, since, as mentioned previously, subharmonic emissions can be generated from both inertial and non-inertial cavitation activity. Thus, without additional acoustic detection information it is not possible to substantiate this claim.

In a study that was conceptually similar to that of Sokka *et al* (2003), Melodelima *et al* (2003) studied the use of thermal and cavitation effects to generate lesions "deep" (2.5-15 mm) in ex-vivo liver. An unfocused 5.16 MHz HIFU transducer was used. They established the "cavitation threshold" from 0.5 s exposures as being above 60 W/cm^2. This threshold was defined by the detection of hyperechogenicity in a B-mode image after the exposure. No distinction was made between acoustic cavitation and boiling.

This work indicates that the use of a 0.5 s, 60 W/cm^2 'cavitation' exposure prior to a 20 s 14 W/cm^2 'heating' exposure caused a lesion to form 8 mm 'deeper' in the ex-vivo tissue. One significant shortcoming of this study is the lack of data demonstrating that cavitation activity alone caused the increased damage. For example, it is possible that the short high power exposure (the 'cavitation' exposure) led to heating in the tissue which caused the larger lesions. Such thermal enhancement could have generated boiling, causing the observed increase in echogenicity, thus it is difficult to identify whether the 'cavitation' enhancement of the lesions was directly due to acoustic cavitation activity. However, it is also possible that the 'cavitation' exposure caused a greater peak temperature rise resulting in a larger lesion, and the echogenicity (used as an indication of cavitation activity) resulted from this higher temperature (i.e. boiling occurred) but did not directly contribute to the lesion 'enhancement'.

Roberts *et al* (2006) pioneered a non-thermal technique for tissue destruction using high intensity short duration ultrasound pulses. The technique is called histotripsy as it is similar in application to lithotripsy (§3.3) other than it is targeted for soft tissue destruction. As the pulses are typically short (~ 20 μs) with a pulse repetition rate of 100 Hz the tissue destruction is from mechanical processes rather than the thermal effects typically seen from HIFU exposures. In this investigation, homogenised regions of tissue were generated *in vivo* with 1000 or 10000 pulses that, under gross examination, displayed regions with a liquefied core with smooth walls and sharply demarcated boundaries. The therapeutic ultrasound system was able to deliver intensities of 20000 W/cm^2 at a frequency of 0.75 MHz. It was guided by a 2.5 MHz diagnostic imaging probe (General Electric Medical Systems, Wisconsin, USA), which was used to visualise the focal region. A hyperechogenic region was observed in the focus during the exposures, but this dissipated rapidly after the exposure had finished. This technique demonstrates the ability for acoustic cavitation activity to damage tissue.

Liu *et al* (2006) used dual frequency systems in order to cavitation-enhance lesion formation. This system used 1.16 and 0.57 MHz HIFU transducers combined with 28 and 40 kHz planar transducers. The rationale was that a lower (kHz) frequency used in combination with a HIFU (MHz) frequency would increase the probability of cavitation induction in porcine muscle tissue and that the presence of such bubbles would increase the local heat deposition. Both high and low frequency transducers were driven simultaneously for exposure durations of 20-100 s. The paper demonstrates that the dual

frequency system produced larger and more predictably shaped lesions than that using the single high frequency alone. One possible drawback to the implementation of the technique presented was that the lower frequency transducers were aligned perpendicularly to the HIFU transducers, requiring two acoustic windows for access, and a method for aligning the foci within the body. This would be hard to achieve *in vivo* and, even if the HIFU and low frequency beams had the same acoustic axis, bubbles may have been generated pre-focally by the lower frequency component, thus effectively reducing the energy delivered to the designed treatment location as reported by ter Haar and Clarke (1997).

The literature discussed here gives an overview of the effects that cavitation can have on HIFU exposures in tissue and/or phantoms. It is clear from this work that cavitation may play an important role in HIFU treatments. Currently, however, there is generally agreement that cavitation activity gives an enhanced heating effect in addition to the absorption of the acoustic field by an attenuation medium. However, there seems to be some uncertainty as to the exact nature of the cavitation behaviour involved, specifically the differentiation between acoustic cavitation and boiling is often lacking. In order to demonstrate the positive benefits of cavitation activity during HIFU exposures it is important to establish clearly which type of cavitation activity is occurring. Only when this is possible can the lesion enhancement properties of cavitation activity could be fully investigated. Nevertheless, based on the consensus from the literature discussed here, cavitation (either acoustic cavitation or boiling) is likely to play a significant role in future clinical HIFU treatments, and it is this that is the main thrust of the present thesis.

3 – Cavitation detection methods in an ultrasound field

This chapter introduces the concepts behind the different methods employed for cavitation detection in the literature. It provides a broad overview of the different cavitation detection methods, but focuses in more detail on the techniques that are suitable for studies using HIFU fields. There are a number of different cavitation detection techniques that use different mechanisms for the detection of bubbles, which can be ultrasonic, chemical, electrical or optical. Interpretation of the detected signals is discussed in greater depth in Chapter 4.

3.1 Introduction

3.2 Active cavitation detection

There is no standard definition for active cavitation detection so for the purposes of this study it has been classified as any technique that interacts directly with the bubbles. An example is the scattering of a diagnostic ultrasound imaging pulse by a bubble and the detection of the backscatter.

Medwin (1977) gives a review of the ultrasonic methods for the estimation of bubble populations in seawater. Described in this review were in-situ experiments for the determination of these distributions using pulse-echo and continuous wave techniques. The backscattering and extinction cross-section (§2.3) per unit volume were estimated by emitting a pulse (0.5 ms) from the source/receiver which was reflected from a steel plate a known distance away (2-7 m), which was then detected by the source/receiver (properties of which were not specified in this publication). The echo signal recorded on an oscilloscope was compared with those obtained in 'clean water' (i.e. bubble free) which allowed the determination of the absorption and scattering due to the presence of bubbles in the seawater. Relative reverberation between echoes, compared with the preceding echo levels gave an estimation of the scatter in the acoustic path. The continuous wave technique also measured the sound speed, by measuring the number of wavelengths that were detected between two hydrophones a fixed distance apart along the acoustic axis. This study demonstrated that acoustic techniques provided the methods best-suited for measuring the resonance characteristics of a gas bubble to estimate the bubble populations in a bubbly liquid. The techniques described here were suitable for a laboratory application, but it would be difficult to

implement them to investigate bubble generation in a clinical environment. In addition, this system relied on the presence of pre-existing bubbles, but it was assumed that no other large scatterers were present, which could prove problematic when working in tissue in the presence of vasculature and other tissue structures.

Miller (1981) described the use of second harmonic emissions from pre-existing bubbles, injected using a syringe, as a method for the detection of bubbles (4.2 μm) in a flowing liquid (water). The aim of this work was to demonstrate a resonant bubble detector that could have *in vivo* applications The author suggested that the second harmonic signal originated from non-inertial cavitation being driven with a 1.64 MHz ultrasonic field at the cavities' resonant frequency, and re-emitting the higher harmonic of the drive frequency ultrasound. The theoretical section of this paper described calculation of the transmit acoustic parameters required so that second harmonic generation from non-linear propagation or radiation force on the bubble would not be significant factors. The detector was constructed so that it detected resonant bubbles preferentially in a liquid medium. Since these devices were not focused, a detector of diameter smaller than the send transducer was used to interrogate a small volume, in order to further minimise the detection of second harmonic generated from non-linear propagation of the acoustic field. Liquid was allowed to flow through the detector to allow a large volume to be sampled. The radiation force was calculated so that the pressure amplitude of the transmit transducer would not cause the bubbles to exceed 50 cm/s (arterial blood velocity) to avoid it pushing the bubbles out of the detection volume. Two transducers were fixed inside a perivascular cuff that was constructed of acoustic absorber with cut-out sections to allow for acoustic propagation. Coupling gel was used to couple the transducers to the 'artery' (a 2.4 mm plastic tube). The transmit transducer was 4.8 mm diameter with a resonant frequency of 1.64 MHz. The paper describes how each component of the detector was tested and quotes the free-field spatial peak intensity for the 'sending' transducer as 120 mW/cm^2 (0.06 MPa). The receiver, which had a 3.2 mm diameter, was designed to be sensitive to bubbles with a resonant size of 4.2 μm at a drive frequency of 1.64 MHz in order to produce a second harmonic at 3.28 MHz. In conclusion, the paper states that this resonant bubble detector will satisfy two purposes in biophysical research, the detection of pre-existing bubbles, which may interact with an ultrasonic field, and the measurement of cavitation thresholds without involving high amplitude bubble behaviour. A limitation of only

interrogating the second harmonic is that the device would have been only sensitive to bubbles of a resonant size. The detection of superharmonics generated from bubble oscillations could prove problematic as HIFU fields can generate superharmonics from non-linear propagation (§1.3.2 above).

A study by ter Haar and Daniels (1981) investigated the occurrence of ultrasonically induced cavitation *in vivo* in a guinea-pig hind limb. Pulse echo diagnostic ultrasonic imaging (8 MHz) was used to identify hyperechogenicity resulting from 5 minute exposures using a 0.75 MHz ultrasound therapy system (Rank Sonacel Multiphon, Mk 11) with spatially averaged intensities of 80, 150, 300 and 680 mW/cm^2 (pressures not given) in the hind legs of guinea-pigs. The B-mode images were recorded onto film at a rate of 11 Hz, allowing the study of the temporal and spatial evolution of bubble activity. The authors discussed the spatial resolution of the scanner being a limiting factor in the identification of bubbles. Since the scattering cross-section of a bubble is greatest when it is at resonance (§2.3) then it would be these bubbles that give the greatest backscatter for a B-mode scan. However, the authors suggested that the bubbles detected by this system must be larger than those resonant in water (4 μm at 0.75 MHz) since the scanner resolution limit was 5 mm. In fact, they estimated, from the appearance in the B-mode images, that the bubbles seen were in the range 10-100 μm. The authors hypothesised that echoes could be due to scattering from a cluster of bubbles where the individual bubbles are smaller than the scanner's resolution. The authors further suggested that the bubbles were formed due to the negative pressures of the acoustic field, giving rise to acoustic cavitation. A cloud of bubbles from acoustic cavitation must be generated in order for it to be imaged, and it is difficult to estimate whether the frame rate of the scanner was sufficiently fast to image such a bubble cloud before the bubbles would dissolve, leaving a population that does not produce echogenicity. However in a subsequent publication Watmough *et al* (1991) measured a temperature rise of $15^oCW^{-1}cm^2$ (60 s duration) in ex-vivo guinea pig leg for an equivalent system, and it is suggested (Leighton, 1994) that this heating of the tissue could have caused the bubble formation. Irrespective of the mechanism for bubble formation this publication demonstrated that a B-mode image was able to detect cavitation *in vivo*. In the absence of any other detection method, it is not possible to identify whether the cavitation discussed in this paper was from acoustic cavitation or boiling.

Roy *et al* (1990) investigated the acoustic backscatter technique specifically for the detection of inertial (or transient) cavitation generated from microsecond pulses of ultrasound. The system used 10 μs long tone bursts (30 MHz centre frequency) to detect inertial cavitation that was generated from 10 μs pulses at 757 kHz in a suspension of 0.8 or 0.245 μm polystyrene spheres in degassed water. This system was constructed in a Perspex enclosure with the 30 MHz pulse-echo transducer perpendicular to, and confocally aligned with, the 757 kHz transmitter. The inertial cavitation threshold was measured for a range of particle and dissolved gas concentrations using the active cavitation detector. It was shown that as the dissolved gas concentration increases, the inertial cavitation threshold pressure decreased for a suspension of 0.8 μm diameter polystyrene spheres. In addition to the active detection method, a 1 MHz passive unfocused transducer was used to detect scattering of the 757 kHz signal from cavitation bubbles. The authors found that the measured cavitation threshold from the active technique was either lower or equal to that measured using the passive technique at all levels. The authors demonstrated that the high frequency active detection pulse itself did not produce cavitation in the liquids, but they suggested that acoustic streaming and radiation pressure could affect the cavitation threshold, since sweeping more particles through the focal region might increase the probability of exposing cavitation nuclei. The active cavitation detection technique shown here can be used to obtain both temporal and spatial information about cavitation activity. This technique is limited to use in a region in which the scattering can be attributed to cavitation activity and for example might not be suitable for use in perfused tissue as other objects may create scattering and be confused for the presence of cavitation. Nevertheless, the unique broadband emissions are critical to identifying the presence of inertial cavitation. The acoustic interface from HIFU exposures could render this technique problematic for a cavitation detection system like this when trying to use it in conjunction with a HIFU field.

Holland *et al* (1996) used active cavitation detection to investigate damage to rat lungs from acoustic cavitation, following Doppler imaging. They aimed to investigate whether it was possible to observe direct evidence of cavitation *in vivo* caused by diagnostic ultrasound and whether the bubble activity could be related to biological damage. They used a clinical ultrasound scanner (Advanced Technical Laboratories (ATL), Ultramark 9 system, with high definition imaging, UM9 HDI, Seattle, USA) to

generate cavitation and a detection transducer (resonance at 30 MHz) to pulse the targeted region and investigate the echo. The peak negative pressure of the Advanced Technical Laboratories device was measured to be 3.6 MPa for a focal length of 0.8 cm in water. The active cavitation detector used a pulse-echo technique (Roy *et al*, 1990) to observe the backscattered sound. The pulse from the detection system was designed be coincident with the Doppler pulses, in order for the detected signal to be on the same time scale as the therapeutic ultrasound pulse. The authors reasoned that signals on the time scale of a single acoustic cycle (0.25 μs) or the entire ATL scanner's tone burst would be from cavitation, whereas other scatterers would exist for the entire pulse duration (15 μs) of the active cavitation detector. The active cavitation detection technique used for this study was able to identify whether cavitation had occurred *in vivo*. The backscatter technique gives information as to whether or not acoustic cavitation is present, but does not give any specific insight into how the bubble is behaving in response to the ultrasound field that is, the type of cavitation activity occurring. This technique would only be suitable for use with pulsed ultrasound and could not to be used in conjunction with continuous wave HIFU exposures. In addition, as this study was done *in vivo* on rats detection of scattered signals was shallow depths ($\leq$ 2.8 cm, the focal depth of the active cavitation detector was not specified). However, this may not be applicable in the clinical environment where pulse-echo signals would have further to travel, and will be attenuated by the increased tissue path.

Deng *et al* (1996) measured the thresholds for inertial cavitation inception in human blood *in vitro*. Their active cavitation detection system (a focused transducer with a centre frequency of 30 MHz) used the backscattered signal from the cavitation sites to identify whether cavitation occurred. In addition to this, the Doppler shift in reflected signal was used to identify the rapid growth and collapse of cavities. 'Typical cavitation events' shown in this appear to show fluctuations in velocity, measured by the Doppler signal, which occurred over a time period of approximately 1 μs. Assuming that this arises from a single oscillation of a bubble, this would mean that these typical examples of cavitation bubbles were oscillating at a frequency of approximately 1 MHz. The blood was exposed with a focused transducer at 2.5 MHz. Thus, it is difficult to understand why a bubble generated at this frequency would be oscillating at a frequency that is unrelated to drive frequency. The frequency shift of the Doppler signal might be indicating the motion of the cavity's surface monitoring the growth/collapse of a cavity.

However, high acquisition rates would be needed in order to identify this from cavitation oscillating at high MHz frequencies. Inertial cavitation in blood was identified from the combination of the detected voltage signals variation with time and the Doppler signal.

Melodelima *et al* (2004) investigated the effects of cavitation during lesion induction in ex-vivo bovine liver, as discussed in section 2.4. Their active cavitation detection system was a diagnostic ultrasound scanner (Hawk 2102 XDI Scanner, B-K Medical, Germany) which was used to acquire B-mode images after exposures using a high intensity planar ultrasound transducer. Hyperechogenicity in the B-mode images was used to identify the presence of cavitation, but unlike in the ter Haar and Daniels (1989) study, images were only obtained after the exposure had occurred, due to acoustic interference from the high intensity ultrasound exposure. No discussion as to the type of cavitation was presented and it is likely that this technique detected the presence of thermally generated cavitation (§2.1.2) rather than acoustic cavitation, since the hyperechogenicity persisted after the exposure.

3.3 Passive cavitation detection

Passive cavitation detection, refers to the detection of acoustic emissions generated from bubble activity (a discussion of cavitation mediated acoustic emissions can be found in §4.1). The detector does not interact with the bubble, and is thus a passive device. However, the acoustic source driving the cavitation may interact with the bubbles once produced, and so it may be that some of the detected signals might be due to scattering.

Edmonds & Ross (1986) used a passive cavitation detector to record the drive frequency half harmonic and 'noise' produced (presumably broadband emissions) produced from cavitation in a cell suspension (C1300 mouse neuroblastoma). The acoustic emissions were detected using a lens focused 0.5 MHz Panametrics transducer (focal length not specified, diameter of 3.8cm) placed at 45^0 to the acoustic axis of the ultrasound transducer. The ultrasound transducer (1 MHz) gave continuous wave exposures for 5 min using spatial peak intensities of 0.9, 1.7, or 2.6 W/cm^2 (pressures not given). As the half harmonic (0.5 MHz) was of interest a low pass filter (which rejected the fundamental signal) was used to attenuate the drive frequency by 50 dB, the remainder of the signal was then passed through a 20 dB amplifier. This signal was then split between a spectrum analyser (HP 8557A) and a root mean square (rms) voltmeter (HP 3400A). One key aspect of this detection system is that it recorded the time

dependence of the acoustic emissions, which gave insight into the development of the cavitation activity during the 5 min exposures. The paper suggests that the half harmonic was an indication of non-inertial cavitation (referring to work by Miller (1981)) and that the noise build up was due to inertial cavitation, as a result of work by Neppiras (1980). This detector provides a useful basis for a passive cavitation detection system for investigation of the behaviour of subharmonics.

Crum and Law (1995) investigated the relative roles of thermal and non-thermal effects of HIFU exposures for the treatment of benign prostatic hyperplasia. A 4 MHz HIFU transducer (Sonablate, Focus Surgery, IN, USA) was used to expose ex-vivo turkey breast (at 37^{o}C) for 4 s at an in-situ intensity of 2000 W/cm^2 (calibration technique not given). The diagnostic scanner was used to image the HIFU exposures and to monitor any change in echogenicity in the tissue. The electrical drive power supplied to the transducer was recorded using a chart recorder. Acoustic emissions were detected using a focused broadband transducer (specifications not given) con-focally aligned with the HIFU focus and positioned directly opposite, which was connected to a spectrum analyser via a filter and amplifier (specifications not given). The authors found that in some of the exposures, hyperechogenic regions could be observed which corresponded to the time at which an audible emission (dubbed 'popcorn' by the authors) was heard. They found that when this was seen, there was a drop in the transmitted acoustic intensity and that fluctuations occurred in the electrical drive power. Spectral analysis of the emissions detected by the sensor showed the presence of subharmonic and superharmonic (specifically at 2 and 6 MHz) emissions, and also of broadband emissions. They hypothesised that the source of these audible emissions (and the subsequent onset of acoustic emissions and power fluctuations) was from the superheated boiling of a localised region of the tissue that had been rapidly heated by the HIFU field. It was considered that this event was the catalyst for the detection of subharmonic and superharmonics. However, it is not clear whether these were from the superheated bubbles, or that this event seeded other forms of cavitation. Also with strong scatterers present, the superharmonics could have been due to scattering of non-linear components of the HIFU field, but this was not considered.

Everbach *et al* (1997) used a narrow band 20 MHz passive cavitation detector to quantify the amount of inertial cavitation occurring in a sample of human blood exposed to pulsed ultrasound. The sample was exposed to a spatial peak pulse average intensity of 500 W/cm^2 (peak negative pressure of 2.8 MPa) at a centre frequency of 1 MHz, with

varying tone burst durations (20, 100, 200, 500 and 1000 μs) and a pulse repetition frequency of 20 Hz for 60 s. It was suggested that, since the passive detector (unfocused narrow-band 20 MHz transducer) does not interact with the cavitation site, the temporally overlapping signals for each tone burst were independent of each other. The rms voltage from the detector was taken as a measure of the number of cavitation events (bubble collapse). This was calculated using the internal software in the oscilloscope for a single 1 minute exposure. The results show that the cavitation activity, if it had occurred, was indistinguishable above the baseline noise level for exposures in pure blood. However, when a microbubble echo contrast agent (CA) was added (Albunex®) the time averaged cavitation activity increased with increasing pulse duration. Without any secondary confirmation of cavitation activity the increase in detected signal could be a result of the CA scattering ultrasound towards the passive detector. This is, however, unlikely as the centre frequency of the detector was much higher than the exposure frequency. It would however, have been useful to perform Fourier analysis on the time-averaged cavitation activity signal to determine the frequency spectrum of the detected signal in order to investigate other forms acoustic emissions from inertial cavitation. Basing a detection system on the Vrms from a sensor, without analysis of the frequency components of the recived signals may provide inaccurate results since this type of analysis assumes that you only detect signals from bubble activity, which could be misleading. The appendix of this paper shows a frequency spectrum of 'typical cavitational activity' that was detected with a needle hydrophone (Precision Acoustics, Dorset, UK) and not the cavitation detection system used in their study. The spectrum shows a dB scale (50 to -250 dB) with 4 harmonics of the drive signal (1, 2, 3 and 4 MHz) that have amplitudes between 20 and 120 dB greater than the broadband noise identified by the authors as 'typical cavitational activity'. Even though the detection system was centred at 20 MHz it is possible that these harmonics (since they are significantly larger than the broadband noise) contributed to the detected signal giving an inaccurate measure of the cavitation activity.

Poliachik *et al* (1999) used a passive cavitation detector to investigate the effect of HIFU on whole blood, with and without a microbubble CA (the experimental details were similar to those used by Everbach *et al* (1997)). A 1.1 MHz HIFU transducer and a 5 MHz focused hydrophone (2 MHz bandwidth) were used for cavitation generation and passive cavitation detection, respectively. The HIFU transducer was used to expose

the blood samples, usually for 1 s, over the intensity range 560-2360 W/cm^2. The hydrophone was positioned perpendicular to and aligned con-focally with the HIFU transducer. A peak detector was used to detect the spikes in the detected signal, which were presumed to originate from cavitation activity rather than from scattering of the non-linear components of the HIFU field. The data analysis, aimed at determining whether cavitation had occurred, used two different methods. The first technique analysed the acoustic emissions by taking the derivative of the detected peak voltages with respect to time. The resulting value gave an indication of the frequency of cavitation events (i.e. how often they occur). However, only spikes that were greater than five standard deviations from the baseline were counted by this method. This technique would be able to give an indication of the time at which cavitation occurs, whether it was predominantly at the start, middle or end of the exposure. The baseline was described as exhibiting no cavitation acitivity. The second technique calculated the integral of the detected peak voltage data that was above a specified noise level (not quantified) to provide a quantitative measure of cavitation (in mV), which they called "cavitation dose". The publication does not discuss the type of cavitation event being counted, nor do they define what is meant by a cavitation event, so the term dose could be misleading. Although the concept of a cavitation dose is a potentially useful one, the problem with this is the ability to define it in a meaningful quantitative way. Poliachik *et al* (2004) subsequently used the same experimental set-up to investigate the relationship between cavitation and platelet aggregation, and they found that cavitation generated by HIFU exposures was responsible for platelet rupture resulting in aggregation.

Zeqiri *et al* (2003) presented a series of experiments to evaluate the performance of a novel sensor for monitoring broadband acoustic cavitation emissions, particularly in (acoustic) cavitation baths. The sensor was a hollow open-ended cylinder, whose inner surface is a thin film piezoelectric polymer, which acted as a passive detector. The sensor had a bandwidth greater than 10 MHz, (no centre frequency is quoted for the device), but the majority of the detected emissions were below 5 MHz. The outer layer of the sensor consisted of a 4 mm thick coating of acoustic absorber to ensure that only signals generated inside the volume of the sensor were detected. They used a commercial ultrasonic cleaning vessel, operating at 40 kHz with an output power of 1 kW, to create cavitation in a tank of degassed water. The sensor monitored the broadband acoustic signal associated with the oscillation and collapse of inertial

cavitation bubbles. The study relied on the assumption that the broadband noise only originated from inertial cavitation (§4.1). The authors argued that the high frequency (> 1 MHz) broadband emissions were produced either by the shockwave of the collapse of the cavity or by random chaotic oscillations in the cavity. The collapse of a cavity is the more likely explanation, since the oscillation of a population of bubbles at different frequencies would appear as a broadband continuum at the detector. In order to quantify the cavitation activity within the sensor, the broadband integrated energy (*BIE*), shown in equation 3.1, to indicate the white noise generation due to inertial cavitation was used.

$$BIE = \int_{f_1}^{f_2} V_C(f)^2 \, df \tag{3.1}$$

where $V_C(f)$ is the frequency-dependent spectral magnitude of voltage derived from the cavitation sensor output spectrum. The integration was only performed between f_1 = 1 MHz and f_2 = 5 MHz. Measurements were made for ultrasound vessel power settings in the range 5-95% (of the maximum power deliverable). Once the power level was set to above 20%, the *BIE* increased linearly with power setting, showing a direct correlation between cavitation activity and drive power. Below this level no emissions were detected. A linear relationship for inertial cavitation activity with power would not be expected, once the cavitation threshold is exceeded a 'jump' in the detected broadband emissions is expected. This would increase with drive power level but would be expected to plateau. This plateau may not have been reached, or the increase in drive power caused a flow in the liquid providing more cavitation nuclei, which would be integrated into the time-averaged signal. For this reason it would have been useful to see typical time history information from the detector. As the sensor is designed to only detect cavitation within its volume, unlike the focused transducers discussed above, the uses for this sensor are limited to situations where cavitation activity can be generated inside the sensor. However this sensor could provide a useful test apparatus for investigation of cavitation activity from HIFU exposures (§4.3).

Bailey *et al* (2005) used both passive and active cavitation detection to investigate the collateral damage in porcine kidney tissue from shock-wave lithotripsy (Dornier HM3 lithotripter) *in vivo*. For passive cavitation detection they used two single element focused transducers (10 cm diameter, 10 cm radius of curvature, centre frequency 1.1 MHz) that were con-focally aligned with the focus of the lithotripter but positioned

perpendicular to it. Time of flight data acquired by the dual passive cavitation detection system was used to identify the location of cavitation events. The signals from both transducers were high pass filtered (300 kHz, 3202, Krohn-hite, Avon, MA, USA) and 1 ms of data was recorded for each shock-wave with a sample frequency of 5 MHz on a digitiser (Tektronix TDS 520). This system was designed to detect the pressure pulse emitted from bubble collapse. This publication showed that the collapse pressure of a single bubble that was detected by the passive cavitation detection system was of the order of 1 MPa, which is close to the lower end of the peak negative pressures generated from our HIFU transducers (§5.1.2). The use of a dual detection system in this case allowed identification of the position of the cavitation activity. This was only possible as the Lithotripter is pulsed. This is not usually with the case for clinical HIFU exposures as it affects the heating achieved. In addition, HIFU transducers have a higher frequency (~1-5 MHz) which means that the sample rates for the detection system need to be higher. The detection system here did not use any amplification due to the large peak negative pressures used, this may not be possible for HIFU exposures.

Rabkin *et al* (2005) used a combination of active and passive cavitation detection techniques to study the source of hyperechogenicity in diagnostic ultrasound images of HIFU exposed pig muscle *in vivo*. A 3.3 MHz HIFU transducer (focal length 6.3 cm, f-number 0.9) was used to expose the tissue for 10 s using in-situ intensities (spatial peak, temporal average) in the range 220-1710 W/cm^2. The passive cavitation detector was an unfocused broadband single-element transducer with a bandwidth of 0.5-5.5 MHz (V382, Panametrics), that was inserted into a central hole in the HIFU transducer. Hyperechogenicity was assessed using a diagnostic ultrasound scanner (probe C9-5, Advanced Technology Laboratories, ATL Bothell, WA, USA). This was also used as the active cavitation detector during exposures. Passive detection was performed for 1 ms at the start of every 127 ms HIFU pulse. The HIFU was then off for 33 ms during which time the diagnostic imaging (160 ms) and active cavitation detection (200 μs) was performed. In this study, the level of inertial cavitation was calculated from the rms amplitude of the broadband noise over the frequency range 0.5-1.5 MHz. Non-inertial cavitation was calculated from the half harmonic (1.65 MHz) amplitude. Relying solely on this for the identification of non-inertial cavitation especially if broadband emissions are being detected, could lead to misleading conclusions since inertial cavitation can generate half harmonic emissions (§4.1.1). This passive cavitation detection system monitored acoustic spectra that occurred at a frequency below that of the drive in order

to investigate the temporal variation during HIFU exposures. Using the low frequency range meant that acoustic emissions were less attenuated than if they had used the high frequency range, and that the data acquisition rates could be lower. This limited the detection system to a narrow frequency band, rendering the results more susceptible to noise artefact since the spectrum of interest is smaller. The temporal information was correlated with the appearance of hyperechogenicity in the focal region. They showed that cavitation played a role in the appearance of hyperechogenicity, specifically that inertial cavitation occurred within the 0.5 s immediately prior to the appearance of a hyperechogenic region. The gating used provided a number of different techniques that could be used during the exposure. However, one disadvantage of this system is that, for example, the passive detector was only recording for 0.8% of the total exposure time, which might have meant that a significant proportion of the cavitation activity was missed. A better approach is to acquire continuously during the exposure, but this may have a detrimental effect on the active cavitation detection.

Coussios *et al* (2007) investigated the non-invasive monitoring and control of inertial cavitation dynamics from HIFU exposures in a tissue-mimicking (specifications not given) agar-graphite phantom. A 1.089 MHz HIFU transducer (Sonic Concepts H-102, S/N-8) was used to expose phantoms over the in-situ peak negative pressure range of 1.84-4.98 MPa for up to 60 s with a variety of duty cycles. Broadband emission were monitored using a focused 15 MHz passive transducer (7.6 cm focal length, Panametrics Ltd. V319-SU) connected to a data acquisition card via a 40 dB preamplifier (HP 461A) and a 5 MHz high pass filter. The high pass filter was used to remove the fundamental, second, third and fourth harmonics generated by the HIFU transducer, in an effort to ensure that the signal detected by the passive cavitation detector was only from broadband emissions. However, no verification was provided that superharmonics generated from non-linear propagation of the HIFU field were not generated above the fourth harmonic (4.36 MHz). The authors demonstrated that increasing the path length of the passive sensor within the phantom (5, 10, 15 and 20 mm) reduced the amplitude detected. This was only demonstrated at one exposure level (2.16 MPa). It would have been useful to see if this change in path length would have had an effect on the cavitation activity detected, for example, would the cavitation threshold measured in this type of phantom have changed with a different path length, giving a lower/higher threshold. This suggests that cavitation thresholds quoted are dependent on the amount of attenuation in the propagation path between the source and

detector. The authors investigated different duty cycles and the effect on both the amplitude, and the total amount of inertial cavitation activity. As they had found with continuous wave exposures the amplitude of the detected broadband emissions decayed with exposure time. Thus, they used 10, 20 and 40% duty cycles in an effort to maintain the amplitude of broadband emissions throughout the exposure duration. A 20% duty cycle was shown to prevent this decay in the detected broadband emissions, thus suggesting that this was the optimal setting for maintaining cavitation activity throughout the HIFU exposure. However, if the aim of the study was to use cavitation for the enhancement of HIFU treatments a 20% duty cycle may be counter productive since the heating you might gain from more cavitation activity could be lost in reduced heating time, since the thermal effects in HIFU exposures are the dominant factor in lesion formation.

Mast *et al* (2008) used a 32-element unfocused transducer (3.10 MHz) to ablate and B-mode image (not simultaneously) ex-vivo bovine liver tissue in an effort to investigate the acoustic emissions generated during tissue ablation and establish whether any correlation could be established. An unfocused 1 MHz broadband receiver (C302, Panametrics, MA, USA) was positioned perpendicularly to the imaging and ablation transducer and used as a passive cavitation detector. The peak intensity (pressure) amplitudes used (15 mm way from the imaging-ablation transducer) were given as 23, 41, and 64 W/cm^2 (0.83, 1.10 and 1.38 MPa). Total exposure time was 20, 10, or 5 mins. Every 3.3, 1.7 and 0.9 s the ablation was stopped for 30 ms to allow a single B-mode scan, which gave a duty cycle of approximately 97-99%. The aim of this was to ensure that comparable tissue heating occurred for each exposure condition. A sample rate of 10 MHz was used to acquire data from the passive cavitation detector at 100 ms intervals throughout the exposures. It was synchronised such that it did not acquire information during the B-mode image acquisition pulse. The frequency analysis was performed over three distinct frequency regions, the half harmonic (1.55 MHz), broadband emissions (0.3-1.1 MHz) and low-frequency emissions (0.01-0.03 MHz), which were said to represent non-inertial, inertial cavitation and boiling, respectively. However, half harmonic emissions can also be generated by inertial cavitation activity (§2.1.1). Baseline noise levels were established from sham exposures. The temperature was measured using a 0.4 mm needle thermocouple (Type-B, Ella CS, Czech Republic) that was inserted under ultrasound image guidance to a depth of 7.7 ±2.3 mm below the tissue surface. The authors suggested that broadband, low-frequency emissions and

tissue echogenicity may be useful for the non-invasive monitoring and control of exposure parameters during ultrasound ablation. Interestingly, the authors observed that non-inertial cavitation, as identified by the presence of half-harmonic emissions, was rarely seen, and only under 'special conditions' (i.e. for tissue temperatures between 47-49^{o}C for the 0.8 MHz exposure). This was thought to be due to pre-existing bubbles of resonant size (~ a radius of 1 μm at this frequency) being destroyed by the continuous wave sound field. The authors do not discuss the process by which these resonant bubbles could be destroyed, which would presumably be from oscillations or violent collapse. However, they do discuss the possibility of cavitation being generated in the degassed water surrounding the tissue, but this was discounted following tests. As a latex condom was used to hold the tissue in place for the experiments, it appears that this was removed during this test. This may have trapped cavitation nuclei that could have been the source of sporadic half harmonic emissions, which would have been detected by the unfocused passive cavitation detector. The use of an unfocused sensor was practical for this study due to the unfocused ablation device. However, for strongly focused HIFU fields, a focused sensor would be more practical since more reliable spatial information may be obtained.

3.4 Sonochemistry and Sonoluminescence

Chemical reactions that do not occur in the absence of an acoustic field are generally termed sonochemical (Leighton, 1994). It is believed that Sonochemistry is not caused by the direct interaction between sound and the molecular species, since the acoustic wavelength (for frequencies between 0.015–10 MHz) is much greater than the molecular dimensions. Rather, it is thought that acoustic cavitation is the primary cause of these reactions, because of the high temperatures generated during bubble collapse. Sonoluminescence is believed to occur from the recombination of chemical species which cause light emissions, generated from bubble collapse (Suslick *et al*, 1990).

Weissler (1959) studied the role of free radicals in chemical reactions caused by ultrasonic waves. A sample of oxygen (or argon) saturated water contained within a Pyrex test-tube was exposed to 10 minute duration exposures of ultrasound (400 kHz with an acoustic intensity of 2.5 W/cm^2, calibration technique not specified). The test-tube had a rubber bung in one end that contained inlet and outlet pipes to allow bubbling of gas through the solution. During the exposure, the pipes were closed off in order to eliminate the possibility of air mixing with the solution. The sonochemical

yield of hydrogen peroxide, which was believed to be produced by the formation of free radicals from bubble activity in the solution, was measured spectrophotometrically. This finding provides the basis for sonochemical studies.

Leighton *et al* (1988) investigated the correlation of sonoluminescence in aerated water with the acoustic standing wave pattern produced by a physiotherapeutic ultrasound device comprised of a continuous wave ultrasound source with frequencies of 1 or 3 MHz. The experiment was set-up in order to simulate standing waves created inside humans caused when the ultrasound undergoes a partial reflection due to discontinuities. Spatial average intensities of 3.3 W/cm^2 were found to create sonoluminescence in a sample cell. The inside of the cell was painted black to prevent scatter from the sonoluminescence events being detected by the optical system. The optical system consisted of a camera lens, mirror-image intensifier tube and a camera. In order to eliminate outside light sources the experimental apparatus (up to the image intensifier tube) was housed within a light tight enclosure. This publication demonstrated that the light emissions were predominantly located at the antinodes (peak negative pressure of 0.3-0.4 MPa) of the standing waves. Therefore the sonoluminescence was shown be generated in the regions of peak pressure. However, in arrangements where little or no standing wave component was present no sonoluminescence was generated. This could prove problematic if this technique were to be used with HIFU fields as standing waves are avoided so that damage to the HIFU transducer does not occur.

Leighton *et al*, (1990) performed an *in vivo* study into the generation of sonoluminescence in the human cheek, again using standing waves. This work extended the previous study by performing sonoluminescence detection *in vivo*. The human cheek was selected for study as it was thin, with low attenuation compared with other regions of the body, allowing for optical and acoustic measurements, and the tissue air interface would also cause partial standing waves. The sonoluminescent photons were collected by a light guide and channelled to a red-sensitive photomultiplier (EMI 9658R), whose output was measured by a 5C1 photon counting system and 5C14 pulse height analyser (EG&G Brookdeal Electronics Ltd.). Sonoluminescence was generated by a 1 MHz Therasonic 1030 (Electro Medical Supplies) ultrasound system, operating at intensities up to 2 W/cm^2 (the author reported that the volunteers experienced discomfort above this level). A sealed bag containing aerated water (the dissolved oxygen levels were not given) was sometimes placed between the light guide or transducer and cheek, the

reasons for this were not given. The number of sonoluminescence events in the human cheek were not statistically significant (student's *t*-test) when compared with background measurements from sonoluminescence generated in the aerated bag alone. This was attributed to two factors, firstly no sonoluminescence occurred, or secondly that its level was sufficiently low that attenuation in the cheek meant the photon intensity was below the detectable level of the experimental technique. Using this second reason as a hypothesis the authors calculated the minimum amount of light intensity from sonoluminescence that the system would be able to detect. This study highlights the difference between detecting cavitation activity in a readily cavitating medium (e.g. aerated water) and in living tissue. The detection threshold was critical in identifying cavitation activity in this experiment. This is an important consideration when discussing cavitation thresholds in tissue.

Coleman *et al* (1992) used sonoluminescence combined with focused passive cavitation detection to investigate the cavitation activity in tap water exposed to shock-wave lithotripsy. This study used two, nominally identical, 1 MHz electrohydraulic shock-wave lithotripters (Dornier HM3 and EEV Ltd., Lincoln). The reason for this was the passive cavitation and sonoluminescence detection were performed at two separate centres. Light emissions were recorded from the water, around the focal region, using a fast photomultiplier (PM) tube (EMI 9789B), which was positioned perpendicular to the shock-wave propagation direction. The tube was encased in an opaque cylinder in order to shield the PM from the light flash generated from the electrical discharge of the lithotripter. Aluminium foil (50 μm thick) was used for windows on the opaque cylinder to provide negligible acoustic attenuation but remain opaque to the light discharge. The need to maintain opacity around the PM tube was the reason why the passive cavitation detection and sonoluminescence detection were performed separately. This study demonstrated that acoustic and light emissions were detected simultaneously (when corrected for the different propagation speeds) from cavitation generated from the primary and secondary shock-waves from a lithotripter pulse. This study demonstrated the practical limitations which occur when trying to undertake different cavitation detection methods simultaneously. The ability to generate sonoluminescence in tap water and to be able to correlate this with signals obtained during passive cavitation detection would be a powerful tool in the investigation of cavitation activity from HIFU exposures. However, it is unclear whether sufficient acoustic cavitation could be

generated to cause detectible sonoluminescence with the HIFU transducers used for this thesis.

Birkin *et al* (2002) reported an electrochemical technique for the detection of two sonochemical reactions, the Weissler and Fricke reactions. The Weissler reaction is the production of iodine from a potassium iodine solution through the generation of free radicals typically from an ultrasound exposure. The Fricke reaction results from exposure of an acidified solution of Fe^{2+} to ultrasound (or ionising radiation) which generates free radicals, which then oxidise Fe^{2+} to Fe^{3+}. These were generated inside an ultrasonic reactor using a 27 kHz piezoelectric transducer. Electrochemical reactions were required to allow detection of the chemical change caused by the sonochemical reaction. These were performed in a 'flow cell', comprised of three electrodes within a Perspex body: a working electrode (the material of this changed according to the sonochemical reaction of interest), a stainless steel counter electrode and a reference electrode. A peristaltic pump was used to flow the solution around the circuit containing the sonochemical reactor and 'flow cell'. This detection technique allowed the sonochemical reaction to be measured as a function of time. There was an initial delay of 20-30 s before the exposed solution reached the flow cell, but after this, the sonochemical reaction could be monitored in real time. The flow cell was encased within a Faraday shield suggesting that this measurement technique was sensitive to RF noise. The need for this type of electrical shielding, although not discussed in the publication, suggests that the sensitivity of this detection technique would be effected by RF sources, for example the power amplifier typically used to drive HIFU transducers. The ultrasonic reactor had a volume of 320 cm^3 in which the sonochemical reaction took place. The volume of a typical HIFU focus is ~0.3 cm^3 (§6.1.1). It would be difficult to generate enough free radicals from this focal volume for the electrochemical reaction inside the 'flow cell' to be above noise levels.

Kanthale *et al* (2008) investigated experimental and theoretical aspects of sonoluminescence using dual frequency ultrasound exposures. A pulsed (20% duty cycle) 20 kHz horn transducer (Branson B-30, diameter = 45 mm) was operated at a fixed drive power (6.3 W) in conjunction with a 355 kHz 'high frequency' transducer (Allied Signal transducer, diameter = 55 mm) operated at variable drive powers, to exposure air saturated water for 30 s. The sonoluminescence was measured using a Hamatsu end-on photomultiplier tube, where the detected signal was read on an oscilloscope (Tektronix, TDS 320) and stored on a desktop computer. This study

showed that the use of the dual frequencies (under specific drive conditions) resulted in enhancement (>30-fold increase) of the sonoluminescence signal. A technique for increasing cavitation activity would be useful in HIFU studies, as it may provide a controllable way of increasing the heating caused by cavitation activity. The authors point out that there were some drive settings which caused a decrease in the cavitation activity, possible due to radiation pressure moving the bubbles out of the antinodes. However, they also hypothesised that the increase in bubble population in the antinodes may result in coalescence, causing the formation of larger bubbles that would not collapse. This highlights that an increase in the bubble populations using a lower frequency transducer might cause a detrimental effect.

3.5 Impedance change measurement

This technique for detecting cavitation arises from the measurements of the 'motional impedance' of an ultrasound transducer (Neppiras and Fill, 1969). The name generally refers to the impedance bridge technique to monitor the loading of a transducer. This technique can detect bubbles since their backscatter can alter the loading, and thus alter the signal recorded by the impedance bridge. Depending on the electrical circuitry used, it should be possible to detected very small changes in the loading of the transducer, making this technique very sensitive to bubble activity.

Neppiras and Coakley (1976) performed a detailed study of bubble activity in water (the gas content was varied between that of 'gassy tap water' and of degassed water, with mixtures of the two) using a focused (diameter and radius of curvature of 4.8 cm) 1 MHz acoustic field. In addition to optical and acoustic monitoring (2.5 MHz focused transducer), this study used a motional impedance bridge (see Figure 3.1) to measure acoustic impedance changes from cavitation activity. It is worth noting that the impedance change technique refers to the electrical drive system and not acoustic impedance, although it is the latter that generates the backscatter that causes an electrical impedance change in the ultrasound drive system.

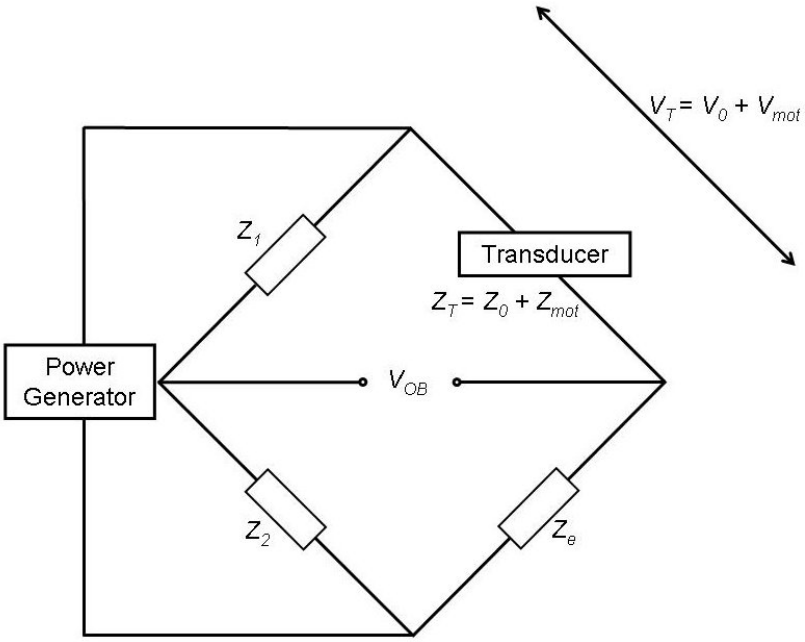

Figure 3.1. A schematic diagram of the motional impedance bridge that was used in the study by Neppiras and Coakley (1976), for further explanation see text.

Initially, the bridge was balanced with the transducer unloaded and driven off resonance. In this state the motional impedance (Z_{mot}) is zero and the bridge balances the clamped electrical impedance (Z_0), ensuring the off balance voltage (V_{OB}) is zero. This gives the balance condition,

$$Z_1 Z_e = Z_2 Z_0 \tag{3.2}$$

When the transducer is driven, $Z_{mot} \neq 0$, and the bridge is not balanced, which creates an off balance voltage. This leads to the relationship for V_{OB}

$$V_{OB} \propto \frac{h_e \xi_t R_2}{(R_1 + R_2)} \tag{3.3}$$

where h_e is the electromechanical constant and ξ_t is the oscillatory amplitude of the transducer face. For simplicity, the electrical impedance has been written as its real component, resistance (R_n), neglecting the imaginary part. Equation 3.3 shows that the off balance voltage is directly proportional to the transducer face amplitude. The pulse duration and frequency of the detected V_{OB} as functions of the acoustic intensity and time were recorded. This study showed that V_{OB} increased linearly with the drive voltage. However when bubbles were generated (as demonstrated by the detection of acoustic emissions) the signals increase more rapidly (not quantified) than the drive voltage. It was hypothesised that the presence of bubbles decreased the acoustic

impedance of the water causing a near proportional increase in the bridge signal. This technique has been demonstrated to be a useful for quantifying the levels of backscatter likely to be caused by bubbles within the acoustic field. However, its application to a medium such a tissue, which contains inhomogeneities (e.g. blood vessels), could cause detected changes in the bridge signal in the absence of bubbles, giving a false positive reading. It would thus be necessary to combine it with a secondary form of cavitation monitoring.

Leeman and Vaughan (1980) used the apparatus described above, but with an unfocused transducer to create cavitation. They found that the plane wave transducer was unable to cause sufficient backscatter to affect V_{OB} but detected subharmonic emissions. This showed that the impedance bridge technique was not able to detected cavitation when the bubble population was insufficient in a confined area.

Thomas *et al* (2006) monitored cavitation using the electrical drive voltage, during lesion formation from (2 MHz) HIFU exposures in polyacrylamide phantoms containing bovine serum albumin (BSA). The phantoms were exposed for 5 s at an in-situ peak pressure of 12.3 MPa. An rms to dc converter chip (Analog Devices, AD637) was used to measure the rms voltage across the HIFU transducer during the exposures, at a sampling rate of 40 Hz. It was suggested that the peak fluctuations seen in the rms drive voltage corresponded to constructive interference between the outgoing and reflected HIFU wavefronts, where the minima in the fluctuations were due to destructive interference. The transparency of the phantoms used allowed direct comparison between the progression of the front surface of the lesion with the fluctuations in the rms drive voltage, where as this type of comparison would not be possible in tissue.

3.6 Direct observation

Direct observation refers to the technique whereby scattered light is used to observe bubble activity in an acoustic field.

Willard (1953) directly observed cavitation activity generated in water from exposures made using a 2.5 MHz focused transducer at a intensity of 1800 W/cm^2 (peak pressure of 7 MPa). The bubbles were illuminated by a high intensity water cooled, 1000 W, mercury arc lamp, which was either pulsed at 60 Hz or was on continuously. A number of different cameras (SLR) were used to record the images from directly above the tank. Firstly, a hand held camera that provided one to one scale images

acquired at speeds of 10 or 100 frames per second (fps) was used. It was found that the higher exposure rate had a lower chance of recording the sporadic events, where as the slower rate improved chances of recording multiple events in one frame, which appeared as a single brighter event, observable by eye. The second camera was operated at 24 to 64 fps, with the arc lamp in pulsed mode. This configuration meant that there was a 120 cycle (2.4 s) of illumination with alternating light and dark periods. It was found that due to the sporadic nature of the cavitation events this camera often missed events and meant that observation of the time evolution of bubble activity was not possible. This system did not allow observation on time scales that would relate to single bubble activity, but rather the coalescence of a number of bubbles into observable clouds. A third camera was used in an attempt to achieve better time resolution. It was operated at speeds of a few hundred up to 1000 fps, which meant that it was possible to record successive frames of a single cavitation cloud, which could also be observed by the users. The final (fourth) camera used was a variation on the third camera. It was used with the arc lamp continuously on and it recorded directly onto 100 feet of film at an effective frame rate of approximately 185 fps. This allowed the authors to record all cavitation events during the exposures with the temporal information provided by the location of the film (depending on film speed). Using this detection technique Willard was able to identify a sequence of events for the cavitation activity observed. Firstly, stable nuclei were dragged into the focal region by radiation pressure and streaming. This is unexpected since the peak pressures occur in the focal region, which is where it would be expected that the majority of the cavitation bubbles would form. It could be that radiation pressure forces cavitation out of the focal region, while the pre-focal pressure is sufficient to generate cavitation. The author called this the 'pre-initiation' stage. The next stage, 'initiation' occurred when, above resonant sized bubbles stream into the focal region (these were visible by the eye). The final, 'catastrophic' stage occurred when these above resonance bubbles broke-up into a cloud of smaller bubbles (which was accompanied by a 'loud snapping noise'). It was found that this sequence of events occurred in degassed and aerated water. However, the authors do not quantify the gas content of the water. This study was able to identify cavitation activity with sufficient sensitivity that it was possible to identify three specific stages of cavitation activity in water, which occurred over time frame of a few milliseconds. In this study the authors claim to be able to view cavitation bubbles generated by a 2.5 MHz ultrasound field. However, a resonant bubble at this frequency would be approximate

2.6 μm in diameter, which would not be seen by the naked eye. Visual observation was used in this paper to confirm the presence of cavitation cavity. This would suggest that the results discussed here refer to clouds of cavitation bubbles rather than to single events. In addition, the acquisition rates would be to slow to capture events occurring at MHz frequencies.

Crum and Nordling (1979) used direct observation in order to determine the velocity of transient acoustic cavitation exposed to a standing wave. The acoustic cavitation wave was generated within an acoustic resonator that consisted of two matched cylindrical transducers (55 kHz) separated by a thin glass cylinder mounted between them. The resonator generated acoustic cavitation at its geometric centre, directly underneath the glass cylinder. A high speed stroboscope and camera were positioned at one of the flat parts of the cylinder in order to image the cavitation. The photographs were mostly taken using a 35 mm camera with a shutter speed of 1/15 s. This shutter speed was used so that it would increase the probability of observing a cavitation event during image acquisition. This experimental method allowed them to identify 'feathery' tracks that were caused by transient acoustic cavitation within the standing wave field created by the ultrasound transducers. These tracks were comprised of multiple bubbles that were travelling as a group (due to streaming) and retained their clustered configuration. This technique highlights the limitations of a direct observation technique for observing events with the time scales of MHz frequency ultrasound, since even at this lower frequency only activity on the macroscopic scale could be observed.

Luther *et al* (2001) used a high-speed (2250 fps) observation technique to monitor acoustic cavitation generated from a standing wave field created using plane wave 20 kHz transducer, with peak anti-node pressures of 0.2 MPa. A CCD camera (KSV, HiSIS, 2002) was used to take 2250 fps in order to observe the bubble activity in this standing wave field within a tap water filled Perspex cuvette (5 x 5 x 10 cm). Two methods were used to illuminate the bubbles. Firstly, short LED flashes (3 μs) synchronised to the acoustic driving pulse and camera acquisition time, to backlight the bubbles. This caused them to appear as dark regions in the images. Secondly, CW side lighting was used so that the camera recorded scattered light from the bubbles. This technique resulted in short streaks since the bubbles were moving during the image acquisition. Digital image processing was used to extract the bubbles positions, sizes, and shapes. The authors claim that this system was able to track individual bubbles,

since the CCD was 1x1 cm^2 with 256x256 pixels, giving a spatial resolution of approximately 40 μm. The radius of a resonant bubble at this frequency would have been 320 μm, so this would have been possible. However, the frame rate would not have been sufficiently high in order to monitor the oscillations of bubbles at this frequency. This technique would however not be suitable for MHz frequency ultrasound.

3.7 Summary

This chapter has discussed the different detection methods that have been used to identify cavitation activity. An aim of this present study is to design and construct a cavitation detection system for ex-vivo and eventually in-vivo and clinical use (§1.2.2). However, from a review of the literature it seems that no two cavitation detection techniques are the same. This makes the identification and quantification of the relative sensitivity and efficacy of each technique difficult. It would seem that direct observation was the most sensitive technique to acoustic cavitation activity since it was possible to identify cavitation on the single bubble scale. However, this technique would be the least useful clinically. Similarly, sonochemistry and sonoluminescence would be impractical to implement for clinical applications, and the sensitivity of these measurements relies on the volume of solution exposed and the detection technique used to identify chemical changes. Pulse-echo ultrasound (a form of active cavitation detection) would be the next most sensitive detection technique as it is used to directly interact with the bubble, and in some of the publications discussed above was shown in interact with a single bubble. This has the disadvantage of not being able to be used simultaneously with HIFU exposures. Passive cavitation detection is a commonly used technique, but is the most difficult to quantify. This technique relies on the secondary process of acoustic emission, for which, depending on the apparatus used for detection, sensitivity can vary significantly. It is not clear from the literature if it is possible to identify single bubble activity, or whether this type of detection technique is only looking at multiple bubbles. Passive cavitation detection can be used *in vivo* but the interpretation of the detected acoustic emissions remains critical. This will be investigated further in this thesis.

An ideal in-vivo cavitation detection system would be able to distinguish between the different types of acoustic cavitation and boiling (Chapter 2) produced during a HIFU exposure. As the detection technique is a secondary goal compared with

successful HIFU treatment, in order to perform pulse-echo active cavitation detection the HIFU exposure would need to be pulsed (Rabkin *et al*, 2005). This technique relies on scattering from bubbles, and so, in in-vivo application, it could give false positives from scattering from other sources (bone, tissue interfaces etc) within the body. It can however, give a high degree of spatial information, but only during the HIFU 'off time'. The use of pulse-echo techniques to interrogate cavitation in the focal field only when with the HIFU field is off, would mean that the heating from the HIFU exposure would be reduced unless the exposure time is increased. Therefore a compromise between the allowable 'off time' (~ms) and the frequency at which the cavitation activity would be interrogated is required.

Unlike active detection methods, passive cavitation detection does not interfere with HIFU treatment delivery regime and the detected acoustic emissions (subharmonics, superharmonics and broadband emissions) can be a reliable indicator of bubble activity (discussed in Chapter 4) since they are generated from bubble motion. However, these signals are likely to be very weak in comparison to those from HIFU field, and thus would need significant RF filtering and amplification. Accurate interpretation of the acoustic emissions would also be critical in discerning bubble behaviours, which should allow identification of non-inertial and inertial cavitation.

Impedance change seems to be a useful technique for monitoring backscatter from bubbles that would be easy to implement in any HIFU drive system. The main problem with this technique arises from the interpretation of the signals, since it only indicates a source of scatter at the HIFU focus, and it is unclear from the literature how sensitive this technique would be to, for example, a single bubble. Nevertheless, it would be possible to monitor this throughout the HIFU exposure.

No single cavitation detection technique is thought to be sufficient to provide a comprehensive picture of the cavitation activity generated by HIFU exposures for an in-vivo detection system. This review therefore suggests that it would be prudent to mix different complementary detection methods, such as, for example, the use of passive and active cavitation detection with impedance change measures. Direct observation or sonochemical/sonoluminescence does not have any direct in-vivo application. However they could be used to provide quality assurance for the in-vivo cavitation detection system. For example, if a high speed camera could be used to identify single bubble behaviour in conjunction with the in-vivo cavitation detection system it would provide a calibration technique for the detection system. It could also be used to compare the

detection thresholds of indirect measures as a function of the number of events (i.e. to determine the sensitivity). Unfortunately a high speed camera was not available for this study, but a sonochemical study was done.

4 – Development of a cavitation detection system

This chapter details the development and construction of the detection system used for the cavitation studies described in subsequent chapters.

4.1 Acoustic Emissions

A pre-existing bubble driven by an acoustic wave will oscillate and, in turn, emit pressure waves (Neppiras, 1980). These emitted pressure waves are referred to as acoustic emissions. In an introductory paragraph, Leighton (1994) described the characteristics of these emissions as a function of the drive power, which would determine the in-situ acoustic peak pressures. When the drive power is "low", the bubble oscillates linearly and only emits pressure waves at the ultrasound drive frequency (f_0). However, at higher drive power it can undergo non-linear oscillation, including collapse, and the acoustic emissions generated may comprise broadband emissions and superharmonics ($n_i f_0$), ultraharmonics ($(2n_i+1)f_0/2$) and subharmonics (f_0/n_i) of the drive frequency (where n_i is a positive integer). These acoustic emissions are described in more detail below.

4.1.1 Subharmonic

The origins of subharmonic emissions remain unclear despite having been the focus of numerous research efforts (Vaughan, 1968; Neppiras, 1969a; Neppiras, 1969b; Lauterborn, 1976; Prosperetti, 1977; Neppiras, 1980). Leighton (1994) discussed the possible sources of subharmonic from bubbles driven by a linear acoustic field. His discussion is summarised here.

Subharmonic emissions from inertial (transient) cavitation may be generated by a prolonged bubble expansion phase, and delayed collapse. Thus, if the bubble were to survive the initial collapse and undergo motion such as the example shown in Figure 4.1(b), surviving several acoustic cycles before collapse, subharmonic emissions may be emitted. The probability of generating subharmonic emissions decreases as the order of subharmonic increases. Neppiras (1980) proposed a second mechanism for the generation of subharmonic emissions from inertial cavitation activity. Consider a bubble that is near the pressure threshold between non-inertial and inertial cavitation activity, and with an equilibrium radius near the size that would be resonant at $f_0/2$.

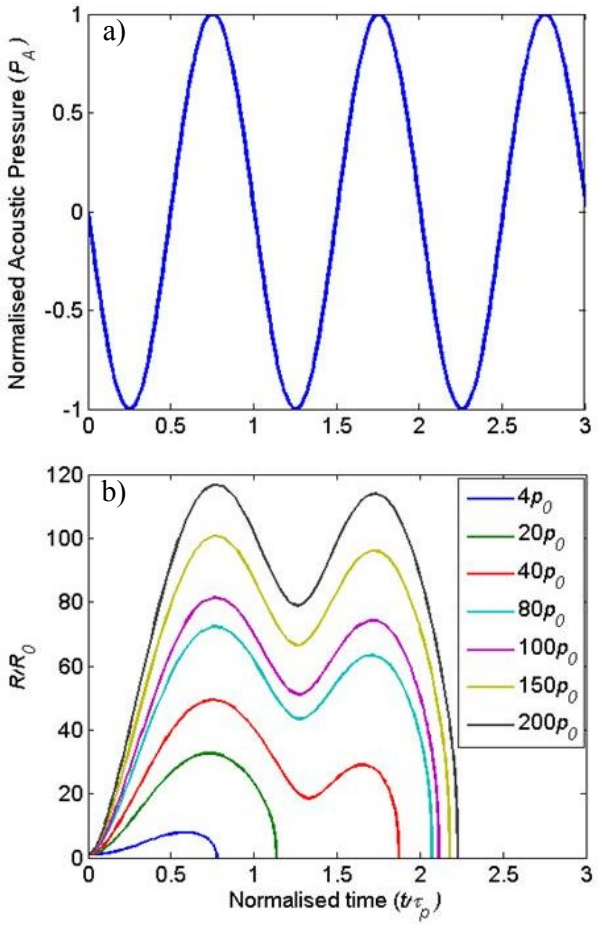

Figure 4.1. Radius-time curves (b) for a 1 μm bubble in a 500 kHz showing the effect of increasing P_A (shown as multiples of p_0 in the figure legend) on an air bubble in water. The time is measured in multiples of the acoustic period, which is shown in (a). These plots are calculated from results shown in Leighton (1994).

The periodic unstable oscillations from a bubble, driven at twice its resonant frequency, close to the pressure threshold, could generate subharmonic emissions. This type of behaviour is shown in Figure 4.2 (Neppiras, 1980). This numerical solution, predicts that a bubble with an equilibrium radius of 260 μm (which would have a linear resonance at 13.1 kHz) driven at 24.5 kHz, and therefore executing approximately 13 cycles for around 25 acoustic cycles, would undergo oscillations that could generate subharmonic.

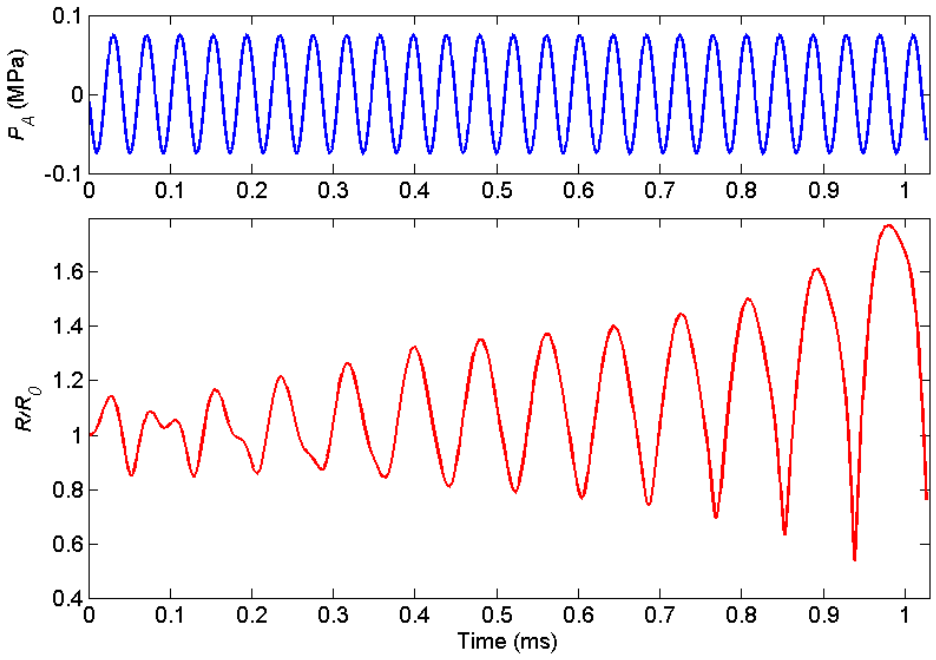

Figure 4.2. Unstable motion of a bubble driven at twice its linear resonant frequency, where R_0 = 260 μm, P_A = 0.075 MPa and f_0 = 24.5 kHz (Neppiras, 1980).

Neppiras (1980) summarised the possible mechanisms for subharmonic emissions from non-inertial (stable) cavitation. The first of these is the generation of surface instabilities. Faraday (1831) was the first to report the appearance of waves at half of the driving frequency, on the surface of water. These Faraday waves, on the surface of a bubble, could be a source of subharmonic emissions (Neppiras, 1969a; Neppiras, 1969b). However, a study by Strasberg (1956) showed that sound emissions caused by so-called "shape" oscillations resulted in a negligible sound pressure. Strasberg (1956) found a rapid fall-off in the velocity potential with distance from the bubble. This rapid decay suggests that subharmonics would only be detected close to the bubble. A more detailed discussion has been provided by Leighton (1994). A second mechanism for subharmonic emission from non-inertial cavitation may be from driving bubbles that are twice the resonant size for the ultrasound driving frequency. Eller and Flynn (1969) published a calculation of the threshold acoustic pressure required for a bubble to emit a signal at half the ultrasound drive frequency. Neppiras (1969a) suggested that generation of $f_0/3$ (or higher integer multiples of this n_i) subharmonics through this mechanism is unlikely due to the inability of the bubbles to grow to the sizes required. Leighton (1994) comments that it is unlikely that subharmonic signals are solely caused

by emissions from bubbles that are integer multiples of the resonant size for the ultrasound field. As an example, he showed that no bubbles of sufficient size were present (using a direct observation technique) and demonstrated that subharmonic emissions were still detected (Leighton *et al*, 1993).

This section has discussed the different possible mechanisms by which subharmonic emissions may be generated by both non-inertial and/or inertial cavitation. The half harmonic ($f_0/2$) is the first in the series of subharmonics, and will be referred to specifically throughout the rest of this study.

4.1.2 Broadband Emissions

Broadband emissions are thought to originate from inertial cavitation only, and the cause of these emissions is presumed to be the steep shock fronts associated with collapsing cavities (Neppiras, 1969a).

4.1.3 Superharmonics

The origins of superharmonic emissions can be deduced by considering the oscillations of a bubble by representing the nonlinear response of this system with a power series expansion (Leighton, 1994).

$$\Phi(t) = \in_0 + \in_1 \zeta_d(t) + \in_2 \zeta_d^2(t) + \in_3 \zeta_d^3(t) + ... \quad (4.1)$$

where $\Phi(t)$ is the amplitude response of a bubble to a driving force ($\zeta_d(t)$) and $\in_n$ is the coefficient of the n^{th} term. If the driving force is an ultrasound wave at a single frequency, this would give an acoustic pressure of $P(t) = P_A\cos(\omega t)$. Substitution of this into equation 4.1 demonstrates how superharmonics of the drive frequency can be present. For example, the ζ_d^2 term gives a harmonic at twice the drive frequency from the $2\cos^2(\omega t) = 1 + \cos(2\omega t)$ term, and the ζ_d^3 term would produce a harmonic at three times the driving frequency. Superharmonic emissions are generally associated with the non-linear stable oscillations characteristic of non-inertial cavitation (Miller, 1981).

4.1.4 Ultraharmonics

Lauterborn (1976) suggested that ultraharmonic emissions can be generated from bubbles driven by an ultrasound frequency that is below their resonance. Ultraharmonic emissions are usually reported to be associated with the non-linear bubble oscillations

that generate subharmonic emissions (Eller and Flynn, 1968; Neppiras, 1969; Prosperetti, 1975; Leighton, 1996).

The mathematical description of a non-linear oscillator (Equation 4.1) does not account for the generation of ultraharmonics. In order to do this, it is necessary to use a different mathematical model. Prosperetti (1976) describes some general features of non-linear systems using the Duffing equation to describe the non-linear oscillation,

$$\frac{d^2X}{dt_d^{\,2}} + f\frac{dX}{dt_d} + \Omega_0^{\,2}X = F\cos\Omega t_d + \Gamma X^3, \tag{4.2}$$

where Γ is a real constant with dimensions of ms^{-2}. Using this equation, Prosperetti demonstrated that this non-linear system could result in large amplitude oscillations at frequencies above the drive frequency that may include ultraharmonics.

Basude and Wheatley (2001) highlighted an apparent lack of interest in the use of ultraharmonic emissions for bubble detection, even though they could be generated by the non-linear pulsations from both non-inertial and inertial cavitation. Superharmonics were often monitored in preference to these since they would be generated more readily by non-linear bubble oscillations. However, in HIFU where non-linear propagation of the acoustic field can generate significant superharmonics (§1.3.2), ultraharmonics could prove a useful insight into the bubble activity.

4.1.5 Summary

Acoustic Emission	Non-inertial Cavitation	Inertial Cavitation
Subharmonics, $\frac{f_0}{n_i}$		
Ultraharmonics, $\frac{(2n_i+1)f_0}{n_i}$		
Superharmonics, $n_i f_0$		
Broadband,		

Table 4.1. The possible acoustic emissions that can be generated from inertial and non-inertial cavitation, where blue is possible and red is not possible.

Table 4.1 shows the possible acoustic emissions generated during acoustic cavitation. This suggests that a passive cavitation detection system needs to monitor multiple emissions in order to differentiate between non-inertial and inertial cavitation.

4.2 Passive cavitation detection system

A passive cavitation detection system generally comprises four basic components. The first is a passive sensor, used to convert the pressure waves it detects into an electric signal. A second element in a detection system provides for filtering and amplification of this electric signal. Filtering in this context refers to the use a physical RF filter, which may be used as part of the analogue signal processing of the detected signal. The third element, data acquisition, is the component in which the electrical signal is digitised and stored. Finally, signal processing is used to analyse the detected signal. A simple example of such processing would be the performance of a fast Fourier transform on the detected signal to identify its constituent frequency components.

This description of a passive cavitation detection system serves mainly to highlight the different components are required and is by no means an exhaustive list of the possible elements that could be used. For this study, the main area of interest was to use a passive cavitation detection system to investigate the acoustic cavitation activity, during continuous wave exposures, using a 1.7 MHz HIFU transducer in a variety of target media. The following sections describe the components used for the passive cavitation detection system in this study.

4.2.1 *Sensors*

Two types of passive sensors, constructed using polyvinylidene fluoride (PVDF) or a piezoceramic, were used. As discussed in the previous section, a passive cavitation detection system is most effective when used to monitor different acoustic emissions simultaneously. This requires that the use of either a single sensor with broadband sensitivity, or of a combination of sensors.

The PVDF sensor used was designed and built at the National Physical Laboratory (Teddington, UK), for the measurement of cavitation activity in ultrasonic cleaning baths (Zeqiri *et al*, 2003a). This novel sensor was a hollow, open-ended cylinder, of which the inside surface was a 110 μm PVDF film. The outer part of the cylinder was a 4-mm thick acoustic absorber designed to attenuate MHz frequency ultrasound (Zeqiri *et al*, 2003a). This design means that it should only be sensitive to cavitation events

occurring within the hollow region of the cylinder. Figure 4.3 shows reflection measurements made using a network analyser (HP8712ES, Agilent systems, Waterloo, Canada), which shows the relatively flat, broadband response of the sensor over the 0.1-10 MHz range. A decrease in the reflected energy would be an indication of the transducer converting this energy from electrical to acoustic energy. This 'NPL sensor' was used to perform preliminary studies into the cavitation activity that could be induced within ex-vivo bovine liver tissue (§4.3). Tissue samples were prepared (§5.4) that completely filled the hollow volume of the sensor (diameter 34 mm, length 32 mm). The geometry of the sensor, meant that it was most sensitive to emissions occurring along its central axis, therefore the HIFU focus was targeted here. This sensor provided a useful tool for preliminary studies of cavitation activity, but clearly was unsuitable for human clinical applications.

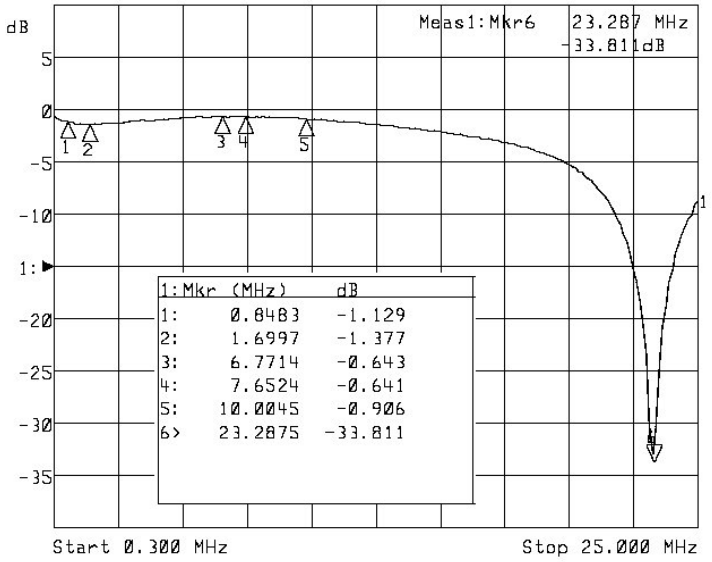

Figure 4.3. Electrical reflection measurements over a range of 0.3-25 MHz, for the NPL sensor. The markers show data at frequencies of interest.

In an effort to develop a passive cavitation detection system that would be more relevant clinically, piezoceramic focused transducers, with centre frequencies of 1, 7.5 and 10 MHz, were tested. The depth in tissue at which it is possible to investigate acoustic emissions depends on the focal length of the sensor. For the ex-vivo applications described here, a minimum focal distance of 25 mm was required. However, for the study involving whole perfused porcine livers this was longer, as will be discussed in §10.4.

A 1 MHz focused sensor (Panametric, 1.5 cm diameter, focal length 4 cm) was used to investigate signals that were below the drive frequency (~1.7 MHz). Figure 4.4 shows network analyser electrical reflection measurements for the 1 MHz sensor. The response of this sensor was such that it was suitable for investigation of subharmonics up to and including the half harmonic and low frequency broadband emissions (0.1-0.8 MHz). The half harmonic at 1.7 MHz (0.85 MHz) is marked in the figure. This device was usually used in conjunction with either the 7.5 or 10 MHz sensor.

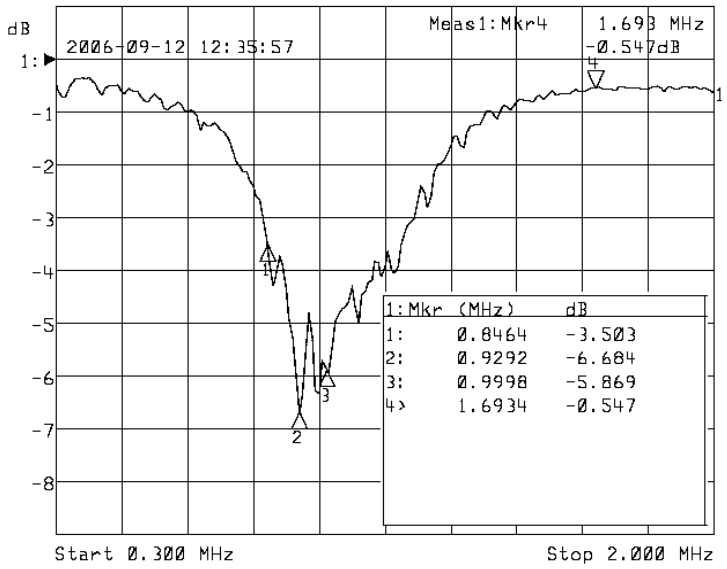

Figure 4.4. Electrical reflection measurements over the range 0.3-2.0 MHz for the 1 MHz focused passive cavitation sensor.

When used in conjunction with the 1 MHz sensor, the 7.5 MHz sensor (Aerotech Laboratories, Lewistown, PA, 25 mm diameter, 70 mm focus, 139303HR) was used to investigate acoustic emissions above the drive frequency. This includes superharmonics, ultraharmonics and high frequency broadband emissions. Figure 4.5 shows the electrical reflection measurements for the 7.5 MHz sensor, made using a network analyser. This demonstrates that this sensor sensitive over the range 0.3-10 MHz.

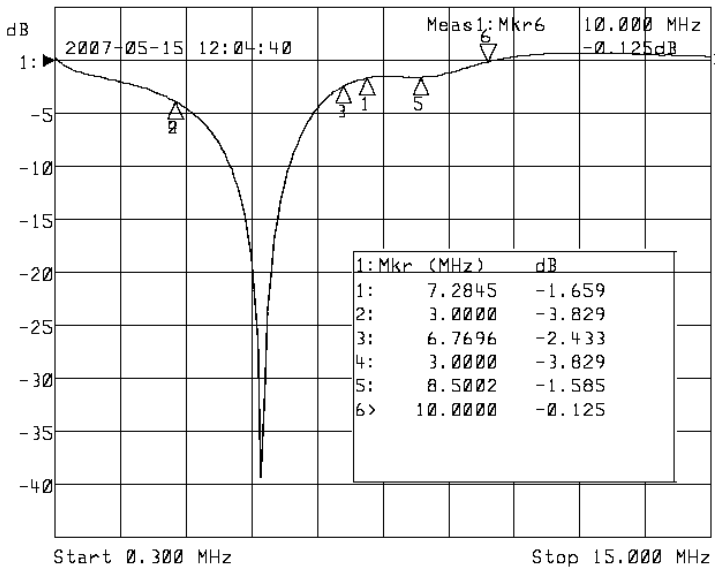

Figure 4.5. Electrical reflection measurements over the range 0.3-15.0 MHz for the 7.5 MHz focused sensor used in the passive cavitation detection system.

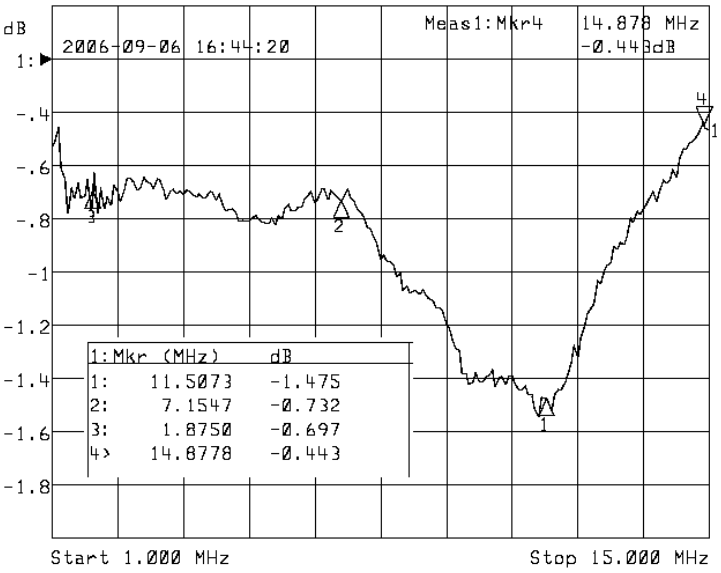

Figure 4.6. Electrical reflection measurements over the range 1-15.0 MHz for the 10 MHz focused passive cavitation sensor.

Figure 4.6 shows the electrical reflection measurements for the 10 MHz sensor (Panametric, 3.0 cm diameter, focal length 4.5 cm), made using a network analyser. This sensor was used predominantly for the detection of all acoustic emissions above the drive frequency, which was used in mainly in conjunction with the 1 MHz.

The beam profiles of the individual sensors were measured using a membrane hydrophone whilst being driven at the manufacture's specified centre frequency (See §5.3.2 for a description of the measurement technique).

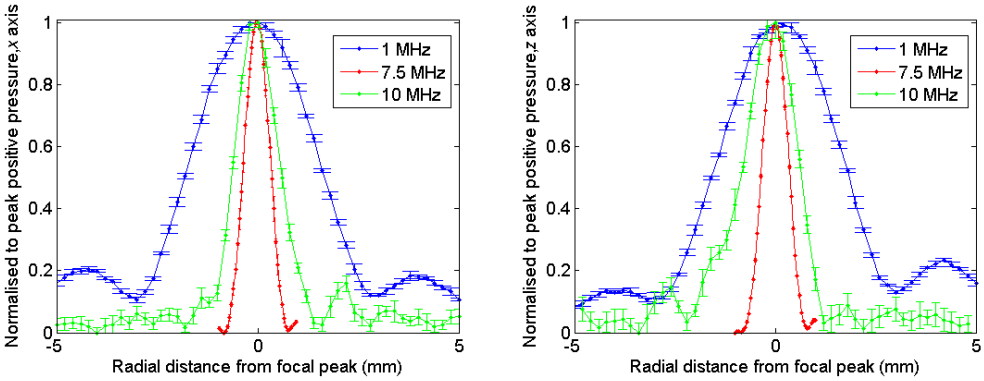

Figure 4.7. The radial beam profiles for the 1, 7.5 and 10 MHz sensors used in the passive cavitation detection system measured in two orthogonal directions. Error bars shown are given by the standard deviation of the average value (n = 5). Beam dimensions are given in Table 4.2.

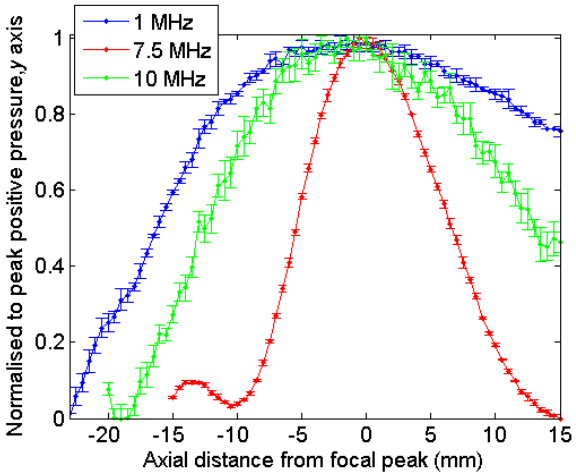

Figure 4.8. The axial beam profiles for the 1, 7.5 and 10 MHz passive cavitation sensors. Error bars shown are given by the standard deviation of the average value for n = 5.

Figure 4.7 shows the radial beam profiles and Figure 4.8 the axial profiles for the three sensors. Both figures show that the sensors have different focal volumes. The 1 MHz sensor had the widest focus and the 7.5 MHz sensor the smallest focal volume.

Sensor	Axial FWHM	Radial FWHM$_x$	Radial FWHM$_z$	FWHM Volume
1 MHz	40 ±0.5 mm	4 ±0.2 mm	4 ±0.2 mm	2680 mm^3
7.5 MHz	12 ±0.5 mm	1 ±0.05 mm	1 ±0.05 mm	50 mm^3
10 MHz	30 ±0.5 mm	2 ±0.2 mm	2 ±0.2 mm	503 mm^3

Table 4.2. The axial and radial full width half maxima (FWHM) pressure of the sensors used in the passive cavitation detection system. The FWHM volume is calculated using the assumption that the focal region is an ellipse. Uncertainty shown is the spatial precision over which the measurements were taken with the 3-D automated gantry.

Table 4.2 shows the measured FWHM and calculated associated volumes for the different sensors used. These values give an approximation to the relative volumes of the sensors that would be sensitive to acoustic cavitation. The 1.7 MHz HIFU transducer used in this study ('Mauve' transducer, see §5.1.2), and for clinical applications, had a FWHM volume of 440 mm^3 (Visioli *et al*, 1999). Assuming that acoustic cavitation is primarily generated within the HIFU focus (i.e. and does not occur in pre-focal peaks or side lobes), the ability of the passive detection system to identify acoustic cavitation depends on the overlap of these two volumes. Since the focal length, for these sensors are shorter than the focal length of the HIFU transducer (15 cm), it was not possible to align them along the acoustic axis. It was generally necessary to position them so that they were at an angle (90^0 or 45^0) to the direction of propagation of the HIFU field, which meant that the overlap of these volumes was reduced as shown in Figure 4.9. For both orientations, there is a small region that would be sensitive to cavitation activity, and the difference in overlap is small for the two intersection angles. Generally, the 1 MHz sensor was used simultaneously with either the 7.5 or 10 MHz sensors to achieve a system that was sensitive to subharmonics, superharmonics, ultraharmonics, and broadband emissions.

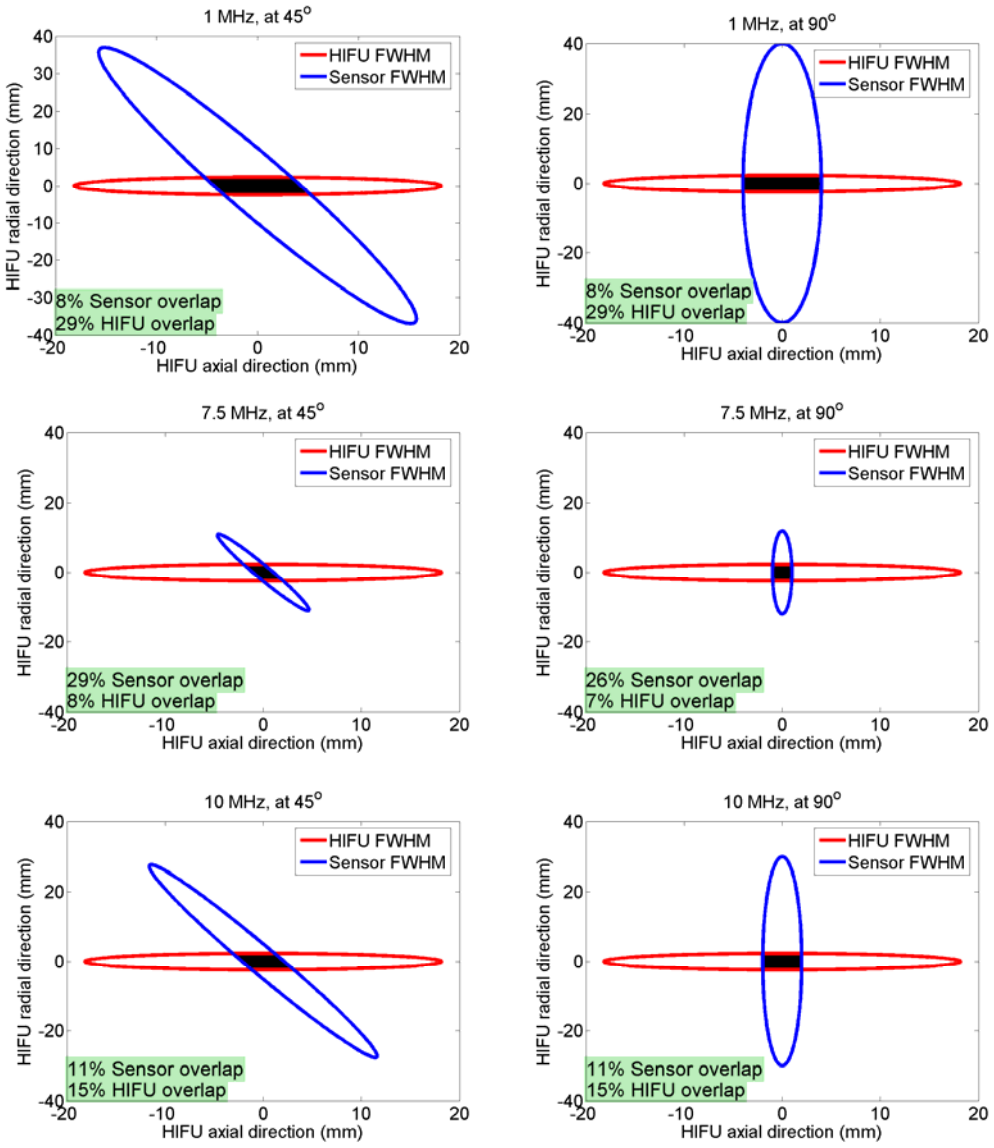

Figure 4.9. 2-D representation of the axial FWHM pressures for the HIFU transducer and three passive sensors showing the region of overlap of these areas with the sensors orientated at 45 and 90^0. The percentages shown give the approximate area of overlap compared with the area represented by the FWHM of the Sensors and HIFU transducer.

For use in experiments, the sensors were aligned with the HIFU focal peak using a pulse-receive technique. Short pulses (~80 cycles) from the HIFU transducer were reflected from a spherical target and detected by the sensors approximately perpendicular to the target. The sensors were positioned on opposite sides of the HIFU beam such that the detected signal was maximised, which meant that they were co-aligned with the focal peak of the HIFU transducer in water (this technique is similar to

the pulse-echo technique described in §5.3.2). Alignment of the sensors in this way ensured that both of the different sensors FWHM would overlap at the focal peak of the HIFU transducer. However, since less than 30% of the HIFU transducers FWHM area overlapped with that of the sensors a significant proportion of the HIFU beam was not interrogated by them. This brings into doubt the ability to provide quantitative values of the total cavitation activity within the HIFU focal region, unless it is assumed that the detected signals were representative of the acoustic cavitation activity occurring throughout the focal region of the HIFU transducer. In interpreting the different acoustic emissions, it should be remembered that it is possible that the different sensors, even when used simultaneously may detect acoustic cavitation from different locations in the HIFU focus. However, particularly for a threshold study, using incremental increases in HIFU pressure, it would be expected that acoustic cavitation would be generated first in or close to the region of the focal peak, where both sensors are able to detect bubble activity.

4.2.2 *Filtering and amplification*

The aim of filtering and amplification in a passive cavitation detection system is to remove unwanted signals, and in particular the HIFU drive frequency, detected by the sensor, and to optimise detection sensitivity for the rest. This is particularly important when working with HIFU fields. Miller (1981) calculated that a 3 μm resonant bubble, oscillating in a 1.64 MHz ultrasound field of peak pressure 0.02 MPa, emits a pressure wave with amplitude approximately 10 Pa (‘measured’ 6 mm from source). Pressure waves with amplitudes in the MPa range which are common in HIFU fields may generate cavitation related pressure amplitudes that are approximately four orders of magnitude smaller than drive pressure. Filtering and amplification are therefore necessary to optimise the detection of acoustic emissions in most passive cavitation detection systems. In this study, acoustic cavitation was generated using 1.7 MHz HIFU transducers, and filters were chosen specifically for this frequency. In this section, only the radio frequency (RF) filters placed between the sensor and the acquisition system are discussed, and not the software filtering that was performed on the digitised data.

Four filters have been used, in different configurations, in the passive cavitation detection system. These are a high pass (HP), low pass (LP), notch (NF) and a band pass (BP) filter. All were provided by Allen Avionics, Inc, Mineola, NY. A low pass filter (F5099,) was used to attenuate frequencies above 0.85 MHz with a response of 25

dB/decade (Figure 4.10(a)). For example, this attenuated a 1.7 MHz signal by 80 dB. However the half harmonic ($n_i = 2$) emissions from bubble activity were only attenuated by 0.7 dB.

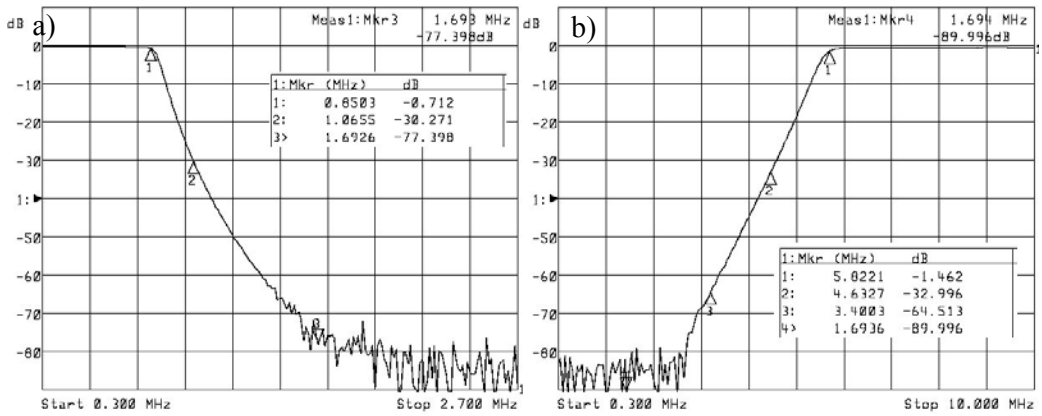

Figure 4.10. Electrical transmission measurements for the (a) LP and (b) HP filters used in the passive cavitation detection system.

The high pass filter (F5100) was used to pass frequencies above 6 MHz with a response of 25 dB/decade (Figure 4.10(b)). For example, the 1.7 MHz signal was attenuated by 90 dB. These two filters provided the filtering for the majority of studies using the 1 and 10 MHz sensors. However as the system developed, band pass and notch filters were introduced into the system.

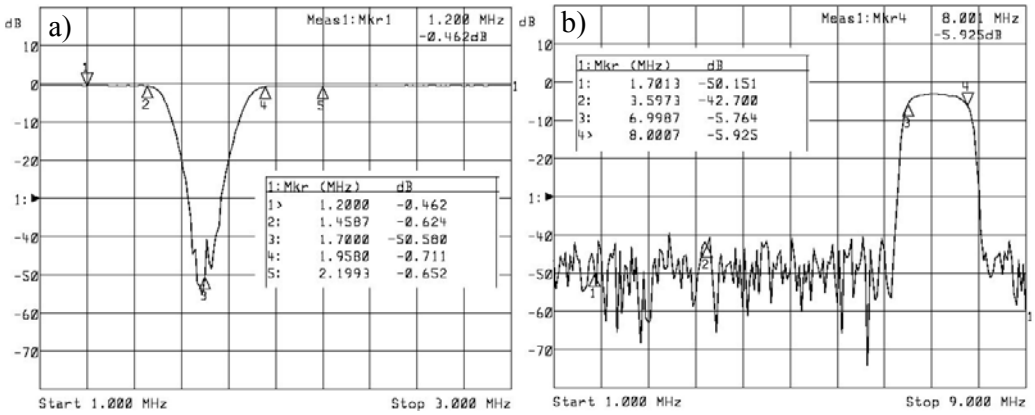

Figure 4.11. Electrical transmission measurements for the NF (a) and BP (b) filters used in the passive cavitation detection system.

The notch filter (F5181) was used specifically to remove the 1.7 MHz component of the detected signal. This filter had a 50 dB/decade response (Figure 4.11(a)), and attenuates

the 1.7 MHz component by 50 dB. It was used in conjunction with the other filters, as it provided additional attenuation of the drive frequency. The band pass (F5204) filter was the final addition to the passive cavitation detection system replacing the HP filter, and was used in conjunction with the 7.5 MHz sensor. This filter had a 40 dB/decade response (Figure 4.11(b)) and an attenuation of 50 dB at 1.7 MHz.

Two models of pre-amplifier were used. The first was a HP461A pre-amplifier (Agilent Technologies Inc, Santa Clara CA, USA), which had a broadband response of 0.001-150 MHz and a user selectable amplification of 40 or 60 dB. In an effort to reduce the RF noise in the detection system, these pre-amplifiers were replaced with some low noise pre-amplifiers with a noise factor of 2.5 dB. These Advanced Receiver Research pre-amplifiers (7866, Ar^2 Communication Products, Burlington, CT, USA) had a broadband response between 0.1-30 MHz with a 20 dB amplification. This lower amplification meant that two or more pre-amplifiers were used in series (generally separated by filters) to achieve an amplification close to that of the HP461A pre-amplifiers. Figure 4.12 shows a comparison of the frequency response of these two pre-amplifiers.

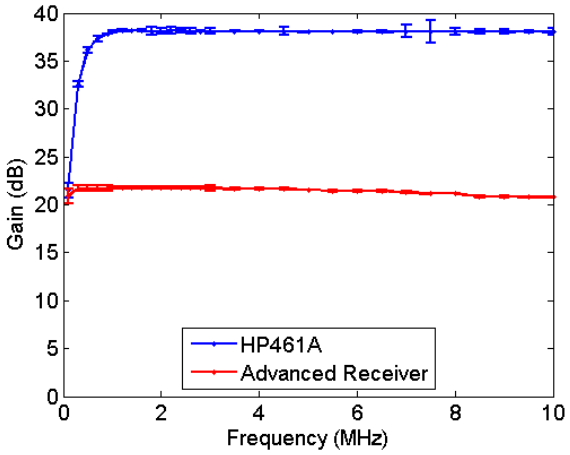

Figure 4.12. The frequency response between 0.1-10 MHz for both pre-amplifiers used in the cavitation detection system.

Figure 4.12 shows that both pre-amplifiers had a linear response over 1-10 MHz, however that of the HP461A response drops off steeply below this frequency, which affects the half harmonic (0.85 MHz) measurements.

4.2.3 Data acquisition

The analogue signal generated by the sensors, filtering, and amplification is digitised at the data acquisition stage. There were two main considerations in the design of this system. Firstly, the sample rate of the digitisers needed to be sufficiently high such that the Nyquist criterion was satisfied for the highest frequencies of interest. In this study, this was 12.5 MHz, which would require a minimum sample rate of 25 MHz. The second consideration was the ability to record a continuous dataset on multiple channels for at least the shortest exposure used (2 s).

Preliminary studies were conducted using the peak detection function on the frequency analysis software of a digital oscilloscope (Waverunner LT3422, LeCroy Ltd, Abingdon, Oxfordshire, UK). This oscilloscope was connected to a computer (Dell Notebook), via an RS232 cable, in order to download the peak spectrum from each exposure. For this initial study, the peak amplitude of the detected half harmonic (0.864 MHz) was recorded for a 2 s exposure. However, the drawback to this technique was that it was not be possible to identify fluctuations in detected half harmonic during the exposure. As discussed at the beginning of this chapter, monitoring a single frequency related to acoustic emissions is not sufficient for differentiating between the different types of acoustic cavitation activity which occur during HIFU exposures.

The oscilloscope used in the preliminary studies was replaced with a custom-built data acquisition system, specifically designed to acquire data continuously from multiple (up to 8) channels (i.e. from the two separate sensors) for at least 2 s. The system used two 4-channel, 8-bit data acquisition cards, an MI.2021 (50 MS/s) and an MI.2031 (100 MS/s) from Spectrum Systementwicklung Microelectronic GMBH (Grosshansdorf, Germany). Both cards were installed within a desktop computer (P4SCT, SuperMicro Computer Inc, San Jose, CA, USA), which was chosen as its motherboard had a dual PCI bus into which both cards could be installed. In an effort to maintain sufficient sample frequencies on multiple channels, the system was operated in 'first in first out' (FIFO) mode. This allowed data to be recorded continuously from the cards and transferred it directly to the PC during data acquisition. Since these cards only had a hardware buffer size of 16 MS, this meant that the maximum time two channels, operating at 50 MS/s, could store continuously was 160 ms. Upgrading the onboard memory buffer to sizes that could store at least 2 s was considered to be too costly. Thus, the onboard RAM of the computer was used to buffer the acquired data, which

was then written to the computer's hard drive after completion of the acquisition. This provided a lower cost solution than purchasing data acquisition cards with sufficient on board memory, but was the reason why dual PCI buses were needed. The operation and setting of the cards were controlled using a C++ program, provided by the card manufacturer. However, this program required some modification in order that the two cards could be run synchronously in FIFO mode. This modification allowed their operation in a master/slave configuration, which meant that it was possible to acquire data simultaneously on up to eight separate channels. The greater number of channels used meant a reduction in available buffer size, which in turn led to a trade off between sample frequency and length of acquisition time. For example, using four channels (two per card) at a sample rate of 40 MHz gave a maximum acquisition time of 2.04 s. An important aspect of programming the system for each acquisition was ensuring that the dynamic range of each card was set appropriately for the exposure levels used. This generally meant that the amplitude of the detected signals filled approximately 80% of the dynamic range selected. A MatLab (v 7.0.1 R14, MathWorks Inc, Natick, MA, USA) routine was written to inspect the dynamic range setting after each exposure so that it was possible to adjust the setting for subsequent exposures. Figure 4.13 shows an example of the output from this program, in this case, 4 channels were used and an indication of the amount of the 8-bit (±128 levels) dynamic range that were filled is given. Ensuring that the dynamic range setting was optimised meant that the system was able to distinguish between the different frequencies of interest and minimising quantisation error. As the system recorded the data as signed 8-bit integer values into binary format, it was critical that the dynamic range settings used were known in order to convert them back into the detected voltage signal. The main disadvantage of this data acquisition technique was that it was not possible to view the recorded signals during the exposures.

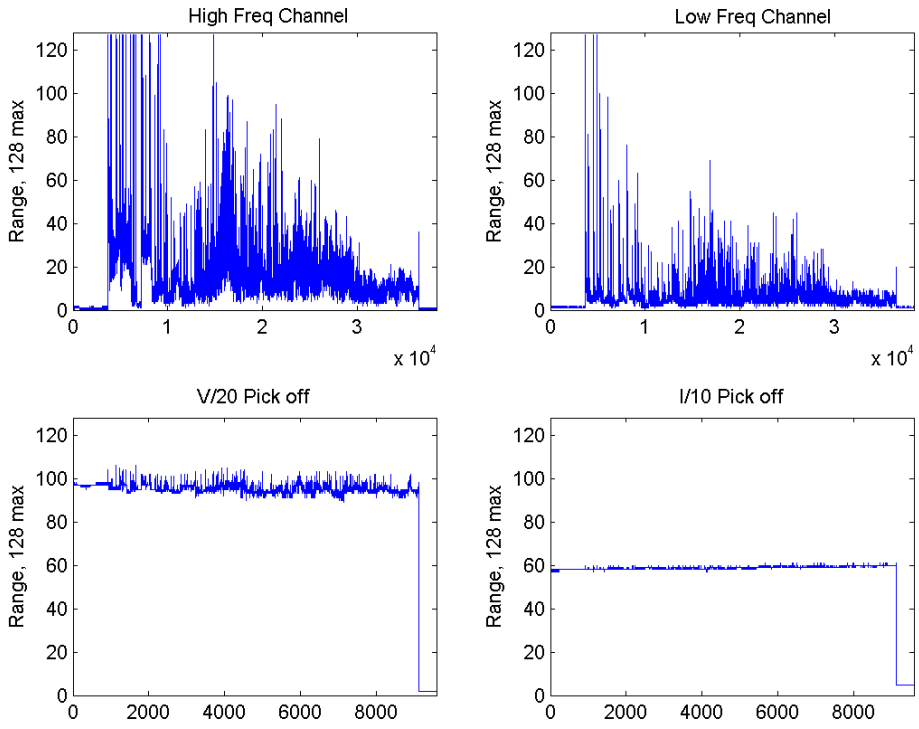

Figure 4.13. An example of the output from the MatLab routine used to check the dynamic range setting for each exposure. The vertical axis gives the value of the detected signal as a signed 8-bit integer level, and the horizontal axis is the length of the data set, each value was averaged over 16384 points. The term 'Pick off' referes to the device that was used to monitor the drive voltage and current, which is described in section 5.1.1.

For acquisition times longer than 16 s (the maximum possible continuous acquisition time with a sample frequency of 20 MHz and up to 8 channels), the proprietary oscilloscope software supplied by the card manufacturer was used (SBench). This software was operated in a similar way by acquiring 37 data sets per second of length 4096 points at regular intervals. This acquisition mode meant that it was possible to acquire signals over a much long period (limited by the PC storage capacity) but could only acquire data as short snapshots, which whilst not ideal for studying the transient nature of acoustic cavitation was useful to monitoring long exposures in which none occurred.

4.2.4 Signal processing

The data acquired from each exposure was stored in an 8-bit binary format on the hard disk of the data acquisition computer. Each operational channel generated a single file

of up to 350 MB, depending on sampling frequency and acquisition time. Converting these files into ASCII format increased the size further, making it impractical to view directly the recorded voltage signal from the sensors. Instead, it was necessary to perform frequency analysis on the data to investigate the specific frequencies of interested that were related to bubble activity.

The signals from the passive cavitation detection system were always split into two channels of data, regardless of whether single or dual sensors were used. Each data set was processed individually, but using a similar technique. A MatLab program was used to read and covert the data back into a voltage/time format. This was done on sequential sub-data sets, as it was not possible to do this on a complete data set as it exceeded the memory allocation for the MatLab software. This program then performed fast Fourier transforms (FFT) on the voltage data of a user specified data set length (of either 4096, 8192 or 16384 points). A Hanning window function was applied to every voltage/time data set prior to performing the FFT (Smith, 1997) to minimise spectral leakage.

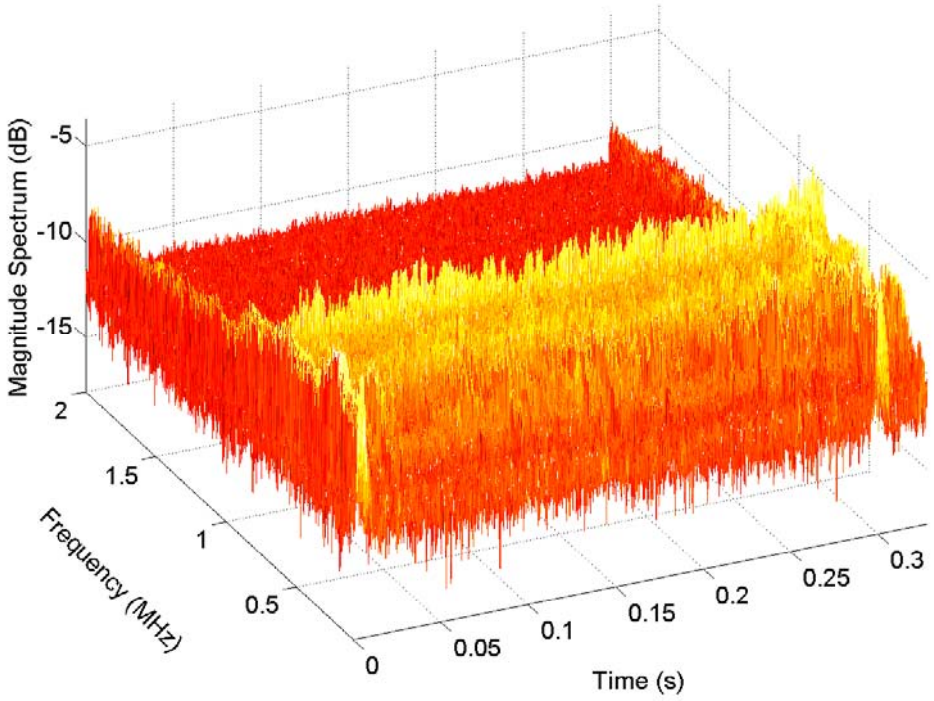

Figure 4.14. The frequency spectra detected using the 1 MHz sensor with the low pass filter at a sample rate of 25 MHz for the first 0.3 s of an 1700 W/cm^2 (2.02 MPa) exposure using a 1.69 MHz HIFU transducer in degassed water. Half harmonic and broadband emissions can be seen in this plot.

Figure 4.14 and Figure 4.15 show truncated spectra after the separate FFT calculations on the data acquired from the 1 and 10 MHz sensors. The exposure was 2 s in length, however only 0.3 s subsets of this could be plotted due to memory limitations in the computer running MatLab. These figures highlight the problems encountered when processing and displaying data of this quantity and type.

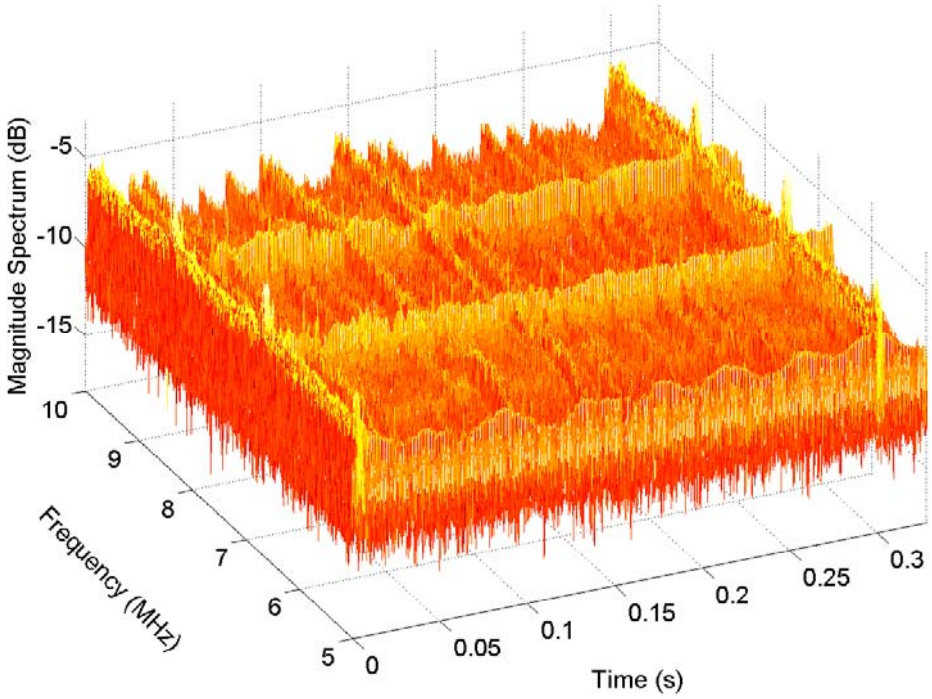

Figure 4.15. The frequency spectra for the first 0.3 s of an 1700 W/cm^2 (2.02 MPa) exposure using a 1.69 MHz HIFU in degassed water, detected using the 10 MHz sensor with the high pass filter (§6.1.2) with a 25 MHz sample rate. Broadband emissions and superharmonic can be seen in this plot.

For the data shown in these figures, the FFT calculations were performed over 16384 points for which the data acquisition rate was 25 MHz. The settings used for the acquisition and processing of the data give this data set a temporal and spectral resolution of 0.6 ms and 1.5 kHz, respectively. In these plots, it is possible to identify, half harmonic (0.846 MHz), broadband emissions and superharmonics (6.77 and 8.46 MHz), but it is not possible to identify ultraharmonics.

In an effort to quantify the specific frequencies of interest, the MatLab program was able to perform peak amplitude detection for each frequency over a narrow bandwidth. This included the half harmonic (0.846 MHz), ultraharmonic (7.62 MHz) and 4th superharmonic (6.77 MHz). The peak value was measured with a tolerance of ±5

times the spectral resolution. These values were stored at each time point for which an FFT calculation was performed.

Broadband emissions were obtained using a two step process. Firstly, a comb software filter was applied in order to remove any contribution from the super and ultra harmonics (as shown in Figure 4.16). This software filter sets the amplitude of the spectrum for a region 0.2 MHz wide around each harmonic to zero, as shown in Figure 4.16(a). This process leaves only broadband frequency information, as shown in Figure 4.16(b). Secondly, integration over the discontinuous frequency band show in Figure 4.16(b) gives the amplitude of broadband emissions.

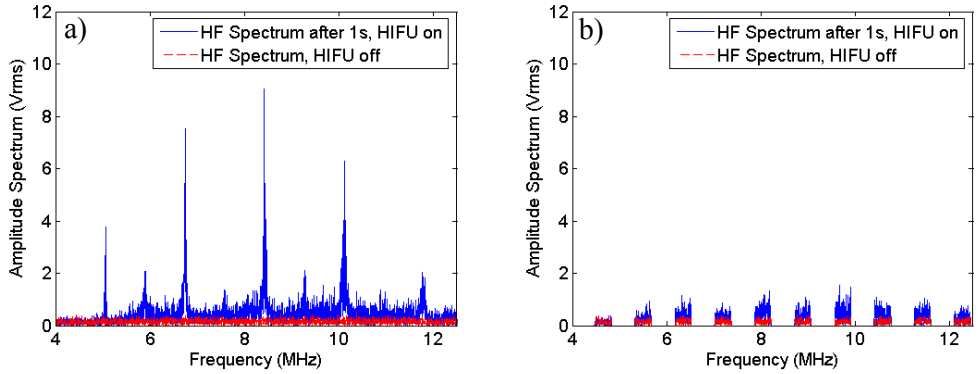

Figure 4.16. A high frequency broadband spectrum (4.0-12.5 MHz) recorded 1 s (using 214 data points) into the 4 s HIFU exposure at an I_{sp} of 2200 W/cm^2, (2.32 MPa) of degassed water without software filtering (a) and with software filtering (b) to remove the super and ultraharmonics.

These signal processing techniques were used to monitor the different acoustic emissions described in section 4.1. Subharmonics, superharmonics, ultraharmonics and broadband emissions were monitored simultaneously for the duration of each HIFU exposure. Specifically, the first subharmonic, generally referred to as the half harmonic (0.846 MHz), the fourth superharmonic (6.77 MHz), the '$9f_0/2$' (n_i = 4) ultraharmonic (7.62 MHz) and broadband emissions. The broadband emissions were generally separated into two frequency bands, referred to as 'high' (~4-12.5 MHz) and 'low' (~0.1-0.8 MHz) frequency broadband emissions and this filtering was done for both bands. This refers to whether they lay above or below the HIFU drive frequency. These specific frequencies were chosen for all of the acoustic emissions since they generally represented the best compromise between RF filtering and attenuation (in tissue) of the higher frequency signals. Figure 4.17 shows an example of the typical emissions

detected from a HIFU exposure in degassed water, for a 2 s with I_{sp} = 1700 W/cm^2 (2.02 MPa).

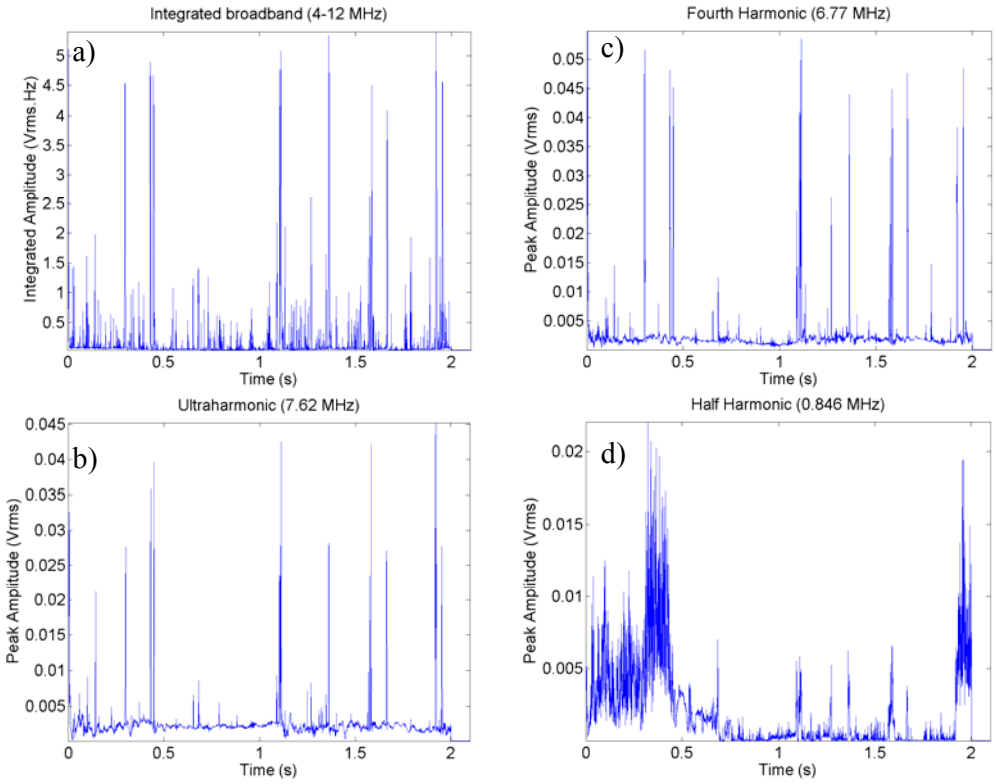

Figure 4.17. The fluctuations in the (a) detected integrated broadband, (b) ultraharmonic, (c) fourth harmonic, and (d) half harmonic signals as a function of time, for the exposure described in Figure 4.14 and Figure 4.15.

Two further programs were used to analyse the processed acoustic spectra data. The first program integrated the acoustic emissions over the exposure. This gave a single value at each time point that represents the total time integrated emissions from a single exposure, thus allowing the comparison between multiple individual exposures at different HIFU intensities. The second had a similar function, but gave a binary output based on whether or not the emissions detected in an exposure were above a specified noise level. This technique identified the percentage of exposures that were above this noise level in order to attempt to identify pressure thresholds.

Noise, in the context of this study, was defined as any signal that was detected by the passive cavitation detection system that did not result from cavitation activity. In order to measure this, a sham exposure was carried out each time a set of experiments (generally on a day-to-day basis) were performed. A sham exposure was done at the

highest drive level used for the experiment with the HIFU transducer disconnected from the drive chain. An example of a sham exposure is shown in Figure 4.18.

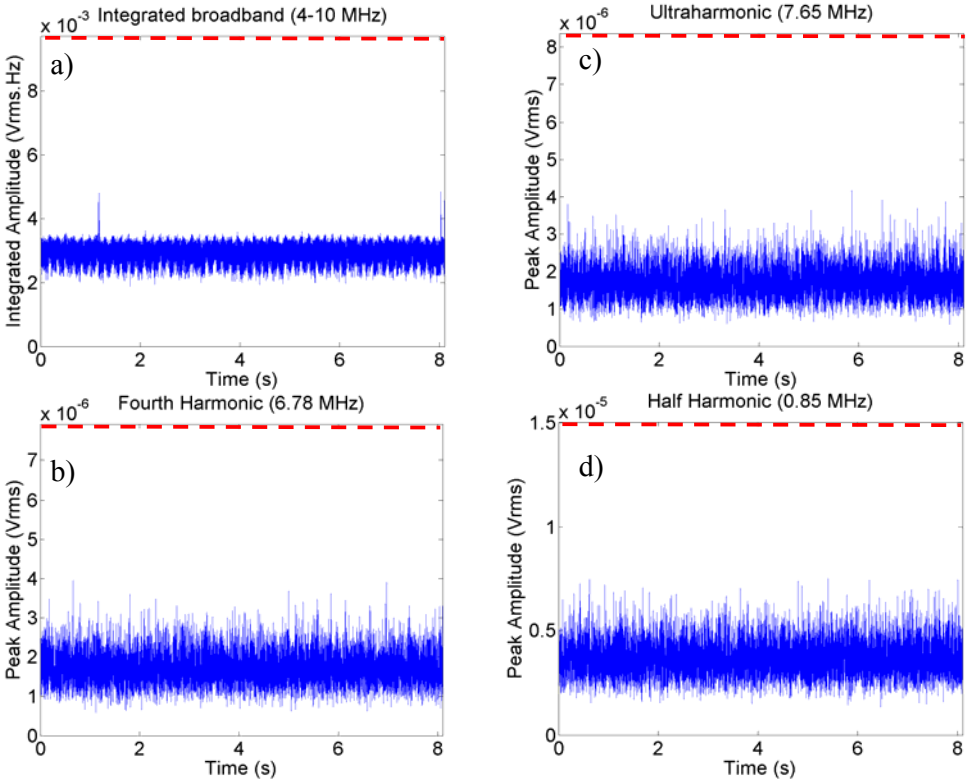

Figure 4.18. The detected spectra from a sham exposure at a drive level of -1 dBm using the 1 and 7.5 MHz passive sensors, where (a) detected integrated broadband, (b) ultraharmonic, (c) fourth harmonic, and (d) half harmonic. The dashed red line indicated the noise level that would be obtained from this sham exposure.

This measurement allowed the estimation of the noise detected by the system for a single exposure, which could vary depending on the combination of sensors/filters/amplifiers used. In addition, the acquisition time was always continued longer than the HIFU exposure and the 'off time' data was used to provide an additional estimation of the noise level in the system, when the RF drive chain was not active. The noise level was defined as twice the peak value, either from sham or 'off time' measurements (the largest of the two), detected. However, the MatLab routine that was used to decide whether a signal was above noise contained more stringent conditions. Detected spectra were required to exceed five times the noise level for a minimum of five (none sequential) data points. This more stringent condition was used since the binary output of this program needed to be insensitive to, for example, noise spikes (Figure 4.18(a)) that could sometimes be generated from switching on/off the HIFU

drive system, in order to reduce the chances of false positive identification of acoustic cavitation activity.

This suite of programs, developed during this project, allowed the detailed inspection of the acoustic spectra arising from HIFU exposures and resultant bubble activity.

4.3 Preliminary data obtained using the NPL sensor

The aim of this study was to investigate the variation of the half harmonic emission (0.846 MHz) with HIFU intensity for a fixed exposure of 2 s, in ex-vivo tissue. This series of experiments provided the initial basis for the design of the passive cavitation detection system.

Figure 4.19 shows the experimental set-up used for the detection of acoustic cavitation in ex-vivo liver. Since the available filtering meant this system could only monitor emissions below the drive frequency, it was not possible to differentiate between types of acoustic cavitation activity. The Mauve HIFU transducer (1.69 MHz, 8.4 cm diameter, 15 cm focal length) was used to nucleate cavitation in samples of degassed ex-vivo ox liver (either one or two days after slaughter). The liver was stored in a refrigerator and for experimental day 1, was degassed for 1h, and for day 2, for 2h. The central axis of the NPL sensor was aligned to be coincident with the HIFU beam axis.

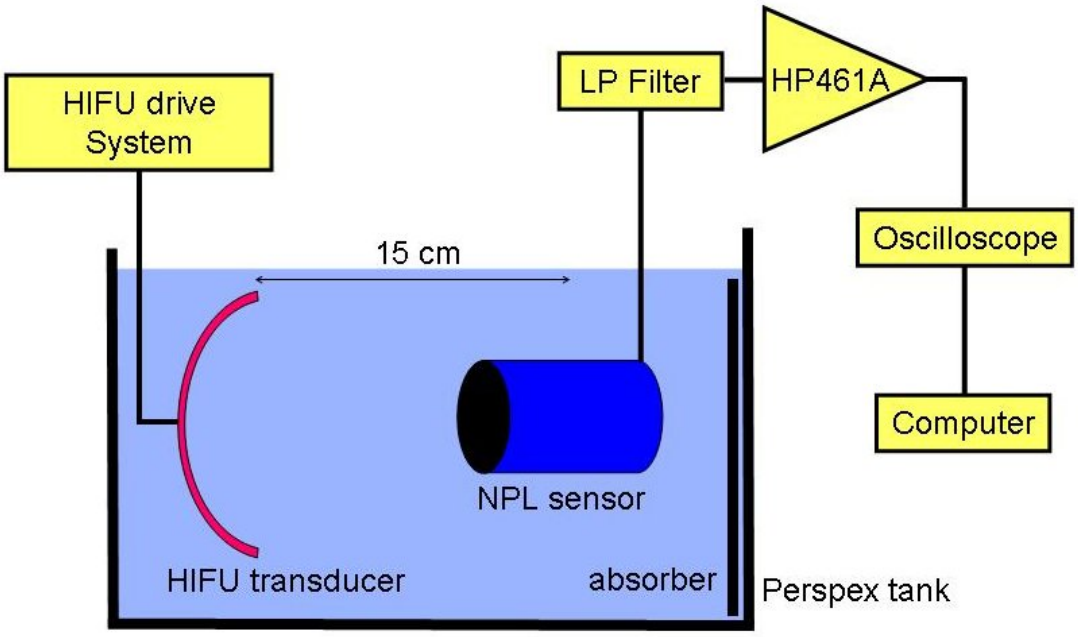

Figure 4.19. A schematic diagram of the experimental set up used for the preliminary studies during the development of a passive cavitation detection system.

Tissue samples were cut to fit inside the NPL sensor (§5.4) and to fill its volume completely. A timer (0.1 s resolution) was used to control the HIFU exposure duration, which was fixed at 2 s for these ex-vivo studies. It triggered (5V TTL) both a function generator (Agilent, 33120A) and the data acquisition oscilloscope (LeCroy Waverunner LT3422). The HIFU drive signal was passed to an amplifier (ENI A300, +55dB). The PCD sensor was mounted on a 3-axis gantry to allow positioning of the HIFU focus within it, through the use of a pointer (§5.1.3). The output from the sensor was low pass filtered and amplified to allow investigation of the 'low frequency' broadband emissions and the half harmonic. The oscilloscope was used to perform and display FFT's during the exposure. The frequency spectrum (0.01-2 MHz) of the detected signal was transferred from the oscilloscope to a PC via an RS232 cable. As the acoustic emissions could not be stored in real time, only the spectrum where the maximum value of the half harmonic occurred during the exposure was saved.

The tank water used for the experiment was vacuum degassed (§5.2). More than 200 individual samples from approximately 30 bovine livers were exposed to HIFU fields using in-situ spatial peak intensities (I_{sp}) of 370-3280 W/cm^2 (§5.3.1).

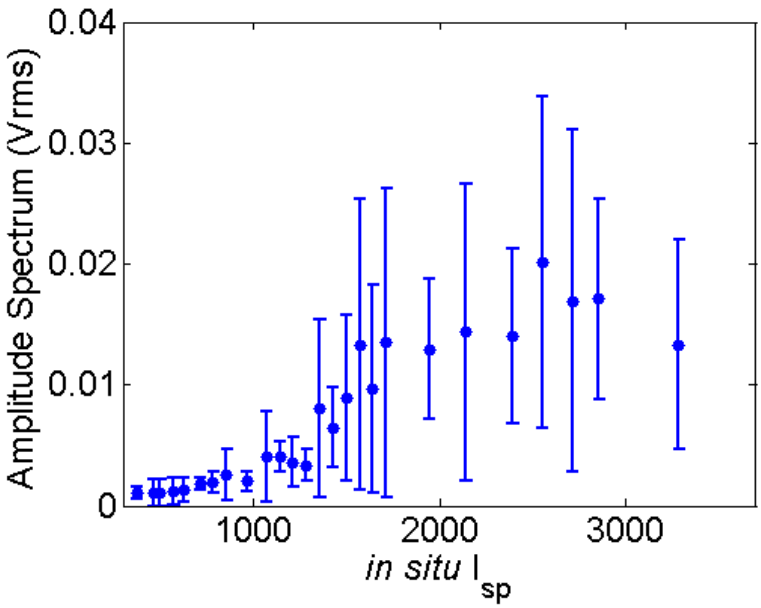

Figure 4.20. The averaged peak amplitude of the detected half harmonic emissions. Error bars shown are given by the standard deviation ($3 < n < 25$) of the average measurements.

Figure 4.20 shows the averaged peak detected amplitude for the half harmonic during 2 s HIFU exposures. It suggests that half harmonic was not detected below 625 W/cm^2, but since the oscilloscope was performing the FFT calculations during the exposures, it was likely that this procedure meant that there were off times while these calculations were performed. Thus, it was not possible to identify accurately the HIFU intensity at which the half harmonic emissions occurred. An interesting feature of this data is that beyond 1360 W/cm^2 there is not only an increase in the average values but also an increase in their spread (i.e. the standard deviation is larger). This might suggest that a different mechanism comes into play beyond this point. This figure highlights some of the drawbacks of using peak detection in cavitation studies. In addition, there is no way of determining at what point during the exposure the peak half harmonic signal occurred. The monitoring of this single acoustic frequency limits the interpretation of the results, since the half harmonic can be generated by non-inertial and inertial cavitation. It was for these reasons that the passive cavitation detection system which incorporated several channels, and which recorded for the duration of the HIFU exposures was developed.

A further aim of the preliminary study was to investigate the effect of using 1 or 2 day old tissue.

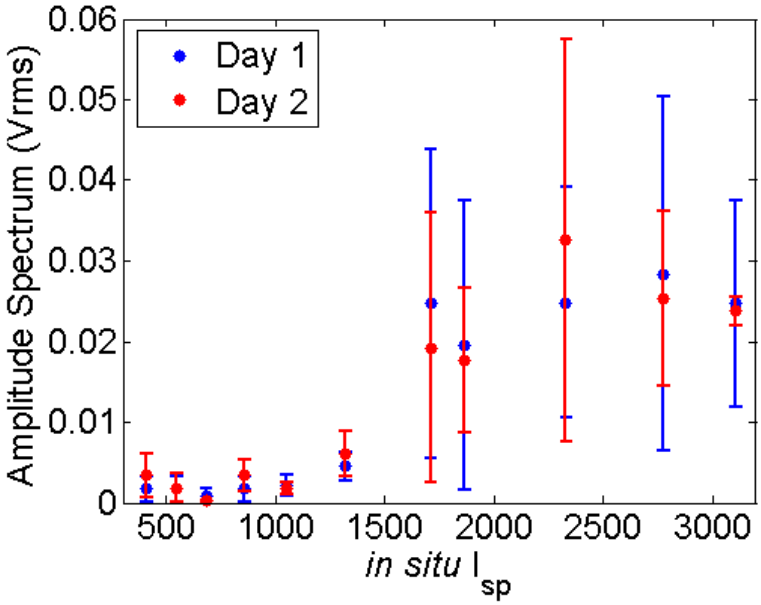

Figure 4.21. The averaged peak amplitude of the detected half harmonic emissions, which have been separated into exposures performed on 1 and 2 day old tissue. Uncertainty shown in the data is the standard deviation (n = 4-6).

Figure 4.21 shows a comparison between the average peak amplitude of the detected half harmonic in ex-vivo tissue from 2 s HIFU exposures averaged over either one or two day old tissue which was degassed for 1 or 2 hrs, respectively. The key aspect of this data is that there does not seem to be a significant difference between the emissions that were detected. There is variation in the uncertainty in the measurements, but this does not seem to be related to the age of the tissue. This study or analysis demonstrated that the tissue degassing techniques used were sufficient to enable comparison between acoustic spectra detected from tissue that is either one or two days old.

4.3 Active cavitation detection methods

Two forms of active cavitation detection were used in conjunction with the passive cavitation detection system. Commercially available diagnostic ultrasound imaging was used to identify hyperechogenicity that was thought to have been caused by bubble activity (as reviewed in §3.2). Measurement of electrical drive power fluctuation has been classified as active cavitation detection since the electrical impedance change (§3.5) is caused by backscatter of the HIFU field, again from bubbles.

4.3.1 Ultrasound diagnostic imaging

A Z.One (Zonare Medical Systems, Mountain View, CA, USA) diagnostic ultrasound scanner was used in this study. The scanner was used with either a linear L10-5 probe (centre frequency 8 MHz, MFCD1313, 14 Hz frame rate, 6 cm imaging depth) or curvilinear C5-2 probe (radius of curvature 5 cm, field of view angle 65^{o}, centre frequency 1.96 MHz, and imaging depth 18 cm); both probes are shown in Figure 4.22.

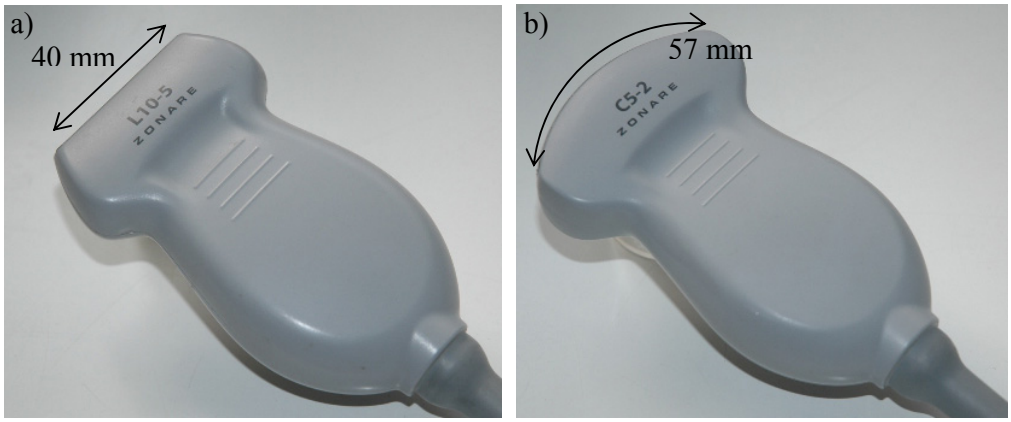

Figure 4.22. Photographs of the L10-5 (a) and C5-2 (b) diagnostic ultrasound probes that were used for active cavitation detection in this study.

The principle idea behind this device is that it scans in 'zones' which are wider than conventional single scan lines. As a result of this, the acquisition time required to produce an image is reduced. In addition to being able to view the B-mode image in real time on the scanner display, it could be stored as in-phase and quadrature sinusoidal components (*I/Q* data). This data could be downloaded from the scanner to a flash-based storage device using a communication program, TeraTerm Pro (v2.3) on a PC connect to the imaging device via an RS232 port. Zonare provided two MatLab programs that were used to reconstruct the B-mode and RF data from the downloaded *I/Q* data, for a more detailed discussion please refer to Civale (2007). An example of the B-mode and RF data that could be reconstructed using this code is shown in Figure 4.23.

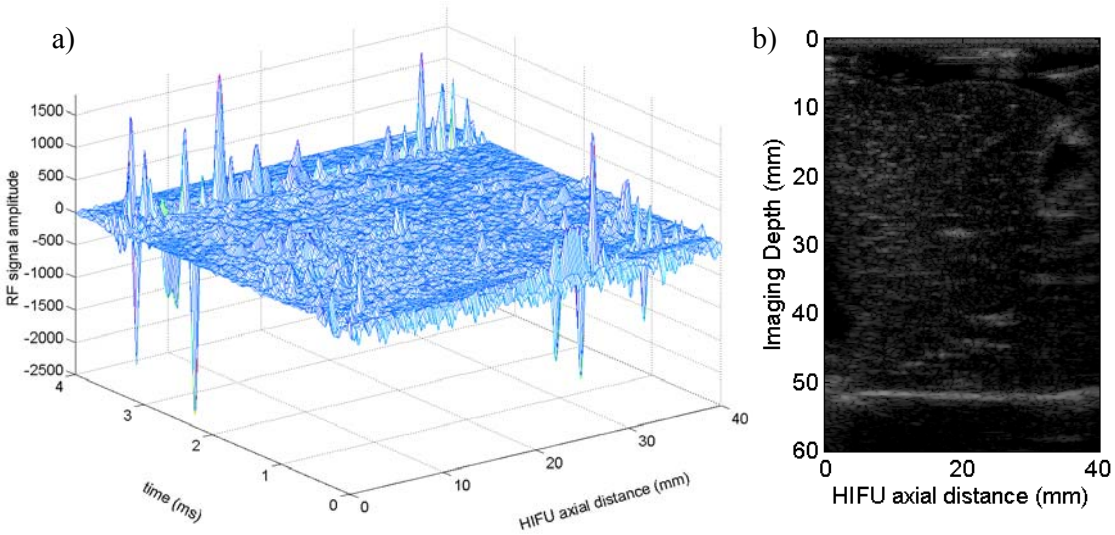

Figure 4.23. A plot of the (a) RF data from a single frame of data recorded on the Zonare scanner, which was generated using the MatLab program with the corresponding (b) B-mode image in ex-vivo bovine liver tissue, which had not been exposed to a HIFU field.

Having access to this data made it possible to perform frequency analysis on the RF data and further image analysis on the B-mode images, such as performing a simple image subtraction between two frames. This highlighted any change in the image as a result of a HIFU exposure, such as the appearance of hyperechogenicity or shadowing. Unfortunately, the RF from the HIFU transducer interferes with the B-mode image making observation of the image difficult. Figure 4.24 shows a B-mode frame that has been partially obscured due to the interference while the HIFU field is on. The level of acoustic interference seen in B-mode images acquired during HIFU exposures increases as the exposure intensity increases.

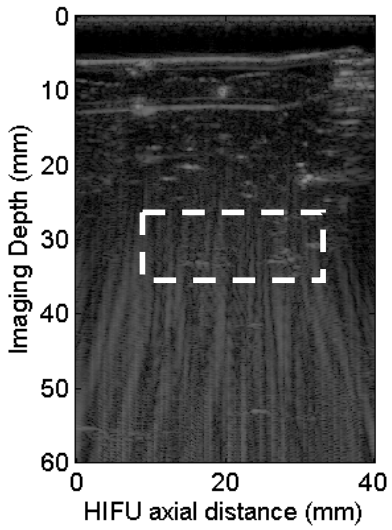

Figure 4.24. A B-mode image that was acquired during a HIFU exposure of ex-vivo bovine liver tissue. The interference pattern obscures part of the image. The white box indicates the approximate position of the HIFU focal region.

4.3.2 Electrical drive power fluctuations

Monitoring both the drive voltage (V) and current (i) as described in (§5.1.1), allowed the average electrical drive power (P) to be calculated using:

$$P = \frac{1}{N\tau}\int_{0}^{N\tau} V(t)i(t)dt\,, \tag{4.3}$$

where the integration was performed in the steady state over 500 acoustic cycles (N) with period τ. Alternatively, V_{rms} of the drive voltage was calculated over N cycles when it was only possible to monitor the drive voltage. It was assumed that changes in the electrical impedance of the HIFU transducer due to reflected energy caused the electrical drive power to fluctuate from the average value. In order to test that these fluctuation were not simply due to instability in the drive system or measurement techniques, the HIFU drive system was driven into a dummy load (8322 Tenuline co-axial attenuator, 30 dB, 200 W input, 50 Ω impedance, Bird Electronics Corp., Cleveland, OH, USA). This mimicked the drive of a HIFU transducer, but without the possibility of any electrical impedance change.

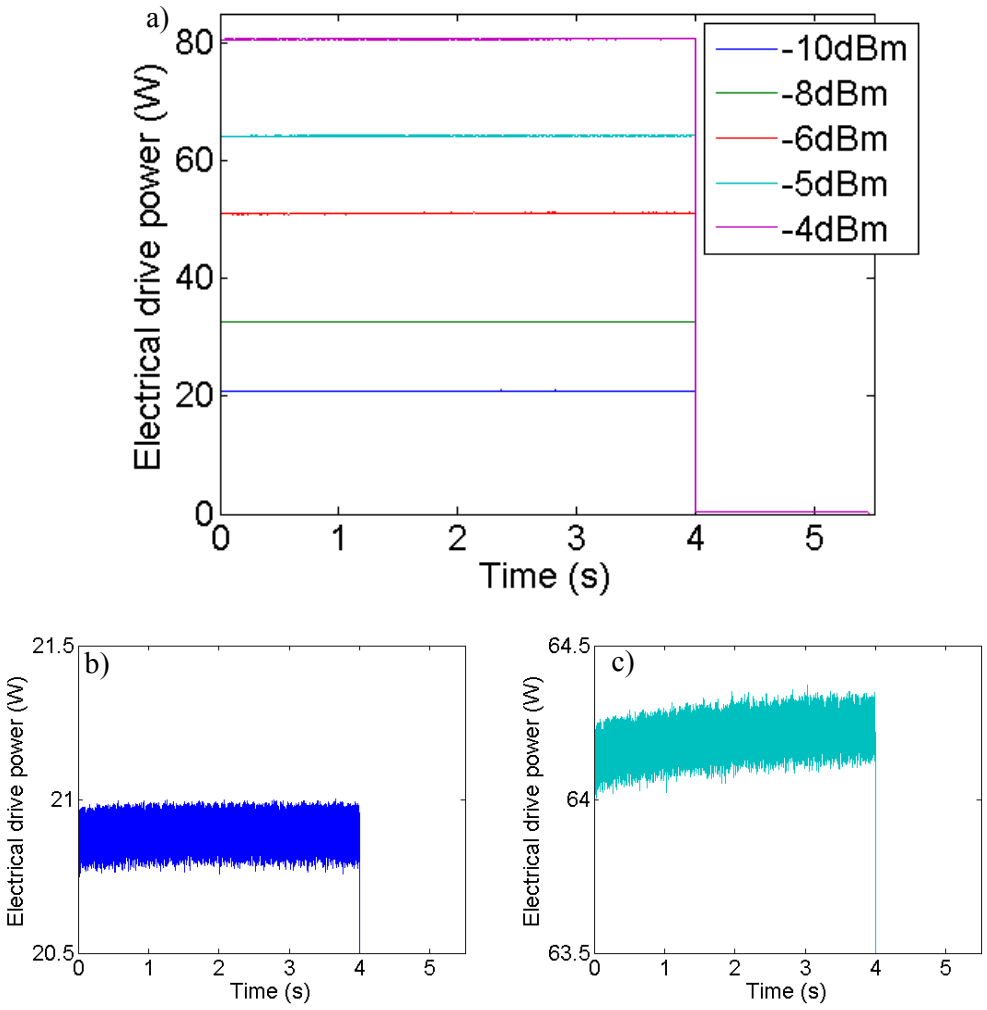

Figure 4.25. (a) The calculated electrical drive powers for 4 s exposures with the HIFU transducer replaced with a dummy load. The legend shows the drive level used for each exposure. (b) and (c) show the expanded drive power scales for the -10 and -5 dBm exposures, respectively.

Figure 4.25 shows the calculated power that obtained when driving the HIFU drive system at power levels equivalent to those used to drive the HIFU transducers. The expanded scales shown in Figure 4.25(b) and (c) give an approximation to the uncertainty of these measurements. Thus, power fluctuations from the average value that have a magnitude greater than ±0.125 W are greater than the uncertainty in the measurement and drive system.

4.4 Cavitation Thresholds

Apfel (1981) summarised three different pressure thresholds for a single spherically oscillating bubble. The Blake threshold (§2.3) is the first of these and describes the

threshold conditions for the mechanical growth of a gas bubble. A second threshold is the acoustic pressure required to cause rectified diffusion of gas into a bubble. Finally, the transient cavitation threshold described the minimum acoustic pressure required to cause the bubble wall velocity to approach the speed of sound during collapse. From these classifications, a diagram was produced for the prediction of these cavitation thresholds for a range of pre-existing bubble sizes. However, Apfel stresses that these plots are meant to be interpreted semi-quantitatively as the regions are not as specifically defined as the models would suggest. This is due to the approximations that were used to formulate these models. A more detailed discussion is given by Leighton (1994). The main difference between the thresholds discussed by Apfel is they are related to pre-existing bubble activity rather than the pressure threshold required to cause the formation of cavitation. A threshold for bubble nucleation, i.e. the minimum pressure required for the formation of cavitation from trapped gas was discussed in section 2.2, but this model was not applicable at MHz frequencies. Thus, there is no general mathematical description for the probability or pressure required for the formation of cavitation in liquids or tissue exposed to HIFU frequencies. This probably explains why cavitation thresholds are usually obtained empirically, using various cavitation detection methods (§3.1).

There is no generally agreed or defined term for a cavitation threshold in HIFU studies. Since it is not possible to observe cavitation activity in tissue visually, and active and passive cavitation detection rely on recording different aspects of behaviour associated with bubble activity, quoted thresholds must relate to the level at which specific acoustic emissions are detectable. As discussed in Chapter 3, there is no standard method for cavitation detection or calibration technique for such systems. The ‘detectable’ cavitation threshold has been previously described in terms of the negative pressure needed to produce acoustic emissions during HIFU exposures by, for example, Hynynen, 1991; Vyhodtseva *et al*, 1995; Holt and Roy, 2001; Melodelima *et al*, 2004; Khokhlova *et al* 2005; Rabkin *et al*, 2005. Datta *et al* (2006), for example, used a dual passive cavitation detection system to identify half harmonic and high frequency broadband emissions and report thresholds for non-inertial and inertial cavitation in porcine blood plasma. They assumed that, in the absence of high frequency broadband emissions, half harmonic emissions were from non-inertial (stable) cavitation to define their stable cavitation threshold criterion.

Both acoustic cavitation (i.e. both inertial and non-inertial) and boiling bubbles can act as scatterers (Khokhlova *et al* 2005) of ultrasound. This may make it difficult to distinguish between them when using active cavitation detection alone. Therefore, the addition of passive cavitation detection is necessary to allow identification of thresholds for different types of acoustic and non-acoustic bubble activity.

The cavitation thresholds described in this thesis are the minimum in-situ peak negative pressures and/or spatial peak intensities that cause detectable acoustic emissions, audible emissions, power fluctuations and/or hyperechogenicity from single HIFU exposures between 2-10 s in duration. In order to exceed this threshold criterion, a detectable mechanism, for example half harmonic, would need to occur at any point during an exposure but have an amplitude that would exceed the noise level established from a sham measurement, as defined earlier in this chapter. It is important to stress that these thresholds refer to the detectable thresholds under these experimental conditions. It is likely that cavitation is generated at lower intensities (pressures) than quoted, however the system described here is unable to differentiate this from noise (i.e. if the signals are attenuated to a level that the sensor is unable to detected). Thus, these 'detectable cavitation thresholds' are likely to be an over estimate, by an amount related to the noise levels of the detection system.

Using the cavitation detection system described in this chapter it was possible to identify pressure thresholds for the occurrence of non-inertial, inertial cavitation and boiling during HIFU exposures in degassed water and tissue, as reported in chapters 6 to 10.

5 – Experimental methods for HIFU transducer alignment and calibration

5.1 HIFU equipment

5.1.1 HIFU drive system

The general set-up for the HIFU drive system used in this project consisted of five basic components, shown in Figure 5.1:

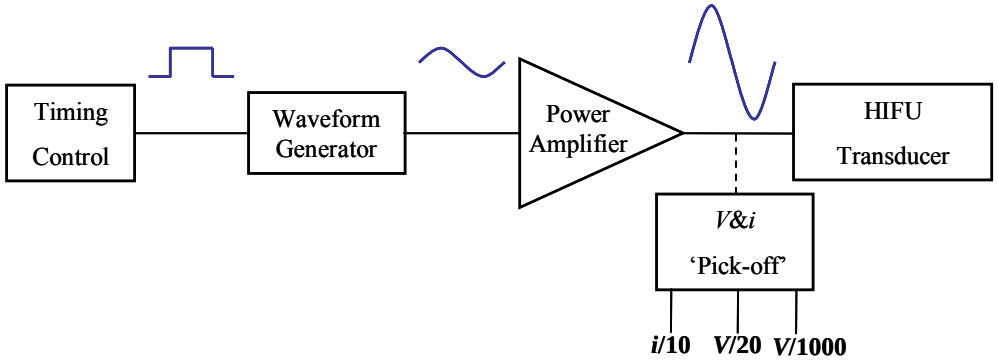

Figure 5.1. The five basic components of the HIFU drive system

A timer (5 V TTL output to BNC) was used to trigger a waveform generator (Agilent, USA, 33120A, 15 MHz function generator). The timer was used to provide a TTL trigger for continuous wave exposures (CW), of durations between 0.01 and 99999 s, with a temporal resolution of 0.01 s. The waveform generator provided a sine wave at the desired frequency. This device was used in one of two modes. Firstly, for CW exposures, the waveform generator was externally triggered by the timer box. Secondly, it could be used to provide a "burst" of a given number of cycles with a user specified "burst frequency" i.e. number of pulses per second. The resulting signal was amplified by one of two broadband power amplifiers (ENI A300/A500, +55dB/+60dB), which drove the HIFU transducer. These power amplifiers were switched on to warm up for at least 1 h prior to use, to ensure a stable output. The output from the waveform generator varied the electrical drive level for the system. The power level is quoted in *dBm* (i.e. the power ratio referred to 1 mW) only as a relative level for the output of the transducer (~ -22 to 0 dBm); this relationship is detailed further in section 5.3. A voltage (V) and current (i) 'Pick-off' box (Figure 5.2) was connected between the power amplifier and the HIFU transducer for every HIFU exposure. This allowed i and V to be

monitored at reduced levels (*V*/20, *V*/1000 and *I*/10) in order to protect the measurement apparatus. This system was designed and constructed in-house for use in the Teleson I clinical HIFU system (Vaughan *et al*, 1994).

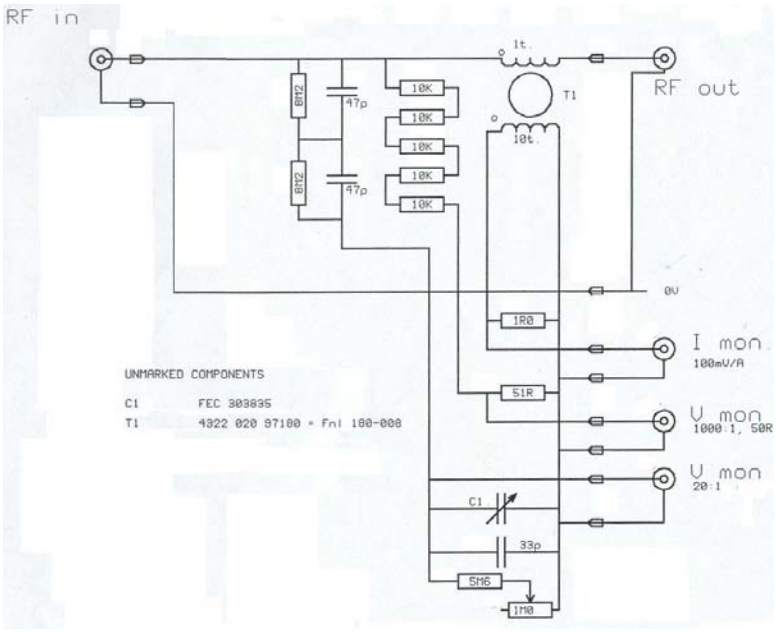

Figure 5.2. Electrical circuit diagram of the voltage and current 'Pick-off' box, used in the HIFU drive system.

The voltage is measured using potential divider circuits, where the current is measured using an induction loop.

5.1.2 HIFU transducers

A number of HIFU transducers with active elements composed of either piezocomposite or piezoceramic materials, were used. All transducers used, with one exception (1.7 MHz, Imasonic), were single element devices. Table 5.1 details selected physical properties of each transducer used in this project.

Description	Drive Frequency (MHz)	Element Diameter (cm)	Radius of Curvature (cm)	F Number	Element material
Mauve - single element	1.693	8.4	15.0	1.79	Piezoceramic
Green - single element	0.898	9.4	13.0	1.39	Piezoceramic
Imasonic - 10 element array	1.70	11.0	15.0	1.36	Piezocomposite

Table 5.1. Selected physical properties for the HIFU transducers used.

The two HIFU transducers used for the majority of experiments are described in more detail below. However the same calibration techniques were used for all transducers detailed in Table 5.1.

The 'Mauve' transducer consisted of a single piezoceramic (PZT4) element (Channel Industries, CA, USA), spherical bowl, focused device with a housing that was constructed at the Institute of Cancer Research, as shown in Figure 5.3(a). The element has a focal length of 15 cm, an active aperture diameter of 8.4 cm and is air backed. For all HIFU experiments it was driven at a frequency of 1.693 MHz.

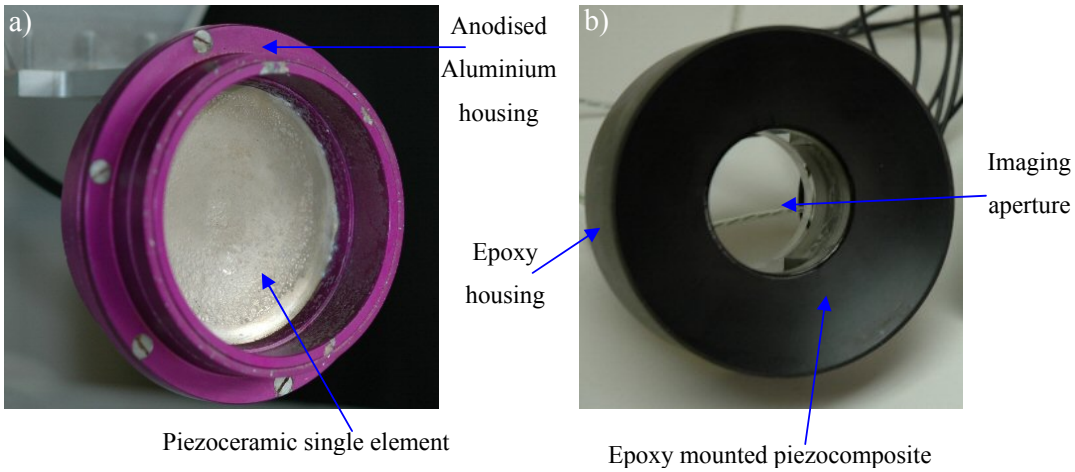

Figure 5.3. Photographs showing the front faces of the (a) 'Mauve' and (b) 'Imasonic' HIFU transducers.

The 'Imasonic' transducer was a piezocomposite array (Imasonic SA, Besançon, France), which had a spherical bowl geometry with a focal length of 15 cm, shown in Figure 5.3(b). The array was comprised of 10 equal area parallel linear elements as shown in Figure 5.4. The outer diameter was 11 cm, and it had a working frequency of 0.9 to 2.1 MHz. 1.7 MHz was the frequency chosen to deliver HIFU. A coupling box was used to drive all 10 elements simultaneously from a single RF amplifier. Thus the electrical voltages applied to each individual element were in phase. A 5 cm diameter central aperture allowed co-axial diagnostic ultrasound imaging to be aligned co-axially with the HIFU beam.

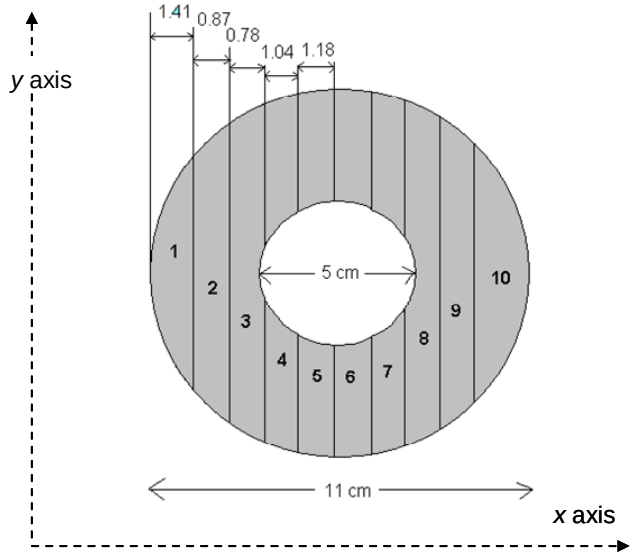

Figure 5.4. A schematic diagram of the 10 equal area elements of the Imasonic HIFU transducer.

Resonant frequency and electrical impedance measurements were made for the all transducers using a network analyser (HP8712ES, Agilent Technologies, Santa Clara, CA, US) in reflection mode. Figure 5.5 shows a log magnitude reflection measurement over the 0.3-6.0 MHz range for the 'Mauve' transducer. It can be seen from this plot that its fundamental frequency was at 541 ± 0.5 kHz. However this transducer was always driven at 1.693 MHz since the energy absorption at this frequency is higher and thus made it easier to induce tissue damage (Chapter 1). It had been constructed in this fashion for structural strength. An element with a fundamental frequency of 541 kHz is three times as thick as one at 1.693 MHz. However, for simplicity 1.693 MHz will always be referred to here as the fundamental or drive frequency, (f_0), of the 'Mauve' transducer.

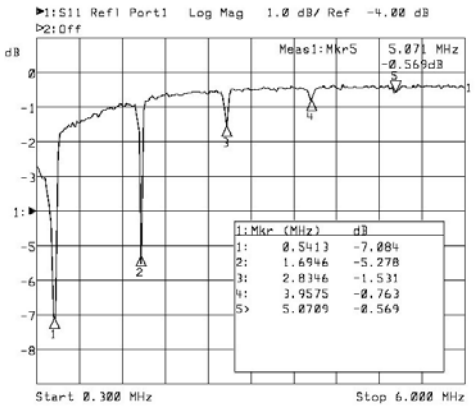

Figure 5.5. Reflection electrical impedance measurements plotted as log magnitude of the reflected voltage over a frequency range of 0.3-6.0 MHz, for the 'Mauve' transducer. The markers highlight the first 5 harmonics of this transducer. These measurements were performed with the transducer submerged in water.

The measured real impedance magnitude of the transducer at 1.693 MHz in water was approximately 16.9 Ω. Therefore, an impedance matching transformer was usually used between the HIFU drive system (Figure 5.1) and the Mauve transducer.

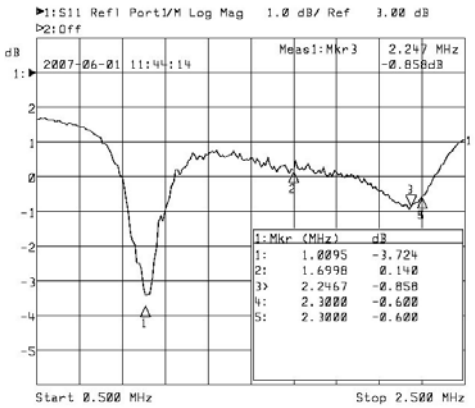

Figure 5.6. Reflection electrical impedance measurements plotted as log magnitude of the reflected voltage over a frequency range of 0.5-2.5 MHz, for the Imasonic transducer. These measurements were performed with the all 10 elements of the transducer connected, and with the device submerged in water.

Figure 5.6 shows the reflection measurements over the range 0.5-2.5 MHz for the Imasonic transducer. The Imasonic transducer has a much broader response (over 0.5-2.5 MHz) than the Mauve transducer. Even though a peak at a lower frequency exists (1.01 MHz) the drive frequency of this transducer will always be referred to herein as 1.7 MHz. The electrical impedance for each element of the Imasonic transducer was

designed to be 50 Ω, however as these were connected in parallel the combined impedance was approximately 7 Ω. An impedance matching circuit was connected between the power amplifier and 'Pick-off' box to improve the electrical efficiency of this transducer.

5.1.3 HIFU transducer alignment

Parallel rails, on which equipment could be mounted, were situated above the tank for every experiment in which the HIFU transducer was used in a horizontal alignment (Figure 5.8). Every HIFU transducer used had an associated pointer to aid initial alignment with the target. The most commonly used type of pointer, shown in Figure 5.7(a), could be attached to the standardised transducer mount system in place of the transducer. It was comprised of two parts, the first screwed onto the mount on the rails. The second, a solid cylinder with a pointed tip which slid into this, included a rule so that the appropriate focal depth could be selected. The pointer shown in Figure 5.7(a) is the one used to align the Mauve transducer. When the rear transducer housing was positioned at zero on the rule, the pointer tip was at the distance of the focal peak. Alignment of the Imasonic and Green transducers was performed similarly. The Siemens transducer had a point built into its transducer housing.

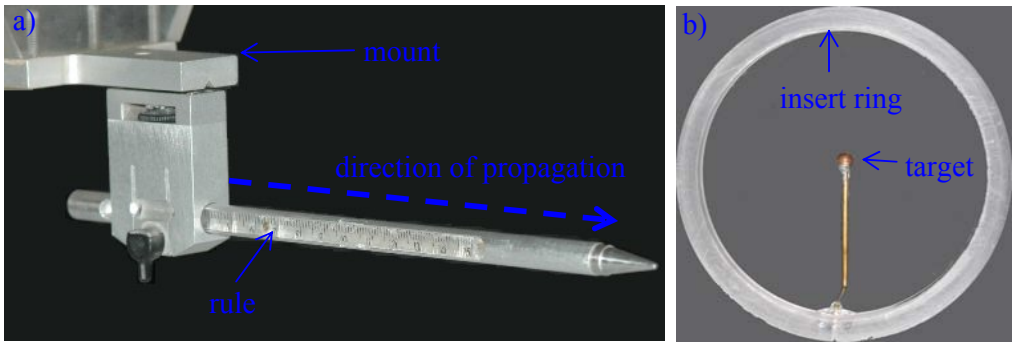

Figure 5.7. Photographs showing the pointer (a) that was used to align the focal peak of the Mauve transducer with the pulse-echo alignment target (b).

Alignment using the pointers was accurate to ±2 mm, in the axial direction (*y* axis). The pointer was aligned with the pulse-echo target, which gave a first approximation for the HIFU alignment. Once this had been achieved the pointer was swapped for the HIFU transducer to refine the alignment using a pulse-echo technique. Generally, the HIFU transducers were mounted onto the rails in a fixed mount (only the *y* axis could be

adjusted). However the sample holder (Figure 5.27) was mounted on a micrometer gantry which, in turn, sat on the rails.

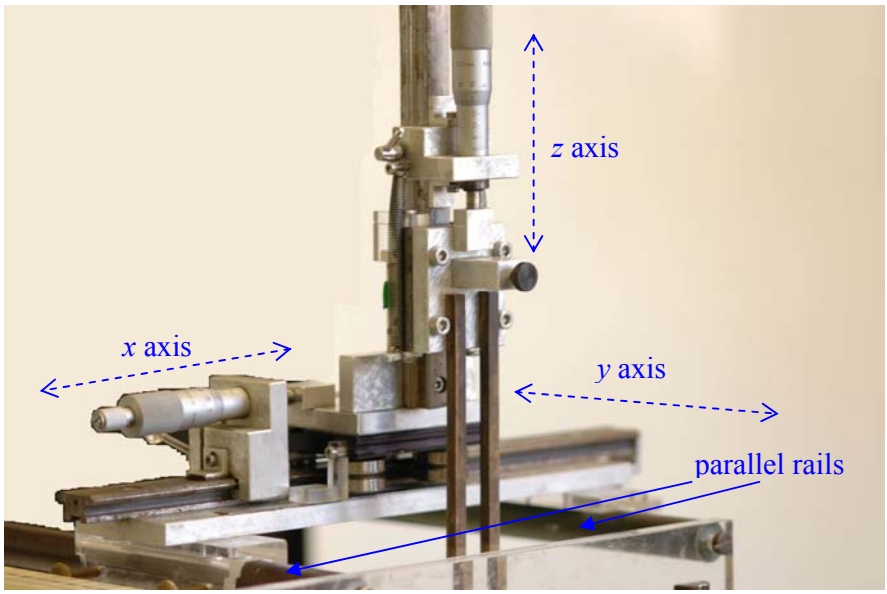

Figure 5.8. The micrometer gantry on the parallel rails.

Using micrometer adjustments, a pulse echo alignment target (Figure 5.7(b)), which fitted into the sample holder, could be positioned to give the maximum reflected signal. The location of the target in the holder was used to define where the position of the focal peak of the HIFU beam. The alignment target was usually recessed by 20 mm from the front face of the sample holder, as this was the default focal depth for the work described in this thesis. However the micrometer gantry could be translated (*y* axis) on the rails if a different focal depth was required. Pulse-echo alignment was generally undertaken with the same exposure settings as were used for plotting the acoustic field in 3-D (§5.3.2) i.e. significantly lower power than used to obtain tissue damage, 80 cycles. The *V*/20 connection of the 'Pick-off' box was connected into the Spectrum data acquisition system to measure the pulse-echo signal. This system was triggered by the waveform generator, which was set to internal trigger mode. Once a pulse-echo signal was recorded, the micrometer gantry was scanned in *x* and *z* (Figure 5.8), to locate the maximum signal at the focal peak, with special attention being paid to avoiding targeting side lobes. Lastly the axial direction (*y* axis) was maximised.

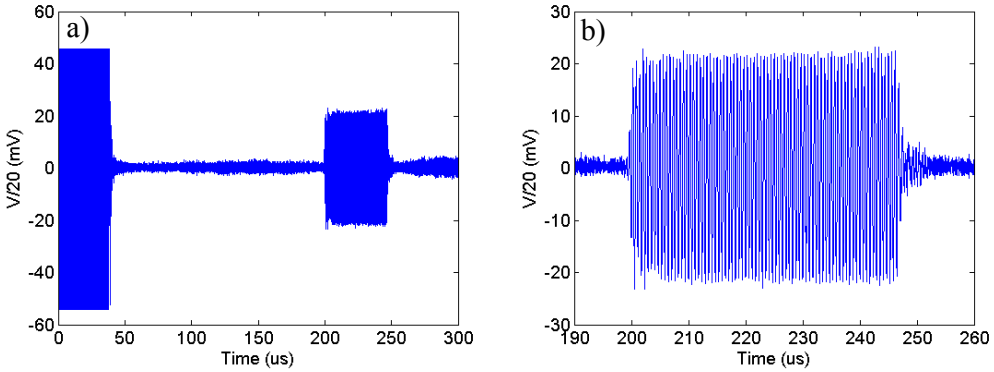

Figure 5.9. An example of a pulse-echo signal detected from the target in Figure 5.28(b) when using the Imasonic transducer (a), (b) shows the expanded section of the echo.

Figure 5.9 shows the pulse-echo signal from the Imasonic transducer. If the sound speed in the degassed water is assumed to 1500 m/s (at 20^{o}C) this gives a time of flight of around 100 μs for the burst to travel to the target. Thus the echo should be received at approximately 200 μs, as is seen in Figure 5.9(b). Note, that the actual drive signal is approximately 100 times that seen at the start of Figure 5.9(a) since the dynamic range of the data acquisition system was set to ±50 mV in order to resolve the echo signal.

5.2 The water degassing system

Degassed water was used as the coupling medium in order to minimise the formation of cavitation during HIFU experiments. Tap water was degassed in house using a custom built vacuum system.

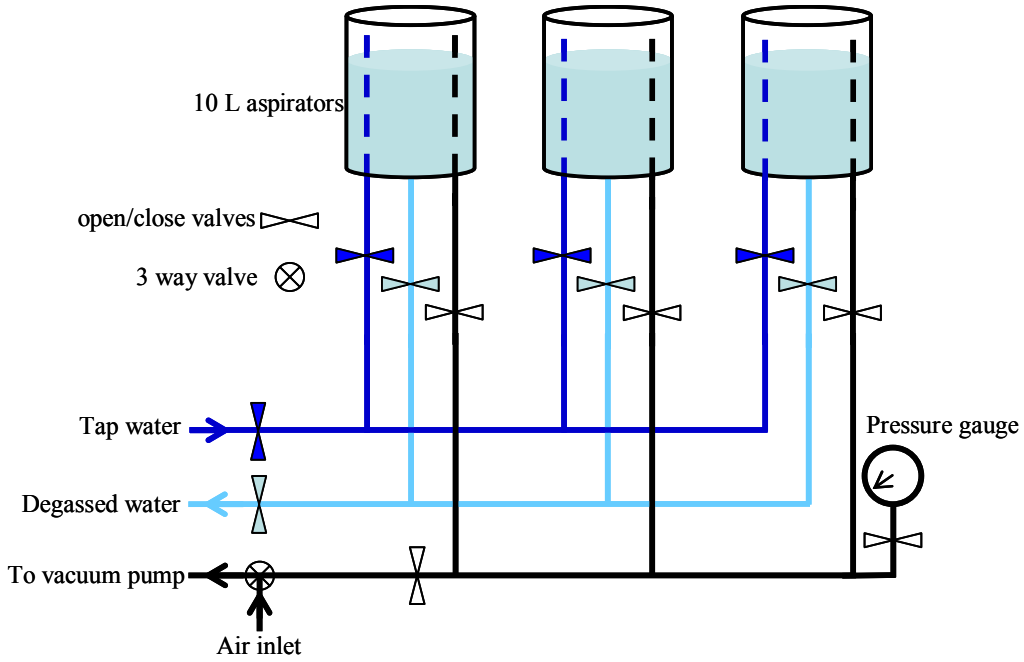

Figure 5.10. A schematic diagram of the system used for vacuum degassing tap water.

The degassed water system, shown in Figure 5.10, comprised 3 inverted 10 litre capacity glass aspirators mounted above head height. Each 'bottle' was fitted with a spray nozzle through which it was water filled, a vacuum pipe and a drain pipe. To fill the system with tap water, the drain and water inlet valves were closed, the vacuum valves all opened and the 3-way valve was directed to the vacuum pump, evacuating the air from the bottles. The 3-way valve was then closed while the bottles were filled with tap water, through the spray nozzle, in order to prevent too much water vapour from entering the pump. Use of a spray increased the surface area of the water in contact with the vacuum, to improve the rate of degassing. Once the bottles are 80% filled (to avoid over filling the bottles) the water inlet valves were closed. The reservoirs were left for at least 12 h under a vacuum of 0.85 MPa before the water was used. Figure 5.11 shows the dissolved oxygen meter (HQ30d, with a LDO101 dissolved oxygen probe, HACH

LANGE Ltd, Manchester, UK) measurements of the degassed water after 12 h under vacuum, compared with measurements taken after a 5 h experiment and in tap water.

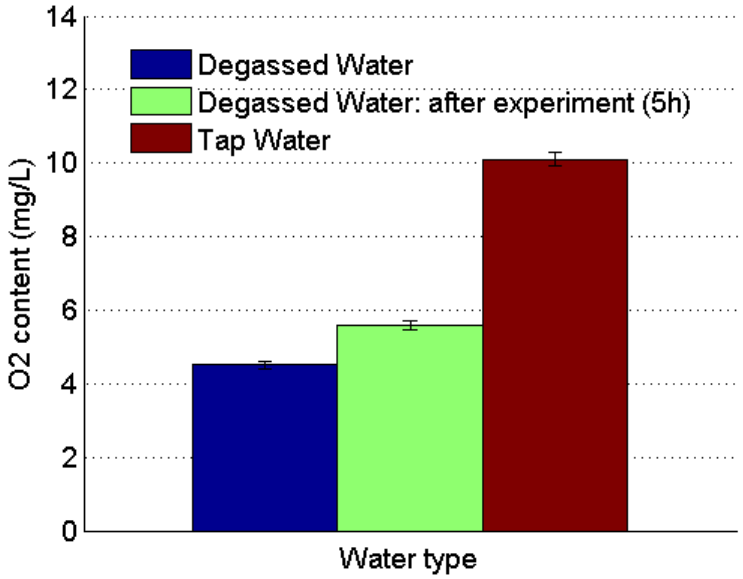

Figure 5.11. A plot showing the dissolved oxygen content in the degassed water compared with tap water. Error bars shown are given by the standard deviation of average measurement, where $n = 3$.

In order to drain, the system the 3-way valve is opened to release the vacuum and then the degassed water valves are opened and water drains out under gravity. The system also included a vacuum flask between the bottles and the vacuum pump (not shown in Fig 5.10) that was a used to collect any overspill water, in order to prevent it from reaching the vacuum pump. This also prevented oil contamination of the degassed water if the anti-suck back valve on the inlet of the vacuum pump were to fail.

5.3 HIFU calibration techniques

5.3.1 *Radiation force balance*

A radiation force balance was used to measure the acoustic power for each HIFU transducer regularly throughout the duration of this project.

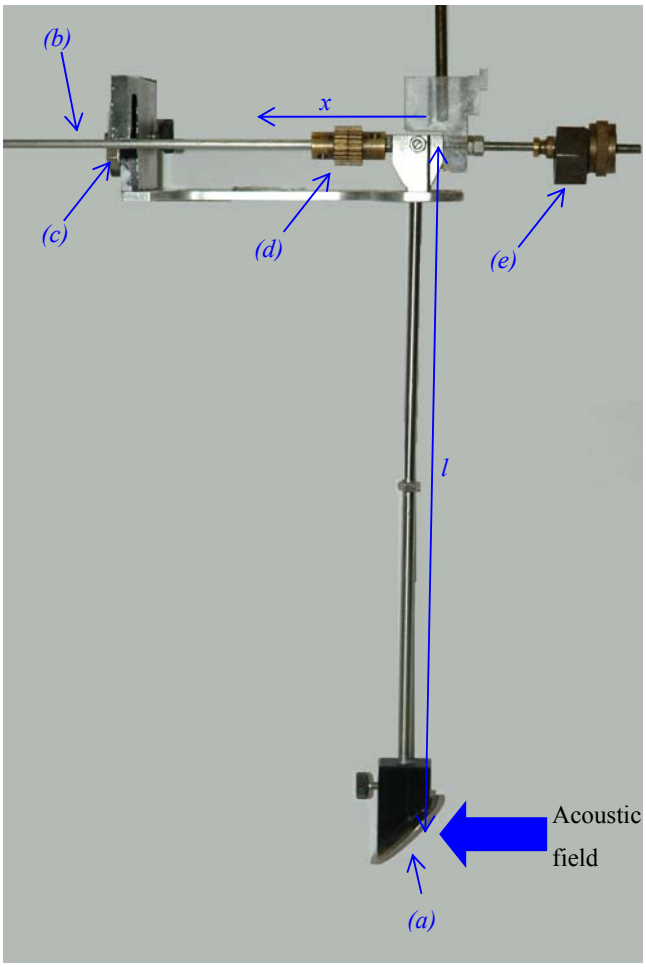

Figure 5.12. A photograph showing the radiation force balance used to perform acoustic power measurements. The reflecting stainless steel coated target (a), horizontal rod (b), equilibrium level (c), masses (d) and counter-balance masses (e) are shown. The length of the vertical rod (*l*), mass displacement (*x*) and direction of the acoustic field are shown. Measurements were made after first balancing the horizontal rod following submersion of the target in degassed water.

Figure 5.12 shows a photograph of the radiation force balance used. The counter-balance (e) was positioned in order to set the equilibrium point to be level with the rod. This position varies depending on the user, amount of water in the tank, and how many masses were used. When an acoustic field is incident on the reflecting target (a), the

balance is displaced such that the longer arm of the horizontal rod (b) moves above the equilibrium level (c). To get the horizontal rod (b) back to the equilibrium level (c), the mass (d) was moved in the direction of x, such that the force balance returned to equilibrium. Once this has been achieved x was recorded. Given that l and x are the length of the vertical rod and displacement of the mass required to counterbalance the radiation force, by equating moments about the pivot it is possible to derive the radiation force (F_{rad}) acting on the target.

$$F_{rad} = \frac{mgx}{l}, \tag{5.1}$$

where m and g are the mass, and acceleration due to gravity. If the speed of sound (c) is known then the acoustic power (W) can be estimated from F_{rad} as follows (Davidson, 1991):

$$W = F_{rad}c, \tag{5.2}$$

At the focal peak of a HIFU field the acoustic pressure profile can be approximated to a Gaussian shape (Figure 5.17). This neglects the contribution of the side-lobes in the acoustic field, as observed in section 5.3.2. By measuring the 6 dB radial beamwidth (§5.3.2) and as the acoustic power it is possible to estimate the acoustic intensity (I). Hill *et al* (1994) have defined a quantity, I_{sal}, is the acoustic intensity spatially averaged over the area enclosed by the half-pressure-maximum contour measured under linear conditions (I_{sal}). This quantity may be used to derive the spatial peak intensity (I_{sp}) from the relationship:

$$I_{sp} = 1.8I_{sal} = \frac{1.56W}{A} = \frac{1.56F_{rad}c}{A}, \tag{5.3}$$

where A is the square of the 6 dB radial beamwidth (pressure full width half maximum). It is worth emphasising that three important assumptions are made in the estimation of I_{sp}: firstly since the reflecting target has an effective radius of 23 mm which is considerable larger than the 6 dB beamwidths, (all < 5 mm), the side-lobes are included in the measured acoustic power. Secondly, the beamwidth is assumed to have been measured under linear acoustic propagation conditions. This is discussed in more detail in the next section. Thirdly, this model assumes that the acoustic field is a plane wave, which is approximately the case in the focal zone of a HIFU transducer

Practically, in measuring of F_{rad}, the reflecting target is placed approximately 1 cm in front of the focus, because of the large negative pressures generated during high power measurements. This was done to minimise the effects of acoustic cavitation,

which interferes with the acoustic field propagation causing instability in the balance (§2.1) resulting in unreliable measurements. However, the entire acoustic beam is still intercepted. During these measurements, the peak *i*/10 and *V*/1000 were measured, so that it was possible to calculate the electrical drive power. Figure 5.13 shows the I_{sp} (a) and peak electrical drive power (b) for both the Imasonic and Mauve HIFU transducers as a function of dBm level. In this figure, it can be seen at the same electrical drive power that the Imasonic gives a lower output than the Mauve transducer. This could be due to driving a 10 element transducer from a single RF amplifier.

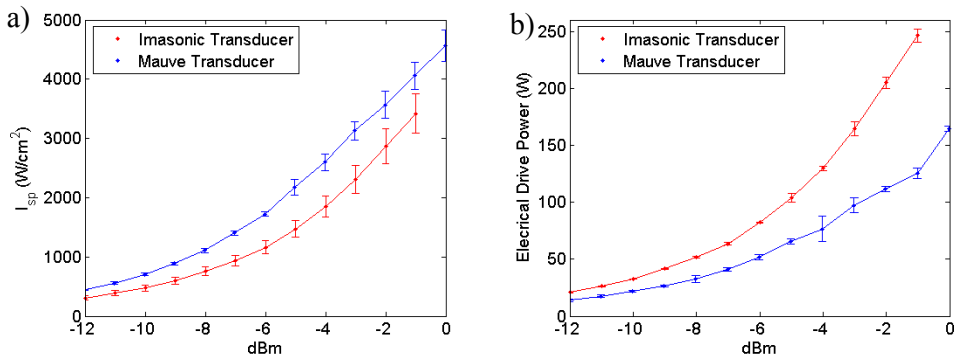

Figure 5.13. The spatial peak intensity (a) and electrical drive power (b) as a function of drive setting (*dBm*), for both the Imasonic and Mauve HIFU transducers. Error bars shown are given by the standard deviation of all measurements (~25) made between 12/2004 and 02/2007.

Experimentally the *dBm* level used on the waveform generator provides a convenient setting to alter for HIFU experiments. However, by performing a force balance calibration it is possible to relate these power levels to the acoustic output characteristics of the HIFU transducer used.

5.3.2 Membrane hydrophone

Direct acoustic field measurements were performed using the polyvinylidene difluoride (PVDF) membrane hydrophone (GEC Marconi, UK). This device had two purposes. Firstly, it was used to measure the acoustic field in 3-D space at different drive levels. Even at the low drive powers (-16 dBm) setting used for these measurements the acoustic field was non-linear, for example, the -16 dBm drive level with the Mauve transducer gives peak positive and negative pressures of 2.04 and 1.28 MPa ±17%, respectively. Secondly, it was used to measure the peak pressures at the focus of the HIFU field over the entire range of drive levels (from -12 to 0 dBm).

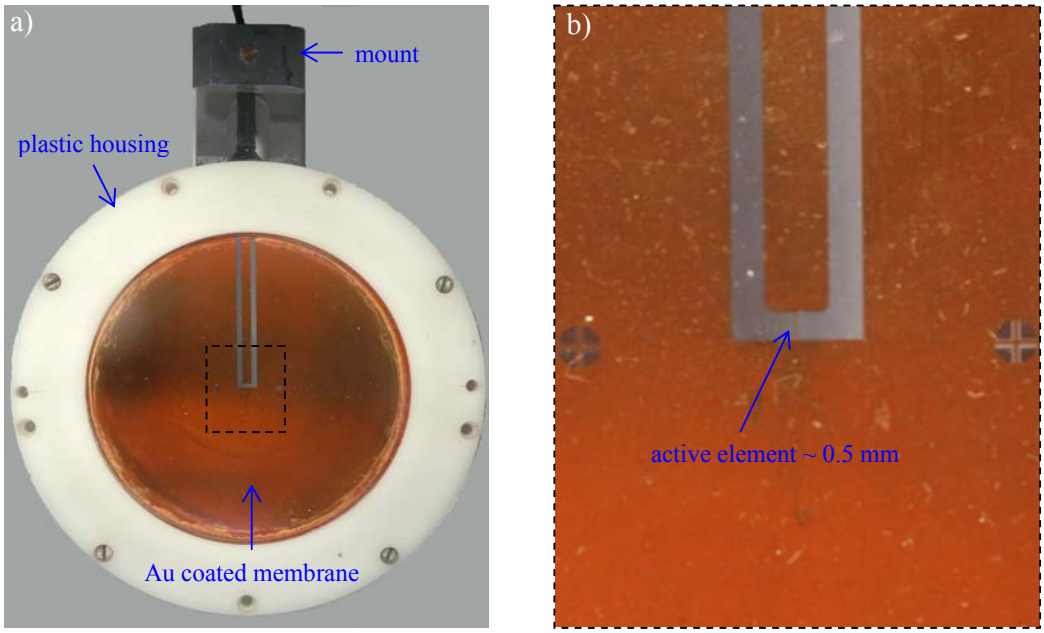

Figure 5.14. (a) Photograph of the GEC-Marconi PVDF membrane hydrophone, (b) shows a magnified view around the active element (~0.5 mm wide) on the hydrophone.

Figure 5.14 shows the PVDF membrane hydrophone used for acoustic field measurement. Figure 5.14(b) shows a magnified view of the region outlined by the dashed box in Figure 5.14(a), showing the active element, which has an approximate width of 0.5 mm. For 3-D acoustic field measurements, the HIFU transducer was driven with between 40 and 80 acoustic cycles. The minimum number of cycles was used to allow the transducer to have sufficient 'on' time to reach the maximum acoustic pressure output and be stable. A burst frequency rate of 100 Hz was used, giving an approximate duty cycle of 0.5%, at a drive frequency of 1.7 MHz. This low duty cycle was used so as not to damage the piezoelectric material, to prevent the generation of standing waves in the measurement tank and to avoid nucleating acoustic cavitation in the degassed water.

RF power pickup by the hydrophone at this duty cycle meant that it was not possible to measure the acoustic field at positions within 7 cm of the HIFU transducer front face. This problem was avoided by ensuring that hydrophone data was only acquired while the drive pulse was off. A schematic diagram of the automated system used to measure the 3-D acoustic field is shown in Figure 5.16. The 3-D automated gantry allowed movement in three orthogonal axes (x, y and z) using of 3 independent stepper motors

controlled by a motion controller (Max 3040, Agile systems, Waterloo, Canada). Optical encoders provided position feedback. A pair of limit switches on each axis was used to restrict the range of movement available using the motion controller, which was controlled by software running on a PC.

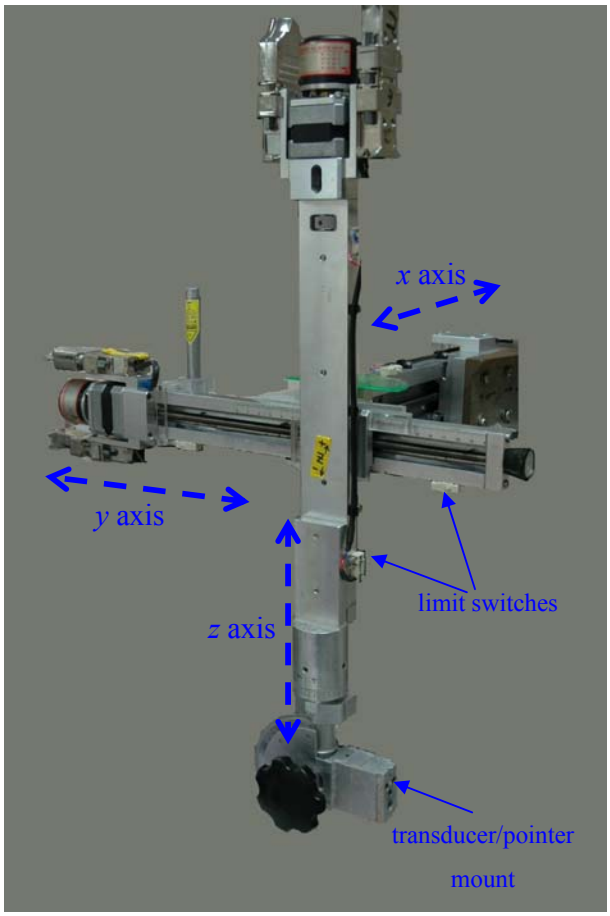

Figure 5.15. A photograph of the automated 3-D gantry used for beamplotting.

The HIFU transducer was attached to the lower part of the gantry (Figure 5.15), while the membrane hydrophone was maintained in a fixed position (at a precisely set angle). An in-house written computer program was used to control the position of the transducer, and the PC running the software was able to acquire data on an oscilloscope (LeCroy Waverunner LT342L, LeCroy Corporation, Chestnut Ridge, NY, USA) via a GPIB connection (Agilent). This allowed automatic acoustic field measurements to be made in 1, 2 or 3 pre-defined directions with spatial resolution ± 0.05 mm. The motion controller had programmable output, which was used to trigger the HIFU system.

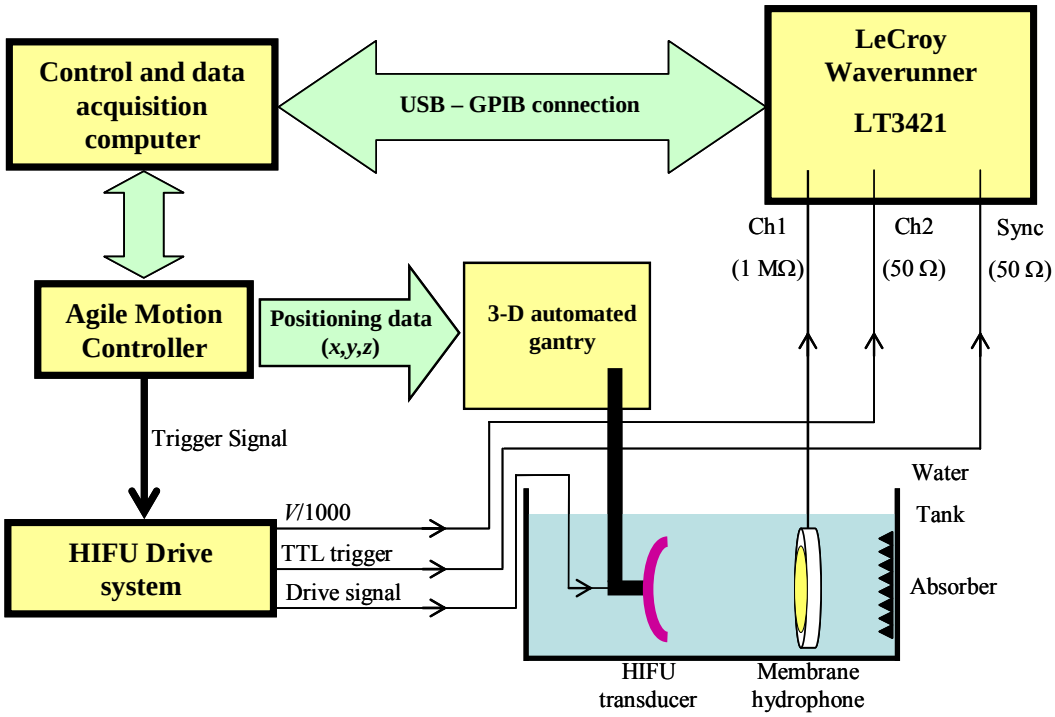

Figure 5.16. A schematic diagram of the automated system used to measure the acoustic field in 3-, 2-, or 1-D or at a fixed position. The absorber was located approximately 5-10 cm from the hydrophone and was used to minimise the formation of standing waves.

The transducer was scanned in the three orthogonal directions using an iterative process such that the focus of the transducer was coincident with the hydrophone's active element. A protractor was attached to the mount of the hydrophone so that the angle of the device could be set precisely. The HIFU transducer and membrane hydrophone were aligned parallel to each other. Either 3 or 5 repeat measurements, depending on the size of a scan, of the peak positive and peak negative voltage of signals from both the hydrophone and the drive (V/1000) were acquired, and the data was averaged at each position using the computer software. The number of repeat measurements was varied depending on the size of the scan, being reduced for large area scans. The software only recorded a value when it had automatically set the dynamic range for each channel to maximise the resolution for each measurement. Scans could be performed in 1, 2 or 3 dimensions with a minimum step size of 0.05 mm. High resolution 3-D scans were avoided, due to the time that they took to complete. The peak positive and negative voltage readings were recorded and converted to acoustic pressure, using a conversion factor of 32 mV/MPa (at 1.7 MHz) provided by the National Physical Laboratory (NPL,

Teddington, UK). Figure 5.17 shows 1-D radial (x & z) beamplots for the Mauve transducer.

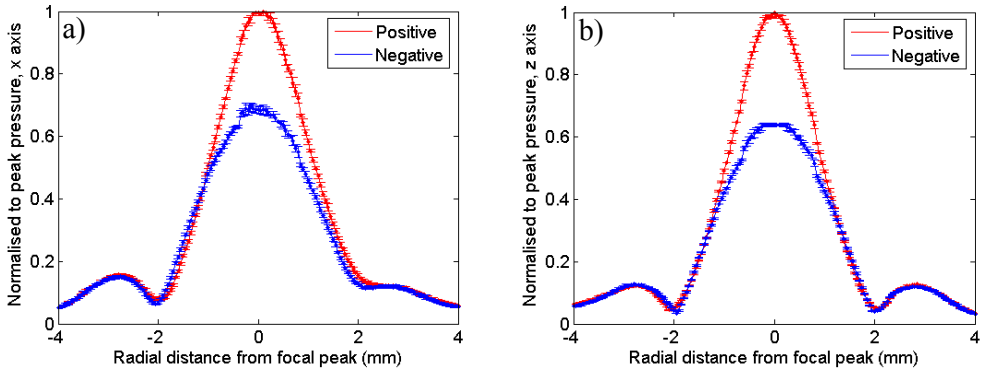

Figure 5.17. 1-D radial beamplots showing the normalised positive and negative pressures for the *x* (a) and *z* (b) axis of the Mauve transducer, for a drive level of -18 dBm. Uncertainties shown in the plots are the standard deviation of five repeat measurements.

From the data shown in Figure 5.17(a) the 6 dB beamwidth of the Mauve transducer is found to be 2.4 ± 0.2 mm. This value was used in equation 5.3 to calculate the I_{sp} levels for this transducer. Figure 5.18 shows similar beamplots for the Imasonic transducer.

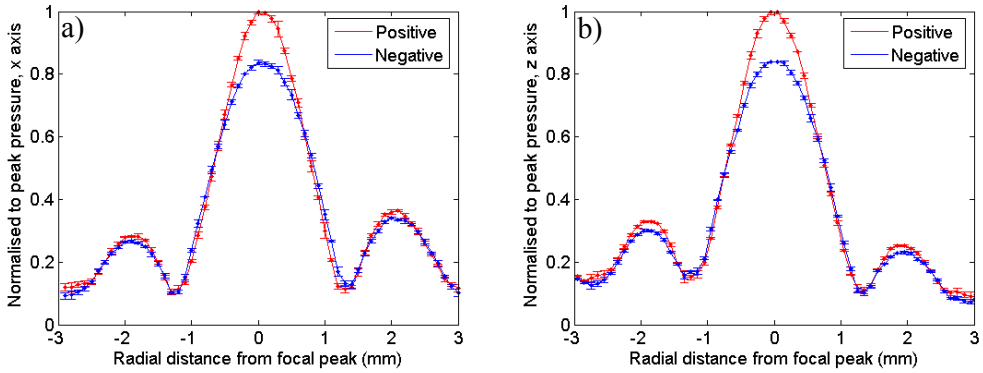

Figure 5.18. 1-D radial beamplots showing the normalised positive and negative pressures for the *x* (a) and *z* (b) axis of the Imasonic transducer, for a drive level of -18 dBm. Uncertainties shown are the standard deviation of the repeat measurements.

From the data shown in Figure 5.18(a), the 6 dB radial beamwidth of the Imasonic transducer used in equation 5.3 to calculate the I_{sp} levels was 1.4 ± 0.05 mm.

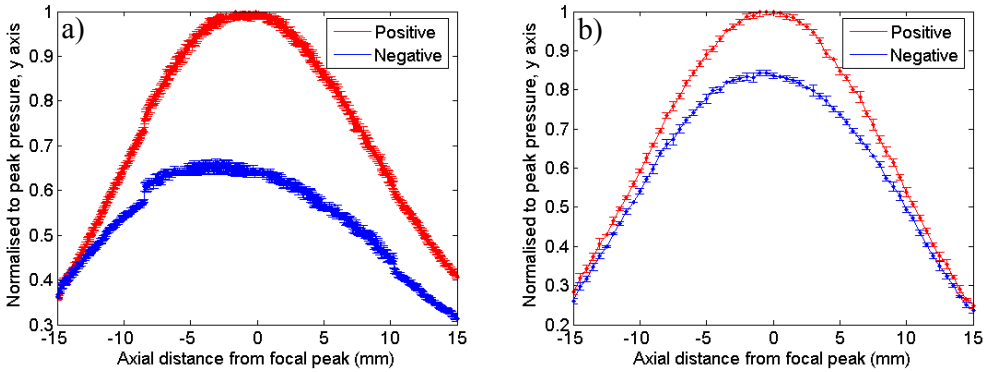

Figure 5.19. 1-D axial beamplots showing the peak positive and negative pressures for both the Imasonic (a) and Mauve (b) HIFU transducers, for a drive level of -16 dBm. Uncertainties shown in the plots are the standard deviation of the repeat measurements.

The data in Figure 5.19 shows the positive and negative pressures for the Imasonic and Mauve HIFU transducers. The beamplots for both transducers were measured at a drive level of -16 dBm. It is clear from the figures above that the beamplots were not obtained under linear conditions, even at a low drive setting. This raises concerns about the accuracy of these measurements and their applicability in practical usage. This is the topic of a recent paper (Shaw and Hodnett, 2008). However, as these calibration techniques are widely used to characterise the output of an ultrasound transducer (Rivens *et al*, 1999; Denbow *et al*, 2000; Kun and Wan, 2004).

The second application of the membrane hydrophone was to measure the peak pressures of the acoustic field at the focus of the transducer as a function of applied drive. Figure 5.21 shows a schematic diagram of the apparatus used. Since only measurements at the focal peak were required, it was not necessary to use the automated gantry system. Instead, peak pressure measurements were undertaken with the transducer position fixed and the membrane hydrophone mounted on a manually operated micrometer gantry (Figure 5.8). During hydrophone alignment (§5.1.3) the waveform generator was used with internal triggering to produce short bursts (~80 cycles, with a duty cycle of 0.5%). After alignment the waveform generator was triggered externally using an FPGA card (see below) to ensure that pulses were only transmitted when measurements were required A field-programmable gate array (FPGA) card was developed, in-house (Ma *et al*, 2007), to allow interleaving of HIFU and imaging. It was used for this application as it could provide the trigger signal for a single burst. Manually triggered single bursts were used in order to minimise the risk of

cavitation damage to the hydrophone, as it was necessary to expose at negative pressures that could generate acoustic cavitation at longer exposure times (Chapter 6). Repeated bursts, even at a low duty cycle, were thought to represent a more significant cavitation risk to the hydrophone. It is for these reasons that beamplots were not created at the highest drive powers used in these studies. However, Figure 5.20 shows that the focal peak of the Mauve HIFU transducer does not vary over the drive level range of -22 to -8 dBm.

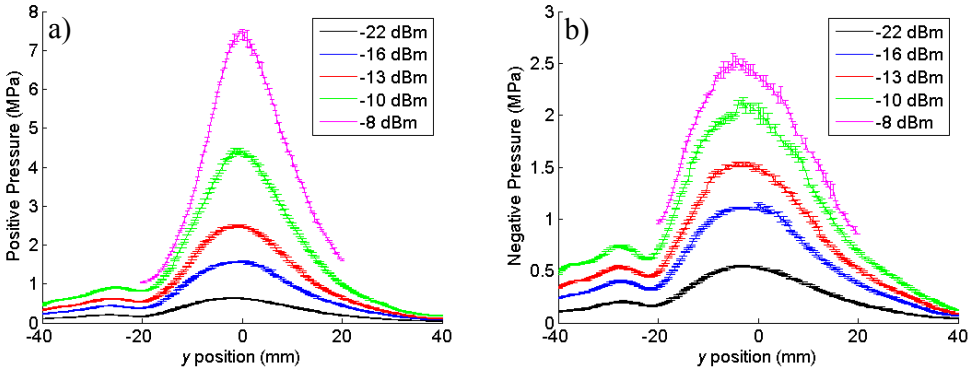

Figure 5.20. 1-D beam plots of the positive (a) and negative pressures of Mauve transducer with -22, -16, -13, -10, and -8 dBm drive powers. Error bars are calculated from the standard deviation of the average value where $n = 5$.

The Spectrum data acquisition system (§4.2.3) had SMA connectors, while the hydrophone had a BNC connector. Thus a switchable gain pre-amplifier (x1 or x5 gain, Kenelec, Type 55641, Hampton Hill, UK) was connected between the hydrophone and data acquisition system to maintain the correct capacitance of the hydrophone. The gain of the pre-amplifier was set to x1, as the device was only being used to allow connection of the hydrophone to the data acquisition system. Incorporation of the pre-amplifier meant that the calibration factor for the hydrophone into pressure measurements needed correction.

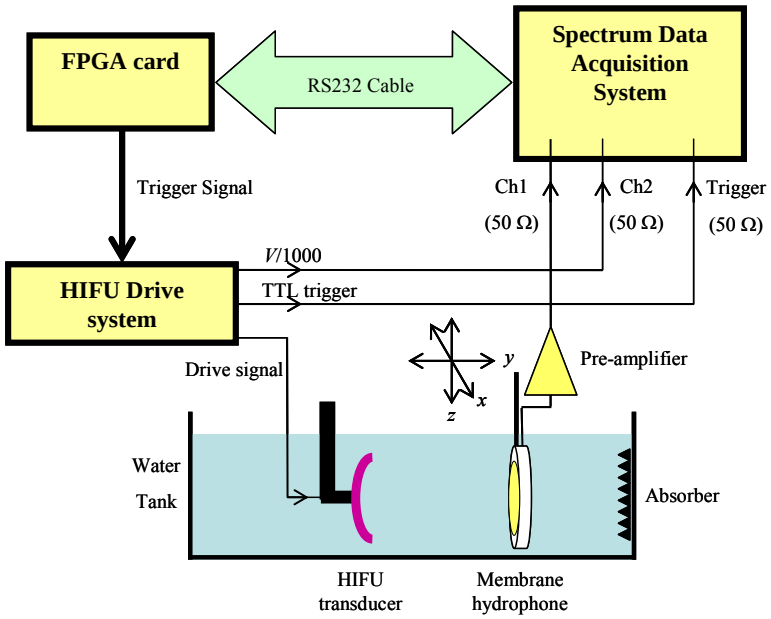

Figure 5.21. A schematic diagram of the set up used to measure the peak positive and negative pressures for HIFU transducers. Unlike the beam plotting system, the transducer position is fixed, the hydrophone is mounted on a manual micrometer gantry. An FPGA card is used to trigger the HIFU drive only when a measurement is required. The pre-amplifier is used to couple the hydrophone output to the data acquisition system. The entire waveform is recorded using an acquisition system described in §4.2.3.

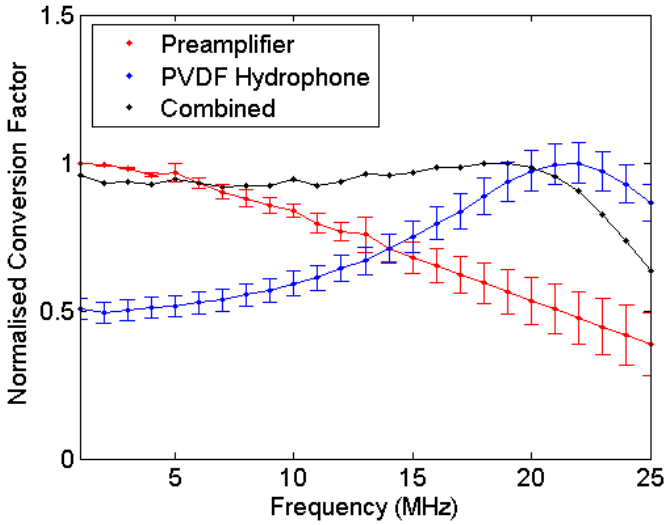

Figure 5.22. The frequency dependence of the normalised conversion factors for the pre-amplifier, hydrophone and the two combined. Normalised values are shown for a comparison between the frequency responses of the individual conversion factors. However, the combined calibration factor has units of mV/MPa, since the calibration factor for the pre-amplifier is an absolute value. Uncertainty shown for the pre-amplifier is calculated from the standard deviation of 3 measurements, whereas for the hydrophone a value of 10% uncertainty came with the calibration provided by NPL.

Figure 5.22 shows the frequency response of the hydrophone calibration factor. All HIFU transducers used had a drive frequency ≤ 3 MHz (Table 5.1). Acoustic field measurements were assumed to be made under linear propagation conditions, -22 to -16 dBm, depending on the transducer used. It was assumed that the conversion factor closest to the drive frequency would give an accurate pressure level. However, this effect is pressure dependent, such that the higher pressure waves will become more distorted over the same propagation distance. An example of this is shown in Figure 5.23(a) and (c), where approximately five acoustic cycles from the Mauve transducer of a low (-22 dBm), approximately linear, pressure pulse are compared with a high (-4 dBm) pressure pulse. Figure 5.23(b) and (d) show the frequency components of the 80 cycle pulse for both these exposure levels.

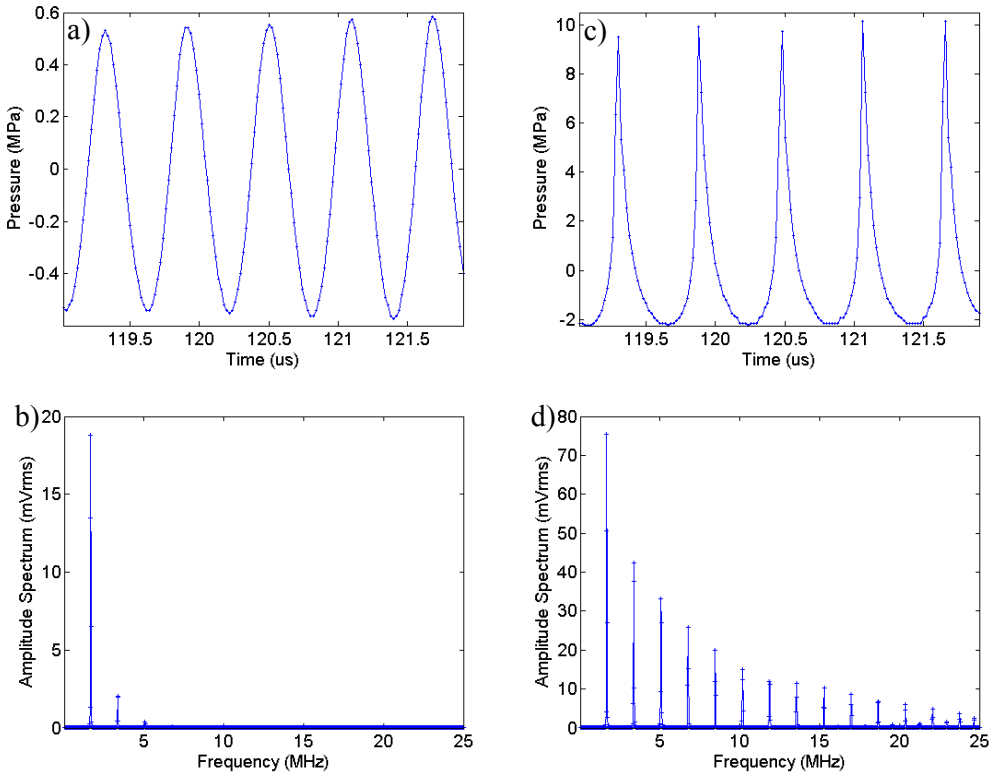

Figure 5.23. A plot of the focal peak to peak amplitude of 5 acoustic cycles (close to the start of the pulse) of an 80 cycle pulse from the Mauve transducer driven at -22 dBm (a) and -4 dBm (c) measured with the membrane hydrophone. (b) and (d) show the frequency amplitude spectrum of the entire pulse in (a) and (c), respectively. The conversion of these drive settings to intensity is shown in Figure 5.13.

The higher pressure pulse, in Figure 5.23(c), shows a shocked wave due to the non-linear propagation of the HIFU field in degassed water. The data shown in Figure 5.23(d) demonstrates that only 42% of the time-domain signal measured by the

hydrophone is at the fundamental frequency, compared with 89% for the data shown in Figure 5.23(b). Summing the individual harmonic contributions for the first 5 harmonics in Figure 5.23(d) gives approximately 95% of the total time domain signal. Therefore, as the conversion factor (Figure 5.22) varies by 4% over this range a single average conversion factor of 38.19 mV/MPa can be used to approximate the measured peak pressures with this hydrophone.

An RS232 cable connected the FPGA card to the data acquisition system. This allowed the user to program the card and generate a manual software trigger for each burst. For each burst, the data acquisition system typically recorded 0.1 ms of the received pulse at the hydrophone and the electrical drive signal, measured by the *V*/1000 connection described earlier. This process was repeated at least three times for each exposure level between -22 and -1 dBm. The upper limit of this range is determined by 1 V input to the power amplifier. However, for the Mauve transducer the upper range was limited to -4 dBm to avoid damage to the hydrophone.

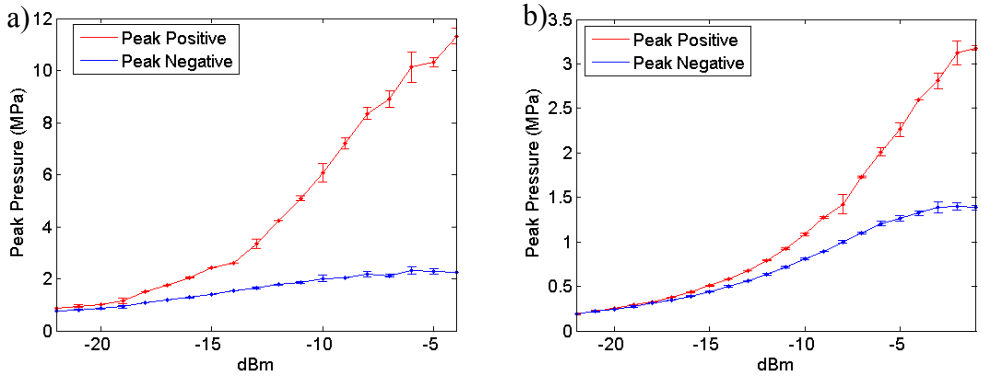

Figure 5.24. Peak pressure measurements for the Mauve (a) and Imasonic (b) HIFU transducers. Error bars shown are given by the standard deviation of three repeat measurements.

Figure 5.24 shows the peak positive and negative pressures for both the Mauve and Imasonic HIFU transducers measured using the membrane hydrophone. It can be seen that for both HIFU transducers, the non-linearity in the acoustic field increases with the drive level, since the peak positive and negative pressures diverge as the drive level increases. This effect is greatest for the Mauve transducer (Figure 5.24(a)). Figure 5.25 shows contributions of the fundamental (f_0) and subsequent four superharmonics to the total time domain signal that was measures using the membrane hydrophone over the dBm range showed in Figure 5.24. It shows that at a drive level of -5 dBm the contribution of the fundamental frequency is approximately 30% of the total time-

domain signal using the Mauve HIFU transducer (Figure 5.25(a)), compared with 65% for the Imasonic transducer (Figure 5.25(b)).

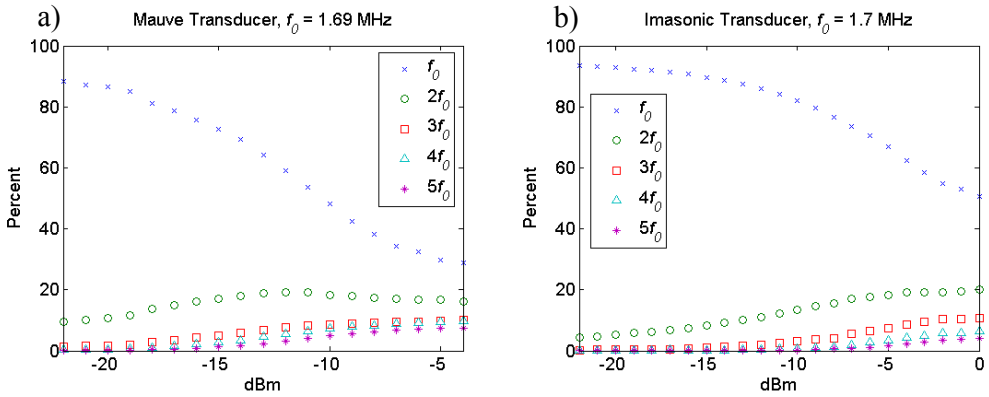

Figure 5.25. Percentage contributions to the total detected time-domain signal from individual harmonics as measured using the membrane hydrophone for both HIFU transducers.

The focal length for these two HIFU transducers were the same but it appears from the data shown in Figure 5.25 that superharmonic generation from non-linear propagation is a more significant factor with the Mauve transducer.

A membrane hydrophone has been used to measure the peak pressures of the HIFU field at drive levels that exceeds those used in the cavitation threshold measurements in subsequent chapters. No lasting damage was observed on the hydrophone after numerous measurements had been taken. The data shows that non-linear propagation can have a significant effect on the detected waveform, which highlights potential problems when considering the interaction of the HIFU field with tissue. For a further discussion of this problem, see Shaw and Hodnett (2008).

5.4 Ex-vivo tissue preparation

The freshly excised ex-vivo bovine liver used in this study was collected from an abattoir and stored overnight in a refrigerated room (5-10^{o}C). Whole livers were cut into samples using the two corers shown in Figure 5.26. The larger (Figure 5.26(a)) was used to core samples of 51 mm diameter to fit into the Perspex holder shown in Figure 5.27. The smaller (Figure 5.26(b)) was used to core out samples to fit into an NPL broadband cavitation sensor (described in §4.3). Cored samples were submerged in degassed water, and vacuum degassed for 1 h (on the first day after collection) or 2 h

(on the second day after collection). A preliminary study (§4.3) established that this tissue degassing regime gave similar cavitation activity between the two days. The older tissue would be expected to have greater gas content (from more autolysis).

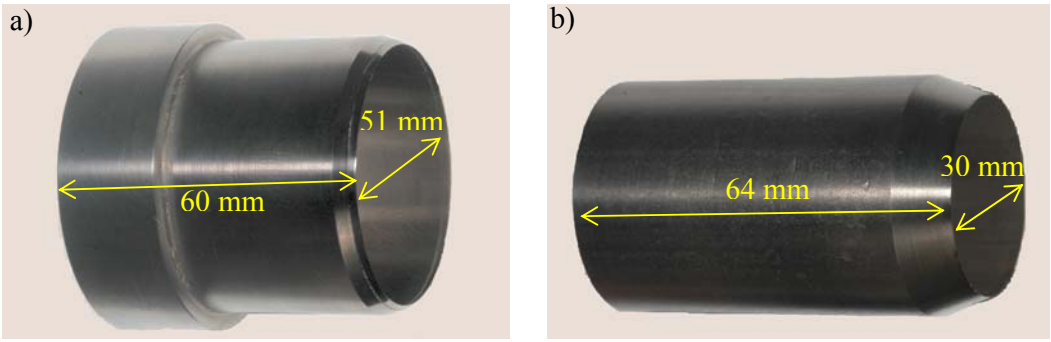

Figure 5.26. The large (a) and small (b) diameter corers used to produce cylindrical samples of ex- vivo liver tissue.

A cylindrical Perspex framed tissue holder with acoustically transparent 19 µm thick Mylar windows (front, back, and wrapped around the length of the cylinder – as defined in Figure 5.27) had been designed and was used to allow HIFU propagation along the length of the tissue sample whilst allowing simultaneous diagnostic ultrasound imaging from above.

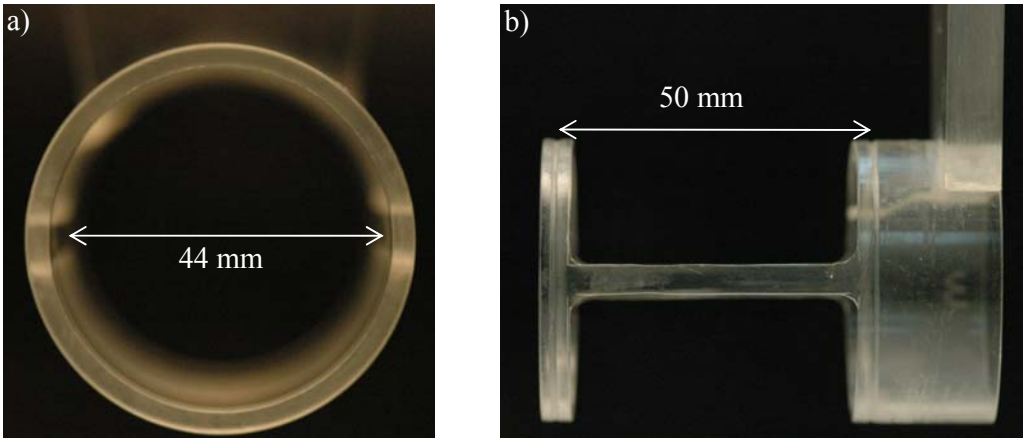

Figure 5.27. Cylindrical Perspex tissue holder used in both degassed water (Chapter 6) and ex-vivo (Chapters 7 and 11) experiments. The front face is shown in (a) and the side view (b) shows length of the holder with the front face to the left hand side and the back face to the right hand side. For clarity, Mylar windows are not shown.

A Perspex tube with a Mylar membrane on one end was inserted into the rear of the holder to hold cylindrical tissue samples (up to 45 mm in length, in place, but compressed to 40 mm in the tissue holder). Samples were compressed to prevent tissue displacement during HIFU exposures.

5.5 Sample photography

Once cylindrical tissue cores had been exposed to HIFU, they were dissected along the acoustic axis with a skin graft knife in order to expose the lesion. If a lesion was present in the sample it was photographed in a holder (Figure 5.28) using a digital camera (Nikon D70) with a macro lens (Nikon, 105 mm, f/2.8D).

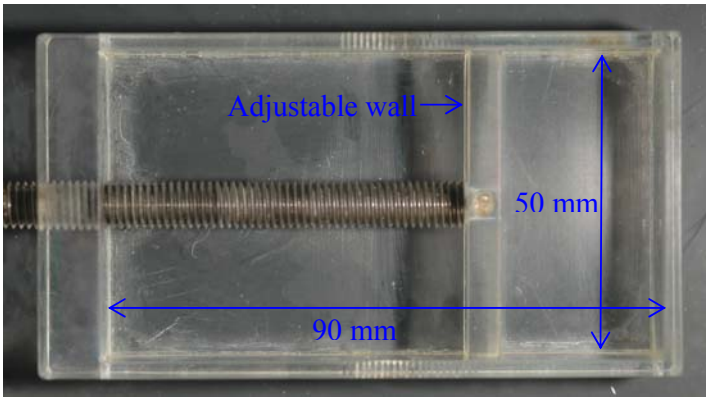

Figure 5.28. The Perspex sample holder, used to compress the cut samples back to the size they were during HIFU exposure and to hold them for photography.

When using the holder in Figure 5.28, the camera was positioned 42 cm above it. It was configured to acquire images with a resolution of 3008 x 2000 pixels, which gave a resolution of 14 µm per pixel. The adjustable wall of the sample holder allowed different length samples to be held, and was positioned so that the samples were compressed to the same extent as when they were mounted in the cylindrical holder for HIFU exposures. A schematic diagram of the photography set up is shown in Figure 5.29. This included a flash gun mounted either side of the camera. These were aligned at approximately 45° to the sample holder. The flash guns were arranged such that they illuminated the furthest region of tissue from them, to minimise direct reflections into the camera lens and shadowing from the side of the holder. Cross polarising filters were placed in front of the flash guns and in front of the camera lens (this filter being

orientated at 90^{o} to the other two) to produce photographs with good contrast between the normal tissue and lesion, and to eliminate specular reflections from the tissue surface.

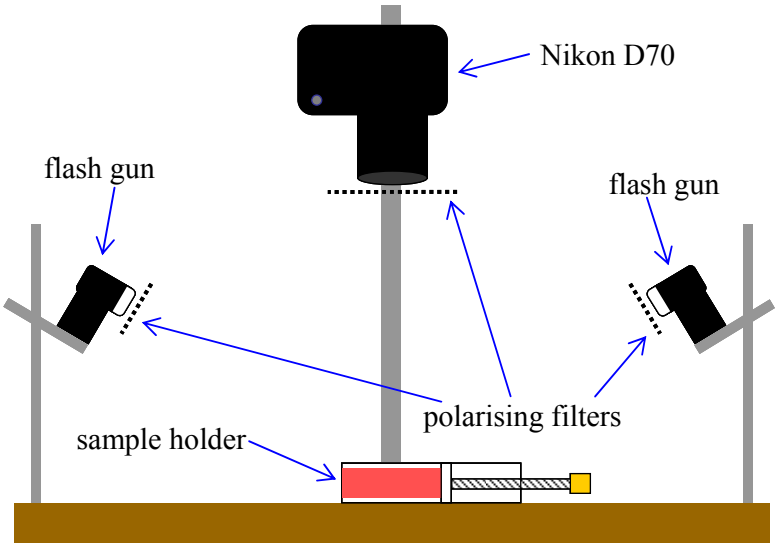

Figure 5.29. The sample photography set up. Flash guns were angled at approximately 45^{o} to illuminate the area furthest away, thus minimising reflections and shadowing. Polarising filters were added to minimise specular reflections and to improve the contrast between lesioned and non-lesioned tissue.

The camera was operated in manual mode the flash guns were linked and triggered simultaneously by the camera. This system was also used to photograph exposed samples of kidney (Chapter 9) and perfused liver tissue (Chapter 10). For larger samples a Nikon AF-S, 18-135 mm, f/3.5-5.6G lens could be used. However where a sample was too large to fit under the system shown in Figure 5.29, the camera was operated free hand. A MatLab routine was written in order to measure the lesion dimensions (length, width and area) from the photographs taken with this system. The user was required to specify the start, end, top and bottom (maximum width was selected) of the lesion. Area was calculated using boundary recognition. The contrast between the lesioned and normal tissue allowed the program to define an outline of the lesion, within this boundary the number of pixels were added together giving the total area contained within the boundary. The pixel size was calibrated using a reference distance in the image (e.g. a ruler) and they were assumed to be square. Figure 5.30 shows a 'test lesion' that had been photographed by this system and subsequently analysed using the MatLab program. The four positions on the lesion indicate the locations where the user has defined the length (2-1) and width (4-3) of the lesion.

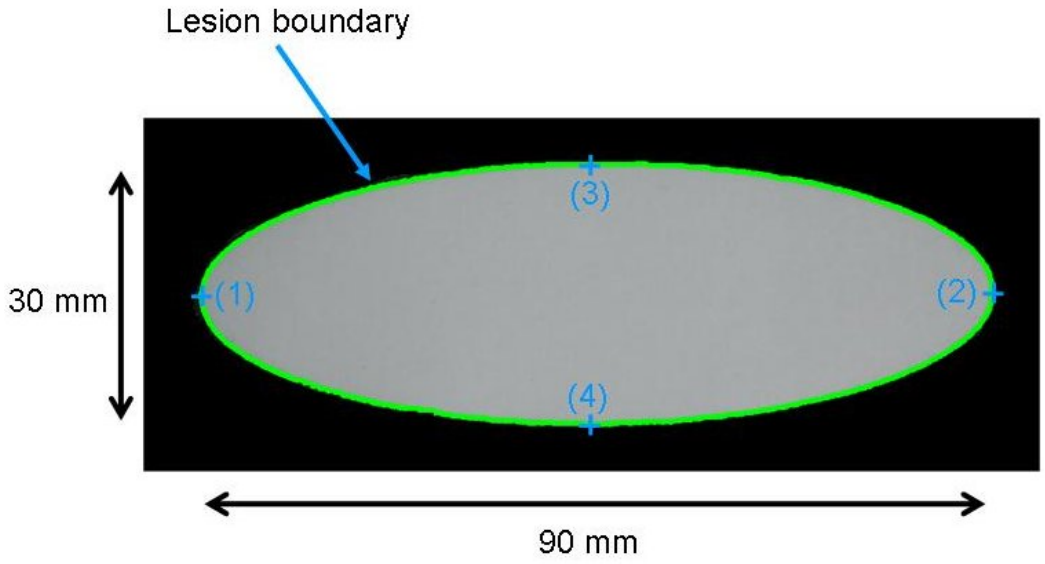

Figure 5.30. A photograph of a 'test lesion' that has been processed by the lesion analysis program. The green line indicates the lesion boundary, and the four points show how the user would calculate the length (2-1) and width (4-3) of the lesion.

The average (n = 5) length, width and area of this 'test lesion' (Figure 5.30) was measured to be 89.8 ±0.25, 29.5 ±0.11 mm and 2080 ±9.5 mm^2, where the uncertainty in these measurements the standard deviation of the average value. This process was repeated with every lesion photograph in this study and lesions that had artefacts (e.g. blood vessels) were discounted.

5.6 Summary

This chapter has outlined the basic HIFU equipment and transducer calibration techniques (based on a radiation force balance and membrane hydrophone) used for this project. Calibration details for the two transducers used most widely for this project have been given. The acoustic pressures and spatial peak intensities measured will be referred to in all subsequent chapters. The photography system developed to obtain high resolution images of highly specularly reflecting tissue surfaces has also been described.

6 – Acoustic cavitation detection in liquid media

This chapter describes the use of the cavitation detection system in non-attenuating media, namely degassed water and potassium iodide (KI) solution, in which heating cannot occur, but acoustic cavitation may. The studies performed in these two different media are presented separately, with the sonochemical study presented first.

6.1 Sonochemical Study

A sonochemical reaction was used as an indicator of inertial cavitation, in an attempt to understand the emissions detected by the passive cavitation detection system (described in §4.2) from HIFU exposures of a KI solution better.

$$H_2O \rightarrow H^+ + OH^+ \tag{6.1}$$

$$I^- + OH^+ \rightarrow OH^- + I^+ \tag{6.2}$$

$$I^+ + I^- \Leftrightarrow I_2^{+-} \tag{6.3}$$

$$2I_2^{+-} \rightarrow I_2 + 2I^- \tag{6.4}$$

Equation 6.1 describes the production of free radicals (OH^+) in solution from the generation of inertial cavitation from HIFU exposures. Equations 6.2-6.4 describe the Weissler reaction (Birkin *et al*, 2002; Birkin *et al*, 2003) in which free radicals are scavenged, leading to iodine production. This molecular iodine production (I_2) causes an increase in absorbance in the UV spectrum (300-400 nm). The aim was to use these sonochemical reactions in conjunction with passive cavitation detection to provide a secondary indication of inertial cavitation activity.

6.1.1 Methods

The 1 and 10 MHz passive sensors with the high and low pass RF filters were used as part of the passive cavitation detection system, which was described in section 4.2. The Mauve (1.69 MHz) HIFU transducer, micrometer gantry and degassed water from the degassing system which were all described in Chapter 5 were used for this. The sonochemical test solution (KI) was mixed to a concentration of 0.1 mmol/dm^3 (Birkin *et al*, 2002) in an appropriate volume of pure water (1 L). Individual samples of KI solution (approximately 2 ml) were exposed in a specially designed (20x15 mm) holder (Figure 6.1) to 1.69 MHz ultrasound. The holder was designed such that it enclosed the focal field of the HIFU transducer (16x2 mm) and was sufficiently large that acoustic

windows, for cavitation monitoring, could be cut into its sides without loss of structural integrity, but as small volume as possible was used in order to maximise the measurement sensitivity. This cylindrical Perspex holder, shown in (Figure 6.1(b)) slotted into a Perspex block, which held in place a second piece of Clingfilm covering the rear window. This block was attached to the micrometer gantry described in section 5.1.3, which allowed precise motion for the targeting of the HIFU in the KI solution.

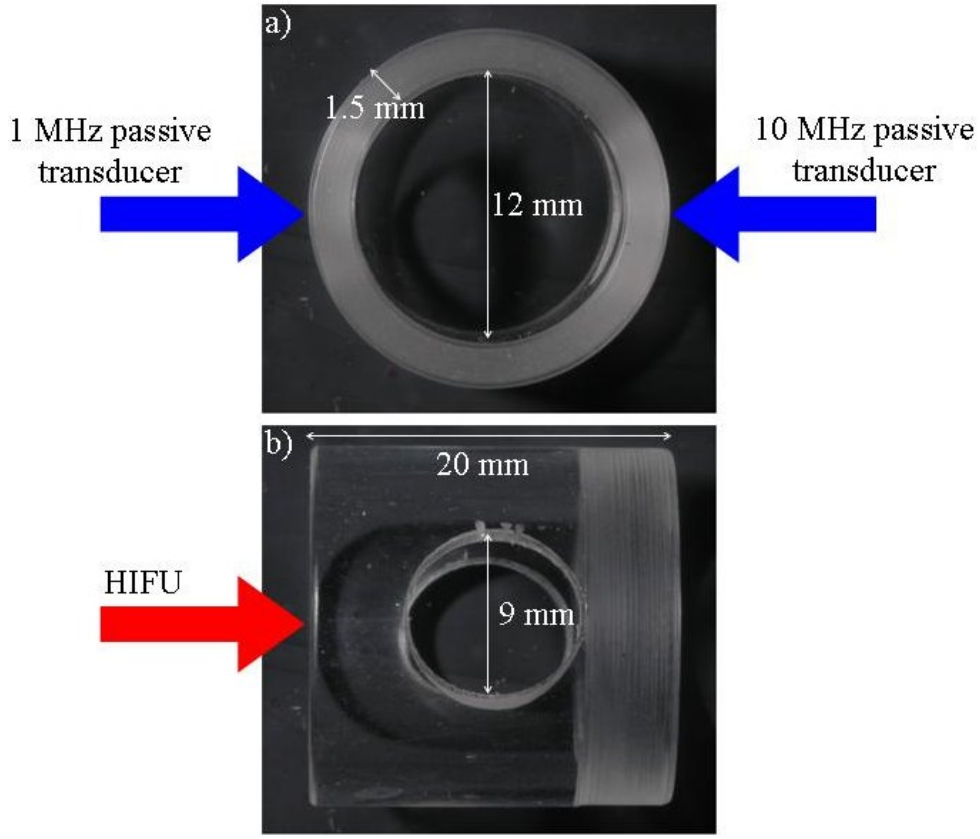

Figure 6.1. Photographs of the front (a) and side (b) of the cylindrical Perspex holder, which contained the KI solution used for the sonochemical study. The two pieces of cling film used to provide the front sides and rear acoustic windows are not shown in the photograph. The frosted part of the holder shown in (b) was slotted into the Perspex block which held the rear acoustic window in place and located the sample holder in the acoustic field.

The holder was first positioned using the pointer so that the focal peak of the HIFU was located approximately at the centre of the front surface. By using the pulse-echo technique (§5.3.2) to locate the sides of the holder it was possible to determine the centre point of the holder more accurately by location of four points in opposing pairs on the holder (typically centre top, bottom, left and right). This was done by movement

of the micrometer gantry. Once the HIFU beam was aligned with the central axis of the holder it was possible to translate the whole arrangement in the axial direction so that focal peak was in the centre of the acoustic windows used for the passive cavitation detectors. Both the HIFU field and passive cavitation detectors were aligned prior to the introduction of the KI holder.

The sonochemical solution was exposed for 5, 10, 16 or 60 s using an I_{sp} (peak negative pressure) range 440-3100 W/cm^2 ±20% (1.80 to 2.38 MPa ±17%) with individual values of 440, 550, 700, 880, 1100, 1400, 1700, 2200, 2500 and 3100 W/cm^2 (1.80, 1.88, 2.04, 2.08, 2.10, 2.20, 2.30, 2.32, 2.35 and 2.38 MPa). The data acquisition system (§4.2.3) was not able to record continuously for 60 s, so the proprietary software, SBench, was used to acquire 'snapshots' of length 4096 points (~0.2 ms) of the acoustic spectra throughout the exposure. This worked by acquiring 37 datasets per second at regular intervals, giving a duty cycle of approximately 1%. The signal processing techniques described in section 4.2.4 were used on each of these datasets to yield the variation with time of the specific peak or bands of frequencies of interest. Once the KI had been exposed to a single HIFU exposure, the 2 ml volume of solution was transferred, using a 5 ml syringe, into a 2 ml Eppendorf tube. The holder was dried out each time before being refilled with KI solution for the next exposure.

The relative absorbance between 270-400 nm of the exposed solutions was measured in a spectrometer (UV/VIS Lambda EZ 201, PerkinElmer, Waltham, MA, USA) and was recorded. A quartz cuvette (2 ml volume) was used when measuring the spectrum since it is transparent to the UV spectrum investigated. Figure 6.2 shows the decay in measured absorbance (ABS) for an exposed KI sample left at room temperature (20^{o}C) for an hour. The absorbance was measured approximately 30 mins after the exposure, as this was the most suitable time to measure after a series of between 3-5 exposures had been carried out.

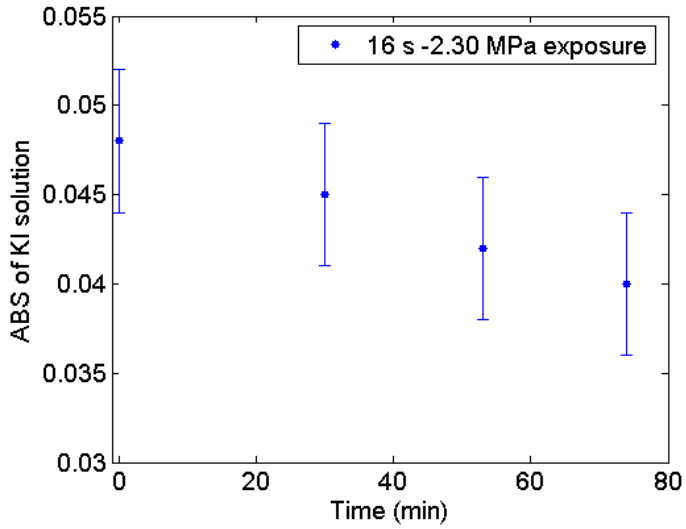

Figure 6.2. Decay in the absorbance at 350 nm, following a single 16 s exposure at 1400 W/cm^2 (2.30 MPa) as a function of time. The uncertainties plotted here show the variation in absorbance measured from an unexposed sample.

The active and passive cavitation detection techniques described previously (4.2 and 4.3) were used during each exposure. However, B-mode imaging was not used as no acoustic window into the solution was available.

6.1.2 Results

The data presented in this section are from single HIFU exposures, of a KI solution, with durations of 5, 10 or 16 s over the I_{sp} (peak negative pressure) range 440-3100 W/cm^2 ±20% (1.80 to 2.38 MPa ±17%). Figure 6.3 and Figure 6.4 show typical acoustic spectra acquired during two 10 s HIFU exposures of the KI sonochemical solution. These plots are typical in that the peak amplitude fluctuates rapidly during the exposure, in some instances these fluctuations can occur over approximately 1 ms, which is the temporal resolution of this system. In addition, the amplitude and frequency increases with exposure intensity (pressure), as can be seen in the difference between these two plots.

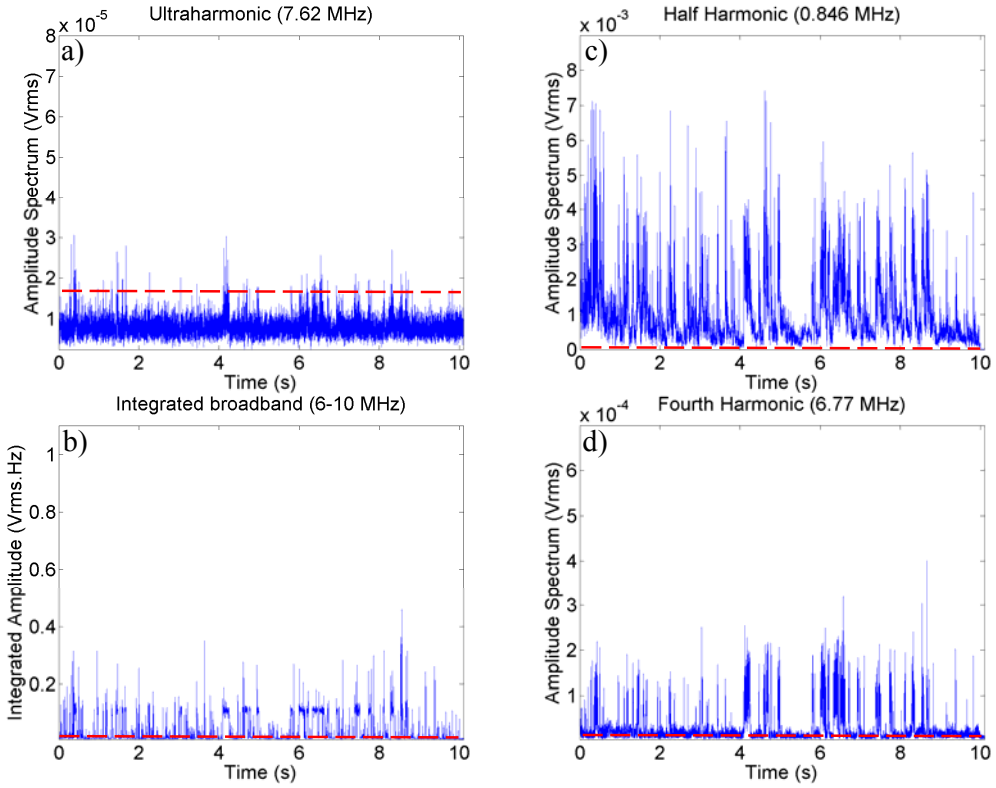

Figure 6.3. Acoustic spectra detected with the passive cavitation detection system from a single 10 s exposure at 1700 W/cm^2 (2.30 MPa) in the KI solution. The red dashed line indicates the peak noise level measured from a sham exposure.

Figure 6.3(c) show that the amplitude of the detected half harmonic emissions from this exposure did not drop below the noise level throughout the exposure. The amplitudes of the acoustic spectra shown in Figure 6.4 were all above the noise level indicated by the dashed red line throughout the exposure.

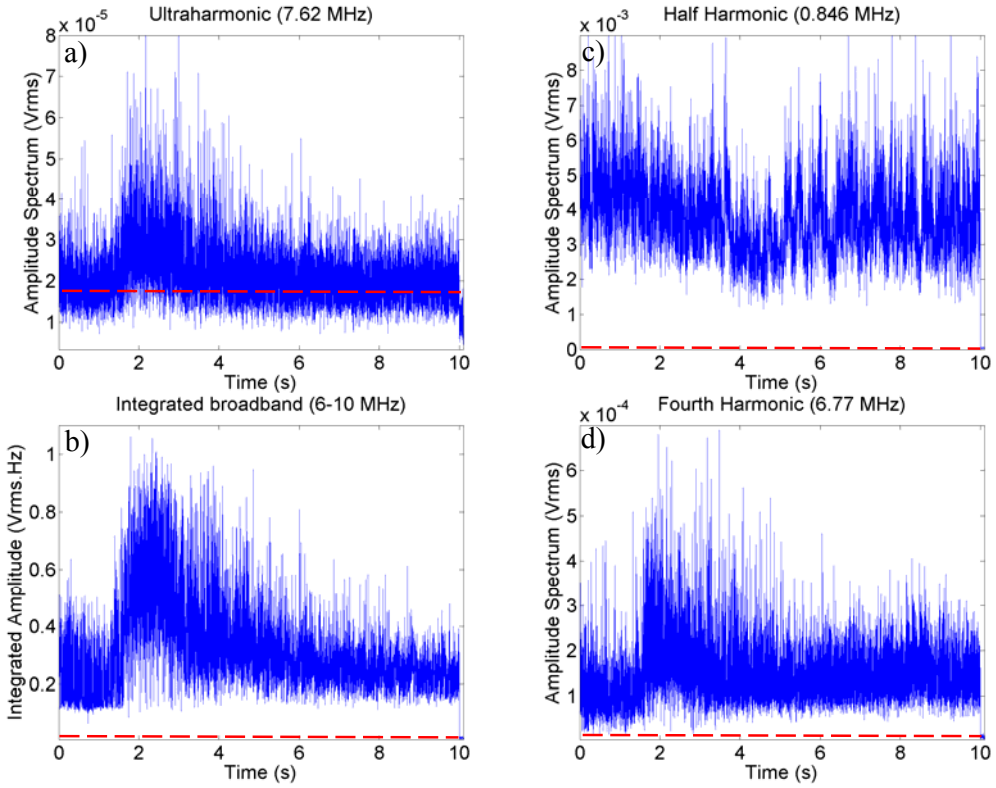

Figure 6.4. Acoustic spectra detected with the passive cavitation detection system from a single 10 s exposure at 3100 W/cm^2 (2.38 MPa) in the KI solution. The red dashed line indicates the peak noise level measured from a sham exposure.

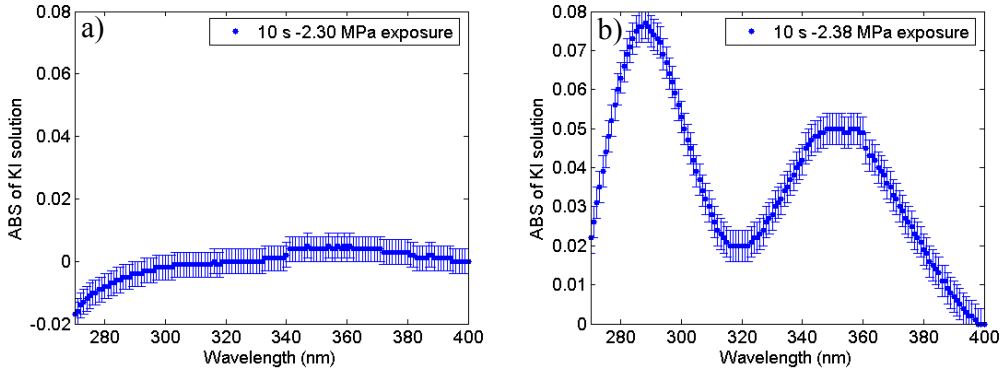

Figure 6.5. The measured absorbance over the UV spectra of the two KI solutions from the exposures described in (a) Figure 6.3 and (b) Figure 6.4. The error bars in the plots is the measured variation in absorbance at 350 nm of an unexposed sample. Negative absorbance in (a) was due to an ABS difference between the reference sample and this exposure.

Figure 6.5 shows the UV absorbance spectra from two KI solutions that were exposed for 10 s to (a) 1700 W/cm^2 (2.30 MPa) and (b) 3100 W/cm^2 (2.38 MPa) HIFU. Figure 6.5(b) shows the peaks due to the absorbance of light at these wavelengths by the

molecular iodine in the solution (Birkin *et al*, 2002), produced by the sonochemical reaction in the solution.

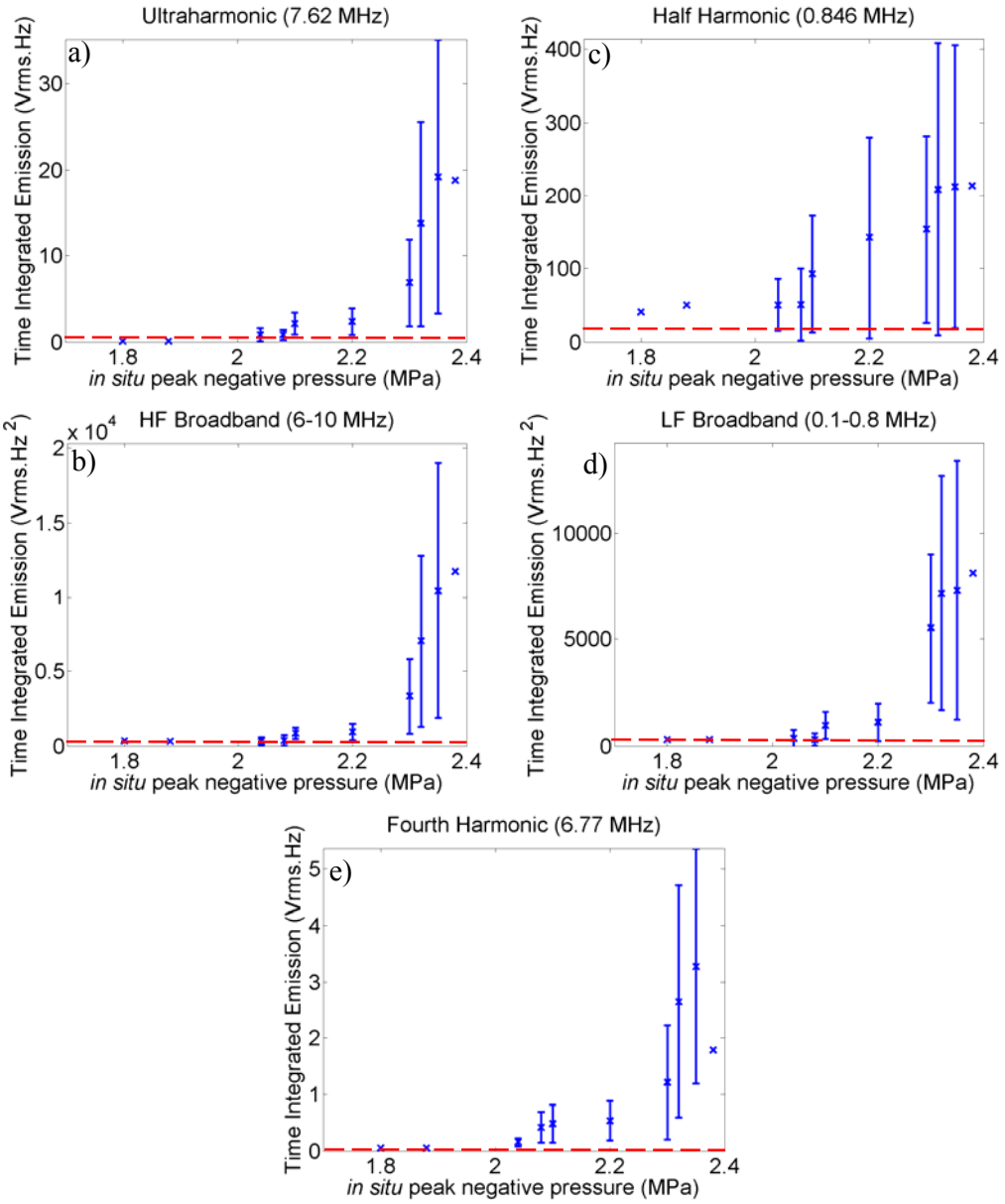

Figure 6.6. The averaged total time integrated (a) ultraharmonic (7.62 MHz), (b) HF broadband emissions (6-10 MHz), (c) half harmonic (0.846 MHz) (0.1-0.8 MHz), (d) LF broadband emissions and (e) fourth harmonic (6.77 MHz) shown over the range of peak negative pressures used. Uncertainty, where shown, is the standard deviation for n = 3-5. The red dashed line indicates the peak noise level measured from a sham exposures.

Figure 6.6 shows the averaged total time integrated emissions for the acoustic spectra monitored with the dual frequency passive cavitation detection system during the 5, 10

and 16 s exposures in the KI sonochemical solution. This shows that half harmonic emissions (Figure 6.6(c)) were detected above the noise level at peak negative pressures greater than 1.80 MPa, while broadband emissions (Figure 6.6(b) and (d)) were detected above 2.10 MPa.

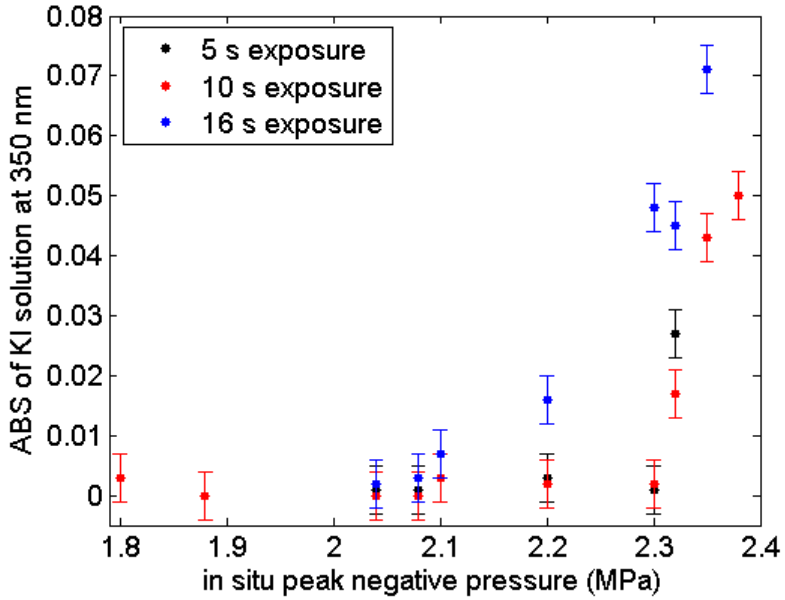

Figure 6.7. The measured absorbance (ABS) of UV at 350 nm in KI solutions exposed for 5, 10 and 16 s. The uncertainty shown is that of the measured absorbance at 350 nm of an unexposed sample.

Figure 6.7 shows the measured absorbance of KI samples for 5, 10 and 16 s exposures over the I_{sp} (peak negative pressure) range 440-3100 W/cm^2 ±20% (1.80 to 2.38 MPa ±17%. For the 5 and 10 s exposures a sonochemical change is only measured at 2200 W/cm^2 (2.32 MPa), whereas the 16 s exposures yielded a sonochemical change at 1100 W/cm^2 (2.10 MPa). It can be seen that for the 5 and 10 s exposures where broadband emissions are detected first with the passive cavitation detection system, no change in the absorbance was measured within the uncertainty in the measurements up to 1700 W/cm^2 (2.30 MPa). However, for the 16 s exposures a sonochemical change was detected at the sample pressure level at which broadband emissions are first detected.

6.1.3 Discussion

The aim of the sonochemical study was to use a secondary indicator of inertial cavitation activity with which to compare detected acoustic emissions. Molecular Iodine, generated from free radical production when a KI solution was exposed to HIFU, was used to indicate that inertial cavitation had occurred during an exposure. A

specially designed holder was used to contain a volume of KI solution as close as possible to that of the focal field (Figure 6.1). A number of problems restricted the holder size, firstly in order to provide acoustic windows for the passive cavitation detection system, 9 mm diameter holes were cut into the side of the holder. As the thickness of the holder was 1.5 mm, this meant that the minimum size for it to retain structural integrity was 20x15 mm. The inner dimensions of the holder give a volume of approximately 2260 mm^3, where the approximate volume of the focal region was 70 mm^3, meaning that the volume of the holder was approximately 30 times that of the focal region. The second problem was to ensure that the sonochemical holder was watertight when submerged in degassed water. This was achieved by putting Clingfilm over the front and side windows and holding it in place with two rubber O-rings either side of the side acoustic windows. The rear window was held in place when the cylindrical holder was inserted into the Perspex block mount. This technique ensured that the holder was watertight, while allowing easy access for changing the sonochemical solution.

Figure 6.4(b) and Figure 6.5(b) show the broadband emissions and absorbance spectra of a sample of KI solution, which had a HIFU exposure of I_{sp} = 3100 W/cm^2 (2.38 MPa) for 10 s. The lower I_{sp} exposure shows no increase in UV absorbance (at 350 nm), however there were broadband emissions, indicative of inertial cavitation. For the higher I_{sp} exposure (Figure 6.4) there is clearly sonochemical activity (Figure 6.5(b)), and the broadband emissions are higher in amplitude and occur more frequently. At the lower I_{sp} exposure (Figure 6.5(a)), absence of sonochemical change may be due to the spectrophotometry detection threshold not having been exceeded. This reflects the number of Iodine molecules in solution needed to cause a change in the absorbance detectable by spectrophotometer. Unfortunately, this calibration data was not available for this device. Another factor to be considered is that the total volume of the solution is approximately 30 times that of the HIFU focal region, and even if inertial cavitation were generated within the focal region, the solution might be sufficiently dilute as to not exceed the lower limit discussed previously. This is likely to be the reason that a 16 s exposure was needed before the sonochemical change occurred at the same I_{sp} (pressure) at which broadband emissions were detected. Figure 6.6 shows that for this length of exposure it was possible to induce a detectable sonochemical change at a peak negative pressure of 2.10 MPa, but that it was not possible for similar 5 and 10 s exposures. A number of samples (n = 3) were exposed for 60 s at a peak negative

pressure of 2.08 MPa, in order to investigate whether a sonochemical change could be generated in the absence of broadband emissions. The longer time was used to give sufficient time for enough sonochemical reactions to have occurred to overcome the dilution problem. However, no sonochemical change was detected in the absence of broadband emissions.

For an I_{sp} of 3100 W/cm^2 (2.38 MPa), both broadband emission (Figure 6.4(b)) and sonochemical change (Figure 6.5(b)) were detected. Thus, there is little doubt that acoustic cavitation occurred, and more specifically that it was inertial cavitation. The number of inertial cavitation events can be estimated in relation to the number of Iodine atoms produced. It is possible to calculate the concentration of iodine from the absorbance at 350 nm, using the Beer-Lambert law (Atkins, 1995):

$$\textit{Absorbance at a wavelength} = \textit{concentration*path length*extinction coefficient} \quad (6.5)$$

The path length is the distance light travels in the spectrometer (10 mm) and the extinction coefficient is 26500 mol^{-1}cm^{-1} (Suslick *et al*, 1997). Therefore the relationship can be rewritten:

$$\textit{Iodine concentration} = \textit{ABS}/26500 \quad (6.6)$$

Using this relationship and the absorbance at 350 nm from Figure 6.5(b), the concentration of molecular iodine was calculated to be $1.88*10^{-6}$ mol/dm^3. The volume of the container was $2.0*10^{-3}$ dm^3. This gives an iodine production of 3.76 nmol, or approximately $2.3*10^{15}$ iodine atoms. In theory, one free radical can liberate a single iodine atom. However, this could not be confirmed experimentally in this study. In addition, it is not possible to identify whether a single free radical would be liberated from a single bubble collapse, but it has been assumed to be so here, for the purpose of this derivation. If the reaction were assumed to have a 60% conversion rate, this would give the estimate that $1.4*10^{15}$ free radicals were created during a 10 s HIFU exposure. Thus if it were possible to estimate the number of bubble collapses generated during this exposure it could be possible to quantify the level of broadband emissions with an estimation of the number of inertial cavitation events that occurring during the exposure.

6.2 Degassed water study

6.2.1 Introduction

The aim of the degassed water study was to test the detection system in a minimally attenuating medium that is known to cavitate in order to give a useful comparison with the ex-vivo results (§7.2.2) (Flynn, 1964; Neppiras, 1980; Walton and Reynolds, 1984). Since the acoustic absorption of water is negligible, focal heating is unlikely, and thus cannot affect acoustic cavitation occurrence, and boiling bubbles were not generated.

6.2.2 Methods

The passive cavitation detection system described in the previous methods section and in Chapter 4 were used in this experiment. Active cavitation detection was provided by the linear probe with the Zonare diagnostic ultrasound scanner (§4.3) and the electrical drive power was monitored. The Mauve HIFU transducer (1.69 MHz) was used to expose degassed water provided by the degassing system, both are described in Chapter 5.

Degassed water was exposed to 2 or 4 s HIFU exposures over a spatial peak intensity (I_{sp}) range of 300-2200 ±20% W/cm^2 (peak negative pressure range of 1.43 to 2.32 ±17% MPa). For a degassed water volume (~27000 cm^3) significantly larger than the focal volume of the 1.69 MHz Mauve transducer (~0.3 cm^3), it was verified experimentally that multiple exposures, such as those used in this study, did not change its acoustic cavitation threshold. Data from this study can be seen in Figure 6.10, which shows the total time integrated emissions from over the I_{sp} range 300-2200 W/cm^2 (1.48 to 2.32 MPa) for 4 s HIFU exposures. The three time points were 0, 2.5 and 5h after the start of the experiment, which was approximate 1 h after the degassed water had been added to the tank, as this was the time taken to align the passive cavitation detectors with the HIFU focal peak. Approximately 20 HIFU exposures 2200 W/cm^2 (2.38 MPa) were performed between the measurements for these data sets. The data in Figure 6.10 shows that acoustic emissions were not detected a lowest exposure levels at any point during the experiment. However it can be seen that the peak amplitude of these measurements varied, but this could be related to the transient nature of acoustic cavitation activity.

Since radiation force causes streaming and moves the bubbles away from the transducer, the tissue holder shown in Figure 5.28 (§5.4) with the front Mylar window

inserted to reduce acoustic streaming was used for this experiment. The rear window was not used, in order to both allow bubbles to stream out of the holder and ingress of unexposed water. The experimental set-up shown in section 7.2.1 was used for each exposure.

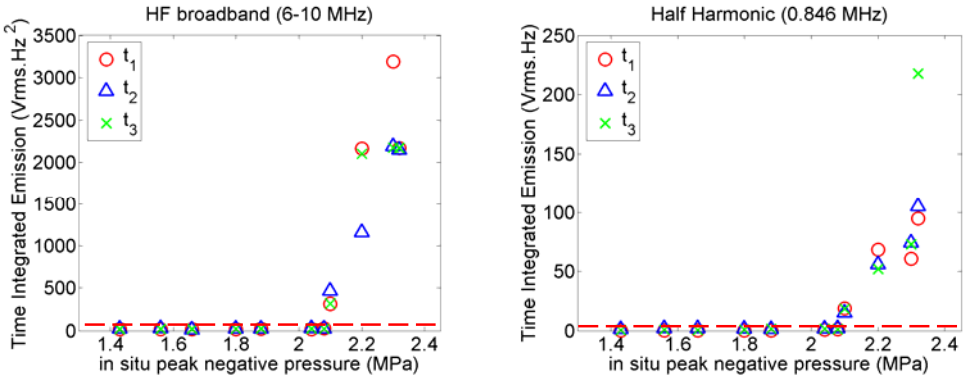

Figure 6.8. The total time integrated emissions for three series of 4 s exposures in degassed water over the same exposure range at different time points, t_1 = 0 h, t_2 = 2.5 h and t_3 = 5 h. The red dashed line indicates the peak noise level measured from a sham exposure.

6.2.3 Results

Examples of emissions repeatedly seen during multiple (n ~ 50) HIFU exposures of degassed water are shown in Figure 6.9 and Figure 6.10. These examples were chosen as they were typical of the signals detected at these power levels, showing that the amplitude and frequency of the detected emissions increased with intensity.

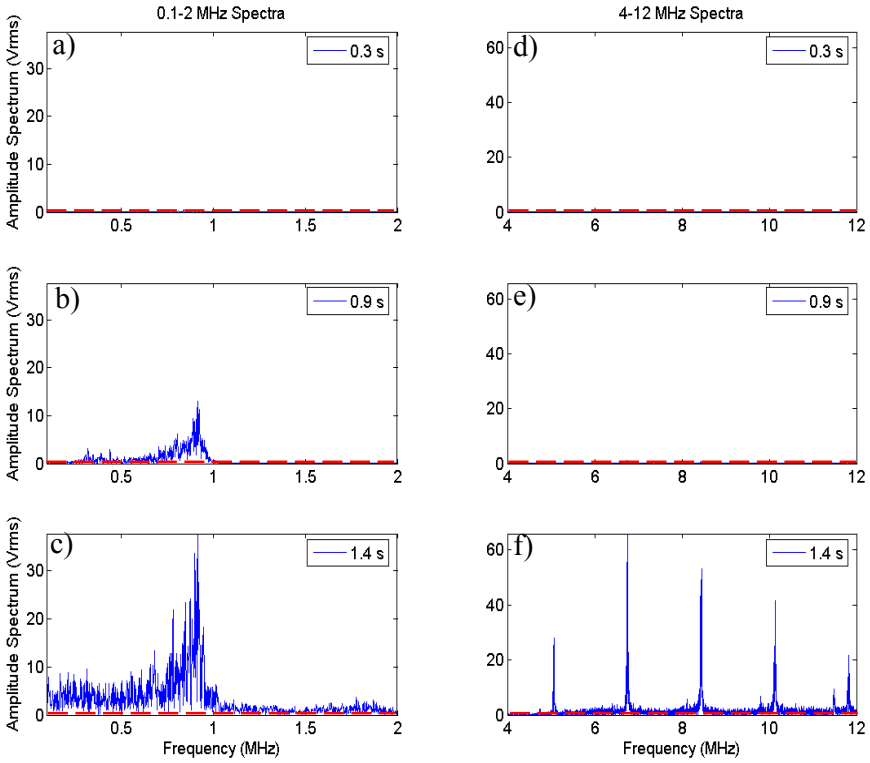

Figure 6.9. The low (a-c) and high (d-f) frequency spectra detected at three separate times (0.3, 0.9 and 1.4 s) during a 4 s HIFU exposure, [I_{sp} = 1100 W/cm^2 (2.10 MPa)] of degassed water. A Hanning window function and 214 data points were used to generate each of the FFT spectra. The red dashed line indicates the peak noise level measured from a sham exposure.

Figure 6.9 shows the spectra detected at three different time points during a single 4 s exposure with I_{sp} = 1100 W/cm^2 (2.10 MPa). Figure 6.9(a)-(c) and (d)-(f) show the spectra detected using the 1 and 10 MHz transducer, respectively. At 0.3 s, no acoustic emissions were detected above the indicated noise level. Only half harmonic emissions were detected at 0.9 s, whereas 4th, 5th, 6th and 7th harmonics (6.77, 8.47, 10.2 and 11.9 MHz) and broadband emissions (4-12 MHz) were seen at 1.4 s.

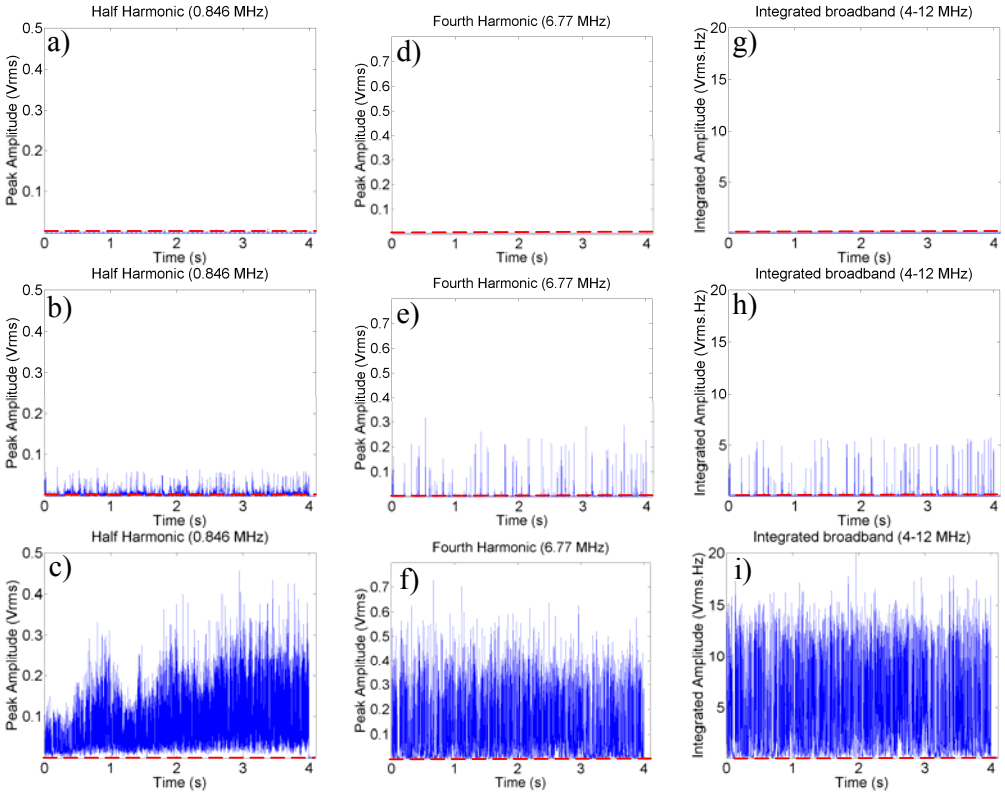

Figure 6.10. Sample spectra acquired from three individual 4 s HIFU exposures in degassed water, with I_{sp} (pressure) of (a, d and g) 300 W/cm^2 (1.43 MPa), (b, e and h) 1100 W/cm^2 (2.10 MPa) and (c, f and i) 2200 W/cm^2 (2.32 MPa). (a-c) Half harmonic (0.846 MHz) emissions, (d-f) fourth harmonic and (g-i) integrated (4-12 MHz) broadband emissions. The red dashed line indicates the peak noise level measured from a sham exposure.

Figure 6.10 shows a comparison of the acoustic emissions detected at three different I_{sp} exposure levels (peak negative pressure) at 300 (1.43 MPa), 1100 (2.10 MPa) and 2200 (2.32 MPa) W/cm^2. This figure shows that as the exposure intensity is increased the amplitude and frequency of the detected acoustic spectra increase. For the lowest exposure used in this study, (Figure 6.10(a), (d) and (g)) no acoustic spectra above the noise level were detected. Figure 6.11 shows the expanded electrical drive power measurements for the three exposures shown in Figure 6.10. In Figure 6.11(b) and (c), the expanded scales highlight the electrical drive power fluctuations seen. As with the detected acoustic spectra, the increase in the amplitude and frequency of the electrical drive power fluctuations can be seen.

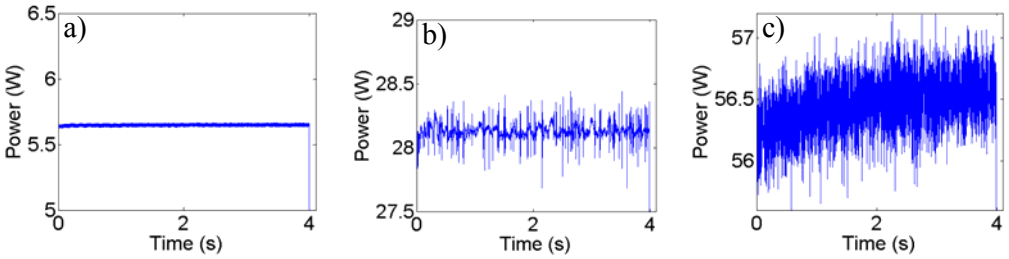

Figure 6.11. The electrical drive power derived from the measured HIFU drive voltage and current is shown for the three exposures in degassed water shown in Figure 6.10. (a) 300 W/cm2 (1.43 MPa), (b) 1100 W/cm^2 (2.10 MPa) and (c) 2200 W/cm^2 (2.32 MPa). The power scale has been expanded to show the range of fluctuation rather than emphasising the drive level. This shows an approximate fluctuation of ± 3 % about the nominal drive level.

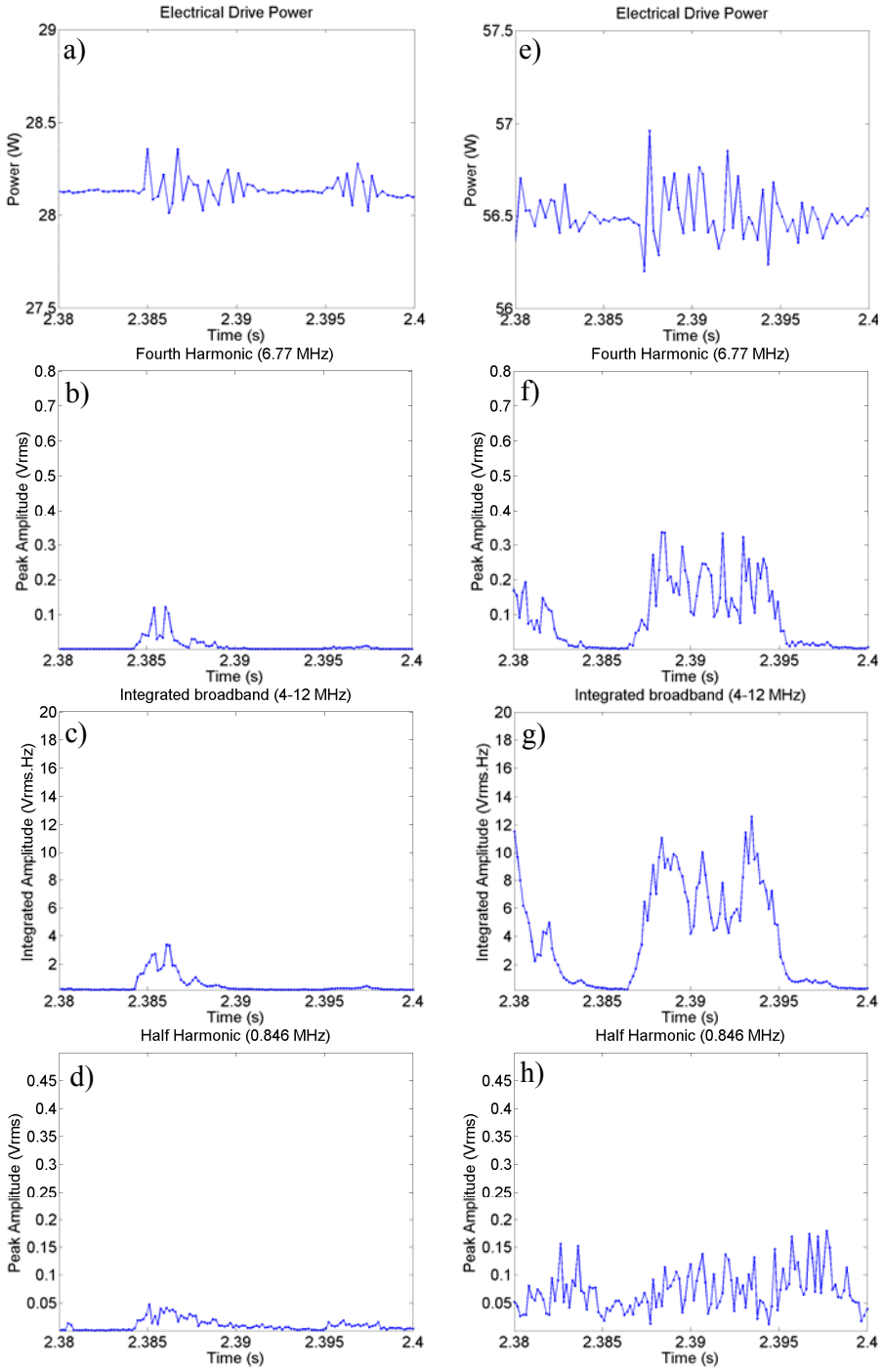

Figure 6.12. Cavitation monitoring measurements made between 2.38 and 2.40 s during 4s long 1100 W/cm^2 (2.10 MPa) (a-d) and 2200 W/cm^2 (2.34 MPa) (e-h) exposures in degassed water. (a, e) Drive power, (b, f) fourth harmonic, (c, g) broadband emissions and (d, h) half harmonic.

Figure 6.12 shows the measured electrical drive power for the 3 exposures shown in Figure 6.10. Power fluctuations can also be seen in Figure 6.11 (b) and (c). The plots show a temporal correlation between the start of power fluctuations and the detection of

fourth harmonic and broadband emissions and half harmonic emissions at the lower power (Figure 6.12(d)). The uncertainty in the power measurements was measured (§4.3.2) as ± 0.2 W using the highest drive level and with a dummy load to mimic the transducer. In order to determine whether these power fluctuations coincided with any of the detected emissions it was helpful to expand the time scale. Figure 6.12 shows the power fluctuations and acoustic emissions detected between 2.38 – 2.40 s for the 1100 and 2200 W/cm^2 exposures. It shows that the power fluctuations are initiated at the same time as the broadband and fourth harmonic emissions.

Figure 6.13 demonstrates that the majority of the energy in the power fluctuations at both drive levels is at the drive frequency (1.69 MHz).

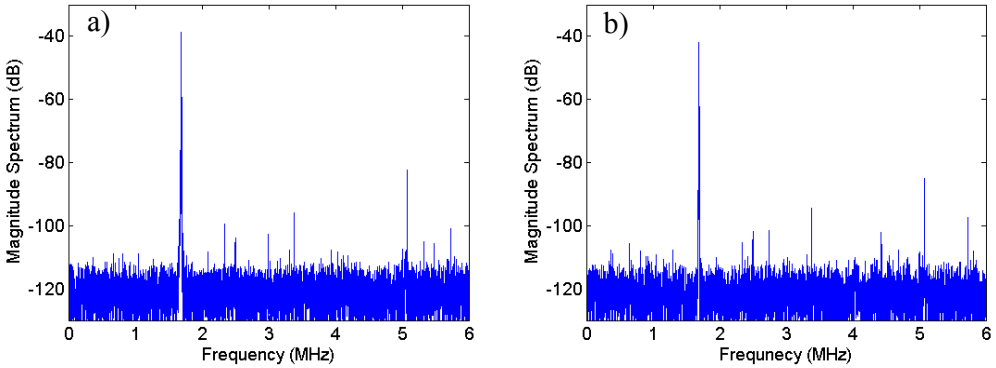

Figure 6.13. The spectral content of the drive voltage at 2.39 s for (a) 1100 W/cm^2 and (b) 2200 W/cm^2 exposures in degassed water. This shows that the fluctuations occur at the fundamental frequency (1.69 MHz) as no other harmonics can be seen.

Figure 6.14 and Figure 6.15 show a combination of the results of active and passive cavitation detection at two time points (0.21 and 2.43 s) during a 4 s 1700 W/cm^2 (2.30 MPa) HIFU exposure in degassed water. Figure 6.14(a) and (c) show the B-mode images acquired at these time points. The interference caused by the HIFU field (§4.3.1) is present in both images, but its location in the scan is different. Figure 6.14(b) and (d) show the frequency analysis of these two frames highlighting the frequency band around the second harmonic (3.39 MHz) of the HIFU drive frequency. These images show the location with respect to the HIFU focal peak of the approximate position of the interference. Figure 6.14(e) demonstrated the audible emissions that were recorded during the HIFU exposure. Audible emissions can be seen to be detected intermittently over the 6-18 kHz range, with the peak amplitude frequency at approximately 17 kHz. The white boxes highlight the two time points for which the expanded frequency spectra

are displayed in Figure 6.15. These expanded spectra round 0.21 and 2.43 s show that the broadband emissions (4-12 MHz) correlate in time with the electrical drive power fluctuations as seen in Figure 6.12, whereas the half harmonic emissions (Figure 6.15(b) and (e)) do not. Figure 6.15(c) and (f) show that the detected broadband emissions are discrete.

Figure 6.16 shows the percentage of exposures in degassed water over the exposure range that generated acoustic spectra that were above the noise level specified in section 4.2.4. The acoustic emissions in these plots (Figure 6.16(b), (c), (e) and (f)) show an distinct pressure threshold at which the detected emissions are above the noise level. Once the exposure I_{sp} was equal to or greater than 1400 W/cm^2 (2.20 MPa) acoustic emissions were detected for 100% of exposures. Figure 6.17 shows the averaged emissions integrated over the total time for the acoustic spectra monitored with the dual frequency passive cavitation detection system during all of the 4 s exposures in degassed water. The data shows a similar trend to that presented in Figure 6.16, however the uncertainty in the average measurement increases considerably after 1400 W/cm^2 (2.20 MPa). The red dashed line indicates the peak noise level measured from a number (n = 3) of sham exposures acquired throughout the study in degassed water. The average time integrated emissions shown in this figure generally increase in an exponential fashion with increasing intensity (pressure).

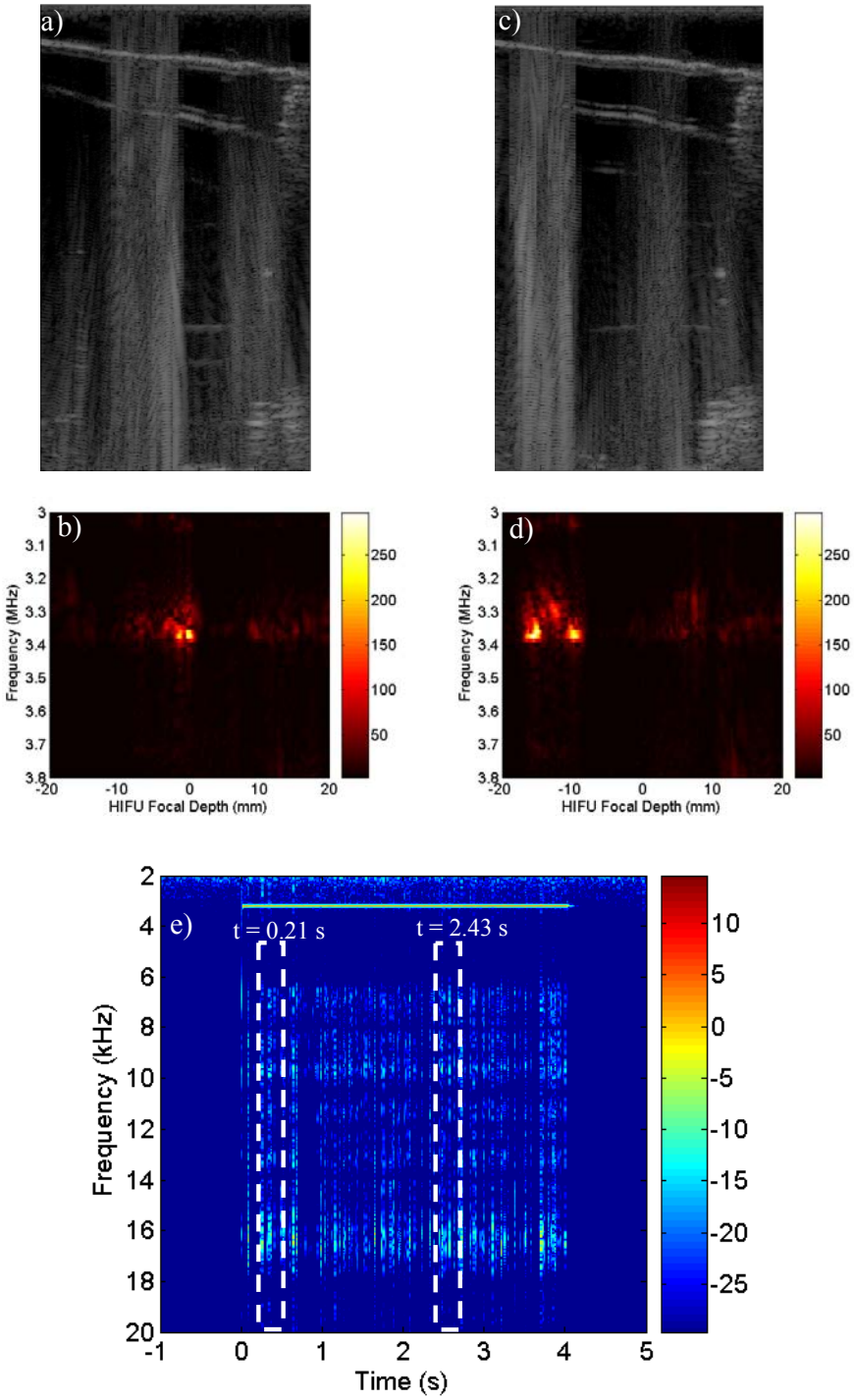

Figure 6.14. The two ultrasound imaging frames shown were taken during a single 4 s 1700 W/cm^2 (2.30 MPa) exposure in degassed water (a) 0.21 and (c) 2.43 s into the exposure. (b) and (d) are frequency maps from frames in (a) and (b), respectively. The HIFU focal plane is at 0 mm (in (b) and (d)) and the beam propagated from right to left (in all figures except (e)). (e) shows the audible emissions detected during this exposure. Note that the maximum emissions lie between 16-18 kHz, which is higher than the maximum audible frequency detected from ex-vivo exposures (§7.2.2). The colour scale is logarithmic.

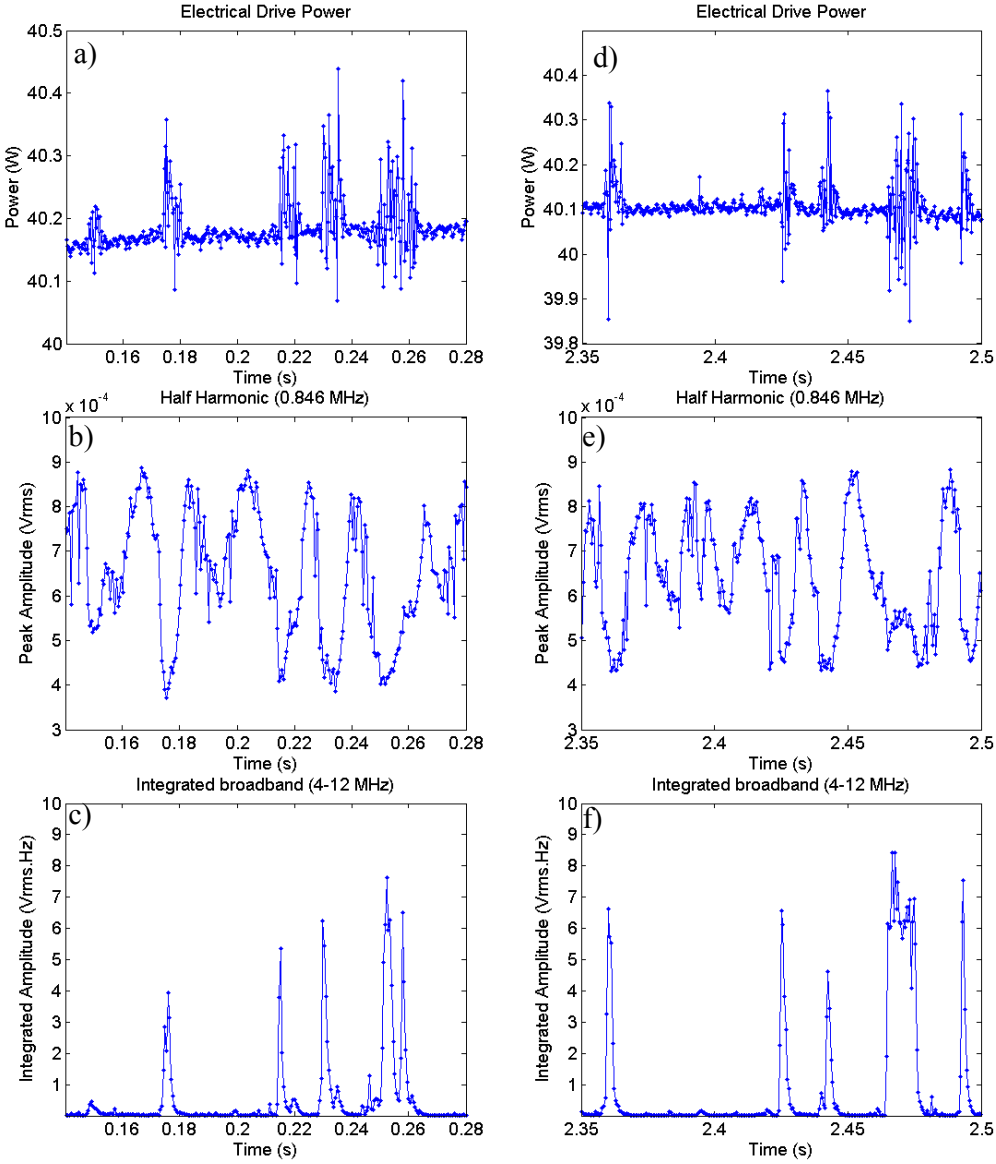

Figure 6.15. Drive power and acoustic emission data from the exposure shown in Figure 6.14. The fourth harmonic data has been omitted as it showed a similar trend to the broadband emissions. The time scale was chosen to show emissions at approximately the same times (left column at 0.21 and right column at 2.43 s) as shown in Figure 6.14.

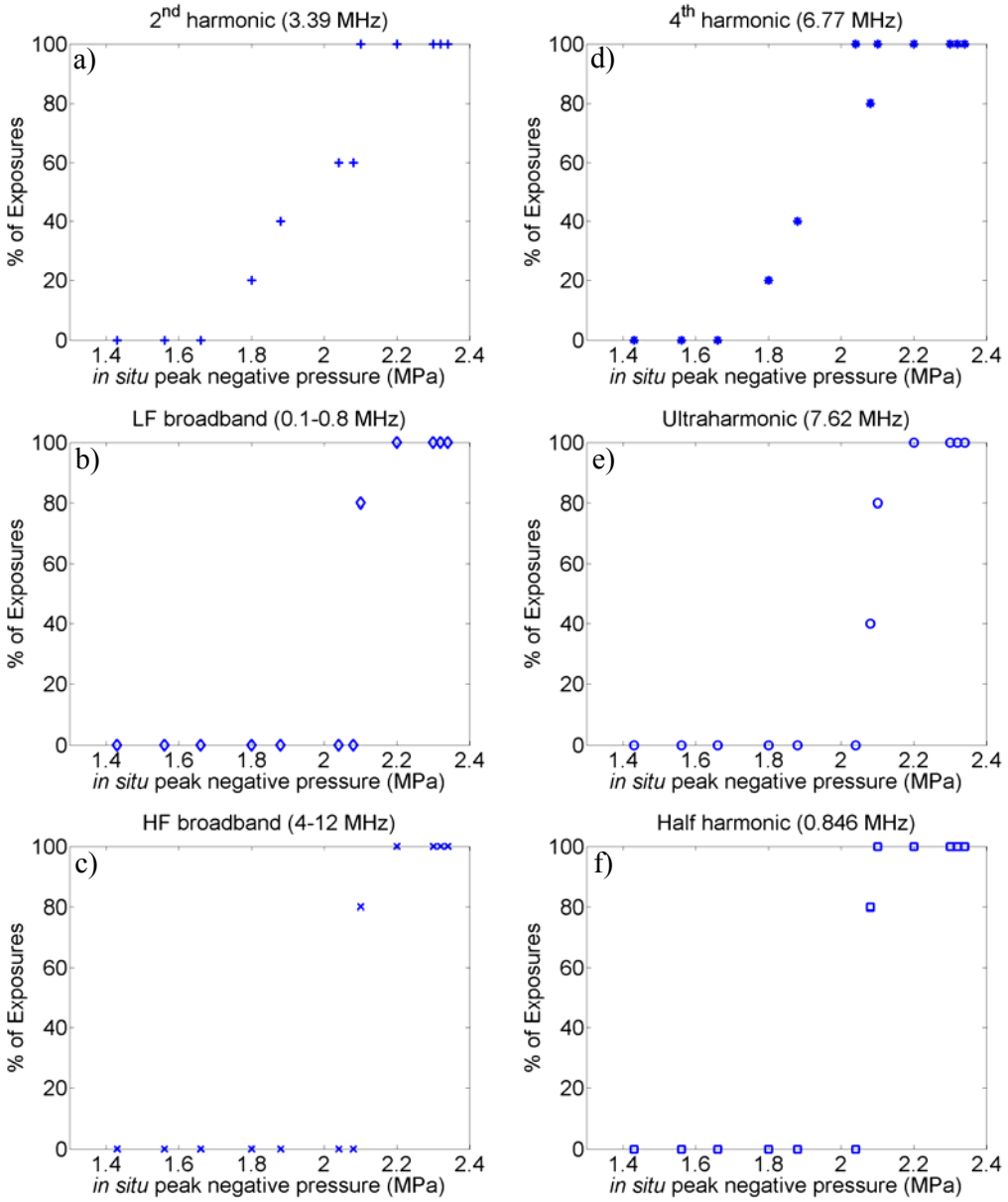

Figure 6.16. The percentage of exposures in which acoustic spectra were detected as being greater than the noise level criteria specified in section 4.2.4 at any point during the 4 s exposures. The signals were measured over the range 300-2200 W/cm^2 (1.48-2.32 MPa) where n = 3-5 for each exposure level.

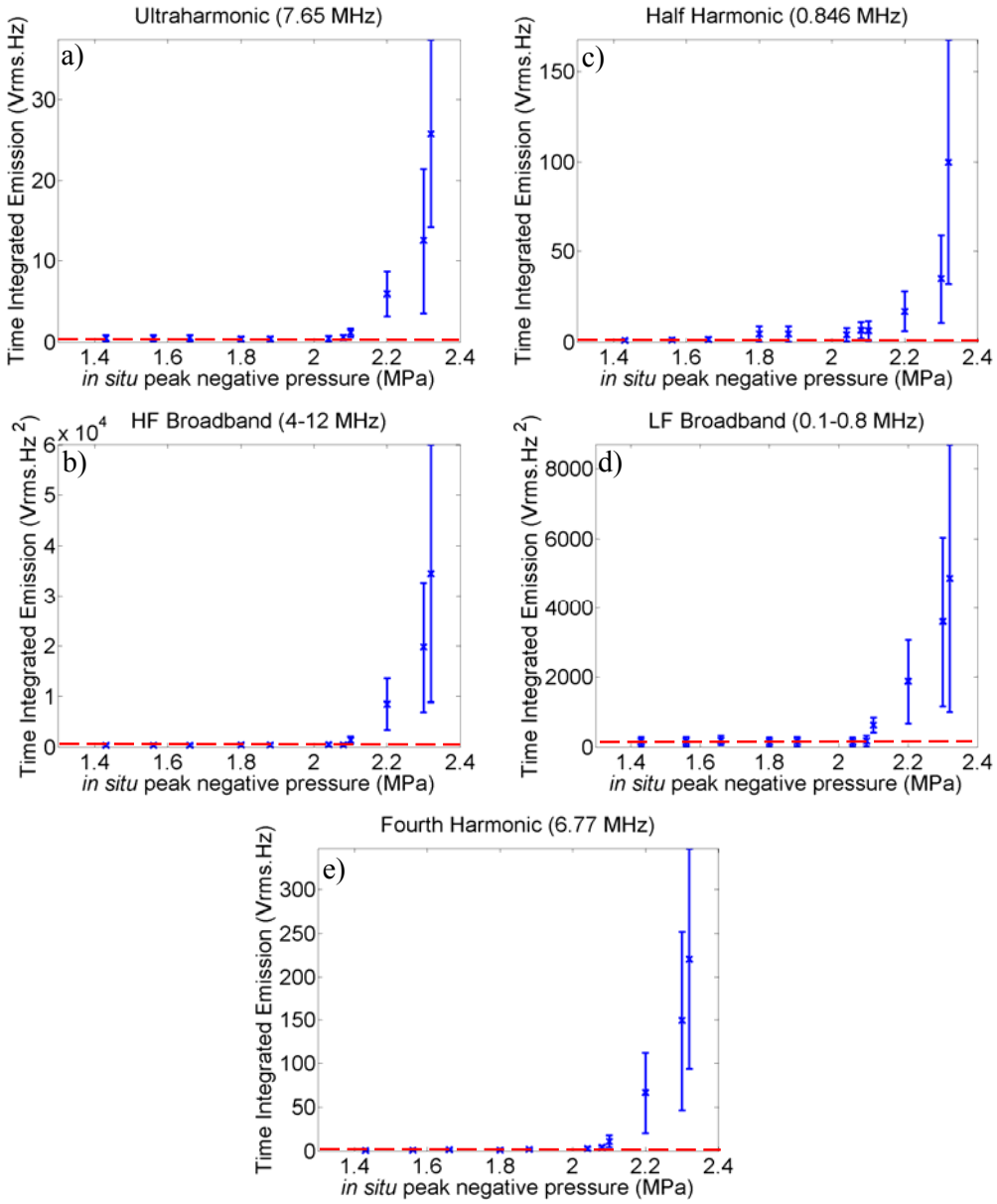

Figure 6.17. The averaged total time integrated (a) ultraharmonic (7.62 MHz), (b) HF broadband emissions (4-12 MHz), (c) LF broadband emissions (0.1-0.8 MHz), (d) half harmonic (0.846 MHz) and (e) fourth harmonic (6.77 MHz) shown over the range of peak negative pressures used. Uncertainty, where shown, is the standard deviation for n = 3-5. The red dashed line indicates the peak noise level measured from sham exposures.

6.2.4 Discussion

The aim of this study was to investigate the relevance of different ways of detecting cavitation activity in ex-vivo tissue (§7.1), with the eventual goal of determining the best technique for future in-vivo monitoring. Experiments in degassed water are useful to test a detection system that could then be used in an in-vivo application, since it is a

readily available medium and could be used to perform regular quality assurance tests with an in-vivo system. An advantage of this medium is that it may be possible to combine it with a form of direct observation in an effort to quantify the acoustic emissions detected (§4.1). The identification of specific cavitation activities was possible by using this novel suite of multiple complementary simultaneous cavitation detection methods (acoustic emissions, impedance change, active cavitation detection, and audible emissions).

The results acquired in degassed water (Figure 6.9 to Figure 6.17) demonstrate how the cavitation detection system behaved in a liquid propagation medium maintained at a constant temperature (20 ± 2^{o}C). In degassed water, unlike in tissue, acoustic streaming can occur. This means that bubbles are not trapped but can move around. This, and the transient nature of acoustic cavitation, may explain why the different emissions are seen at separate time points during the same exposure. Half harmonic (0.864 MHz), fourth harmonic (6.77 MHz) and broadband (4-12 MHz) emissions were detected during a 4 s exposures above 1100 W/cm^2 (Figure 6.10(d), (e) and (f)). Below this intensity level (1100 W/cm^2), only half harmonic was detected. No acoustic emissions were detected (Figure 6.10(a), (b) and (c)) below 400 W/cm^2. Since half harmonic emissions can be generated from both inertial and non-inertial cavitation, the absence of broadband emissions suggests that at 440 W/cm^2 (1.80 MPa) they are the result of non-inertial (stable) cavitation. It is not possible to make this distinction for the higher intensity exposures (Figure 6.10(g), (h) and (i)) due to the presence of broadband emissions. The literature, reviewed in sections 2.4 and 3.3, suggests that the presence of broadband emissions indicates the occurrence of inertial (transient) cavitation. Figure 6.11 demonstrates that the drive power fluctuations correlated temporally with broadband emissions, but were not observed when only half harmonic emissions were detected. This suggests that the drive power fluctuations relate to inertial cavitation but not to non-inertial (stable) cavitation. Nevertheless, they could also be due to an increase in the bubble population at the higher intensities required to generate inertial cavitation. It is likely however that the population of bubbles presents a scattering cross section of sufficient size to cause a level of backscatter that was detected by the electrical drive power monitoring system (this topic is discussed further in §7.2.3). Figure 6.11 shows that the drive power fluctuations are sensitive to scatter caused by acoustic cavitation in degassed water.

Figure 6.14 and Figure 6.15 show B-mode data, frequency maps, audible emissions, drive power fluctuations and acoustic emissions for a single degassed water exposure, above the inertial cavitation threshold, at two time points (0.21 and 2.43 s). Figure 6.14(a-d) shows that the B-mode interference pattern increase observed in water was caused by scattering from acoustic cavitation bubbles. These plots are representative of the results seen at this exposure level, and show a similar pattern to the higher intensity exposures in Figure 6.9(d)-(i). Acoustic streaming may have caused a bubble cloud to move out of the focus of the HIFU beam, and the detection zone of the passive cavitation detectors. The B-mode frames have a ±70 ms (14 Hz frame rate) temporal resolution compared to ±1 ms for the passive cavitation detection system. Therefore, it is probable that the events seen in Figure 6.14(b) and (d) are directly correlated with emissions shown in Figure 6.15, but it is not possible to be certain. By submerging the microphone in the water tank it is possible to detect audible emissions (8-20 kHz), as shown in Figure 6.14(e). These audible emissions were only found to occur at an intensity level at which inertial cavitation is detected

Table 6.1 shows a summary of the acoustic emissions/power fluctuations detected and the threshold intensities and pressures at which they occur for degassed water, as shown in Figure 6.17.

I_{sp} (W/cm^2)/Peak Negative Pressure (MPa)	Half Harmonic (0.846 MHz)	Broadband Emissions (6-10 MHz)	Drive Power Fluctuations	Audible Emissions (8- 20 kHz)
I < 440 (1.80)	No	No	No	No
440 (1.80) > I > 1100 (2.10)	Yes	No	No	No
I > 1100 (2.10)	Yes	Yes	Yes	Yes

Table 6.1 A summary of intensities at which acoustic emissions, power fluctuations and audible emissions (8-20 kHz) occur with 4 s HIFU exposures in degassed water.

The acoustic emissions shown in Figure 6.10(d)-(i) are above the inertial cavitation threshold for this medium as determined by the measurements shown in Figure 6.16 and Figure 6.17. However, the plots show significant differences in the detected magnitude and temporal behaviour of the emissions at different exposure levels. At 1100 W/cm^2 (Figure 6.10(d)-(f)) the detected broadband emissions occur more sporadically than during the 2200 W/cm^2 exposure. This is most likely to be due to less cavitation activity occurring. As the intensity (peak negative pressure) is increased, even above the inertial

cavitation threshold, detectable inertial cavitation events are more likely to occur during a given time. Figure 6.12 shows the acoustic emissions and power fluctuations for ±10 ms subsections of data around 2.39 s for the 1100 (a-c) and 2200 W/cm^2 (d-f) exposures. During this time period, the 1100 W/cm^2 exposure shows very few acoustic emissions and power fluctuations, even though the exposure is above the inertial cavitation threshold. The 2200 W/cm^2 expanded plots show that when the amplitude of the broadband emissions are at a minimum (Figure 6.12(g)) the power fluctuations are also at a minimum (Figure 6.12(e)). However the half harmonic emissions do not follow the same pattern (Figure 6.12(h)). This suggests that inertial cavitation plays the dominant role in causing the scatter seen in the power fluctuations and B-mode interference (Figure 6.14(a) and (c)).

Figure 6.13 shows the spectral content of the drive voltage for the two intensities (1100 and 2200 W/cm^2) under consideration. This, and the spectrum of the measured current (not presented), showed that only the fundamental drive frequency was detected, potentially as a result of the limited bandwidth of the transducer. This suggests that the power fluctuations were caused predominantly by from the backscatter of the fundamental frequency, most probably from short-lived bubbles (the source of which is moving stable cavitation or inertial cavitation). This preliminary study of the acoustic emissions detected during exposure of degassed water provided an improved understanding of sources of the emissions detected during ex-vivo tissue exposure to HIFU.

6.3 Conclusions

The ultraharmonic (7.62 MHz), half harmonic (0.846 MHz), fourth harmonic (6.77 MHz), broadband emissions (6-10 MHz), audible emissions (8-20 kHz), electrical drive power fluctuations and diagnostic imaging were monitored over the length of the exposures, as part of the 'full spectrum' approach to cavitation detection in degassed water. This 'full spectrum' approach was used to determine the non-inertial and inertial cavitation thresholds in degassed water, exposed to a 1.69 MHz HIFU beam. Non-inertial cavitation was found to occur at peak negative pressure greater that 1.80 MPa ±17%, where inertial cavitation occurred at the greater peak negative pressure of 2.10 MPa ±17%. It was also observed that electrical drive power fluctuations occurred at the same time as broadband emissions. This suggests that monitoring of the drive power during a HIFU exposure could give useful information about cavitation activity.

A sonochemical study gave a secondary indication that inertial cavitation occurred during some HIFU exposures. However, a problem with this study was that since the detection threshold for the sonochemical change using UV absorbance spectra was low, that it was not possible to detect such an effect for exposures of 5 or 10 s below a peak negative pressure of 2.38 MPa. A 16 s exposure was able to produce a sonochemical change at the exposure level at which broadband emissions were detected (1100 W/cm^2 or 2.10 MPa) in degassed water. Since the sonochemical change was assessed by a change in the UV spectrum, it was not possible with the current apparatus to monitor how the sonochemical change varied as a function of the exposure time, as can be achieved with the acoustic emissions. Clinical application of a sonochemical reaction could be difficult as the solution would need to be localised specifically in the region where the HIFU ablation was being targeted, and detection of any sonochemical change would be difficult since the solution would be diluted in the body. However, if these significant technical obstacles could be overcome, it might provide a useful estimation of the inertial cavitation activity that had occurred during the procedure.

7 – Cavitation detection in ex-vivo bovine liver tissue

This chapter investigates the cavitation activity generated from single HIFU exposures in ex-vivo bovine liver tissue. Simultaneous single and dual passive cavitation detection systems, audible emission monitoring, electrical drive power measurements and B-mode imaging are used to study the cavitation activity comprehensively using the Mauve and Imasonic HIFU transducers.

7.1 Introduction

A number of different techniques used for cavitation detection have been discussed in Chapter 3. This study used novel simultaneous passive and active cavitation detection, impedance change and audible (1-20 kHz) emission monitoring to investigate acoustic cavitation and boiling generated in ex-vivo bovine liver tissue by HIFU exposures. As discussed in chapter 2, temperature affects cavitation dynamics. As tissue temperature rises, the pressure threshold required to generate acoustic cavitation falls, since the partial pressures of the vapour and/or gas dissolved in the tissue increase. Therefore, less tension is needed in the tissue for the inception of cavitation at elevated temperatures. To understand further the process of boiling, cavitation detection was conducted with simultaneous thermocouple measurements. The aim of this study was to establish whether temperature measurements could be made using intensities at which boiling occurs. However, thermocouples, both fine wire (constructed in-house using 50 μm Constantan and Manganin wire (GoodFellows Ltd, UK)) and hypodermic needles (K-type, Omega Engineering Ltd., Manchester, UK) are known to contain errors in their temperature measurements, such as viscous heating artefacts (Fry and Fry, 1953; Carnochan *et al*, 1985), thermal conduction along the wire among others (Morris *et al*, 2007). The thermocouple itself, may introduce cavitation nuclei, affecting the cavitation activity for the ex-vivo tissue. The study outlined below investigates this potential problem with invasive thermometry in HIFU fields.

7.2 Cavitation study using dual 1 and 10 MHz passive transducers

7.2.1 Methods

The freshly excised ex-vivo bovine liver used in this study was collected from an abattoir and stored overnight in a refrigerated room (5-7^{o}C). Individual cylindrical

samples (50 mm diameter and 45 mm long) were cut, submerged in degassed water, and degassed for either 1 h (on the first day after collection) or for 2 h (on the second day after collection). The degassing process involved placing the container with the tissue submerged in degassed water into a vacuum chamber and maintaining a vacuum (~0.85 MPa) for the specified time. A preliminary study (§4.3) established that this tissue degassing regime resulted in the average peak amplitudes of the half harmonic emissions that were the same within the uncertainty range for both days. The older tissue will have undergone more autolysis and thus be expected to have greater gas content. The degassing procedure reduces this. Tap water was degassed by holding it under a vacuum of 0.85 MPa for at least 12 hours (§4.3).

A 1.69 MHz focused bowl piezoceramic transducer (f-number 1.79, focal length 15 cm) was used for the study. The intensity (free field spatial peak) was calibrated using a radiation force balance (Hill *et al*, 1994). Repeat measurements gave a spread in intensity values of ±10% (n = 16). Systematic errors in the measurement technique amount to no more than ±10%. The intensity values quoted therefore have an error of ±20%. Free field peak negative pressure values were measured for 80 cycle pulses using a calibrated 0.5 mm element PVDF membrane hydrophone (GEC Marconi, UK). The spread in repeat measured peak negative pressures was ±7% (n = 9). In addition, the calibration factor (provided by the National Physical Laboratory) has an associated 10% error. This gives a total uncertainty of ±17% in quoting the peak negative pressures. The free field intensity and pressure were corrected to give in-situ levels using a value of 0.11 Np/cm for the attenuation at 1.7 MHz for liver (Duck, 1990). This value, however, neglects the effects of non-linear propagation on the harmonic content of the HIFU field. All HIFU exposures are quoted as in-situ spatial-peak intensities (I_{sp}) with the in-situ focal peak negative pressure given in brackets.

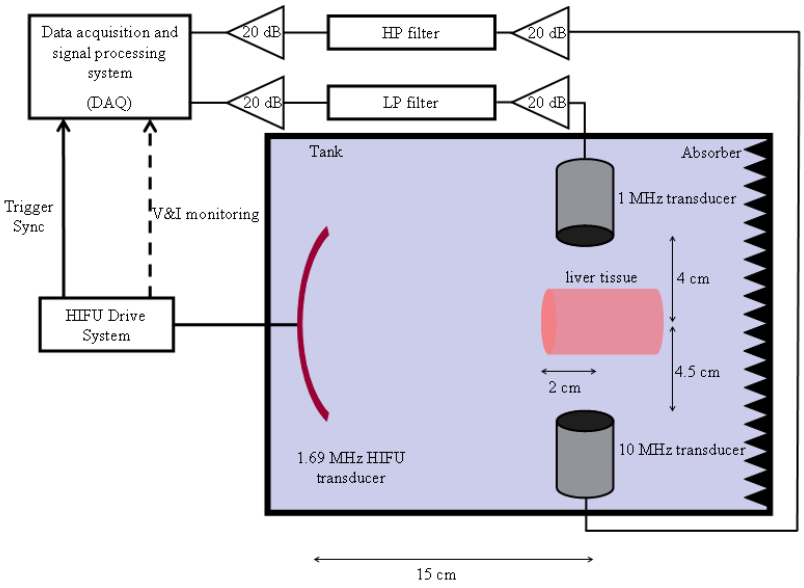

Figure 7.1. A plan view of the experimental set-up used for the ex-vivo bovine liver tissue study. The high pass filter (HP) has a cut off frequency of 6 MHz where the low pass filter cut off was at 0.85 MHz, more details of these filters are given in section 4.2.2.

This setup allowed simultaneous investigation of a wide band of different acoustic emissions. Specifically, the half harmonic (0.845 MHz), the fourth harmonic (6.77 MHz), ultraharmonic (7.62 MHz) and frequency broadband emissions (0.1-0.8 and 4-12 MHz) were studied.

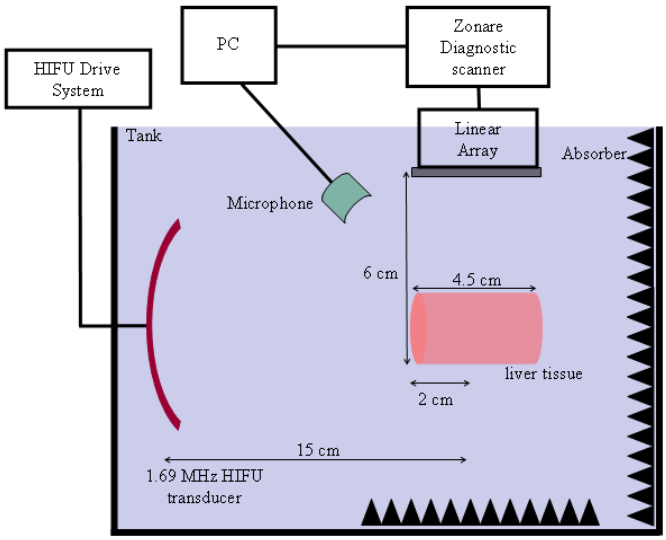

Figure 7.2. A side view of the experimental set-up used for the HIFU exposed ex-vivo bovine liver tissue study. This shows the relative positioning of the diagnostic ultrasound system and the microphone.

Figure 7.2 shows the diagnostic scanner (Zonare Medical Systems, Mountain View, CA, USA), with an L10.5 probe (centre frequency 8 MHz, MFCD1313, 14 Hz frame rate, 6 cm imaging depth), which could be used before, during and after HIFU exposure. The scanner could provide a real time view (typically at 14 Hz) of the sample region but the image was susceptible to interference during HIFU exposure. All the available image data was downloaded to a PC after each acquisition. The IQ data for each frame was converted to RF and B-mode data using a MatLab routine, which was provided by Zonare (Chapter 4).

The 1 and 10 MHz sensors were aligned with the focal peak of the HIFU, by optimising the received pulse (~ 0.2% duty cycle) from a 40 cycle HIFU burst which was reflected from a spherical target (shown in Figure 7.3). The target in Figure 7.3 was designed to have the ball bearing located at the focus of the 10 MHz sensor (45 mm). The sensor was positioned to receive the maximum reflection from the ball bearing as described in section 5.3.2. The *V*/20 channel on the 'pick-off' box in the HIFU drive system was used since it was not possible to resolve these signals when using the *V*/1000 channel. Alignment of the 1 MHz sensor was achieved by maximising the received signal reflected from the ball bearing. The diagnostic imaging array was also aligned with the focal peak by imaging the same target. Since the target was positioned perpendicularly to the HIFU axis it was possible to alter the imaging position until the maximum reflection from the ball bearing was observed. This could be positioned to a precision of ±1 mm since it was mounted on the manual 3-D gantry (§5.1.3). The signal processing and data analysis was performed using the methods outlined in section 4.2.4.

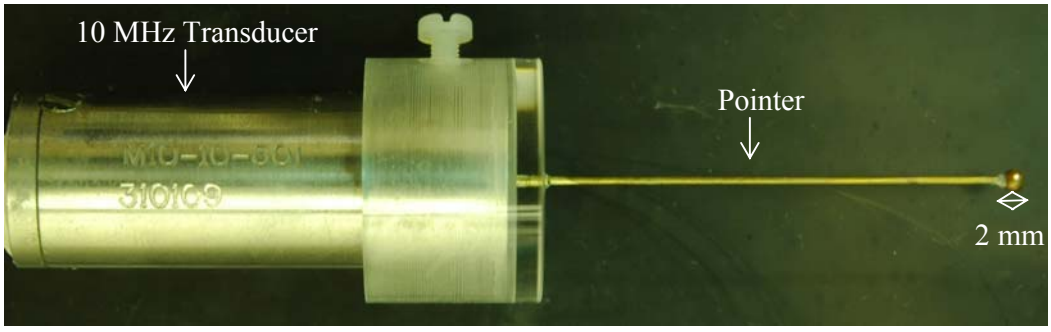

Figure 7.3. A photograph of the 2 mm ball pulse-echo target mounted on the 10 MHz passive sensor so that it is located at it's focus.

Audible emissions (1-20 kHz) were monitored using a battery operated microphone (Partridge Electronics, Essex, UK, CHK00627, frequency response 0.03-17 kHz, 80 dB signal/noise), connected to a personal computer with audio encoding software (Smart PC Recorder, v2.5), which sampled the audible emissions at a rate of 44.8 kHz and with 16-bit resolution. The *.wav* data was then analysed using a spectrum analysis code written in MatLab. The microphone was placed in a condom to allow it to be immersed into the water tank in an attempt to maximise the detected signals.

A cylindrical Perspex framed tissue holder with acoustically transparent 19 μm thick Mylar windows (front, back, and wrapped around the length of the cylinder – as shown in §5.4, Figure 5.28) was designed and used to allow unimpeded HIFU propagation from the front of the tissue sample to the back, and provided acoustic windows for simultaneous diagnostic ultrasound imaging from above. An absorber was placed at bottom of the Perspex tank to minimise reflections. A Perspex tube with a Mylar membrane was inserted into the rear of the holder to hold in place cylindrical tissue samples up to 45 mm in length, but compressed to 40 mm in the tissue holder. Each liver sample was subjected to a single 2-5 s long HIFU exposure. Following removal from the holder it was dissected by cutting along the sound axis to reveal lesion size and shape. If a lesion was created in the ex-vivo tissue, the sample was re-compressed to 40 mm prior to being photographed using the system described in section 5.5, Figure 5.29.

The focal plane of the HIFU was set 20 mm deep in the tissue (Chapter 5). The capsular surface of the liver always faced the transducer, in order to mimic a clinical HIFU path. Four second exposures were chosen, as they represent the longest times used previously in a clinical trial (Visioli *et al*, 1999). The ex-vivo in-situ exposure ranges used were 210-1785 W/cm^2 ± 20% (peak negative pressure range 1.21 to 2.05 MPa ±17%), this range being separated into 15 exposure intensities (pressures) of 210, 250, 290, 310, 390, 500, 630, 710, 790, 890, 1000, 1110, 1210, 1570 and 1785 W/cm^2 (1.21, 1.32, 1.40, 1.52, 1.59, 1.72, 1.76, 1.765, 1.77, 1.81, 1.86, 1.90, 1.94, 1.96 and 1.99 MPa).

7.2.2 *Results*

The results shown are representative of data obtained from experiments carried out on 22 separate ex-vivo livers, each of which provided 10-15 samples. The following three figures show acoustic spectra recorded at the different acoustic cavitation regimes, defined as exhibiting 1) non-inertial (stable) cavitation only (Figure 7.7), non-inertial

and inertial (transient) cavitation (Figure 7.8), non-inertial, inertial cavitation and boiling occurring during the 4 s exposure (Figure 7.9). The first data set is from a I_{sp} of 290 W/cm^2 (1.32 MPa) for 120 s HIFU exposure and demonstrates the formation of a lesion in the thermal regime (Figure 7.4). A 4 s exposure at this level would not generate a lesion. Figure 7.7 to Figure 7.9 show four time varying acoustic spectra that were detected by the dual passive cavitation detection system for these different exposure regimes.

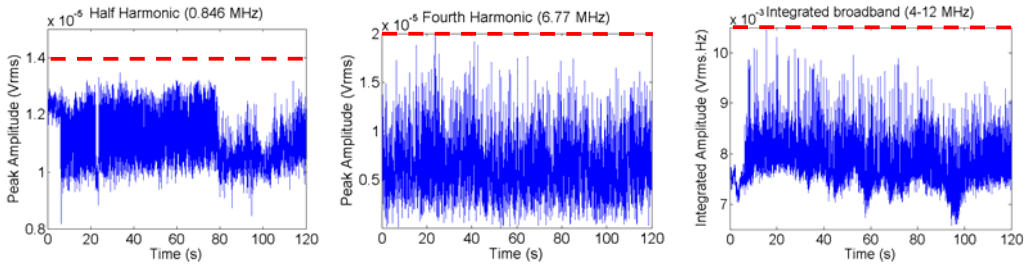

Figure 7.4. Half harmonic (a), fourth harmonic (b) and Broadband emissions (c) for a 120 s free-field exposure at I_{sp} 290 W/cm^2 (1.32 MPa) in ex-vivo liver tissue. Note the scaling factor of 10^{-5} on (a) and (b). All values plotted on these graphs are either equal to or less than the peak noise level measured from a sham exposure (red dashed line). Diagnostic imaging was not used during this exposure. .

Data from the first exposure regime is shown in Figure 7.4. This shows a lack of all the acoustic emissions indicative of bubble activity for intermittently sampled data (~37 points per second) during a 120 s exposure 290 W/cm^2 (1.32 MPa). Figure 7.5 shows the lesion generated in the ex-vivo tissue from this exposure. No audible emissions were detected.

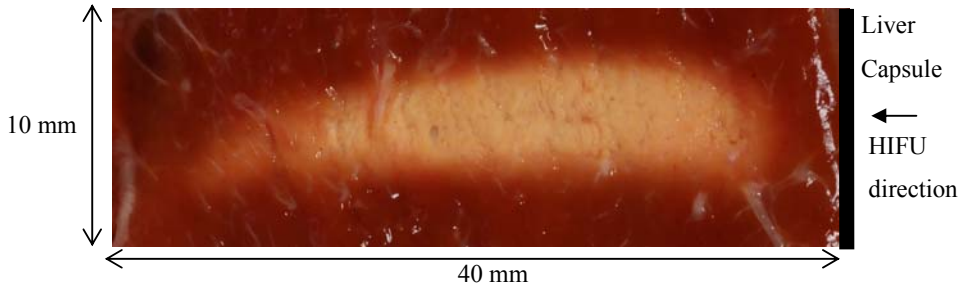

Figure 7.5. Lesion produced by a 290 W/cm^2 (1.32 MPa) 120 s exposure of ex-vivo tissue at a focal depth of 20 mm. The HIFU field propagated from right to left.

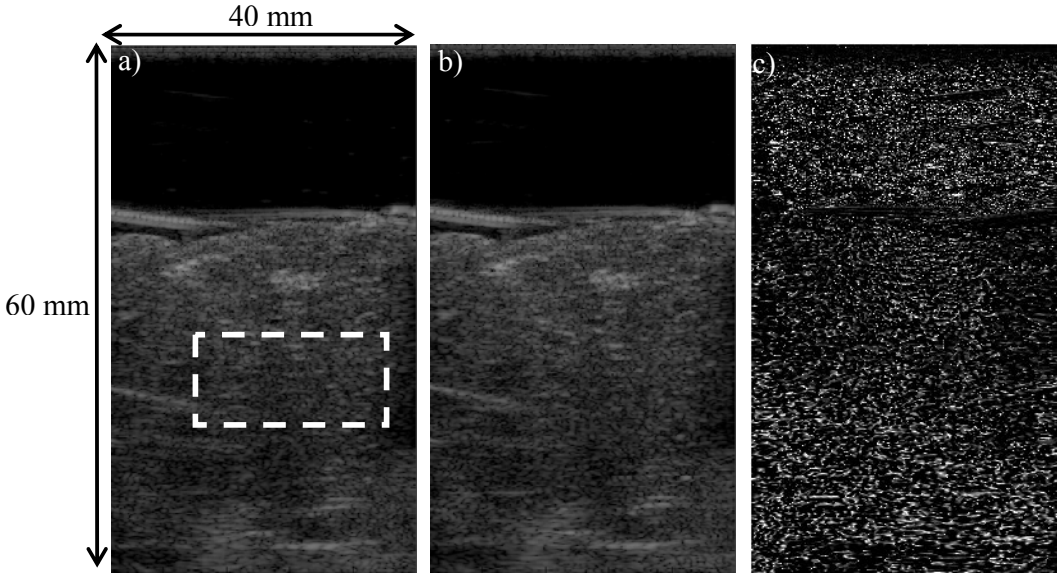

Figure 7.6. Two B scan frames acquired immediately (a) before and (b) after the 290 W/cm^2 (1.32 MPa) 120 s exposure. (c) is a subtraction image of the two frames shown in (a) and (b). It shows that there is no hyperechogenicity change between the frames acquired before and after the exposure. The HIFU propagates from right to left. The approximate focal zone is indicated by the dashed white box.

Figure 7.6 shows two B-mode frames acquired using a Zonare diagnostic scanner (8.5 MHz) immediately before and after the HIFU exposure shown in Figure 7.4. No change in echogenicity can be seen in the frames acquired after the exposure (Figure 7.6(b)).

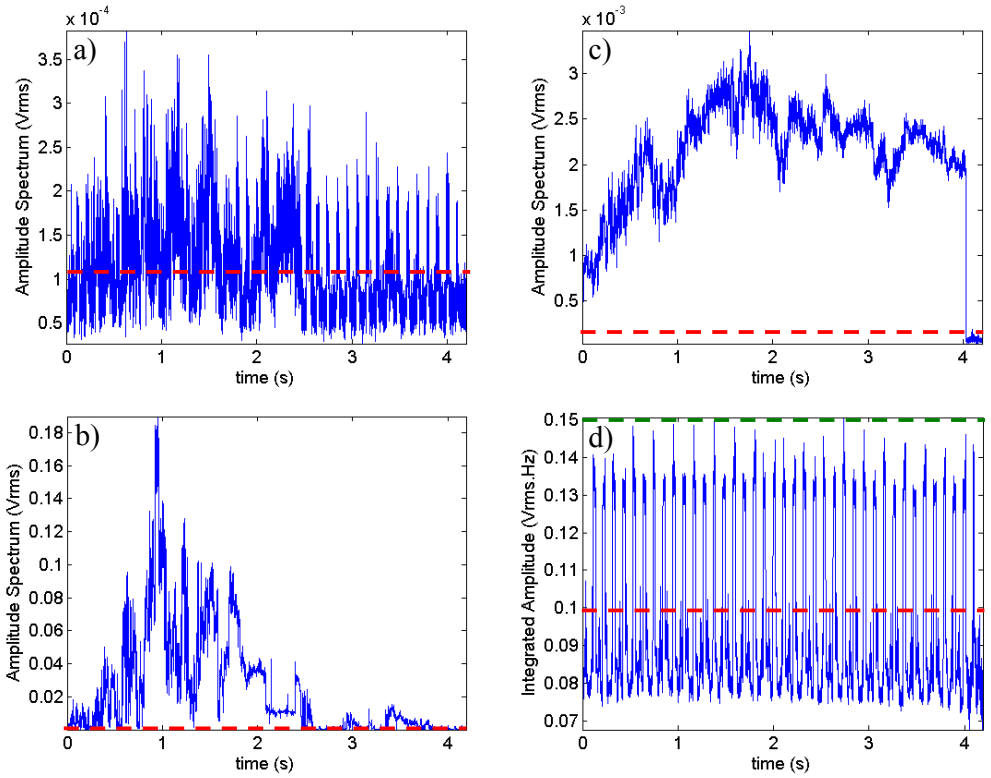

Figure 7.7. The emission spectra acquired from a 4 s HIFU exposure at 310 W/cm^2 (1.52 MPa), which shows the (a) ultraharmonic (7.62 MHz), (b) half harmonic (0.846 MHz), (c) fourth harmonic (6.77 MHz), (d) integrated broadband (4-12 MHz). Diagnostic imaging was performed during the exposure. Amplitude scales have been maximised for presentation purposes. The dashed red line indicates the peak noise level measured from a sham exposure, where the green line indicates the peak noise generated from the diagnostic imaging in (d).

Figure 7.7 is an example of the detection of ultraharmonic (7.62 MHz) and half harmonic (0.846 MHz) emissions above the noise level (dashed red line). Figure 7.7(d) shows the broadband signals detected when the diagnostic imaging was on during the exposure, which is highlighted by the green dashed line. This noise can be seen in the other spectra, for example in the ultraharmonic (Figure 7.7(a)), but is not as pronounced.

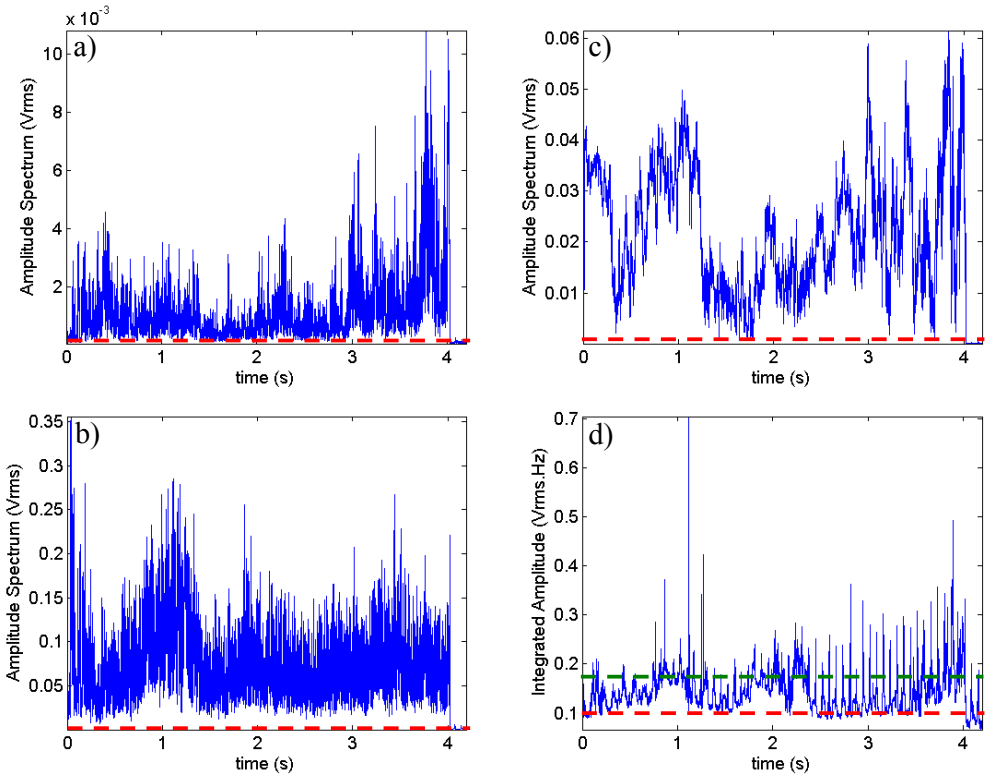

Figure 7.8. The emission spectra acquired from a 4 s HIFU exposure of 790 W/cm^2 (1.77 MPa), which shows the (a) ultraharmonic (7.62 MHz), (b) half harmonic (0.846 MHz), (c) fourth harmonic (6.77 MHz), (d) integrated broadband (4-12 MHz). Diagnostic imaging was performed during the exposure. Amplitude scales have been maximised for this exposure. The dashed red line indicates the peak noise level measured from a sham exposure, where the green line indicates the peak noise generated from the diagnostic imaging in (d).

At an intensity of 790 W/cm^2 the peak amplitude of the detected fourth harmonic (Figure 7.8 (c)) signal is approximately 60% higher than in the data shown in Figure 7.7(c) (for a 40% increase in the electrical drive power (Figure 7.11(a) and (b))).

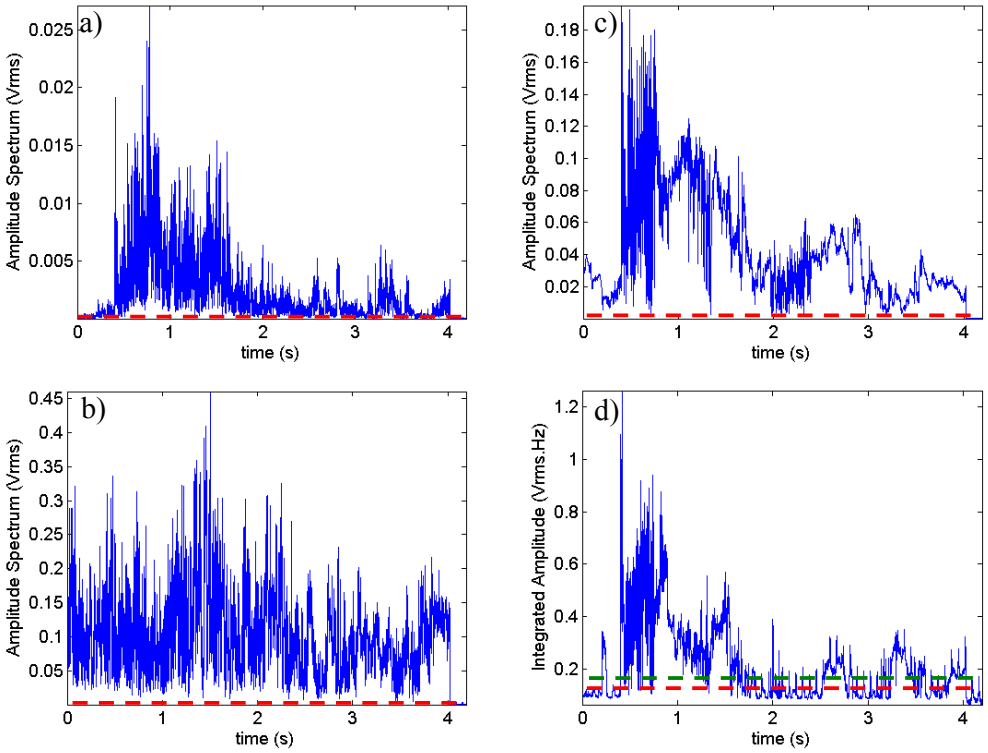

Figure 7.9. The emission spectra acquired from a single 4 s HIFU exposure of 1570 W/cm^2 (1.96 MPa), which shows the (a) ultraharmonic (7.62 MHz), (b) half harmonic (0.846 MHz), (c) 4th harmonic (6.77 MHz), (d) integrated broadband (4-12 MHz). Diagnostic imaging was on during the exposure. Note that amplitude scales have been maximised for this exposure. The dashed red line indicates the peak noise level measured from a sham exposure, where the green line indicates the peak noise generated from the diagnostic imaging in (d).

Figure 7.9 shows that there is more than a 300% increase in the peak amplitude of the detected fourth harmonic (Figure 7.9(c)), which occurs at 0.4 ±0.001 s. Figure 7.10 shows broadband emissions acquired from two separate exposures in ex-vivo tissue with (Figure 7.10(a)) and without (Figure 7.10(b)) diagnostic imaging on during the exposure. In Figure 7.10(b) the interference caused by diagnostic imaging can be seen to start at approximately 0.25 s after the end of the 4 s exposure.

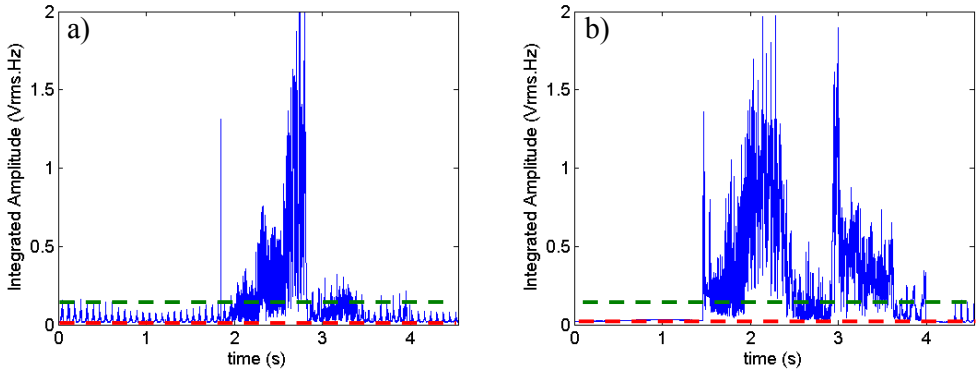

Figure 7.10. The measured broadband emissions for two 1210 W/cm^2 (1.94 MPa) 4 s exposures in separate ex-vivo liver samples, with (a) and without (b) diagnostic imaging. The dashed red line indicates the peak noise level measured from a sham exposure, where the green line indicates the peak noise generated from the diagnostic imaging.

Figure 7.11 shows the calculated drive power for the three ex-vivo tissue exposures described above. There is an approximately 100% increase of the power for each increase in the exposure intensity. Figure 7.11(c) shows fluctuations in the calculated power of ±5.25 W from the average power level, where the fluctuations during the exposures at the two lower power levels are within the noise levels measured in §4.2.4. The first of these fluctuations occurs at the same time point as the increase in the detected fourth harmonic emissions show in Figure 7.9(d). Figure 7.12 shows electrical drive power fluctuations be seen for in-situ I_{sp} levels ≥1000 W/cm^2 (1.86 MPa) and they occur earlier in the exposure as I_{sp} is increased.

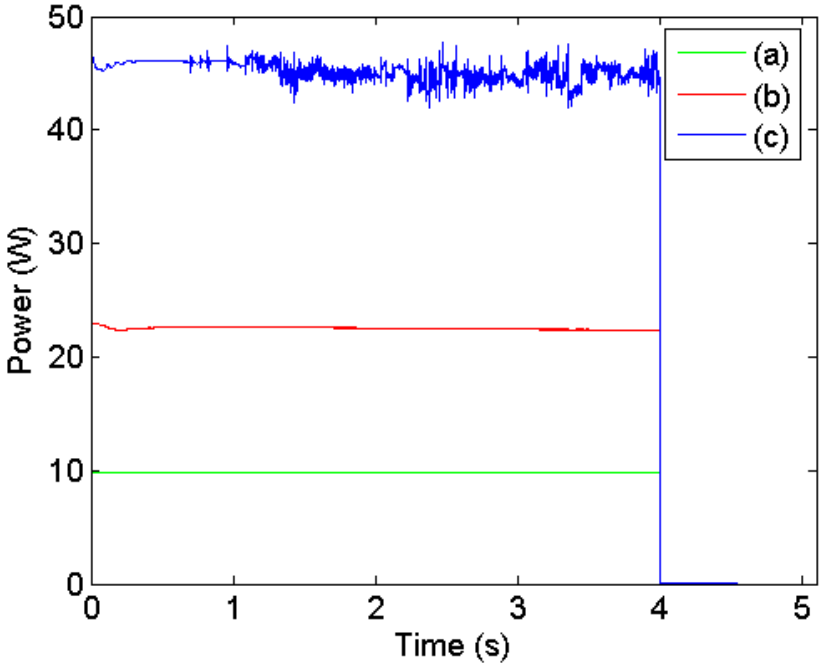

Figure 7.11. The calculated drive powers for the 4 s exposures shown in (a) Figure 7.7, (b) Figure 7.8, and (c) Figure 7.9, which are exposures in the three different cavitation regimes.

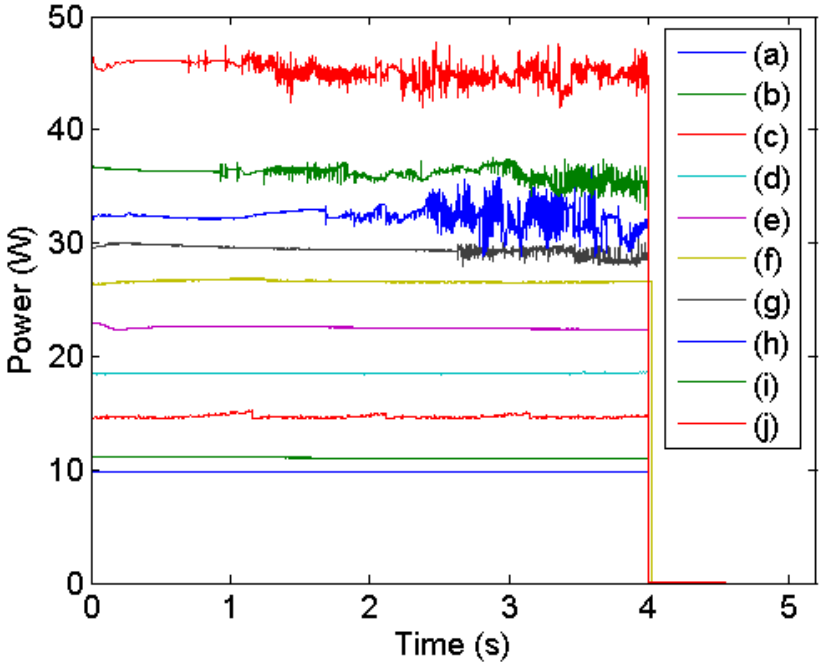

Figure 7.12. The measured power for 4 s exposures in ex-vivo tissue at (a) 310 W/cm^2 (1.52 MPa), (b) 390 W/cm^2 (1.59 MPa), (c) 500 W/cm^2 (1.72 MPa), (d) 630 W/cm^2 (1.76 MPa), (e) 790 W/cm^2 (1.77 MPa), (f) 890 W/cm^2 (1.81 MPa), (g) 1000 W/cm^2 (1.86 MPa), (h) 1110 W/cm^2 (1.90 MPa) (i) 1210 W/cm^2 (1.94 MPa) and (j) 1570 W/cm^2 (1.96 MPa).

Figure 7.13 shows photographs of typical lesions created using 4 s exposures using the I_{sp} range 630-1570 W/cm^2 (1.76-1.96 MPa). Detectable lesions were only generated above 630 W/cm^2 (1.76 MPa), as shown in Figure 7.13(g). At 630 W/cm^2 (1.76 MPa), which is within the first cavitation regime (i.e. non-inertial cavitation only), the lesion is very faint and centred approximately around the HIFU focal peak. Figure 7.13 curves (e) and (f), show lesions generated at 790 and 890 W/cm^2 (1.77 and 1.81 MPa) respectively, which are in the second cavitation regime (non-inertial and inertial cavitation). Pre-focal damage and 'holes' (see below) are seen for exposures above 1000 W/cm^2 (1.86 MPa), which corresponds to the exposure level at which the power fluctuates (Figure 7.12) and is in the third cavitation regime (acoustic cavitation and boiling), these lesions have been described as 'tadpole'-like in appearance (Watkin *et al*, 1996).

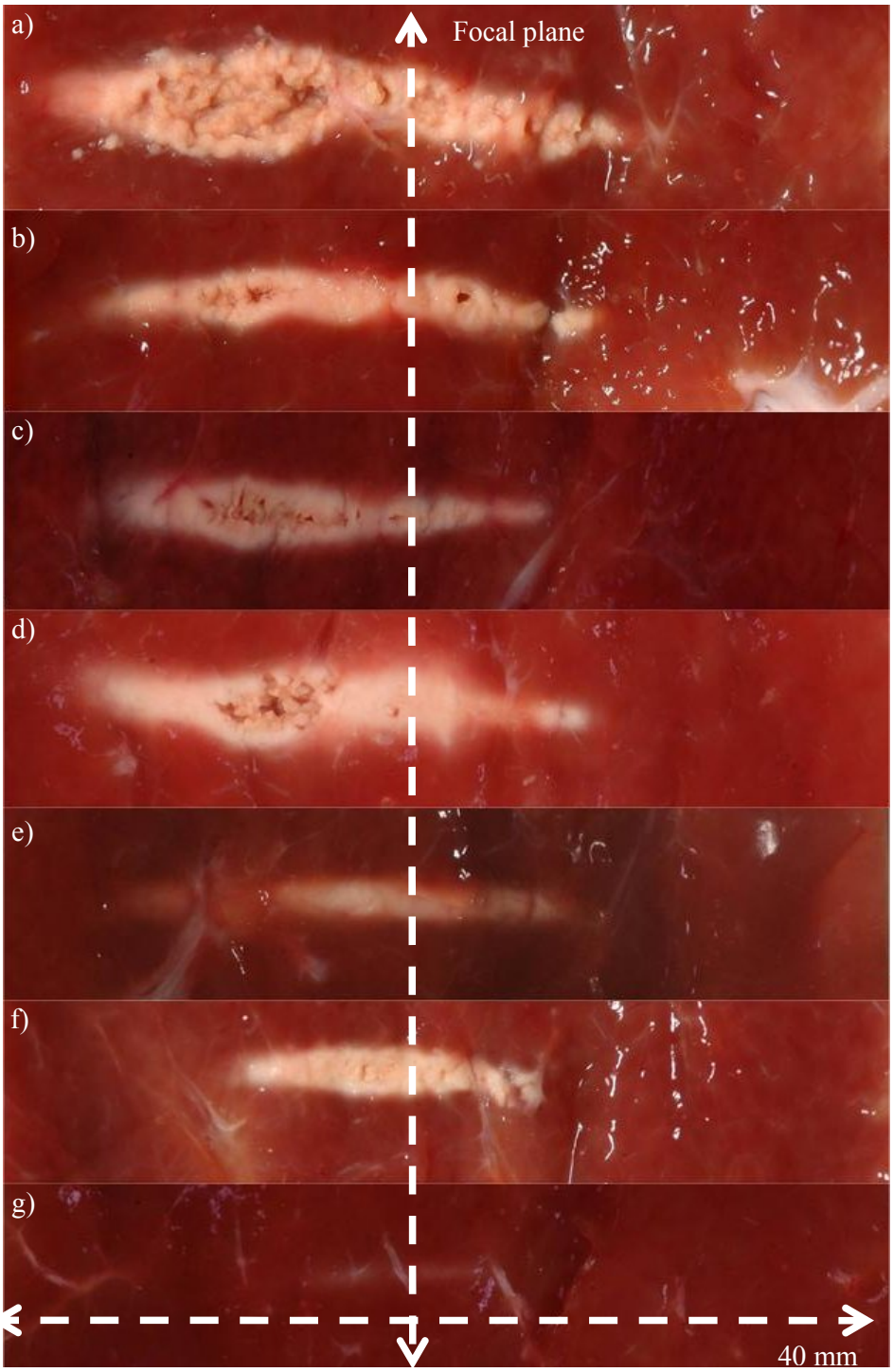

Figure 7.13. Photographs of typical lesions created in ex-vivo tissue from 4 s exposures in at (a) 1570 W/cm^2 (1.96 MPa), (b) 1214 W/cm^2 (1.94 MPa), (c) 1110 W/cm^2 (1.90 MPa), (d) 1000 W/cm^2 (1.86 MPa), (e) 890 W/cm^2 (1.81 MPa), (f) 790 W/cm^2 (1.77 MPa) and (g) 630 W/cm^2 (1.76 MPa). The vertical dashed arrow marks the approximate focal peak of the HIFU field. In all images, the HIFU field propagated from left to right.

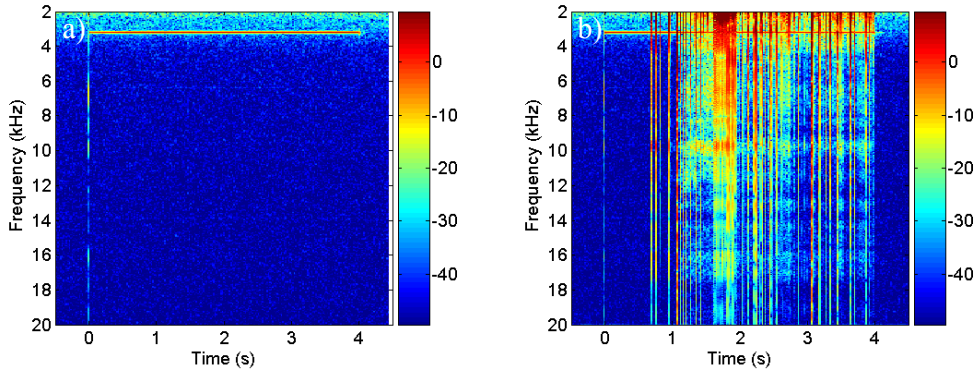

Figure 7.14. Audible frequency spectra (2-20 kHz) recorded with the microphone during the (a) 790 W/cm2 (1.77 MPa) exposure and (b) 1000 W/cm^2 (1.86 MPa) exposures shown in Figure 7.12. The constant 3.5 kHz tone is from a buzzer that indicates when the HIFU field is on. The noise spike seen at 0s is from generated from the HIFU drive system.

Figure 7.14 shows the audible emissions (1-20 kHz) recorded using the microphone for two 4 s exposures in ex-vivo bovine liver tissue. Audible emissions were detected during the 1000 W/cm^2 (1.86 MPa) exposure from 0.65 ± 0.02 s onwards. This corresponds to the time point at which power fluctuations start to occur in Figure 7.12(j). Figure 7.15 show B-mode frames acquired using the Zonare diagnostic scanner (8.5 MHz) immediately before and after the HIFU exposures shown in Figure 7.14. No change in echogenicity can be seen in the frame acquired after the exposure at the 790 W/cm^2 (1.77 MPa) exposure (Figure 7.15(i)), even when the post exposure image is subtracted from the pre-exposure one. For both of these exposures the diagnostic imaging was switched on immediately (±0.5 s) after the exposure had finished.

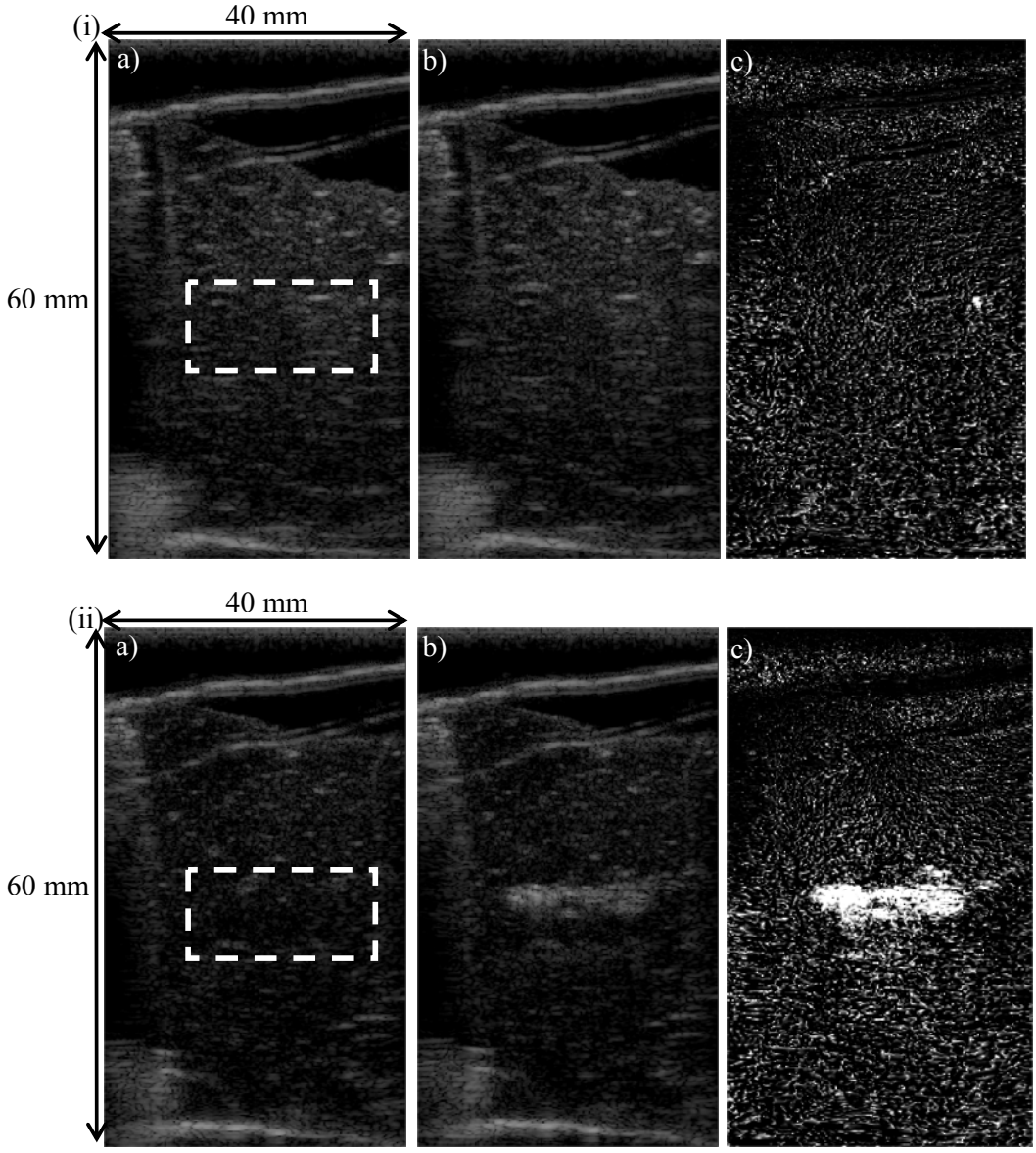

Figure 7.15. Two B scan frames acquired immediately before (a) and after (b) a 4 s HIFU exposure at (i) 790 W/cm2 (1.77 MPa) shown in Figure 7.14(a) and (ii) 1000 W/cm^2 (1.86 MPa) shown in Figure 7.14(b). The subtraction image shows that there is no echogenicity change between the frames acquired before and after the exposure. The HIFU field propagates from right to left. The approximate focal zone is indicated by the dashed white box. (i) is in the cavitation exposure regime where acoustic cavitation only is occurring, but (ii) is in the regime for acoustic cavitation and boiling.

The data described above has shown examples of the detected acoustic spectra from the three different regimes of cavitation activity. Data presented in Figure 7.16 to Figure 7.24 provide an in depth examination of the cavitation activity in the acoustic cavitation

only and acoustic cavitation and boiling regimes, and gives more detail about the trends observed in the diagnostic imaging data acquired throughout the HIFU exposure.

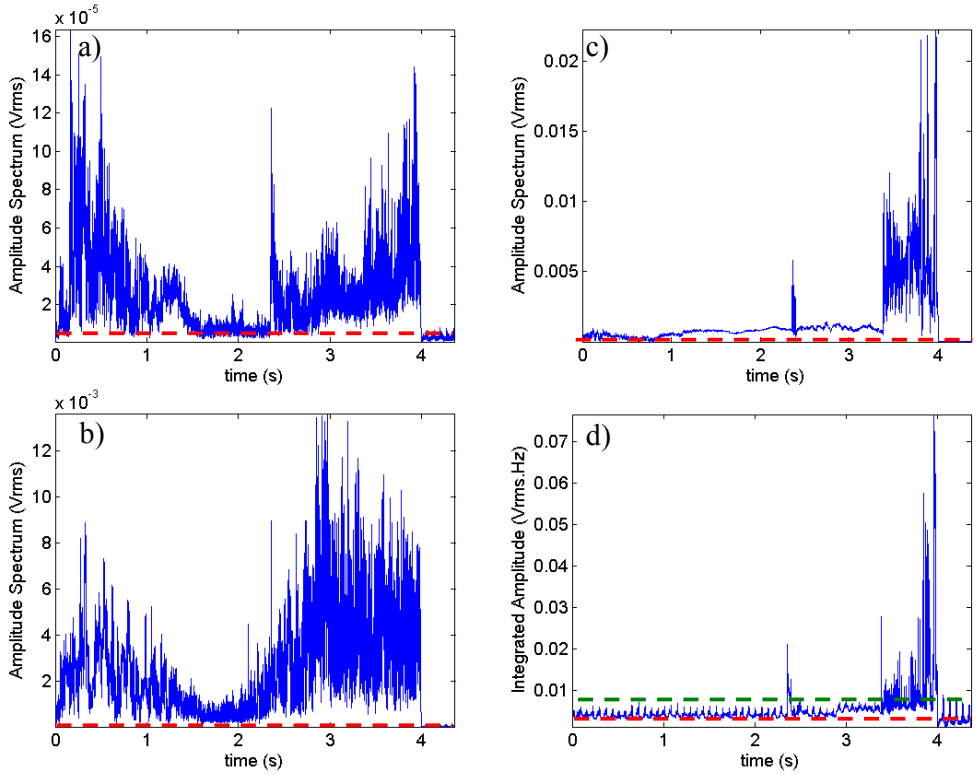

Figure 7.16. The emission spectra acquired from a single 4 s HIFU exposure at 1000 W/cm^2 (1.86 MPa), which shows the (a) ultraharmonic (7.62 MHz), (b) half harmonic (0.846 MHz), (c) 4th harmonic (6.77 MHz), (d) integrated (6-10 MHz) broadband. Diagnostic imaging was on during the exposure. Amplitude scales have been maximised. The dashed red line indicates the peak noise level measured from a sham exposure

Ultraharmonic, half harmonic, fourth harmonic, and broadband emissions are detected throughout the exposure shown in Figure 7.16. In Figure 7.16 (c) and (d) there is a significant increase in the magnitude of the signals detected after 2.3 and 3.3 s. However, between these events there is a reduction in the signals detected.

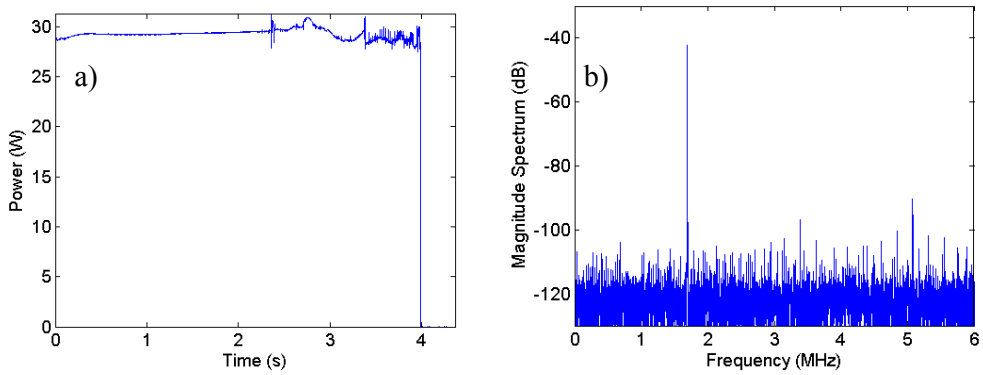

Figure 7.17. The calculated drive power for the ex-vivo exposure shown in Figure 7.16 at 1000 W/cm^2 (1.86 MPa) (a). (b) shows the frequency spectra for the drive voltage calculated from the 1000 W/cm^2 (1.86 MPa) exposures at 2.3 s.

Figure 7.17 shows the power calculated for the ex-vivo liver exposure shown in Figure 7.16, and the frequency spectrum of the drive voltage at 2.3 ±0.001 s. Fluctuations in the drive power can be seen after 2.3 s in Figure 7.17(a). The frequency spectrum at this time point (Figure 7.17(b)) shows no harmonic content apart other than fundamental frequency (1.69 MHz).

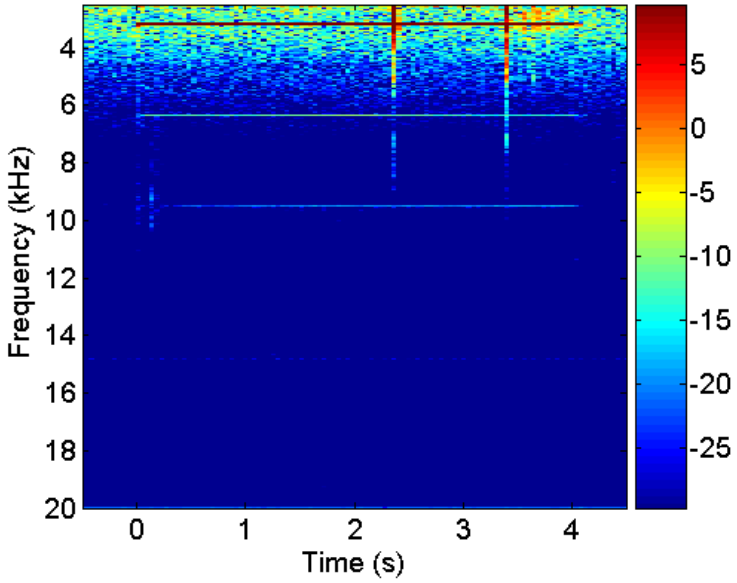

Figure 7.18. Audible (2-20 kHz) spectra recorded with the microphone during the 1000 W/cm^2 (1.86 MPa) exposure shown in Figure 7.16. The constant 3.5 kHz tone is from a buzzer indicating when the HIFU is on, also two higher harmonics of this buzzer can also be seen which were not present in Figure 7.14. The presence of these was due to the timer box being located closer to the microphone. Emissions are observed between 2-8 kHz, at 2.3 and at 3.3 s.

Brief audible signals, in the 2 to 8 kHz range, can be seen in Figure 7.18 during the 1000 W/cm^2 exposure, after approximately 2.3, and 3.3 s. This data was sampled at a rate of 44.8 kHz and the analysis software used 2048 points in each FFT calculation, resulting in a temporal resolution of 0.05 s.

Figure 7.19 shows the lesions generated from the 1000 W/cm^2 (1.86 MPa) HIFU exposure shown in Figure 7.16. The lesion has grown asymmetrically "forward" towards the HIFU transducer, this trend was observed in the lesions shown in Figure 7.13. Figure 7.19(b) shows a 'hole' within the lesion. This damage has a different appearance from that of a blood vessel (Figure 7.19(c) solid line box).

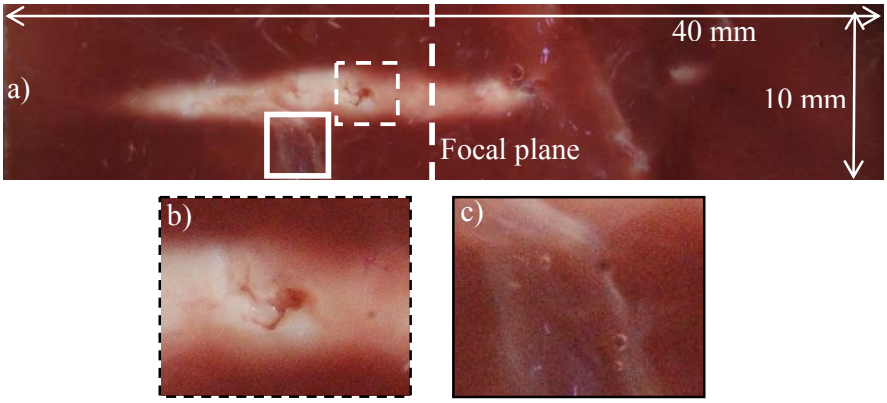

Figure 7.19. Lesion generated in ex-vivo bovine liver tissue at 1000 W/cm^2 (a, b) and (c) for a single 4 s exposure. The HIFU field propagated from left to right. The dashed zoom box (b) shows a hole in the lesion and the solid line box (c) shows a blood vessel.

Figure 7.20 shows five B-scans acquired during the 1000 W/cm^2 exposure. Each frame shows tissue 60 mm deep and 40 mm wide, with the HIFU propagating from left to right.

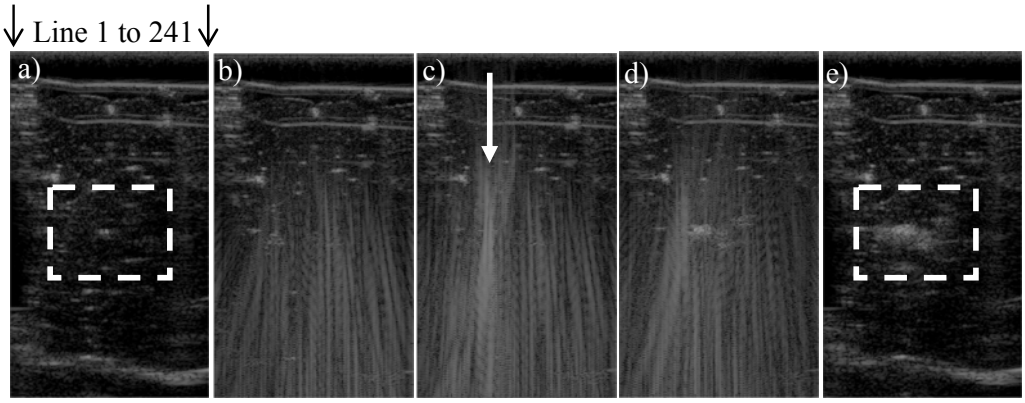

Figure 7.20. Five B-scan frames acquired with a Zonare scanner (L10-5 Probe) during the 4 s 1000 W/cm^2 exposure in ex-vivo tissue, shown in Figure 7.16. (a) Before, (b) 2.29 s, (c) 2.35 s (d) 3.30 s into and (e) after the HIFU exposure (timings have a precision uncertainty of ± 0.07 s.

Figure 7.20(b) demonstrates the acoustic interface pattern seen when the HIFU was active during image acquisition. The pattern changes appearance at 2.35 s and at 3.30 s (Figure 7.20(c) and (d)), with an increase of the bright interference signal apparent on the left hand side of the image (arrowed). These frames were recorded at approximately the times at which audible emissions were detected (Figure 7.18). Figure 7.21 shows that the interference pattern was caused predominantly by the 2nd, 3rd and 4th superharmonics (3.38, 5.07 and 6.77 MHz) of the HIFU drive frequency. These integer harmonics lie within the bandwidth of the scanner array. In this study, observation of these transient, localised increases in interference was common in B-mode scans taken during HIFU exposures gave audible emissions. Figure 7.22 shows frequency maps (between 3-4 MHz) of the frames in Figure 7.20(c) and (d) i.e. the FFT amplitude (colour scale) of the frequency components detected in each line of the image. In Figure 7.22(a) the maximum detected signal lies approximately 15 mm beneath the surface of the tissue. The highlighted region in Figure 7.20(e) shows a large area of increased echogenicity, which is associated with the presence of boiling at around this position in the tissue. The expanded subtraction image in Figure 7.23 shows the shrinkage of the hyperechogenic region with time after HIFU exposure. In the absence of the HIFU field, this hyperechogenicity can only be caused by increased scatter of the imaging beam.

This is demonstrated in Figure 7.24 which shows the spectra of the image data before (a) and immediately after (b) HIFU exposure.

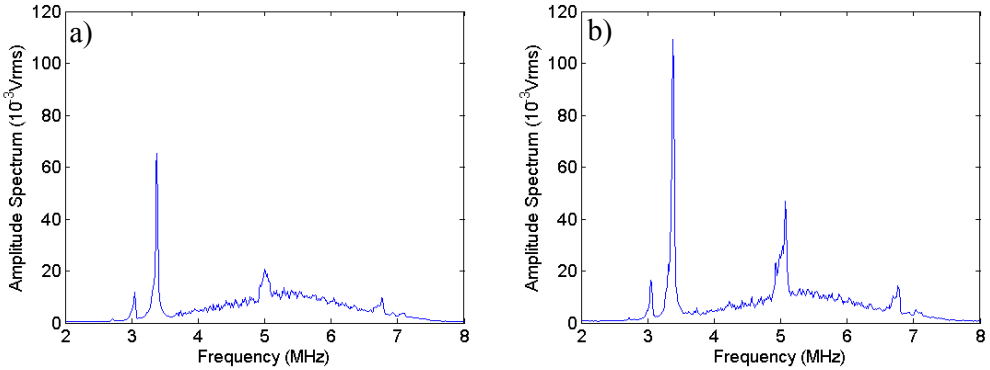

Figure 7.21. Average frequency spectra for the B-mode image frames show in (a) Figure 7.20(b) and (b) Figure 7.20(c). These were calculated by averaging the FFT spectra over a 13 by 60 mm window (i.e. lines 90-160 over the full image depth).

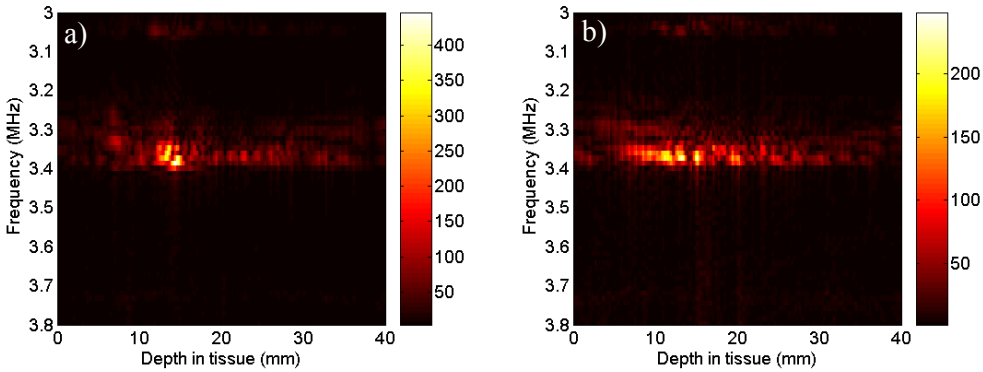

Figure 7.22. Frequency maps (between 3 and 4 MHz) obtained from the frames shown in Figure 7.20 (c) and (d). (a) is 2.35 s and (b) 3.30 s into the HIFU exposure. The colour scale indicates the FFT amplitude; note the difference in magnitude between (a) and (b). The horizontal axis is the depth in the tissue sample at which the signal is detected (0 mm is the first image line). The focal plane of the HIFU was set at 20 mm. Analysis over a wider frequency band did not reveal any extra information.

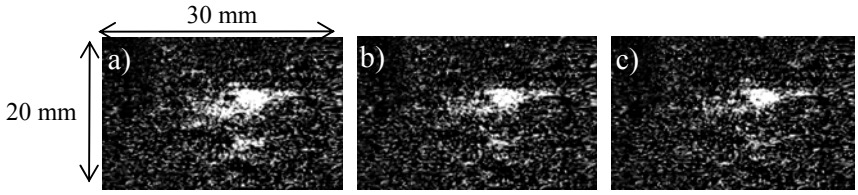

Figure 7.23. Subtraction B-scan images generated by subtracting an image frame obtained before HIFU exposure from image frames obtained at (a) 0 s (see Figure 7.20(e)) (b) 4.3 s and (c) 7.1 s (± 0.07 s) after the exposure ended. The scale is the same for all images.

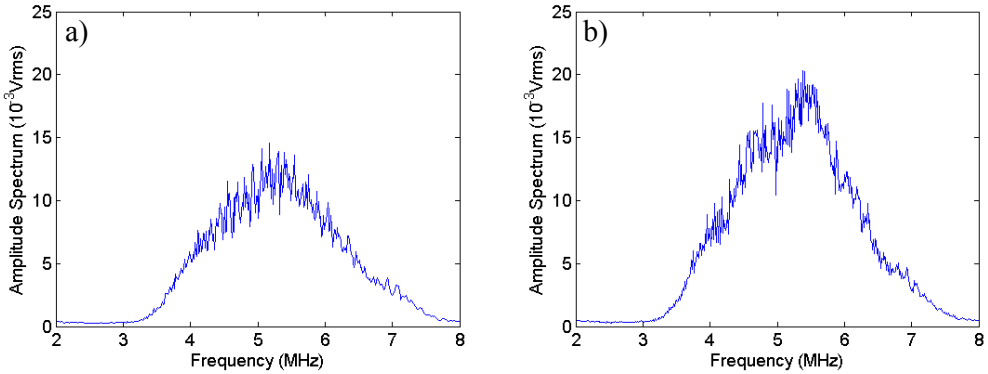

Figure 7.24. Frequency spectra for B-mode frames shown in (a) Figure 7.20(a) before HIFU exposure and (b) in (e) at least 0.07 s after a HIFU exposure which caused a hyperechogenic region. The spectra were calculated by averaging the FFT data over a 13 by 60 mm window (i.e. lines 90-160 over the full image depth).

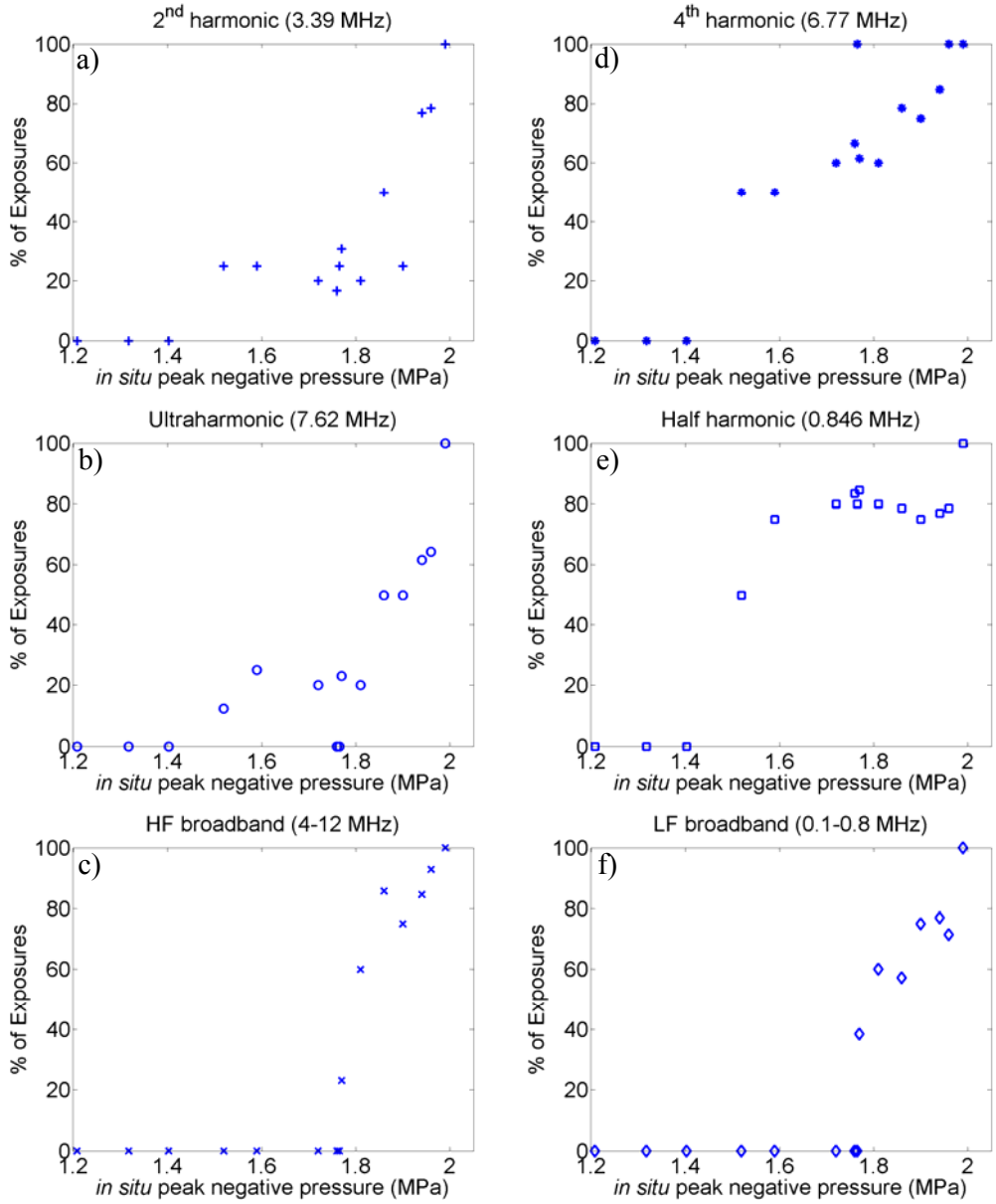

Figure 7.25. The percentage of exposures in which acoustic spectra were detected as being greater than the noise level criteria specified in §4.2.4 at any point during the 4 s exposures. The signals were measured over the range 210-1785 W/cm^2 (1.21-1.99 MPa) where for n = 3-14 for each exposure level.

Figure 7.25 shows the percentage of exposures that had a detectable signal that was greater than the noise level (§4.2.4). It shows that for the exposure range 210-290 W/cm^2 (1.21 to 1.40 MPa) no acoustic spectra were detected that exceeded the noise threshold. Superharmonics (3.39 and 6.77 MHz) were detected above this level with increasing likelihood. The acoustic emissions of ultraharmonic and half harmonic that are indicative of non-inertial cavitation (in the absence of broadband emissions) were detected at intensities greater than or equal to 310 W/cm^2 (1.52 MPa). Figure 7.25(b)

shows that no ultraharmonic was detected above the noise level for exposures at 630 or 710 W/cm^2. This result is most likely to be due to the limited number of samples at these exposures (n = 3), and the use of diagnostic ultrasound imaging which increases the noise threshold level. Broadband emissions (Figure 7.25(c) and (f)) were detected at intensities greater than or equal to 790 W/cm^2 (1.77 MPa). It is not possible to identify from this data at what intensity (pressure) boiling occurred during the 4 s HIFU exposures. Figure 7.26 shows the averaged lesion dimensions for the 4 s exposure over the peak negative pressure range used in this study.

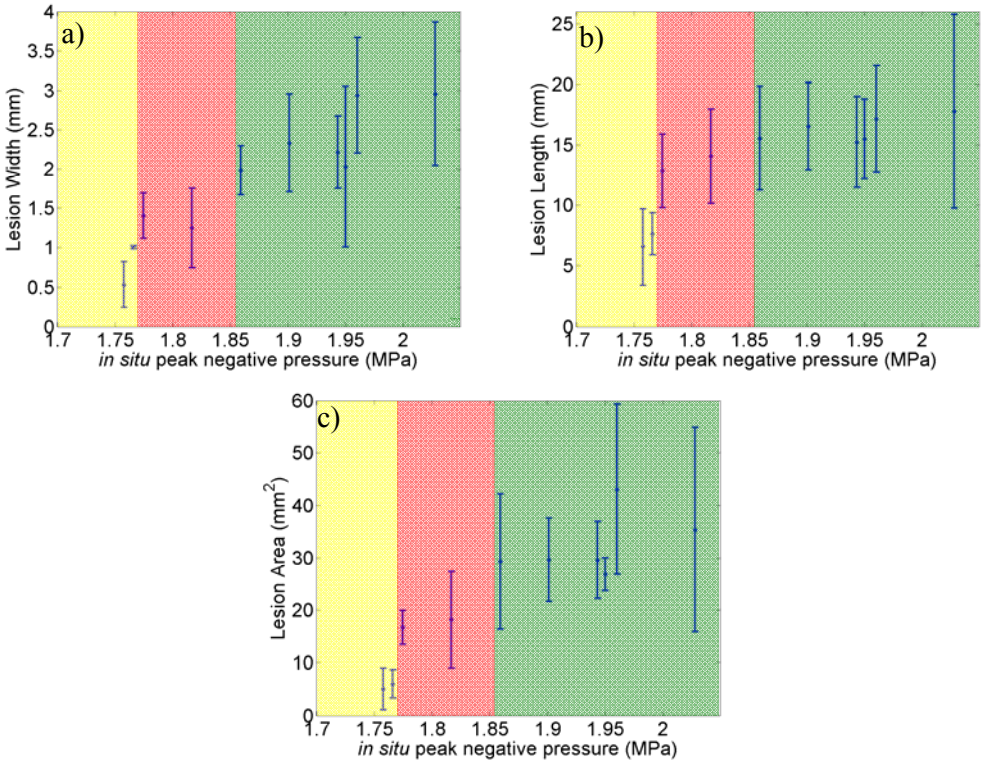

Figure 7.26. The averaged measured lesion (a) length, (b) width and (c) area for peak negative pressures that generate a lesion from a single 4 s exposure. The uncertainty shown is the standard deviation of the average value, for n =3-16. The three colours are used to describe approximately the three cavitation regimes, non-inertial cavitation only (yellow), non-inertial and inertial cavitation (red) and acoustic cavitation and boiling (green).

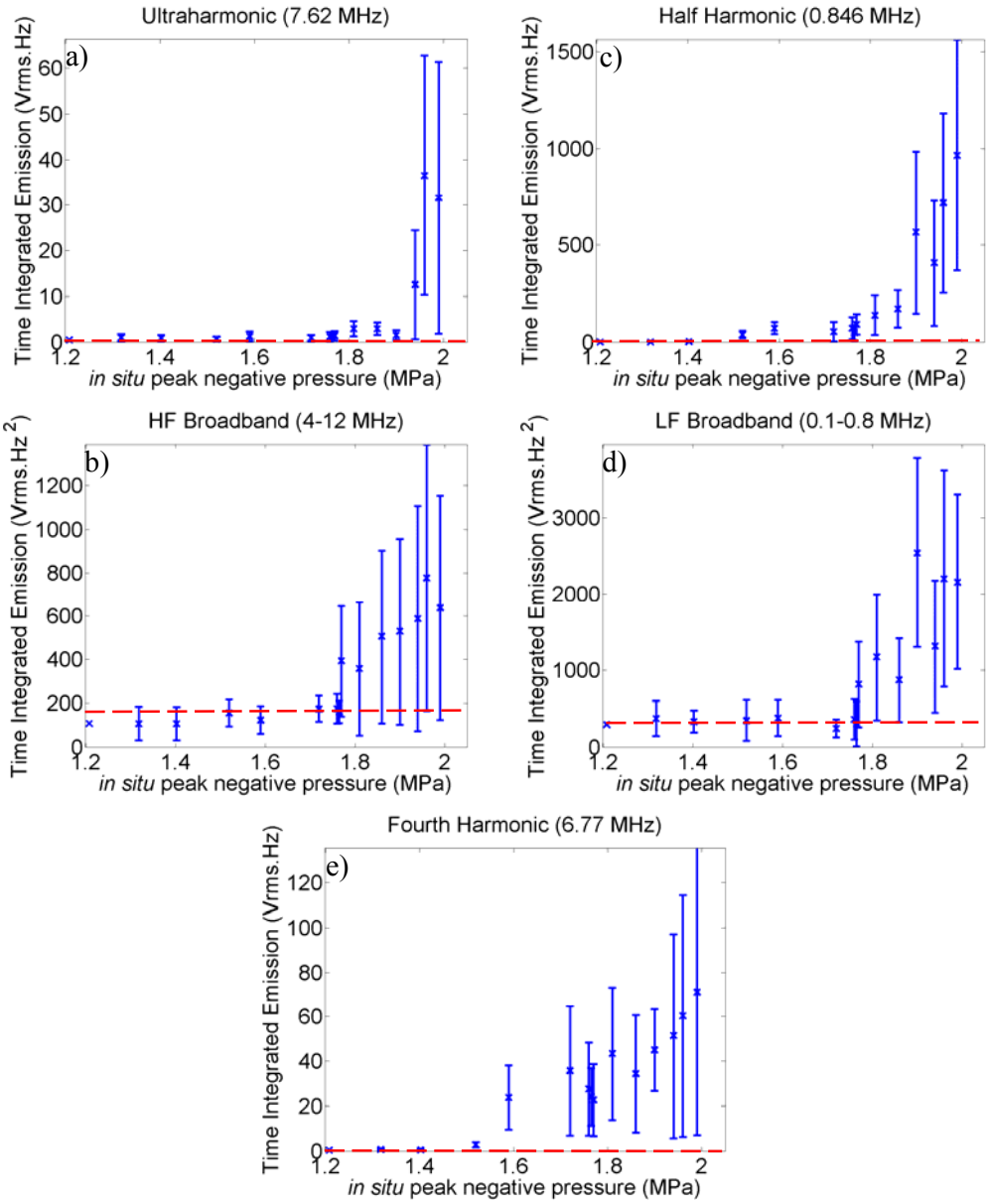

Figure 7.27. The averaged total time integrated (a) ultraharmonic (7.62 MHz), (b) HF broadband emissions (4-12 MHz), (c) LF broadband emissions (0.1-0.8 MHz), (d) half harmonic (0.846 MHz) and (e) fourth harmonic (6.77 MHz) shown over the range of peak negative pressures used. Uncertainty, where shown, is the standard deviation for n = 3-21. The red dashed line indicates the peak noise level measured from sham exposures.

Figure 7.27 shows the averaged total time integrated emissions for the acoustic spectra monitored with the dual frequency passive cavitation detection system during the 4 s exposures in ex-vivo bovine liver tissue. The data in this figure highlight the differences in the detected amplitudes of the acoustic spectra. Uncertainty in the broadband emissions increases with the exposure intensity. The detected ultraharmonic (Figure

7.27(a)) emissions increase significantly in the regime where boiling occurred ($\geq$ 1000 W/cm^2 or 1.86 MPa).

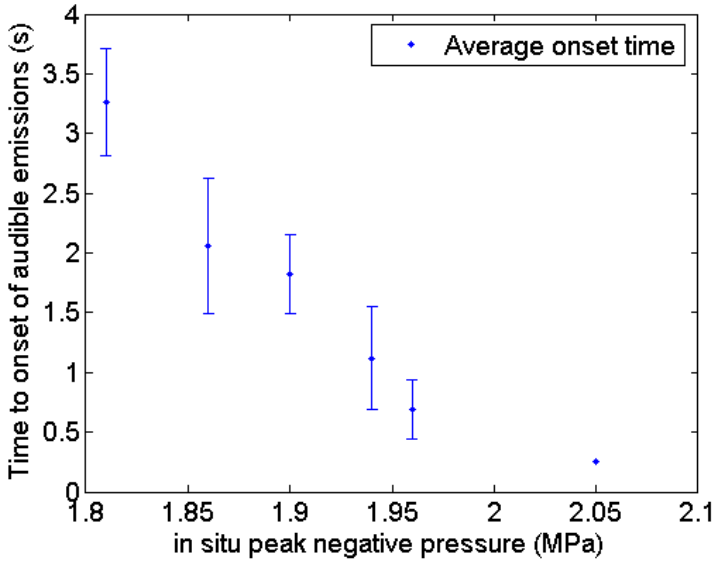

Figure 7.28. The average onset time to the first occurrence of audible emissions in ex-vivo tissue exposed to a HIFU field, for 4 s HIFU exposures targeted 20 mm deep in tissue. *n* = 3-17 on the data points with error bars representing standard deviation, *n* = 1 for the point without.

Figure 7.28 shows the average time into an exposure for audible emissions to be detected ('onset') as shown in Figure 7.14(b) and Figure 7.18. The transient nature of the detected acoustic emissions meant that it was not possible to apply the same 'onset' criteria to this data. Figure 7.29 shows the percentage of 4 s HIFU exposures in ex-vivo bovine liver tissue exhibiting hyperechogenicity, electrical drive power fluctuations and/or audible emissions (2-20 kHz). At exposure levels greater than or equal to 100 W/cm^2 (1.86 MPa) these indicators of boiling were detected in more than 75% of the exposures. Interestingly they were also detected for some of the exposures for the exposure level 890 W/cm^2 (1.81 MPa).

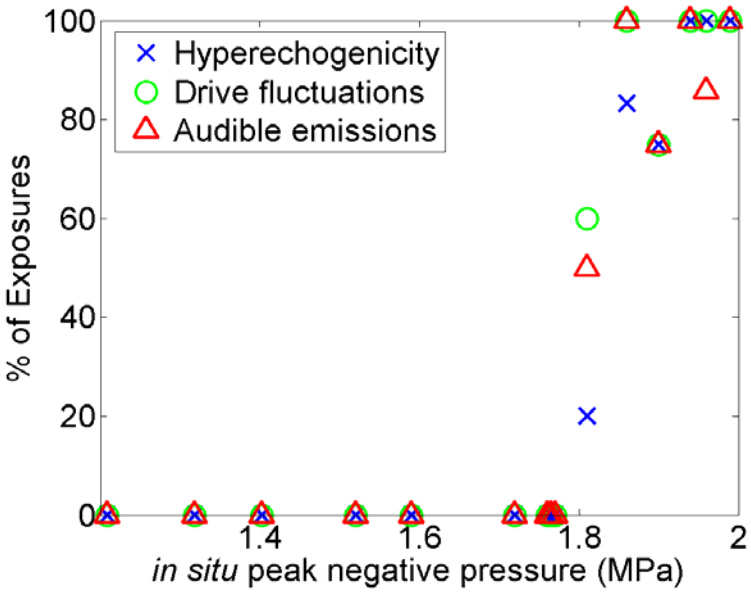

Figure 7.29. The percentage of 4 s HIFU exposures that exhibited hyperechogenicity after the exposure, electrical drive power fluctuations and/or audible emissions during the exposure. These mechanisms were measured over the range 210-1785 W/cm^2 (1.21-1.99 MPa) where for n = 3-14 for each exposure level.

7.2.3 Discussion

Significant differences between cavitation activity in tissue and water (§6.2.3) are to be expected for a number of reasons. Firstly, ultrasound energy is absorbed in tissue leading to a range of effects from reversible heating to irreversible damage during exposure. In all cases, there will be thermal gradients across the HIFU focal region. Not only will varying tissue temperature affect acoustic cavitation nucleation, but also as the temperature approaches 100^{o}C, intra- and/or extra-cellular water may undergo thermal exsolution of gas vapour (boiling). Secondly, the attenuation and absorption coefficients of most tissues (including liver, but not fat) increase with frequency (Duck, 1990). Higher frequency emissions from bubbles will therefore be attenuated more than those at lower frequencies. Finally, the only publication (Leighton *et al*, 1990) to compare the ability to produce inertial cavitation in tissue and water showed that sonoluminescence was not detectable in the human cheek. The authors hypothesised that a lack of nucleation centres was the most likely explanation for this finding.

The exposure at 290 W/cm^2 (1.32 MPa) for 120 s provides an example of a lesion (Figure 7.5) generated in the absence of any detectable acoustic emissions or drive

fluctuations. B-mode imaging (Figure 7.6) showed no increase in echogenicity even though a lesion 30 mm by 5 mm was created in the tissue. This suggests that the initial claim that this lesion was generated only from thermal effects was valid. This highlights a potential problem with the ability of diagnostic ultrasound guided clinical HIFU to detect damage. Thermally generated lesions may not be able to be identified on a diagnostic imaging system in the clinical environment. Figure 7.7 to Figure 7.9 show the acoustic emissions detected from exposures that are in the three different cavitation threshold regions (§7.2). These plots show the variations over time of an ultraharmonic (7.62 MHz), half harmonic (0.846 MHz), fourth harmonic (6.77 MHz) and integrated broadband emissions (6-10 MHz). Figure 7.10 shows the acoustic interference caused from active cavitation detection (ultrasound imaging) operating at a frequency (Figure 7.24) within the passive detection bandwidth (4-12 MHz). This highlights a potential problem of using active and passive cavitation detection simultaneously. The problem would be most significant when broadband emissions are of a similar level to the noise caused by passive sensor "listening" to the diagnostic imaging pulse (Figure 7.8(d)). In the absence of any broadband emissions Figure 7.7(d) shows that the noise introduced from diagnostic imaging is approximately 50% higher than that measured during a sham exposure. However, Figure 7.8(d) shows that if there are broadband emissions greater than the baseline noise level, the noise from the scanner is superimposed upon this. A second form of active cavitation detection was used, namely monitoring the HIFU drive electrical power (e.g. Figure 7.11(c)). This method does not directly interfere with passive acoustic monitoring. Figure 7.12 shows that power fluctuations occurred during 4 s exposures of $\geq$1000 W/cm^2 (1.86 MPa). These coincided with the generation of lesions with pre-focal damage and observable 'holes' in the tissue (Figure 7.13). As discussed in section 2.4, Watkin *et al*, (1996) and Meaney *et al*, (2000) observed and modelled this effect but were unclear as to its origin, believing that cavitation, acoustic or boiling were possibly responsible. The data shown in this chapter indicate that the cause of the 'tadpole' shape lesions is from the occurrence of boiling in the tissue. Figure 7.14 and Figure 7.15(ii) show that audible emissions and hyperechogenicity occur at the same exposure levels and times as power fluctuations.

For the 790 W/cm^2 (1.77 MPa) 4 s exposure (Figure 7.8), power fluctuations were negligible (Figure 7.11(b)), even though broadband emissions were detected (Figure 7.8(d)). In experiments in degassed water (§6.2.3), power fluctuations correlated with the presence of broadband emissions. It may be that the extra attenuation (of the 1.69

MHz fundamental frequency) by tissue in the round trip of the scattered HIFU, leads to insufficient backscatter to cause detectable power fluctuations. However, it could also be due to a lower number of bubble nuclei in ex-vivo tissue, compared to water. For the 1000 W/cm^2 (1.86 MPa) 4 s exposure, power fluctuations (Figure 7.17(a)) and audible emissions (Figure 7.18) were detected after 2.35 s. As these two events occurred simultaneously, it is hypothesised that the boiling bubbles cause sufficient backscatter to generate power fluctuations. Figure 7.22(b) shows how boiling events occur at different locations in the tissue, which could be why a break in the audible emissions was seen between 2.35 and 3.30 s. There is also a corresponding significant increase in detected emissions (Figure 7.16(c) and (d)) at these time points. The increase in the level of the fourth harmonic detected at the receiver is more likely to be due to backscattering of this high frequency (6.77 MHz) by the larger bubbles that were generated through boiling than due to the presence of acoustic cavitation bubbles. In order to investigate this it is possible to first assess which contributes more effectively to scattering at the fundamental (1.69 MHz) and fourth harmonic (6.77 MHz): micron-sized bubbles undergoing inertial cavitation or resonant oscillations, or larger, mm-sized 'boiling' bubbles. The backscattering cross-section $\Omega_{\mathrm{cV}}^{\mathrm{b\text{-}s}}$ per unit volume of a cloud of linearly-pulsating bubbles is given by (Leighton, 1994)

$$\Omega_{\mathrm{cV}}^{\mathrm{b\text{-}s}} = \frac{1}{4\pi}\int \Omega_{\mathrm{b}}^{\mathrm{scat}} n_{\mathrm{b}}(R_0)\mathrm{d}R_0 \qquad \text{for } (kR_0 << 1) \tag{7.1}$$

where $n_{\mathrm{b}}(R_0)$ is the number of bubbles per unit volume having a radius between R_0 and $R_0+\mathrm{d}R_0$, and $\Omega_{\mathrm{b}}^{\mathrm{scat}}$ is the scattering cross-section of each linearly oscillating bubble (§2.3)

$$\Omega_b^{scat} = \frac{4\pi {R_0}^2}{((\omega_0/\omega)^2-1)^2+(2\beta_{tot}/\omega)^2} \qquad \text{for } (kR_0 << 1) \tag{7.2}$$

where ω_0 is the circular resonance frequency of the bubble, ω is the circular driving frequency, and β_{tot} is an appropriate damping factor (of dimensions 1/time) for the bubble (Eller, 1970). Figure 7.30 shows a plot of $\Omega_{\mathrm{b}}^{\mathrm{scat}}$ for air bubbles in water exposed at 1.69 and 6.77 MHz under 0.1 MPa static pressure, in the radius range up to 10 μm (note that the geometrical scatter from a 10 μm bubble produces a cross-section of similar magnitude to that which occurs at the local maximum associated with a resonant bubble). Boiling bubbles of ~mm size will therefore contribute very significantly to

backscatter at 1.69 and 6.77 MHz, although Figure 7.30 cannot be extended to these radii because of the $kR_0 << 1$ limitation of equations 7.1 and 7.2.

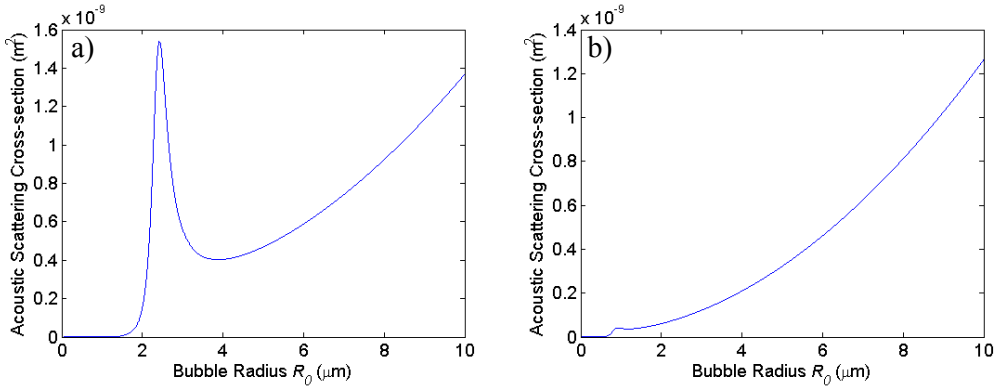

Figure 7.30. The acoustic scattering cross-sections for a single bubble (the size of which is shown on the abscissa) exposed to (a) 1.69 MHz and (b) 6.77 MHz ultrasound.

The power fluctuation at 2.3 s in Figure 7.17(a) caused peak-peak power fluctuations of 2% of the drive power. Assuming the HIFU beam cross-section to be $2*10^{-6}$ m^2, and that this fluctuation is caused by the sudden appearance in the field of a number N_b of resonant bubbles (for which from Figure 7.30(a), $\Omega_b^{scat}=1.54*10^{-9}$ m^2, and from Figure 7.30(b) $\Omega_b^{scat}=0.4*10^{-10}$ m^2), then, assuming their distribution causes incoherent radiation at 15 cm, from equation 7.1 we can estimate that $N_b*1.54*10^{-9}/(4\pi)=0.02*2*10^{-6}$, that is, N_b ~300 and ~12500 bubbles, for 1.69 and 6.77 MHz ultrasound, respectively. Although resonant bubbles are unlikely to undergo the assumed linear pulsations in this field, this estimate for N can be regarded as a conservative estimate because nonlinear pulsations would not scale with the linear ones, and would radiate a proportion of their emission at other frequencies. Therefore, it seems more likely that a 2% fluctuation in power is due to a 2% change in the geometrical area presented to the beam by scattering boiling bubbles, than by rapid fluctuations in the population of smaller bubbles. Note that the power fluctuations observed in degassed water (where it is not possible to generate boiling bubbles using HIFU) are very much smaller, (e.g. 0.2% of the drive power in §6.2.3 Figure 6.11(a)) corresponding to fluctuations due to a few dozen smaller bubbles in the population. In ex-vivo liver tissue, power fluctuations are only seen when boiling occurs (Figure 7.29), as evidenced by audible emissions and hyperechogenicity in B-mode imaging.

The backscattered 4th harmonic could result from the 1.69 MHz primary frequency of the HIFU field causing bubbles resonant at 1.69 MHz to radiate at their 4th harmonic, by bubbles resonant at 3.38 MHz radiating at their 2nd harmonic (6.67 MHz) after being driven by the 2nd harmonic of the HIFU field (3.38 MHz), or by bubbles resonant at 6.67 MHz radiating at 6.67 MHz after being driven by the 4th harmonic of the HIFU field. When subharmonic excitation is considered, there are clearly a plethora of ways in which, through various resonances, bubbles in a population spanning several octaves in radius could contribute to the detected 6.67 MHz signal. However all such emissions would be attenuated by spherical spreading, and by the viscous absorption of this high frequency ultrasound (6.67 MHz). An alternative mechanism would be backscatter of the fourth harmonic (6.67 MHz) energy generated through nonlinear propagation of the HIFU field by mm-sized 'boiling' bubbles.

Figure 7.30(b) demonstrates that a linearly-pulsating resonant bubble exposed to an ultrasound frequency of 6.77 MHz has a scattering cross-section which is over an order of magnitude smaller than that of a resonant bubble at 1.69 MHz. The difference in the geometrical backscattering cross-section of an mm-sized 'boiling' bubble between these two frequencies will be much less. Thus, it is possible to assume that scattering of the fourth harmonic generated through nonlinear propagation of the HIFU field is responsible for the detected fourth harmonic signal (Figure 7.16(d)). The component of the fourth harmonic due to the nonlinear ultrasonic wave incident on a boiling bubble in the focus of a HIFU beam can be estimated from hydrophone calibrations in degassed water. It is recognised that, in tissue, both nonlinearity and absorption may be increased through the presence of bubbles. Using drive settings equivalent to those shown in Figure 7.17(a), Figure 7.31(a) shows the harmonics in the HIFU field in degassed water.

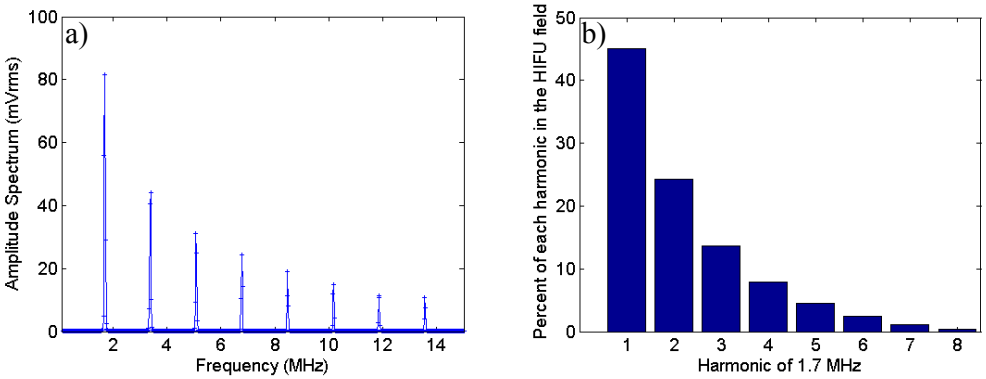

Figure 7.31. (a) The measured amplitude spectrum (0.01-15 MHz) of individual harmonics, in an 80 cycle HIFU pulse at 47.5 W electrical drive power. (b) Percentage contribution to the time-domain signal of the first 8 harmonics. This was calculated from the total time-domain signal divided by the contribution of each harmonic.

Figure 7.31(a) shows the Vrms voltage of each sinusoidal component of the time-domain signal measured by the hydrophone. Summing the individual harmonic contributions for the first five harmonics in Figure 7.31(b) gives 95% of the total time domain signal. The pressure in the HIFU field was calculated from the measured time-domain voltage signal multiplied by a frequency dependent conversion factor (provided by calibration of the hydrophone by National Physical Laboratories, Teddington, UK). This calibration factor fluctuates by approximately 4% over this frequency range (1-9 MHz) and so averaging gives a corrected conversion factor which accounts for 95% of the original time-domain voltage signal. Applying the averaged conversion factor to the time-domain voltage signal gives a total peak positive pressure of 10.5 MPa. From Figure 7.31(b), it can be seen that the fourth harmonic (6.77 MHz) contributes approximately 8% of the total voltage signal measured by the membrane hydrophone at the HIFU focal peak. Hence, the peak positive pressure component of the fourth harmonic, which could be incident on a boiling bubble (correcting for attenuation of 20 mm of liver) is 0.7 MPa. The next step is to estimate the radiated pressure from a resonant bubble at the fourth harmonic (6.77 MHz). Equation 7.3 can be used to calculate the pressure radiated from a bubble (Leighton 1994).

$$\frac{p}{p_\infty} = \frac{\rho}{p_\infty}\left[\frac{R}{r}(\ddot{R}R + 2\dot{R}^2) - \frac{\dot{R}^2}{2}\left(\frac{R}{r}\right)^4\right] + 1 \ , \tag{7.3}$$

where p is the radiated pressure, p_∞ is the pressure far from the bubble, R is the bubble radius and r is the distance away from the bubble wall. The two terms within the square

bracket in equation 7.3, are the acoustic (left term) and the kinetic (right term) components of the radiated pressure (Leighton, 1994).

The Rayleigh-Plesset equation (§2.3) was solved for a resonant bubble (R_0 = 0.91 μm) at 6.77 MHz to give R and $\dot{R}$. The acceleration term, $\ddot{R}$ was calculated from the derivative of $\dot{R}$. Figure 7.32 shows the acoustic and kinetic components of equation 7.3 during a collapse.

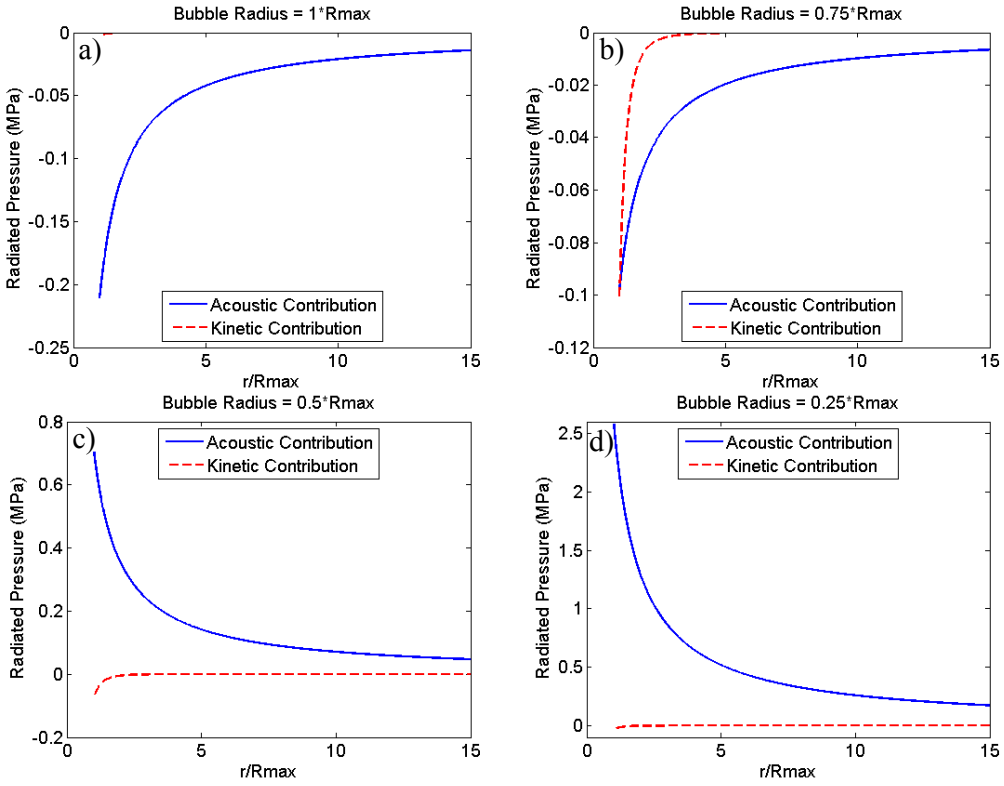

Figure 7.32. The pressure radiated by a resonant bubble as a function of distance from the bubble wall, *r*. Four points during the collapse of the bubble are shown, which are *R* = *Rmax* (a), *R* = 0.75**Rmax* (b), *R* = 0. 50**Rmax* and *R* = 0.25**Rmax* (*Rmax* = 2.6 μm).

Figure 7.32 shows that the kinetic term of the Rayleigh-Plesset equation is only significant at positions less than a micron from the bubble wall. If we assume that this is unlikely to be important, then any radiated pressure incident on the surface of a boiling bubble would come from the acoustic term of equation 7.3. Figure 7.32 shows that the radiated pressure is at a maximum when the bubble radius is near its minimum (*R* = 0.25**Rmax*). Figure 7.32(d) shows that a resonant bubble would need to be located approximately 8 μm away in order for it to produce the same incident pressure on a

boiling bubble as caused by the fourth harmonic component of the HIFU field. For example, it would take approximately 100 coherently resonating bubbles, 1 mm away from the boiling bubble to generate the same incident pressure as the fourth harmonic component of the HIFU field at this drive level. It is therefore concluded that the source of the 6.67 MHz signal detected in this experiment is the generation, through nonlinear propagation, of the fourth harmonic of the HIFU field, which is backscattered by 'boiling' bubbles.

One interesting result of this study is the increase in the broadband signals observed simultaneously with audible emissions (2-20 kHz) and power fluctuations of 4 s HIFU exposures in ex-vivo bovine liver tissue (Figure 7.16). The audible emissions caused by the formation/growth of a boiling bubble have been observed in the 2-20 kHz range (Figure 7.18). The increase in broadband emissions would not necessarily be expected to be generated from boiling bubbles. However it is possible that these bubbles generate sufficient nuclei to generate inertial cavitation. One other concern is that if boiling is occurring, it is likely that the temperatures will be up to 100^{o}C and the vapour pressures could be high enough to restrict the violent collapse of the bubble. The negative pressure at the 1000 W/cm^2 exposure level was 1.86 MPa, but the positive pressure was 7.63 MPa.

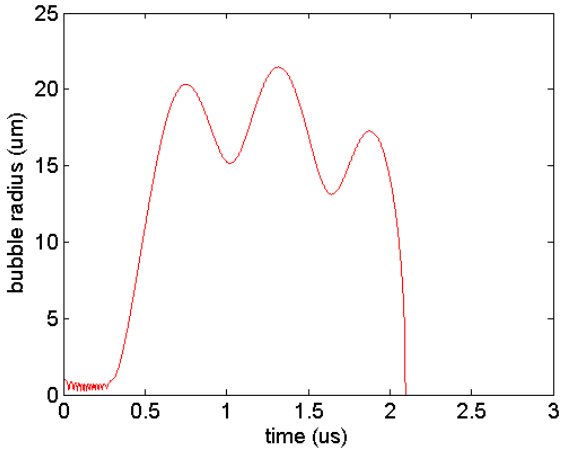

Figure 7.33. The response of a 1 μm bubble exposed to 1.7 MHz, 7 MPa peak pressure (in a linear acoustic field), which was modelled using the Rayleigh-Plesset equation. The viscosity and vapour pressures were altered to simulate the bubble oscillating in 100^{o}C water.

Figure 7.33 shows a solution of the Rayleigh-Plesset equation which suggests, within the limitations of this model, that at this peak positive pressure and elevated temperature

a bubble can collapse (Figure 7.33). A 1 μm radius was chosen as it represents an approximation to the size of the bubbles generated from this acoustic field.

Figure 7.20 shows image frames acquired before the exposure, during the exposure but before boiling, during boiling and after the HIFU exposure. During boiling there is an increase in the interference pattern (Figure 7.20(c) and (d)). This increase is predominantly caused by scattering of superharmonics (Figure 7.21(a) and (b)). It is not possible to resolve the distance from the diagnostic transducer at which the boiling occurred, but it is presumed that it occurred in the same plane as the acoustic axis. Figure 7.22(a) shows a colour frequency map of the first frame taken following tissue boiling. The maximum second harmonic detected by the diagnostic scanner lies approximately 15 mm deep into the ex-vivo liver tissue. This corresponds to the region in which a hole was found in the tissue on subsequent dissection (Figure 7.19). It seems likely that since the increase of interference from this location which corresponded in time with the power fluctuations and audible emissions, a boiling bubble generated at this time (2.35 s) and caused the damage seen in the tissue. Hyperechogenic regions such as these (Figure 7.15(ii)) were only observed after HIFU exposure when audible emissions had been detected during the exposure. Hyperechogenicity persisted for some time after the exposure (Figure 7.23), but the region was observed to reduce in size. This could be due to tissue cooling and the condensation of vapour generated from thermal exsolution into a fluid. An increase in the broadband and fourth harmonic was also detected at this time (Figure 7.16(c) and (d)). However, if this occurred 15 mm deep (along the HIFU beam axis) in the tissue, this is outside the focal regions of both the passive cavitation detectors, and the detectors should therefore not have been sensitive to this boiling event. Conversely, if the boiling event and the broadband emissions are not occurring in the same region, then the probable acoustic shielding from the boiling bubbles would cause a drop in the intensity (pressure) in the focal region of the HIFU (and the detectors), and decreased emissions would been observed. The events that occurred outside the focal fields of the passive cavitation detectors could have been of sufficient amplitude that the detectors were still sensitive to these events. Thus, it is most likely that the boiling event that occurred at this particular time was sufficient to seed inertial cavitation bubbles in sufficient numbers that the passive cavitation detection system was able to detected them outside the focal region of the 10 MHz sensor. Unfortunately, it is not possible to predict the location of these events

since it would have been useful to compare them with a boiling event occurring in the focal region. It might be expected, however, that boiling occurs at the focal peak of the HIFU field but this event occurred away from this position. This suggests that a secondary mechanism was also invoved, maybe the presence of cavitation activity enhancing the heating effect (§2.4).

Using a combination of simultaneous passive and active cavitation detection, power fluctuation and audible emission measurements, it was possible to identify intensities (pressures) for the occurrence of: (i) half harmonic (0.846 MHz) emissions only, (ii) half harmonic and broadband (4-12 MHz) emissions and (iii) half harmonic, broadband and audible emissions with 'increased scatter' (i.e. detected impedance change, passively detected superharmonic scatter and B-mode echogenicity increase). This was achieved by looking at in-situ spatial peak intensity and peak negative pressure ranges of 210-1785 W/cm^2 and 1.21-1.99 MPa respectively, for 4 s exposures. Furthermore, by assuming that, in the absence of broadband emissions, the half harmonic indicates non-inertial cavitation (e.g. Datta *et al* 2006) and that audible emissions indicate boiling, thresholds for specific types of bubble activity were identified in degassed water (§6.2.4) and ex-vivo liver samples. The cavitation pressure thresholds identified for 4 s exposures in ex vivo bovine liver tissue were taken from Figure 7.25 and Figure 7.27.

	Non-Inertial Cavitation	**Inertial Cavitation**	**Boiling (for 4 s exposures)**
Degassed Water (*n* =50)	$\geq$ 440 W/cm^2 $\geq$ 1.80 MPa	$\geq$ 1100 W/cm^2 $\geq$ 2.10 MPa	N/A
Ex-vivo bovine liver (*n* >50)	$\geq$ 310 W/cm^2 $\geq$ 1.52 MPa	$\geq$ 790 W/cm^2 $\geq$ 1.77 MPa	$\geq$1000 W/cm^2 $\geq$ 1.86 MPa
Degassed Water* (*n* =10)	< 0.65 MPa	< 0.65 MPa	N/A
Porcine Blood Plasma* (n =32)	0.39 MPa	0.50 MPa	N/A

Table 7.1. Peak negative pressures required to generated cavitation activity in degassed water and ex-vivo bovine liver tissue, compared with those published by Datta *et al* (2006), marked with *.

Non-inertial cavitation occurred at (1.69 MHz) HIFU intensities greater than 310 W/cm^2 ±20% (1.52 MPa ±17%). Inertial cavitation occurred at HIFU intensities greater than 786 W/cm^2 ±20% (1.77 MPa ±17%). For the 4 s exposures used here, boiling occurred at HIFU intensities greater than 1000 W/cm^2 ±20% (1.86 MPa ±17%). Table

7.1 shows a summary of the cavitation threshold data for degassed water and ex-vivo bovine liver compared with data published by Datta *et al* (2006). The differences in degassed water thresholds is most likely be due to the difference in ultrasound frequency, Datta *et al* used 0.12 MHz whereas 1.69 MHz was used in this study. Acoustic cavitation will occur at lower pressures at lower frequencies (Apfel and Holland, 1991). The exposure time was the same (4 s) for the majority of this study. However, as intensity increases, boiling will occur earlier as demonstrated by the relationship between intensity and onset time of audible emissions (2-20 kHz) in Figure 7.28. Onset time was defined as the point at which the amplitude of the detected fourth harmonic increased by at least a factor of 10 within 5 data points in time, which corresponded to a rapid change over 5 ms of the exposure. This is consistent with higher intensities reducing the time taken to reach 100°C. In a previous study (McLaughlan *et al*, 2005), the variation of "onset" time of the fourth harmonic (6.77 MHz) between 800-2000 W/cm^2 was demonstrated.

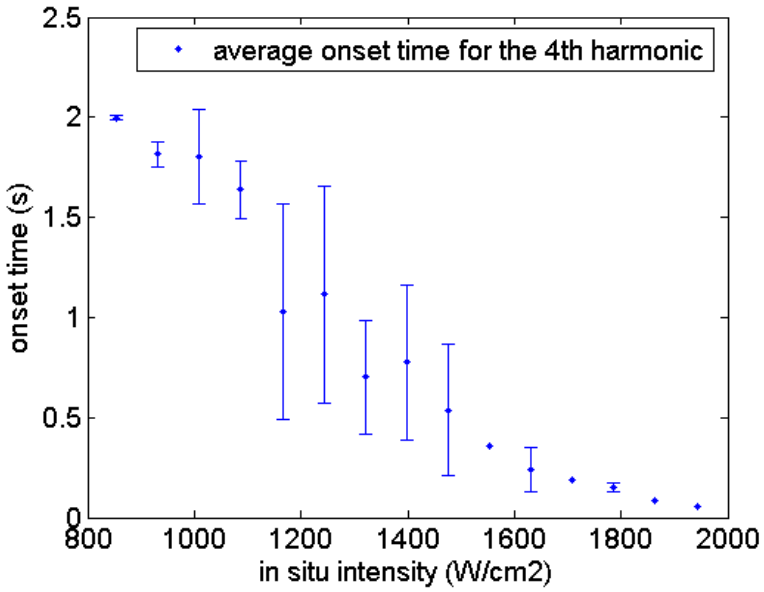

Figure 7.34. The average onset time for the 4th harmonic in ex-vivo tissue exposed to HIFU. For 2 s HIFU exposures targeted 15 mm deep in tissue. *n* =3-20 for the points with uncertainty bars, *n* <3 for the ones without. The uncertainty is calculated from the standard deviation.

Figure 7.34 shows the onset time for a given intensity for the fourth harmonic, which indicates an increase in the scatter of the non-linear HIFU components due to boiling. It can be seen that as HIFU intensity is increased, the time to onset decreases. The maximum variability in the measures is approximately 1 s which is similar to the

maximum variability in the onset time for the audible emissions (Figure 7.28). It is worth noting that the onset time for the audible emissions is here defined as the first occurrence of emissions in the 2-20 kHz) range (excluding the 3.5 kHz buzzer signal). The lesion dimensions shown in Figure 7.26 are the measured average length, width, and area for this series of experiments in ex-vivo bovine liver tissue. Figure 7.26(c) shows that at peak negative pressures exceeding the boiling threshold (>1.86 MPa) the area of the lesions reaches a plateau. The lesion length (Figure 7.26(a)) shows a similar trend to the area, whereas the width (Figure 7.26(b)) continues to increase with higher negative pressures. This shows that the boiling bubbles have a significant effect on the shape of the lesion (Figure 7.13(a) and (d)) causing what are typically called 'tadpole' shaped lesions. However, it does not appear that acoustic cavitation has an effect on the size of the lesion.

7.3 Tissue heating study

7.3.1 Methods

The significant difference between the cavitation detection system described in this section and that in the last one, is that a single sensor, which is mounted on the HIFU transducer in order that it will remain aligned even if the HIFU source is moved between exposures, is used. This gave the ability to track cavitation detection with the movement of the HIFU transducer, giving greater flexibility in the positioning of the target tissue. It also represents a move towards a more clinically relevant detection system. A modification was made to the Imasonic transducer mount that allowed a 7.5 MHz passive transducer (§4.2.1) to be mounted and con-focally aligned with the Imasonic transducer. Figure 7.35(a) shows a photograph of the Imasonic transducer with the 7.5 MHz passive transducer attached. In this configuration a curvilinear probe (C5-2, radius of curvature 5 cm, field of view angle 65^{o}, centre frequency 1.96 MHz, and imaging depth 18 cm) was inserted into the rear of the Imasonic transducer to allow coaxial imaging. This probe was recessed 14.4 mm from the front face of the Imasonic transducer (Figure 7.35(b)). The 7.5 MHz passive transducer mount was designed such that it was possible to adjust the distance from the HIFU transducer (z) and the angle of the device (between y and z). This system was attached to the 3-D automated gantry (§5.1.3) and could be moved under manual or computer control with a precision of ±0.1 mm.

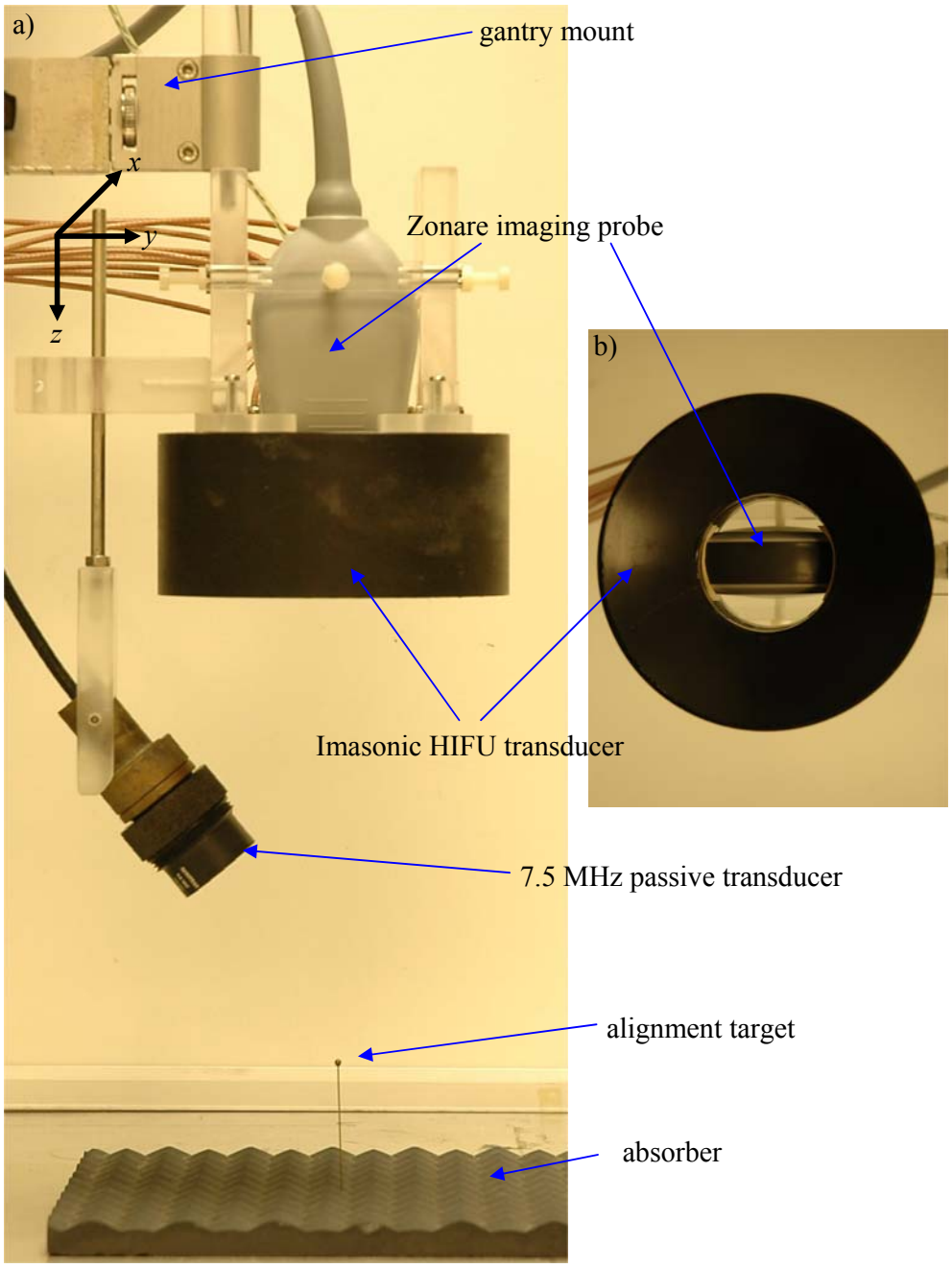

Figure 7.35. A photograph (a) of the experimental set-up using the 7.5 MHz passive transducer. The water tank has been omitted for clarity. (b) the front face of the Imasonic transducer and Zonare Imaging probe viewed down their sound axes.

Alignment of this system was achieved with a pulse-echo target (Figure 7.35(a)), which was a 1 mm ball bearing mounted on a 0.5 mm brass rod. Firstly, the target was located using diagnostic ultrasound. This gave a rough alignment with the HIFU focus, and was sufficient for the first stage of the alignment process. Then the HIFU transducer was

pulsed to refine this alignment (§5.1.3). Positioning of the Zonare imaging probe could be refined such that the focal peak of the HIFU was located on the alignment target (±5 mm). Finally, the 7.5 MHz passive transducer was aligned using an echo of a pulse produced by the HIFU transducer (±0.1 mm). Once this received signal had been maximised, the 7.5 MHz passive transducer was fixed in place. This method allowed these three devices to be aligned with the HIFU focal peak, which could then be targeted on any suitable location in the ex-vivo tissue.

The 7.5 MHz passive cavitation detection system used the DAQ computer described in the last section. For this single sensor the filtering and amplification was changed, as shown in Figure 7.36.

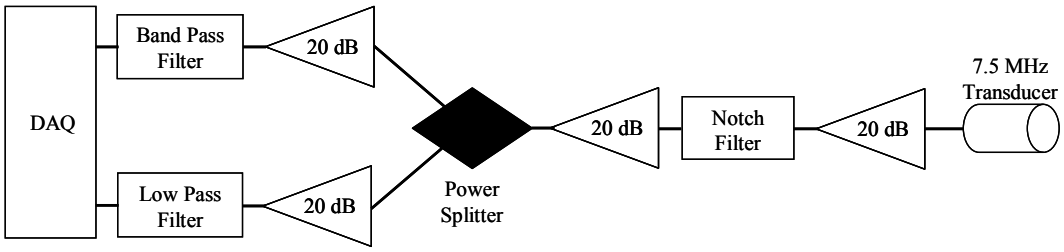

Figure 7.36. A schematic diagram of the filtering and amplification used with the 7.5 MHz HIFU transducer mounted passive cavitation detection system.

In addition to the low pass filter described in the last section, a notch (NF) filter (Allen Avionics, F5181, band reject frequency 1.5-2 MHz, -50 dB attenuation at 1.7 MHz, -50 dB/decade) and a band pass (BP) filter (Allen Avionics, F5204, band pass frequency 7-8 MHz, -50 dB attenuation at 1.7 MHz, -40 dB/decade) were used to minimise RF pickup from the drive signal, and acoustic interference from the HIFU system.

In order to investigate the effect of temperature on the cavitation threshold described in the previous section, ex-vivo tissue samples were heated to 40 ±2^{o}C. Rectangular 10x10x5 cm ex-vivo tissue samples were used for this study. The collection and preparation of these samples was that described in section 7.2.1. As the HIFU transducer and passive cavitation detection system were both coupled to the 3-D automated gantry movement, it was possible to perform multiple exposures in a single sample. A Perspex frame with front and rear Mylar membranes (12 cm diameter aperture) was used to hold the ex-vivo tissue sample in place for exposures in the vertical (z) plane.

The tissue was submerged in degassed water which was heated to 45°C. It took approximately 50 mins for the temperature of the tissue and degassed water to equilibrate at 40 ± 2°C. It was held at this temperature for approximately 2 h, which was not sufficient length of time to cause an irreversible damage in the tissue. The thermal dose is usually quoted in terms of equivalent minutes at 43°C (t_{43}), which refers to the time it takes to achieve complete cell death at 43°C (240 min) (Sapareto and Dewey, 1984). For example at 56°C this time is reduced to 1.75 s (Hill, 2004). Thus the tissue would need to be held at 42°C (the upper limit for the temperature range) for 480 min, or 8 h for irreversible damage to occur. Figure 7.37 shows a schematic diagram of the tissue heating system used.

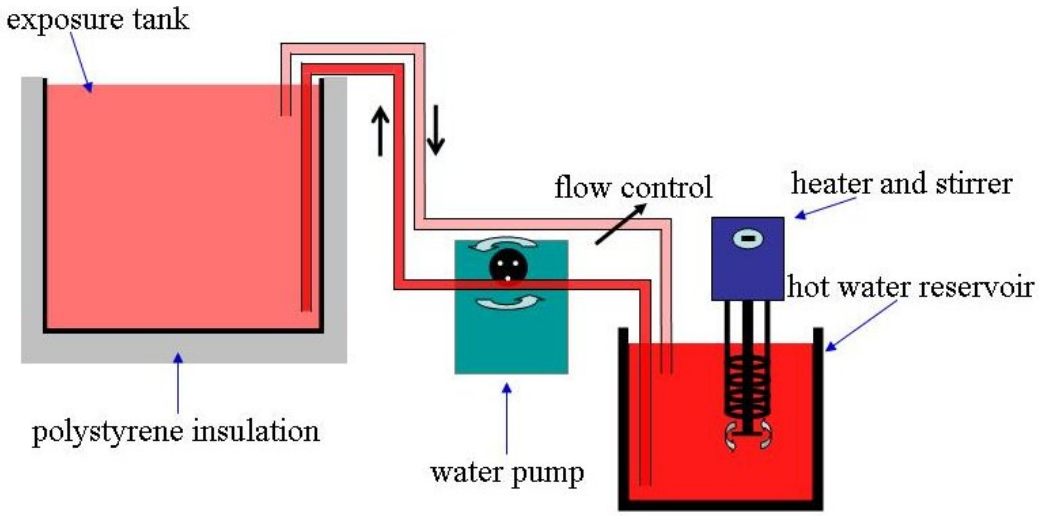

Figure 7.37. A schematic diagram of the heating apparatus used to heat the ex-vivo bovine liver tissue. The HIFU apparatus (Figure 7.35) has been omitted for clarity.

Degassed water was circulated between the exposure tank (start temperature 20°C) and hot water reservoir (start temperature 60°C) until the temperature in the exposure tank was 45°C. The temperature in the hot water reservoir was maintained by a programmable heating and stirring element (Figure 7.37). Once the temperature of the ex-vivo tissue had reached the desired level, then the flow of degassed water between the two tanks was halted, to avoid disturbing the detectors. Two hypodermic needle thermocouples were used to monitor the temperature of the ex-vivo tissue and degassed water. The thermocouple in the tissue was located approximately in the centre of the tissue sample, but outside of the region targeted by the HIFU field and the water thermocouple was located next to the HIFU transducer. It was found that the

temperature of the tissue varied by approximately 2°C over the time it took to expose the tissue (~ 2 h). One disadvantage of this set-up was that the HIFU transducer was submerged in the heated water, it was thus necessary to re-calibrate the transducer at the higher temperature. It was found that for the same drive level the acoustic output of the Imasonic HIFU transducer was reduced by an equivalent 1 dBm level in the drive system (§5.1.2), compared to operation in the 20°C tank water.

The passive cavitation detection system, described in the previous section was used for each exposure. The microphone system described in section 7.2.1 was submerged in the exposure tank for this study. Diagnostic imaging was performed before and immediately after the HIFU exposure using the Zonare diagnostic ultrasound system and the probe described in the previous section.

The HIFU focal peak was targeted at a depth of 15 mm in ex-vivo bovine liver tissue. A range of 10 separate I_{sp} (peak negative pressure) values between 280–3010 W/cm^2 ±20% (1.00 to 2.25 MPa ±20%) was used to investigate the cavitation threshold of the tissue at 20 and 40°C, during 4 s exposures. The 10 individual exposure levels were, 280, 340, 430, 540, 670, 830, 1050, 1320, 1650 and 3010 W/cm^2 (1.00, 1.11, 1.23, 1.32, 1.48, 1.58, 1.74, 1.86, 1.99 and 2.25 MPa). A 4x4 2-D (*x* and *y*) array of exposures with a 10 mm separation in order to maximise the available tissue were performed in each tissue sample. Two rows of surface marker lesions were made either side of the row of exposures in the *x* direction.

7.3.2 *Results*

Figure 7.38 shows six B-mode frames acquired at 10 minute intervals when the ex-vivo bovine liver sample was heated in a water bath to 40°C. It can be seen that as the temperature of the tissue and degassed water increases, the surface of the tissue appears to move towards the imaging probe.

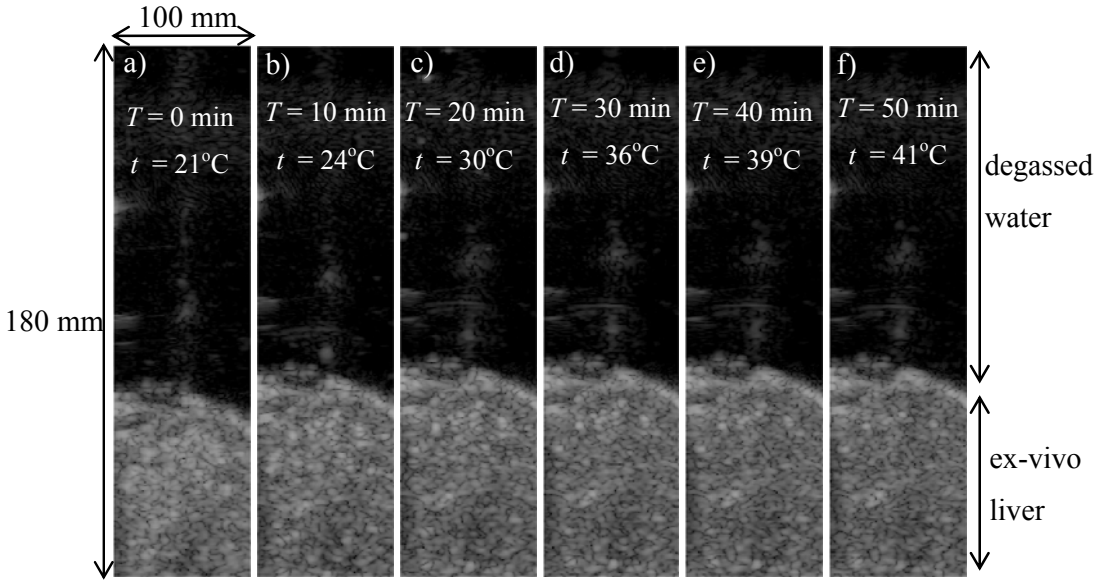

Figure 7.38. Six B-mode frames acquired during water-bath heating of ex-vivo bovine liver, where the temperature (T) at a specific time (t) is shown on the image.

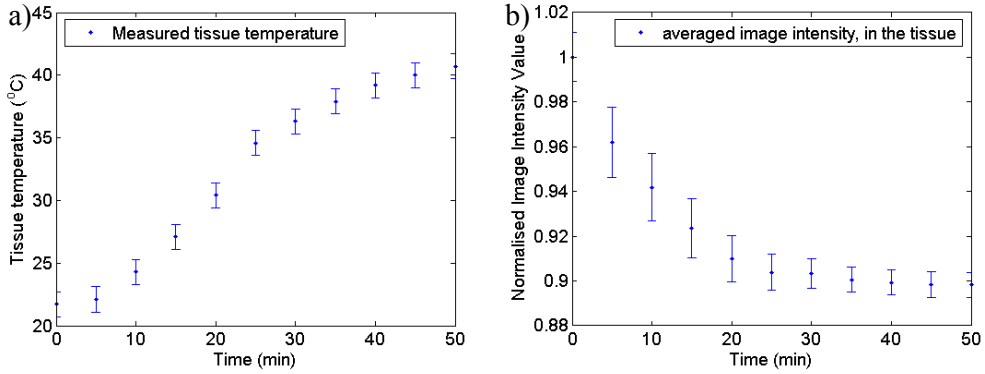

Figure 7.39. The measured tissue temperature approximately in the centre of the sample (a) during heating and the normalised average image intensity in the tissue in the B-mode image (b). Uncertainty in the temperature measurements is the error in the measurement of the tissue. The uncertainty in the normalised average image intensity is the standard deviation of the image intensity for the ex-vivo liver pixels.

The normalised average image intensity in Figure 7.39(b) shows a decrease with increased in temperature Figure 7.39(a). Average image intensity was normalised to the peak value detected at t = 0 min. Image intensity was the sum of the greyscale values of the manually identified tissue region in the B-mode image. The shift in position at the end temperature meant that the position of the HIFU focal peak was corrected for this apparent shift. Figure 7.40 to Figure 7.42 show typical examples of the acoustic spectra that were detected during the 4 s HIFU exposures in ex-vivo tissue at 20 and 40°C.

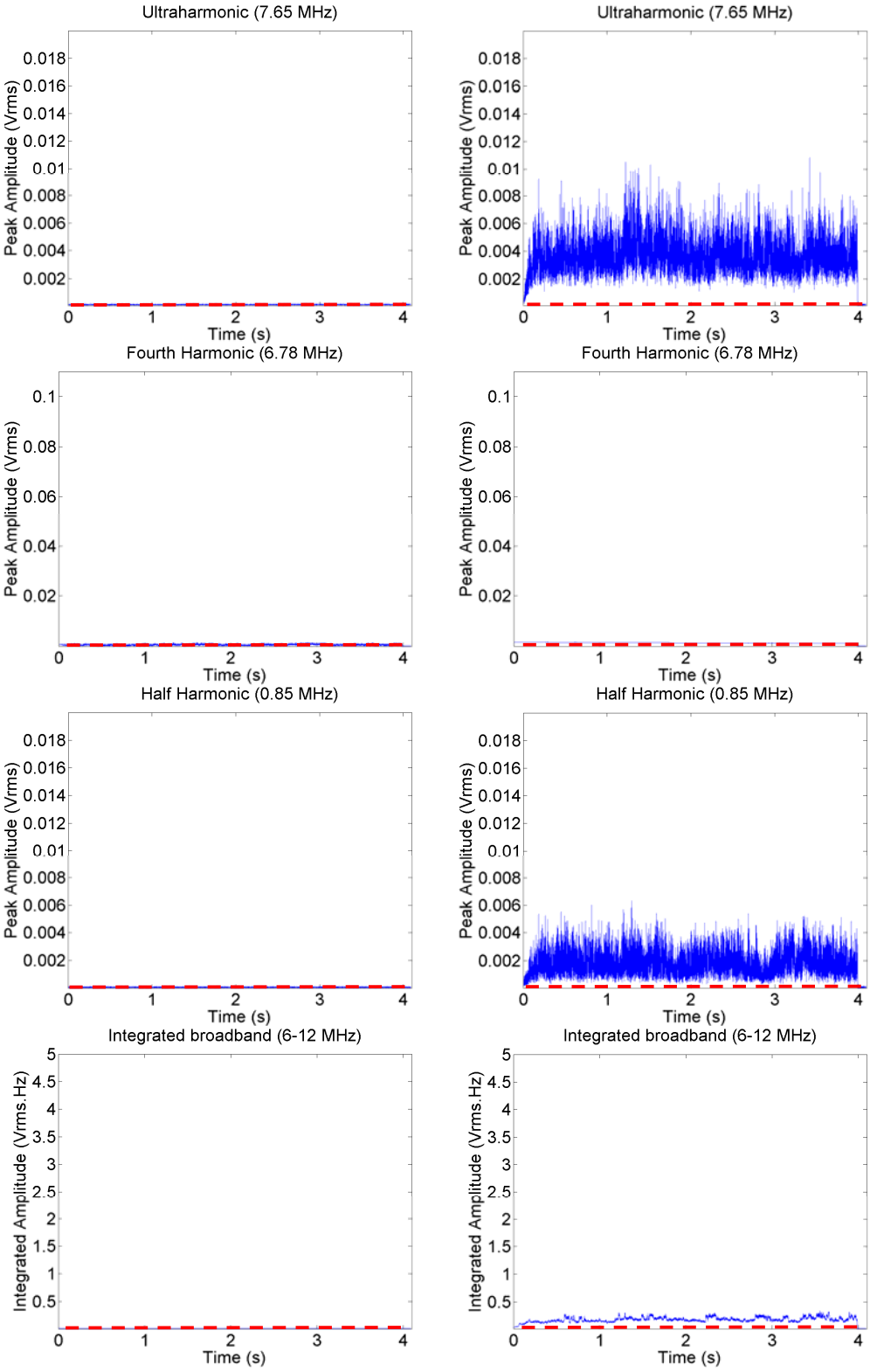

Figure 7.40. The acoustic spectra detected during a 4 s 540 W/cm^2 (1.32 MPa) in ex-vivo bovine liver tissue at 20^{o}C (left column) and 40^{o}C (right column). The red dashed line indicates the peak noise level measured from a sham exposure.

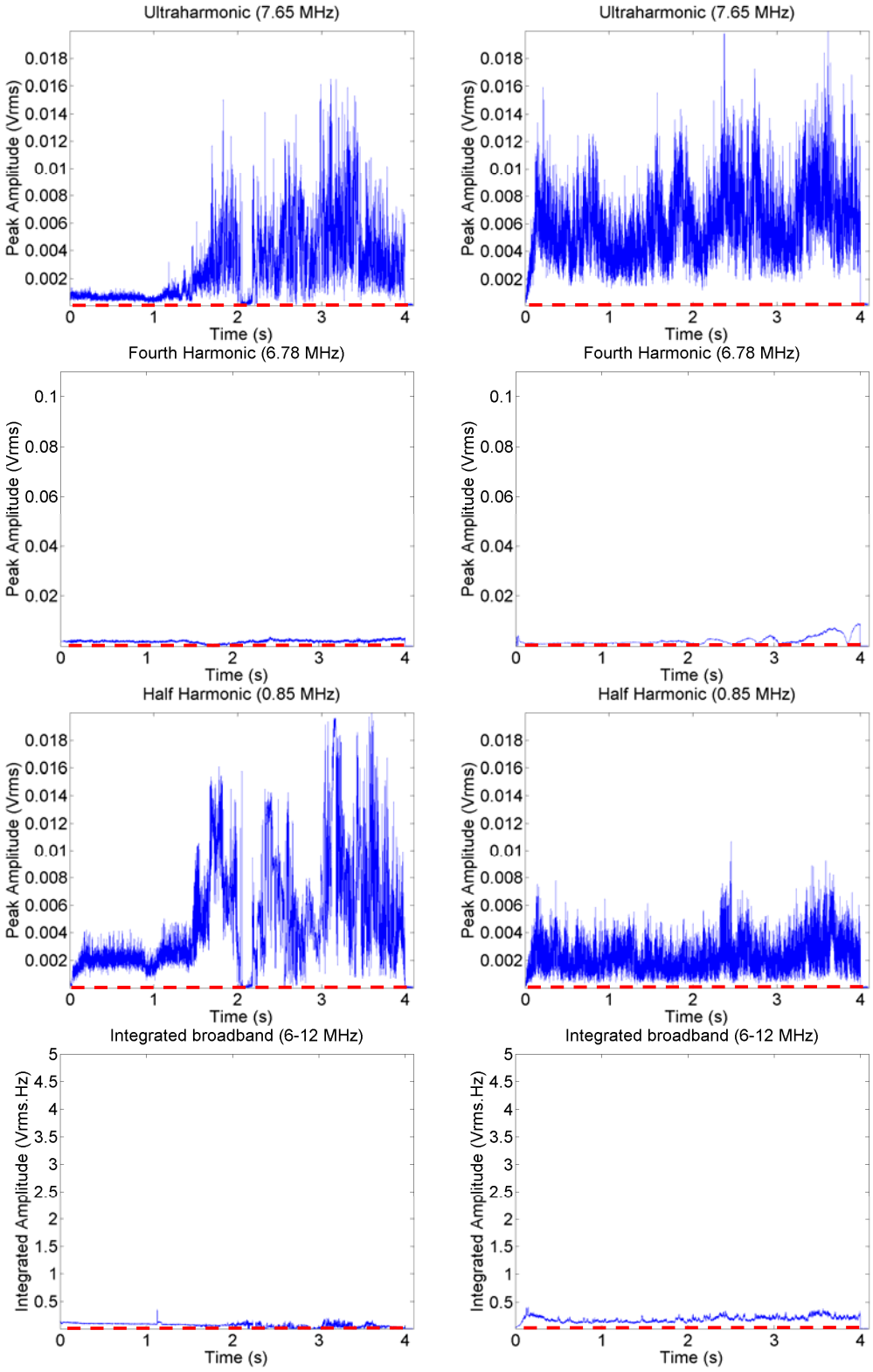

Figure 7.41. The acoustic spectra detected during a 4 s 1050 W/cm^2 (1.74 MPa) in ex-vivo bovine liver tissue at 20^{o}C (left column) and 40^{o}C (right column). The red dashed line indicates the peak noise level measured from a sham exposure.

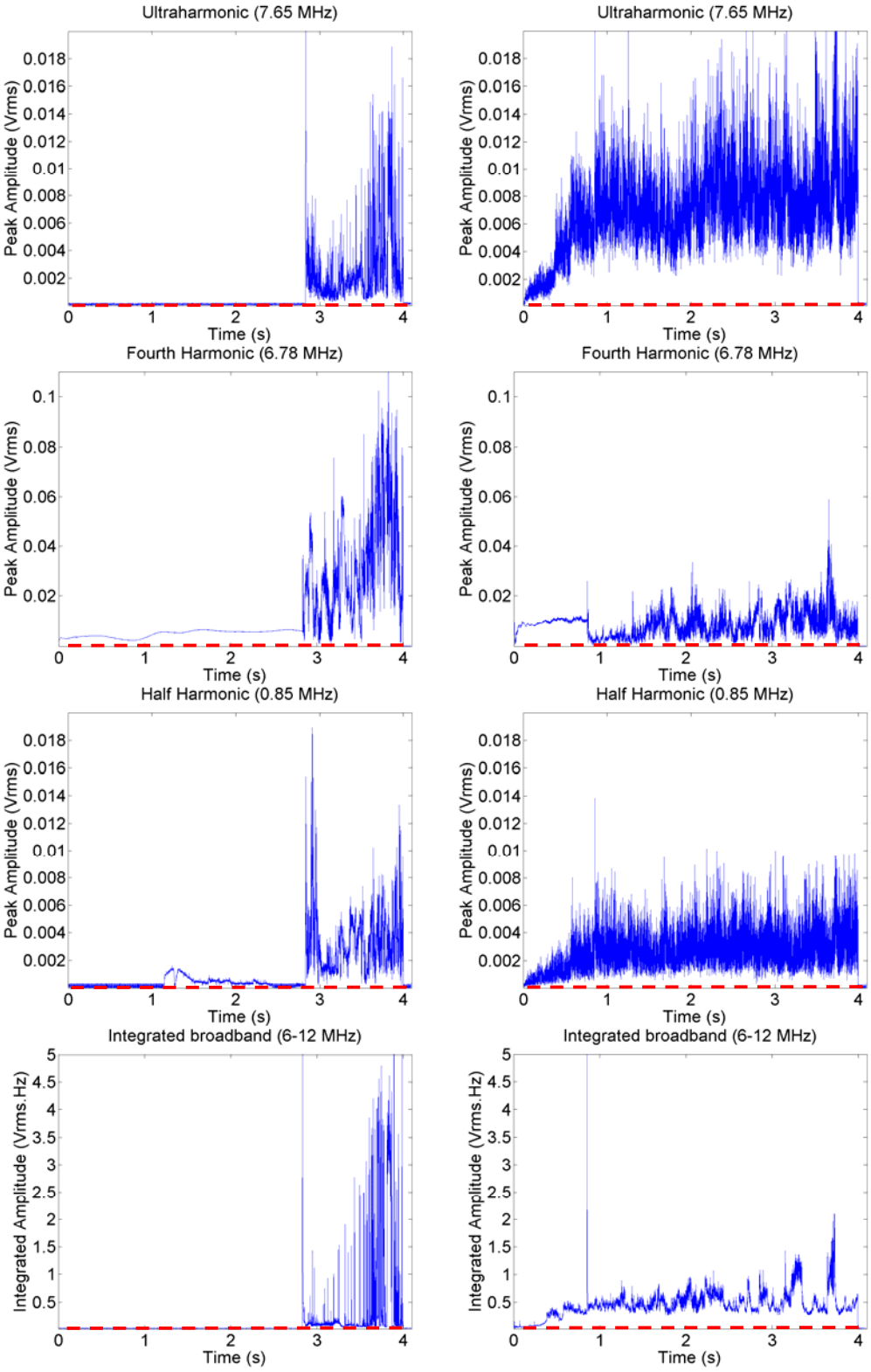

Figure 7.42. The acoustic spectra detected during a 4 s 1650 W/cm^2 (1.99 MPa) in ex-vivo bovine liver tissue at 20^{o}C (left column) and 40^{o}C (right column). The red dashed line indicates the peak noise level measured from a sham exposure.

Figure 7.40 shows that for 540 W/cm^2 (1.32 MPa) exposure at 40^{o}C acoustic emissions were detected above the peak noise level measured from a sham exposure, where for the equivalent exposure at 20^{o}C no acoustic emissions were detected. When the emissions are detected, they showed the typical behaviour of amplitude variation with time. The 4 s HIFU exposures at 1050 W/cm^2 (1.74 MPa) and either 20 and 40^{o}C showed acoustic emissions detected throughout the 4 s exposure (Figure 7.41). Figure 7.42 shows two exposures at 20 and 40^{o}C for an in-situ I_{sp} = 1650 W/cm^2 (1.99 MPa), where boiling occurred for both of these exposures. However, at 20^{o}C this occurred at approximately 2.8 s, whereas at 40^{o}C it occurred at approximately 0.5 s.

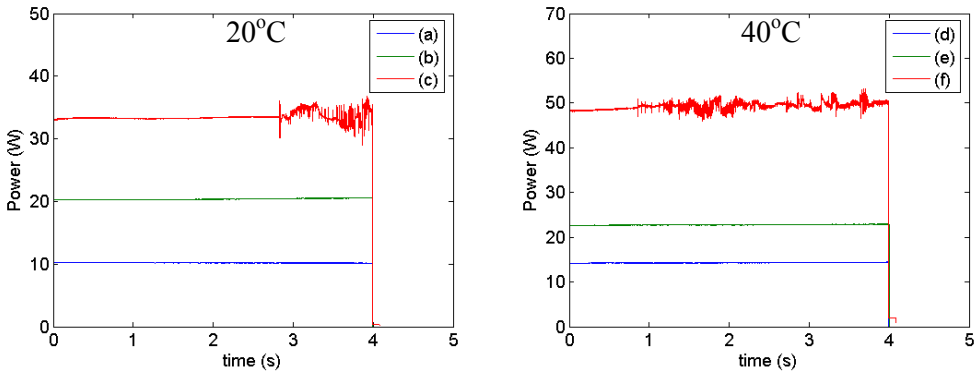

Figure 7.43. The measured power during the six exposures described above, where the exposure intensities are (a, d) 590 W/cm^2 (1.32 MPa), (b, e) 1050 W/cm^2 (1.74 MPa) and (c, f) 1650 W/cm^2 (1.99 MPa). Note that at 40^{o}C higher levels of electrical drive power were required to achieve equivalent acoustic output to that at 20^{o}C.

Figure 7.43 shows the measured electrical drive power of the exposures shown in Figure 7.40 to Figure 7.42. The total time integrated average acoustic spectra shown in Figure 7.44 give a comparison between the detected emissions at 20 and 40^{o}C. Acoustic spectra were detected at lower peak negative pressures when the ex-vivo tissue was warmer. For example half harmonic emissions (Figure 7.44(c))) were detected at 340 W/cm^2 (1.11 MPa) for the exposures of tissue at 40^{o}C, where this was 830 W/cm^2 (1.58 MPa) for 20^{o}C. This is consistent with the study performed using the Mauve HIFU transducer (Figure 7.27(c)). Similarly broadband emissions were detected at 340 W/cm^2 (1.11 MPa) for the exposures of tissue at 40^{o}C, whereas this was 1050 W/cm^2 (1.74 MPa) for 20^{o}C which is consistent with the study performed using the Mauve HIFU transducer within calibration uncertainty (Figure 7.27(b) and (d)).

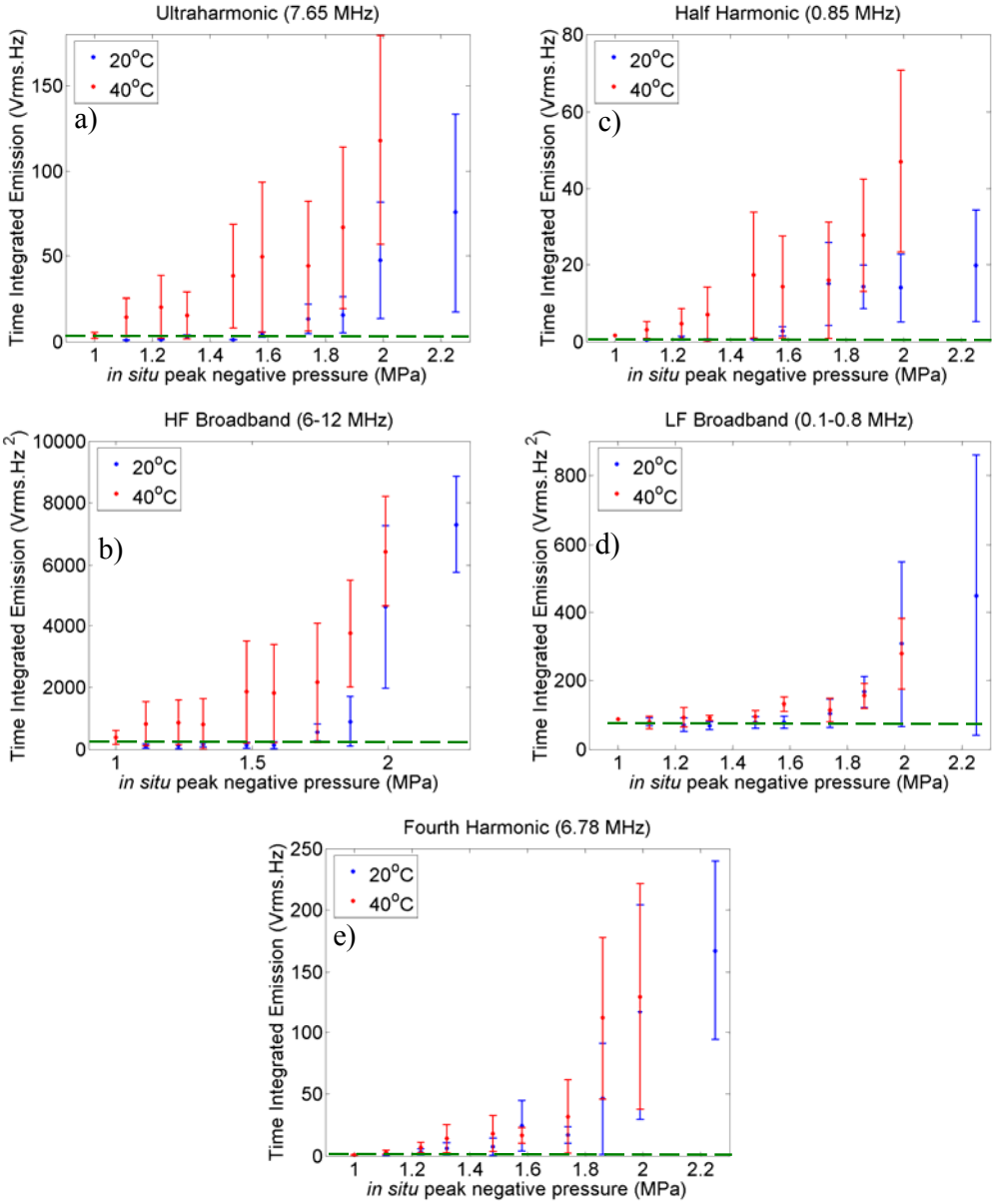

Figure 7.44. The averaged total time integrated (a) ultraharmonic (7.65 MHz), (b) HF broadband emissions (6-12 MHz), (c) LF broadband emissions (0.1-0.8 MHz), (d) half harmonic (0.85 MHz) and (e) fourth harmonic (6.78 MHz) shown over the range of peak negative pressures used. Uncertainty, where shown, is the standard deviation for n = 4-5. The green dashed line indicates the peak noise level measured from sham exposures.

7.3.3 Discussion

The system used to heat the tissue to a uniform elevated temperature (40°C) worked in such a way that it was necessary to hold the degassed water at the elevated temperature. The effect of this on sound speed can be seen in Figure 7.38, as the surface of the tissue

appears to shift towards the imaging transducer. Figure 7.39 shows another effect, namely that as temperature increased there was a small decrease (~10%) in the total image intensity of the ex-vivo tissue. However, the aim of this study was to see if it was possible to detect any increase in the echogenicity of the ex-vivo tissue as a result of it being heated to 40 ±2^{o}C. The reduction of the averaged image intensity (Figure 7.39(b)) demonstrated that this was not a successful technique for determining whether gas has been released as a result of increased rate of autolysis due to the elevated temperature of the tissue over the time scales used.

The acoustic spectra shown in Figure 7.40 to Figure 7.43 show that at 40^{o}C acoustic emissions were detected at exposures below the acoustic cavitation thresholds for tissue at 20^{o}C. However, boiling occurred at the same exposure intensities at both temperatures, but generally occurred earlier in the exposures at 40^{o}C (Figure 7.43). In this study the boiling threshold was unaffected by the higher start temperature. Figure 7.44 gives a comparison between the total time integrated acoustic spectra detected over the exposure range used in this study. It shows that at the elevated temperature acoustic spectra were detected below the acoustic cavitation thresholds for ex-vivo tissue at 20^{o}C.

7.4 Thermocouple measurements

Cylindrical samples (§7.2.1) of ex-vivo tissue were cut, and thermocouples were inserted under diagnostic imaging guidance approximately 20 mm deep (axial direction) into them. Two different thermocouple types were used for this study: fine-wire thermocouples, constructed in-house by soldering 50 μm constantan and manganin wires (wire diameter 50 μm, K-type), and a hypodermic needle Omega© K-type thermocouple (diameter 200 μm, nT, copper-constantan). All wire thermocouples were calibrated in a water bath against a mercury-in-glass thermometer over a temperature range of 28-40^{o}C. To minimise the introduction of air or impurities, each thermocouple, after cleaning with alcohol and being stored in degassed water, was inserted under water. The focal peak of the Imasonic transducer was aligned on each thermocouple using 1-D axial scans. Temperature scans were carried out at a free-field temporal average intensity of 40 W/cm^2 at 5 steps/mm over a 4 mm transaxial range and 20 mm axially at 1 steps/mm, with data being recorded using software written in house. The temperature history was recorded using this software, which controlled a DMM 2000 digital multi-meter (Keithley Instruments Inc., FL, USA). At each position, the

HIFU was turned on for 1 s and the tissue was then allowed to cool for 5 s before the next exposure. Electrical noise resulted in a ±0.2^{o}C uncertainty in measured values for each thermocouple. Transaxially, the thermocouple junctions were aligned with the focal region of the HIFU field to a precision of 0.2-0.4 mm, depending on the diameter of the thermocouple. Localisation along the HIFU beam axis was achieved to at an accuracy of about 1 mm. Temperature rise versus time data were obtained at the focal peak in the HIFU field. Fifteen seconds of data were recorded: 5 s before exposure, 5 s during HIFU exposure, and 5 s during cooling.

Passive cavitation detection was performed using both systems described in sections 7.2.1 and 7.3.1. The dual passive cavitation detection system (§7.2.1) was used initially. When using the experimental set-up described in section 7.2.1, ensuring that the thermocouple was implanted in the correct location was time consuming and sometimes required several attempts before correct insertion was achieved. The arrangement described in section 7.3.1, for the single passive sensor (7.5 MHz) was used in favour of the dual system as the alignment of the thermocouple with the HIFU focal peak ensured that the focal peak of the passive cavitation detection system was in the correct location.

Two or three repeat measurements were made with each thermocouple at a range of different in-situ I_{sp} values, over the range 110-1550 W/cm^2 (0.36 to 1.34 MPa) in 8 increments. These were 110, 140, 170, 260, 410, 630, 1000 and 1550 W/cm^2 (0.36, 0.43, 0.52, 0.62, 0.76, 0.89, 1.25, and 1.34 MPa). 5 s exposures at these levels were found to avoid visible tissue damage i.e. they were below the lesioning threshold. This made it possible to expose the same region repeatedly, once the temperature had returned to the baseline. Once a complete data set had been acquired, a single lesioning exposure in the range of 2510-4580 W/cm^2 (1.61 to 2.02 MPa) was performed. All exposures were repeated in separate tissue samples without a thermocouple to provide a comparison between the detected acoustic emissions obtained with and without a thermocouple *in situ*.

7.4.1 *Results*

The results presented in this section represent typical thermocouple and cavitation detection measurements taken in ex-vivo bovine liver tissue. Temperature histories for needle (NT) and fine wire (FWT) thermocouples measurements were taken over the range 110–1550 W/cm^2 ±25% (0.36 to 1.34 MPa ±22%) in ex-vivo bovine liver tissue. The increase in the uncertainty of the in-situ intensity (pressure) measurements is due to

the inability to insert the thermocouple at exactly 20 mm deep, in the tissue sample. Using the diagnostic imaging it was possible to measure the depth of the thermocouple in the tissue and it has been assumed that it was at located at a depth of 18 ± 4 mm and the in-situ intensities (pressure) have been calculated accordingly.

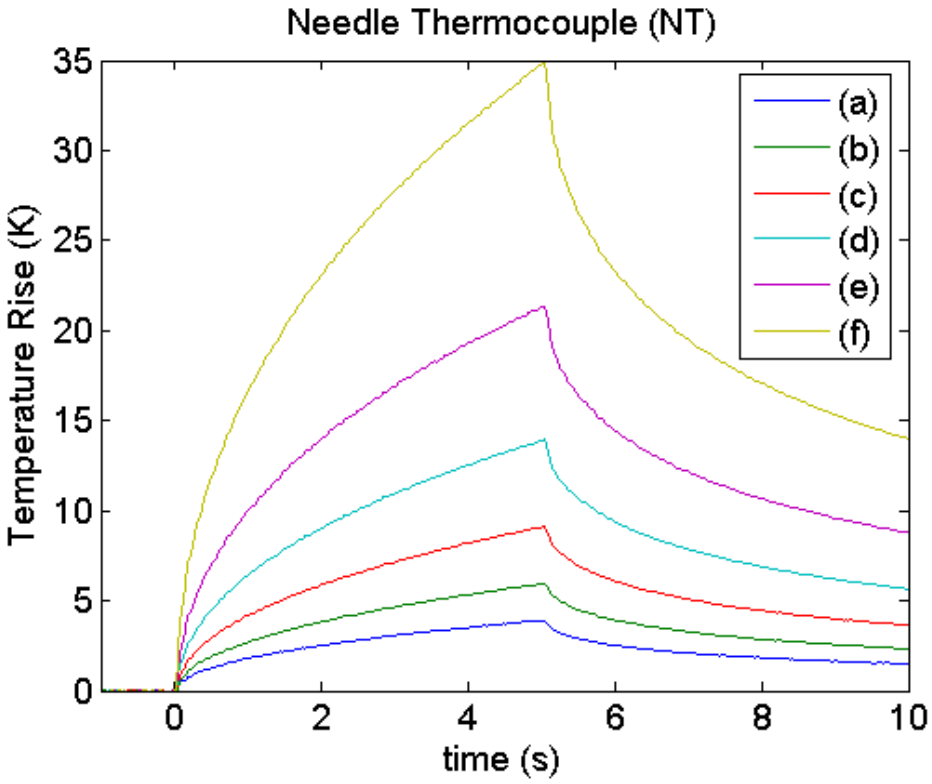

Figure 7.45. Temperature-time data for needle thermocouple measurements of 5 s HIFU exposures at (a) 170 W/cm^2 (0.52 MPa), (b) 260 W/cm^2 (0.63 MPa), (c) 410 W/cm^2 (0.76 MPa), (d) 630 W/cm^2 (0.89 MPa), (e) 1000 W/cm^2 (1.13 MPa) and (f) 1550 W/cm^2 (1.34 MPa) in ex-vivo bovine liver tissue. Uncertainty levels have been omitted for clarity but ±1 K (n =2-3).

Figure 7.45 shows typical temperature histories measured during 5 s exposures at the HIFU intensities detailed in the caption. A needle thermocouple was used for these measurements. The plots show examples of the temperature-time plots obtained from this study with between 1-3 repeat measurements being made at each intensity level. The steep rise at the start of the exposure is due to viscous heating at the thermocouple junction and has not been corrected in these plots.

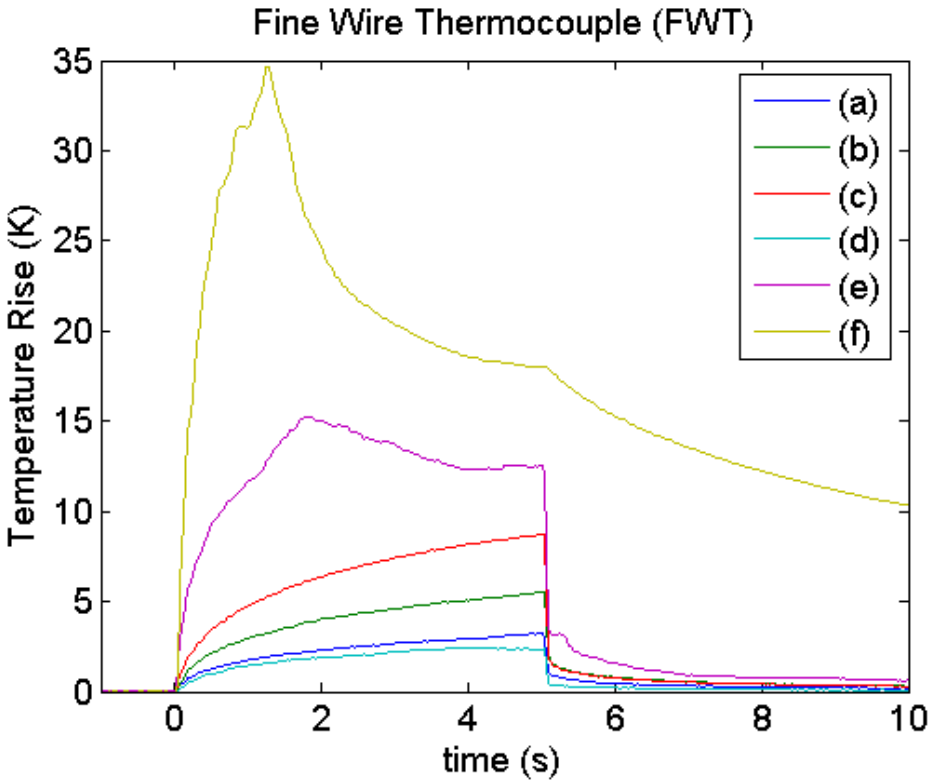

Figure 7.46. Temperature-time data for fine wire thermocouple measurements of 5 s HIFU exposures at (a) 170 W/cm^2 (0.52 MPa), (b) 260 W/cm^2 (0.63 MPa), (c) 410 W/cm^2 (0.76 MPa), (d) 630 W/cm^2 (0.89 MPa), (e) 1000 W/cm^2 (1.13 MPa) and (f) 1550 W/cm^2 (1.34 MPa) in ex-vivo bovine liver tissue.

Figure 7.46 shows typical temperature histories measured during 5 s exposures at increasing HIFU exposure intensities using the Imasonic transducer. Between 3-5 repeat measurements were made at each intensity level. Fine wire thermocouples were used for these measurements. The temperature histories in curves (e) and (f) show fluctuations in the measurements that can be associated with acoustic cavitation activity.

Figure 7.47 to Figure 7.49 show a comparison between the detected spectra with no thermocouple, a needle thermocouple and a fine wire thermocouple (Figure 7.46) in the ex-vivo tissue. At the 170 W/cm^2 (0.52 MPa) exposure level (Figure 7.45(a) and Figure 7.46(a)) only a low amplitude (~0.04 Vrms.Hz) of broadband emissions was detected between 4.3 and 5s. A similar trend was observed during the 260 W/cm^2 (0.63 MPa) exposures, where low amplitude broadband emissions were detected throughout the 5 s HIFU exposure. Broadband and half harmonic emissions were detected during the 5 s exposure at 630 W/cm^2 (0.89 MPa) with a fine wire thermocouple (Figure 7.46(d)), no other emissions were detected with the needle thermocouple or in the absence of a thermocouple.

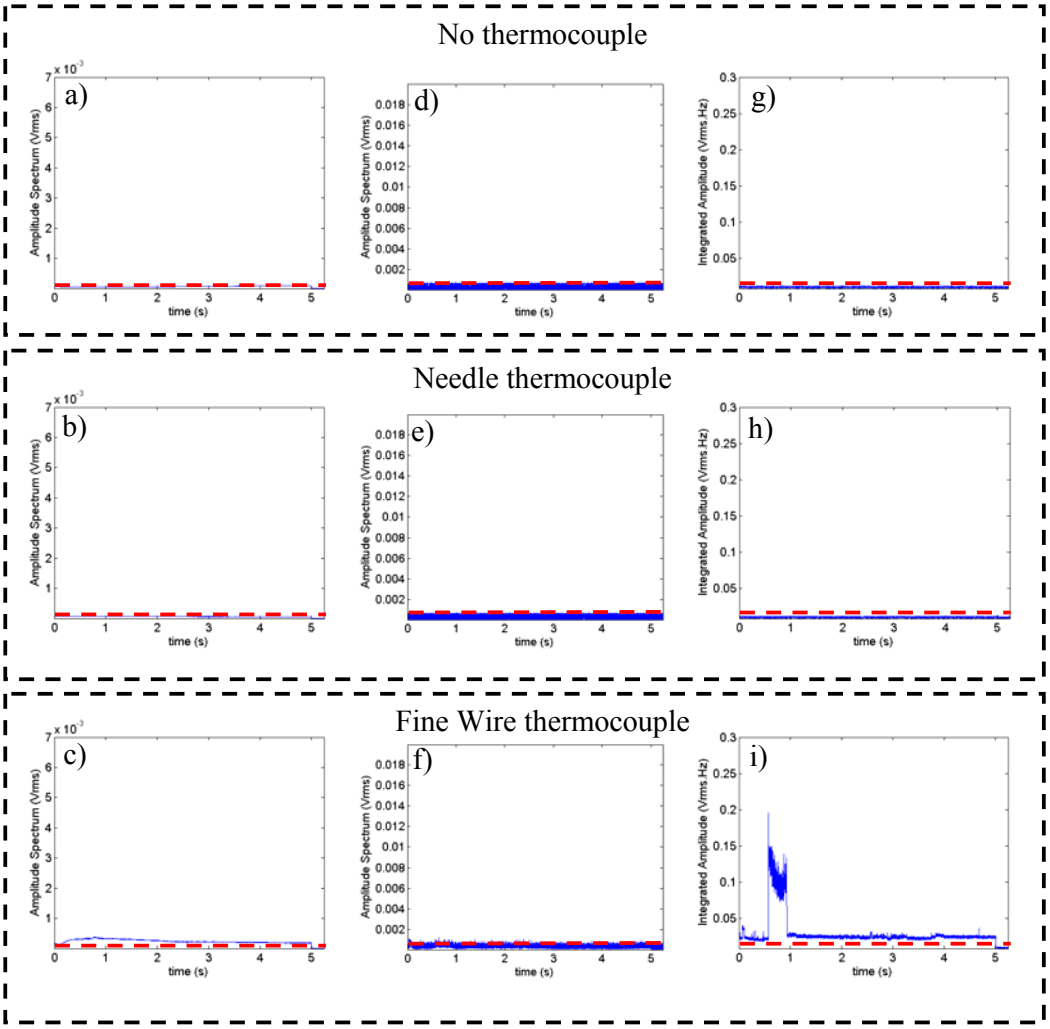

Figure 7.47. The detected fourth harmonic ((a)-(c)), half harmonic ((d)-(f)) and broadband emissions ((g)-(i)) for single 630 W/cm^2 (0.89 MPa).

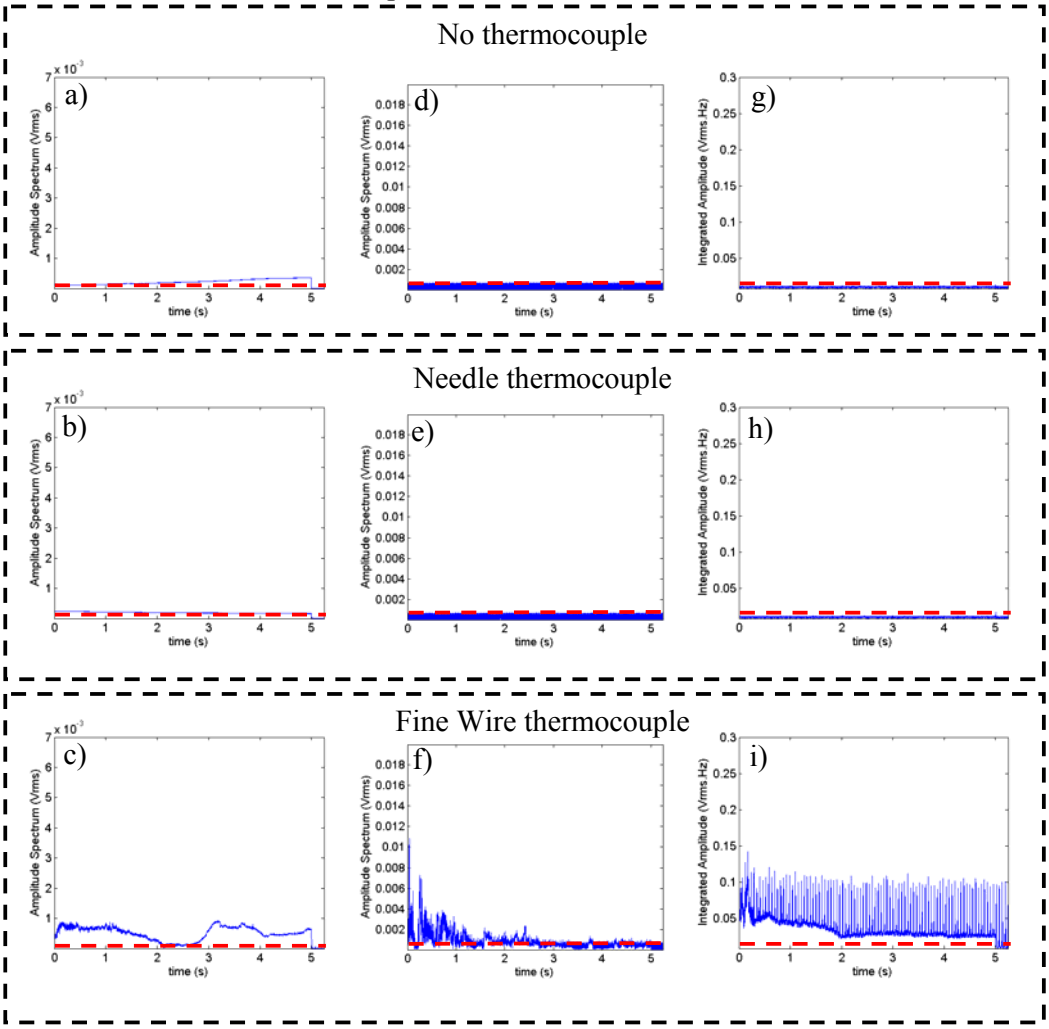

Figure 7.48. The detected fourth harmonic ((a)-(c)), half harmonic ((d)-(f)) and broadband emissions ((g)-(i)) for single 1000 W/cm^2 (1.13 MPa) exposures.

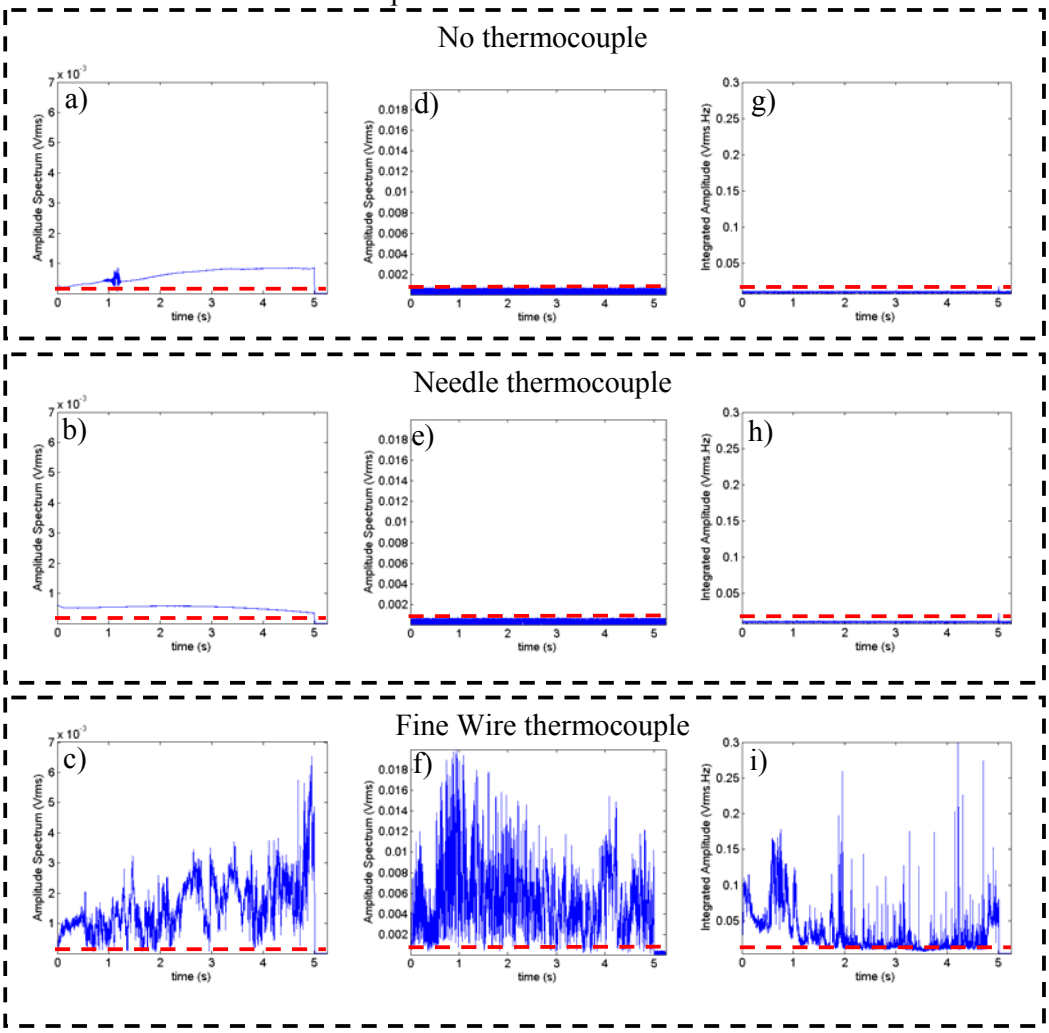

Figure 7.49. The detected fourth harmonic ((a)-(c)), half harmonic ((d)-(f)) and broadband emissions ((g)-(i)) for single 1550 W/cm^2 (1.34 MPa) exposures

The following figures show in detail the acoustic signals detected, temperature histories, power measurement, audio measurements and B-mode images for three separate 5 s 4580 W/cm^2 (2.02 MPa) exposures with (i) a needle, (ii) a fine wire and (iii) no thermocouple. This exposure is above the boiling threshold for ex-vivo bovine liver tissue in the absence of a thermocouple. Figure 7.50 shows the temperature histories of two separate exposures in ex-vivo bovine liver tissue at 4580 W/cm^2 (2.02 MPa) measured with a FWT and NT. Both show a decrease in temperature 1 s into the 5 s HIFU exposure.

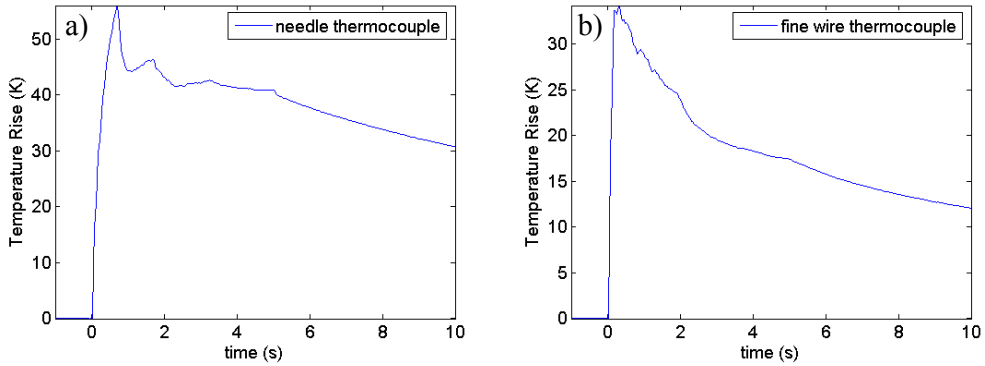

Figure 7.50. Two 5 s exposures in separate ex-vivo tissue samples at 4580 W/cm^2 (2.02 MPa) with (a) a needle thermocouple and (b) a fine wire thermocouple. Note the scale difference between the plots.

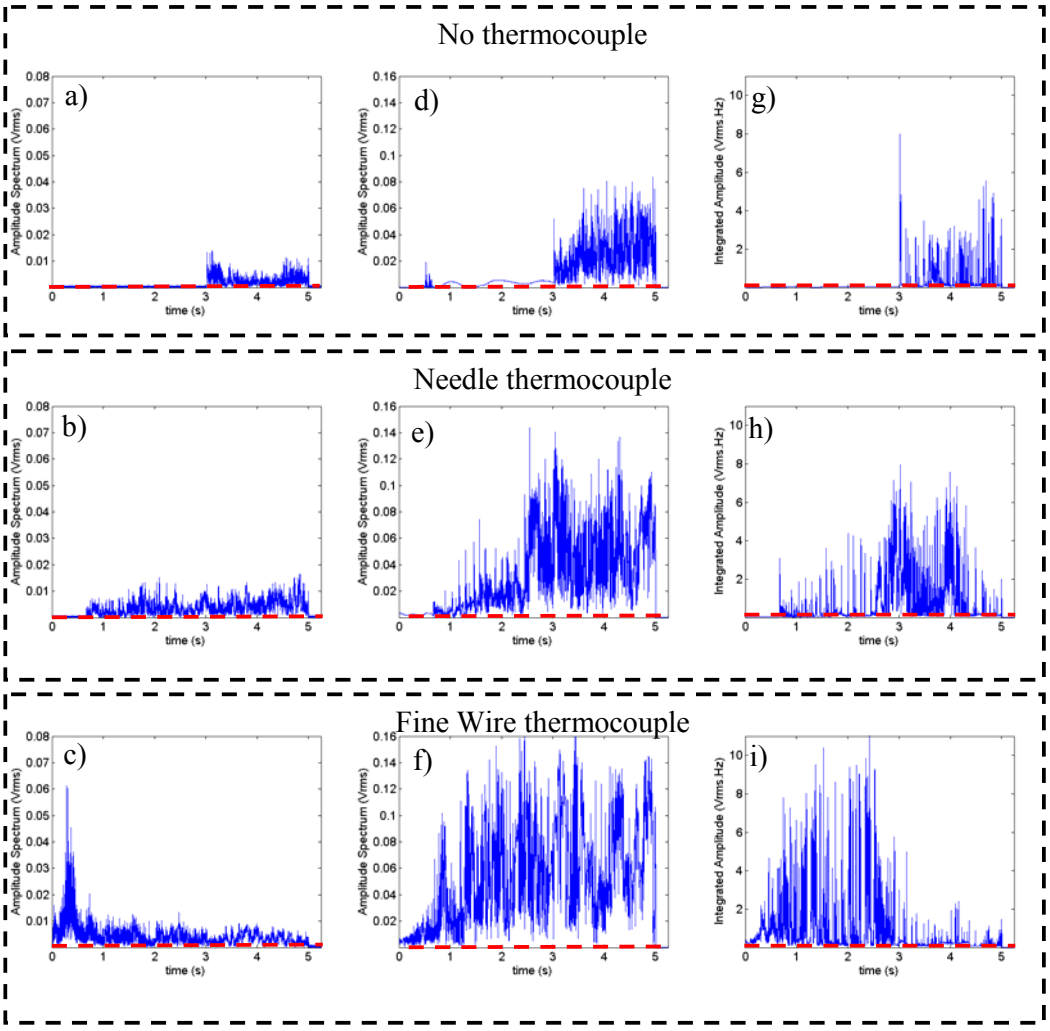

Figure 7.51. The detected fourth harmonic ((a)-(c)), half harmonic ((d)-(f)) and broadband emissions ((g)-(i)) for single 4580 W/cm^2 (2.02 MPa) exposures. Note the increased vertical scale compared with the acoustic spectra plotted in Figure 7.47 and Figure 7.49.

The data shown in Figure 7.51 are from three separate exposures in ex-vivo bovine liver tissue with and without thermocouples in place. The results show that in the absence of a thermocouple the acoustic emissions are seen to begin after 3 s. Acoustic emissions appear approximately 0.75 s into the exposure where the NT was in place. When the FWT is present, it is not possible to identify a time at which they began. Figure 7.52 shows the power measured during the three exposures.

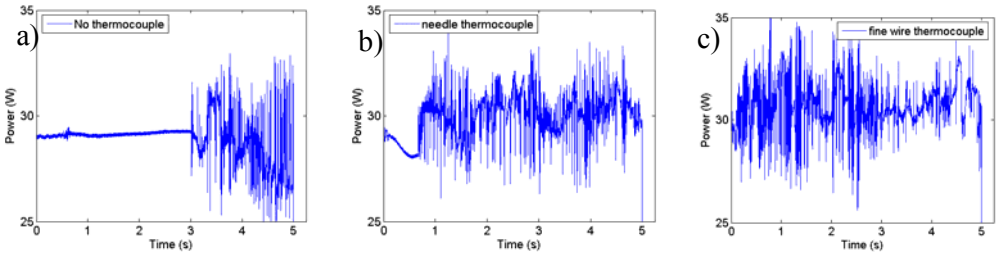

Figure 7.52. The measured drive power for the exposures in Figure 7.51, with the thermocouple types shown in the legends. Note that the vertical axis has been expanded around the average power measurement, 30 W.

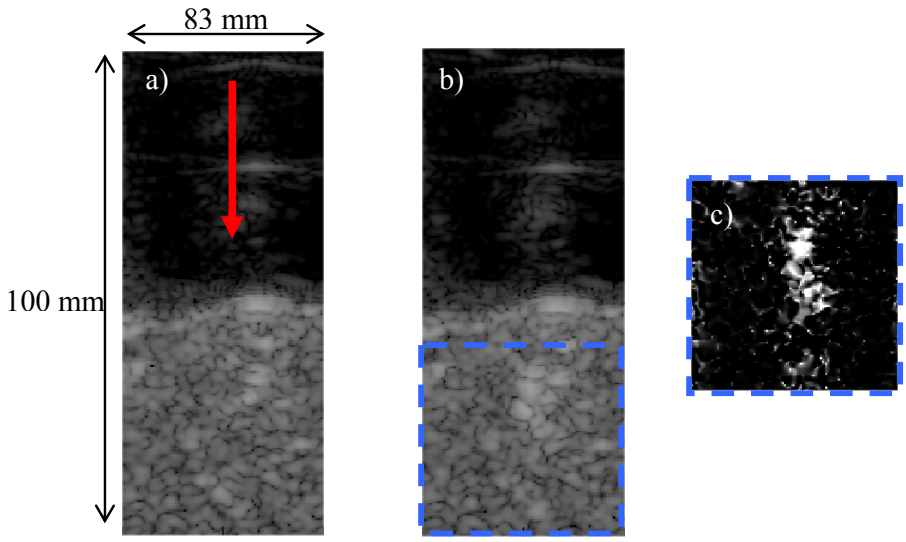

Figure 7.53. B-mode images acquired (a) before and (b) after (< 0.5 s) the 5 s exposure in ex-vivo tissue without a thermocouple. The B-mode images have been cropped to show the region of interest as the imaging depth with this transducer (Zonare C-5) was set at 180 mm. (c) shows a subtraction image of the region of interest depicted by the blue box in b). The red arrow indicates the direction of propagation of the HIFU field.

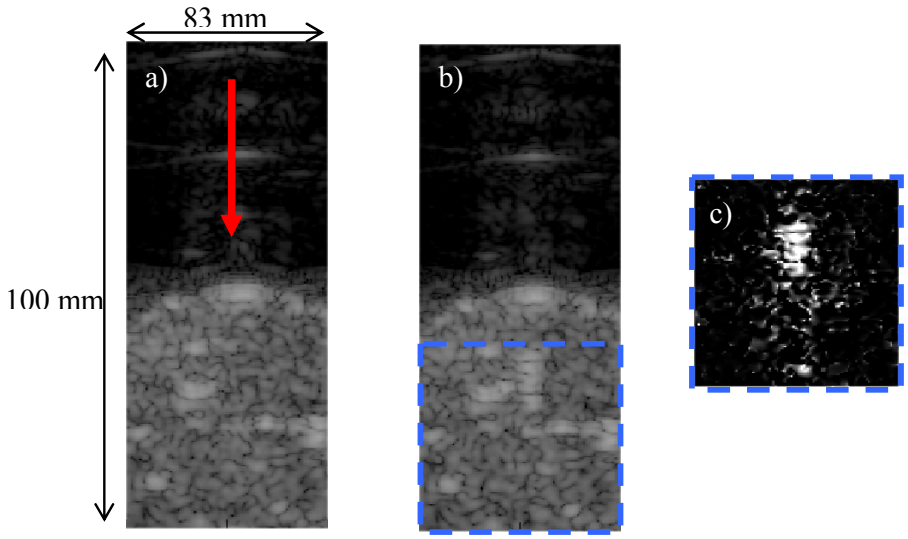

Figure 7.54. Two B-mode images acquired (a) before and (b) after the 5 s exposure in ex vivo tissue with the needle thermocouple (Figure 7.50(a)). (c) shows a subtraction image of the two frames shown in (a) and (b). The red arrow indicates the direction of propagation for the HIFU field.

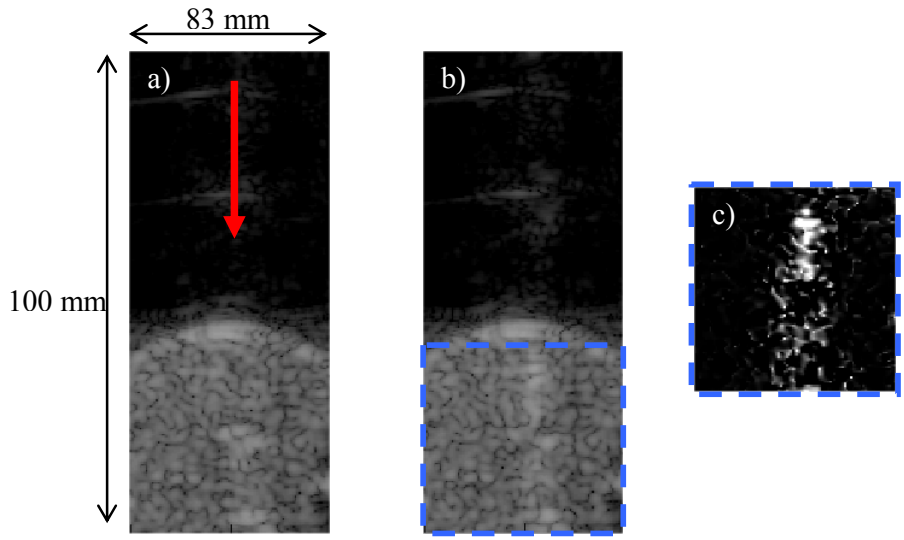

Figure 7.55. Two B-mode images acquired (a) before and (b) after the 5 s exposure in ex vivo tissue with the fine wire thermocouple (Figure 7.50(b)). (c) shows a subtraction image of the two frames shown in (a) and (b). The red arrow indicates the direction of propagation for the HIFU field.

Figure 7.53 to Figure 7.55 show B-mode images and subtraction images, for a smaller region of interest, for the three exposures with no thermocouple, a needle thermocouple and a fine wire thermocouple, respectively. Hyperechogenicity was observed in each of these three exposures. However, it is not as pronounced as previously when the L5-10 linear imaging probe was used, since these images were acquired along the acoustic axis and so viewed the focal region "end on".

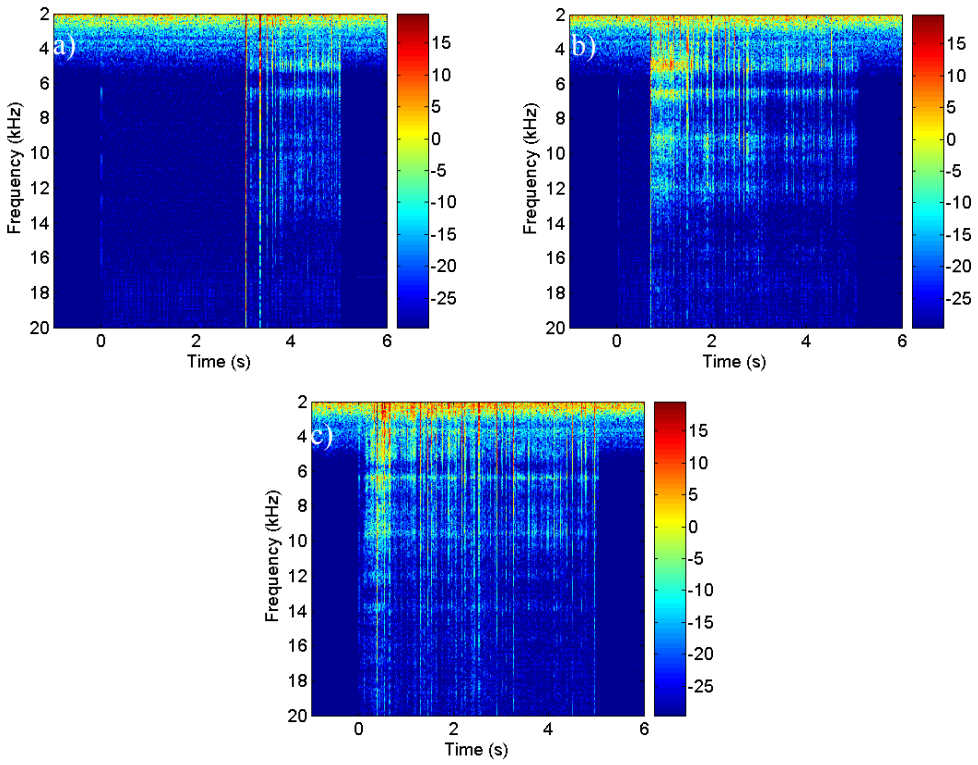

Figure 7.56. Audible (2-20 kHz) spectra acquired during exposure (a) without a thermocouple, (b) with a needle thermocouple and (c) with a fine wire thermocouple. The HIFU drive system used for these exposures did not use the timer box, and so the 3.5 kHz tone seen previously is absent (Figure 7.18).

Audible emissions can be seen for the three exposures shown in Figure 7.56. Note that the onset time for the audible emissions corresponds to the time at which acoustic emissions began for these exposures (Figure 7.51).

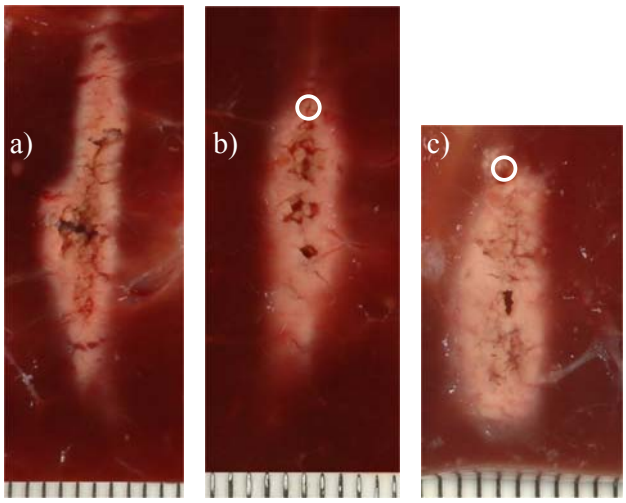

Figure 7.57. Photographs of the lesions generated from the 5 s 4580 W/cm^2 (2.02 MPa) exposures (a) without a thermocouple, (b) with a needle thermocouple and (c) with a fine wire thermocouple. markings on the rule shown in each photograph are 1 mm. This also indicates the surface of the tissue that was facing the HIFU transducer. The white circle shows the approximate location of the thermocouples, which were inserted parallel to the tissue surface. Note that the HIFU focal peak was localised on the thermocouple.

Figure 7.57 shows the lesions that were generated from the exposures described above. Due to the handling and dissection process it was not possible to preserve the location of the thermocouples for the photographs. 'Holes' related to the occurrence of boiling can be seen for each of these lesions. For this exposure level very little or no tissue damage can be seen 'behind' the thermocouple (relative to the direction of propagation of the HIFU field). The lesion generated with a FWT in place has grown closer to the surface of the tissue.

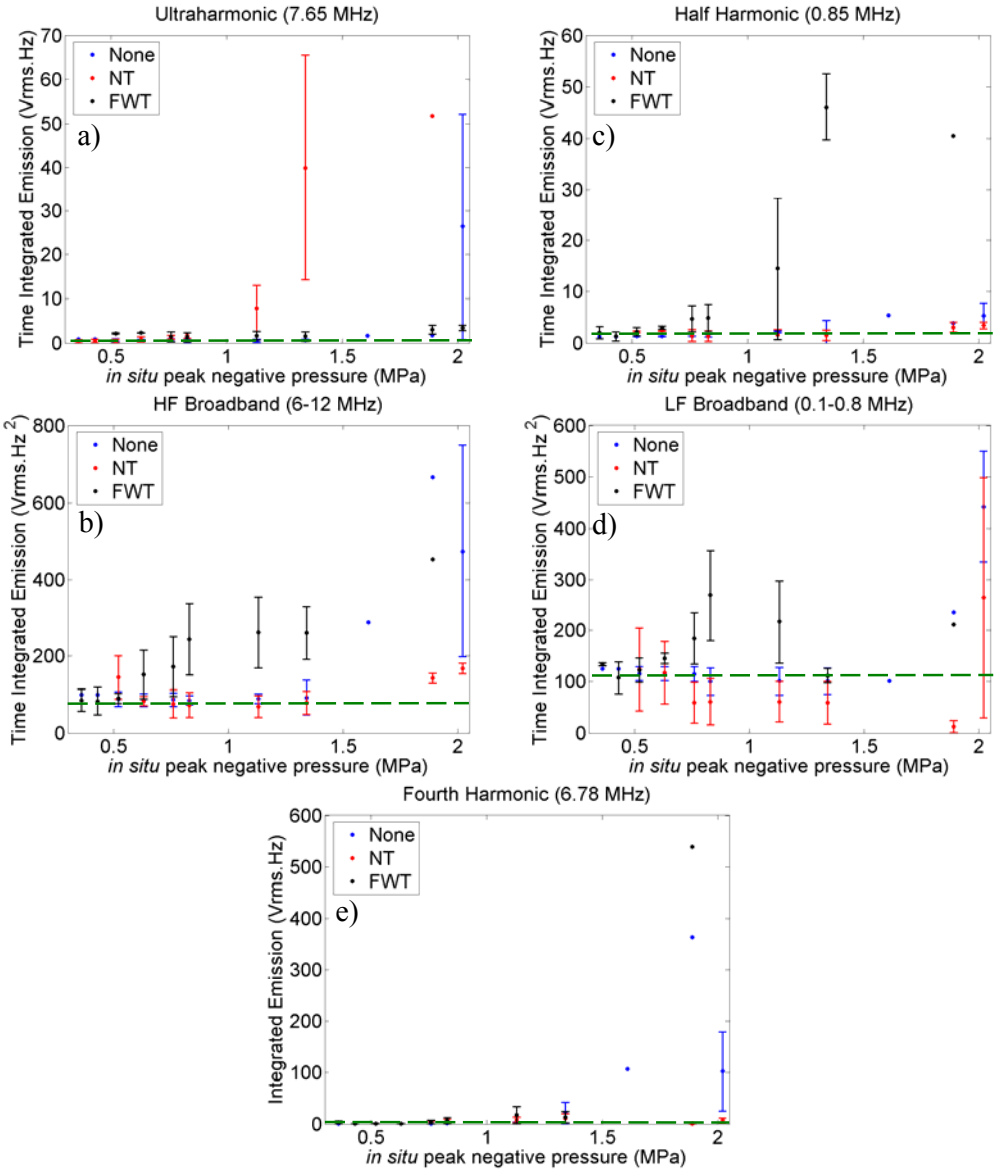

Figure 7.58. The averaged total time integrated (a) ultraharmonic (7.65 MHz), (b) HF broadband emissions (6-12 MHz), (c) LF broadband emissions (0.1-0.8 MHz), (d) half harmonic (0.85 MHz) and (e) fourth harmonic (6.78 MHz) shown over the range of peak negative pressures used, for no thermocouple (None), with a needle thermocouple (NT) and with a fine wire thermocouple (FWT). Uncertainty, where shown, is the standard deviation of the average value, for n =3-13. The green dashed line indicates the peak noise level measured from sham exposures.

Figure 7.58 shows the averaged total time integrated emissions for the acoustic spectra monitored with the 7.5 MHz frequency passive cavitation detection system during the 5 s exposures using the Imasonic HIFU transducer, in ex-vivo bovine liver tissue. This shows that the acoustic emissions are detected below the pressure thresholds, previously established for ex-vivo bovine liver tissue (Figure 7.27). The average amplitude of the

acoustic emissions detected when a NT was used, were below the noise level of the system, even when acoustic emissions were detected at these expsoure levels without any thermocouple.

7.4.2 Discussion

The combination of temperature monitoring with cavitation detection gave insight into how the introduction of needle and fine wire thermocouples into tissue can affect the acoustic cavitation threshold. Figure 7.45 shows temperature histories for six exposure levels, 110–1550 W/cm^2 ±25% (0.36 to 1.34 MPa ±22%), in the same ex-vivo tissue sample measured with a needle thermocouple. The peak temperature rise (Figure 7.45(f)) was 35 K (which gives a temperature at the end of the exposure measured by the needle thermocouple of 55^{o}C). However, the viscous heating artefact (Fry and Fry, 1954), overestimates temperature due to the HIFU field, and the thermal conduction along the wire reduces the temperature. Out of these for these short exposures the viscous heating artefact is the dominant factor affecting the peak temperature rise caused by a HIFU exposure. No lesion formed during any of these sets of exposures. All of the temperature histories show the typical heating and cooling curves expected from a 5 s exposure in ex-vivo tissue, including the artefacts in these types of temperature measurements. Figure 7.46 shows temperature histories measured using a fine wire thermocouple with the same exposure parameters. Acoustic cavitation activity occurred during the temperature measurements. Figure 7.46 curves (d), (e) and (f), and this could explain the source of the abnormalities in these measurements. Figure 7.47 curves (c), (f) and (i) show the acoustic spectra acquired during the temperature measurement in Figure 7.46(d). This temperature was lower than would have been expected from the trend shown at lower HIFU intensities of the same plot, and when using a needle thermocouple (Figure 7.45(d)). Broadband emissions (Figure 7.47(i)) are detected throughout this exposure, with a large increase between 0.5-1.0 s. During this period it is likely that acoustic cavitation shielded the thermocouple and thus gave a reduced temperature measurement. The bubble population has been discussed in section 7.2.3 in reference to the cause of acoustic scattering. It was concluded that the population was likely to be insufficient to cause the scatter detected. However, in this context it is be very likely that bubbles would have been generated on the surface of the thermocouple, and since it was approximately 50 μm in diameter a small number of resonant bubbles might be able to sufficiently shield the device causing the reduction in heating seen

here. The exposure in Figure 7.46(f) shows a shielding effect (temperature drop), which corresponds to the time at which there is a peak in the detected fourth harmonic (Figure 7.48(f)). This could have been due to increased scatter from the shielding bubbles. The highest exposure, shown in Figure 7.46(f), peaked at the same temperature as the equivalent exposure using a needle thermocouple (Figure 7.45(f)). However this temperature rise occurred in approximately 1.2 s, where as it took 5 s for the exposure using a needle thermocouple. The acoustic emissions (Figure 7.49(f) and (i)) show acoustic cavitation activity throughout the exposure. Peak emission activity was at approximately 1.2 s, which corresponded to the maximum temperature measurement. Cavitation may be due the imperfections, or to a crevice (§2.2, Figure 2.5) trapping a gas pocket on the surface of the fine wire thermocouple, that when exposed to a HIFU field, forms into an acoustic cavitation bubble and oscillates, causing frictional heating on the thermocouple junction. After this (>1.2 s) a potential shielding effect is seen (Figure 7.45(f)) due to acoustic cavitation in the absence of boiling.

The negative pressures (0.36 to 1.34 MPa) that generated the acoustic spectra shown in Figure 7.47 to Figure 7.49 are below the acoustic cavitation threshold for ex-vivo tissue (§7.2.2). However, the introduction of a fine wire thermocouple lowers the cavitation threshold, with acoustic emissions detected at a peak negative pressure of 0.52 MPa (Figure 7.58). This effect was not seen when using a needle thermocouple. This is most likely due to the construction of the device where the junction is set in a stainless steel cover, which would minimise the trapping of gas. That is needle thermocouples probably have fewer sites on their surface which can trap gas. Figure 7.46 highlights some of the problems caused by acoustic cavitation when trying to make temperature measurements using a fine wire thermocouple. Figure 7.50 curves (a) and (b) show temperature histories when needle and fine wire thermocouples were used during two separate 5 s 4580 W/cm^2 (2.02 MPa) exposures, (above the boiling threshold (§7.2.2) for ex-vivo tissue). Both temperature histories show shielding after approximately 0.75 and 0.1 s for the exposures using the needle and fine wire thermocouples, respectively. It is at both of these points that active (Figure 7.52(b) and (c)) and passive (Figure 7.56(b) and (c)) detection indicate the occurrence of boiling. This is supported by the observation of hyperechogenic regions (Figure 7.54 and Figure 7.55) after the HIFU exposures. The power fluctuations (Figure 7.52) for these exposures, and one without a thermocouple show that boiling occurs earlier in the exposure with the introduction of a thermocouple. This would suggest that the presence

of the thermocouple has an effect on the heating caused by the HIFU. This is shown in the comparison of the lesions generated without, and with a needle or fine wire thermocouple (Figure 7.57(a), (b) and (c), respectively). The lesion generated without a thermocouple (Figure 7.57(a)) was the longest and when either type of thermocouple was used, the majority of the resulting lesion formed pre-focally (i.e. in front of the thermocouple which was located at the focal peak). This suggests that the presence of a thermocouple interferes with the HIFU field causing the energy to be deposited in the pre-focal region.

Figure 7.58 shows that the presence of a fine wire thermocouple lowers the acoustic cavitation threshold, where as the presence of a needle thermocouple does not have an effect on the acoustic cavitation threshold. Therefore, it is not advisable to use FWT's in conjunction with cavitation threshold studies.

7.5 Conclusions

In tissue, audible emissions, drive power fluctuations and B mode imaging of the HIFU focal region appear to identify the occurrence of boiling bubbles effectively. For clinical applications, monitoring drive power fluctuations would probably be the easiest to implement. Monitoring of audible emissions in a clinical environment should be possible, but care would need to be taken in the interpretation of the audible emissions, particularly in the presence of a heartbeat from the patient. If the drive power fluctuations could be monitored in 'real time' it could give a direct indication, that boiling is occurring during the treatment, which could aid treatment planning. Furthermore, using these methods simultaneously it is possible to categorise lesion generation into three distinct types, and thus to specify the following cavitation thresholds: exposure levels at which no acoustic (ultrasonic or audible) emissions, or power fluctuations are detected during the 4 s exposures (cavitation free); exposures for which half harmonic emissions only are detected (i.e. non-inertial cavitation only); an exposure region in which broadband and half harmonic emissions are detected simultaneously during one exposure (i.e. inertial cavitation threshold) and finally exposure levels where audible emissions and power fluctuations are detected (i.e. boiling and acoustic cavitation). Thus lesions may involve (i) only thermal effects (those caused by absorptive HIFU heating), (ii) thermal effects and acoustic cavitation or (iii) thermal effects, acoustic cavitation and boiling bubbles.

In the in ex-vivo liver samples investigated here, it was possible to identify three pressure thresholds for these cavitation activities, that have been summarised in Table 7.1. It was observed in this study that boiling bubbles caused lesion growth towards the HIFU transducer. These lesions tended to have a 'tadpole' shape, where the tissue damage does not correspond to the location and shape of the full width half maxima of the HIFU focus. It was generally seen that the on-set of boiling caused an increase in the detected acoustic emissions. This suggested that the boiling events acted as a catalyst, causing the seeding of acoustic cavitation. The increase of cavitation activity could have resulted in a localised enhanced heating effect, which may have contributed to the shape distortion of the generated lesions when boiling occurred. However, no significant effect in the lesion shape was observed in the presence of acoustic cavitation alone. Only for lesions in which boiling occurred was it possible to identify hyperechogenic regions in B-mode images or subtracted B-mode images. The location of these regions of hyperechogenicity was where the lesion formed, but did not fully represent the lesioned area, and their size reduced with time. These regions coincided with areas of characteristic tissue destruction not associated with thermal denaturation of tissue i.e. millimetre sized holes,

In an effort to measure the peak temperature caused by HIFU exposures where boiling occurred it was first necessary to investigate any effect that locating a thermocouple at the focal peak might have on the cavitation threshold. It was found that the fine wire thermocouples (50 μm) used lowered the acoustic cavitation threshold (the lowest pressure at which acoustic emissions were detected was 0.43 MPa), but a needle thermocouple (200 μm) has no statistically significant effect on the acoustic cavitation threshold. However, when using both types of thermocouples the presence of cavitation could cause shielding effects pre-focally region, which added to the inaccuracies in the measurement of the tissue temperature with thermocouples. This effect meant that it was not possible to estimate the peak temperatures generated accurately when boiling was observed. However, the peak temperature measured by the needle thermocouple before the effects of shielding were obvious was 75^{o}C. The viscous heating artefact could mean that this temperature may be up to a 50% overestimation of the actual heating (Morris *et al*, 2008). Estimation of the actual temperature reached in this measurement was not possible.

The detection system used in this chapter was able to identify when acoustic cavitation (non-inertial and inertial) and boiling occurred during single 4 s exposures of ex-vivo bovine liver tissue. However increasing the temperature of the tissue (from 20 to 40^{o}C) caused the acoustic cavitation threshold to drop, as acoustic emissions were detected at I_{sp} = 340 W/cm^2 (1.11 MPa). At this stage, it is not clear whether this is due to more favourable conditions for the formation and activity of acoustic cavitation or the greater gas content in tissue due to an increase in the rate of autolysis. The system used a 'full spectra' approach to cavitation detection, however for clinical applications this system, and hence the amount of data required, could be streamlined. For example, if the onset of boiling was of key interest, then only one parameter, such as power fluctuation (or audible emissions, or super harmonics) might be monitored.

8 – An ex-vivo tissue study with extra-corporeal clinical HIFU systems

8.1 Introduction

This chapter investigates cavitation detection techniques suitable for use with current available clinical HIFU treatment systems, and compares the use of unfocused and focused passive cavitation detection systems. The JC extra-corporeal HIFU system (Chongqing HAIFU™ Technology Company Limited, Chongqing, P.R. China) is a commercially available ultrasound guided HIFU system that has been in clinical use in China since 1997 (Wu *et al*, 2004). This system was used in this study, and has been in clinical trials at the Churchill Hospital (Oxford, UK) since 2002 (Kennedy *et al*, 2004). Greyscale (echogenicity) changes in the B-mode images have been observed in clinical treatments (Wu *et al*, 2005) with this system.

The Terason 2000 ultrasound system (Teratech Corp., Burlington, MA) belonged to Boston University College of Engineering, where it had been demonstrated that it could be used for passive cavitation detection (Farny, 2007). Professor R. Roy and Dr. C. Farny were collaborators on this project. As discussed in section 3.3, most passive cavitation detection systems use a focused transducer because of the increased spatial sensitivity. In contrast, the Terason system comprises a diagnostic ultrasound transducer that can be operated passively (i.e. the output pulse voltage is set to 0 V), creating a detection system with the spatial coverage of a diagnostic ultrasound scan beam. The Terason software allows the acquisition of the beamformed RF signals from which the B-mode images are normally generated, even when the output is off. As this device was used in passive mode, the received signals were from signals resulting from the HIFU exposure. Spectral analysis could then be performed on this RF data as the probe was connected directly into the beamforming device, which was connected into a Laptop computer. The RF data was stored on this computer and converted, after the exposure, into a MatLab readable format using proprietary software, provided by the manufacturer. Previous extensive calibration and testing of this system (Farny, 2007), allowed optimum operating values to be used in this study. The primary aim was to assess the relative sensitivity of the focused and unfocused passive sensors to cavitation activity when used in conjunction with the Mauve HIFU transducer or the JC HIFU

system. In addition to this, it was possible to assess the cavitation activity that occurs during clinical HIFU treatments as these exposure conditions could be recreated in ex-vivo bovine liver tissue. This meant that it was also possible to investigate the hyperechogenicity observed during HIFU treatments (Wu *et al*, 2005) and to determine whether these could be correlated with lesion area. Track lesions were generated with the JC HIFU system, and emitted acoustic signals were monitored by the Terason system. It was therefore possible to investigate the ablation from these tracks in association with the detected acoustic spectra, in order to determine whether this activity has any observable effect on lesion generation.

8.2 Materials and Method

8.2.1 Single exposures using the Mauve Transducer

A 1.69 MHz focused bowl piezoceramic transducer (f-number 1.79, focal length 15 cm), which had been previously used in Phase I and II clinical trials at the Royal Marsden NHS Foundation Trust, was used in this study. The free-field spatial peak intensity and peak negative pressure were calibrated using the radiation force and hydrophone methods, described in section 5.3.1. The data acquisition, data processing and tissue preparation procedure were those described in sections 4.2.4 and 5.4. The Zonare ultrasound system (§4.3.1) was replaced for these studies with the Terason 2000 ultrasound system. A single focused 10 MHz passive transducer was connected to the data acquisition system (DAQ) described in section 4.2. The filtering and amplification used is show in Figure 8.1.

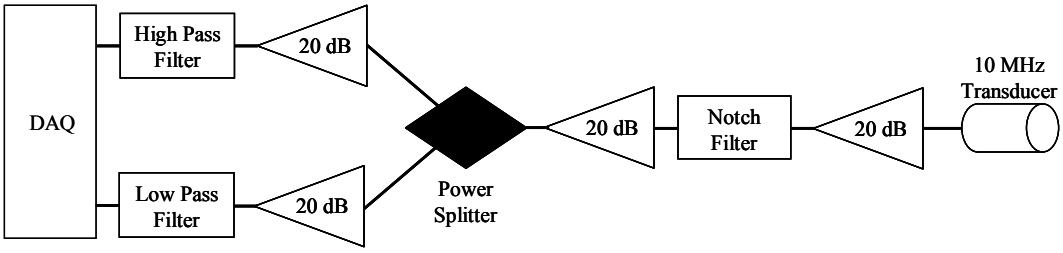

Figure 8.1. A schematic of the amplifcation and filtering used with the 10 MHz transducer.

A notch filter (NF), low pass (LP) filter and high pass (HP) filter (§4.2.2) were used to minimise RF pickup from the drive signal, and acoustic interference from the HIFU system. Four 20 dB preamplifiers were used with the 10 MHz passive transducer. The

power splitter was used to split the signal detected from the 10 MHz passive sensor into two. This allowed a replication of the detection techniques used with the dual passive cavitation detection system described in section 7.2.1.

The Terason scanner was aligned, using the 1 mm diameter ball bearing pulse-echo target (§5.1.3), along the acoustic axis and centred on the focal peak of the HIFU field in imaging mode. This configuration meant that the Terason was sensitive to acoustic emissions originating from ±10 mm of the focal peak. The frame rate of the Terason scanner was fixed at 15 Hz for use with the Mauve transducer.

Ex-vivo liver tissue was exposed over an in-situ I_{sp} (peak negative pressure) range of 310–1570 W/cm^2 (1.52 to 1.96 MPa) with a fixed 4 s exposure time. A total of 45 exposures were performed in different tissue samples taken from approximately 18 livers. These exposures meant that the Terason system was used to detected acoustic spectra from the different cavitation regimes discussed in section 7.2.3.

8.2.2 *JC extra-corporeal HIFU system*

This system used a 1.75 MHz HIFU transducer (f-number 0.81, focal length 12.2 cm), consisting of a 15 cm diameter plane piezo-electric disc with an aluminium alloy lens. A central 4.5 cm diameter hole allows a diagnostic ultrasound probe to be aligned co-axially with the HIFU field. 1-D HIFU tracks were made by switching the transducer on and translating it in a radial direction at constant speed. 1, 2 and 4 mm/s transducer speeds were used at each of five acoustic power settings, namely, 120, 170, 220, 270 and 330 W. The linear track length was fixed at 20 mm, but the treatment system performed two passes (the second in the reverse direction) over each targeted region. Thus, for example, a 20 mm track at a speed of 1 mm/s took 41 s to complete. The extra second, which was due to the 'turn around time' when the scanned track changed direction for the return pass over the targeted region, was present at each speed setting. The JC HIFU system (Figure 8.2) included a combined HIFU treatment and ultrasound imaging head mounted on a combination of three mechanical gantries (Figure 8.2) in a degassed water reservoir (Figure 8.2(e)) situated in the centre of the treatment table (Figure 8.2(d)). Next to the mechanical gantry there was a unit containing an amplifier and frequency generator (Figure 8.2(c)). This RF drive system was completely enclosed, but it allowed the deflection on meters labelled anode voltage and current to be read. This was the only information available to the user to monitor the power setting, but it was not possible to identify any power fluctuations (§7.2.1).

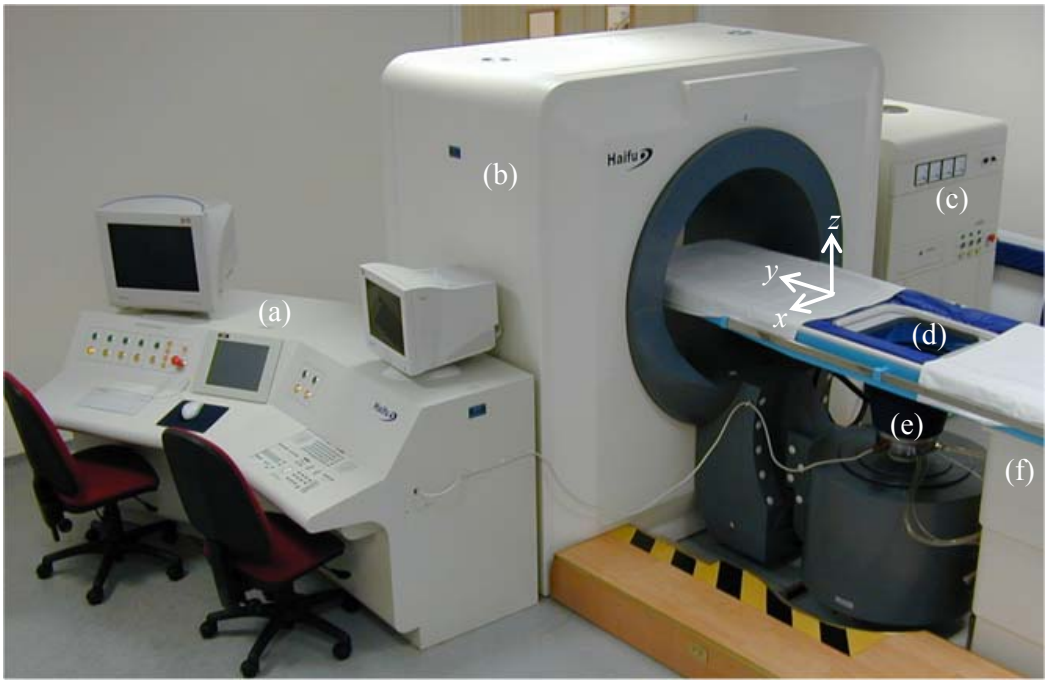

Figure 8.2. A photograph of the JC extra-corporeal HIFU system. (a) Operator console (left) diagnostic ultrasound imaging (right), (b) gantry housing, (c) RF drive system, (d) degassed water bath opening, (e) degassed water bath and transducer housing and (f) treatment bed. The three orthogonal axes indicate the translational degrees of freedom for the HIFU transducer, where *z* is the axial direction and *x* and *y* are radial directions.

All linear tracks were performed along the *x*-axis. The operator console was used to position the HIFU transducer and set the exposure conditions. It housed the diagnostic ultrasound system that was used to align the focal peak of the HIFU field with the alignment target, and acquire B-mode images before and after HIFU exposure. The focal depth in the ex-vivo tissue was fixed at 30 mm.

Passive cavitation detection was undertaken with both the 10 MHz passive transducer and the Terason ultrasound system. The signal processing and data analysis was performed using the techniques outlined in section 4.2. The DAQ system used was only able to record continuously for ~16 s, so for 1 and 2 mm/s track speeds it was only be able to record samples during the total exposure time. The DAQ system was manually triggered to start acquiring data at 0, 2, 3, 4 or 5 s into the HIFU exposure, with a precision of ~0.25 s. The Terason scanner could acquire data over the entire HIFU track length and exposure time at a frame rate of 8, 14 and 30 Hz for track speeds of 1, 2 and 4 mm/s, respectively. Spectral analysis of this data was performed using the

methods developed by Farny (2007). The resultant data gave spatial and temporal variations of the detected broadband emissions and the sum of the detected integer harmonic content. For ease of comparison between different exposure parameters, both of these quantities were integrated over the track length and exposure time to provide a 'Total time integrated' acoustic emission quantity.

A Perspex tank which could house the tissue sample, Terason probe and 10 MHz passive sensor was constructed to sit on top of the degassed water bath (Figure 8.3). The tank could be split into 3 sections using removable Perspex walls. Each removable wall had a 5x5 cm window with a Mylar membrane (~ 19 μm thickness) on one side to provide an acoustic imaging window. The wall were removable so that the alignment target could be used since the Mylar membranes would have restricted this.

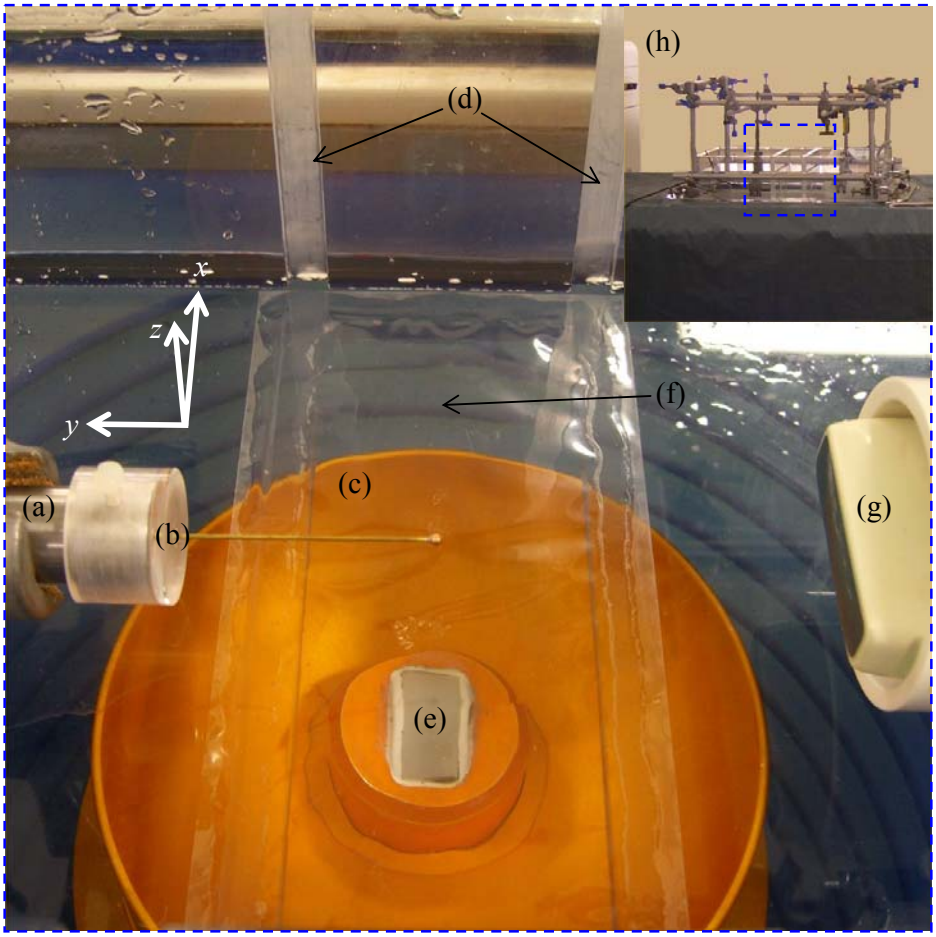

Figure 8.3. (a) the 10 MHz passive transducer, (b) the pulse-echo alignment target, (c) the HIFU transducer, (d) slots for removable walls, (e) diagnostic transducer, (f) a Mylar membrane, (g) Terason probe and (h) and insert showing the Perspex tank sitting on the degassed water bath in the treatment bed of the HIFU system.

When the removable walls were in place a central volume of 20 x 6 x 11 cm was created, into which the ex-vivo liver tissue was placed. As the tissue was cut 1 cm wider than the 6 cm separation, it meant that the compression from the walls held the tissue in place, but still allowed the tissue to be translated in the *x* direction. A second unused tissue sample was placed on top of the sample that was exposed to ensure its position did not shift during the exposure. The tank had an acoustic window (Figure 8.3(f)) to allow HIFU and diagnostic imaging of the sample, while avoiding liver and blood contamination of the degassed water bath built into the HIFU system. The pulse-echo target (Figure 8.3(b)) was designed to be at the focus of the 10 MHz passive transducer and was used to align it with the Terason scanner and the HIFU beam. All devices were aligned with a common point, the centre of the treatment track (0 mm). The focal peak of the HIFU beam was positioned on the alignment target by using the device's treatment planning software and the diagnostic imaging transducer. This was achieved since the planning software indicated the location of the HIFU focal peak, superimposed on the B-mode image, and the location of this focus could be shifted such that it aligned with the pulse-echo target. A precision of ±5 mm was achievable with this system. The Terason system was manually positioned such that it was centred on the track, but was be able to record emissions throughout the HIFU transducer's movement along the track.

B-mode images were acquired using the diagnostic ultrasound system built into the JC HIFU system before, and after, each HIFU exposure, the treatment software automatically switched this scanner off during the HIFU exposures (this could be seen from the lack of interference in the passive detection system). After the 1D-track had been created in the tissue, surface marker lesions were put approximately ± 10 mm from the track edges (*x* direction). The marker lesions aided dissection of the sample in approximately the same plane as the diagnostic imaging was acquired. Lesions were photographed using a digital camera mounted on a clamp stand. The area of the lesion and any greyscale change (echogenicity) was measured using boundary recognition software in the image processing toolbox in MatLab (The MathWorks, Inc. Natick, MA, USA).

The acoustic power output of the HIFU system was calibrated using radiation force techniques described by Kennedy (2004).

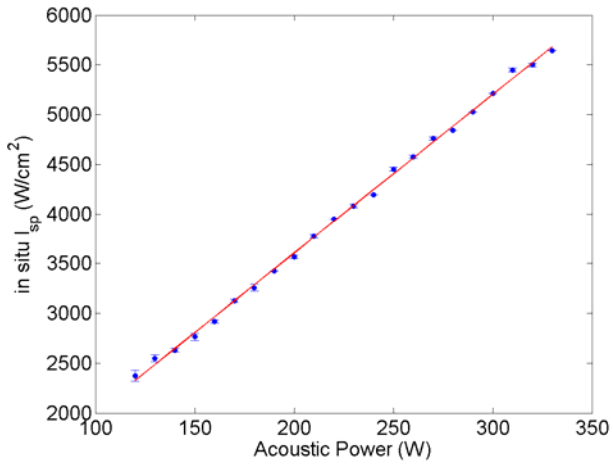

Figure 8.4. Comparison of the acoustic power and the corresponding I_{sp} values for these settings for the JC HIFU system. The uncertainty shown is the standard deviation of the averaged value from 3 measurements. The red line is a linear fit to the data.

Figure 8.4 shows the calculated in-situ I_{sp} values, from the measured free field values, for the corresponding acoustic power setting for the HIFU system. The device geometry meant that it was not possible to measure the peak negative pressure using the methods described in section 5.3.1. Using the relationship (Hill, 2004):

$$I_{sp} = \frac{p_{pp}^2}{2\rho c}, \tag{8.1}$$

where ρ = 1000 kg/m^3, water density, c = 1480 m/s, the sound speed in water and p_{pp} is the in-situ peak to peak pressure free field I_{sp} could be obtained. Rearranging equation (8.1) to find the in-situ peak to peak pressure yields the values shown in Table 8.1.

Acoustic Power (W)	in-situ I_{sp} (W/cm^2)	in-situ peak to peak pressure (MPa)
120	2380	8.40
170	3140	9.63
220	3940	10.80
270	4750	11.86
330	5640	12.92

Table 8.1. Calibration of the acoustic power settings, measured in-situ I_{sp} and the calculated in-situ peak to peak pressure values.

Without any knowledge of the linearity of the HIFU transducer used, it is not possible to disassociate the peak negative pressure value from the calculated peak to peak pressure values shown in Table 8.1, but they are likely to be lower. For example a peak positive pressure of 11.49 MPa with the Mauve transducer (§5.1.2), relates to a peak negative pressure of 2.34 MPa.

8.3 Results

8.3.1 Single exposures using the Mauve Transducer

The aim of the single exposures was to compare the use of the Terason diagnostic ultrasound scanner (detailed in §8.2.1) with the 10 MHz passive cavitation detection system (§8.2.2) using a HIFU system that had been extensively characterised with ex-vivo tissue. Figures 8.5 to 8.10 show the detected acoustic emissions for three I_{sp} (peak negative pressure) values, lying in the three exposure regimes of: non-inertial cavitation, inertial cavitation and boiling for single 4 s exposures.

Data acquired from the 10 MHz passive cavitation detection system shows the detected fourth (6.77 MHz) and half (0.846 MHz) harmonics, high frequency broadband emissions (4-12 MHz) and measured electrical drive power for these three exposure intensities of 310, 860 and 1210 W/cm^2 (1.52, 1.82 and 1.94 MPa). Figure 8.5 shows the data recorded during a 4 s exposure in ex-vivo tissue for an in-situ I_{sp} = 310 W/cm^2 (1.52 MPa) in which a lesion was formed with non-inertial cavitation activity only.

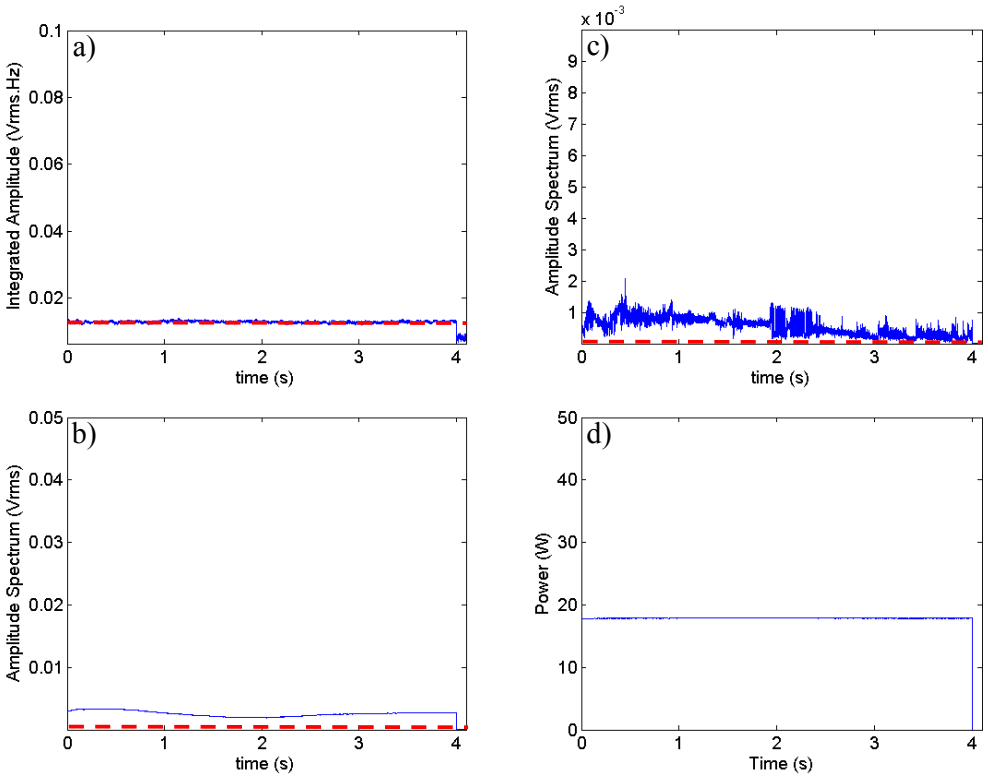

Figure 8.5. The (a) broadband emissions, (b) detected fourth harmonic, (c) half harmonic emissions and (d) measured electrical HIFU drive power for a 4 s exposure with I_{sp} = 310 W/cm^2 (1.52 MPa). The red dashed line indicates the peak noise level measured from a sham exposure.

The half harmonic is the only acoustic emission detected above noise levels during this exposure. Fourth harmonic signals were detected, which were thought to be due to scattering of the non-linear components of the HIFU drive field. The drive power was constant throughout the exposure. Figure 8.6 shows that no emissions were detected using the Terason ultrasound system in passive cavitation detection mode.

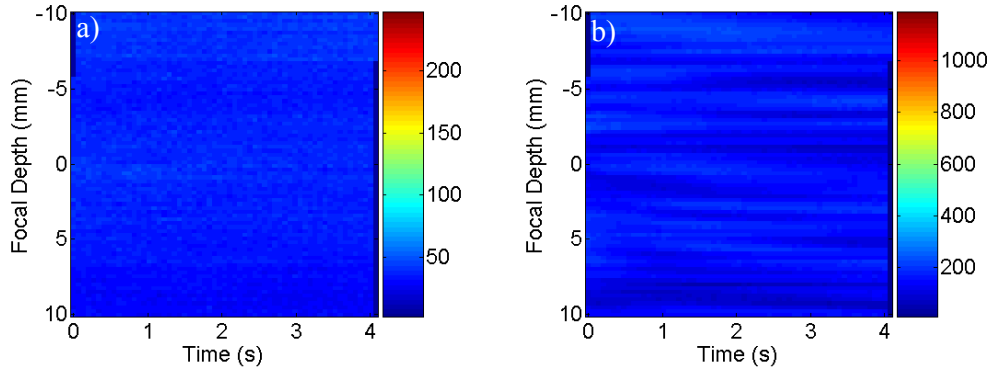

Figure 8.6. The (a) integrated broadband emissions and (b) integrated harmonics ±10 mm from the HIFU focal peak (located at 0 mm) for the exposure described in Figure 8.5 acquired using the Terason system. Note the difference in the colour scales (units of Vrms.Hz).

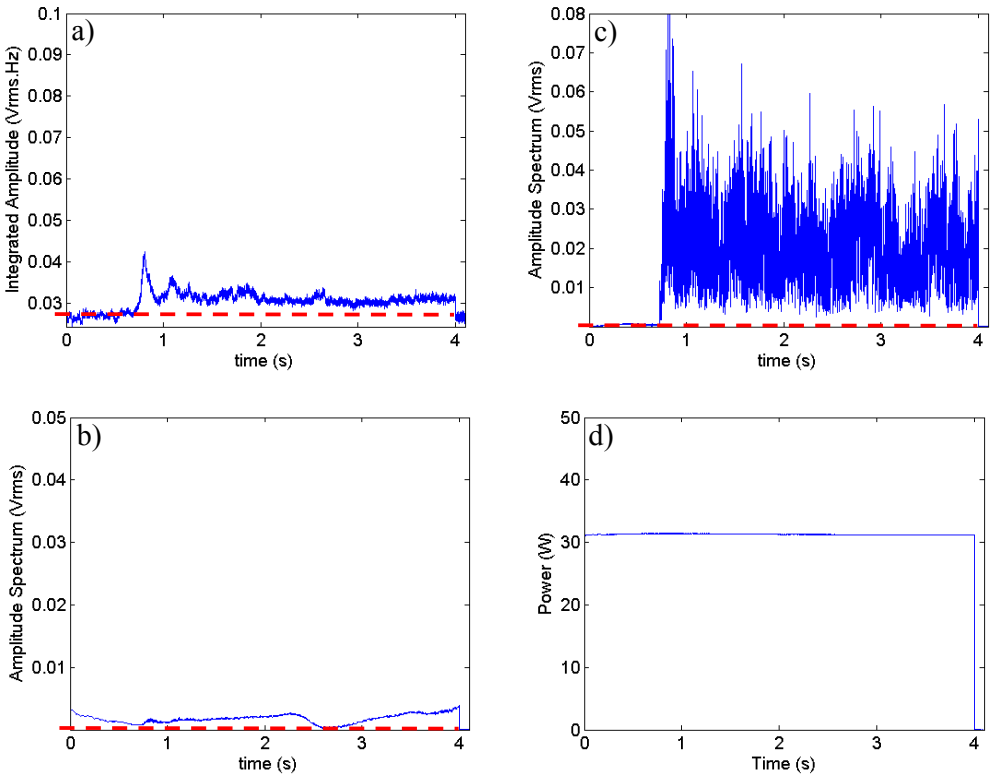

Figure 8.7. The (a) detected broadband emissions, (b) fourth harmonic, (c) half harmonic emissions and (d) measured drive power for a 4 s exposure with I_{sp} = 860 W/cm^2 (1.82 MPa). The red dashed line indicates the peak noise level measured from a sham exposure.

Figure 8.7 shows that half harmonic and broadband emissions occurred during this 4 s exposure at 860 W/cm^2 (1.82 MPa). Figure 8.8(b) shows an increase in the detected harmonics which is mostly located at the focal peak of the HIFU field (0 mm). Figure 8.8(a) shows no broadband emissions are detected above noise.

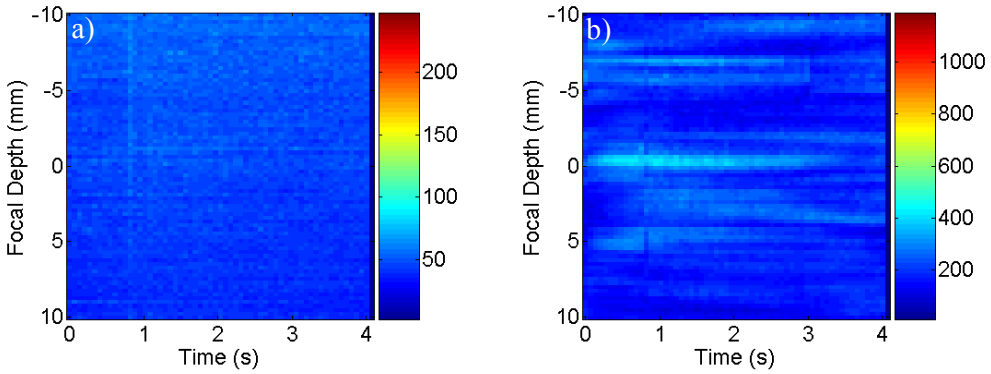

Figure 8.8. The (a) integrated broadband emissions and (b) integrated harmonics ±10 mm from the HIFU focal peak (located at 0 mm) for the exposure describes in Figure 8.7. Note that the colour scales have been set to be equal to equivalent measurements at different intensities. The colour scale has the linear units of rms.Hz.

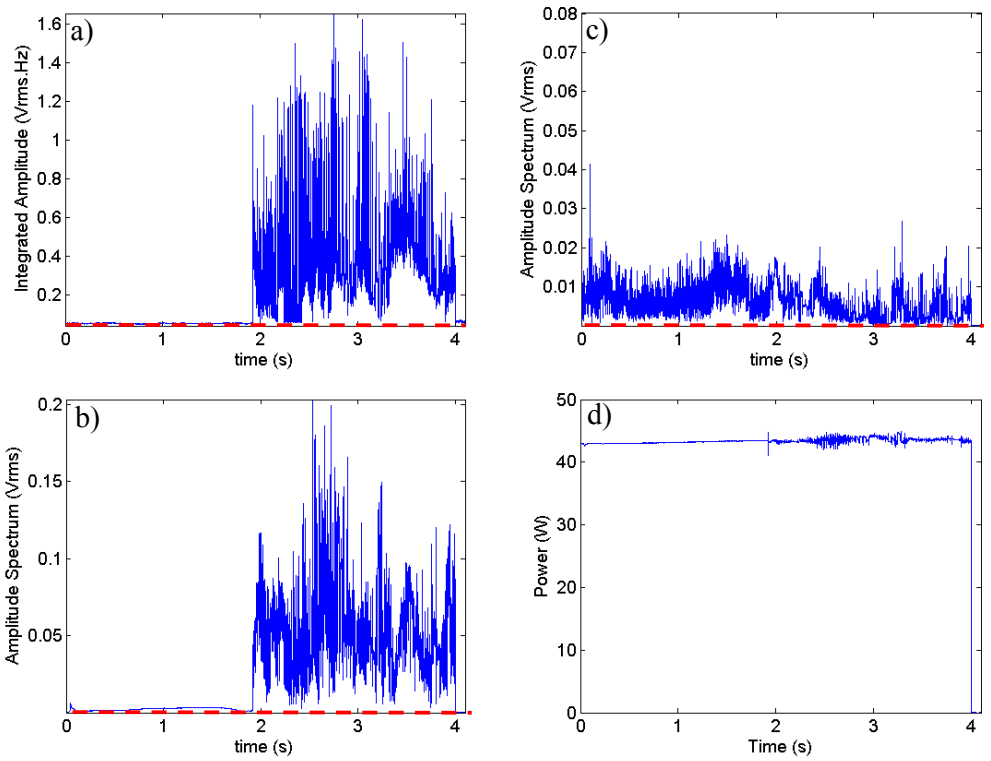

Figure 8.9. The (a) broadband emissions, (b) fourth harmonic, (c) half harmonic emissions and (d) measured drive power for a 4 s exposure with I_{sp} = 1210 W/cm^2 (1.94 MPa). The red dashed line indicates the peak noise level measured from a sham exposure.

Figure 8.9 shows that the increase in the broadband emissions and fourth harmonic correspond to the time at which power fluctuations are seen (after approximately 1.9 s) for the 1210 W/cm^2 (1.94 MPa) exposure. The half harmonic emissions fluctuate

throughout the entire exposure, but the peak value is lower than that seen at 860 W/cm^2 (1.82 MPa) (Figure 8.7(d)).

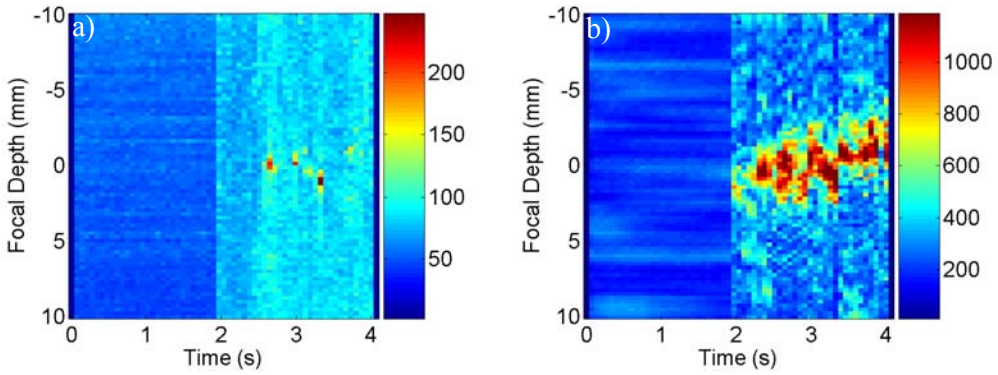

Figure 8.10. The (a) integrated broadband emissions and (b) integrated harmonics ±10 mm from the HIFU focal peak (located at 0 mm) for the exposure described in Figure 8.9. Note that the colour scales have been set to be equal to equivalent measurements at different intensities. The colour scale has the linear units of rms.Hz.

Figure 8.10 shows an increase in the broadband emissions and harmonics detected by the Terason at the same time as those observed with the focused detector in Figure 8.9(a) and (c). The figures shown above are typical examples of the acoustic emissions, detected harmonics and the measured drive powers seen for the three exposures in each of the cavitation regimes, discussed in section 7.2.3. It was found that half harmonic emissions occurred at peak negative pressures above 1.52 MPa ±17%, broadband and half harmonic emissions at peak negative pressures above 1.77 MPa ±17% and boiling occurred above 1.86 MPa ±17% for single 4 s exposures.

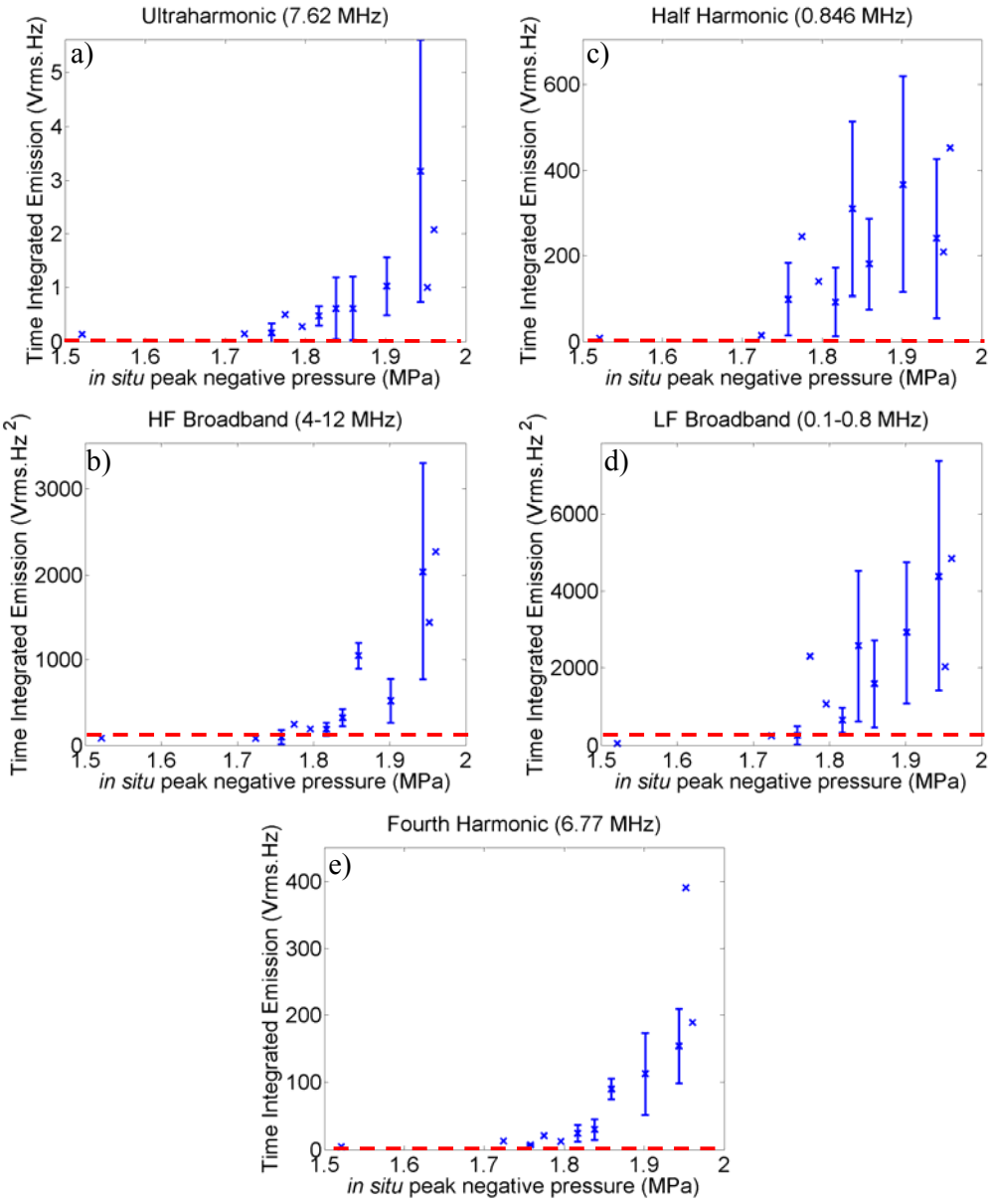

Figure 8.11. The averaged total time integrated (a) ultraharmonic, (b) half harmonic, (c) high frequency broadband emissions, (d) low frequency broadband emissions and (e) fourth harmonic. Uncertainty, where shown, is the standard deviation n = 3-9. The red dashed line indicates the average peak noise level measured from sham exposures.

Figure 8.11(a) and (c) show the time integrated ultraharmonic and half harmonic emissions for the range of peak negative pressures used in this investigation. It shows the ultraharmonic and half harmonic emissions were detected at peak negative pressures above 1.52 MPa. Figure 8.11(b) and (d) show the averaged time integrated broadband emissions over the range of peak negative pressures used in this investigation with the mauve transducer. It shows that broadband emissions are detected above the noise for

peak negative pressures greater than 1.77 MPa. Figure 8.11(e) shows the time integrated fourth harmonic signal detected by the 10 MHz passive cavitation detection system. Figure 8.12 shows the measured lesion area for the intensity range 790-1570 W/cm^2 (1.77 to 1.96 MPa).

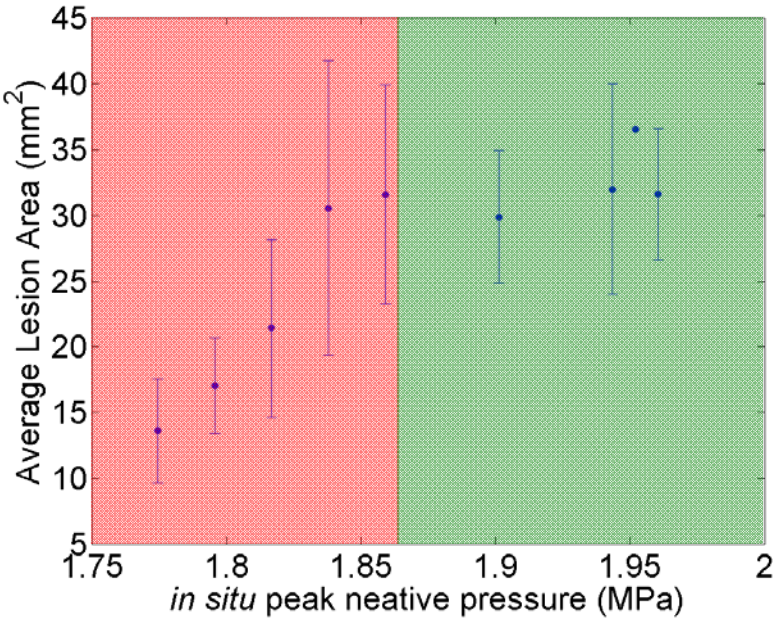

Figure 8.12. The averaged measured lesion area for the range of peak negative pressures that generated a lesion during a 4 s exposure. Uncertainty shown is the standard deviation of the average value, for n = 3-9 repeated measurements. The two colours are used to approximately describe the cavitation regimes, of non-inertial and inertial cavitation (red) and acoustic cavitation and boiling (green).

8.3.2 JC extra-corporeal HIFU system

All the exposures described in this section were 20 mm linear tracks, made at speeds of 1, 2 and 4 mm/s and acoustic power levels of 120, 170, 220, 270 and 330 W in liver. Figure 8.13 and Figure 8.14 shows examples of the acoustic spectra detected at the 1 mm/s track speed for each acoustic power level, detected using the Terason (Figure 8.13) and 10 MHz passive sensor cavitation detection systems (Figure 8.14). The 10 MHz passive system was only able to acquire continuously for 16 s thus the spectra shown in Figure 8.14 represent only a section of the total exposure. At this speed the total exposure time was 41 s, where the 'turn around' occurred at 21 s. The 'V' shape seen in the acoustic spectra detected with the Terason system is due to the shifting focal position in time. The 10 MHz passive sensor was aligned with the 0 mm point in these plots. Figure 8.14 shows that half harmonic emissions were detected at all drive powers at this track speed. A peak can be seen in the broadband and harmonic signals detected at approximately 13 s at the acoustic drive power of 330 W for both the detection systems.

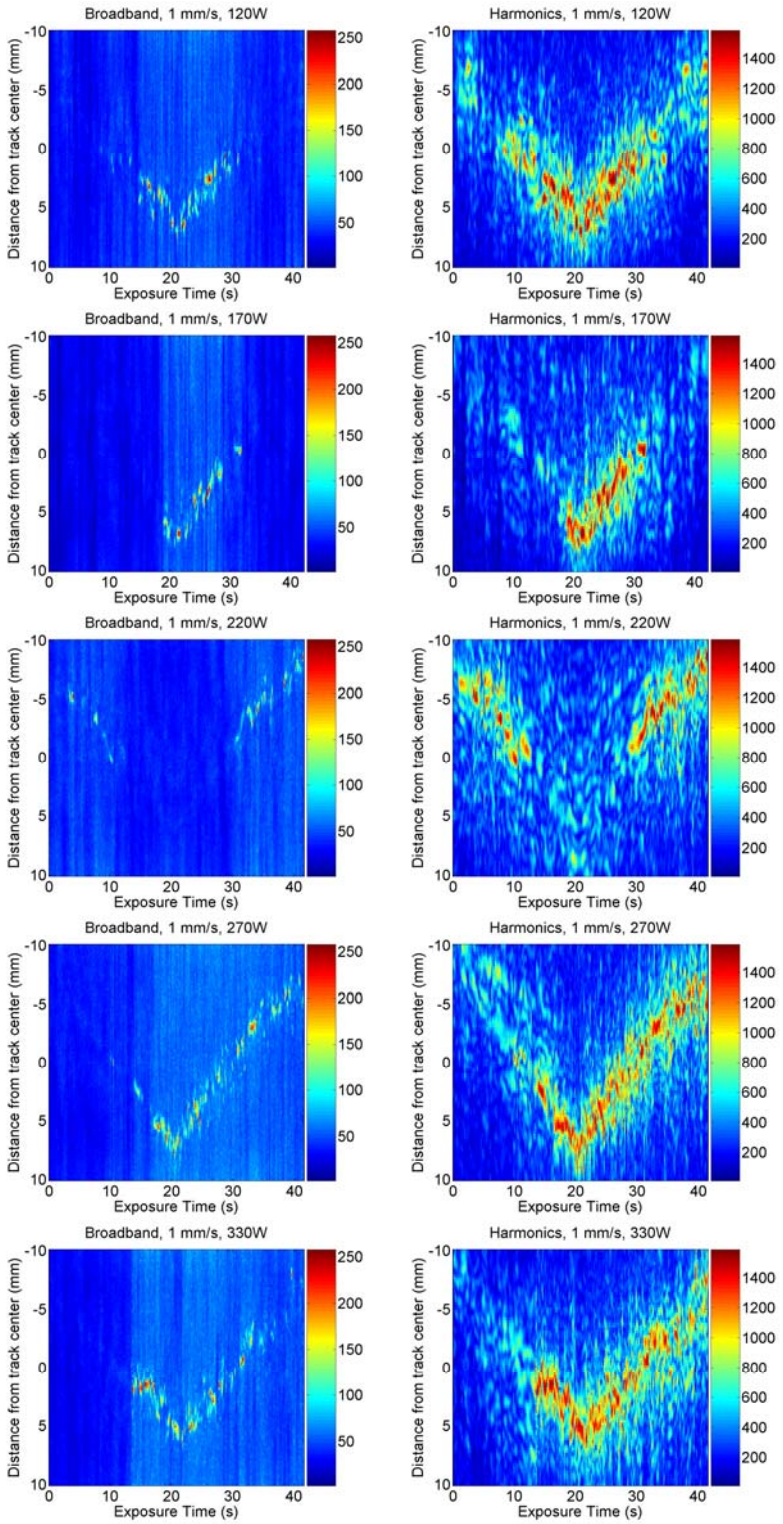

Figure 8.13. The (left) integrated broadband emissions and (right) integrated harmonics detected using the Terason during the 1 mm/s track speed exposures at 120, 170, 220, 270 and 330 W acoustic power levels. The colour scale has the units of rms.Hz. The start of the track is located at -10 mm and the 10 MHz passive cavitation detection system is aligned with the centre of the track (0 mm).

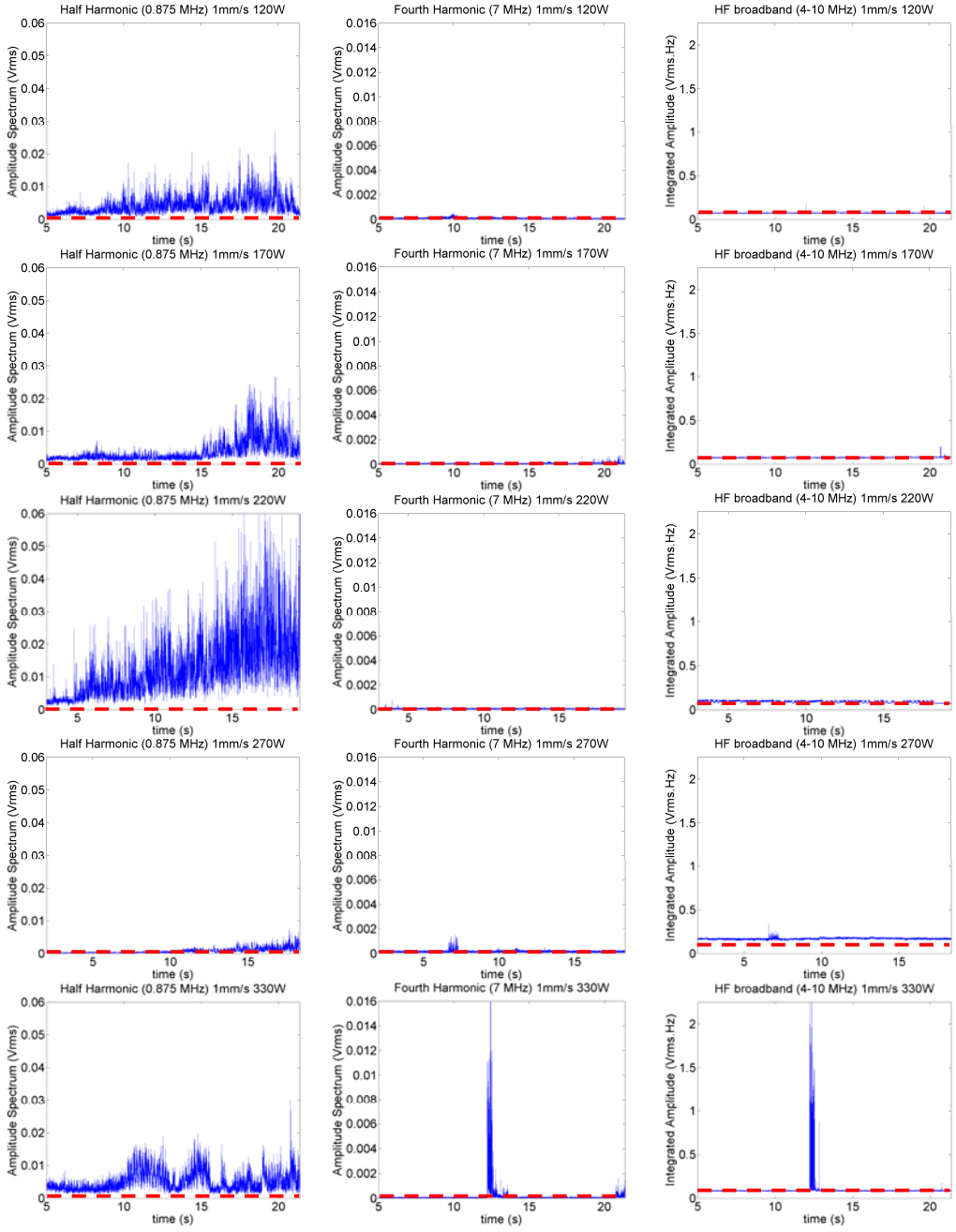

Figure 8.14. The (left) half harmonic emissions (middle) fourth harmonic, (right) broadband emissions using 10 MHz focused sensor from a track speed of 1 mm/s at 120, 170, 220, 270 and 330 W acoustic power. The dashed red line indicates the peak noise level measured from a sham exposure.

Figure 8.15 and Figure 8.16 show the detected spectra using the Terason and 10 MHz passive detection systems, for a 2 mm/s track speed at all acoustic drive powers.

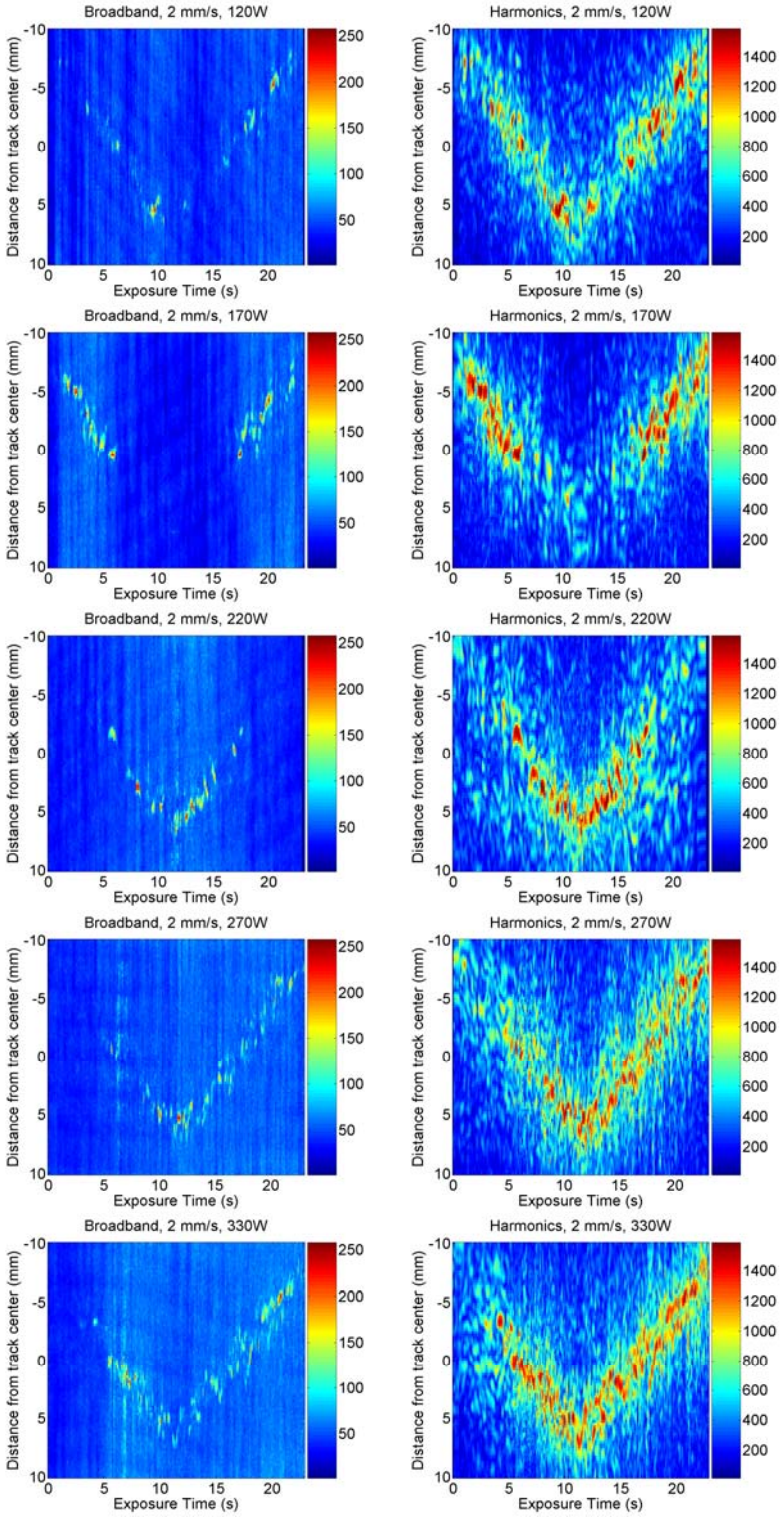

Figure 8.15. The (left) integrated broadband emissions and (right) integrated harmonics detected using the Terason during the 2 mm/s track speed exposures at 120, 170, 220, 270 and 330 W acoustic power levels. The colour scale has the units of rms.Hz. The start of the track is located at -10 mm and the 10 MHz passive cavitation detection system is aligned with the centre of the track (0 mm).

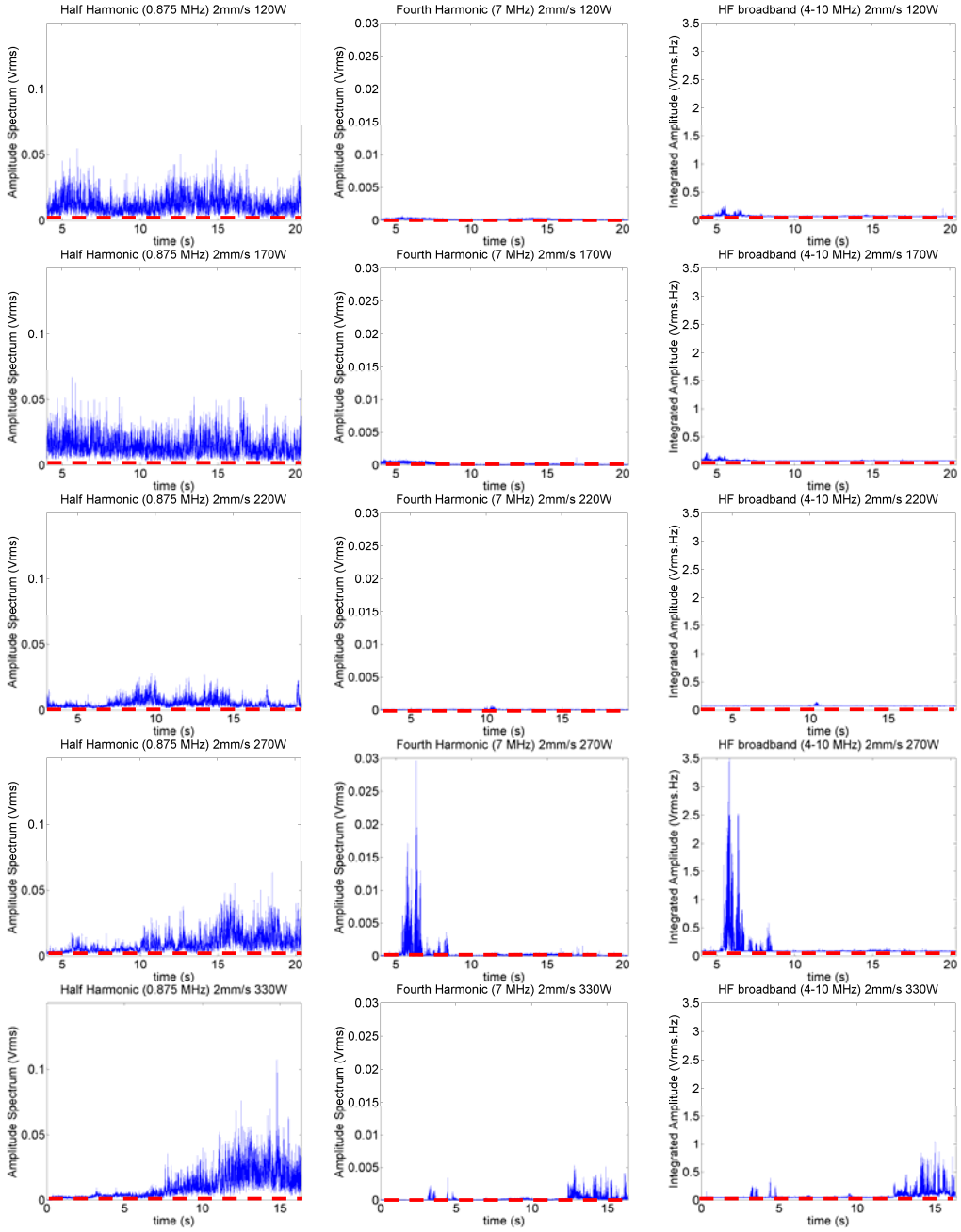

Figure 8.16. The (left), half harmonic emissions (middle) fourth harmonic, (right) broadband emissions using 10 MHz focused sensor with a track speed of 2 mm/s at 120, 170, 220, 270 and 330 W acoustic power. The dashed red line indicates the peak noise level measured from a sham exposure.

The left hand column in Figure 8.16 shows that half harmonic emissions were detected by the 10 MHz detection system at all acoustic drive power levels. The peaks in the broadband emissions and fourth harmonics correspond to the time points at which the HIFU focal peak crossed the focal region of the 10 MHz sensor (5 and 16 s).

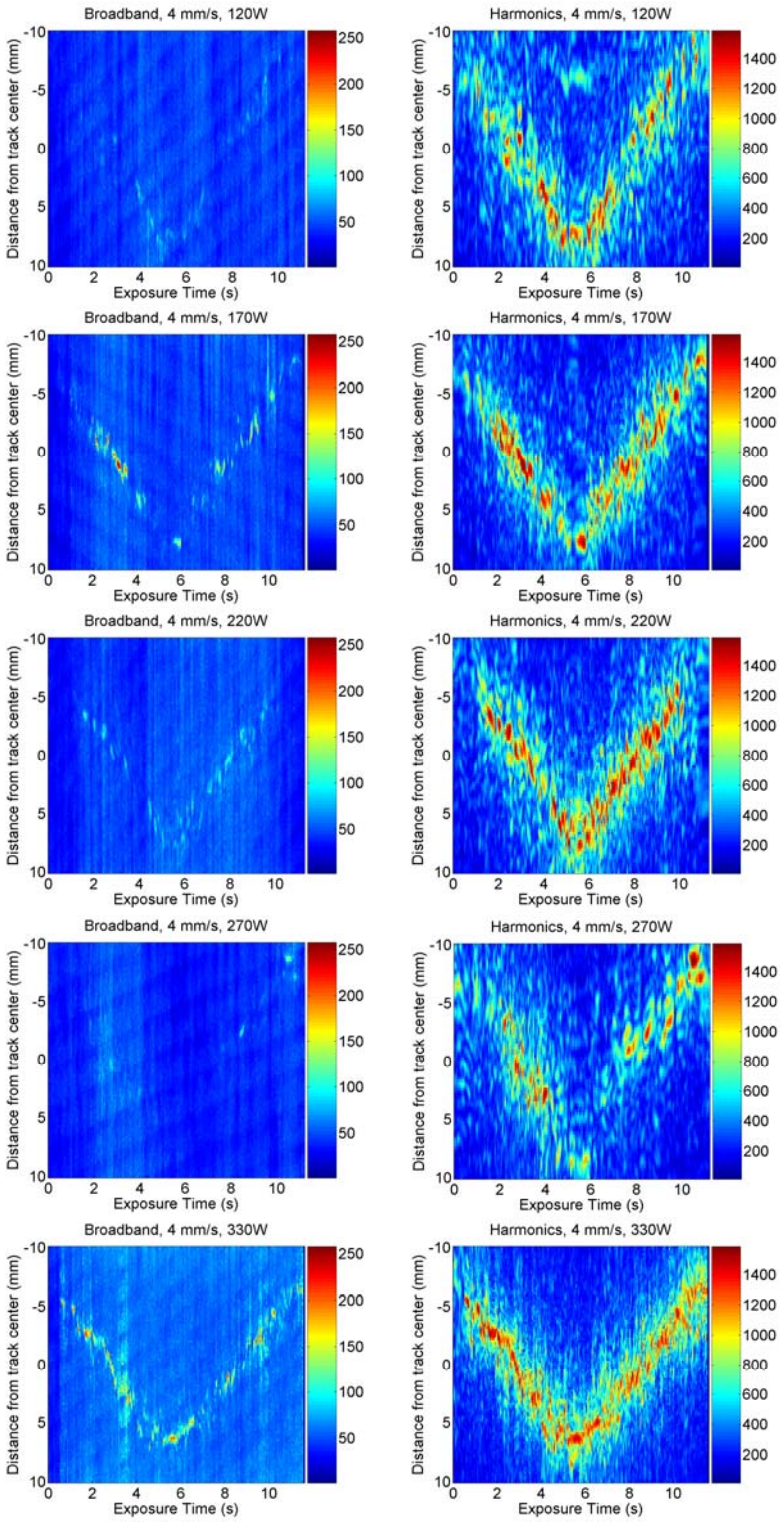

Figure 8.17. The (left) integrated broadband emissions and (right) integrated harmonics detected using the Terason during the 4 mm/s track speed exposures at 120, 170, 220, 270 and 330 W acoustic power levels. The colour scale has the units of rms.Hz. The start of the track is located at -10 mm and the 10 MHz passive cavitation detection system is aligned with the centre of the track (0 mm).

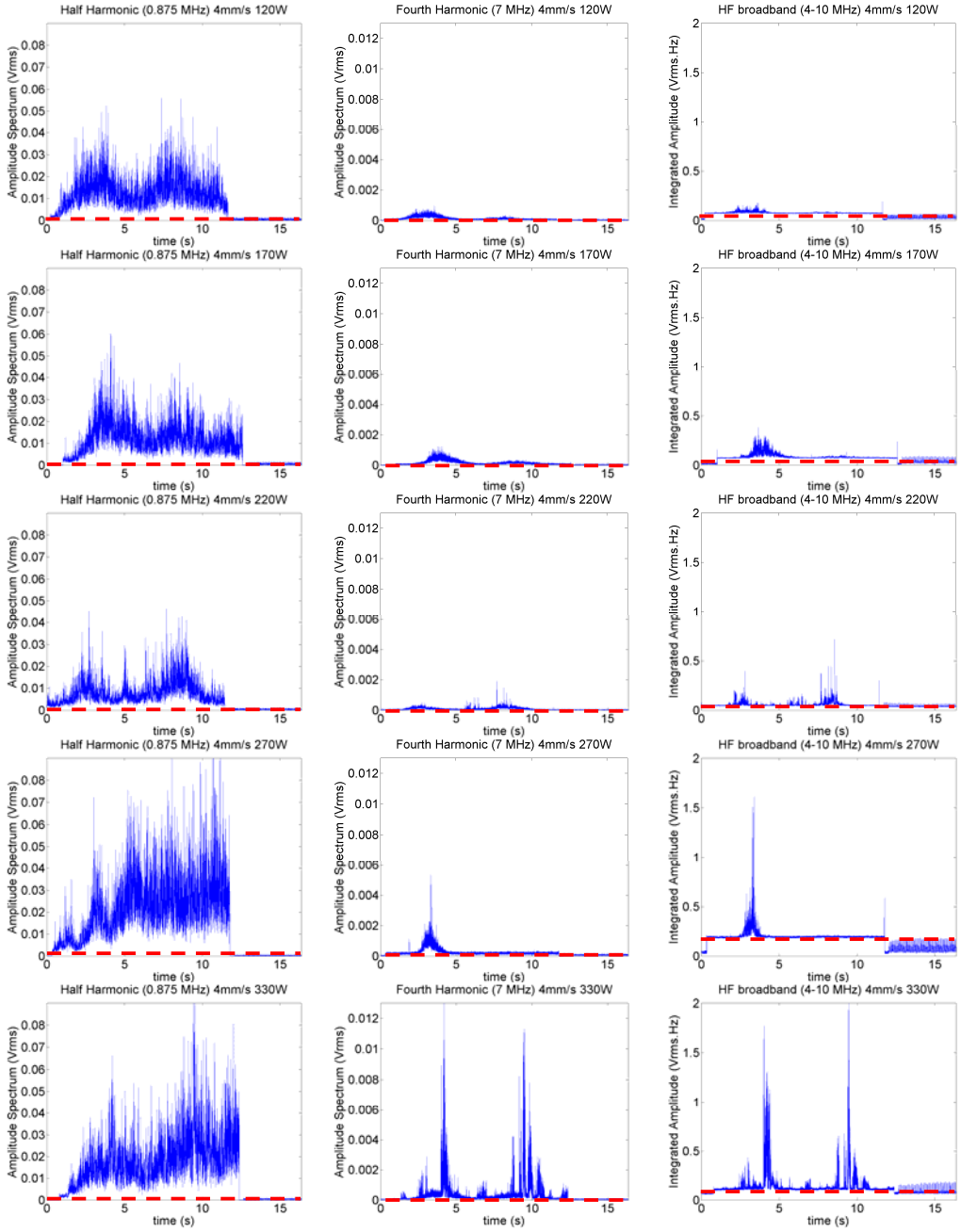

Figure 8.18. The (left), half harmonic emissions (middle) fourth harmonic, (right) broadband emissions using 10 MHz focused sensor with a track speed of 4 mm/s at 120, 170, 220, 270 and 330 W acoustic power. The dashed red line indicates the peak noise level measured from a sham exposure.

Figure 8.17 shows that harmonics are detected by the Terason system for the duration of the exposure, and are maximum at the focal peak. Broadband emissions were detected throughout the 11 s exposure at the acoustic drive power level of 330 W. For exposures at a track speed of 4 mm/s the 10 MHz passive detection system was able to record for the complete duration of the exposures. Peaks in the broadband emissions and fourth

harmonic can be seen at the times at which the focal peak of the HIFU transducer passes through the focal region of the 10 MHz sensor (at 2.5 and 7.5 s) in Figure 8.18. Half harmonic emissions are generally detected throughout the exposure with the peak amplitude signal not always being when the HIFU field was in the focal region of the 10 MHz sensor. For example, at 270 W the peak half harmonic emissions were at the end of the exposure (~11 s) when the HIFU focal peak was approximately 9-10 mm away.

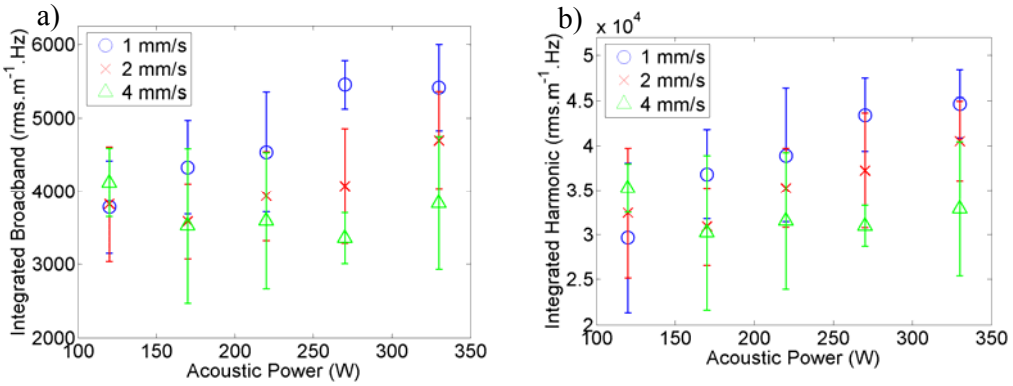

Figure 8.19. The total time and area integrated broadband (a) and detected harmonic (b) emissions for track speeds of 1, 2 and 4 mm/s. Integrated values have been weighted to account for different exposure lengths and frame rates. Uncertainty shown is the standard deviation of the average value, for n = 3-5.

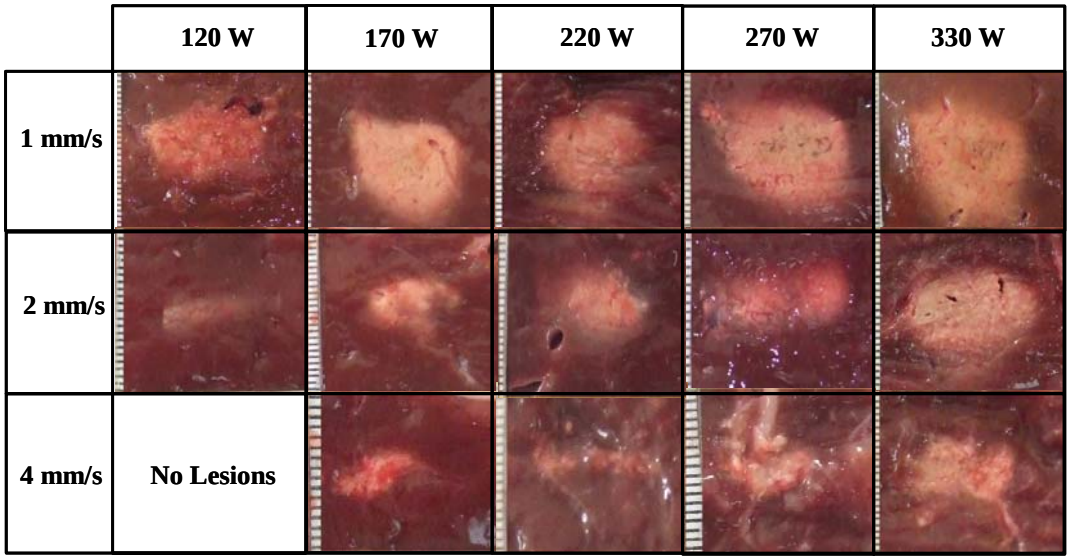

Figure 8.20. Examples of the lesions generated from the different exposure parameters in ex-vivo bovine liver tissue. The incremented scales show 1 mm spacing.

Figure 8.19 shows the total acoustic spectra integrated over the width of the focal track (20 mm) and the exposure time. The uncertainty in the average measurements, at 2 and

4 mm/s, makes it difficult to identify a difference in the level of the integrated broadband and harmonics. The greatest total acoustic spectra was seen for the 1 mm/s track speed for acoustic power setting of 170 W and greater.

Figure 8.20 shows examples of the lesion shapes and sizes created during the HIFU exposures. For the lowest acoustic power at the fastest track speed, of 4 mm/s, no lesions were found in the ex-vivo bovine liver tissue. Exposures at a track speed of 1 mm/s gave the largest volumes of damage.

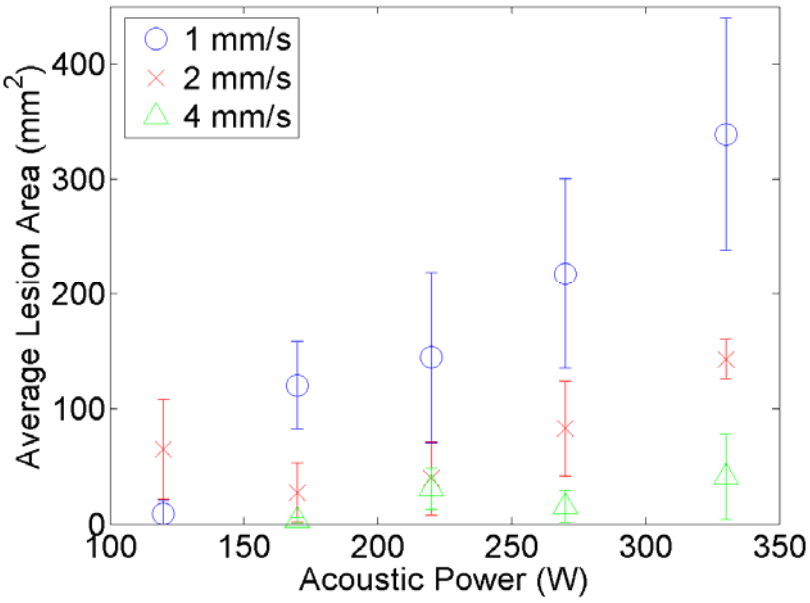

Figure 8.21. The average measured lesion area for track speeds of 1, 2 and 4 mm/s. Uncertainty shown is the standard deviation of the average value, for n = 3-5.

Figure 8.21 shows the average measured lesion area for each track speed. It shows that the 1 mm/s track speed generated the greatest area of tissue damage for the 170-330 W exposures. The largest lesion was generated at 330 W with the slowest track speed.

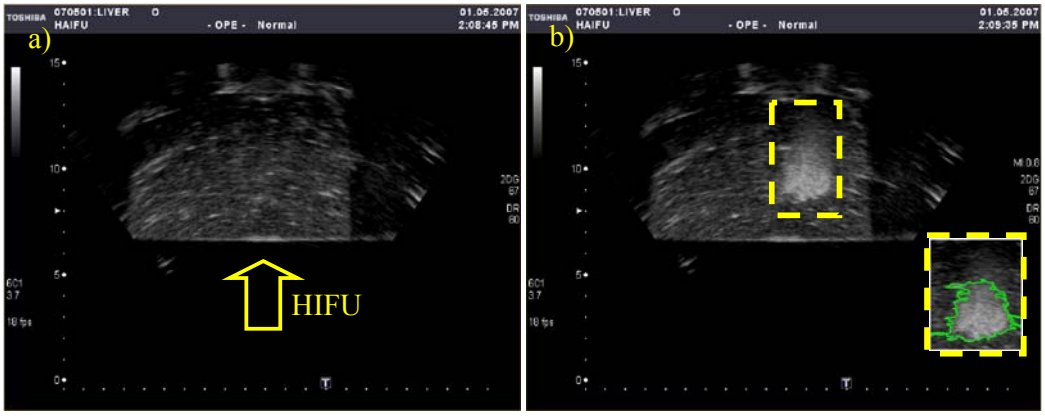

Figure 8.22. B-mode images acquired immediately before (a) and after (b) a 120 W exposure with a 1 mm/s track speed, shown in Figure 8.20. The yellow dashed line indicates the expanded area shown in the insert. This insert shows a green line around the area identified as having increased echogenicity or greyscale change compare to the image taken before the exposure.

Figure 8.22 shows an example of the B-mode images acquired using the diagnostic ultrasound scanner built into the JC extra-corporeal HIFU system. Figure 8.22(b) shows the echogenicity or greyscale change typically seen after a 1 mm/s HIFU exposure, which can be compared to the measured area of the lesion.

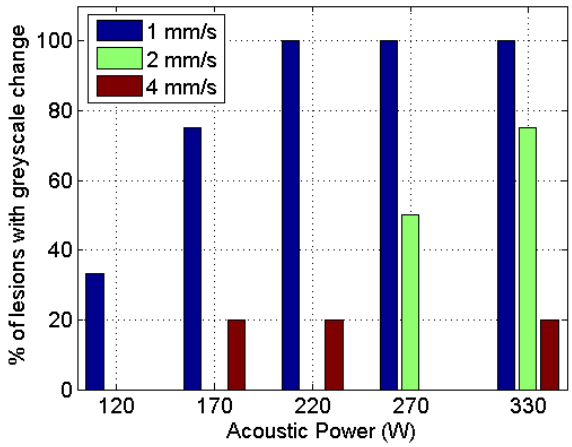

Figure 8.23. A plot of the percentage of lesions generated in ex-vivo liver tissue that showed a greyscale change for all track speeds and acoustic power settings. n = 3-5 for each exposure parameter.

Figure 8.23 shows the percentage of lesions generated in ex-vivo liver tissue that showed echogenicity or greyscale change in the B-mode images acquired after an exposure. 100% of exposures at the 1 mm/s track speed above 220 W acoustic power had echogenicity change indicating that boiling occurred (§7.2.2). Hyperechogenicity

was seen 20% of the time for the exposures at 170, 220 and 330 W. All track speeds at 330 W resulted in hyperechogenicity for at least 20% of the exposures.

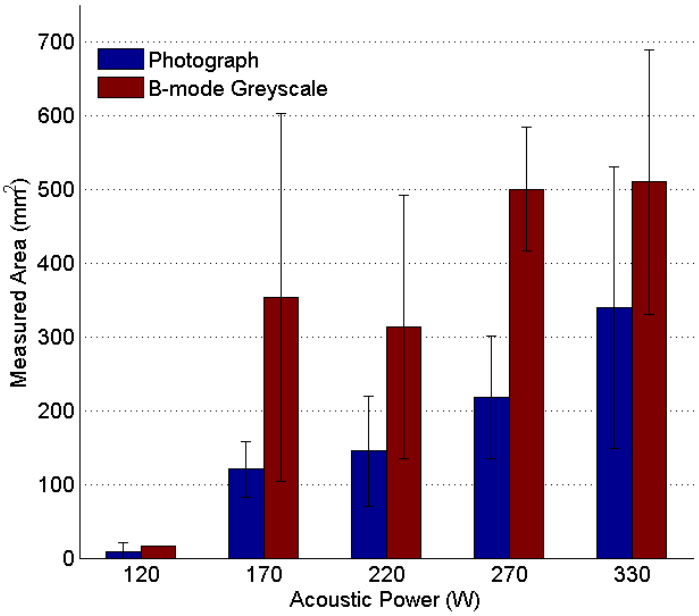

Figure 8.24. The measured area of the lesion compared with the area of greyscale change in the B-mode image, which is acquired immediately after the HIFU exposure at a track speed of 1 mm/s. Uncertainty shown is the standard deviation of the average value, where $n \geq 3$.

Figure 8.24 shows a comparison between the measured lesion area and greyscale change, for a track speed of 1 mm/s. It shows that the hyperechogenicity would overestimate the lesioned area if it were to be used as a treatment guide.

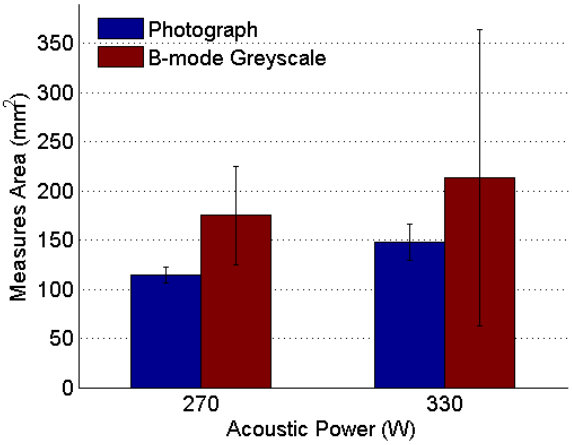

Figure 8.25. The measured area of the lesion compared with the greyscale change in the B-mode image, which is acquired immediately after the HIFU exposure that had a track speed of 2 mm/s. Uncertainty shown is the standard deviation of the average value, where $n \geq 3$.

Figure 8.25 shows a comparison between the measured lesion area and greyscale change, for a track speed of 2 mm/s, and the area estimated from hyperechogenicity. The B-mode appearance overestimates the damage seen in the tissue, but the uncertainty is large.

8.4 Discussion

8.4.1 Single shots using the Mauve Transducer

The exposure conditions used here were specifically chosen to cover the cavitation threshold regimes discussed in section 7.2.3. This study demonstrated that it was possible to use a single 10 MHz passive detector to monitor the same spectra as done with a dual passive cavitation detection system (§7.2).

Figure 8.5 to Figure 8.10 show examples of the acoustic spectra detected using both the 10 MHz and Terason passive detectors for 4 s exposures in ex-vivo bovine liver tissue. For exposures below the boiling threshold (< 1.86 MPa, for 4 s), no spectra were detectable above noise levels by the Terason system (Figure 8.8). For exposures above the boiling threshold (Figure 8.10), the Terason shows an increase in the detected emissions, which corresponds to those detected by the 10 MHz passive cavitation detection system (Figure 8.9(a) and (b)). However, the increase, in both the broadband and harmonic emissions, were detected over the length of the Terason scanners active element, with the largest detected signal amplitude being at the focal peak (Figure 8.10(b)) of the HIFU transducer. Detection of these emissions over the 20 mm width of the Terason scanner could be due to the combination of a weakly focused detector, and an isotropically radiating emitter or scatterer.

Figure 8.11 shows the averaged detected spectra using the 10 MHz passive cavitation detection system. They show the same threshold pressures that were detected with the dual passive cavitation detection system (§7.2.2, Figure 7.27). The averaged lesion area (Figure 8.12), for this data set, shows that the lesion area plateaus as the boiling threshold is exceeded (> 1.86 MPa, for 4 s). This is the same trend observed in the ex-vivo tissue study presented in Chapter 7, where it was thought likely to be due to the presence of boiling bubbles in the focal or pre-focal region causing energy to be

reflected (i.e. power fluctuations and harmonic detection) and the generation of 'tadpole' style lesions (Watkin *et al*, 1999; Meaney *et al*, 2000).

8.4.2 JC extra-corporeal HIFU system

The I_{sp} calibration (Figure 8.4) demonstrates that even at the lowest acoustic power setting (120 W) of the JC extra-corporeal HIFU system the exposure is above the non-inertial cavitation threshold shown in section 8.3.1. The acoustic spectra detected by the Terason system show that there is no clear correlation between the position of the HIFU focal peak and the detection of broadband emissions in the tissue samples (Figure 8.13Figure 8.15 or Figure 8.17). For example, it is not possible to identify that the peak amplitude of broadband emissions could not be clearly identified with the 'second pass' of the HIFU focal peak in the lesion track. However, the detection of broadband emissions correlated with the detection of non-linear harmonics from the focal region. Figure 8.13 to Figure 8.18 show examples of simultaneously detected spectra for both the 10 MHz and Terason passive cavitation detection systems for all exposure conditions. Acoustic emissions were detected at the lowest acoustic power level and slowest track speed (Figure 8.14). The Terason system detected broadband emissions and harmonics at all acoustic power levels. These acoustic power levels corresponded to in-situ I_{sp} values that exceeded the boiling threshold observed using the Mauve HIFU transducer. However, it was likely that due to the movement of the HIFU transducer the tissue was not heated to boiling levels for track speeds of 2 (only 120, 170 and 220 W) and 4 (all acoustic powers) mm/s, as evidence by the absence of hyperechogenicity on the B-mode image. As the 10 MHz passive cavitation detection system was aligned only with the centre point of the track (0 mm), the focal peak of the HIFU passed through its focus at only two time points during the exposure. For the longer exposure times, 21 and 41 s, it was not possible to record signals at both time points. At a track speed of 4 mm/s it was expected that the detected signals with the largest amplitude would occur at 2.5 and 8.5 s (extra second due to 'turn around time'), as seen in the 120 and 220 W acoustic power levels shown in Figure 8.18. However, this was not the finding for the half harmonic emissions at the 270 W acoustic power level (e.g. Figure 8.18), where no direct correlation between the distance of the HIFU focus from the centre of the track and the amplitude of the detected emission was apparent.

For the single exposure using the Mauve HIFU transducer, and taking into account the window length needed for the FFT computation, the spectral resolution for the 10

MHz system was 1250 Hz, compared to 15 Hz for the Terason system. The Terason's temporal resolution is thus approximately two orders of magnitude less than the 10 MHz system.

Figure 8.19 shows a plot for all the total time integrated broadband (a) and harmonic (b) emissions for all track speeds. This is an integration of the emissions seen over the width of the detector (20 mm) during the entire exposure. It can be seen that for the different track speeds the total amplitude of the detected spectra increases with acoustic power. The slowest track speed (1 mm/s) generated the largest total amplitude of integrated emissions. Figure 8.21 shows that the lesioned area is largest at this lower track speed. It is not possible to determine whether this is directly due to the maximum total amplitude of detected acoustic spectra, as it could also result from the fact that this exposure was ~20s longer than that at 2 mm/s.

The diagnostic ultrasound scanner was used to capture B-mode images before and after each HIFU exposure. Figure 8.22 shows such images for a 120 W track exposure produced at 1 mm/s. A greyscale (hyperechogenicity) change can be seen after exposure (Figure 8.22(b)). In order to assess the efficacy of using this greyscale change as an indication of the lesioned area, boundary identification (§5.5) that was used to calculate the area over which greyscale change occurred. Figure 8.23 shows the percentage of lesions generated that had a greyscale change. It is important to note that greyscale change was also observed when a lesion was not generated ($n \sim 2$), which was found on inspection to be due to the presence of blood vessels between 2-5 mm in diameter. These occurrences were discounted from the measurements. Figure 8.24 and Figure 8.25 show a comparison between the average measured lesion and greyscale areas in the digital photographs and B-mode images, respectively. For track speeds of 1 and 2 mm/s the measured greyscale overestimates the lesion size, and thus does not give a good indication of treated regions. This demonstrates that the use of hyperechogenicity to estimate the area of a lesion would most likely result in the overestimation of a treated region, potentially resulting in a failed treatment.

8.5 Conclusions

A preliminary study using the Mauve HIFU transducer showed the 10 MHz passive cavitation detection system was able to detect broadband, fourth harmonic and half harmonic emissions over the same acoustic pressure ranges at the dual 1 and 10 MHz

system described in section 7.2. This system was used in conjunction with the Terason passive cavitation detection system, which was also capable of detecting broadband emissions and harmonics. The Terason system was only capable of detecting broadband and harmonic emissions above noise for exposures that exceeded the boiling threshold (1000 W/cm^2 ±20% or 1.86 MPa ±17%, for 4 s exposures). It was shown for this study, which agreed with the trend previously seen (§7.2.2) that the lesioned area for 4 s exposures reached a plateau as the boiling threshold was exceeded.

The JC extra-corporeal clinical HIFU system was used with the two simultaneous passive cavitation detection systems. The cavitation activity that occurred during single 20 mm tracks for different track speeds and acoustic power settings was monitored. The Terason system shows that there was no significant correlation between the position of the HIFU focus during the exposure and the point at which the peak amplitude signals were detected. This suggested that cavitation activity was more determined by the existence of cavitation nuclei in specific regions of tissue. The slowest track speed (1 mm/s) was shown to produce the peak levels of cavitation activity during the HIFU exposures. In addition, diagnostic ultrasound imaging provided before and after images of the ex-vivo tissue. When the area of the greyscale change observed was compared with the actual lesioned area, the greyscale change observed always overestimated the lesioned area by between 40 and 70%, depending on the acoustic power level used. This suggests that greyscale change is not a reliable indicator of lesioned area in ex-vivo tissue, and that one should be cautious of applying this criterion to in-vivo applications.

The 10 MHz passive cavitation detection system could only record continuously for up to 16 s, which meant that for slower track speeds (1 and 2 mm/s) acoustic spectra was only recorded for 16 s of the total exposure time (the acquisition start time was varied). In addition, the focal peak of the HIFU system only passed the focus of this sensor twice during each track. It was seen that the amplitude of the half harmonic shows little correlation with the location of the HIFU focal peak. This suggests that the passive sensor was capable of detection of acoustic emissions from outside its focal region. However, this seemed to only generally apply to the half harmonic when it was observed at the same time as the broadband emissions, as is typical in response to a boiling event, as also observed in section 7.2.2.

The Terason system provided an overview of the cavitation activity during the HIFU exposures. This was due to its ability to monitor the entire length of the track simultaneously, and for the whole duration of the HIFU exposure. This is the main

advantages of this system over the 10 MHz system. However the Terason was only investigating broadband and harmonic emissions, and not subharmonic emissions.

The two cavitation detection systems have different strengths, but it seems that there is a compromise between spatial resolution, temporal resolution and sensitivity to acoustic emissions. This suggests that a passive weakly focused sensor would be unsuitable for the detection of cavitation activity in the absence of boiling. A thus a possible solution for this would thus be to couple the cavitation detection to the motion of the HIFU treatment system, as was done in Chapter 10 in a perfused liver study. This could be in the form of an existing diagnostic scanner which is built into the HIFU system (if the appropriate functionality exists) but this would still be limited by the temporal resolution and 'signal detection' sensitivity. A focused detector which is co-aligned with the HIFU focus would achieve this, but would not be as sensitive temporally.

9 – Ex-vivo porcine kidney tissue study

9.1 Introduction

This chapter investigates the cavitation activity generated from single 1.7 MHz HIFU exposures in ex-vivo porcine kidney tissue made using the Imasonic HIFU transducer at 20 and 40^{o}C. Passive cavitation detection systems were used. The location of the kidneys within the body makes the targeting of soft tissue tumours within them, a natural application for extra-corporeal HIFU (Chapelon *et al*, 1992; Watkin *et al*, 1997; Wu *et al*, 2003; Illing *et al*, 2005). Shock-wave lithotripsy is an analogous extra-corporeal technique that is used to treat kidney stones as a non-invasive alternative to surgery.

Lithotripsy uses short duration (~1 μs) higher pressure (~100 MPa) pulses with a repetition frequency of approximately 2 Hz to break kidney stones (Takagi *et al*, 2006). Acoustic cavitation is considered to play a role in the destruction of the kidney stones, however it is also thought to cause unwanted tissue damage (Zhu *et al*, 2004). For these reasons active and passive cavitation detection techniques are used to monitor acoustic cavitation activity during laboratory studies of lithotripsy (Coleman *et al*, 1996; Cleveland *et al*, 2000; Bailey *et al*, 2005). Passive cavitation detection is generally used only to monitor broadband emissions to give an indication of inertial cavitation activity (Zhong *et al*, 1997). Active cavitation detection is generally by means of B-mode imaging and the monitoring of any change in the echogenicity of the focal region (Coleman *et al*, 1995). The peak negative pressures may be at least an order of magnitude greater than those generated in this present study. These differences highlight the different mechanisms for damage that lithotripsy and HIFU cause in tissue. In lithotripsy, mechanical effects cause the damage, where as in HIFU treatments it is predominantly thermal in origin. However, the techniques used to monitor acoustic emissions for the investigation of inertial cavitation activity remains the similar.

The aim of this study was to perform cavitation detection experiments similar to those undertaken in ex-vivo liver, described in section 7.2.1, in order to identify pressure thresholds (if any) for non-inertial, inertial cavitation and boiling. This investigation was undertaken at tissue temperatures of 20 and 40 ±2^{o}C.

9.2 Materials and Method

Whole ex-vivo porcine kidneys were used in this study, after the removal of the outer capsule. They were exposed to HIFU within 12 h of being excised from the animal and were not degassed prior to exposure. The kidneys were exposed to a HIFU field at either 20 or 40 ±2^{o}C, the temperature of the tissue being elevated by heating all the degassed water in the tank using the method described in section 7.3.1. The purpose of this was to investigate whether tissue temperature has an effect on the pressure thresholds for cavitation activity.

The 7.5 MHz passive cavitation detection system, described in section 7.3.1, was used to study the acoustic spectra arising from HIFU exposures. Diagnostic imaging was provided by the curvilinear ultrasound probe (C5-2, radius of curvature 5 cm, field of view angle 65^{o}, centre frequency 1.96 MHz, and imaging depth 18 cm) that was inserted into the rear of the Imasonic HIFU transducer (§7.3.1, Figure 7.35). This system was used, rather than the fixed dual passive cavitation detection system, as it was coupled to the movement of the HIFU transducer and it was therefore possible to maximise the space available for exposures in each kidney. Audible emissions (2-20 kHz) were monitored using the microphone (§7.2.1), submerged into the degassed water tank within a condom, and electrical drive power was calculated from the *V*/20 and *i*/10 measurements using equation 4.3 in order to monitor drive power fluctuations.

Since whole kidneys were exposed, it was not possible to maintain a constant tissue thickness between different exposure positions and between samples (unlike in the ex-vivo liver samples where it was possible to cut them to the required dimensions). However, the focal peak of the HIFU field was placed at a constant depth of 12.5 ±2.5 mm. Each exposure was 4 s long, and the I_{sp} was in the range of 312-3120 W/cm^2 ±25%, divided into 12 increments (312, 390, 490, 610, 760, 940, 1200, 1500, 1870, 2330, 2770 and 3120 W/cm^2). The corresponding measured peak negative pressures for this range were 1.06-2.40 MPa ±22% (1.06, 1.18, 1.31, 1.40, 1.58, 1.68, 1.85, 1.98, 2.12, 2.30. 2.38 and 2.40 MPa). After exposure, the kidneys were dissected and any lesions were photographed (§5.5).

9.3 Results

9.3.1 Ex-vivo kidney exposures at 20°C

The results shown are representative of data obtained from experiments carried out on 12 ex-vivo kidneys, each of which provided positions for 15-20 exposures, at 20 ±2°C.

Figure 9.1 shows the acoustic spectra detected from exposures at three intensities, 610, 940 and 2330 W/cm^2 (1.40, 1.58 and 2.36 MPa). These are typical examples of the regimes where no acoustic cavitation (e.g. the first row in Figure 9.1), inertial and non-inertial cavitation (e.g. the second row in Figure 9.1) and boiling (e.g. the third row in Figure 9.1) was detected. The examples are typical in as much as no acoustic emissions were detected during the three repeat exposures at 610 W/cm^2 (1.40 MPa) exposures, and half harmonic (0.85 MHz) and integrated broadband (6-10 MHz) were detected during three out of the six repeat exposures at 760 W/cm^2 (1.58 MPa) exposures. The 2330 W/cm^2 (2.30 MPa) exposure is one out of eight HIFU exposures in all of which boiling occurred (as indicated by drive power fluctuations, and an sudden increase in the detected fourth harmonic and integrated broadband emissions, Figure 9.1(o, i and l), respectively). Figure 9.2 shows the corresponding detected audible emissions (2-20 kHz), acquired using the microphone, and the B-mode images that were acquired immediately before and after the HIFU exposure, and the subtraction image for a smaller region of interest. This figure is again typical of the results seen in kidney, which were that audible emissions (Figure 9.2(c)) and echogenicity changes (Figure 9.2(f)) were only seen for exposures that generate boiling. In this particular example, audible emissions and fluctuations in the calculated electrical drive power (Figure 9.1(o)) occurred immediately (< 5 ms) after the start of the exposure. Approximately 0.2 s into the exposure, a discrete audible emission with magnitude 20 dB greater than the immediately preceding emissions was detected (Figure 9.2(c)), coinciding with an increase in the fourth harmonic and broadband emissions. When half harmonic emissions were detected (Figure 9.1(b) and (c)), their peak amplitude was similar for exposures at 760 and 2330 W/cm^2.

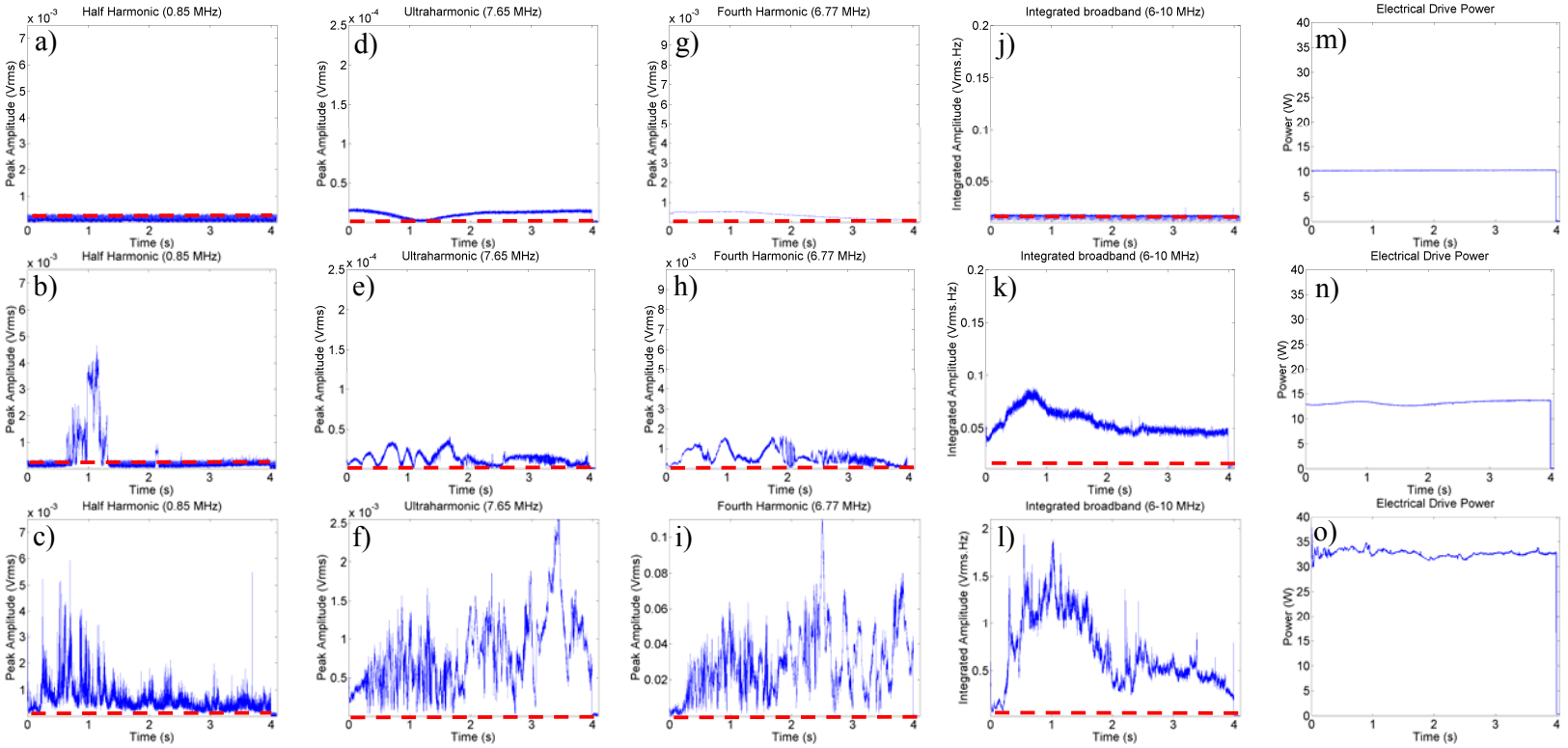

Figure 9.1. The detected half harmonic (a-c), ultraharmonic (d-f), fourth harmonic (g-i), integrated broadband (j-l) and electrical drive power (m-o) for three 4 s HIFU exposures in ex-vivo kidney. I_{SP} for the first row is 610 W/cm^2 (1.40 MPa), the second row 760 W/cm^2 (1.58 MPa), and the third row 2330 W/cm^2 (2.36 MPa). Note the factor of 10 increase in the vertical axis for the detected ultraharmonic (f), fourth harmonic (i) and integrated broadband (l) for the 2330 W/cm^2 exposure. The red line indicates the peak noise level measured during a sham exposure.

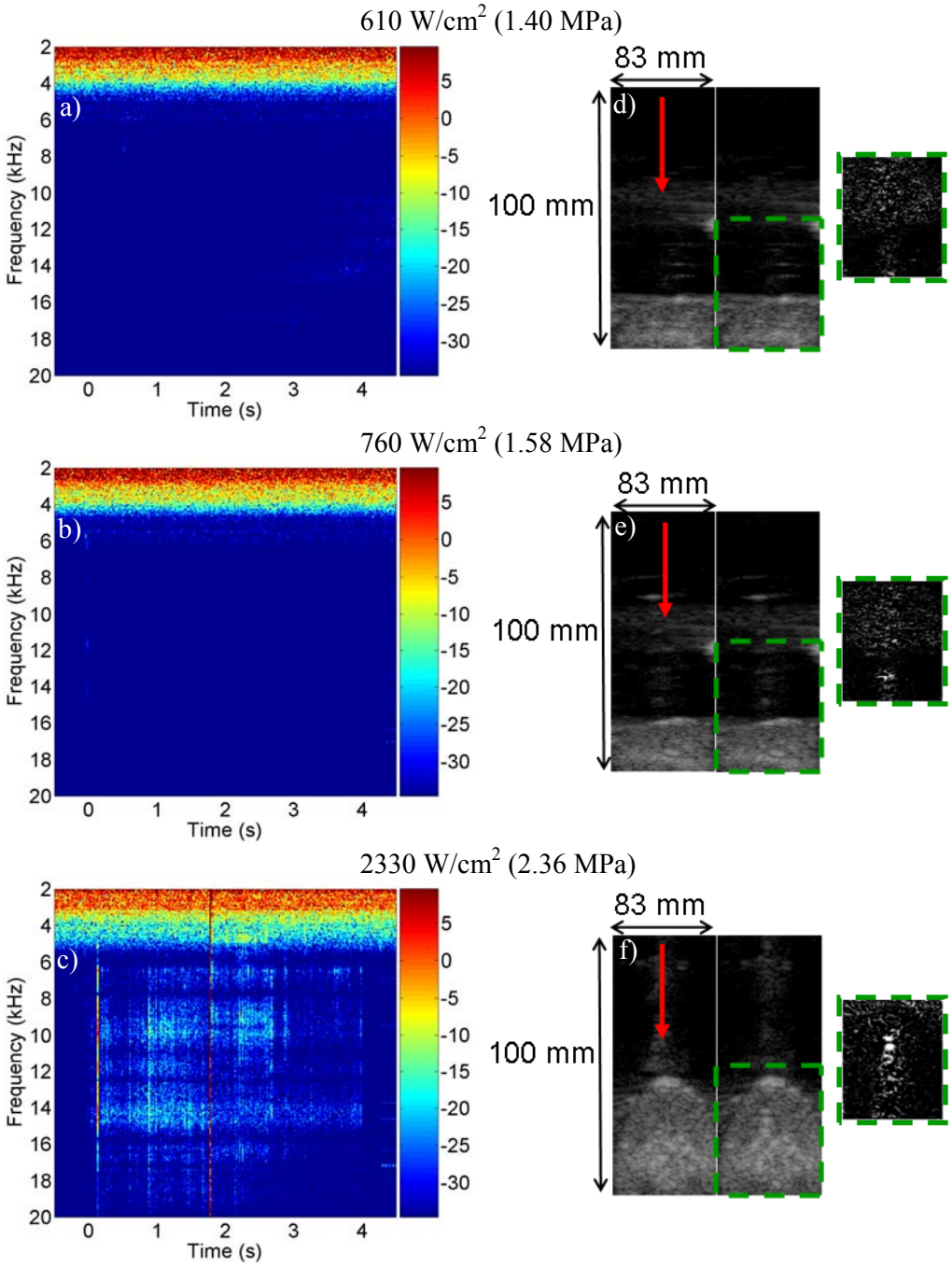

Figure 9.2. The audible emissions (a-c) and B-mode with subtraction (post minus pre) images (d-f) from the (a&b) 610 W/cm^2 (1.40 MPa), (b&e) 760 W/cm^2 (1.58 MPa), and (c&f) 2330 W/cm^2 (2.36 MPa) exposures described in Figure 9.1. The B-mode images shown for each exposure are taken immediately before and after the exposure and the subtraction images show the difference between the two. The colour scale on the audible emissions data is logarithmic. The red arrow indicates the direction of propagation for the HIFU field.

Figure 9.3 shows, for all the kidney experiments, the percentage of exposures for which emissions above the predefined noise threshold detailed in section 4.2.4 were detected.

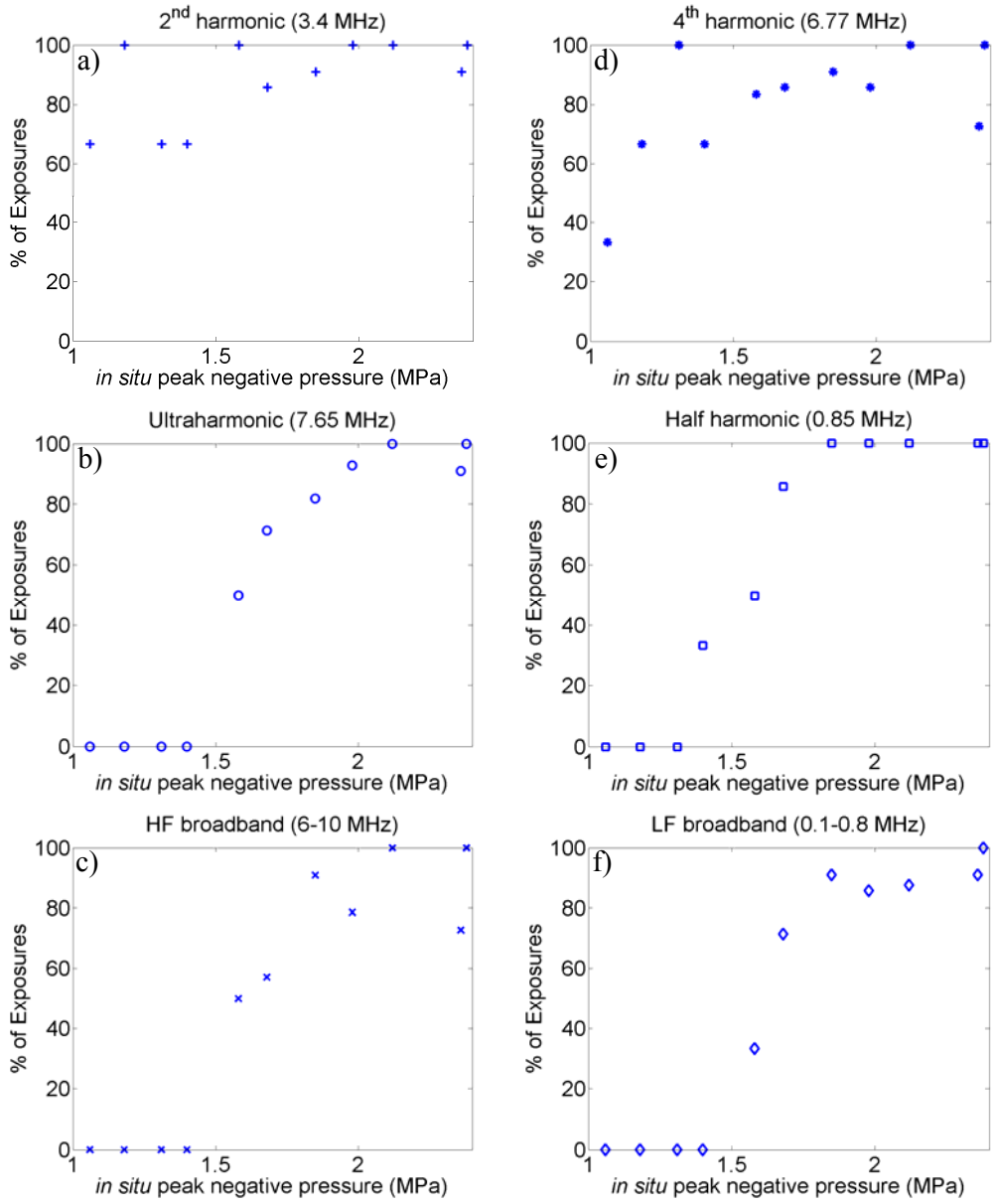

Figure 9.3. The percentage of exposures in which passive cavitation signals greater than the baseline noise level were detected at any point during the 4 s exposures. The signals were measured over the range 312-2770 W/cm^2 (1.06-2.38 MPa), where n= 3-14 for each exposure level.

The second and fourth harmonic data (Figure 9.3(a) and (d)) show that these harmonics, which are most likely caused by scattering of the non-linear components of the HIFU field, were detected over the entire exposure range. Figure 9.3(b, c, e and f) show acoustic spectra generated by bubble oscillation. Below 760 W/cm^2 (1.58 MPa) no ultraharmonic emissions (Figure 9.3(b)) or broadband emissions (Figure 9.3(c) and (f))

were detected above the noise level. As the intensity (pressure) increased the percentage of exposures above the noise level increased. The same trend is observed for the half harmonic emissions (Figure 9.3(e)). This figure gives an indication at the intensity (pressure) levels at which signals are detected above the noise level. Above 1200 W/cm^2 (1.85 MPa) acoustic spectra are detected above the noise for more than 80% of the exposures.

Figure 9.4 shows that B-mode hyperechogenicity was only observed for 4 s HIFU exposures in ex-vivo porcine kidney at 940 W/cm^2 (1.68 MPa) and above. As the in-situ peak negative pressure increases the likelihood of observing a change in echogenicity also increases.

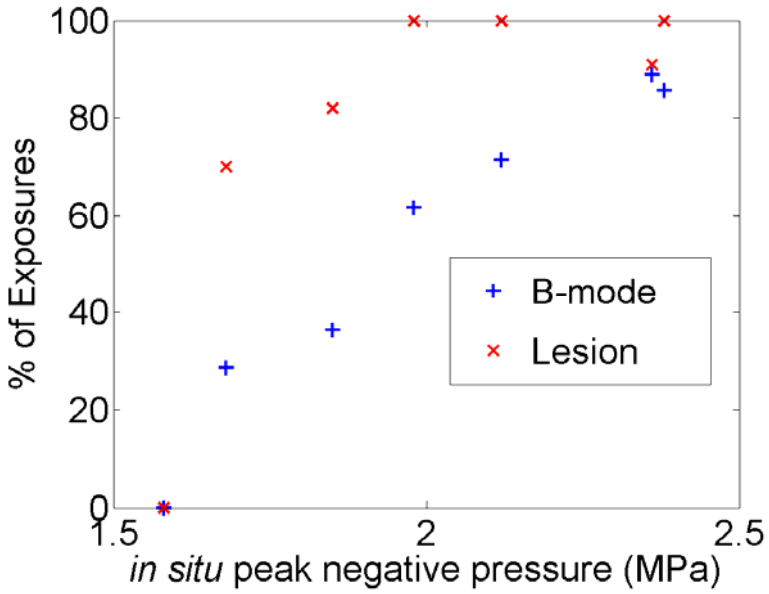

Figure 9.4. The percentage of 4 s HIFU exposures that resulted in B-mode hyperechogenicity (Figure 9.2(f)) after the exposure (+) and a lesion seen in the tissue on dissection (x).

Figure 9.5 shows a comparison between the photograph and the B-mode scan of four exposures during which boiling occurred (as determined by the detection of audible emissions). The B-mode image was acquired (using free hand imaging) approximately one hour after the exposures were performed, and a small amount of echogenicity can still be observed. It is important to note that these B-mode images were acquired using the linear probe (§4.3.1), which is why it was possible to get images at a higher resolution than for those shown in Figure 9.2. The appearance of the hyperechogenicity in this figure shows a more uniform shape than is seen in the photographs of the lesions.

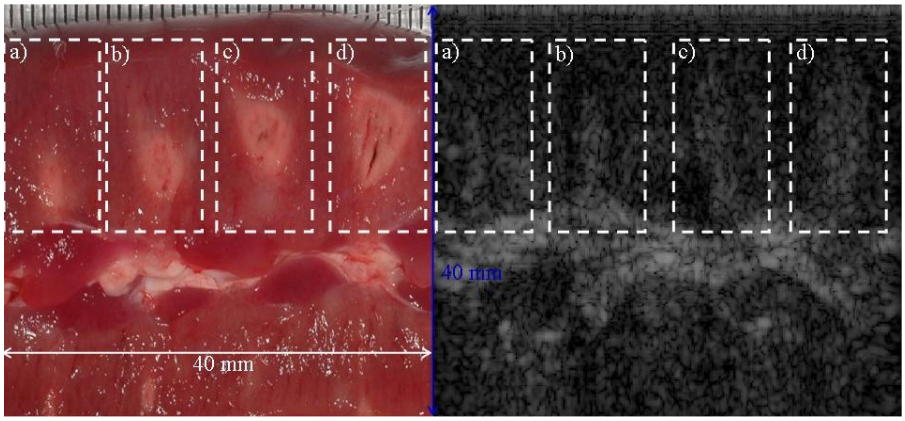

Figure 9.5. A comparison between photographs and a B-mode images of four HIFU exposures in ex-vivo porcine kidney for 4 s at (a) 1870 W/cm^2 (2.12 MPa), (b) 2330 W/cm^2 (2.36 MPa), (c) 2770 W/cm^2 (2.38 MPa) and (d) 3120 W/cm^2 (2.40 MPa).

Figure 9.6 shows the 'onset time', which has previously been defined for ex-vivo bovine liver exposures (§7.2.3), as the time point at which audible emissions, power fluctuations or an order of magnitude increase in the detected fourth harmonic occurs during the exposure. The onset times decrease with increasing intensity (pressure), such that, at the highest exposure, they occur almost instantaneously with the start of the HIFU exposure. Below 940 W/cm^2 (1.68 MPa) no 'onset time' was measured.

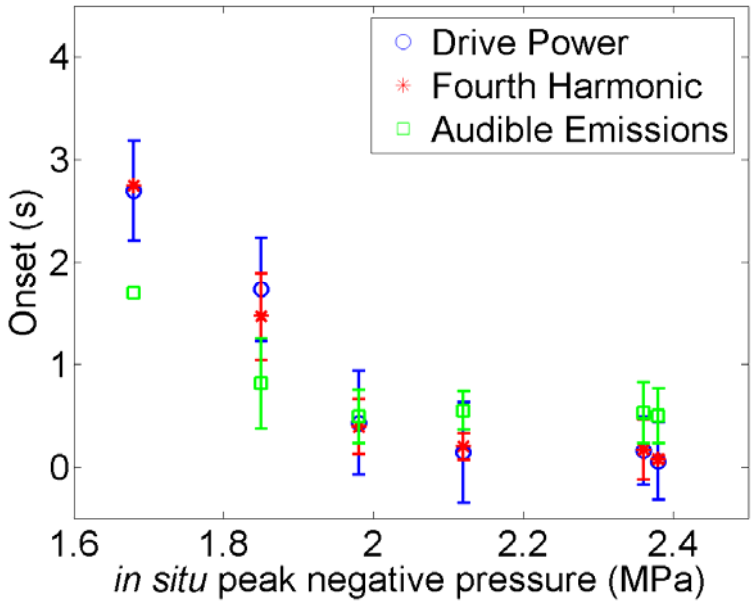

Figure 9.6. A comparison of the average 'onset time' for electrical drive power fluctuations, fourth harmonic increase and audible emissions (2-20 kHz). The uncertainty, where shown, is the standard deviation of the average onset time, when n = 3-14.

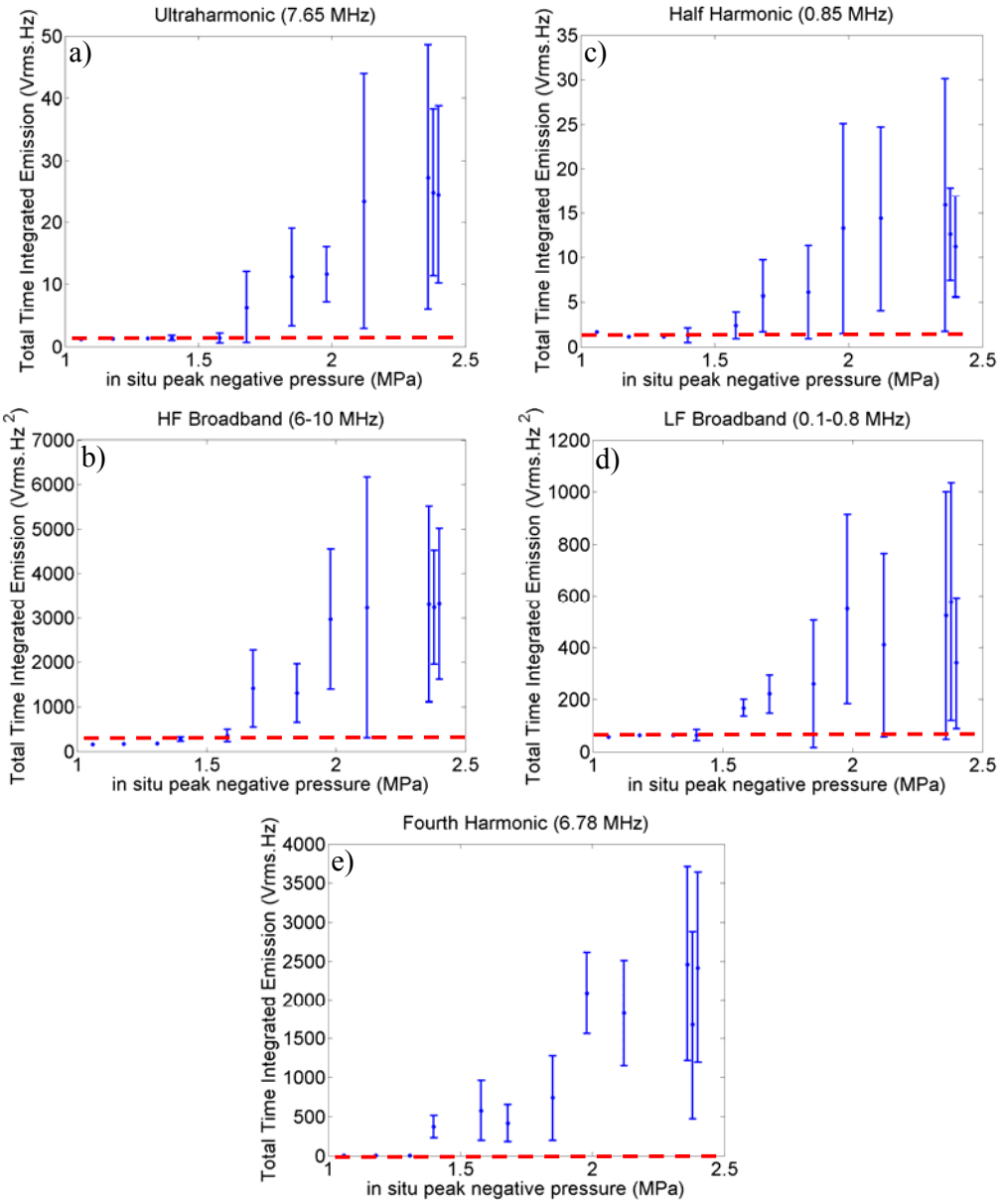

Figure 9.7. The averaged total time integrated (a) ultraharmonic, (b) half harmonic, (c) high frequency broadband emissions, (d) low frequency broadband emissions and (e) fourth harmonic measured in 4 s. Uncertainty, where shown, is the standard deviation of the average value, for n = 3-13. The red dashed line indicates the averaged peak noise level measured from sham exposures.

Figure 9.7 shows the averaged total time integrated emissions for the acoustic spectra monitored with the 7.5 MHz frequency passive cavitation detection system. As the intensity (pressure) increases there is an increase in the detected signal, however the uncertainty value for the data also increases, which means there is a greater spread in the total time integrated emission.

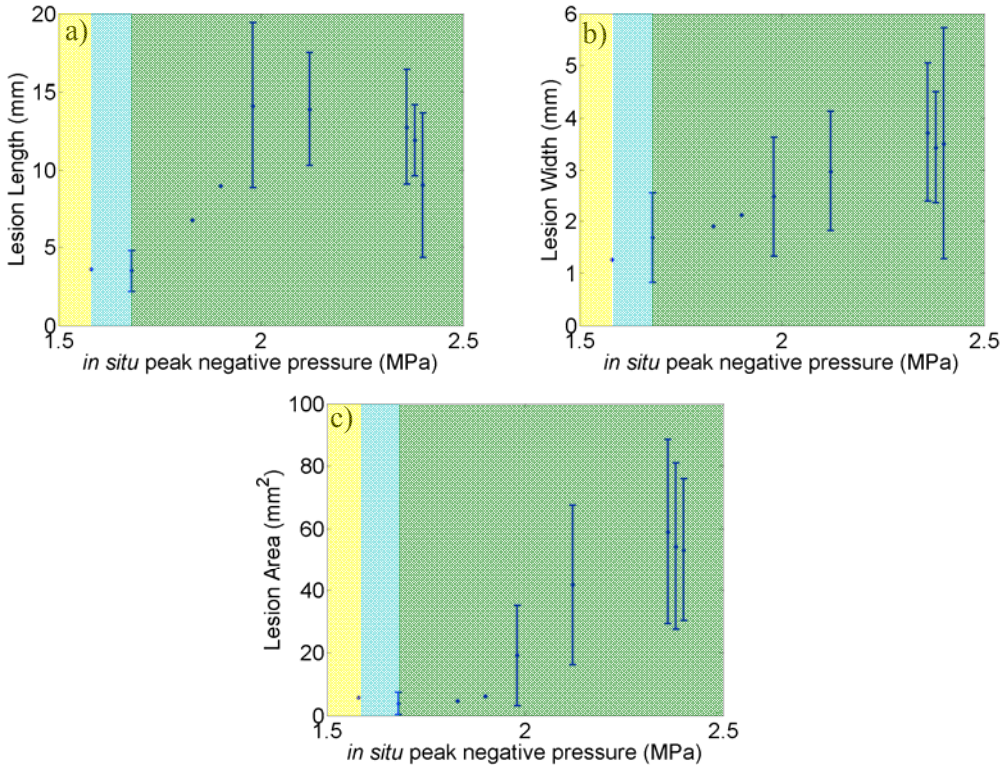

Figure 9.8. The averaged measured lesion length (a), width (b) and area (c) for peak negative pressures that generate a lesion from a single 4 s exposure. Uncertainty, where shown, is the standard deviation of the average value, for n = 3-14. The three colours are used to depict the three cavitation regimes approximately, non-inertial cavitation only (yellow), non-inertial and inertial cavitation (light blue) and acoustic cavitation and boiling (green).

Figure 9.8 shows the lesion dimensions generated from 4 s HIFU exposures in ex-vivo porcine kidney tissue. As the intensity (pressure) increases, the average lesion length in the kidney tissue plateaus, whereas the width of the lesion continues to increase. A similar trend was also observed in lesions in ex-vivo bovine liver (§7.2.2).

9.3.2 Ex-vivo kidney exposures at 40°C

The results shown are representative of data obtained from experiments carried out on 6 separate ex-vivo kidneys, each of which was subjected to 15-20 exposures, at 40 ±2°C.

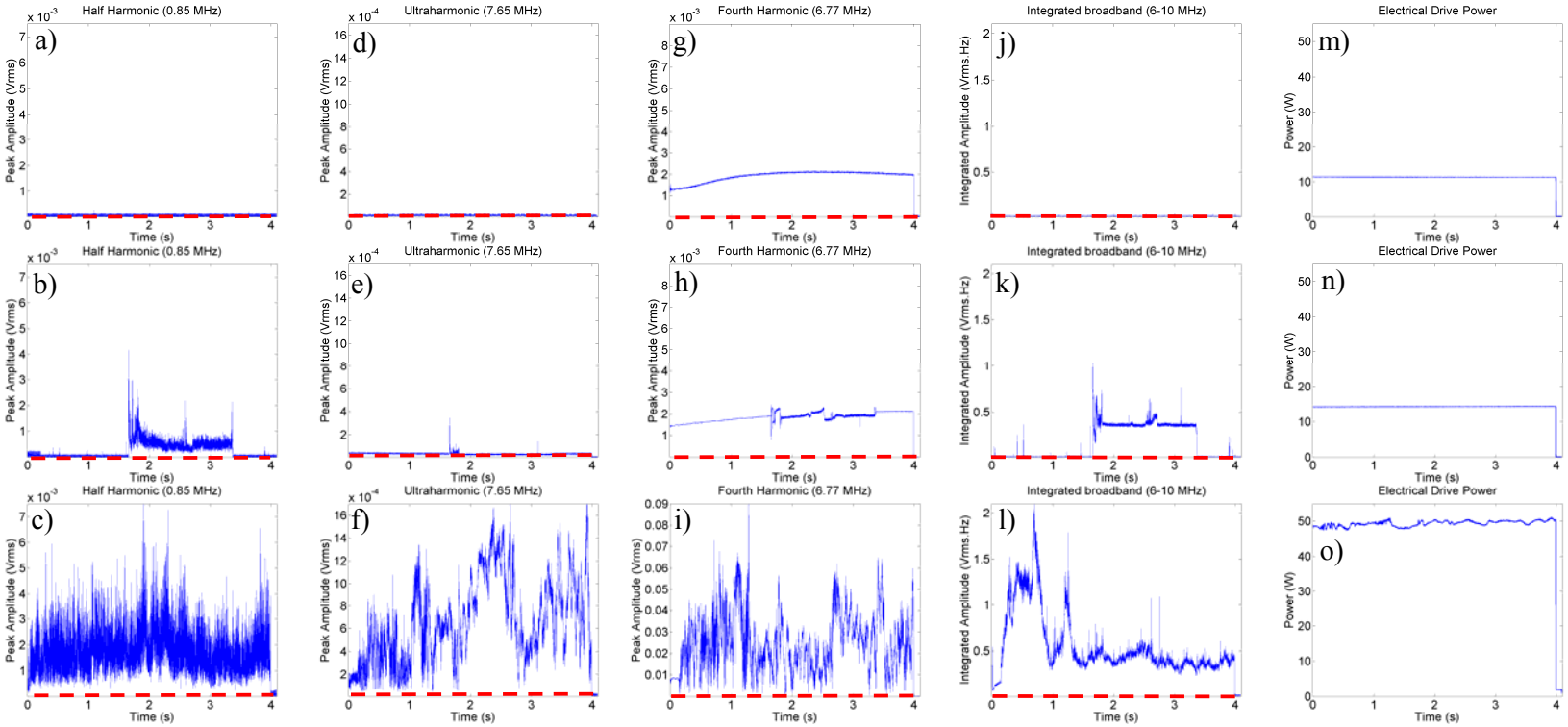

Figure 9.9. The detected half harmonic (a-c), ultraharmonic (d-f), fourth harmonic (g-i), integrated broadband (j-l) and electrical drive power (m-o) for three 4 s HIFU exposures in ex-vivo kidney. Where the first row is at 610 W/cm^2 (1.40 MPa), the second row is at 760 W/cm^2 (1.58 MPa), and the third row is at 2330 W/cm^2 (2.36 MPa). Note the factor of 10 increase in the vertical axis for the detected fourth harmonic (i) for the 2330 W/cm^2 exposure. The red line indicates the peak noise level measured from a sham exposure.

Figure 9.9 shows the acoustic spectra that were detected from three separate exposures of ex-vivo kidney. The three exposures, 610, 940 and 2330 W/cm^2 (1.40, 1.58 and 2.36 MPa) are typical examples of the regimes where no acoustic cavitation, inertial and non-inertial cavitation and boiling, respectively, were detected. The trends seen in this figure are similar to those observed for exposures at 20^{o}C (Figure 9.1), specifically the increase in detected fourth harmonic at 2330 W/cm^2 (2.36 MPa) exposure with the onset of boiling (Figure 9.9(i)). Figure 9.10 shows typical examples of the audible emissions during these exposures and B-mode and subtraction images acquired from 4 s HIFU exposures of ex-vivo kidney tissue at 40 ±2^{o}C. Some artefacts can be seen in Figure 9.10(a) and (b), before and at the end of the HIFU exposure. These are caused by the microphone detecting laboratory noise, including a 'mouse click' before the HIFU exposure, and noise from the power to the motors on the automated gantry (§5.3) being switched on after exposure. Figure 9.10(f) shows an increase in echogenicity in the degassed water caused by the generation of acoustic streaming in the degassed water at this elevated temperature. The acoustic streaming seen here is outside the field of view of the 7.5 MHz passive sensor. This streaming does however cause a bright region in the subtraction image (Figure 9.10(f)), in addition to the one created in the tissue.

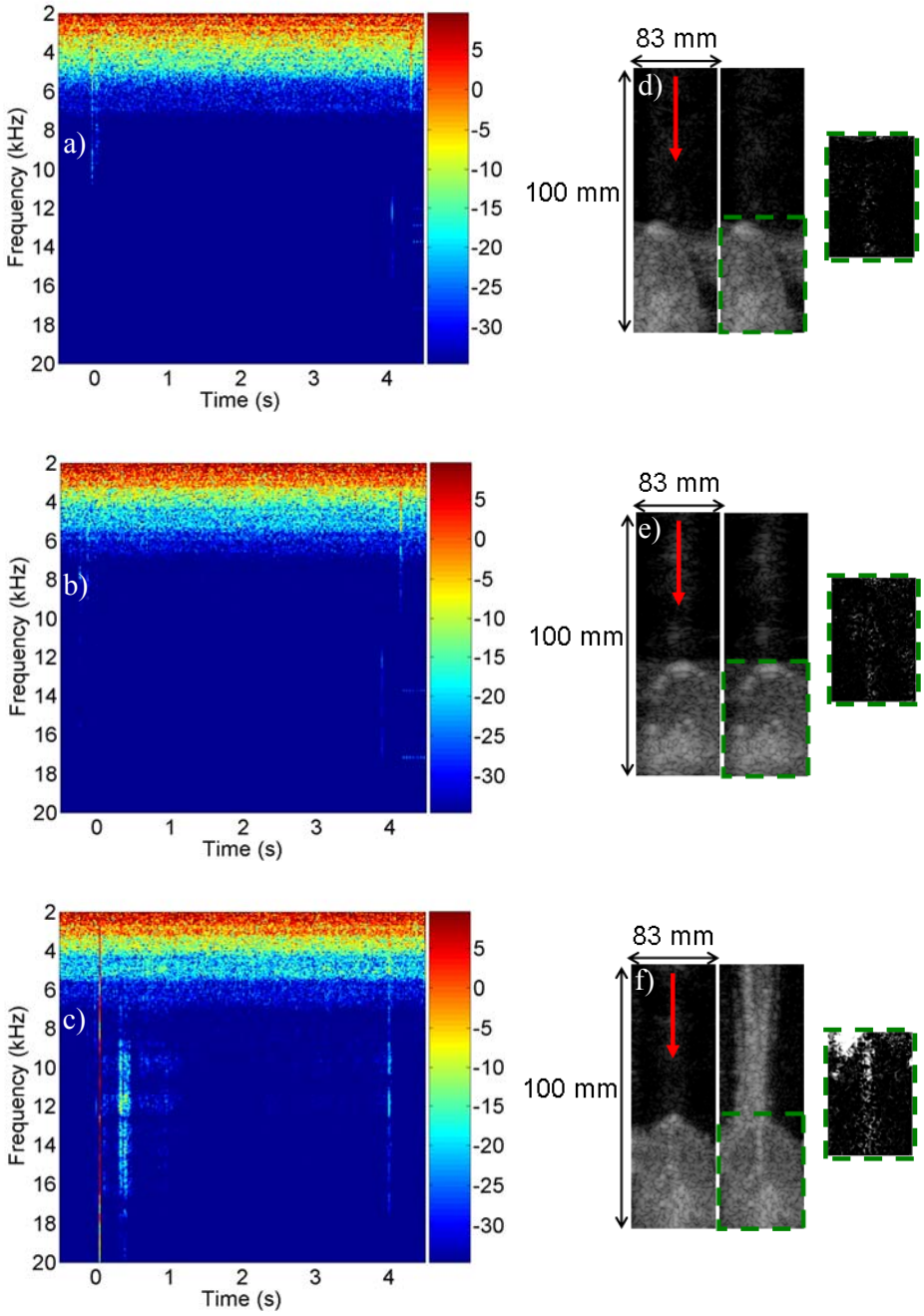

Figure 9.10. The audible emissions (a-c) and B-mode and subtraction images (d-f) from the (a and b) 610 W/cm^2 (1.40 MPa), (b and e) 760 W/cm^2 (1.58 MPa), and (c and f) 2330 W/cm^2 (2.36 MPa) exposures described in Figure 9.9. The B-mode images shown for each exposure were taken immediately before and after the exposure and the subtraction images show the difference between the two. The colour scale on the audible emissions data is a logarithmic scale. Laboratory noise sources were the cause of the emissions seen before ($t < 0$ s) and after ($t > 4$ s) the exposures in (a) and (b). Acoustic streaming in the degassed water caused the echogenic region seen in (f). The red arrow indicated the direction of propagation for the HIFU field.

Figure 9.11 shows the percentage of detected acoustic spectra above the predefined noise threshold defined in section 4.2.4 for all the exposures in this study.

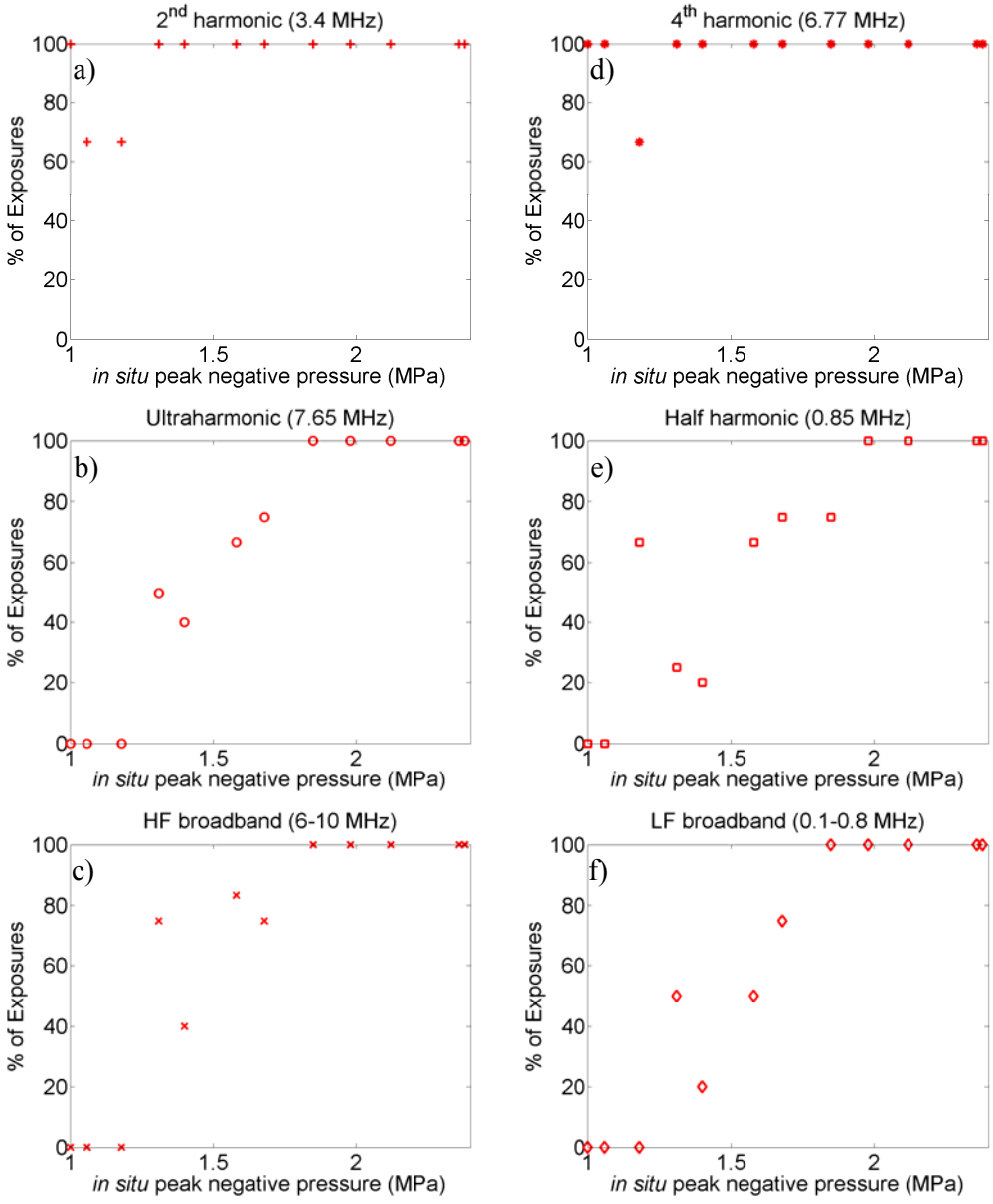

Figure 9.11. The percentage of detected signals, measured with the passive cavitation detection system, which is greater than the noise level at any point during the exposure. The signals are measured during 4 s HIFU exposures over the range 312-2770 W/cm^2 (1.06-2.38 MPa), where n= 3-8 for each exposure level.

The second and fourth harmonic data in Figure 9.11 show that these harmonics, which are most likely to be caused by scattering of the non-linear components of the HIFU field, were detected over the entire exposure range. The same was not true for the

acoustic spectra that were generated from bubble oscillations that are shown in Figure 9.11. Below 480 W/cm^2 (1.31 MPa) no ultraharmonic emissions or broadband emissions were detected above the noise level. This is a lower exposure level than seen for exposures at 20^{o}C (611 W/cm^2 or 1.40 MPa). As the intensity (pressure) was increased the percentage of 4 s exposures above the noise level increased. The same trend is observed for the half harmonic emissions. This figure shows at what intensity (pressure) levels that the passive cavitation detection system detects signals above the noise level i.e. the detectable threshold.

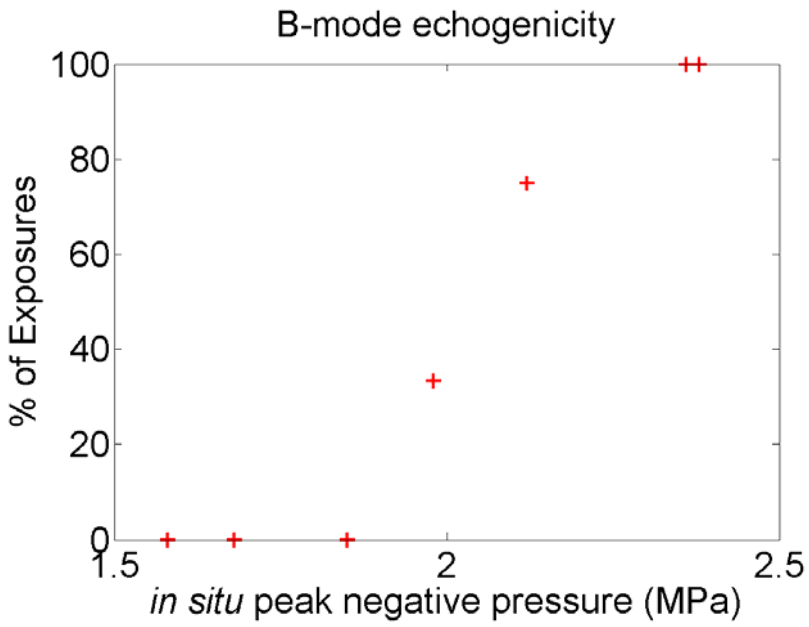

Figure 9.12. The percentage of B-mode images acquired after 4 s HIFU exposures of ex-vivo kidney at 40 ±2^{o}C that resulted in increased B-mode hyperechogenicity (e.g. Figure 9.10(f)).

Figure 9.12 shows that hyperechogenicity was only observed after 4 s HIFU exposures in ex-vivo porcine kidney held at 40^{o}C of ≥1500 W/cm^2 (1.98 MPa). As the in-situ peak negative pressure increases the likelihood of a change in echogenicity increases, just as seen for exposures at 20 ±2^{o}C (Figure 9.4). However, at 40^{o}C the hyperechogenicity occurs at higher intensities (pressures). Figure 9.13 shows the 'onset time' for electrical drive power fluctuations, an increase in fourth harmonic emissions (6.77 MHz) and audible emissions (2-20 kHz). The onset time decreases with increasing intensity (pressure), but unlike for exposures at 20 ±2^{o}C (Figure 9.6), they occur at 1500 W/cm^2

(1.98 MPa) and above. The sample size (n) for the exposures at 40°C was 45, where for 20°C it was 77.

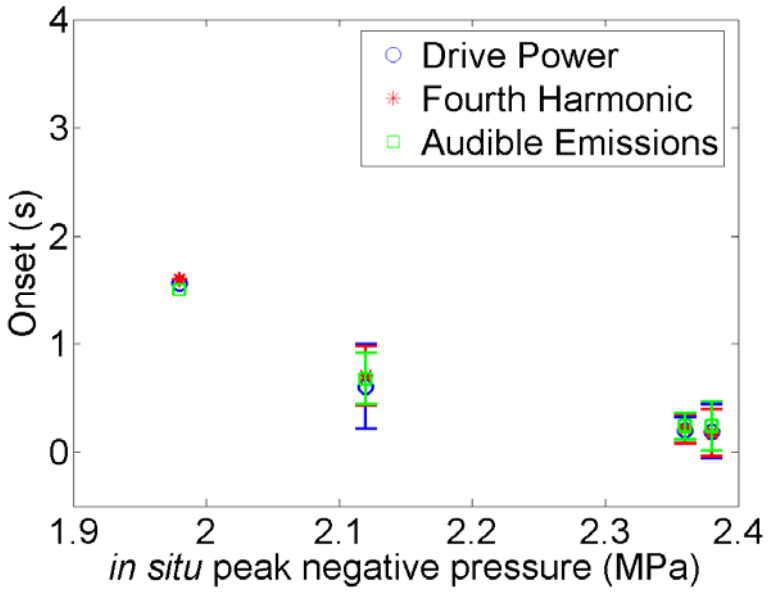

Figure 9.13. A comparison of the average 'onset time' for electrical drive power fluctuations, fourth harmonic increase and audible emissions. The uncertainty, where shown, is the standard deviation of the average onset time, when n >= 3.

Figure 9.14 shows the average total time integrated emissions for the acoustic spectra monitored with the 7.5 MHz frequency passive cavitation detection system during 4 s exposures using the Imasonic HIFU transducer, in ex-vivo porcine kidney tissue at 40°C.

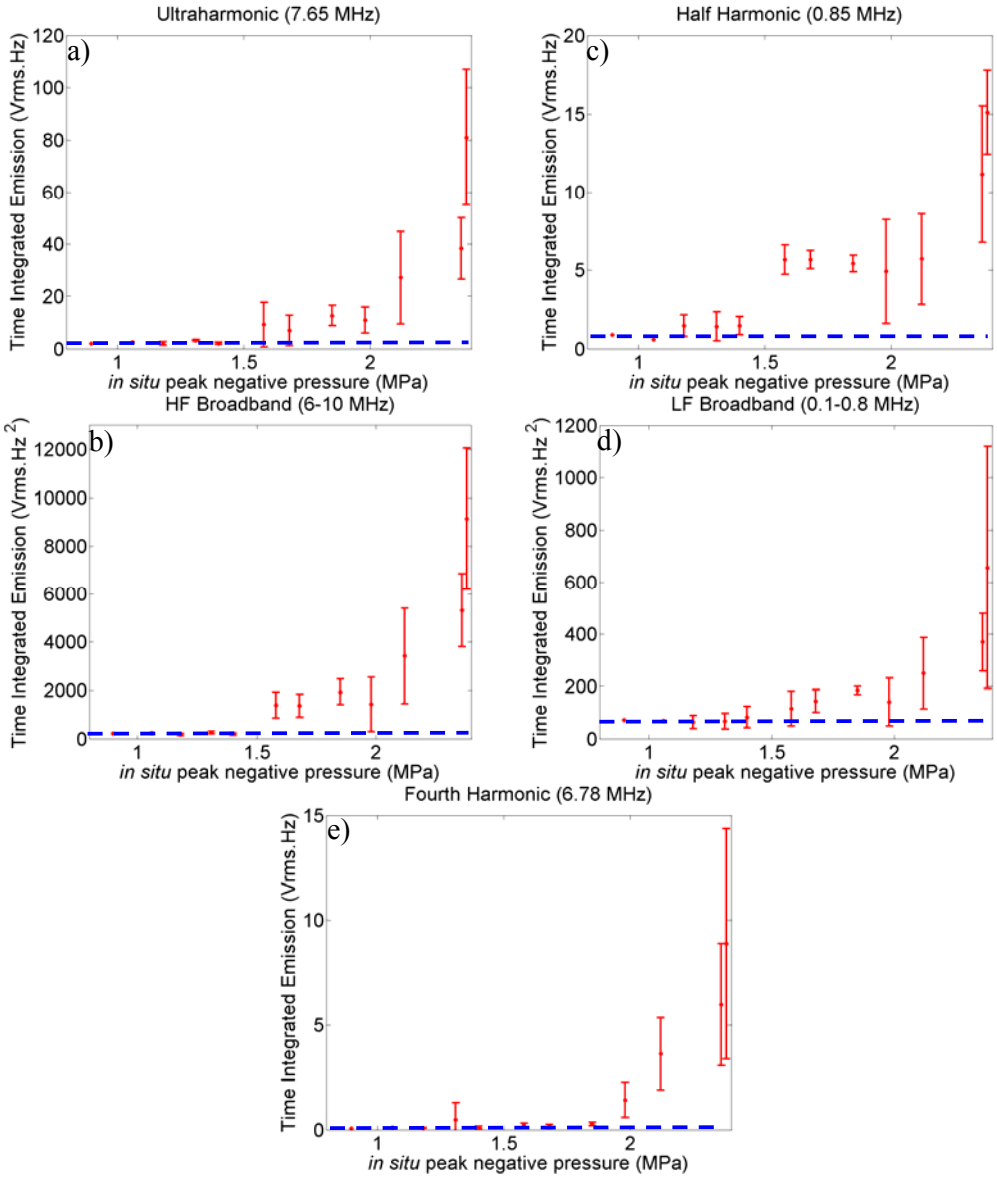

Figure 9.14. The average total time integrated (a) ultraharmonic, (b) half harmonic, (c) high frequency broadband emissions, (d) low frequency broadband emissions and (e) fourth harmonic at 40°C. Uncertainty, where shown, is the standard deviation of the average value, for n = 3-8. The blue dashed line indicates the averaged peak noise level measured from sham exposures.

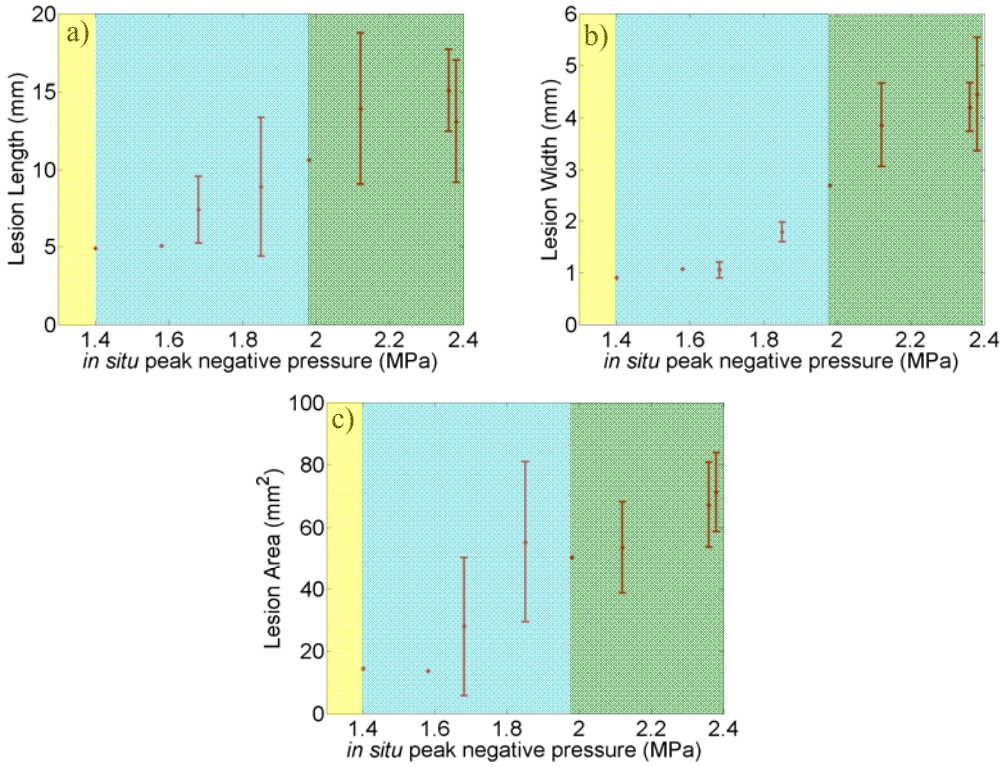

Figure 9.15. The average measured lesion length (a), width (b) and area (c) for peak negative pressures that generate a lesion from a single 4 s exposure. Uncertainty, where shown, is the standard deviation of the average value, for n = 3-8. The three colours are used to depict the three cavitation regimes approximately, non-inertial cavitation only (yellow), non-inertial and inertial cavitation (light blue) and acoustic cavitation and boiling (green).

Figure 9.15 shows the lesion dimensions generated from 4 s HIFU exposures in ex-vivo porcine kidney tissue. As the intensity (pressure) increases, the average lesion length in the kidney tissue plateaus, while the width of the lesion continues to increase. This was also observed with the exposures done at 20 ±2°C (Figure 9.8), however in this case it occurred at the higher intensity (pressure) of 1870 W/cm^2 (2.12 MPa).

9.4 Discussion

This study used a 7.5 MHz passive cavitation detection system to monitor half harmonic (0.850 MHz), fourth harmonic (6.78 MHz), ultraharmonic (7.65 MHz) and broadband emissions (0.1-0.8 and 6-10 MHz) from 4 s HIFU exposures in fresh ex-vivo porcine kidney tissue at 20 or 40°C. A diagnostic ultrasound imaging system was also used to monitor echogenicity change, electrical drive power and a microphone detected audible emissions for these exposures. This detection suite was used to identify the presence of

non-inertial cavitation by the presence of half harmonic emissions only. Inertial cavitation was identified from the presence of half harmonic and broadband emissions during the exposure. Boiling was identified from the simultaneous occurrence of power fluctuations, audible emissions and hyperechogenicity.

At 20^{o}C the ex-vivo kidney data showed that the intensity (pressure) threshold below which non-inertial cavitation was not detectable above noise was 611 W/cm^2 (1.40 MPa), as shown in Figure 9.3(e) and Figure 9.7(b). Inertial cavitation was detected at I_{sp} (pressure) $\geq$ 760 W/cm^2 (1.58 MPa), and boiling occurred $\geq$ 940 W/cm^2 (1.68 MPa) for 4 s HIFU exposures. There is a factor of 10 increase in the peak amplitude of the detected ultraharmonic, fourth harmonic and the high frequency broadband emissions (Figure 9.1(f), (i) and (l)) from the exposure where boiling occurred (2330 W/cm^2 / 2.36 MPa) detected thought this exposure compared to exposures that did not boil (Figure 9.1(e), (h) and (k)). This behaviour is similar to that seen for boiling exposures in ex-vivo bovine liver. The peak amplitude of the half harmonic emissions, for the exposures above the non-inertial cavitation threshold (Figure 9.1(b) and (c)), does not show this trend. This would suggest that boiling had the greatest effect on the presence of inertial cavitation, which could be the result of boiling bubbles seeding small cavitation nuclei that may subsequently undergo violent collapse.

The frequency range detected in the audible emissions (Figure 9.2(c)) is typically 6-20 kHz in kidney. In this example, it is possible to identify two events that caused audible emissions in kidney that had a magnitude greater than 5 dB. These occurred 0.2 and 1.7 s (± 0.02 s) into the HIFU exposure. The first time point also corresponded to an increase in the detected ultraharmonic, fourth harmonic and the high frequency broadband (Figure 9.1(f), (i) and (l)). This is similar to a boiling event that was discussed in section 7.2.3, which generated damage that was described as a ‘hole’ (Figure 7.19). Figure 9.16 shows the lesion that was generated from this exposure.

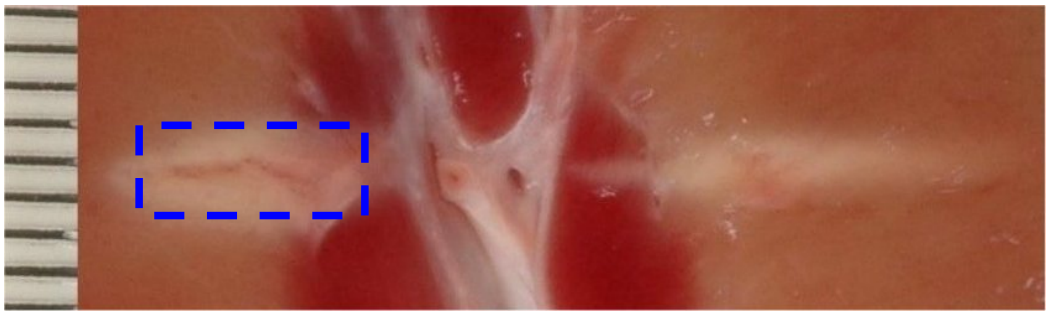

Figure 9.16. The lesion generated in ex-vivo kidney from the 2330 W/cm^2 (2.36 MPa) described in Figure 9.1 and Figure 9.2. The blue box highlights a region of the lesion where damaged characterised as 'holes' were observed. The rest of this lesion is on the other half of the kidney sample. This discontinuity is an artefact of the dissection process. The HIFU field propagated from left to right.

Figure 9.3 gives the percentage of the detected signals, from all exposures, which were above a baseline noise level (§4.2.4). This data gives a first impression of the intensities (pressures) required to generate signals which can be detected by the passive cavitation detection system. The detected second and fourth harmonics (Figure 9.3(a) and (d)) are above the noise level for the entire exposure range. This is most likely results from scattering from inhomogeneities in the tissue (as the kidney is more vascular than liver) of the non-linear HIFU field components. The acoustic emissions shown in Figure 9.3(b), (c), (e) and (f) have an intensity (pressure) threshold for which no acoustic emissions, greater than baseline noise, were detected. However this presentation of the data does not give any indication of the relative amplitude of the detected signals, as is shown for the different acoustic spectra in Figure 9.7. The uncertainly in these measurement was quite large, and in some cases was of the same order of magnitude as the average value. This highlights the variability in these measurements, which is likely to be due to the transient nature of cavitation activity as this data does not give any indication as to how the signals varied with time.

Figure 9.4 and Figure 9.6 show the complimentary data which shows when boiling occurs. In this study of kidney tissue, hyperechogenicity was only observed when power fluctuations occurred, indicating boiling. However, as shown in Figure 9.4, echogenicity was not observed for every exposure that boiled. This is most probably due to the lower resolution of the 1.93 MHz imaging probe compared with the 8.5 MHz linear probe used for the ex-vivo liver studies (§7.2.1). It is also worth noting that this figure shows that the hyperechogenicity did not track with the presence of a lesion. This agrees with the finding in section 8.3.2, that hyperechogenicity is not a good indication of lesion's

size. Another significant difference between these two studies is that the diagnostic imaging plane was parallel to the HIFU field with the kidney but perpendicular to it during the liver study. This gave a much smaller imaging cross-section of the boiled region in the kidney. Figure 9.6 shows the 'onset' times for the phenomena associated with boiling. This shows that as the intensity (pressure) increases the time for the point at which the 'onset' occurs, for these respective phenomena, decreases. The onset for drive power fluctuations and fourth harmonic increase show agreement within uncertainty of these measurements, where the audible emissions do not. This suggests that this phenomenon is the least sensitive in providing temporal information on the occurrence of boiling during the HIFU exposure. This could have been due to environmental laboratory factors as background noise has an effect on the levels of audible emissions that can be detected with the microphone.

Figure 9.7 shows the average total time integrated emissions for acoustic spectra detected with the 7.5 MHz passive cavitation detection system. It shows that there is an increase in the average amplitude of all the acoustic spectra for the exposures where boiling occurred ($\geq$ 940 Wcm^2 or 1.68 MPa), but there is also a large spread in this value, shown by the standard deviations. The reason for this could be due to two factors, firstly there could be greater amplitude signals, as seen in Figure 9.1((f), (i) and (l)), but it could also be that there is more activity during the exposure. This second possibility can be demonstrated by the differences between the detected half harmonic in Figure 9.1(b) and (c), even though they have roughly the same peak amplitude, the higher intensity exposure can be seen to have more activity throughout which would give it a greater time averaged value. This technique might be able to be used to identify a 'cavitation dose', which could be related to tissue damage.

Figure 9.8 shows the averaged lesion dimensions from the 4 s exposures in the ex-vivo porcine kidneys. No lesions were found in the tissue for the 4 s exposures below the inertial cavitation threshold. A trend that was also observed in the ex-vivo liver exposures was that as the HIFU intensity (pressure) increased the length of the lesion plateaued, whereas the width continued to increase. This effect is generally observed for exposures for which boiling occurs, and this is most likely the predominant cause of this. The boiling bubbles act as local scatterers in the tissue, shielding that behind, but causing greater energy deposition in that location, thus causing the lesion to increase in width rather than in length.

The exposure range studied was repeated in ex-vivo kidneys that were elevated to 40 ±2°C. Figure 9.9 to Figure 9.15 show data that has similarities with those already discussed, i.e. the time varying detected acoustic spectra, the detection of audible emissions, hyperechogenicity and electrical drive power fluctuations. However there are some significant differences, which warrant discussion. The first difference is shown by comparing Figure 9.11 with 9.3 and Figure 9.14 with 9.7. It can be seen that the intensities (pressures) required to cause detectable (above baseline noise) acoustic spectra are lower at the higher temperature. This detection of acoustic emissions at lower intensities (pressures) than previously seen (Figure 9.3) would suggest that the elevated temperature has caused a reduction in the acoustic cavitation threshold, as observed in ex-vivo bovine liver tissue (§7.2.3). Contrary to this, and perhaps rather surprising, is the observation that boiling seems to require greater HIFU intensities (pressures) at the higher temperature. This effect could be related to the effect of a temperature change on the available intra- and extra cellular liquid, but this would warrant further investigation.

The lesion dimensions (Figure 9.15) from exposures at this elevated temperature are of a comparable size (Figure 9.8) to those generated at equivalent exposures at the lower temperature. However lesions were created at lower HIFU intensity (pressure) at this elevated temperature, which was expected, as the tissue temperature would need less time to reach 56°C.

9.5 Conclusions

A cavitation threshold study was performed on ex-vivo porcine kidney tissue using active and passive cavitation detection. Since the passive transducer was coupled to the HIFU transducer it was possible to expose the kidney as a whole organ, moving position between each exposure. This more closely represents the clinical application of HIFU than the ex-vivo bovine liver tissue study (Chapter 7). The study was undertaken with the tissue at either 20 or 40 ±2°C. Table 9.1 shows the three cavitation thresholds that were found in ex-vivo kidney, at these two temperatures.

4 s Exposures	Non-inertial Cavitation	Inertial Cavitation	Boiling
Ex-vivo kidney at 20°C (n = 77)	≥ 611 W/cm^2 ≥ 1.40 MPa	≥ 760 W/cm^2 ≥ 1.58 MPa	≥ 940 W/cm^2 ≥ 1.68 MPa
Ex-vivo kidney at 40°C (n = 45)	≥ 485 W/cm^2 ≥ 1.31 MPa	≥ 611 W/cm^2 ≥ 1.40 MPa	≥ 1500 W/cm^2 ≥ 1.98 MPa

Table 9.1. In-situ I_{sp} and peak negative pressures required to generate cavitation activity in ex-vivo porcine kidney tissue, the uncertainty in the intensity and pressure measurements were 25 and 22% respectively.

At both tissue temperatures, exposure conditions were found for three separate regions of cavitation activity. The acoustic cavitation threshold was reduced when the tissue temperature was increased, in contrast to that found for the boiling threshold. Diagnostic ultrasound imagining, electrical drive power fluctuations and audible emissions were all observed during boiling exposures in the kidney. Hyperechogenicity was shown to be a useful indication of boiling but was however limited by the spatial resolution of the diagnostic imaging probe. It was found that the presence of hyperechogenicity was not a reliable indication of the presence of a lesion, as lesions were found without it being observed.

The development of the lesions along the acoustic axis (lesion length) was hindered by the presence of boiling, which also caused a great (often more than doubling) increase of lesion width. However, the increased temperature had little observable effect on the overall lesion size, but meant that the lesioning threshold was reached sooner.

This ex-vivo kidney study has demonstrated that the cavitation detection system can be used in different tissue types and that it has shown consistent results for both ex-vivo kidney and liver tissue.

10 – Perfused porcine liver study

In this chapter an investigation of the cavitation activity occurring, as a result of an HIFU exposure, in a more clinically relevant tissue model than ex-vivo bovine liver is described. This also provided pre-clinical testing of a system that could be used to monitor cavitation activity from shallow extra-corporeal treatments (<50 mm beneath the skin) in a clinical setting.

10.1 Introduction

The ex-vivo tissue used in the experiments described in earlier chapters suffers from autolysis, which starts as soon as the donor animal dies. This causes the generation of gas (Bamber *et al*, 1977). Tissue is degassed in an attempt to reduce this problem, and to provide a closer approximation to in-vivo tissue (Chapter 4). However, it is not possible to eliminate this effect. An ex-vivo porcine liver perfusion system was used in this study in order to maintain normal liver function for the duration of the HIFU experiments (up to 36 h). This system was designed for the preservation of liver for transplantation, and the system has been shown to maintain transplant viability for up to 72 h (Butler *et al*, 2002).

A perfused liver model has some significant differences from ex-vivo tissue. Autolysis, which is negligible in the perfused liver, is an important factor in ex-vivo tissue. This should minimise the number of cavitation nuclei present in the perfused tissue compared to ex-vivo tissue, making the generation of acoustic cavitation more difficult. However, the higher temperature of the perfused tissue (38^{o}C) than that of ex-vivo tissue (20^{o}C) may increase the internal gas/vapour pressures inside the bubbles, leading to the formation of gas/vapour filled cavities at lower negative pressures (Connolly and Fox, 1954). In addition, blood perfusion may cause heat to be lost, affecting lesion formation. Hill *et al* (1994) suggested that this would become significant for HIFU exposures longer than a ‘few seconds’. It is unclear if the addition of blood will effect cavitation activity since although it is know to carry nucleation sites (Chappell and Payne, 2006), a study with 1.1 MHz HIFU exposures found that no ‘significant cavitation activity’ was detected over the spatial average intensities between 560-2360 W/cm^2 (Poliachik *et al*, 1999).

Histological investigation is generally not successful on ex-vivo tissue since the decay of the tissue makes it difficult to distinguish between decay and ultrasound

induced cellular damage. A perfused liver system gives the opportunity to investigate lesions generated by HIFU exposures histologically. Rabkin *et al* (2006) reported the generation of 'voids' inside muscle cells *in-vivo* that had undergone HIFU treatments. These intra- and extra-cellular voids were believed to be produced by cavitation activity and/or boiling. Using 'histotripsy' (§2.4), Roberts *et al* (2002) were also demonstrated histologically that the use of this non-thermal mechanism of damaging tissue resulted in regions of liquefaction which could only have been generated by a mechanical process, e.g. acoustic cavitation.

The aim of this present study was to investigate the cavitation activity in a perfused liver model exposed to HIFU exposures comparable to those investigated *ex vivo* with the aim of providing a close approximation of the tissue to clinical HIFU applications, with the advantage of having no tissue motion.

10.2 Methods

10.2.1 *Perfused porcine liver system*

A cavitation study was performed in a 10 normothermic (porcine body temperature is 38^{o}C), isolated livers perfused with whole heparinised blood. Figure 10.1 shows a diagram of the system used to perfuse the liver.

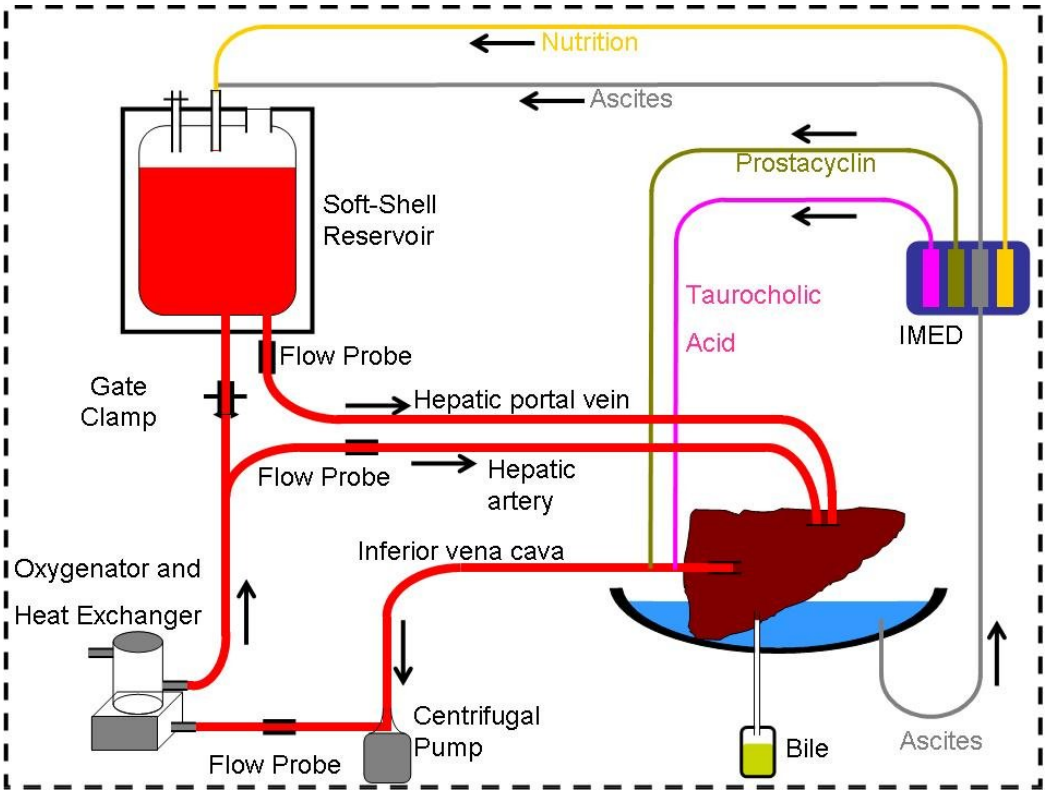

Figure 10.1. Schematic diagram showing the perfused liver system. A centrifugal pump was used to maintain non-pulsatile blood flow, and the heat exchanger maintained normal body temperature (38^{o}C). Blood parameters, such as oxygenation and glucose were maintained as close to their physiological values as possible.

Two 35-50 kg animals were used for each perfusion. The first animal was a blood donor, which provided between five to eight units of blood. These were stored in a fridge until they were needed. The liver from the second animal was surgically excised with great care and placed on the circuit, as described by Butler *et al* (2002), by the surgical staff from the John Radcliffe Hospital (Headington, Oxford, UK).

The perfused liver system was designed to maintain normal synthetic, metabolic and haemodynamic liver function, by maintaining the blood oxygenation level and normal body temperature (Butler *et al*, 2002). In addition, nutrients, prostacyclin and taurocholic acid were infused into the blood. The partial oxygen and carbon dioxide pressures in blood were maintained between 10 and 25 kPa, and between 4.0 and 6.0 kPa, respectively. A blood pH of 7.35 to 7.45 was maintained by controlling the carbon dioxide levels in the blood, by varying air flow affect its removal rate removal rate. The arterial pressure was maintained between 65 and 110 mmHg, whilst the hepatic portal vein pressure was kept below 11 mmHg. Normal blood glucose levels were maintained

between 8 and 15 mmol/l. These parameters were monitored on an hourly basis for the entire duration of each experiment. Heparin (0.8 ml) and antibiotics (5 ml) were injected every four hours. Arterial blood flow rate was maintained at approximately 0.5 litres per minute, and for the hepatic portal vein, 1.5 litres per minute.

The liver was placed in a metallic bowl with a central drain plate through which the ascites were collected and re-circulated into the blood perfusion circuit. For the first eight experiments, the liver was mounted on a number of sterile, perfusate filled gloves in order to raise it above any hard surface and to minimise the amount of degassed water required on top of the liver for acoustic coupling. For the last two experiments the gloves were superseded with degassed water filled sterilised condoms. For these final experiments, the ascites level was raised in order that it provide improved acoustic coupling between separate lobes of the liver.

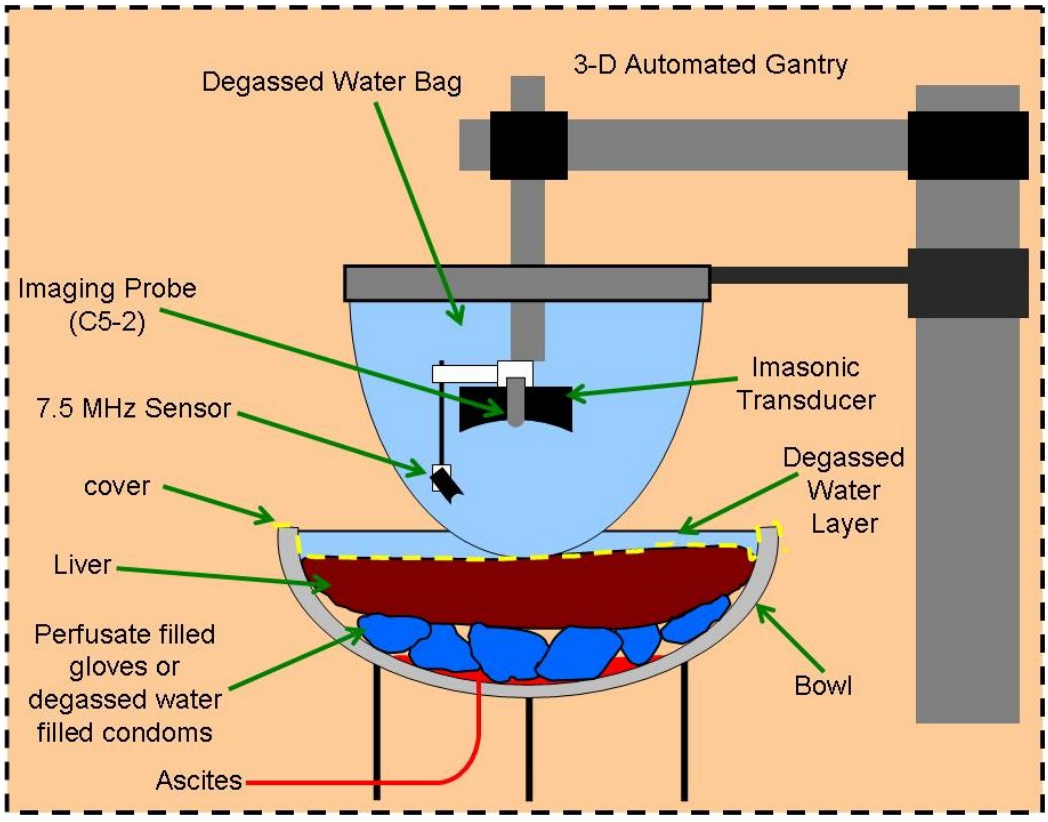

Figure 10.2. Schematic diagram demonstrating how the HIFU exposure of the perfused liver was achieved.

Figure 10.2 shows a schematic diagram of the transducers, water bag and liver positioning for this study. The HIFU transducer and 7.5 MHz sensor used in the passive

cavitation detection system were placed inside a large degassed water filled bag. A sterile cover (bowel bag) was placed on the surface of the liver, and extended over the entire metal bowl. It was filled with a shallow layer of (non-sterile) degassed water. Acoustic coupling between the liver and the HIFU beam was achieved by lowering the larger water bag into contact with the shallower one. This arrangement was used to minimise the pressure that the coupling fluid exerted on the perfused liver.

The 10 strip Imasonic HIFU transducer (§5.1.2) used to expose the liver, at a focal depth of approximately 10 mm, was mounted on the 3-D automated gantry (§5.3). The Zonare C5-2 diagnostic imaging probe (§4.3.1) was mounted within the central imaging aperture of the HIFU transducer.

10.2.2 *Cavitation detection and contrast agents*

The 7.5 MHz passive cavitation detection system, described in section 7.3, was used to study the acoustic spectra generated during 5s HIFU exposures in perfused livers. A number of different passive sensors were considered for this series of experiments. The 10 MHz sensor was unsuitable as its shorter focal length would have restricted the maximum HIFU focal depth to 10 mm. Available, longer focal length sensors (up to 100 mm) were found, in an ex-vivo tissue study, to be a factor of 10 less sensitive than the 10 MHz sensor. The 7.5 MHz sensor was thus a compromise between these two factors. Audible emissions (2-20 kHz) were monitored, in a limited number of the livers, using a microphone, covered by a condom, submerged into the ascites (§7.2.1), and electrical drive power was monitored (§4.3.2).

In an effort to maximise the usable liver volume for exposures, the focal depth of the HIFU was varied. This approach differed from the ex-vivo liver experiments, where it was possible to cut samples to the required dimensions. The focal peak of the HIFU field was placed 10 ±2.5 mm below the liver surface. Each exposure was 5 s long, with an I_{sp} in the range 50-2890 W/cm^2 ±20% divided into 16 levels (50, 70, 110, 170, 260, 320, 400, 500, 640, 790, 980, 1240, 1560, 1950, 2420 and 2890 W/cm^2). For the Imasonic transducer, this gave measured peak negative pressures in the range 0.48-2.14 MPa ±17% (0.48. 0.59, 0.70, 0.81, 0.98, 1.06, 1.15, 1.26, 1.30, 1.43, 1.53, 1.65, 1.77 1.91, 2.01, 2.10 and 2.14 MPa). It is worth noting that each liver was shared between approximately four other experimenters thus it was not possible to use the each entire liver for this study.

For the last three perfused livers in this experimental series, Levovist® (Schering, Berlin, Germany) contrast agent was injected into the hepatic portal vein. The contrast agent was made up to a concentration of 400 mg/ml following the manufacturer's instructions. This concentration gave, in each bottle, 10.5 ml of solution. A single dose of 3 ml was injected before each HIFU exposure. B-mode ultrasound images were acquired before injection, after injection (~10 frames as to minimise bubble destruction) and after the HIFU exposure. The HIFU exposures took place 1-3 mins after injection of the contrast agent, to allow for the post injection B-mode images to be acquired. Each bottle gave enough contrast agent for three HIFU exposures, after which a fresh batch was prepared. The perfused livers, with added contrast agent, were exposed for 5 s over the HIFU intensity ranges of 30-2420 W/cm^2 (0.40-2.01 MPa) over 13 increments of 30, 50, 70, 110, 400, 500, 640, 790, 980, 1240, 1560, 1950 and 2420 W/cm^2 (0.40, 0.59, 0.70, 1.15, 1.26, 1.30, 1.43, 1.53, 1.65, 1.77, 1.91 and 2.01 MPa).

10.2.3 *Lesion photography and Histology*

The photography system (Chapter 5) was transported with the HIFU apparatus for each of 10 perfusion experiments. It was only possible to dissect the liver and photograph any lesions disconnection from the perfusion circuit. On some occasions there was little visible contrast between the lesioned and normal tissue due to darkening of the perfusing blood, which made their identification difficult. In an effort to aid the dissection of the liver, surface "marker" lesions were usually used (similarly to the method described in §9.2). Immediately after the photographs had been taken, the individual liver samples were fixed in 10% normal buffered formalin to allow samples to be processed for histological analysis.

Chaturika Jayadewa, a fellow Ph.D student with a background in biology, performed all the histological processing of these samples. A basic description of the technique used follows, for a more detailed description see Bancroft and Cook (1994). After samples had been left to fix in formalin for a minimum of a week, each was either trimmed to fit into a single histology cassette or cut in half, and placed in two. The samples were taken to wax using a Tissue-tek VIP processor (Miles Scientific, UK), and embedded using a Microm EC-350-1 system (Walldorf, Germany). A Rotary 3003 scientific microtome (PFM, UK) was used to section sample blocks at 5 μm intervals. Sections were taken until the entire lesion was contained on one slide, to ensure minimum tissue loss. The sectioned tissue was placed in a water bath at 45^{o}C until

being transferred to plain glass slides for tinctorial staining. The slides were then placed on a hot plate at 60^{o}C until dry. Hematoxylin and Eosin **(**H&E**)** staining was carried out using a standard working protocol, which allows the examination of tissue morphology.

Once the samples were stained, it was possible to view them using a transmission BX51 microscope (Olympus Optical Co. Ltd, London, UK) with high magnification objectives. The slides were placed onto a motorised scanning stage (Prior Scientific Instruments Ltd, Cambridge, UK) that allowed the entire sample to be scanned at x40 magnification. A desktop computer connected to the microscope and scanning stage, running analySIS (soft imaging system, Munster, Germany) image acquisition software, acquired these images.

10.3 Results

10.3.1 *Cavitation threshold study*

A cavitation threshold study was undertaken in 7/10 perfused liver experiments. Five second duration exposures at a range of in-situ intensities (peak negative pressure) of 50-2890 W/cm^2 ±20% (0.48-2.14 MPa ±17%).

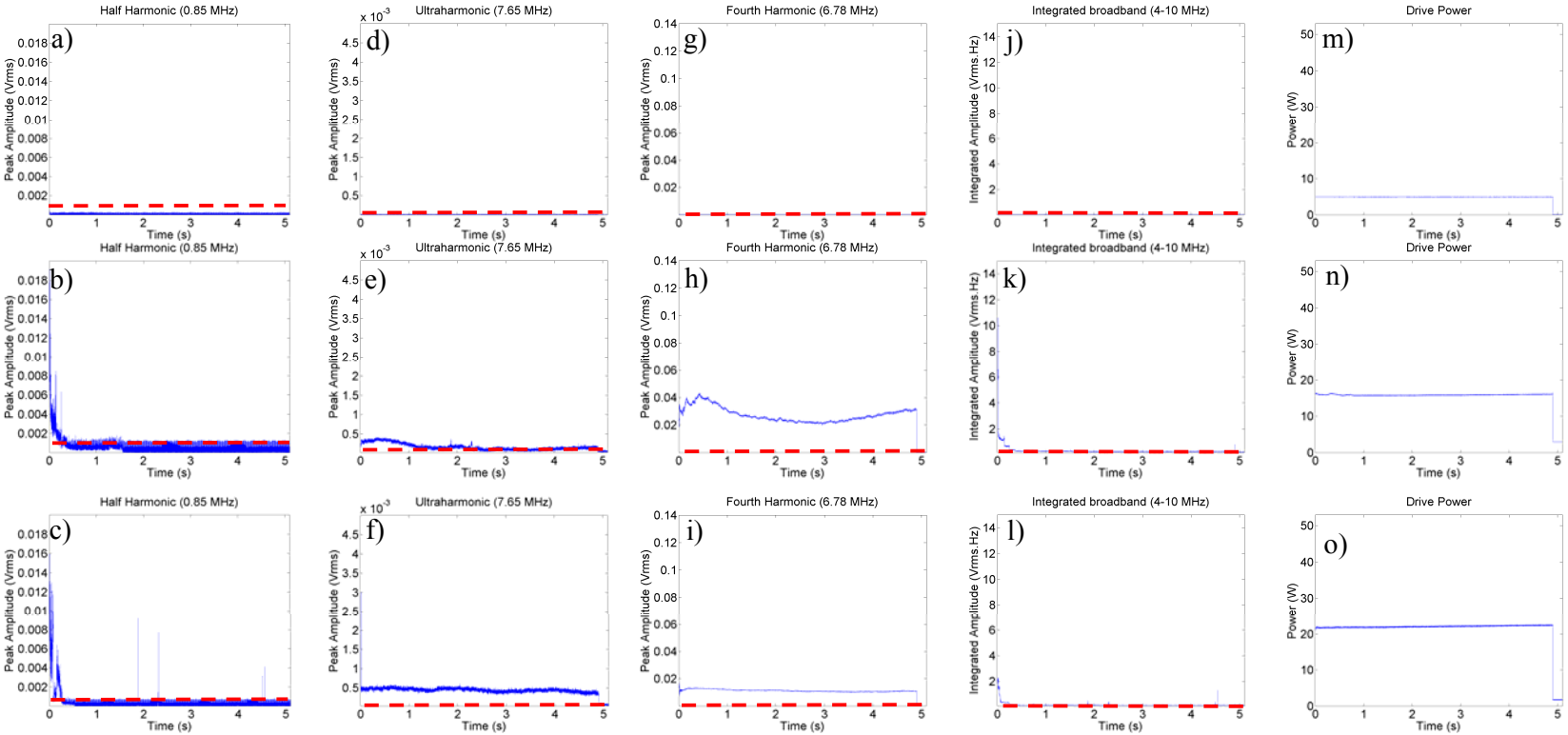

Figure 10.3. The detected half harmonic (a-c), ultraharmonic (d-f), fourth harmonic (g-i), integrated broadband (j-l) and electrical drive power (m-o) for three 5s HIFU exposures in a perfused liver. The first row is at 320 W/cm^2 (1.06 MPa) the second row at 790 W/cm^2 (1.43 MPa), and he third row at 980 W/cm^2 (1.53 MPa). The dashed red line indicated the peak noise level measured from a sham exposure.

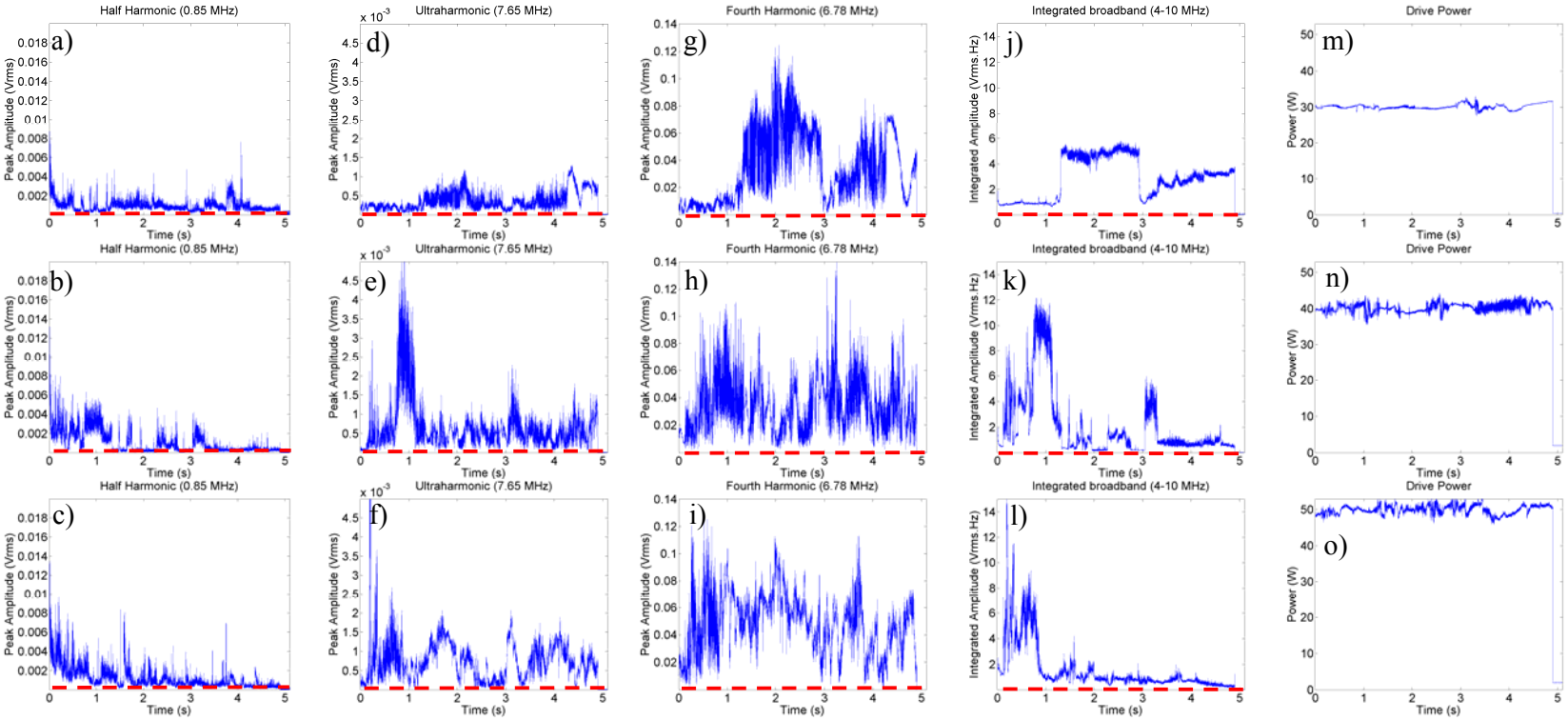

Figure 10.4. The detected half harmonic (a-c), ultraharmonic (d-f), fourth harmonic (g-i), integrated broadband (j-l) and electrical drive power (m-o) for three 5s HIFU exposures in perfused liver. The first row is at 1560 W/cm^2 (1.77 MPa), the second row at 2420 W/cm^2 (2.01 MPa), and the third row at 2890 W/cm^2 (2.10 MPa). The dashed red line indicated the peak noise level measured from a sham exposure.

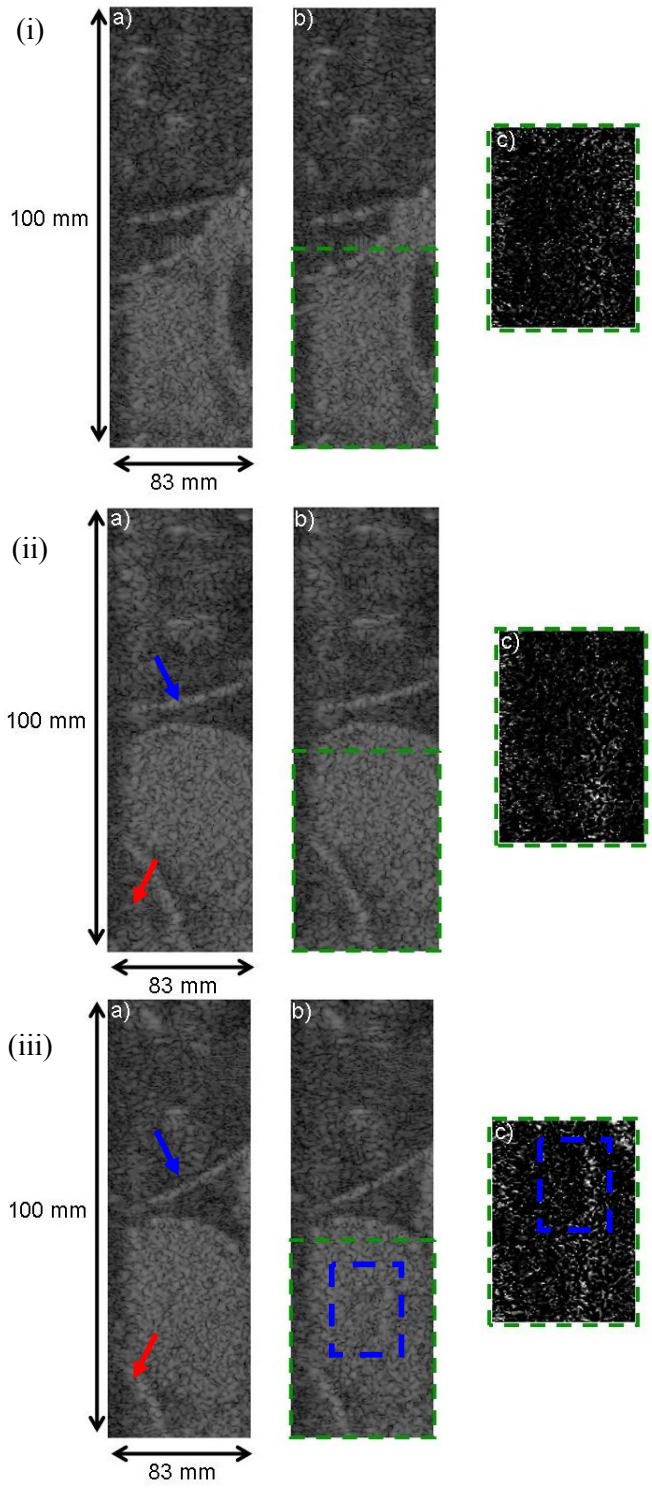

Figure 10.5. B-mode images acquired before (a) and after (b) with the corresponding subtraction image (c) for the 5s HIFU exposures at (i) 320 W/cm^2 (1.06 MPa), (ii) 980 W/cm^2 (1.53 MPa) and (iii) 2890 W/cm^2 (2.10 MPa). The blue dashed box highlights the region of hyperechogenicity. The liver tissue can be seen in the lower half of the images. The cover holding the lower water bath (Figure 10.2) can be seen in the images (blue arrows) as can part of a perfusate filled glove (red arrows) in two of the exposures.

Figure 10.3 and Figure 10.4 show acoustic spectra detected during 5 s exposures in the perfused liver. No acoustic emissions were detected at the lowest exposure level of 320 W/cm^2 (1.06 MPa) (Figure 10.3(a), (d) and (j)). Acoustic emissions can be seen in the higher intensity exposures in Figure 10.3; the majority of the emissions occur from the start of the exposures. No electrical drive power fluctuations were detected during the three exposures shown in Figure 10.3. There is a significant increase in the acoustic emissions detected from the exposures shown in Figure 10.4 as compared with those shown in Figure 10.3. Drive power fluctuations are seen during these exposures, indicating that boiling had occurred. The peak amplitude of the half harmonic emissions (Figure 10.4(a-c)) does not significantly change for these three different exposure levels.

Figure 10.5 shows B-mode images that were acquired before and after a HIFU exposure with the corresponding subtraction image. This figure shows images from three HIFU exposures at 320, 980 and 2890 W/cm^2 (1.06, 1.53 and 2.10 MPa), the liver tissue can be seen in the lower half of the images. The cover holding the lower water bath (Figure 10.2) can be seen in the images (blue arrows) as can part of a perfusate filled glove (red arrows) in two of the exposures. A region of hyperechogenicity can be seen in Figure 10.5(iii), within the blue dashed box. This is difficult to identify from the B-mode images alone, but the subtraction image shows a small region of echogenicity.

Figure 10.7 shows photographs acquired using the microscope system, of the histological tissue sample, where the liver tissue as exposed to 980 W/cm^2 (1.53 MPa) for 5 s. Figure 10.7(a) shows a composite image of multiple scans of cross section of the lesion taken at 40x magnification. Figure 10.7(b) shows the region outlined in (a) at a higher magnification (x200). Figure 10.7(c) and (d) are photographs of the sample taken at the highest magnification (x400). Figure 10.7(c) shows unexposed tissue to provide direct comparison with exposed tissue (d). The most noticeable difference is the increase in extra cellular spacing (shown as white in Figure 10.7(d)), damage that could be caused by of acoustic cavitation. Figure 10.7(b) shows that these regions occur non-uniformly throughout the lesioned area. The difference in the colour (shade of pink) between lesioned and non-lesioned areas (e.g. Figure 10.7(c)) is due to the denaturation of the proteins. The large holes seen in Figure 10.7(a) are vessels (green and blue arrows). Figure 10.6 shows a photograph taken of the dissected liver tissue before the sample was placed into fixative. This surface does not directly correspond to that seen

in Figure 10.7(a) as this section may be deeper into the tissue. However, the blood vessel can be seen at the bottom in both of these images. You can also see the blood in the septae radiating outwards from the lesion. This is thought to be an exaggerated affect due to the blood being heparinised.

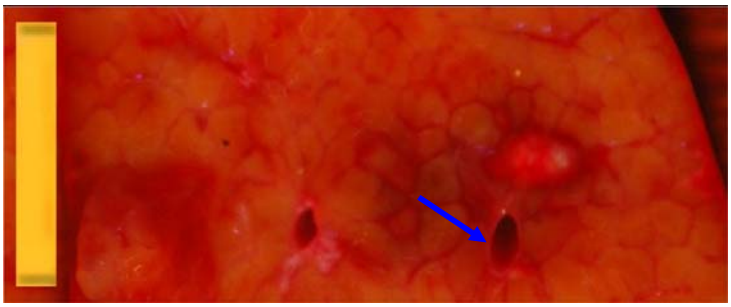

Figure 10.6. Macroscopic photograph of the lesion shown in Figure 10.7, the scale bar indicates 10 mm and the HIFU was incident from the right of the image. The blue arrow indicates a blood vessel.

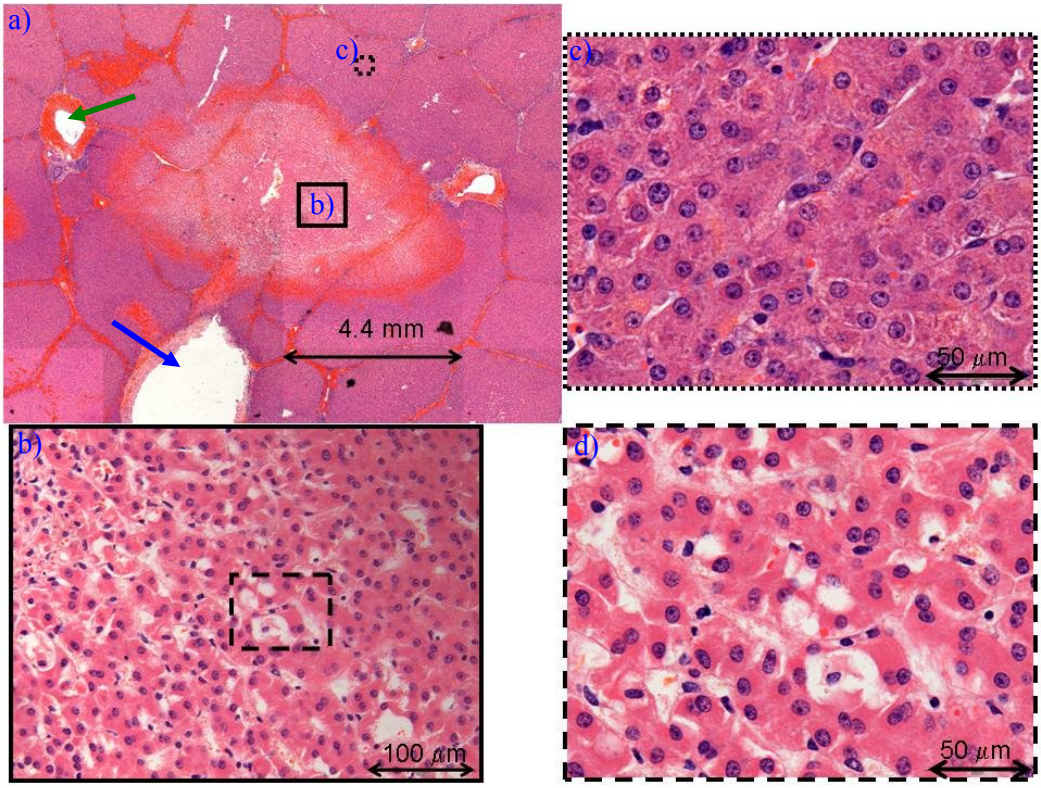

Figure 10.7. Photographs at different magnifications of the H&E stained histological sample of perfused liver exposed to 5 s of HIFU at 980 W/cm^2 (1.53 MPa) (Figure 10.3(c, f, i, l and o)). (a) shows a composite image of multiple views acquired at 40x magnification, (b), (c) and (d) show images taken at higher magnifications, where (c) is unexposed tissue. The blue arrow indicates a blood vessel, where the green one indicates a hepatic triad (artery, vein and bile duct complex).

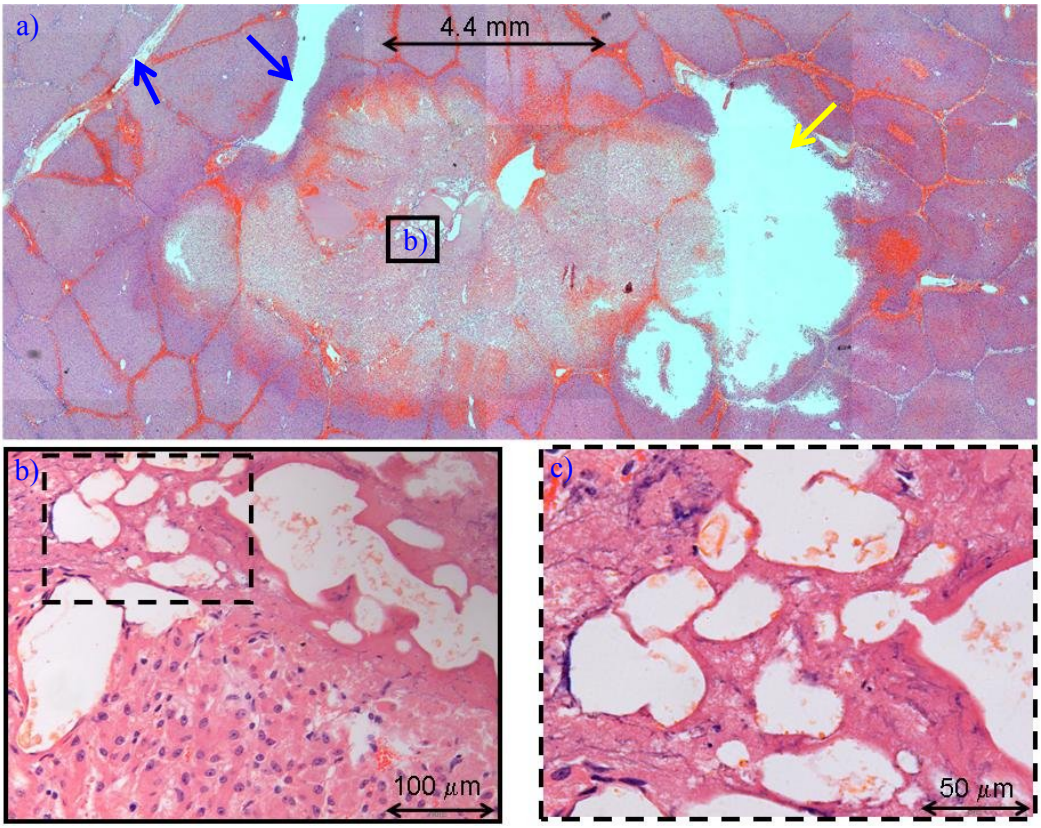

Figure 10.8. Photographs at different magnifications of the H&E stained histological sample of perfused liver exposed to 5 s of HIFU at 2890 W/cm^2 (2.10 MPa) (Figure 10.4(c, f, i, l and o)) .(a) shows a composite image of multiple views acquired at 40x magnification, (b) and (c) show the highlighted areas at higher magnifications. The blue arrows indicate blood vessels, where the yellow arrow shows an artefact introduced from tissue processing.

Figure 10.8 shows photographs of the histology obtained from an exposure in which boiling was seen (Figure 10.4(c, f, i, l and o)). At higher magnification, damage that is only present when boiling occurs can be seen. This is characterised by large holes (compared with those thought to be due to acoustic cavitation) in the tissue surrounded by homogenised regions. Figure 10.9 gives further examples of the histological damage seen when boiling occurs (Figure 10.11). The HIFU intensity was 2420 W/cm^2 (2.01 MPa) for 5 s. An artefact of the histological processing, the vertical 'crack' running from top to bottom in Figure 10.9(a) can also be seen (green arrow). The two expanded regions (Figure 10.9(b) and (c)) show further examples of distinct holes created in the tissue (~2.5 mm). Figure 10.10 shows this lesion immediately before the tissue was placed into fixative. Possible locations of blood vessels within the lesion are highlighted

by blue boxes, which correspond to the locations of the holes seen in the composite histological image (highlighted with blue arrows).

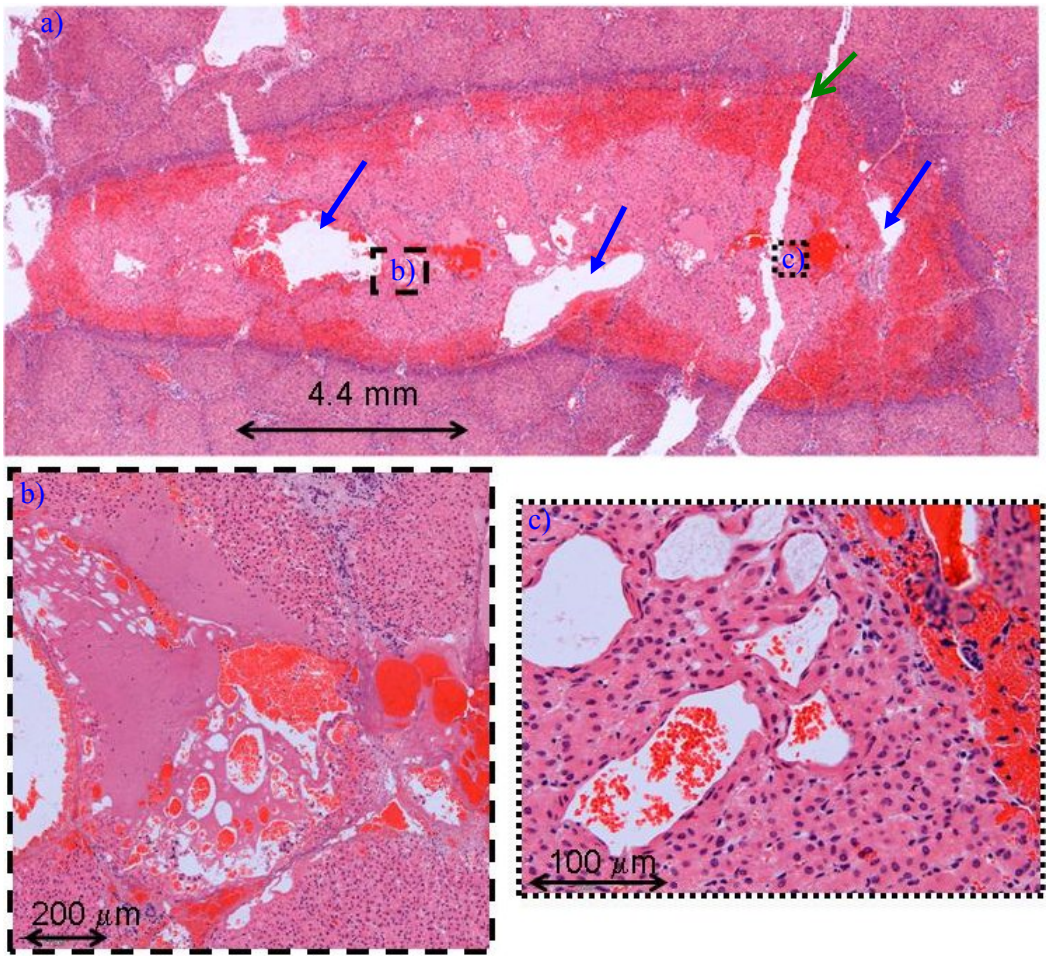

Figure 10.9. Photographs of the histological samples of the 5 s HIFU exposure at 2420 W/cm^2 (2.01 MPa). (a) shows a composite image of multiple slides acquired at 40x magnification, (b) and (c) show the highlighted areas in (a) at higher magnifications. The blue arrows indicate blood vessels, where the green arrow shows a crack in the sample introduced from tissue processing.

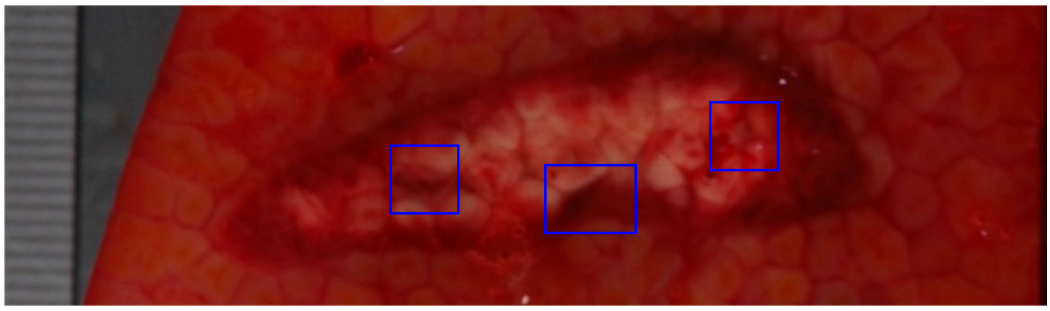

Figure 10.10. A photograph of the lesion shown in Figure 10.9, the scale bar is in 1 mm increments and the HIFU field propagated from right to left in the image. The blue boxes highlight possible locations of blood vessels.

Figure 10.11 shows the acoustic spectra and audible emissions that were detected during the 5 s HIFU exposure shown in Figure 10.9. Figure 10.11(d) shows high frequency broadband emissions, with the peak activity occurring at approximately the same time as the start of the audible emissions at approximately 1.25 s (Figure 10.11(f)).

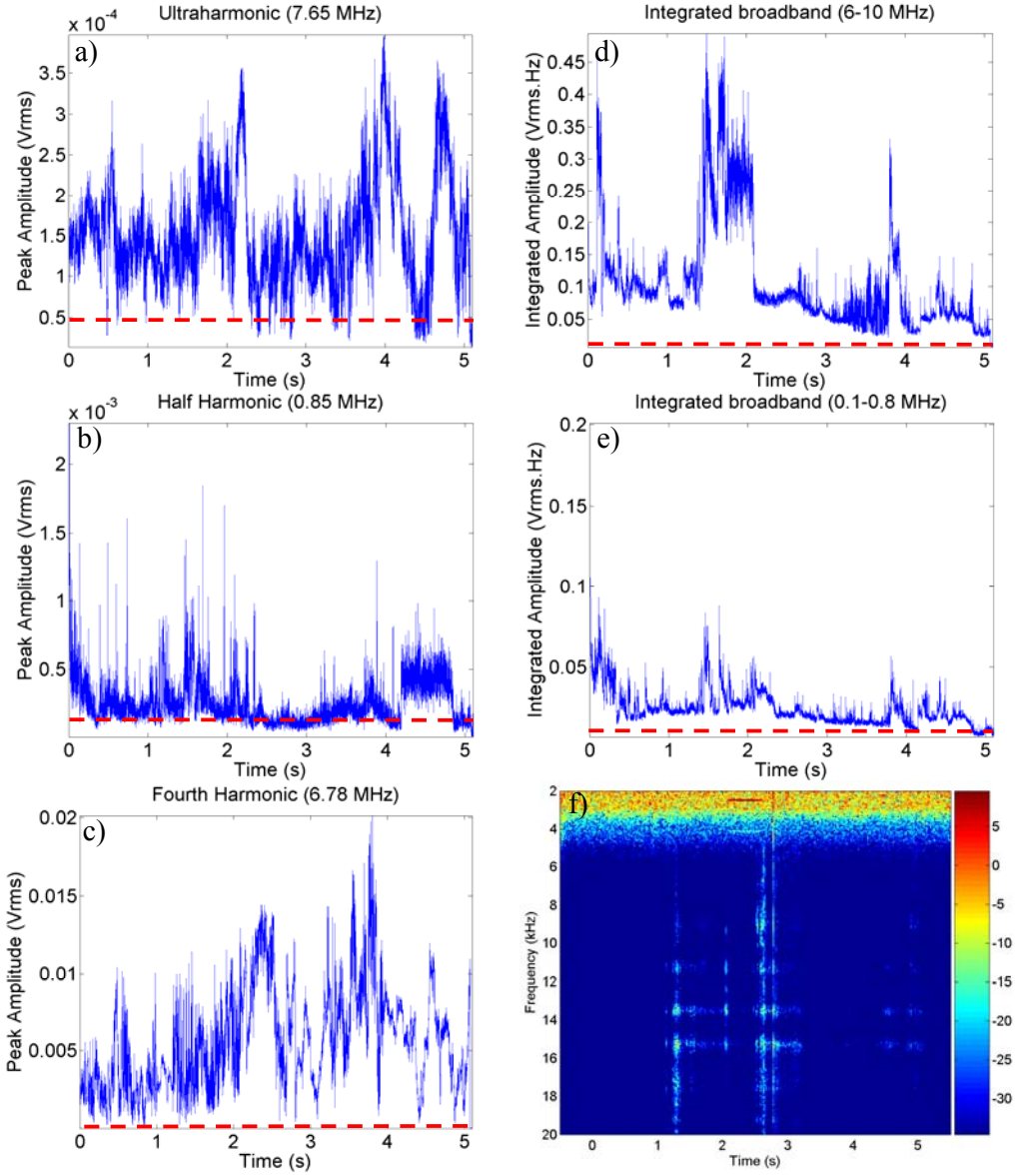

Figure 10.11. The detected (a) ultraharmonic, (b) half harmonic, (c) high frequency broadband emissions, (d) low frequency broadband emissions, (e) fourth harmonic and (f) audible emissions, from a single 5 s 2420 W/cm^2 (2.01 MPa) exposure in perfused liver. The red dashed line indicates the peak noise measured from a sham exposure.

A 2.5 kHz audible tone that occurred after approximately 2.2 s for 0.5s can be seen in Figure 10.11(f). This was due to the microphone detecting the regular beeps, which originated from the equipment connected to the perfused liver.

Figure 10.12 shows the percentage of acoustic spectra, for all exposures in this study, which contained signals above the predefined noise threshold section 4.2.4.

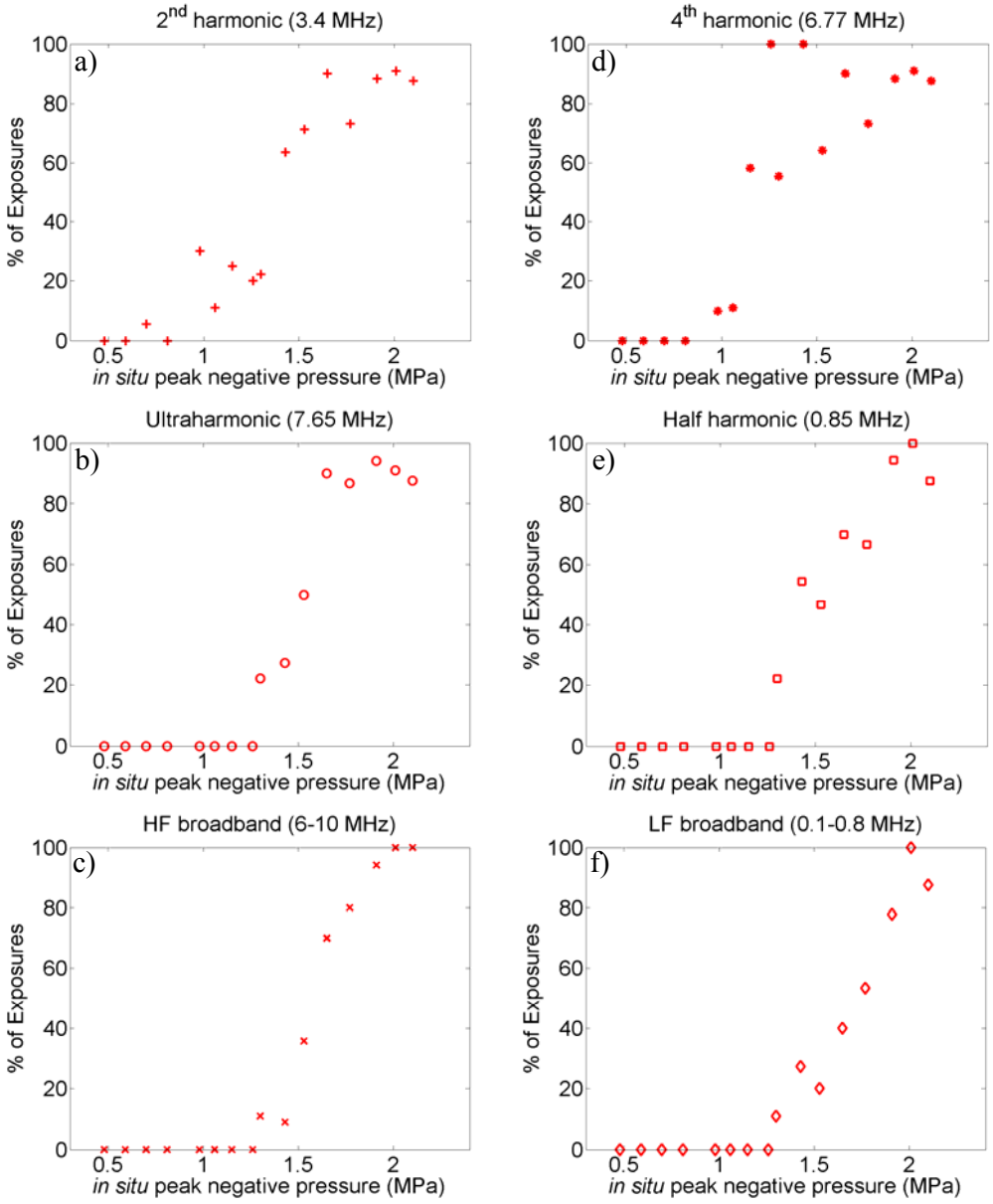

Figure 10.12. The percentage of detected signals, measured with the 7.5 MHz passive cavitation detection system, which are greater than the corresponding noise levels at any time during the exposure. The signals are measured during 5 s HIFU exposures of perfused liver over the range 50-2890 W/cm^2 (0.48-2.10 MPa), where n= 3-18 for each exposure level.

The second and fourth harmonics (Figure 10.12(a) and (d)), (most likely generated from scattering of frequencies arising from non-linear propagation of the drive frequency), were detected at lower drive levels than the signals generated from bubble oscillations (Figure 10.12 (b, c, e and f)). These were only detected above 640 W/cm^2 (1.30 MPa) and, as the intensity (pressure) increases, the probability of an emission being above the

noise level can be seen to increase. This value gives an indication of the threshold for detection of signals above the noise level.

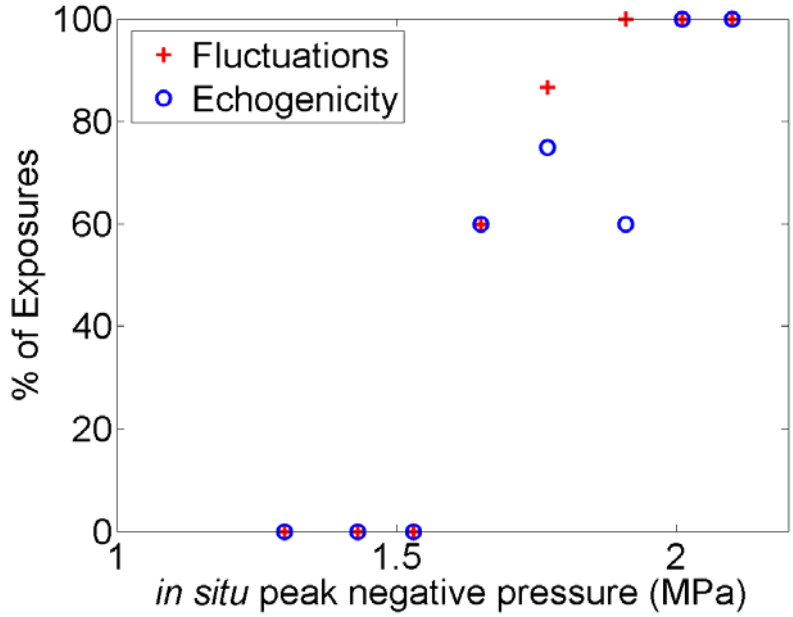

Figure 10.13. The percentage of 5 s HIFU exposures in perfused liver that demonstrated an increase in echogenicity and electrical drive power fluctuations.

Figure 10.13 shows the percentage of 5 s HIFU exposures in the perfused liver during which electrical drive power fluctuations above noise and/or hyperechogenicity were seen. Both indicators only occurred at an exposure level of 1240 W/cm^2 (1.65 MPa) and the probability of occurrence can be seen to increase with intensity (negative pressure). This suggests that boiling occurred during the exposures at and above this level.

Figure 10.14 shows the averaged total time integrated emissions for the acoustic spectra shown in Figure 10.12. As the intensity (negative pressure) increases there is an increase in detected signal. However, the uncertainty in the data also increases, that is, there is greater spread in the total time integrated emission values measured.

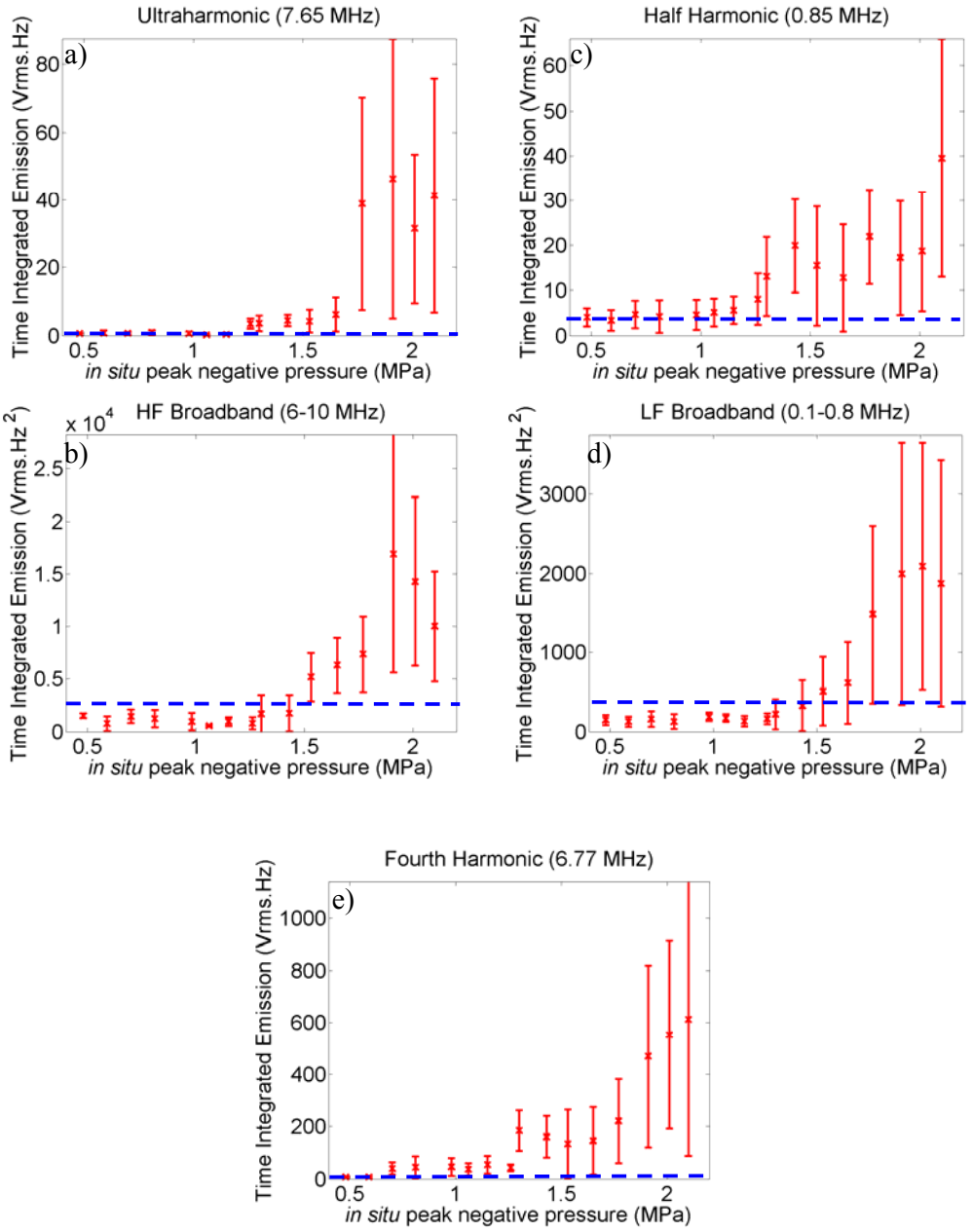

Figure 10.14. The averaged total time integrated (a) ultraharmonic, (b) high frequency broadband emissions, (c) half harmonic, (d) low frequency broadband emissions and (e) fourth harmonic. Uncertainty, where shown, is the standard deviation n = 3-18. The dashed blue line indicated the peak average noise level measured from the sham exposures done in this study.

10.3.2 Cavitation and Contrast Agent study

A study of the effect of introducing Levovist ultrasound contrast agent on cavitation activity was performed using the final three perfused livers. The livers were exposed in different locations, but at the same focal depth, with and without contrast agent at intensities (pressures) in the range 30-2420 W/cm^2 (0.40-2.01 MPa).

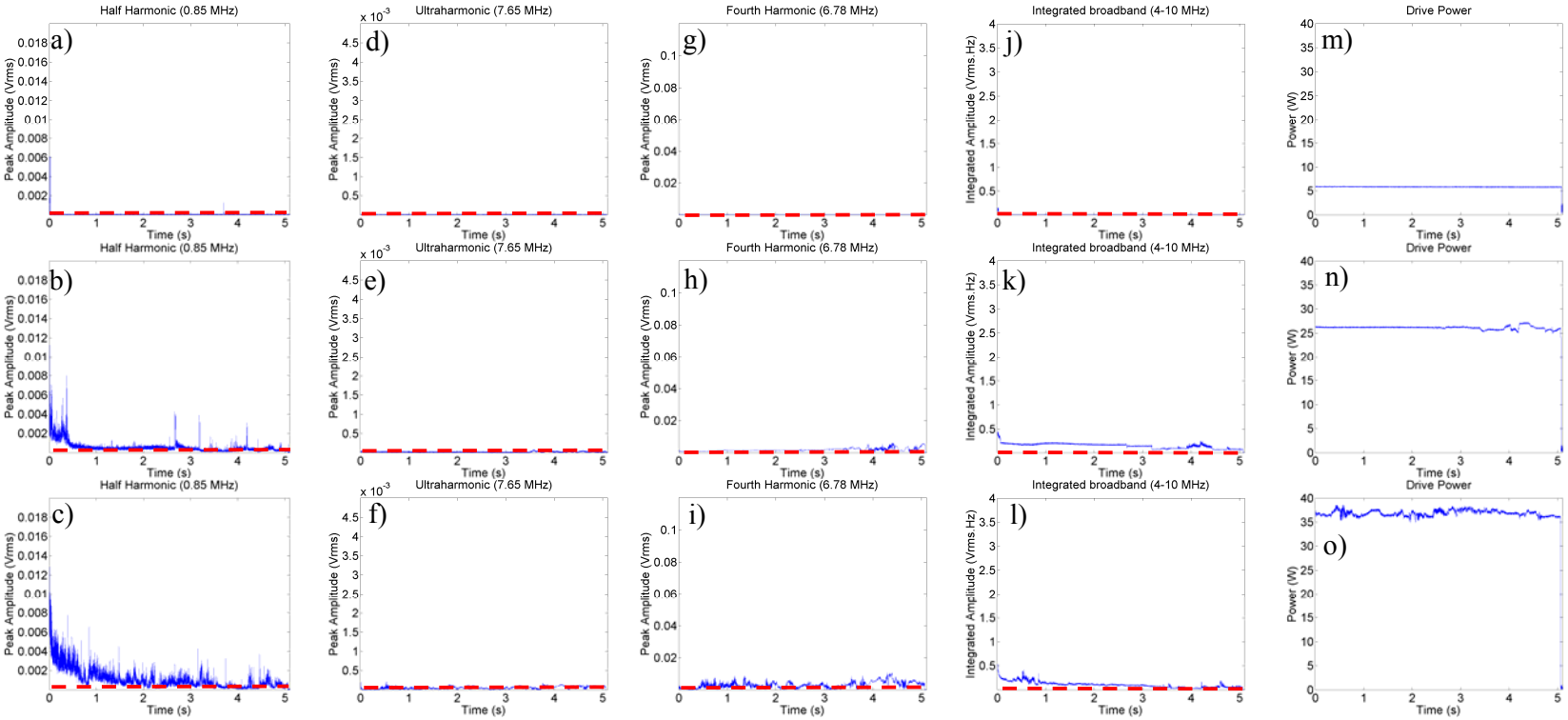

Figure 10.15. The detected half harmonic (a-c), ultraharmonic (d-f), fourth harmonic (g-i), integrated broadband (j-l) and electrical drive power (m-o) from three 5 s HIFU exposures in perfused liver without contrast agent. Where the first row is at 400 W/cm^2 (1.15 MPa), second row is at 980 W/cm^2 (1.53 MPa), and the third row is at 1950 W/cm^2 (1.91 MPa). The red dashed line indicates the peak noise measured from a sham exposure.

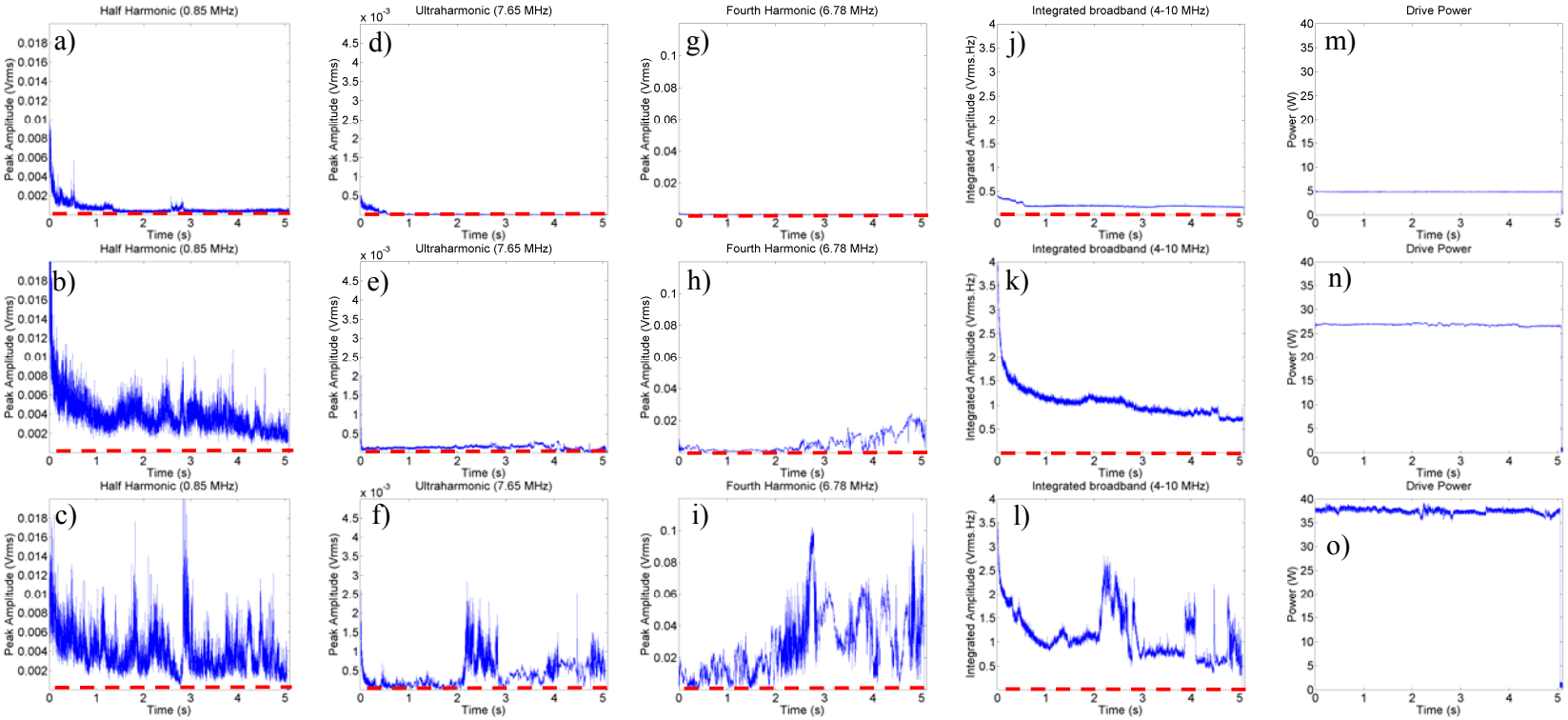

Figure 10.16. The detected half harmonic (a-c), ultraharmonic (d-f), fourth harmonic (g-i), integrated broadband (j-l) and electrical drive power (m-o) for three 5s HIFU exposures in perfused liver with the addition of 3 ml of Levovist immediately prior to the HIFU exposure. Where the first row is at 400 W/cm^2 (1.15 MPa), second row is at 980 W/cm^2 (1.53 MPa), and the third row is at 1950 W/cm^2 (1.91 MPa). The red dashed line indicates the peak noise measured from a sham exposure.

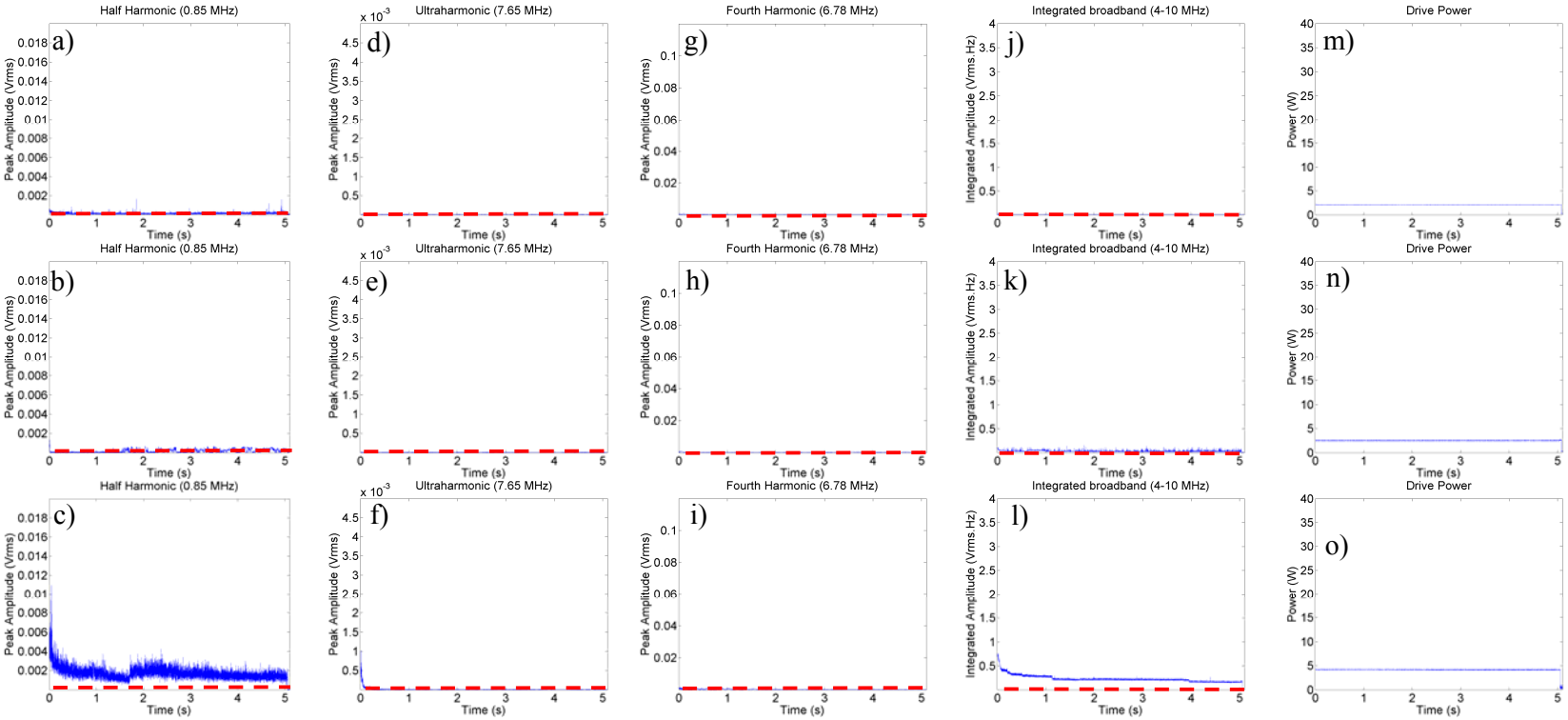

Figure 10.17. The detected half harmonic (a-c), ultraharmonic (d-f), fourth harmonic (g-i), integrated broadband (j-l) and electrical drive power (m-o) for three 5 s HIFU exposures in perfused liver with the addition of 3 ml of Levovist immediately prior to the HIFU exposure. Where the first row is at 30 W/cm^2 (0.40 MPa), the second row is at 70 W/cm^2 (0.59 MPa), and the third row is at 140 W/cm^2 (0.75 MPa). The red dashed line indicates the peak noise measured from a sham exposure.

Figure 10.15 and Figure 10.16 show acoustic spectra and drive power measurements, which were recorded during 5 s HIFU exposures with (Figure 10.16) and without (Figure 10.15) ultrasound contrast agents present. The presence of contrast agent increases the amplitude of the detected acoustic spectra at each exposure levels (compared to Figure 10.15). In addition, Figure 10.16(a, d, g, j and m) shows that acoustic spectra (half harmonic, ultraharmonic, fourth harmonic and broadband emissions) were detected below the cavitation threshold demonstrated in the previous section. Figure 10.17 shows that, in the presence of acoustic contrast agents, acoustic emissions were detected at intensity (negative pressure) levels as low as 30 W/cm^2 (0.40 MPa).

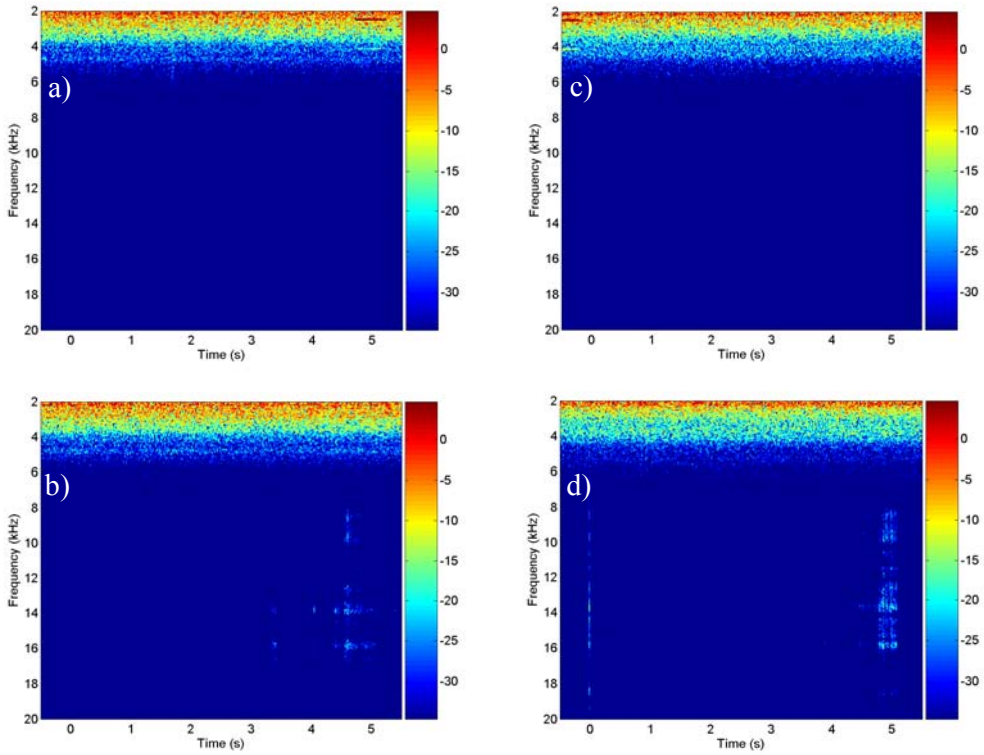

Figure 10.18. The audible emissions that were detected from (a&c) 400 and (b&d) 1950 W/cm^2 (1.15 and 1.91 MPa) 5 s exposures shown in Figure 10.15 and Figure 10.16, (a&b) without and (c&d) with contrast agent. A 2.5 kHz tone can be identified at the start and end of (c) and (d) respectively.

Figure 10.18 shows audible emissions detected from HIFU exposures with and without contrast agent. Figure 10.18(b) and (d) show audible emissions from "boiling" exposures, at 1240 W/cm^2 (1.65 MPa), with and without contrast agent, respectively. Figure 10.18(c) shows that the exposure of the perfused liver in the presence of contrast

agent does not generate audible emissions similar to those detected when boiling occurs. Figure 10.19 shows the measured change in B-mode image intensity (calculated over a rectangular region encompassing the tissue in the frame, Chapter 7) for the perfused liver resulting from the introduction of contrast agent. The images were acquired at a frame rate of 1 Hz and the buffer size of the scanner limited continuous acquisition to 1 minute.

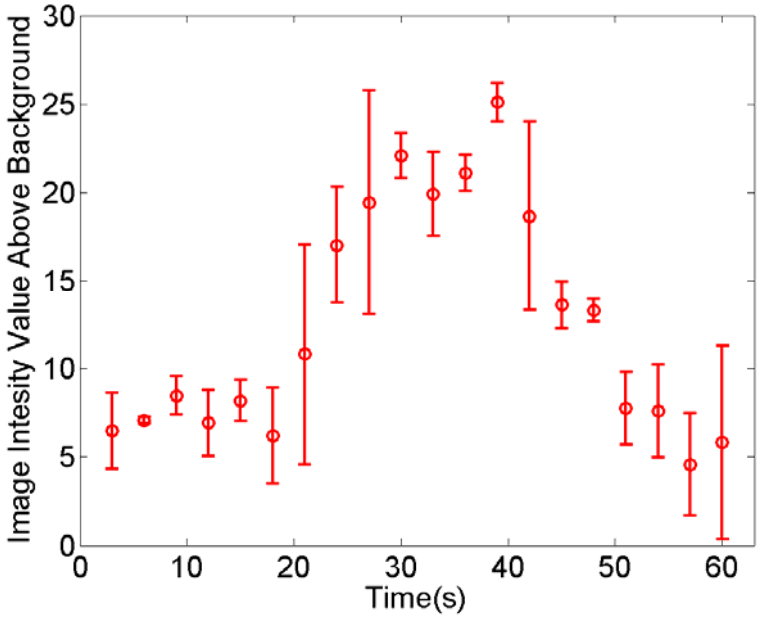

Figure 10.19. A plot showing the change in the image intensity of a B-mode scan for 1 minute starting immediately after contrast had been injected. The image intensity value has been subtracted from a background value measure before contrast injection. The frame rate of the scanner was set to 1 Hz and the uncertainty shown here is the standard deviation of the average of three consecutive frames.

Figure 10.20 shows B-mode images that were acquired before and after HIFU exposure and the corresponding subtraction image. These were acquired from two exposures: 400 W/cm^2 (1.15 MPa) and 1950 W/cm^2 (1.91 MPa), the acoustic spectra for which are shown in Figure 10.15. Figure 10.20(ii) shows an echogenicity change in the subtraction image. Figure 10.21 shows B-mode and subtraction images for the corresponding exposure levels with contrast agent in the liver exposed at ±5 s of the contrast peak (Figure 10.19). It is not possible to identify contrast change in these static images. This was, however, possible in the real time B-mode images displayed on the scanner. The subtraction images (Figure 10.21(d)) show more speckle than comparable

exposures without contrast agent, which seems to increase after the exposures (Figure 10.21(e)).

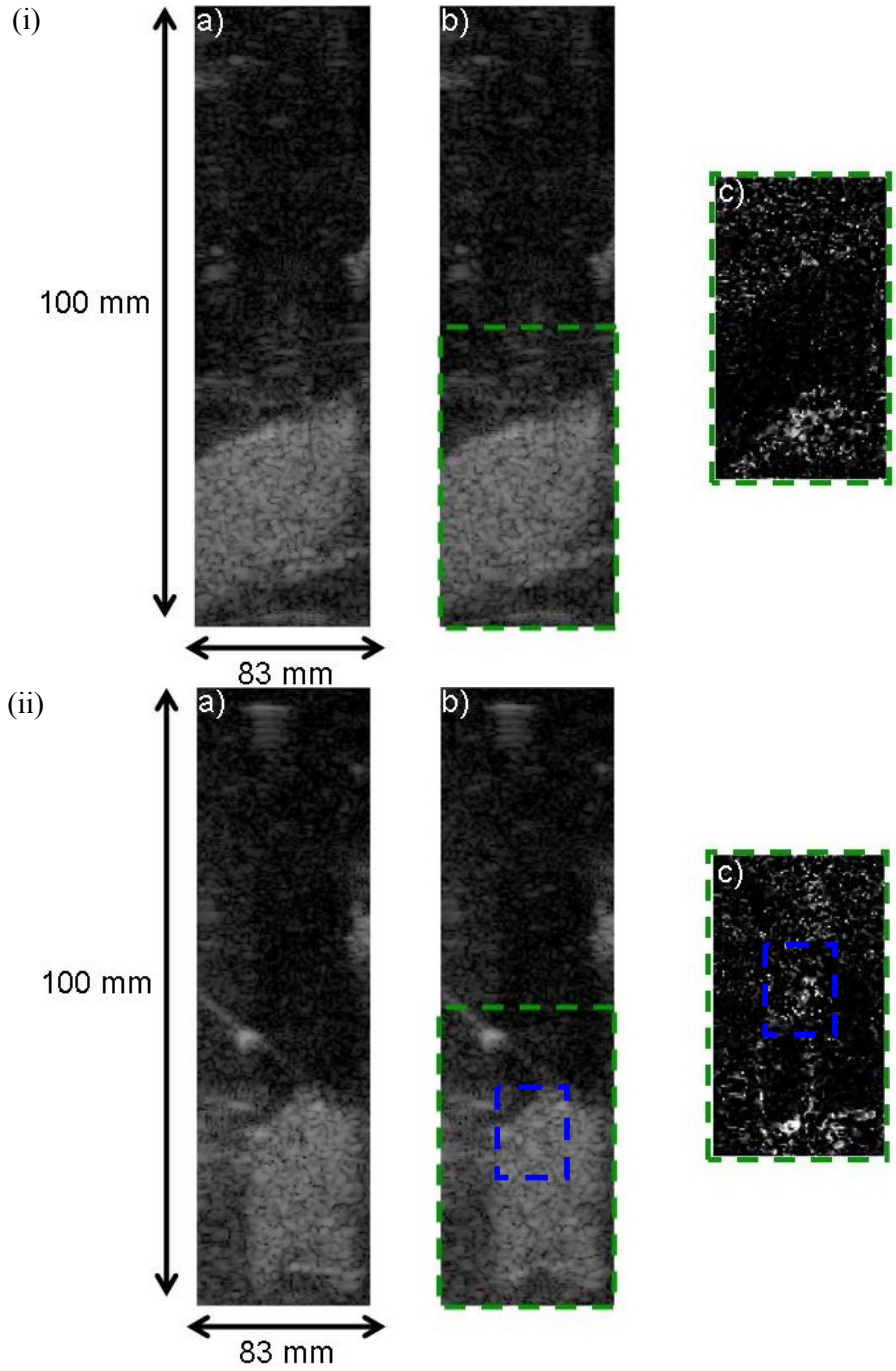

Figure 10.20. B-mode images acquired before (a) and after (b) 5 s HIFU exposures at (i) 400 W/cm^2 (1.15 MPa) and (ii) 1950 W/cm^2 (1.91 MPa), as shown in Figure 10.15, with the corresponding subtraction image (c). The blue dashed box highlights the region of hyperechogenicity.

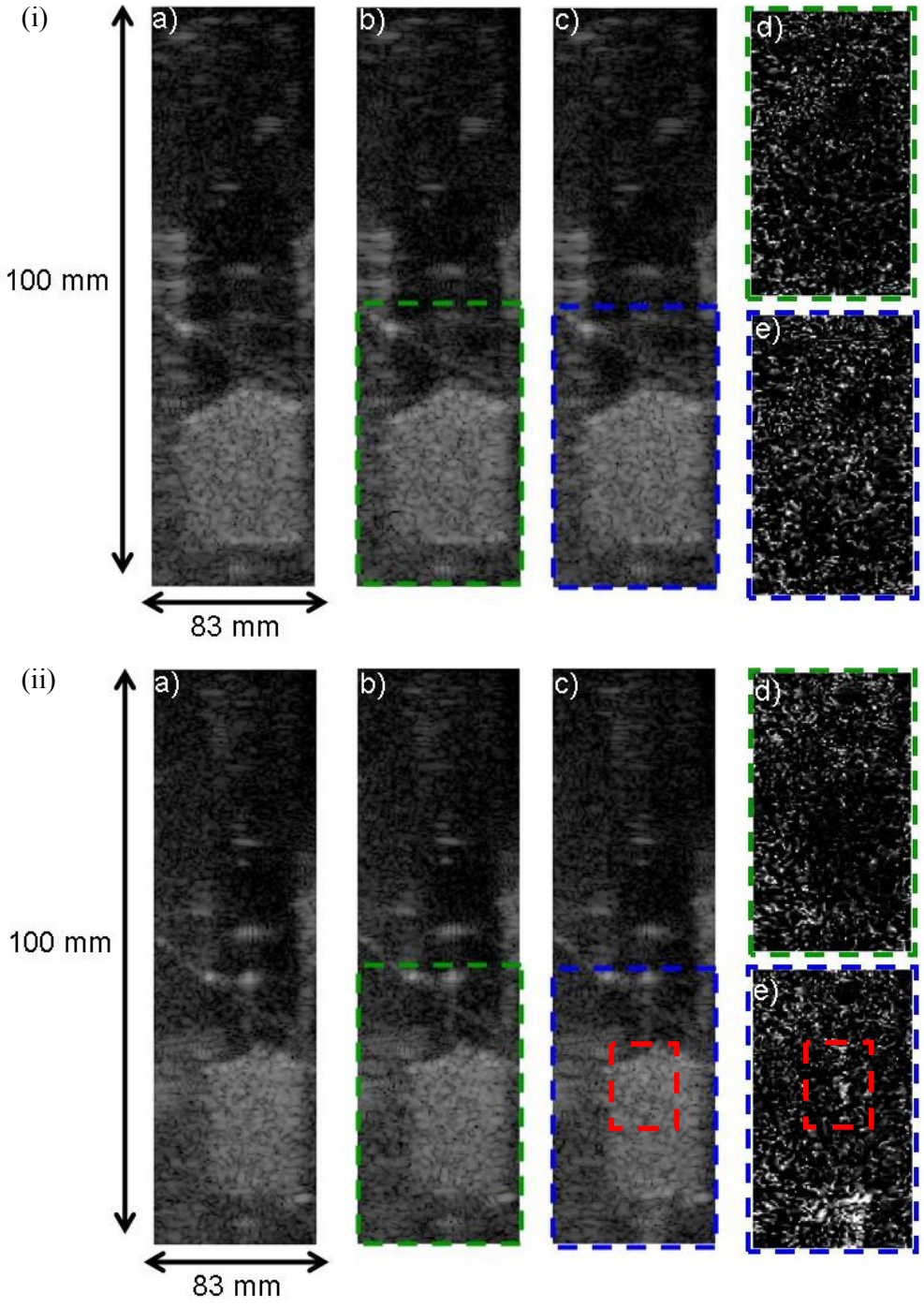

Figure 10.21. B-mode images acquired before contrast agent was added (a), after (<10 s) it was added (b) and immediately after (<5 s) the HIFU exposure (c). The two subtraction images show the effect of contrast only (d), and contrast plus a 5 s HIFU exposure (e). These exposures were at (i) 400 W/cm^2 (1.15 MPa) and (ii) 1950 W/cm^2 (1.91 MPa), as shown in Figure 10.16. The red dashed box highlights the region of hyperechogenicity.

.

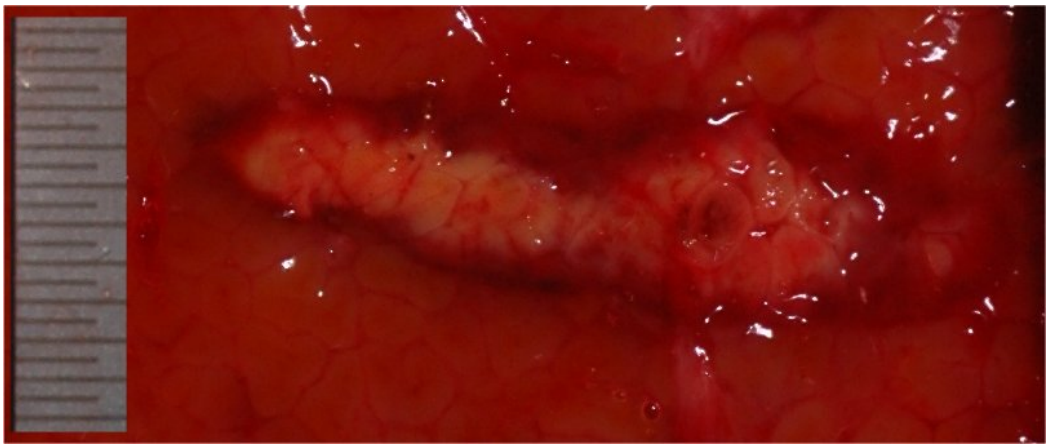

Figure 10.22. Macroscopic photograph of the lesion shown in Figure 10.23, the scale bar is in 1 mm increments and the HIFU field propagated from right to left in the image.

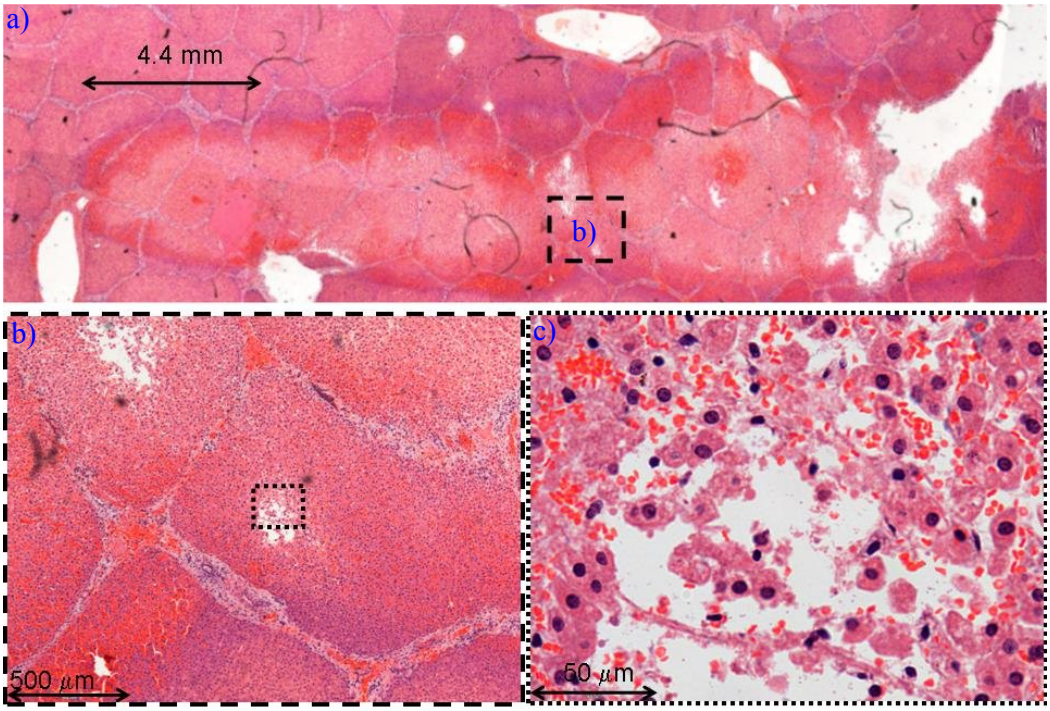

Figure 10.23. Photographs of the histological samples of 5 s HIFU exposures at 1950 W/cm^2 (1.91 MPa). (a) shows a composite image of multiple slides acquired at 40x magnification, (b) and (c) show the highlighted area in (a) at higher magnifications.

Figure 10.23 shows histological images, at increasing magnification, for the 1950 W/cm^2 (1.91 MPa) exposure (acoustic spectra shown in Figure 10.16). A single slice, with magnification of x40, can be seen in Figure 10.23(b). This image has been highlighted since it demonstrates two regions of damage which were unique to all processed samples exposed after the introduction of contrast agent. The higher

magnification area (Figure 10.23(c)) shows one of these regions. It is similar to that seen previously (Figure 10.7(b)), i.e. holes in the tissue, but appears to affect a larger area of tissue. This type of damage was found in all four of the exposures that were processed for histological analysis. Figure 10.22 shows this lesion, photographed immediately before the tissue sample was placed into fixative.

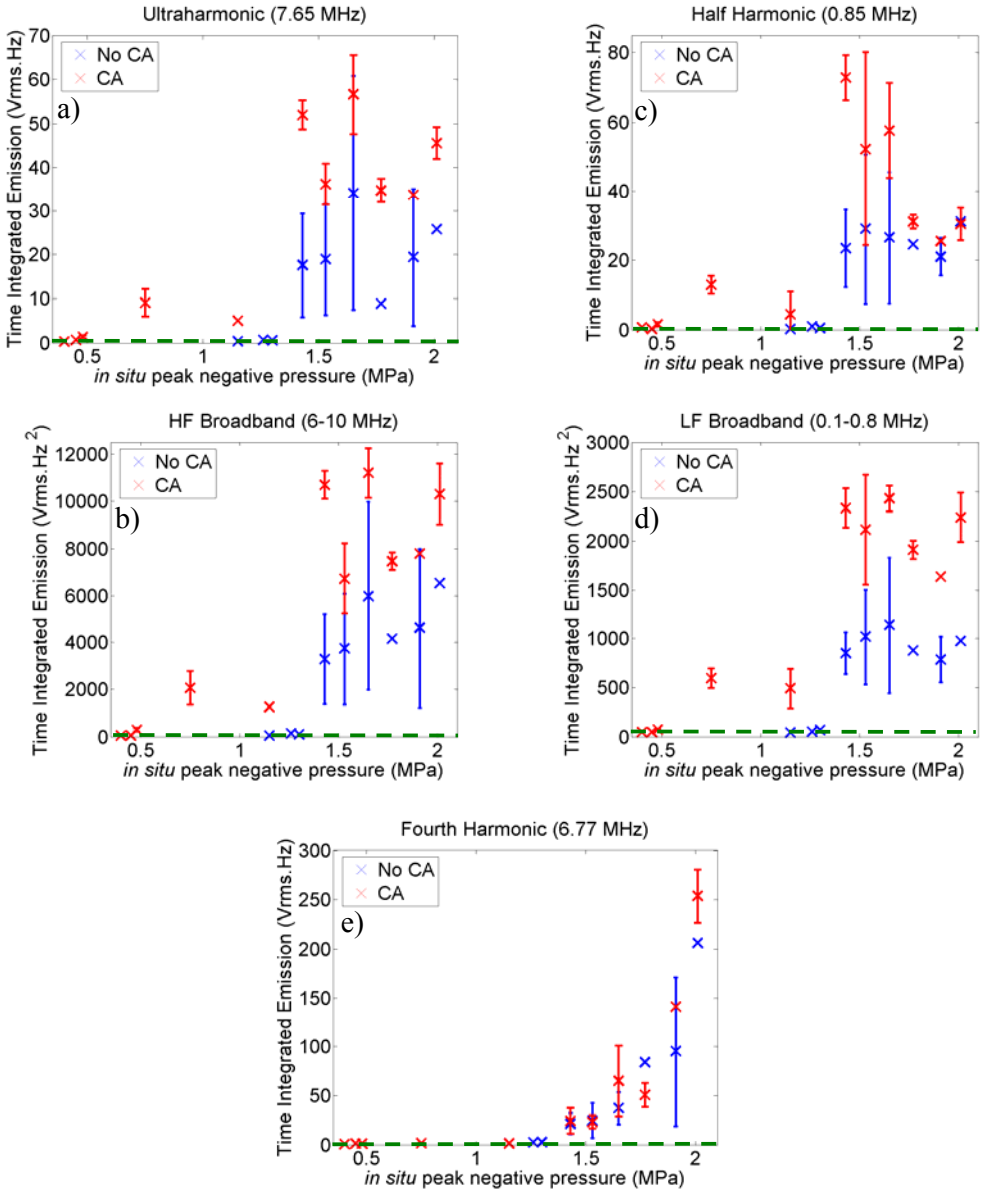

Figure 10.24. The averaged total time integrated (a) ultraharmonic, (b) high frequency broadband emissions, (c) half harmonic, (d) low frequency broadband emissions and (e) fourth harmonic, with (red) and without (blue) contrast agent (CA). Uncertainty, where shown, is the standard deviation n = 3-18. The dashed green line indicated the peak average noise level measured from the sham exposures done in this study

Figure 10.24 is the averaged total time integrated emissions for the acoustic spectra monitored with the 7.5 MHz passive cavitation detection system during the 5 s exposures in perfused liver tissue, with and without contrast agent. This figure shows that the introduction of contrast caused the detection of acoustic spectra at lower intensities (pressures) than seen without contrast agent. The data shown without contrast agent showed that acoustic emissions were detected at intensities (negative pressures) observed in the threshold study (Figure 10.14). However, the uncertainty in the average value is less because of the smaller number of exposures in this study.

10.4 Discussion

The perfused liver model provided the opportunity to deliver HIFU exposures in a similar way to that described by Visioli *et al* (1999) for a clinical trial. The detection system geometry limited the depth at which it was possible to place the HIFU focus to approximately 50 mm. This depth may be representative of a shallow HIFU treatment (Visioli *et al*, 1999). A significant difference however, is the omission of the attenuating overlying tissue layers (skin, fat etc) that may be present and affect the detected acoustic spectra.

In chapters 7, 8 and 9, the cavitation activity observed during HIFU exposures in ex-vivo tissue (bovine liver and porcine kidney) has been generally classified into three categories. Firstly, the situation where no acoustic cavitation is detected, which is identified by the absence of detectable acoustic emissions. Secondly, the case related to non-inertial and/or inertial cavitation where acoustic emissions were detected during the HIFU exposures. Finally, the presence of acoustic cavitation and boiling during the HIFU exposures. In this study, it was not possible to identify different pressure thresholds for the occurrence of non-inertial and inertial cavitation. This is most likely due to the use of the 7.5 MHz probe, and it not being as sensitive to half harmonic emissions.

Since the perfused liver model meant that exposures could be carried out in viable tissue, it was possible to establish that these categories did not result only from the use of ex-vivo tissue. Figure 10.3 and Figure 10.4 show the detected acoustic spectra from typical 5 s HIFU exposures over a range of intensities (pressures). The acoustic spectra shown exhibit the same trend of cavitation activity as observed in ex-vivo tissues, i.e. a time varying amplitude that shows an increase with the occurrence of boiling. The electrical drive power fluctuations seen in Figure 10.4(m, n and o) indicate boiling

activity, which was also identified by hyperechogenicity (Figure 10.5(iii)). Figure 10.13 shows that, for 5 s exposures, intensities (negative pressures) greater than or equal to 1240 W/cm^2 (1.65 MPa), result in echogenicity and power fluctuations. The data in this figure suggests that electrical drive power fluctuations give a more reliable indication that boiling has occurred when compared with B-mode hyperechogenicity. This may be due to the difficulty of identifying the echogenicity in a B-mode image. Figure 10.5(iii) shows a B-mode image in which an increase in echogenicity due to boiling was seen. However, it was difficult to identify this from the B-mode image without the additional information provided by the subtraction image. The 'noise' in the subtraction images more of a problem in this experiment than previously (§9.3.1, Figure 9.2), which provides further difficulty in identifying the presence of echogenic changes. This increase in noise may be due to small motion artefacts associated with the blood flow, as this could cause de-correlation between the pixels in the reference image. Figure 10.7 to Figure 10.9 show photographs of histological samples of lesioned tissue. The histology shown in Figure 10.7 was obtained from a lesion (980 W/cm^2 or 1.53 MPa) for which only acoustic emissions were detected (i.e. no boiling). The higher magnification images (Figure 10.7(b and d)) show damage to the tissue that may have resulted from acoustic cavitation activity. When compared with unexposed tissue (Figure 10.7(c)) this type of damage appears to be unique to the lesioned area. This type of damage was never found to be uniformly distributed throughout the lesioned area; rather it appears in isolated 'patches' in the lesioned area, the location of which varies between similar exposures. As this damage is not often found at the focal peak of the HIFU field where the greatest peak negative pressure would exist, suggesting other factors could have an important role in the presence of cavitation. This could be related to bubble populations in these regions, which in turn could result from a larger local population of cavitation nuclei (§2.2). The corresponding photograph of this lesion (Figure 10.6) shows poor contrast in the tissue (compared to ex-vivo lesions). This is likely to be due to the heparinised blood, used in the perfusion, leaking into the damaged regions caused the red colouring of the lesioned tissue. For these perfused liver experiments, lesion photography was of secondary priority to the histological analysis, which meant that a lesion was sometime not fully dissected in order for it to be processed for histology. Figure 10.8 and Figure 10.9 show examples of the histological sections from lesions that were generated when boiling occurred. The magnified images in these figures show damage that is representative of HIFU exposures in which boiling

occurred since it is only found in these lesions. Figure 10.9(b) shows large damaged regions (>20 μm) that tend to be located within homogenised regions of the lesioned tissue. These large holes (~0.02-2.5 mm) are likely to be caused by a boiling event. Figure 10.9(a) shows multiple locations of this characteristic damage, generally located along the central axis of the lesion where the peak temperature is likely to be greatest.

Figure 10.12 gives the percentage of exposures that generated acoustic spectra greater than the noise level. Acoustic emissions (Ultraharmonic, half harmonic and broadband emissions) were detected at intensities (negative pressures) greater than or equal to 640 W/cm^2 ±20% (1.30 MPa ±17%). As the intensity (negative pressure) was increased, this percentage rose, to a level where it became close to 100%. One key observation from this data is that this threshold is the same for half harmonic and broadband emissions, which means that it is not possible to differentiate between non-inertial and inertial cavitation in this study. The data in Figure 10.13 shows that boiling occurs at 1240 W/cm^2 ±20% (1.65 MPa ±17%). This suggests that, for these exposure conditions, there is a narrow intensity (negative pressure) range (~350 W/cm^2, or 0.24 MPa) in which only acoustic cavitation occurs. This could be a feature of exposures occurring in living tissue, as there are probably fewer cavitation nuclei (because of lower gas content than in the ex vivo case). Harvey *et al* (1944a) observed that in decompression studies (§2.2) bubbles tended not to form in living cells and generally appeared in dead or injured cells. It could be that in the perfused liver tissue, the regions where acoustic cavitation damage was seen was due to the presence of these damaged or dead cells. However, the number of these cells would be limited which could be why this narrow threshold exists between the detection of acoustic cavitation and boiling. This may suggest that the generation of acoustic cavitation in living tissue (even at the elevated temperature) is restricted by the lack of available nuclei. The histological sections would support this, as damage attributed to acoustic cavitation activity is limited to specific locations within lesioned tissue. Thus it is difficult to assess whether the additional damage had an effect on lesion size, since extra damage contained within a lesion would not add anything to the HIFU treatment. This supports the idea that acoustic cavitation occurs preferentially in areas where there are already pre-existing nuclei, and it is the advent of boiling which causes this population to increase.

The use of a perfused tissue model allowed the introduction of ultrasound contrast agent. Figure 10.15 to Figure 10.17 show typical acoustic spectra from HIFU exposures

with and without contrast agent. The data demonstrated that with contrast agent acoustic spectra were detected at intensities (pressure) lower than in their absence. This suggests that contrast agents act as nuclei for acoustic cavitation. Figure 10.18 shows that there is no significant difference between the audible emissions detected with and without contrast agent. There was no apparent effect on the intensity (negative pressure) at which boiling occurred.

A 'dose' of contrast agent (3 ml) was injected into the hepatic vein within 1 min to the HIFU exposure. Figure 10.19 shows a measurement of the image intensity of the B-mode image (background subtracted) over the first minute after the introduction of the contrast agent. This was performed instead of a HIFU exposure, and it shows that there is a peak in the image intensity approximately 20 s after the contrast was added. However, it was observed that the effect of the contrast agent was transient and no increased of contrast in the tissue remained after approximately 5 minutes, when the next 'dose' would be added. This was also confirmed by repeating some experiments after the last 'dose' of contrast agent had been used, and this showed that spectra with a similar appearance to those detected without contrast agent, but occurring at lower intensities (negative pressures). Figure 10.21 shows B-mode and subtraction images acquired from the contrast agent study. From the static images, it is difficult to identify any change in the echogenicity resultant from the contrast agent (prior to any HIFU exposure). However, this was possible when viewing the images directly on the ultrasound scanner. The damage associated with acoustic cavitation seen in histological sections from perfused liver exposed in the absence of contrast agent was observed in those containing contrast agent. It was found, from a limited number samples (n = 4), that this damage affected larger areas (~50-100 μm) in the lesion (Figure 10.23(b) and (c)). This could suggest that the contrast agent leads to more acoustic cavitation activity, a theory supported by the increase in acoustic emissions in their presence (Figure 10.24). However, this damage still seems to occur in isolated regions of the lesioned tissue.

10.5 Conclusion

A cavitation threshold study was performed on seven transplant viable normothermic perfused livers. This investigation provided a first approximation to clinical applications of the cavitation detection system. It was possible to target the HIFU focus at depths up to 50 mm, representing a shallow clinical treatment but was limited by the focal length

of the passive sensor. Active and passive cavitation detection methods were implemented in this study, and it was found that the cavitation activity was similar in trend to that observed previously in ex-vivo tissue, namely identifiable pressure thresholds for acoustic cavitation and boiling. This indicates that the cavitation activity seen in perfused and ex-vivo tissue (discussed in previous sections 7.2.3, 8.4 and 9.4) might be representative of what would be expected *in vivo*. However, one difference was that it was not possible to differentiate between non-inertial and inertial cavitation as half harmonic emissions were not detected in the absence of broadband emissions. This was likely a result of the 7.5 MHz passive sensor used as to detect these emissions. Table 10.1 shows the cavitation thresholds that were found in the perfused liver tissue.

	Acoustic Cavitation	Boiling (for 5s exposures)
Perfused Liver (n ~ 100)	> 640 W/cm^2 ±20% > 1.30 MPa ±17%	>1240 W/cm^2 ±20% >1.65 MPa ±17%

Table 10.1. In-situ I_{sp} and peak negative pressures required to generate cavitation activity in perfused liver tissue at 38^{o}C exposed to a 1.7 MHz HIFU field.

Histology was performed on the lesioned tissue and unique damage attributed to acoustic cavitation or boiling was observed. As part of the study into clinical application of this cavitation detection system, power fluctuations were found to be an accurate and reliable way of indicating the presence of boiling. Detection of audible emissions proved difficult to implement in this set-up, but provided complementary information and could be incorporated into further in-vivo experiments.

In a limited study, (three perfused livers) it was found that the introduction of Levovist ultrasound contrast agent lowered the acoustic cavitation threshold. Acoustic emissions were detected at intensities (negative pressure) of 50 W/cm^2 (0.48 MPa), significantly lower than in their absence (Table 10.1). It was also observed that the amplitude of these emissions were greater when contrast was present, which may explain why the histological damage associated with acoustic cavitation had greater extent than previously seen without contrast agent. This study highlights the possible clinical application of the cavitation detection system developed in this project.

11 – Cavitation enhanced lesion formation

This chapter builds on all the information obtained from the studies in perfused and unperfused ex-vivo liver tissue. The work presented here is designed to answer the basic research question that underpins this study, namely whether cavitation can be used to enhance HIFU treatments. Enhancement in this context is taken as the generation of larger areas of tissue ablation through the use of cavitation. Two approaches to answering this have been investigated, representing the two distinct types of bubble activity identified in this study: acoustic cavitation and boiling.

11.1 Introduction

Devin (1959) discussed three mechanisms by which energy from a propagating acoustic wave could be dissipated by an oscillating bubble (§2.2). These are, energy re-radiation from the bubbles (i.e. acoustic emissions), energy transfer during compression and expansion of the gas, and energy loss through viscous dissipation. Each of these effects could lead to heating in HIFU exposed tissue in addition to the viscous absorption of the ultrasound incident beam itself. There have been a number of studies designed to assess the effects of cavitation on heating (including Hynynen, 1991; Miller and Thomas, 1995; Miller and Gies, 1998; Miller *et al*, 1999; Hilgenfeldt *et al*, 2000; Bailey *et al*, 2001; Holt and Roy, 2001; Sokka *et al*, 2003; Melodelima *et al*, 2004; Rabkin *et al*, 2005; Rabkin *et al*, 2006; Farny, 2007), but there still remains uncertainty as to the exact mechanism by which cavitation can enhance heating, although it is a generally agreed phenomenon (Coussios *et al*, 2007). The mechanisms discussed above are most likely to be relevant to acoustic cavitation, since boiling bubbles are thought to be approximately three orders of magnitude larger than those due to acoustic cavitation generated at MHz frequencies (Khokhlova *et al*, 2006). Boiling bubbles of this size are unlikely to react to the acoustic field as their equilibrium radius is of the same order of magnitude as its wavelength.

Cavitation is thought to be responsible for lesion position shift during HIFU exposures (Watkin *et al*, 1996; Meaney *et al*, 2000). This poses a problem in achieving enhanced heating without affecting the lesion position. However, in this thesis, it has been shown that lesion shift occurs when there is boiling (§7.2.2), and that there are exposure parameters at which only acoustic cavitation occurs. It is unclear whether acoustic cavitation activity had a significant effect on lesions that are formed with these

"boiling" exposure conditions. The HIFU exposures used generated acoustic cavitation without boiling, but no identifiable increase in the lesion dimensions can be observed (§7.2.2 and 9.3.1). Thus, a method of increasing acoustic cavitation activity might be of use. A potential method might employ a 'preconditioning' pulse. This would precede the standard HIFU heating exposure, with the intention of increasing the population of acoustic cavitation bubbles. This might be similar to a single lithotripter pulse (i.e. at high pressure, for a few acoustic cycles) and be designed to nucleate acoustic cavitation activity, which could then interact with the HIFU heating exposure, leading to greater enhanced heating. The frequency of the preconditioning pulse is an important factor, since the pressure needed for acoustic cavitation inception and activity increases with frequency (Apfel, 1984). Apfel and Holland (1991) developed an analytical model for the determination of the threshold pressures that are required for a bubble to undergo a transient collapse.

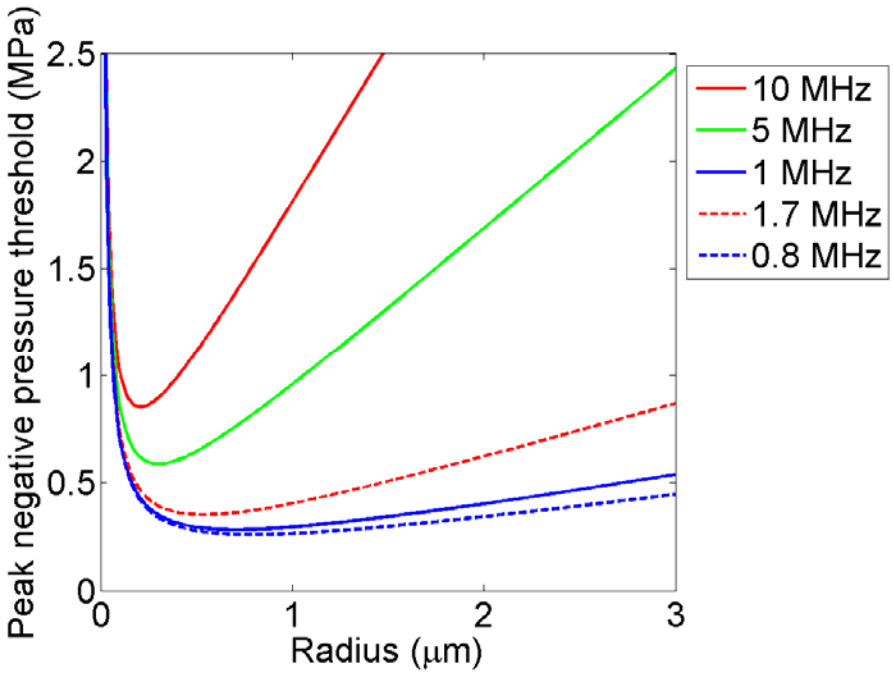

Figure 11.1. A plot of the threshold pressures in water as a function of the initial bubble radius for three ultrasound frequencies (Apfel and Holland, 1991), and the two frequencies used in this study (dashed lines).

Figure 11.1 shows a plot of threshold pressures from this analytical model for exposures at frequencies of 1, 5 and 10 MHz. It clearly shows that as the frequency increases the pressure needed to generate inertial cavitation behaviour also increases. This would

suggest that, in order to maximise the acoustic cavitation activity from a preconditioning pulse, a lower frequency than that used for HIFU exposures (1.7 MHz) would be preferable. Nevertheless, a second consideration is that bubbles generated at a lower frequency are larger, meaning that the HIFU field would not interact as efficiently with these bubbles during the heating pulse. For example, the approximate resonant radius at 0.8 MHz is 4 μm compared with 1.9 μm at 1.7 MHz (§2.2). This suggests that there is a trade off between lower nucleation pressures and the average radius of the bubbles generated. In the absence of an acoustic field a micron sized bubble would be likely to dissolve due to the Laplacian pressure associated with the surface tension (§2.2). This sets the maximum allowable time delay between the preconditioning pulse and the HIFU heating pulse. For example, Neppiras (1980) used the Epstein and Plesset (1950) model to calculate the passive dissolution of a bubble in the absence of an acoustic field. They calculated that a 10 μm bubble would take approximately 1.17 s to dissolve completely away in air-free water, which would suggest that a bubble in degassed water would take longer to dissolve. This could however, be used to advantage in the interaction between the bubble and the HIFU heating field. For example, the delay could be set to allow the bubbles to shrink to be closer to the resonant radius at the HIFU heating frequency (1.7 MHz). This was however, beyond the scope of this study, and may be difficult to implement reliably *in vivo*. However, a preconditioning pulse at 1.7 MHz was also investigated.

Holt and Roy (2001) suggested that viscous dissipation from bubbles provided the most significant contribution to the enhanced heating seen from acoustic cavitation in phantoms. Since inertial cavitation is characterised by rapid growth followed by violent collapse, the viscous contribution may be larger than that from the smaller, stable oscillations from non-inertial bubbles. However, non-inertial bubbles survive longer than a few acoustic cycles and therefore give a viscous contribution over a longer period. It is thus not obvious which type of acoustic cavitation activity would be most desirable for optimisation of the enhanced heating process. The initial aim of this part of the study was to use a preconditioning pulse at a lower frequency than the HIFU heating exposure with the intention of nucleating acoustic cavitation, in order to achieve a detectable change in the lesion size, which could be attributed to an enhanced heating effect.

In previous ex-vivo tissue studies (§7.2), it was observed that boiling caused a significant increase in the scattering of the drive signal from the focal region. This suggested the possibility of using this effect to enhance lesion formation. The placement of a highly reflective region behind the HIFU treatment region should reflect the acoustic field back into the focal zone, leading to greater heating and larger lesion size. The aim of this part of the study was to establish whether the lesion size could be increase by using a reflector in the post focal region.

11.2 Methods

11.2.1 Acoustic cavitation enhancement

A preliminary study found that the use of two individual coaligned HIFU transducers, facing each other, to provide the preconditioning and heating exposures was impractical since the alignment and timing of the two exposures proved problematic. The acquisition of a new transducer, a single element version of the 10 strip Imasonic transducer described in Chapter 5, removed the need for two individual transducers. This was because it was impedance matched to operate over a range of frequencies from 0.8 to 2.0 MHz. It could thus be driven consecutively at frequencies of e.g. 0.8 and then 1.7 MHz. Reflection measurements taken using a Network analyser (§5.1.2), for this single element Imasonic transducer are shown in Figure 11.2.

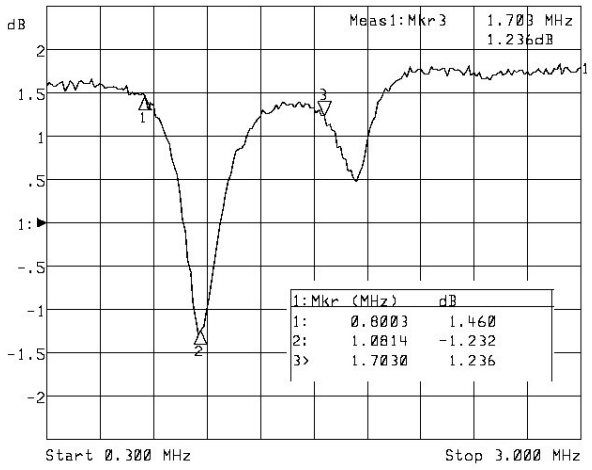

Figure 11.2. Reflection electrical impedance measurements plotted as log magnitude of the reflected voltage over a frequency range of 0.3-3.0 MHz, for the single element Imasonic transducer. These measurements were performed with the transducer submerged in water.

The beamplotting system described in section 5.3.2 was used to characterise the acoustic field from this HIFU transducer at both 0.8 and 1.7 MHz drive frequencies (at -18 dBm drive level). Figure 11.3 shows the resulting axial and two orthogonal radial beamplots for this transducer.

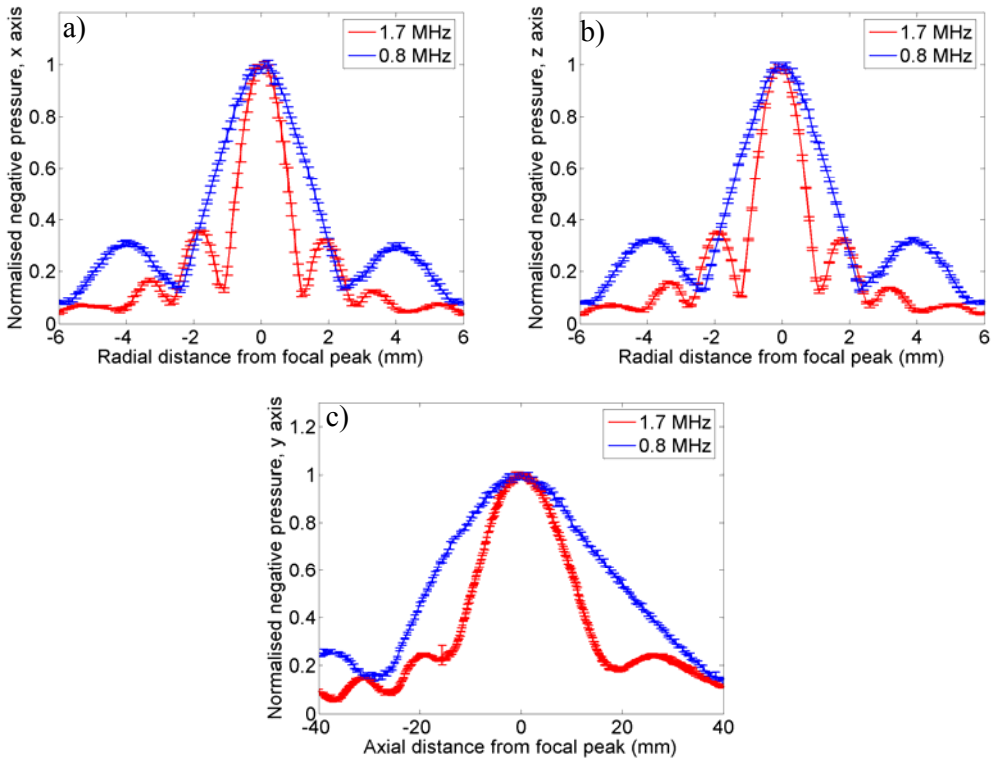

Figure 11.3. The normalised peak negative pressures for the two perpendicular radial ((a), (b)) and axial beamplots of the single element Imasonic HIFU transducer when driven at 0.8 and 1.7 MHz (c).

Drive Frequency (MHz)	Axial FWHM	Radial FWHM$_x$	Radial FWHM$_z$
0.8	38.5 ±0.5 mm	3.0 ±0.1 mm	3.0 ±0.1 mm
1.7	21 ±0.2 mm	1.7 ±0.1 mm	1.7 ±0.1 mm

Table 11.1. The axial and radial pressure full width half maxima (FWHM) of the single element Imasonic HIFU transducer. Uncertainty shown is the precision over which the measurements were taken.

Table 11.1 shows the measured pressure FWHM for this transducer. At 0.8 MHz the beam widths are just under double those at 1.7 MHz. This data has been normalised. These measurements were taken at the same drive voltage (-18 dBm), but the peak value measured at 0.8 MHz was approximately half that measured at 1.7 MHz. The FPGA card (§5.3.2) was used to trigger two function generators which were both connected to the ENI 500 power amplifier (60 dB) via a power splitter (Figure 11.5).

This configuration meant that it was possible to control the preconditioning and heating exposure lengths and delay between the two with a precision of 1 μs.

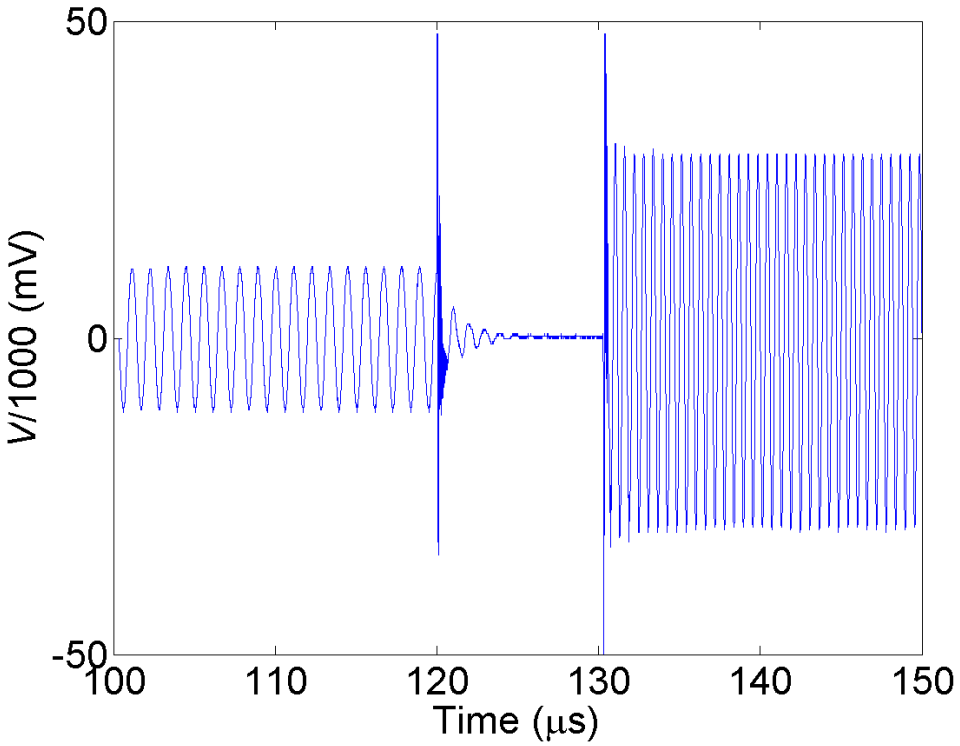

Figure 11.4. The timing between the end of the 0.8 MHz drive pulse (left) and the start of the 1.7 MHz drive pulse (right) as measured using the *V*/1000 channel in the 'pick-off' box. This figure shows a delay of 10 μs, of which the 'ring down' only lasted approximately 5 μs.

However due to the 'ring-down' of this transducer the minimum practical time delay between these two pulses was 6 μs, as shown in Figure 11.4. The power amplifier was then connected to the pick-off box, impedance matcher, and HIFU transducer in the normal way (§5.1.1).

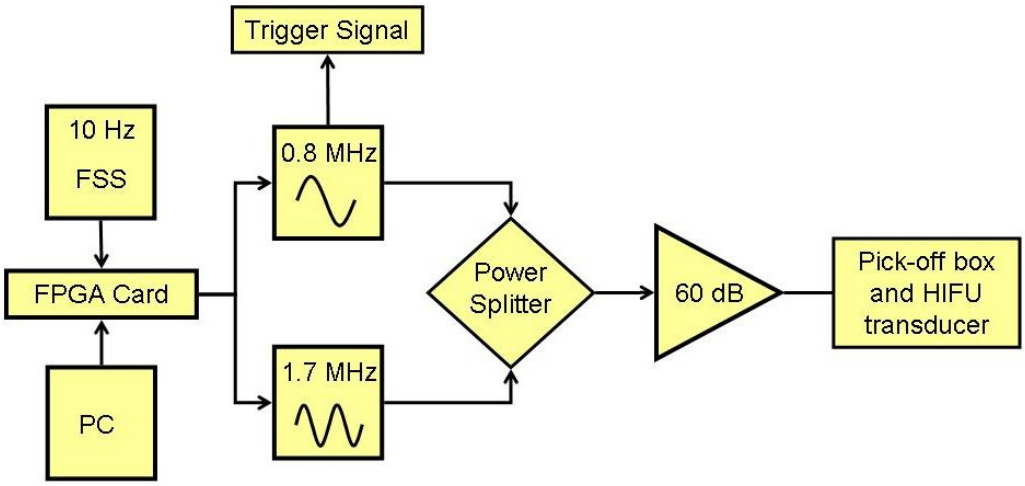

Figure 11.5. A schematic diagram of the HIFU drive system used for the preconditioning study demonstrating how the FPGA card was used to trigger first a 0.8 MHz preconditioning pulse then a 1.7 MHz lesioning pulse, where FSS is the frame synchronisation signal.

Addition of the power splitter meant that a 6 dB correction was needed in the output of the function generator to maintain the drive level that this device was calibrated over. When a preconditioning pulse was not required, this connection on the power splitter was terminated in a 50 Ω load in order to obtain consistent drive levels. The function generator, set to 0.8 MHz (or 1.7 MHz), provided the TTL signal to trigger the passive cavitation detection system which continued data acquisition for the predetermined time set by the acquisition program.

Dual passive cavitation sensors were used, since as has been demonstrated in Chapter 10 that the 7.5 MHz probe was insensitive to the half harmonic emissions. The 7.5 and 1 MHz sensors (§4.2.1) were used to monitor the frequencies above and below the drive frequency (1.7 MHz) used for the heating exposures, respectively. These sensors were arranged in the configuration described in section 7.2.1, but with the 7.5 MHz sensor and band pass filter replacing the 10 MHz sensor and high pass filter. Unfortunately, due to a faulty piece of equipment, it was not possible to monitor $i/10$ with the data acquisition system. This meant that only V_{rms} (not drive power) could be calculated. Diagnostic imaging (Zonare L5-10 probe, §4.3.1) was used to image the focal region immediately before and within 2 s after the HIFU exposures.

A series of 10 experiments using ex-vivo degassed bovine liver tissue prepared as described in §7.2.1 was conducted. Approximately 50 livers, (yielding 10-15 samples per liver), were used in this study. The HIFU exposure was either 4 or 8 s, with in-situ

I_{sp} (peak pressure) of 480, 620, 760, 1030 or 1140 W/cm^2 ±20% (1.66, 1.84, 2.01, 2.13 or 2.32 MPa ±17%). The use of 8 s exposures meant that it was possible to be just above the pressure threshold for lesion formation in order to maximise any observable effect when a preconditioning pulse was used. For each exposure condition, comparisons between the detected acoustic spectra, B-mode echogenicity, audible emissions, and lesion dimensions with and without the use of a preconditioning pulse were made. The delay between the preconditioning pulse and heating exposure was kept constant, but the frequency (0.8 or 1.7 MHz) and number of acoustic cycles in the preconditioning pulse were varied in an attempt to achieve the greatest lesion enhancement. Lesion enhancement was judged from measurement of lesion dimensions with and without the use of a preconditioning pulse to see if any increase in size could be established. The number of acoustic cycles used for the preconditioning exposure, ranged from 5, through 100, 200, 400, 500 to 1000 (6.25, 125, 250, 500, 625 and 1250 μs) at the in-situ peak negative pressure of 3.00 MPa ±17% with the frequency kept constant at 0.8 MHz.

The aim of this study was to use acoustic cavitation in a controllable and repeatable way for the enhancement of lesion formation in ex-vivo bovine liver tissue. A preconditioning pulse, which was deliberately kept short in order to minimise heating whilst still generating acoustic cavitation activity, was used in order to achieve this.

11.2.2 Boiling enhancement

Software written in-house, was used to control both the HIFU exposure (1.7 MHz) and 3-D automated gantry motion (§5.1.3) to generate between two and four lesions, per ex-vivo bovine liver sample, at different focal depths. Cylindrical tissue samples were cut to a length of 5.0 cm and were compressed by 0.5 cm in the sample holder used for HIFU exposure (§5.4). The longer sample was needed so that the two exposures could be placed end to end in the same sample along the axial direction of the HIFU field.

The aim of this study was to generate a boiling lesion centred 35 mm deep in the tissue, followed by a second lower intensity lesion 15 mm deep. It was carried out over 5 different days, on each of which between 5-10 samples taken from approximately 6 livers were used. A 0.5 s exposure at an in-situ I_{sp} = 4400 W/cm^2 (2.73 MPa) was used to generate a boiling lesion, and 990 W/cm^2 (1.47 MPa) for 4 s was used to generated the cavitation free lesion. These two exposure parameters were established from a preliminary investigation in approximately 40 tissue samples. Location of the focal peaks at the two chosen depths meant that the FWHM pressure (at 1.7 MHz) of the

preconditioning boiling exposure and the cavitation free exposure were separated by 0.5 cm (Table 11.1) in an effort to minimise heating from the boiling exposure. Passive cavitation detection, including drive voltage measurement, was used to monitor over the entire exposure time of 6.5 s, which included a delay between the two exposures of 2 s. The delay was due to the time needed for the automated gantry to move the HIFU focus to the second position, for the cavitation free exposure. Diagnostic imaging was performed using the Zonare ultrasound system, which was used to image before, during and after exposures (the total time for ultrasound imaging data acquisition during and after exposure was 9.77 ±0.08 s for a 13 Hz frame rate). The lesion dimensions were measured for each of the three types of exposures; cavitation free, boiling and both combined. For the two individual control exposures (cavitation free and boiling) the lesion dimensions were measured and the total area and length were detrmined by simple addition. The maximum width was taken as the widest measurement from either of these lesion types. These dimensions were then compared to those measured from the lesion generated using both exposures in the same sample. The single sensor (7.5 MHz) passive cavitation detection system (§7.3.1) was pulse-echo aligned with the HIFU focal peak at the location of the 'heating lesion'. The detection system was triggered at the start of the boiling exposure and acquired continuously for 8 s at a rate of 20 and 5 MHz, for cavitation and drive voltage monitoring, respectively. Statistical analysis was performed on the total integrated emissions and lesion dimension values in order to assess whether the preconditioning or boiling enhancement had a statistically significant effect on the detected acoustic spectra and/or the increase in the lesion dimensions. A *t*-test was performed on the individual data sets in order to calculate the *P* values, for which a value below 0.05 was taken to be a statistically significant difference.

11.3 Results

11.3.1 Acoustic cavitation enhancement

In an effort to investigate whether the use of a preconditioning pulse could enhance lesion formation, a number of different parameters were varied.

11.3.1.1 0.8 MHz, 400 cycle, 3.00 MPa preconditioning

The first exposure regime used a preconditioning pulse of length 400 cycles, peak pressure of 3.00 MPa and a drive frequency of 0.8 MHz. A HIFU heating pulse (1.7

MHz) of 4 s duration at in-situ I_{sp} = 1140 W/cm^2 (2.32 MPa) was used. This was chosen since boiling did not occur for these exposure conditions. Data presented in this section were the culmination of three separate experiments using between 180-270 tissue samples taken from 18 ex-vivo bovine livers.

Figure 11.6 shows acoustic spectra from these exposure conditions, with and without the preconditioning pulse. The preconditioning pulse caused a significant increase in all detected acoustic spectra, except ultraharmonic emissions (Figure 11.6(e-f)). This increase was most significant for half harmonic and broadband emissions since without preconditioning these emissions were not detected (Figure 11.6(a&d)) during the 4 s HIFU exposure, and with preconditioning the peak amplitude of the emissions was approximately an order of magnitude greater. The data in Figure 11.7 demonstrates that no electrical drive voltage fluctuations or audible emissions were detected during these exposures, regardless of whether a preconditioning pulse was used.

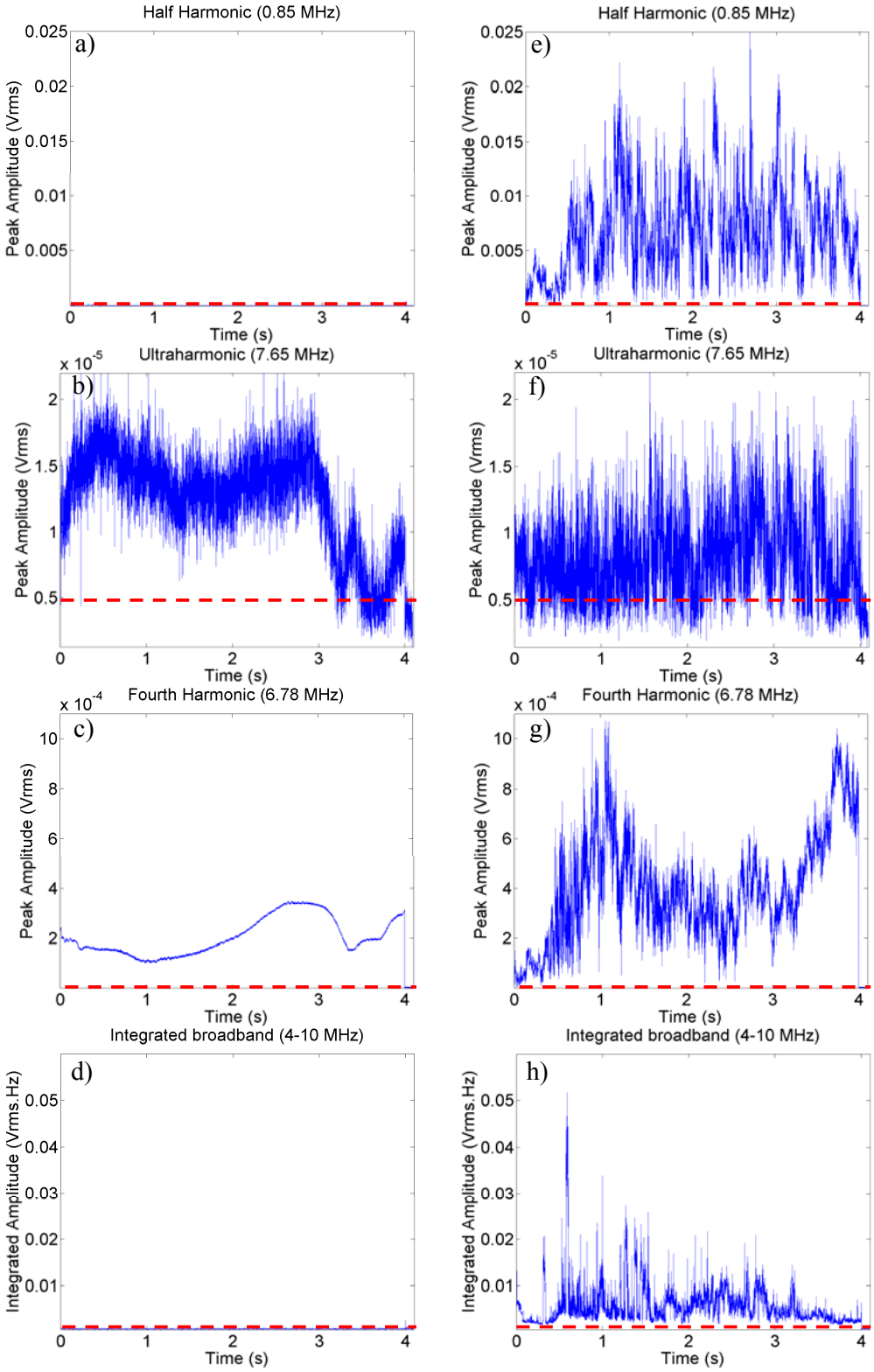

Figure 11.6. The half harmonic (a&e), ultraharmonic (b&f), fourth harmonic (c&g) and broadband emissions (d&h) detected from two 4 s HIFU exposures (1140 W/cm^2 or 2.32 MPa) in ex-vivo bovine liver tissue, with (e-h) and without (a-d) a preconditioning pulse (0.8 MHz, 400 cycle and 3.00 MPa).The dashed red line indicates the peak noise level measured from a sham exposure.

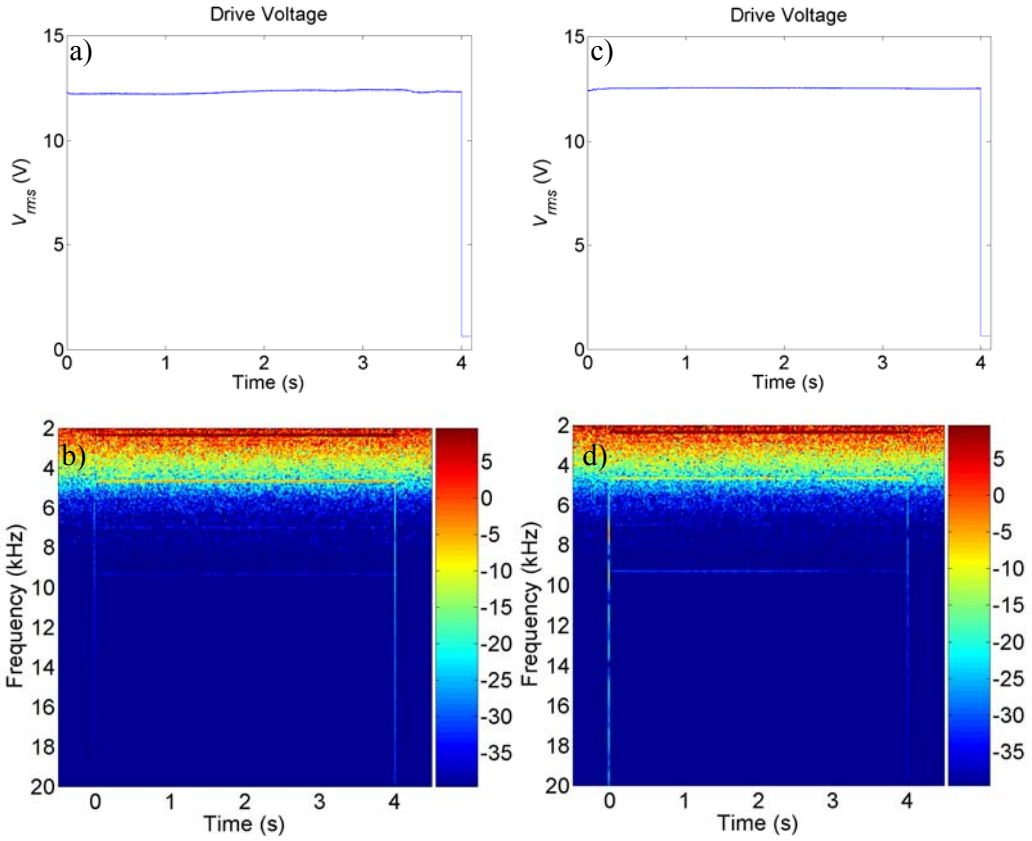

Figure 11.7. The drive V_{rms} (a&c) and audible emissions (b&d) from the 4 s HIFU exposures with I_{sp} = 1140 W/cm^2 (2.32 MPa), shown in Figure 11.6. Where (c&d) is with preconditioning (0.8 MHz, 400 cycle and 3.00 MPa) and (a&b) is without. Each V_{rms} value is calculated over 400 cycles (0.5 ms).

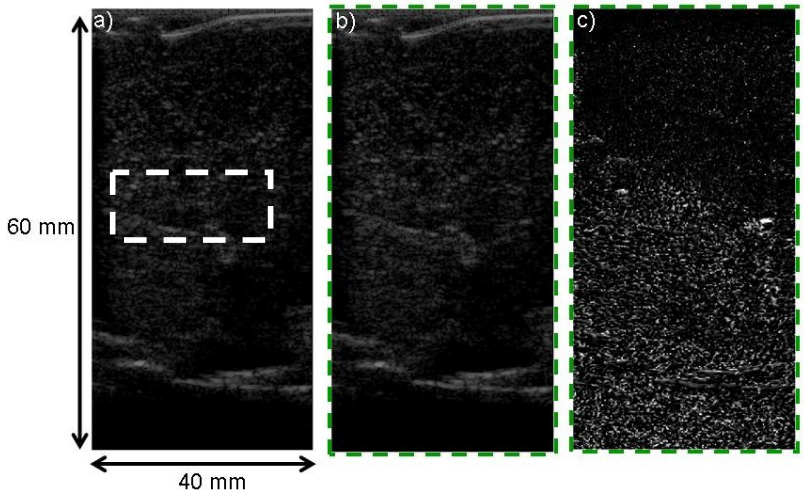

Figure 11.8. The B-mode images taken immediately before (a) and after (b) the 4 s HIFU exposure, where (c) it the subtraction image of these two frames. No preconditioning pulse was used in this exposure. The HIFU field propagated from left to right in these images, where the white dashed box indicates the approximate position of the HIFU focal peak.

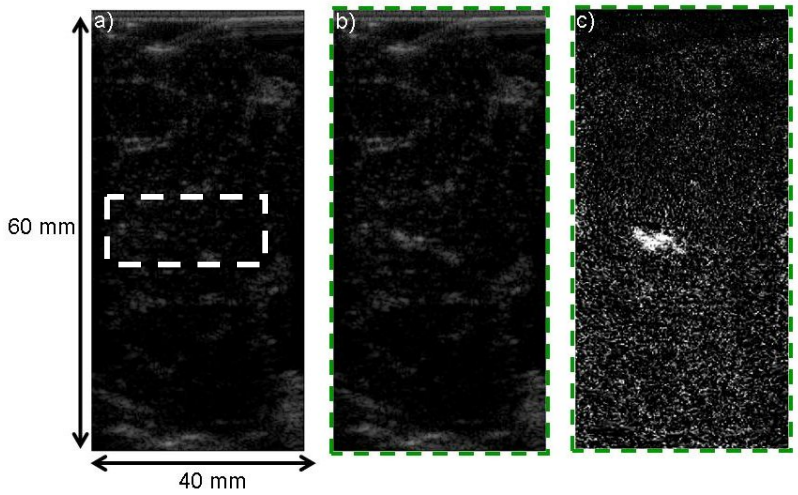

Figure 11.9. The B-mode images taken immediately before (a) and after (b) the 4 s HIFU exposure, where (c) is the subtraction image of these two frames. A 400 cycle, 3.00 MPa *in situ* peak negative pressure preconditioning pulse was used in this exposure. The HIFU field propagated from left to right in these images, where the white dashed box indicates the approximate position of the HIFU focal peak.

Figure 11.8 and Figure 11.9 show the B-mode images and corresponding subtraction images for this sample exposure, with and without preconditioning. The subtraction images show that hyperechogenicity was observed when using the preconditioning pulse (Figure 11.9(c)), in the absence of boiling. Figure 11.10 shows the average total time integrated emissions for all of the 4 s 1.7 MHz HIFU exposures at 1140 W/cm^2 (2.32 MPa), with and without a 0.8 MHz, 400 cycle, 3.00 MPa peak negative pressure preconditioning pulse. As expected from the previous results, there is an increase in the detected half harmonic, ultraharmonic, and broadband emissions, when a preconditioning pulse is used, but there is also an increase in the uncertainly of these averaged values. The scattered non-linear components (second and fourth harmonics) do not show any significant change following preconditioning. The increase in detected acoustic emissions suggests that there was an increase in the acoustic cavitation activity. However, the lesion dimensions in Figure 11.11 show no statistically significant difference ($P > 0.05$).

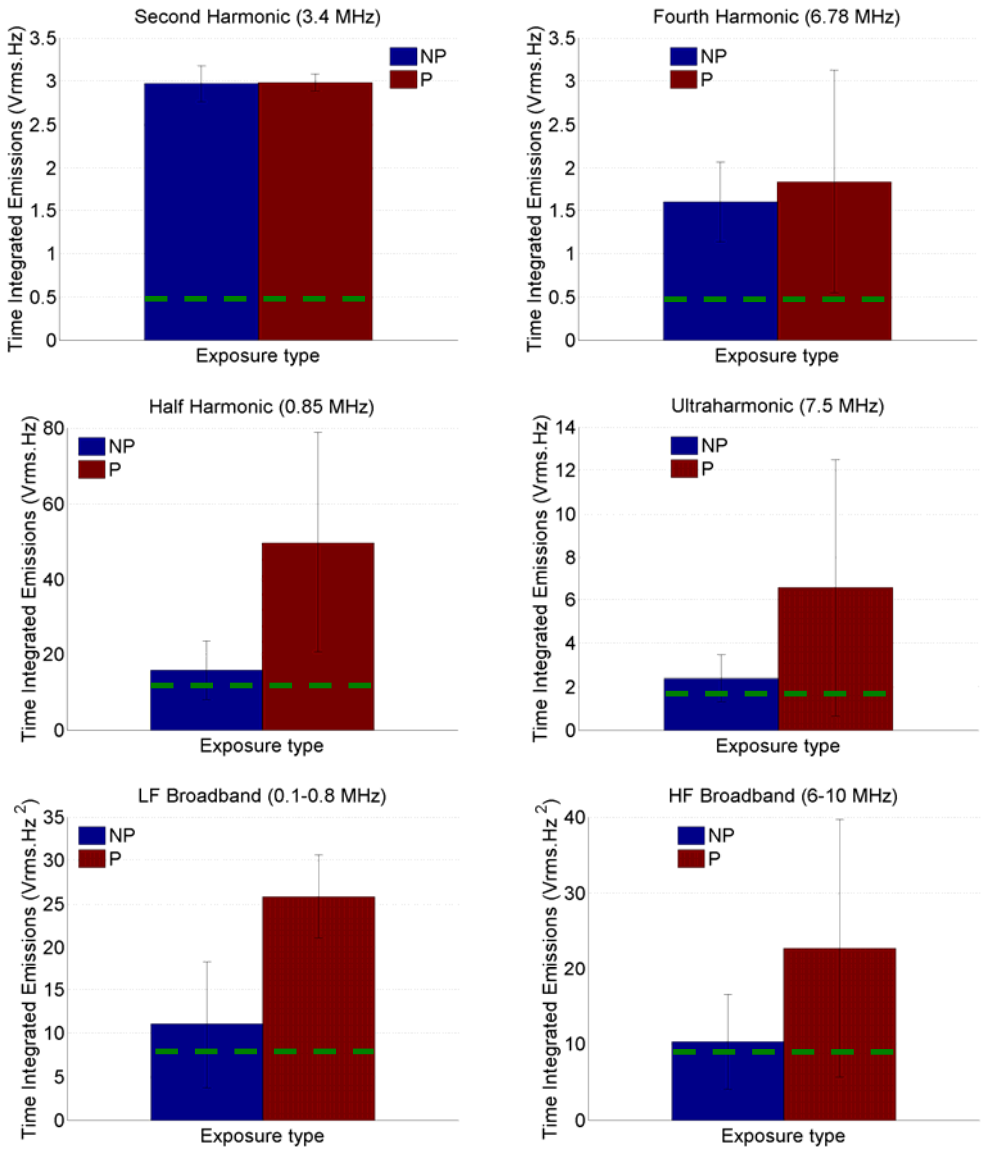

Figure 11.10. The averaged total time integrated emissions for 4 s HIFU (1.7 MHz) exposures at 1140 W/cm^2 (2.32 MPa), with (P) and without (NP) a 400 cycle, 3.00 MPa (0.8 MHz) peak negative pressure preconditioning pulse. Uncertainly shown is the standard deviation of the averaged value, where n = 5. The dashed green line indicated the averaged peak noise level measured from sham exposures.

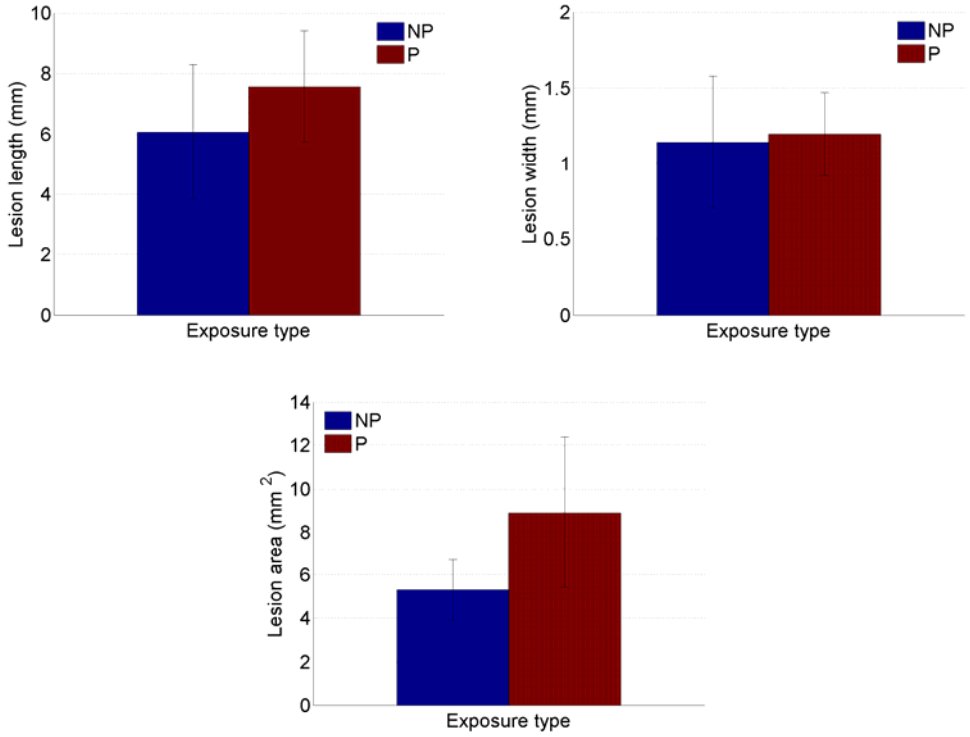

Figure 11.11. Dimensions of lesions generated from the 4 s HIFU exposures at 1140 W/cm^2 (3.62 MPa), with (P) and without (NP) a 500 cycle, 4.29 MPa peak negative pressure preconditioning pulse. Uncertainly shown is the standard deviation of the averaged value, where n = 5, and P > 0.05 for each measurement when comparing exposures with and without preconditioning.

The 0.8 MHz 400 cycle preconditioning pulse has been shown to have a quantifiable effect on the level of detected acoustic emissions as the use of a preconditioning exposure increased the total integrated emissions by up to 100%. However, it had no significant effect on the lesion dimensions.

11.3.1.2 Preconditioning using 0.8 and 1.7 MHz

The previous section has shown that a preconditioning pulse increased the level of detected acoustic emissions and by association the acoustic cavitation activity. However, the increase did not result in a detectable level of increase in the lesion dimensions. In an effort to establish whether the preconditioning frequency would have an effect on this, a study was performed using both 0.8 and 1.7 MHz. After a series of preliminary experiments were performed in ex-vivo bovine liver it was established that an 8 s HIFU heating exposure at in-situ I_{sp} = 760 W/cm^2 (3.04 MPa) produced the

maximum lesion size in the absence of boiling. Figure 11.12 shows three examples of typical acoustic spectra and electrical drive voltage acquired with (i) no preconditioning, or with 400 cycle preconditioning pulses of (ii) 3.00 MPa 0.8 MHz and (iii) at 3.61 MPa 1.7 MHz. The acoustic spectra from case (ii) (Figure 11.12(f-j)) show the greatest amplitude of acoustic emissions. This dataset shows that the maximum acoustic emissions were detected within the first 4 s of the HIFU exposure. There is little difference in amplitude between the acoustic spectra detected without a preconditioning pulse and those preconditioned at 1.7 MHz. An increase in the detected fourth harmonic resulting from the use of a 0.8 MHz preconditioning exposure can be seen in Figure 11.12(h).

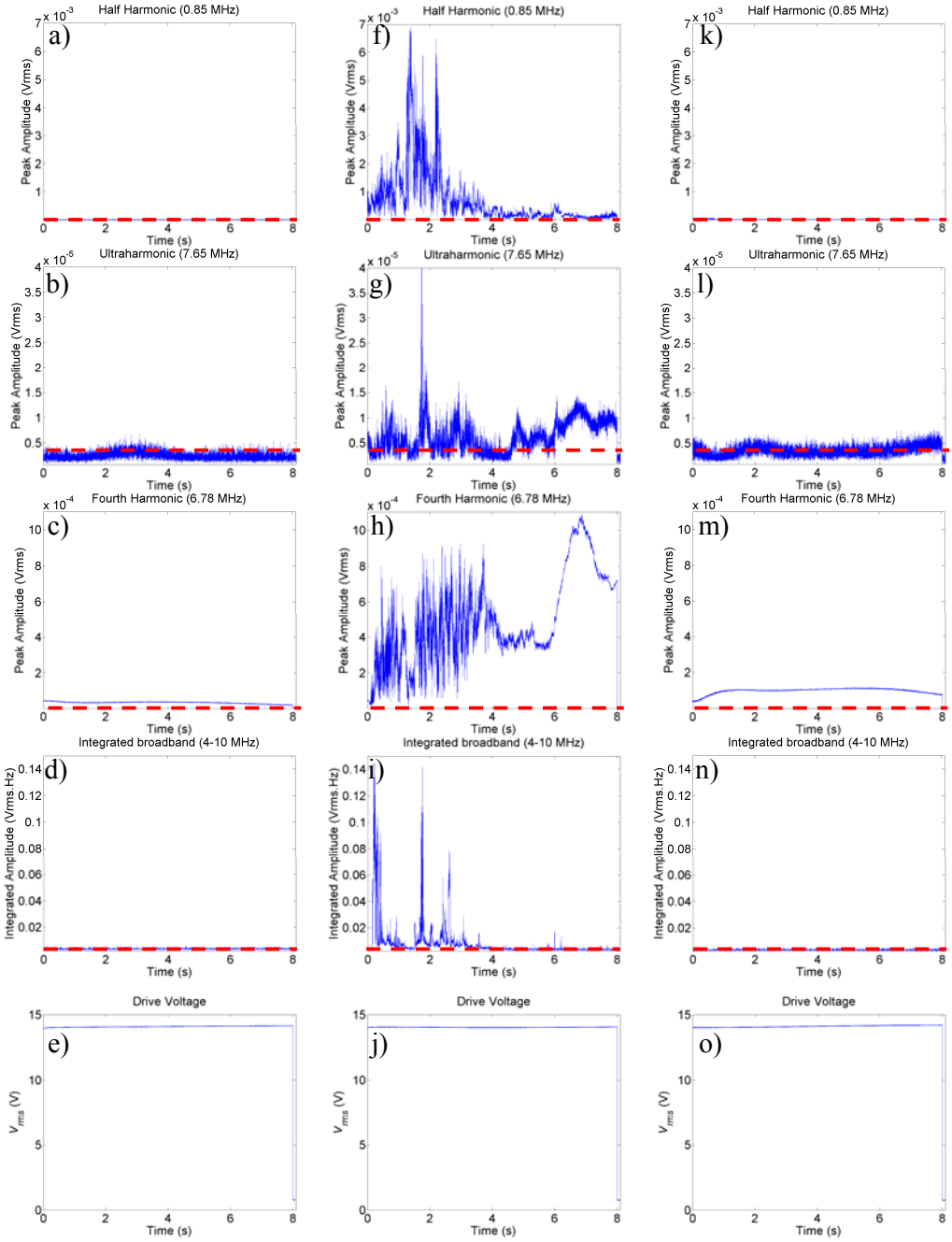

Figure 11.12. The (first row) half harmonic, (second row) ultraharmonic, (third row) fourth harmonic, (fourth row) integrated broadband and (fifth row) electrical drive voltage, for three HIFU exposures, without preconditioning (a-e), with 400 cycles preconditioning pulse at 0.8 MHz (f-j) and with preconditioning at 1.7 MHz (k-o), with peak negative pressures of 3.00 and 3.61 MPa respectively. The dashed red line indicates the peak noise measured from a sham exposure.

Figure 11.13 shows that no audible emissions (2-20 kHz) were detected during these three exposures, suggesting that boiling did not occur. Horizontal lines can be seen in

the spectra that were caused by the microphone detecting the 2.25 kHz buzzer tone and its harmonics (i.e. 4.5, 9.0 and 16.0 kHz) generated by the FPGA card.

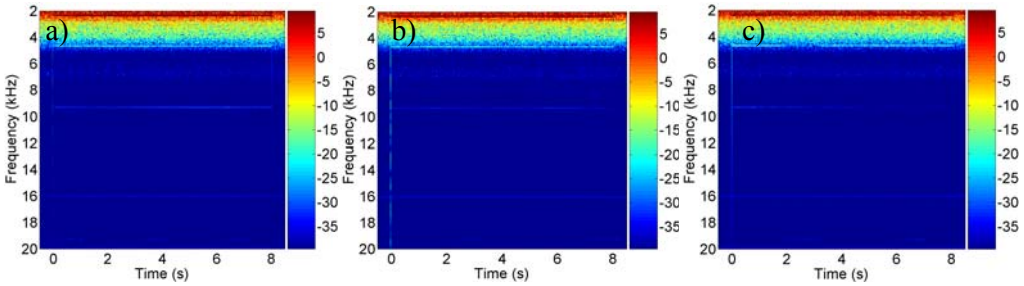

Figure 11.13. The audible emissions detected for the three HIFU exposures, (a) without a preconditioning pulse, (b) with preconditioning at 0.8 MHz and (c) with preconditioning at 1.7 MHz, described in Figure 11.12.

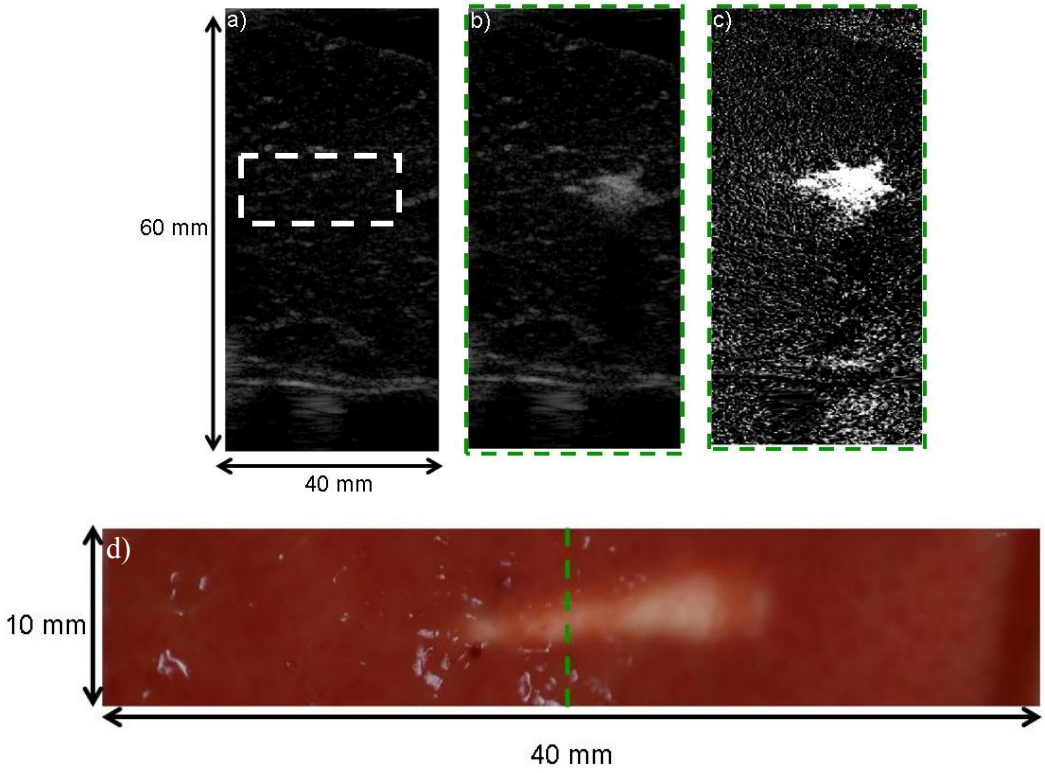

Figure 11.14. The B-mode images taken immediately before (a) and after (b) an 8 s HIFU exposure,(c) is the subtraction image of these two frames. A 400 cycle, 3.00 MPa in-situ peak negative pressure (0.8 MHz) preconditioning pulse was used in this exposure. (d) is the lesion generated from this exposure, where the white dashed box indicates the approximate position of the HIFU focal peak, in the B-mode images and the dashed green line in the lesion photograph represents the position of the focal plane. The HIFU field propagated from left to right in all of these images.

Figure 11.14 shows the B-mode and subtraction images and the lesion photograph from the 8 s HIFU exposure at an I_{sp} = 760 W/cm^2 (2.01 MPa), with a preconditioning pulse

at 0.8 MHz for 400 cycles at a peak negative pressure of 3.00 MPa. The subtraction image (Figure 11.14(c)) shows an increase in echogenicity after this exposure, but in this case in the absence of boiling. The lesion shape shows a 'tadpole' type lesion, but the wider region in this case is post-focal, in contrast to the wider pre-focal region previously seen in this and other studies (Chapter 2).

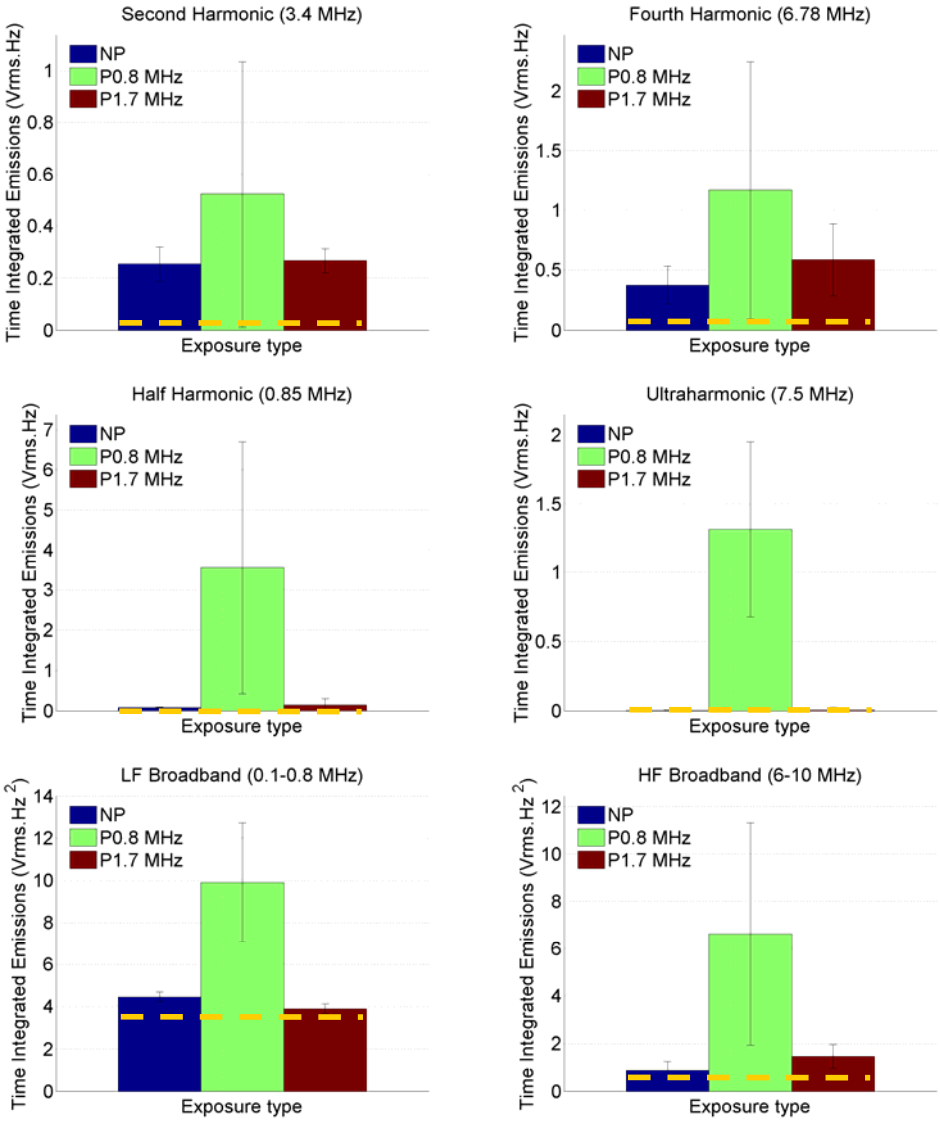

Figure 11.15. The averaged total time integrated emissions for 8 s HIFU exposures at 760 W/cm^2 (3.04 MPa), with (P) and without (NP) a 400 cycle, 3.00 or 3.61 MPa peak negative pressure preconditioning pulse at either 0.8 or 1.7 MHz respectively. Uncertainty shown is the standard deviation of the averaged value, where n = 8, 10 and 4 for without and with preconditioning at 0.8 and 1.7 MHz respectively. The dashed yellow line indicates the average peak noise measured from a sham exposures.

Figure 11.15 shows the average total time integrated emissions for the 8 s HIFU exposure at 760 W/cm^2 (3.04 MPa), with either no preconditioning pulse, a 0.8 MHz or a 1.7 MHz preconditioning pulse. It shows that the use of a 0.8 MHz preconditioning pulse provided a significant increase in all the detected acoustic spectra, whereas the 1.7 MHz pulse did not increase the levels significantly above those detected without a preconditioning pulse.

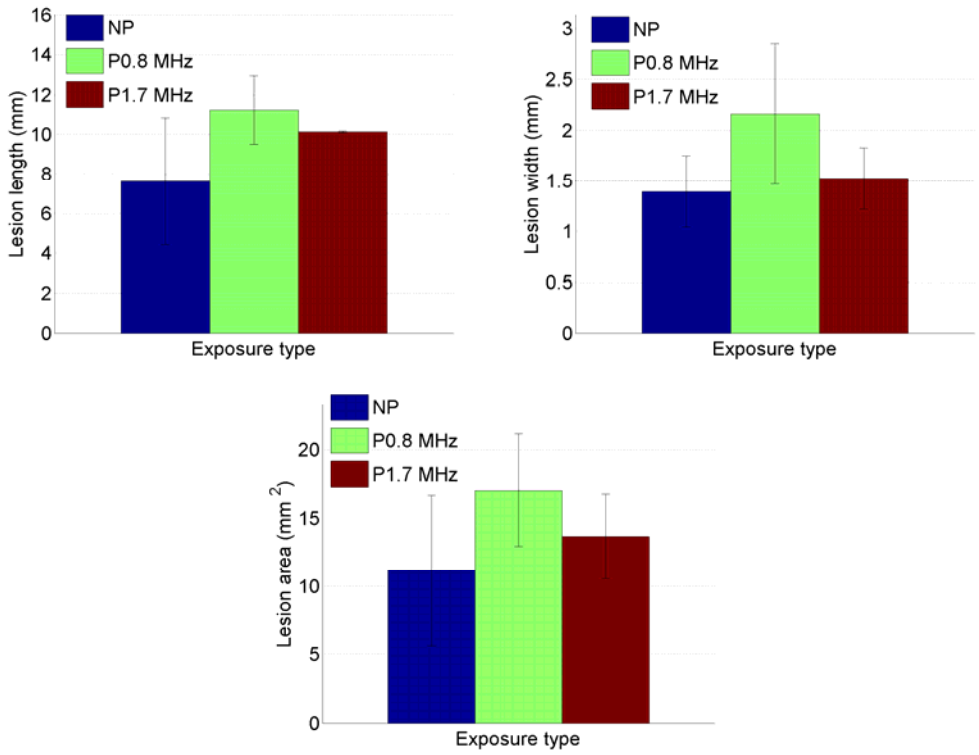

Figure 11.16. The averaged lesion dimensions for a 8 s HIFU exposures at 760 W/cm^2 (3.04 MPa), with (P) and without (NP) a 400 cycle, 3.00 MPa peak negative pressure preconditioning pulse at either 0.8 or 1.7 MHz. Uncertainty shown is the standard deviation of the averaged value, where n = 3-8, and $P > 0.05$ for each measurement when comparing exposures with and without preconditioning (at both preconditioning frequencies).

The lesion dimensions shown in Figure 11.16 demonstrates that there is no significant statistical difference between the different exposure regimes.

11.3.1.3 Variation of the 0.8 MHz preconditioning pulse length

Further acoustic cavitation preconditioning studies were done with a 0.8 MHz frequency pulse, at a peak negative pressure of 3.00 MPa, with the length of preconditioning pulses varied between 0, 5, 50, 100, 200, 500 and 1000 cycles. Figure 11.17 shows a selection of lesions that were generated from these exposure conditions. Only the lesion without a preconditioning pulse shows an ellipsoidal shape, the others all have irregular forms.

The lesion shown in Figure 11.17(c) (50 cycle preconditioning pulse) has the 'tadpole' shape but the widest part of the lesion is post-focal. Acoustic spectra and drive V_{rms} from these exposures are shown in Figure 11.18. The 500 cycle preconditioning pulse gave the largest region of tissue damage (Figure 11.17(e)) and highest peak amplitude acoustic emissions (Figure 11.18(e)). Boiling occurred during three of these exposures (Figure 11.18(c), (e) and (f)), as identified from drive voltage fluctuations and audible emissions (not shown).

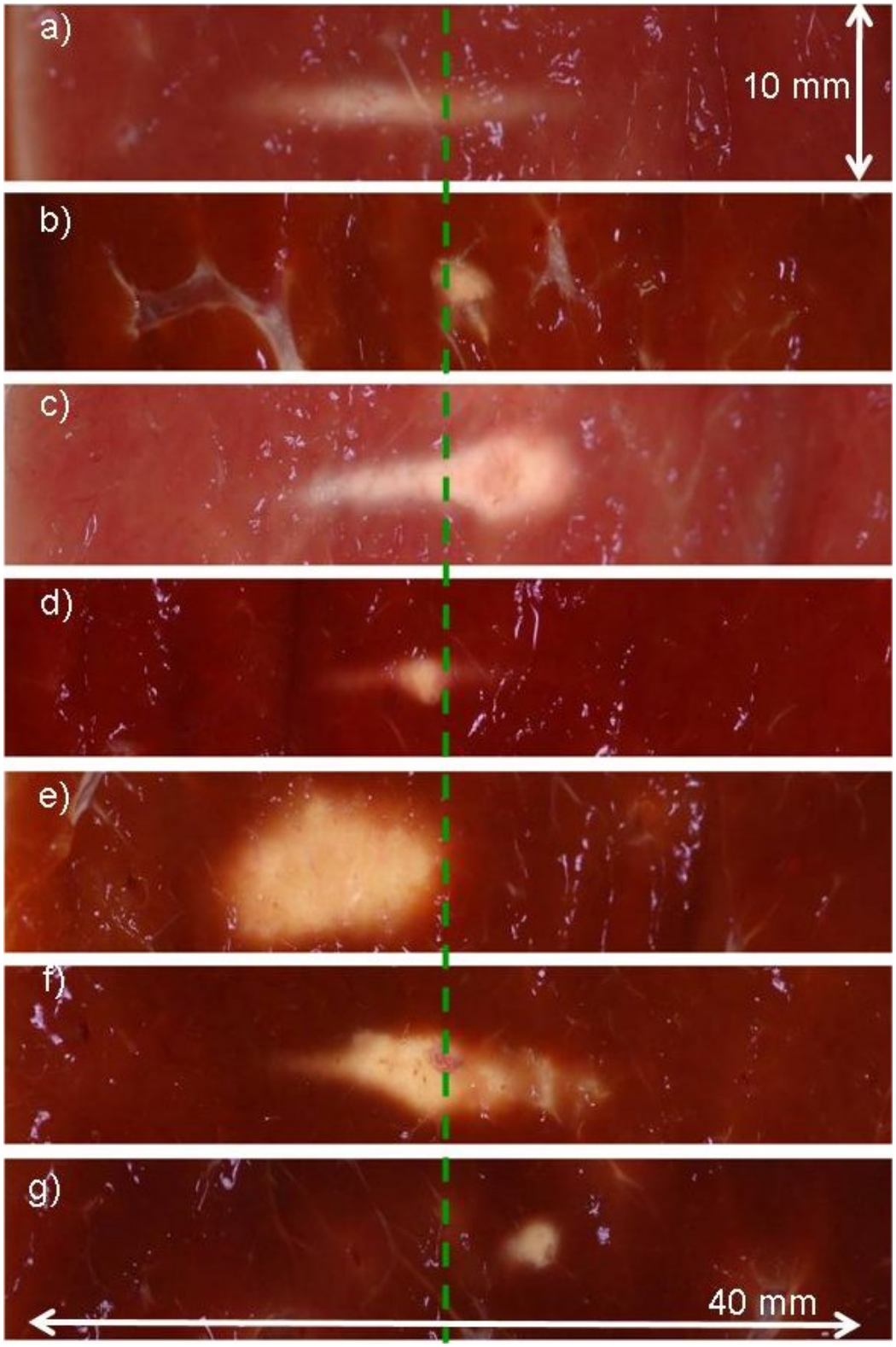

Figure 11.17. Examples of lesions generated using (a) no preconditioning, (b) 5, (c) 50, (d) 100, (e) 200, (f) 500, and (g) 1000 cycles, of a 3.00 MPa peak negative pressure pulse. The HIFU field propagated from left to right, and the green line indicates the approximate position of the focal peak.

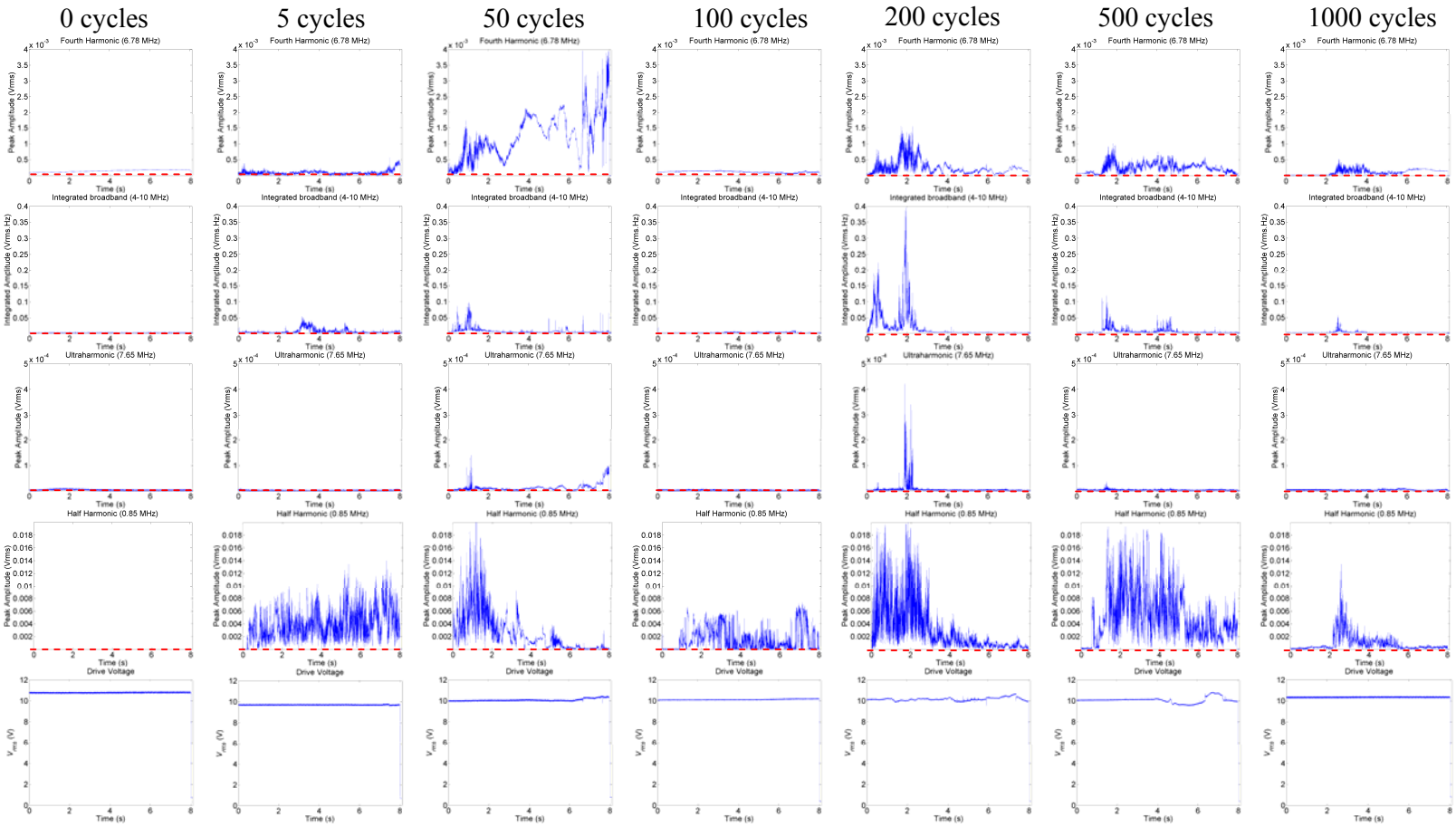

Figure 11.18. Acoustic spectra and electrical drive voltage from the exposures described in Figure 11.17. In columns, from top to bottom, fourth harmonic (6.78 MHz), integrated broadband (4-10 MHz), ultraharmonic (7.65 MHz), half harmonic (0.85 MHz) and V_{rms} drive voltage are shown.

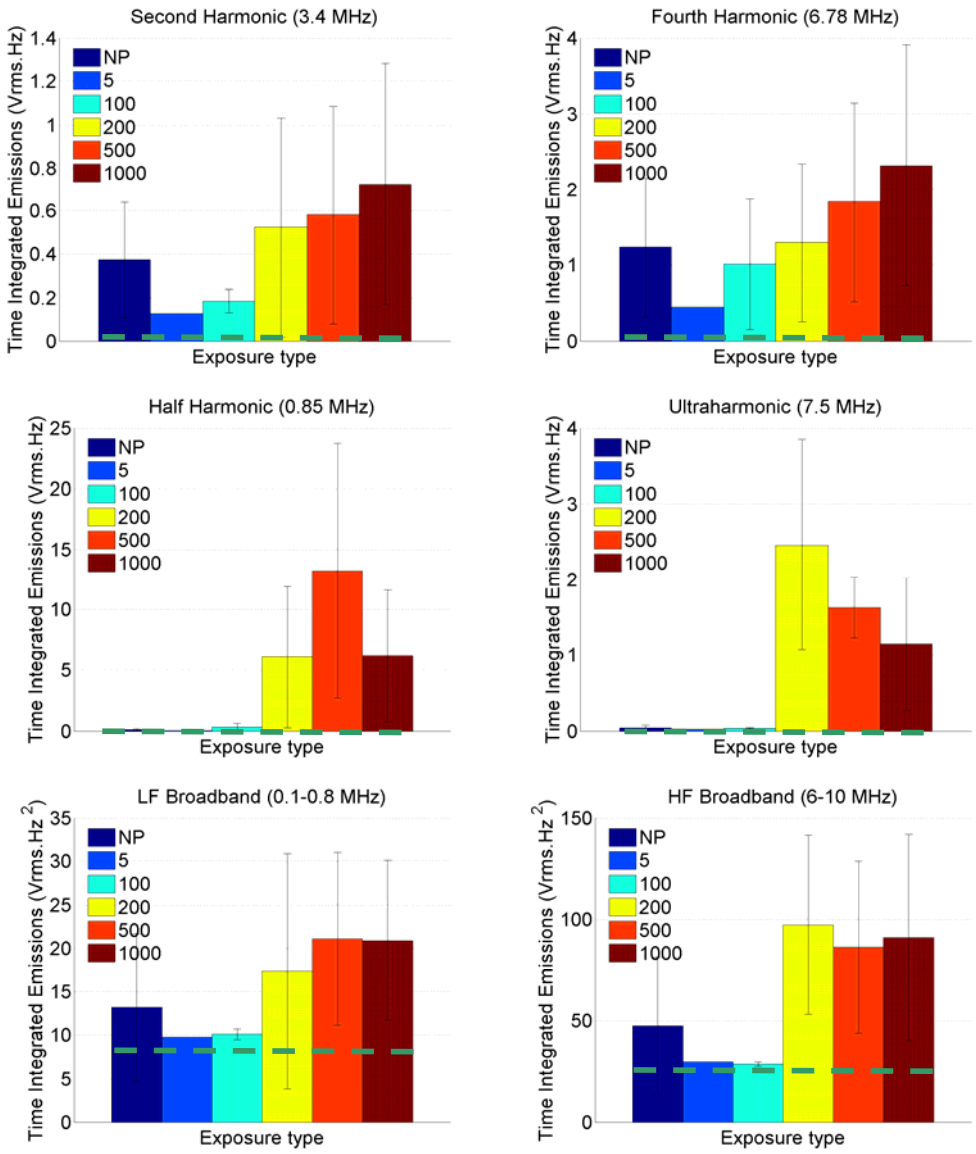

Figure 11.19. The averaged total time integrated emissions for 8 s HIFU exposures at 620 W/cm^2 (2.81 MPa), with no preconditioning (n=6) or a pulse with 5 (n=4), 100 (n=6), 200 (n=5), 500 (n=6) and 1000 (n=6) cycles at a peak negative pressure of 3.00 MPa. Uncertainty is the standard deviation of the average value. The dashed green line indicates the average peak noise measured from a sham exposures.

Figure 11.19 shows that the number of cycles in the preconditioning pulse is not critical. However, the greatest amplitude emissions are detected when 200 or more acoustic cycles are used. Figure 11.20 shows an example of three separate lesions generated when a 200 cycle preconditioning pulse was used. It demonstrates that the number of cycles in the preconditioning pulse does not necessarily dictate the shape of the lesion.

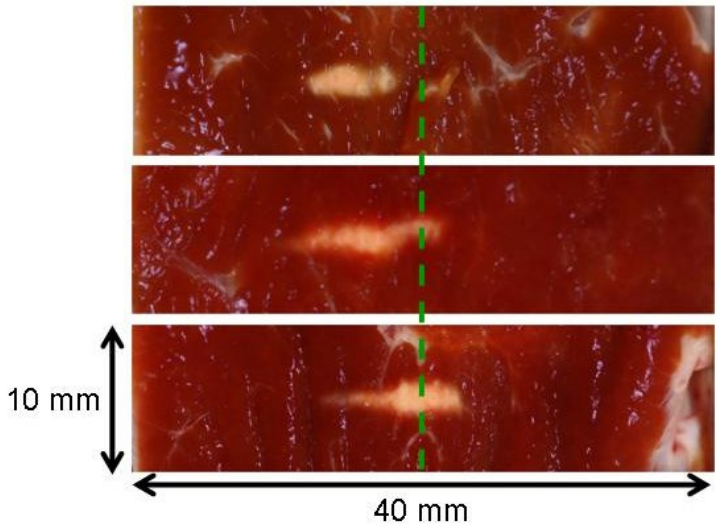

Figure 11.20. Three lesions generated using a 200 cycle preconditioning pulse and a 8 s HIFU exposure at 620 W/cm^2 (2.81 MPa). The green dashed line indicated the approximate position of the HIFU focal peak, where the field propagated left to right.

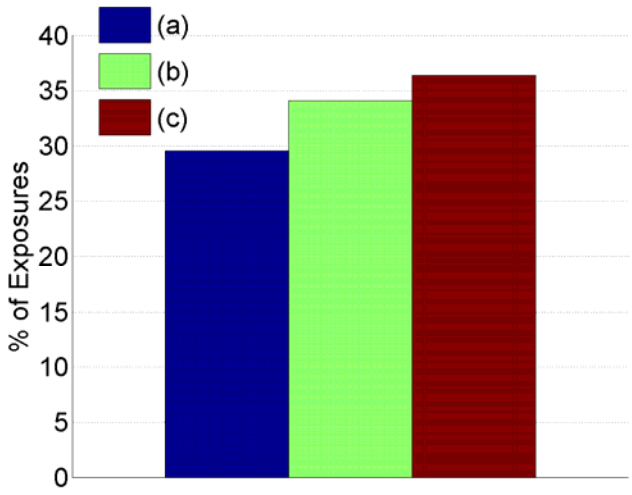

Figure 11.21. The percentage of preconditioning exposures that either had (a) no echogenicity, (b) echogenicity and no boiling or (c) echogenicity and boiling after preconditioned HIFU exposures, $n = 45$.

Figure 11.21 shows that echogenicity was seen in approximately 71% (b+c) of all exposures that included preconditioning, irrespective of whether boiling occurred or not. Echogenicity was not seen in any exposures in the absence of a preconditioning pulse.

11.3.2 *Boiling enhancement*

Examples of lesion generated in ex-vivo tissue samples, by (a) a boiling exposure only, (b) a cavitation free exposure only, and (c) both exposures in the same sample, are presented in Figure 11.22. Blue and green dashed vertical lines approximately indicate the focal peak positions at 15 and 35 mm deep in the tissue, respectively. Lesions generated from the heating only 4 s 990 W/cm^2 (1.47 MPa) exposures are approximately symmetrical in shape and centred around the focal peak position. Boiling exposures (0.5 s at 4400 W/cm^2 or 2.73 MPa) typically generated lesions that were pre-focal and 'tadpole' shaped facing towards the transducer, when both exposures are placed in the same sample, the damage overlaps.

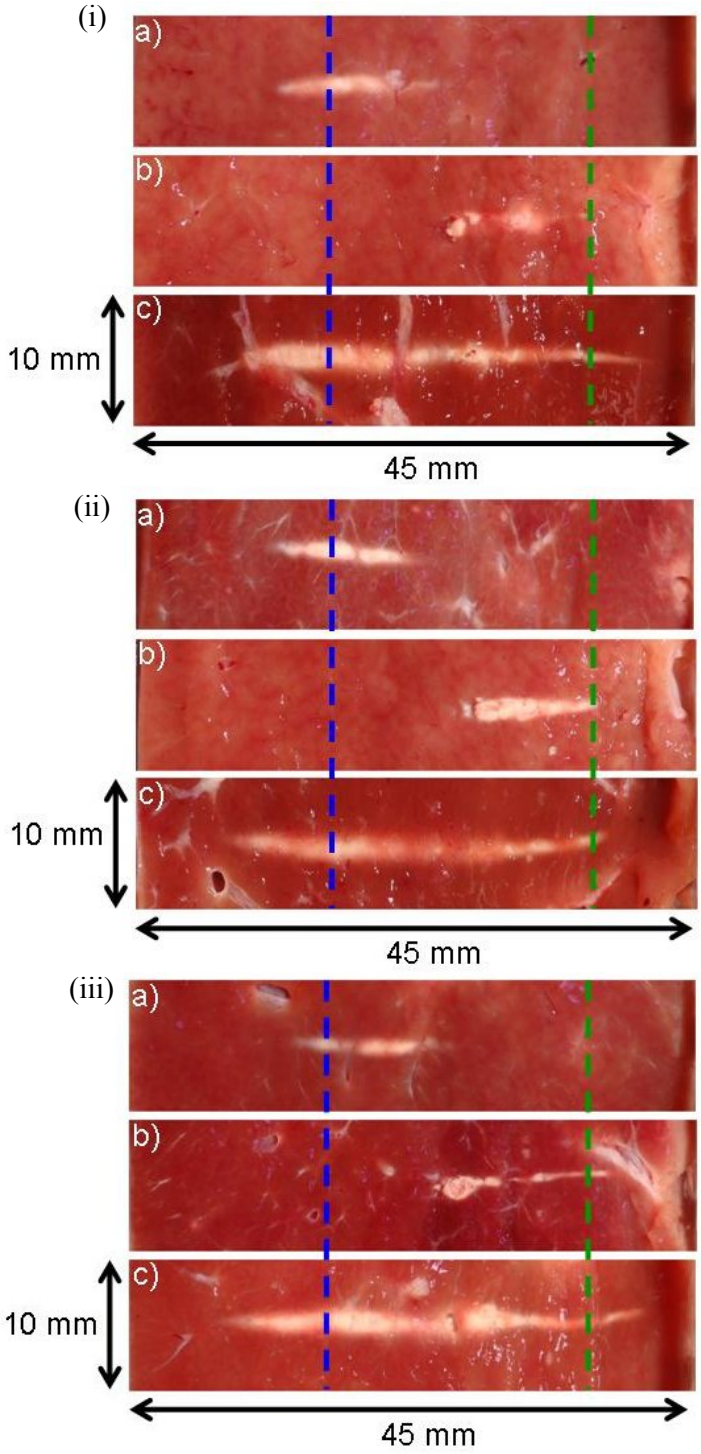

Figure 11.22. Three examples of lesions generated in ex-vivo bovine liver tissue from, (a) 4 s 990 W/cm^2 (1.47 MPa), (b) 0.5 s 4400 W/cm^2 (2.73 MPa) and (c) both exposures in the same sample. In all cases, the HIFU field propagated from left to right. The blue and green dashed lines indicate the approximate position of the HIFU foci at 15 and 35 mm depth in the tissue.

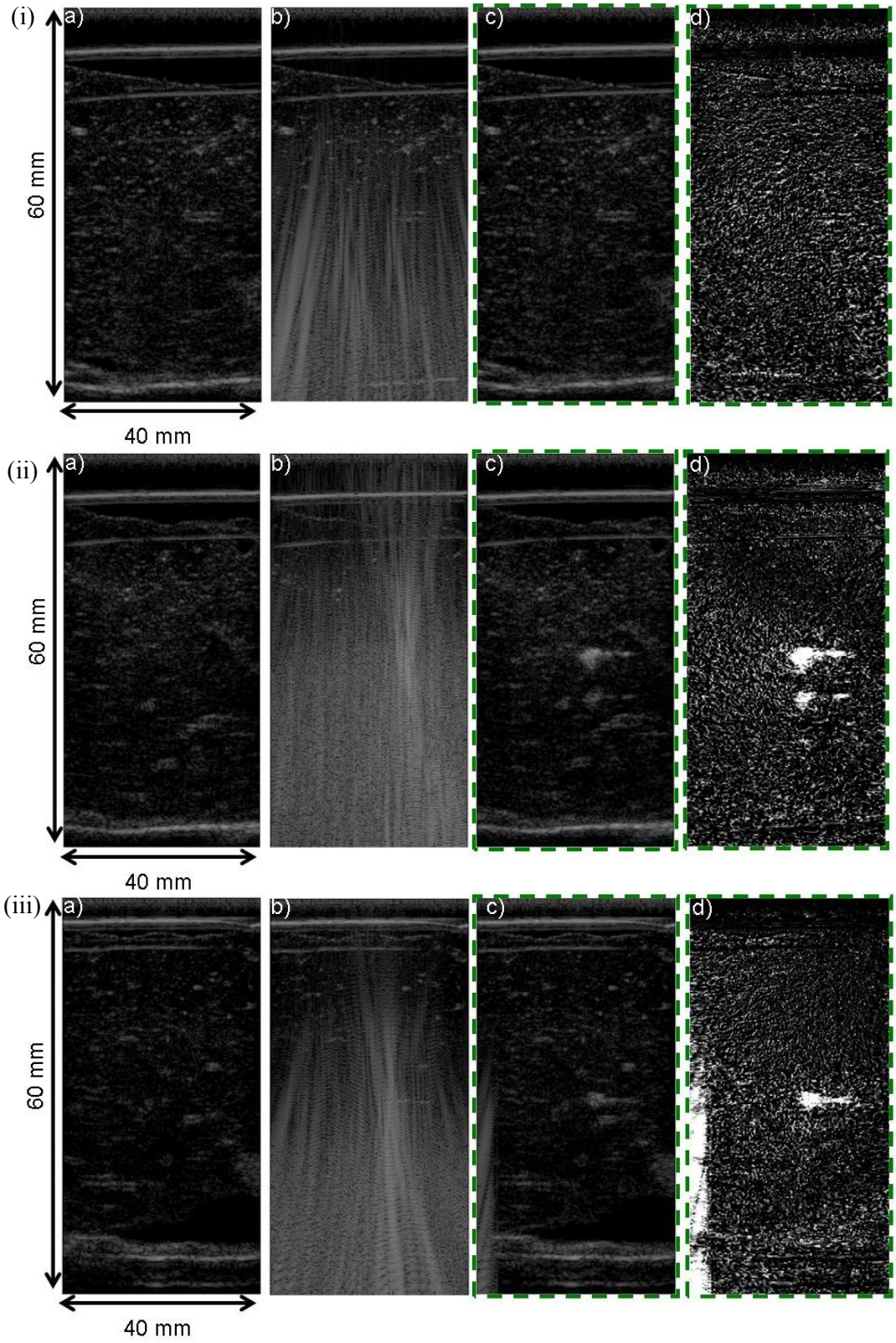

Figure 11.23. B-mode images taken (a) before, (b) during and (c) after HIFU exposure, with (d) the relevant subtraction image, for (i) a cavitation free exposure only, (ii) boiling exposure only and (iii) both exposures, the lesions are shown in Figure 11.22. The HIFU field propagates from left to right.

Figure 11.23 shows hyperechogenicity in the boiling only exposure (Figure 11.23(ii)) and when both exposures were used (Figure 11.23(iii)). The subtraction image in Figure 11.23(ii) shows that the hyperechogenicity caused a double reflection and it appears in two locations at different radial position tissue, in reference to the HIFU field. Interference from the end of the HIFU exposure can be seen in (c) in Figure 11.23(iii), which can also be seen as a bright region in the subtraction image. In the images taken during the HIFU exposures (Figure 11.23(c)) a region of increased interference can be seen in the approximate location of the hyperechogenicity after the HIFU exposure.

Figure 11.24 shows the acoustic spectra and drive voltage measurements acquired during the three exposures. The half harmonic signal is greater than the noise level defined by the sham exposure measurement, however in Figure 11.24(a) this is due to a faulty pre-amplifier which was repaired immediately after this exposure. Half harmonic emissions were not detected from other 4 s exposures at 990 W/cm^2 (1.47 MPa), unless they were preceded by 0.5 s boiling exposures (Figure 11.24(c)). The drive voltage fluctuations can be seen for both the boiling exposures in Figure 11.24(n) and (o). Broadband emissions were detected only during the 0.5 s 4400 W/cm^2 (2.73 MPa) exposures (Figure 11.24(k) and (l)). Half harmonic, ultraharmonic and broadband emissions were detected during the single 0.5 s exposures when the focal peak was approximately 20 mm away from the focal region of the 7.5 MHz passive sensor used in this system. Figure 11.24(o) shows that there was approximately a 2 s delay between the heating and boiling exposures.

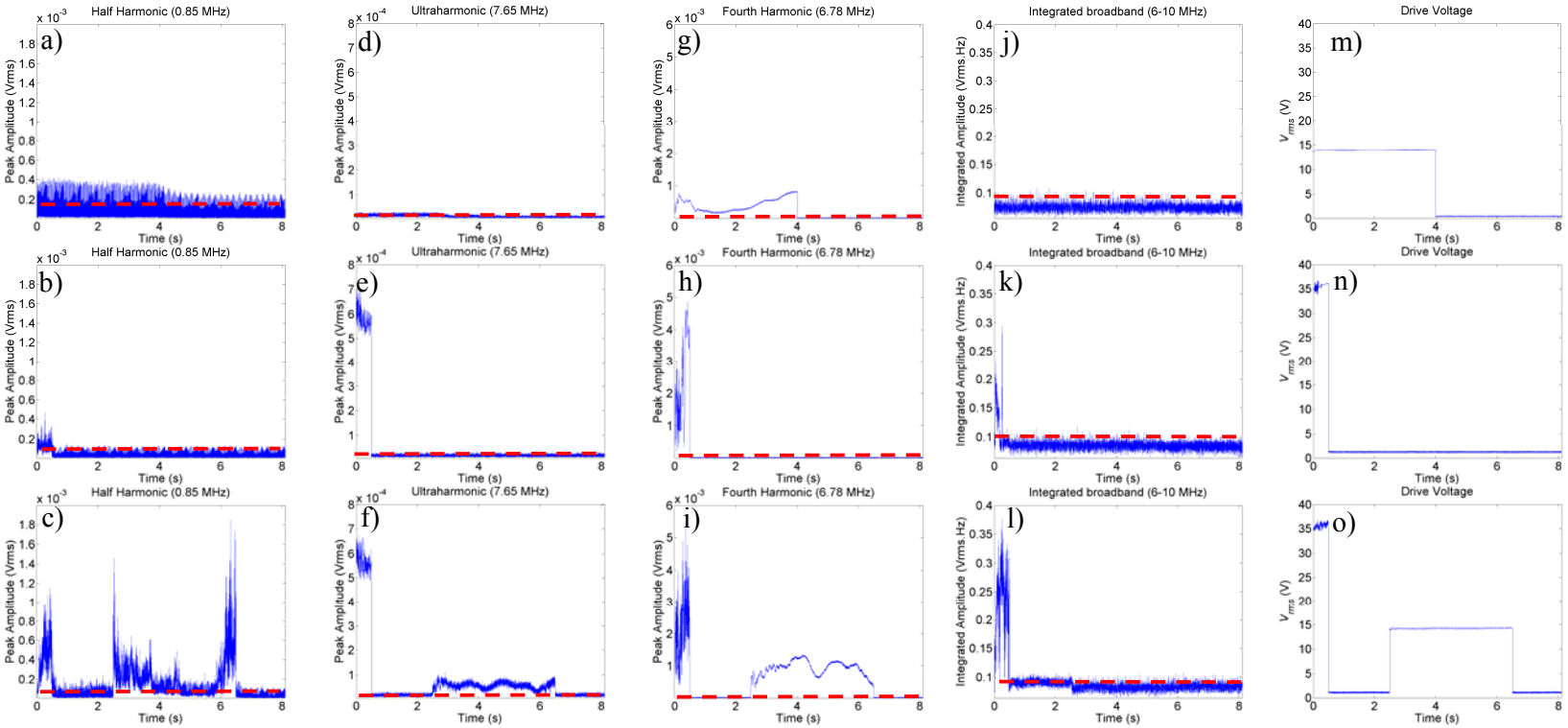

Figure 11.24. The detected half harmonic (a-c), ultraharmonic (d-f), fourth harmonic (g-i), integrated broadband (j-l) and electrical drive power (m-o) for three HIFU exposure types in ex-vivo liver. First row is 4 s at 990 W/cm^2 (1.47 MPa), the second row is 0.5 s at 4400 W/cm^2 (2.73 MPa), and the third row is both exposures in the same sample. The dashed red line indicated the peak noise level measured from a sham exposure.

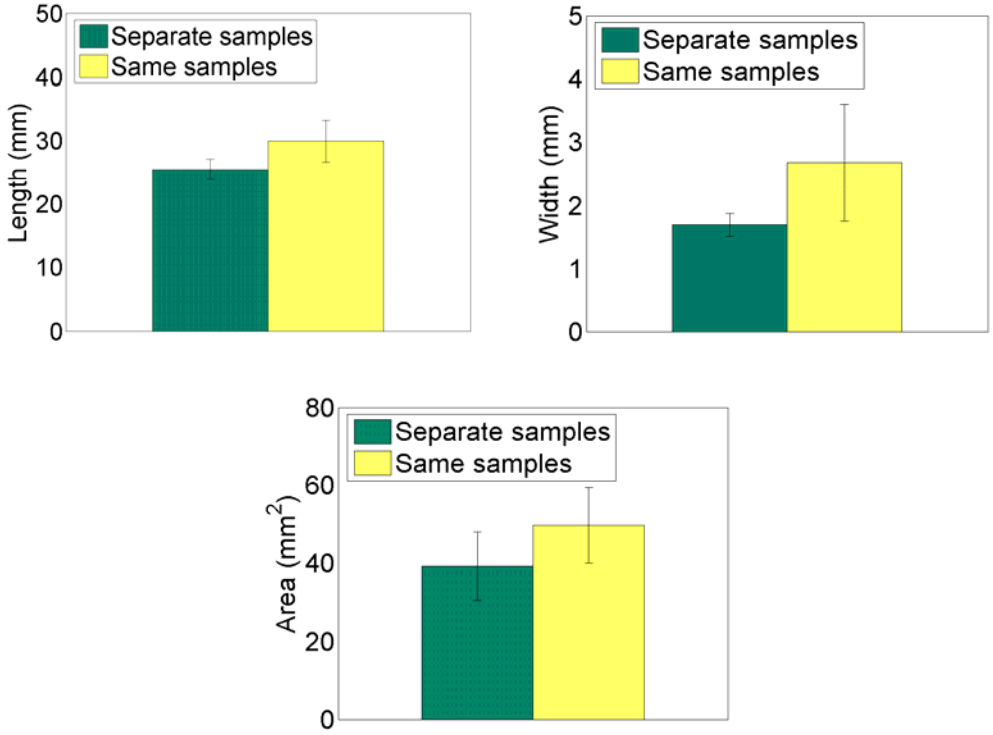

Figure 11.25. Average length (P = 0.001), width (P = 0.004) and area (P = 0.011) for lesions generated with the combined dimensions of the cavitation free and boiling lesions generated separately in different samples, or in the same sample. Uncertainties are the standard deviation of the averaged values.

Figure 11.25 shows the lesion dimensions when a boiling exposure was placed behind, and 2 s prior to, a single cavitation free exposure. These dimensions are compared with the sum of the dimensions measured from the cavitation free and boiling lesions generated in separate samples on their own. Lesion dimensions show a statistical significant increase when a boiling exposure was used for preconditioning.

11.4 Discussion

11.4.1 Acoustic cavitation enhancement

Using a single transducer meant that the focal peak at the two frequencies used (0.8 MHz for preconditioning and 1.7 MHz to produce a lesion) were at the same position. However, Table 11.1 shows that the FWHM pressure at 0.8 MHz was approximately twice that at 1.7 MHz. This suggests that a volume twice that of the focus at 1.7 MHz would be preconditioned, but only if this value represents the threshold pressure

required to generate acoustic cavitation. This would mean that regions outside the HIFU heating zone could experience enhanced acoustic cavitation activity. If this occurred pre-focally (for the 1.7 MHz exposure) it might shield the focal region causing a reduction in lesion size. The only disadvantage of operating a single transducer at two frequencies was that it was not possible to investigate the exposure of tissue to both frequencies at the same time (Liu *et al*, 2006).

A preconditioning pulse may be any type of exposure that precedes the HIFU heating pulse, and there are thus a large number of potential variables for such a pulse, depending on the effect required. For this study, the specific aim was to enhance lesion formation through facilitating a greater amount of acoustic cavitation during a lesioning exposure, which might lead to greater heating and thus enhanced lesion size. The delay between the preconditioning pulse and heating exposure was fixed at the shortest time possible, as limited by the ring down of the HIFU transducer, approximately 6 μs. This study was undertaken in three stages. Firstly, the preconditioning frequency and exposure length (for both the preconditioning pulse and heating exposure) were kept constant. The peak negative pressure of the preconditioning pulse was varied until a value was found which provided a statistically significant difference in either the detectable acoustic emissions or lesion dimensions. Figure 11.6 to Figure 11.11 show data from this study in which it was found that at 3.00 MPa, a 400 cycle preconditioning pulse caused up to a 100% increase in detected acoustic emissions (Figure 11.10). However, Figure 11.11 shows that this increase in acoustic emissions, and by association acoustic cavitation activity, did not have a measurably significant effect on lesion dimensions. It was hypothesised that either the level of acoustic cavitation was insufficient to generate an increase in the heating. This led to a second avenue of investigation in which the HIFU heating exposure length was increased to 8 s, but the intensity was reduced, in an effort to minimise the acoustic cavitation activity that occurred in the absence of preconditioning. A HIFU heating exposure regime was found that generated a repeatable uniformly ellipsoidal shaped lesion in the absence of boiling. Figure 11.12 to Figure 11.16 show that the 0.8 MHz (3.00 MPa) preconditioning pulse selected had a more significant effect on the detected acoustic emissions from HIFU heating exposures than that at 1.7 MHz (at the greater peak negative pressure of 3.61 MPa). A significant observation from the 0.8 MHz preconditioning experiments is that they generated the only hyperechogenic regions seen, during this entire project, in the

absence of boiling (e.g. Figure 11.9 and Figure 11.14). This demonstrates that these exposures have caused an increase in the bubble population which can be detected with diagnostic ultrasound after the exposure. Figure 11.14(d), shows a lesion from such an exposure. It is clear that this lesion has an irregular shape, not only that, but the wider section of the lesion is in the deeper post-focal region. This is another completely novel observation. In the case of boiling exposures, this wider region of damage more usually occurs in the pre-focal region, (sometimes called a 'tadpole' lesion, §2.4). This new finding suggests preconditioning can create bubbles in the post-focal region leading to an increase in lesion width in that region. There was no statistically significantly ($P > 0.05$) increase in the lesion size (Figure 11.16) when using a 0.8 MHz preconditioning pulse, compared with no pulse, or one at 1.7 MHz. The lesions that were generated tended to have irregular shapes, which is unlikely to be clinically useful since an array of irregular lesion shapes, could result in a non-confluent ablated volume, resulting in a failed treatment. The final study in this set was an investigation into the effect of preconditioning pulse length. The data from this are shown in Figure 11.7 to Figure 11.19. The lesions shown in Figure 11.17 that were generated using different numbers of acoustic cycles, produced further irregularly shaped lesions.

The acoustic spectra and V_{rms} drive voltage for these exposures (Figure 11.18) showed increases due to preconditioning. Some of these exposures were found to boil, an effect which never occurred in the absence of a preconditioning exposure under these conditions. This may have been caused by the increase in heating caused by acoustic cavitation activity at specific locations in the tissue. When boiling occurred (~34% of exposures), hyperechogenicity was always seen after the exposure, however this was sometimes the case simply from the use of a preconditioning pulse (~36% of exposures), as shown in Figure 11.21. This figure also shows that no hyperechogenicity was present in approximately 29% of the exposures where a preconditioning pulse was used. Figure 11.19 shows the detected acoustic spectra from the study of the effect of changing the number of acoustic cycles. This indicated that pulses consisting of 200 or more acoustic cycles (≥250 μs) caused the greatest change in the acoustic emissions, by up to 100% compared with those generated without preconditioning. However, lesion formation was generally irregular, as shown in Figure 11.17, and did not show an increase in lesion overall size (data not shown but $P > 0.05$ for all pulse lengths). Thus, the additional acoustic cavitation activity was not enhancing lesion formation in the

desired fashion. It could be argued that, since boiling sometimes occurred (Figure 11.21) in preconditioning exposures, there was localised enhancement of the heating. However, the clinical use of this would be limited as it would not be possible to identify before an exposure if this was going to occur.

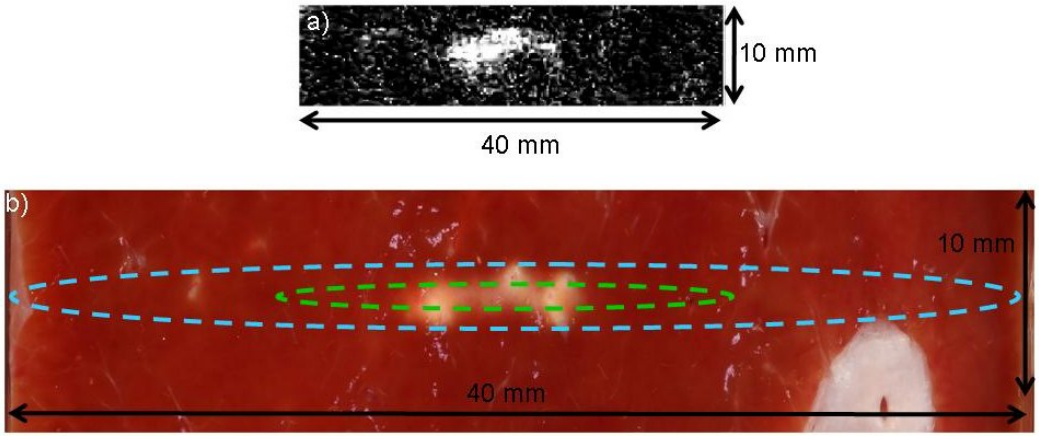

Figure 11.26. The subtraction image (a) and lesion photograph (b) from an 8 s HIFU heating exposure at an in-situ I_{sp} = 620 W/cm^2 (3.04 MPa), using a 400 cycle, 4.29 MPa 0.8 MHz preconditioning pulse. The green and blue ellipses in (b) are representative of the FHWM for the HIFU foci at 1.7 and 0.8 MHz, respectively. Boiling did not occur during this exposure (i.e. no audible emissions and electrical drive power fluctuations were seen).

Figure 11.26(b) shows an example of a lesion generated using a preconditioning exposure. The irregular shape of lesion can be seen to be made up of a number of possible 'hotspot' regions where acoustic cavitation bubbles could have been generated in sufficient numbers to affect the shape of this lesion noticeably and in some cases the structure of the tissue. Small 'holes' can be seen within the lesioned area, these are on a smaller scale (~0.5 mm) than those seen through boiling. It shows that the preconditioning pulse (blue ellipse) exposes a far greater region of tissue than is lesioned, but damage is localised reasonably well within the focal volume of the HIFU heating pulse (1.7 MHz). The regions with apparent increased acoustic cavitation activity may have elevated concentrations of pre-existing nuclei (§2.2). The addition of a preconditioning pulse may not increase the nuclei population uniformly throughout the focal region, but rather may cause greater activity where these nuclei already exist. This point is highlighted in Figure 11.27, where four exposures (0.5 s at 3.00 MPa with 0.8 MHz) in different tissue samples caused different locations of hyperechogenicity,

suggesting that this was due to pre-exciting nuclei in these locations. In addition, no damage was found in any of these samples when dissected after the exposures.

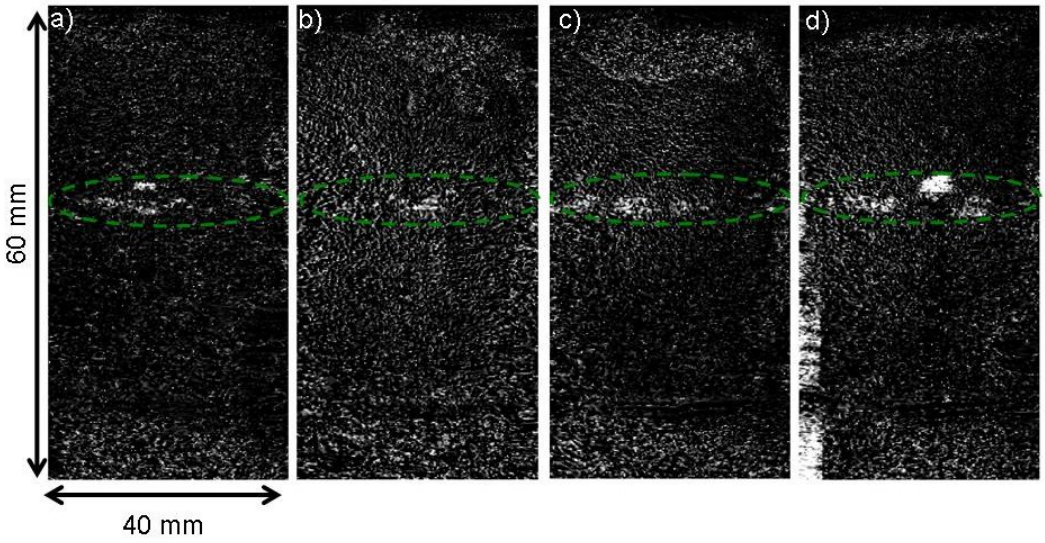

Figure 11.27. Four separate subtraction images of 0.5 s, 3.00 MPa, 0.8 MHz preconditioning exposures, in ex-vivo liver samples. The green ellipse approximately indicates the FWHM pressure of the HIFU focal field at 0.8 MHz. The bright region at the bottom left of (d) is due to the frame capturing the end of the HIFU exposure.

This finding supports the evidence already seen in the perfused liver study (§10.4), where histological analysis of the lesions showed that damage, possibly caused by acoustic cavitation (§10.3.1, Figure 10.7), was found in localised regions within the tissue.

11.4.2 Boiling enhancement

Figure 11.22 shows examples from combining a boiling exposure with a heating exposure in an effort to produce an increase in the lesion dimensions greater than the sum of the two exposures. As seen previously (§7.2.2) the presence of boiling generated a highly reflective region, as demonstrated by the detection of power fluctuations or increased interference in B-mode images (Figure 11.23(c)). By placing this reflective region behind a targeted area it was hoped that is reflective region would cause the energy to reflected into the focal region, causing greater energy deposition and increased lesion dimensions. Hyperechogenicity was present for all of the boiling exposures, which suggested that if enhancement of lesion dimensions was due to bulk heating, rather than an increase in energy deposition through scatter, short boiling

exposures could still be used to check targeting of the HIFU in the tissue. A boiled region could be generated as part of the treatment planning process indicating the outline of the treated region, and thus allowing preliminary assessment of efficacy during treatment delivery. Acoustic emissions were detected during the boiling exposures (Figure 11.24(b-c) and (k-l)) even though the focal region of the 7.5 MHz sensor was located approximately 20 mm less deep in the tissue than the HIFU focal peak. However, this distance is probably an overestimation of the separation as the source of these emissions is most likely to be within the boiled regions, which were always shown, in B-mode images and lesion photographs, to be in the pre-focal region. A more realistic separation estimate would be approximately 10 mm, which demonstrates that the passive cavitation detection system appears to be sensitive to cavitation activity outside the focal region of the sensor. Figure 11.25 shows that the use of a single boiled lesion gave a statistically significant enhancement ($P < 0.05$) of the lesions length, width and area when compared with the lesions generated from a cavitation free and boiling exposures separately. A finite element model, based on the bio-heat transfer equation was used, to calculate the heat deposition due to a linear HIFU field (Civale, 2008) (Chapter 2). This model showed that temperature at the edge of the FWHM pressure at this frequency after the boiling exposure would be approximately 27^{o}C (22^{o}C start temperature) after 2 s cooling. Assuming that the entire area of the cavitation free exposure was at the elevated start temperature of 27^{o}C, it was found that based on the thermal dose model (Chapter 7) this elevated start temperature would generate an ablated area that was approximately 30% larger than when calculated with a 22^{o}C start temperature. This suggests that the maximum increase caused by this bulk heating could account for 30% of the lesion enhancement seen. In these experiments however, the temperature at the focal region of the cavitation free exposure was 23.5^{o}C, only a 1.5^{o}C increase. However, this approximation demonstrates that an 8% enhancement was seen using of this technique.

11.5 Conclusion

Acoustic cavitation has been used to enhance lesion formation in localised regions in ex-vivo bovine liver tissue. The tissue was exposed to preconditioning and heating exposures that were generated consecutively from a single HIFU transducer.

A 0.8 MHz frequency (3.00 MPa) preconditioning pulse was found to generate the greatest increase in detected acoustic emissions from an 8 s HIFU heating exposure at

1.7 MHz (3.61 MPa). The number of acoustic cycles within the preconditioning pulse did not seem to have a significant effect on the acoustic cavitation activity, although in general 200 cycle or longer pulses produced emissions with the largest amplitude during the heating exposure. The preconditioning pulses generated irregularly shaped lesions when compared with equivalent exposures without a preconditioning pulse. This provides an obstacle to the direct application of this technique to clinical use, but demonstrates that acoustic cavitation could enhance the heating from a HIFU exposure. Hyperechogenicity was seen when preconditioning exposures were used in ex-vivo tissue. This was the first time that this effect has been seen in this study without the occurrence of boiling, indicating that there had been a significant increase in acoustic cavitation activity. The lesion enhancement appeared to be generated in localised regions, which may have been related to the presence of pre-existing nuclei in these regions of the tissue. The increased heating, caused by acoustic cavitation, generated temperatures which led to boiling during the 8 s HIFU heating exposure. This gives evidence, in ex-vivo tissue, of the heating effects that acoustic cavitation activity can cause during HIFU exposures.

Boiling exposures were successfully placed 3.5 cm deep in 0.5 s exposures, 2 s prior to a single 4 s cavitation free exposure. Hyperechogenicity was caused when boiling was generated, and persisted until the end of the cavitation free exposure even though boiling was not detected. This causes a reflective region behind the ‘heating’ lesion that was shown to produce a statistically significant increase in the lesion dimensions. In addition to this, drive voltage fluctuations were monitored at these depths (3.5 cm) in tissue and acoustic emissions were detected for activity that was approximately 10 mm away from the focal region of the passive sensor. This technique shows potential for the clinical use of boiling lesions to enhance the lesion dimensions generated from HIFU exposures.

12 – Conclusion and future work

12.1 Cavitation detection

12.1.1 Towards a clinical cavitation detection system

Currently, no clinical HIFU systems have a built in, dedicated system for monitoring cavitation activity during treatments. An aim of this study was to investigate achieving this for a new clinical extra-corporeal HIFU system. Chapter 3 reviews different methods of cavitation detection. Active and passive cavitation detection techniques were chosen as the most appropriate for clinical monitoring. As discussed in section 4.1 no specific acoustic emissions (i.e. superharmonics, ultraharmonics, subharmonics, and broadband emissions) gave a comprehensive indication of the type acoustic cavitation activity occurring from a HIFU exposure. For this reason, a 'full spectrum' passive cavitation detection system was initially designed and implemented. This system was capable of monitoring each type of acoustic emission (in the ranges 0.1 to 0.8 MHz and 4 to 12.5 MHz) simultaneously and for the entire duration of the HIFU exposure. Where monitoring for the entire duration was not possible (> 16 s exposures) intermittent sampling was able to sample the data 37 times a second for an extended period of time (limited by the storage capacity of the system). The filtering and amplification electronics were designed to be most effective for HIFU transducers with a drive frequency of 1.7 MHz, but it would be possible to replace these so that the system could be used at different drive frequencies. Monitoring of the fourth harmonic (6.78 MHz), ultraharmonic (7.65 MHz), half harmonic (0.85 MHz), low frequency broadband emissions (0.1-0.8 MHz), and high frequency emissions (4-10 MHz) gave a comprehensive picture of the acoustic cavitation activity. The fourth harmonic signals were considered to be dominated by scattered non-linear components of the HIFU field, rather than by non-linear bubble oscillation. The remaining acoustic spectra were attributed to the presence of acoustic cavitation because the harmonic content of the drive was software filtered out before analysing the broadband emissions. This passive monitoring equipment could be incorporated into a clinical system with the appropriate choice of passive sensor. Dual and single sensors were used with the passive detection system, after a preliminary study was performed with a novel cavitation sensor from NPL. The focal lengths of these sensors were such that the longest focal length sensor

(7.5 MHz, §4.2.1) would be suitable for shallow HIFU treatments up to 50 mm in depth. The flexibility of the construction of this passive system meant that an appropriate sensor could easily be incorporated into the existing system with minimal modifications. It would be possible to monitor audible emissions (2-20 kHz) in the clinic to detect boiling during treatments. A simple form of this could be the design of a stethoscope with a built in microphone to attach to the patient near the treatment region; this would be connected directly into a computer that could analyse the audio data, preferably in real time, and give feedback about the detected spectra, or perhaps even control an exposure for example by ending it as soon as boiling occurs. The disadvantage of this technique would be the ambient audible noise coming from the patient, for example due to the beating of the heart, which might mask audible emissions from cavitation.

B-mode imaging and electrical drive power (and V_{rms}) monitoring comprised the active cavitation detection used in this study. Monitoring electrical drive power fluctuations was the single most useful, and easiest, method that could be implemented into a clinical system since the measurement hardware was already present in the first clinical prototype developed at the ICR/RMH. Other than Magnetic Resonance Imaging, B-mode ultrasound is currently the only modality used for guiding HIFU treatments (§1.2.2), and as such is already used as an active bubble detection method. The subtraction image technique shown here (Chapter 7) could be incorporated into a diagnostic ultrasound system to give better visualisation of the hyperechogenic regions. However, in a clinical setting, these images would be susceptible to motion artefacts, and thus a technique whereby the acquired images are gated to for example, the respiratory cycle might be needed.

12.1.2 Future work

All the active and passive cavitation data analysis in this study was performed after HIFU exposure had taken place. In order to fully integrate these techniques into a clinical system, real time (or equivalent) feedback would need to be developed. This could be done using the existing system, since the data acquisition cards are fully programmable (in C language), or it would be possible to control them using MatLab, it would thus be possible to write a GUI capable of analysing the data in real time (~ 10 ms) and of providing feedback to the operator. The nature of any feedback system could vary depending on the application. A simple form of this could be to tabulate numerical

values from the detected acoustic spectra, a concept similar to the mechanical index (MI) calculated by, and displayed on, diagnostic ultrasound scanners. All the different cavitation activity detected could be combined to provide either a suite of information for the planning and feedback of HIFU treatments or a single quantitative value.

Suitable passive sensor development would be necessary for clinical use of this detection system. Some significant challenges must be met before this can happen. One of these is improving the location of the passive sensor. During this study (§7.3.1, 9.2, and 10.2.2), the 7.5 MHz sensor was mounted on the side of a HIFU transducer. This had the advantage of coupling the sensor to the movement of the HIFU transducer. Nevertheless, this limited the axial motion of the HIFU transducer since the focal length of the sensor was shorter than that of the HIFU device. An alternative to this would be to use a sensor in a window, such as the imaging hole in the centre of the Imasonic transducers. However, this would prevent the use of diagnostic imaging, which would not be optimal as treatment guidance must take priority over cavitation monitoring, unless it is be possible to design a diagnostic imaging device that could achieve both functions. This has been demonstrated in Chapter 8 with the use of the Terason ultrasound scanner, both as a passive cavitation detection device during the HIFU exposure, and as a diagnostic imaging device before and after the exposure. This detection system was able to monitor emissions from a 40 mm area but was not as sensitive to acoustic emissions as the focused detector used in conjunction with it. This would take collaboration with a diagnostic ultrasound manufacturer in order for this functionality to be incorporated into an existing standard commercial system.

The amplitude of detected acoustic spectra is affected by the filtering, amplification and sensitivity of the detection system used. This varies between different detection systems, and thus a method of calibration is needed in order that the emissions could be compared. One possible way of achieving this would be to use direct observation as a quality assurance technique. If a single bubble could be generated, and driven, by a HIFU field, direct observation would allow monitoring of the radius of the oscillations and association of this with the type of acoustic emissions detected. The amplitude of the detected emissions could be used to quantify the acoustic emissions detected from a HIFU exposure.

12.2 Cavitation thresholds

12.2.1 Cavitation thresholds in degassed water and tissue

The active and passive cavitation detection system was used to study the cavitation activity in a sonochemical solution, degassed tap water, ex-vivo bovine liver and porcine kidney, and perfused porcine liver. It was possible to separate the cavitation activity into two distinct types for HIFU exposures in tissue. The first category is acoustic cavitation, which is generated from the tension in the tissue caused by the negative pressure of the HIFU field (§2.1.1). The second is cavitation generated from the thermal ex-solution of gas vapour from liquid, which is more commonly, but less accurately, referred to as boiling. The system was used to study the acoustic negative pressure thresholds required for detection of non-inertial and inertial cavitation, and boiling.

As the absorption coefficient in the sonochemical solution and degassed water is negligible, it is not possible to generate heating (boiling). This provided an opportunity to study just the acoustic cavitation activity from HIFU exposures. The sonochemical solution (potassium iodide) which produces iodine from the generation of free radicals from inertial cavitation activity (§6.1) gave an independent method for the identification of inertial cavitation. The small HIFU focal region, compared to the sample size, meant that it was difficult to produce a detectable chemical change that correlated with the detection of inertial cavitation induced acoustic emissions until the exposure time was increased to 16 s.

In Chapter 6 it was demonstrated that it was possible to identify pressure thresholds for both non-inertial and inertial cavitation activity in degassed water exposures. These were based on the assumption that the detection of half harmonic emissions in the absence of broadband emissions indicated non-inertial cavitation, whereas inertial cavitation was indicated by the presence of broadband emissions. Audible emissions (2-20 kHz) were also detected during the exposures where broadband emissions were detected, which also corresponded to electrical drive power fluctuations. This suggested that, for these exposure conditions, the bubble population was large enough to cause sufficient backscatter to produce electrical drive power fluctuations above noise. As broadband emissions and audible emissions were detected simultaneously, this suggests that inertial cavitation played an important role in this process.

In ex-vivo bovine liver tissue, it was possible to generate lesions that involved (i) only thermal effects (i.e. due to absorptive HIFU heating), (ii) thermal effects and acoustic cavitation, or (iii) thermal effects, acoustic cavitation and boiling bubbles. Audible emissions, drive power fluctuations and B-mode imaging of the HIFU axial focal region before and after HIFU exposure appeared to identify the production of boiling bubbles. It was not possible to detect audible emissions and electrical power fluctuations from acoustic cavitation alone (unlike in degassed water exposures). The reason for this was hypothesised to be due to the smaller number of cavitation nuclei present in the ex-vivo tissue than in degassed water. B-mode imaging during HIFU exposure showed an increase in the detected interference from the HIFU field when boiling occurred (as this occurred at the same time as audible emissions and drive power fluctuations). Section 7.2.2 described a technique by which this interference was analysed to obtain approximate localisation of these boiling events. After the exposure, hyperechogenicity was always seen if boiling had occurred. This hyperechogenicity gave location information about the lesion, but did not accurately represent its spatial extent. It was observed that the occurrence of boiling caused an increase in the detected acoustic emissions, specifically the broadband emissions (Chapter 7). This increase could be attributed to boiling bubbles seeding acoustic cavitation nuclei. One problem with this hypothesis is that at elevated temperatures the internal pressure of an acoustic cavitation bubble would be higher, restricting the violent collapse that generates broadband emissions. However, solution of the Rayleigh-Plesset equation for these conditions suggested that the bubbles could still collapse since the peak positive pressures generated from the HIFU field were large enough to overcome the increase in inertial pressure. It was not possible to identify any specific tissue damage arising from acoustic cavitation in ex-vivo tissue, however the occurrence of boiling sometimes generated millimetre sized ‘holes’ in the lesioned tissue (§7.2.2, 9.3.1 and 10.3.1). With increasing exposure intensity, boiling occurred earlier in the HIFU exposure.

Thermometry was attempted in order to measure the temperatures for which boiling occurred, but fine wire thermocouples were found to lower the acoustic cavitation threshold in ex-vivo bovine liver tissue (§7.4.2). This was probably due to the trapped gas on the surface of the thermocouple junction which remained despite cleaning in alcohol and soaking in degassed water. The increase in heating measured by the fine wire thermocouple, which corresponded temporally to detected acoustic emissions, was due to activity that was on or near to the thermocouple junction. This represented a

further artefact in this temperature measurement, since this enhanced heating would not occur in the absence of a fine wire thermocouple. Instead of fine-wires, needle thermocouples were used to measure the temperatures that occurred when boiling was observed in the experiments but these measurements proved problematic due to acoustic shielding of the thermocouple since boiling generally occurred in the pre-focal region. This meant that it was not possible to measure the temperature in the focal region when boiling occurred accurately.

The passive cavitation detection system was also used in a study with a commercially available extracorporeal HIFU system (JC HIFU system). It was found that acoustic cavitation and boiling occurred at all the exposure levels that are in routine use clinically. In addition to this, a diagnostic ultrasound system (Terason) was used as a passive detector. It was able to detect any acoustic emissions produced over the entire length (10 mm), of lesion tracks created in ex-vivo tissue but did not have the detection sensitivity of the focused passive sensor used in this study (§8.3.2). The hyperechogenicity generated from producing these tracks did not correlate well with the extent of tissue damage (generally overestimating it) seen in ex-vivo liver, suggesting that this is not an accurate method for the clinical identification of ablated regions.

A pressure threshold study was undertaken in ex-vivo porcine kidney, at 20 and 40^{o}C. The differentiation of acoustic cavitation and boiling was also possible in this tissue type, suggesting that this is a general trend in ex-vivo biological tissues exposed to HIFU. It was found that heating the kidney to 40^{o}C before HIFU exposure caused a reduction in the acoustic cavitation pressure threshold. However, it caused the boiling pressure threshold to increase for the same exposure length. Hyperechogenicity, audible emissions and power fluctuations were observed for exposures in which boiling occurred in this tissue type.

Perfused normothermic transplant viable porcine liver was the final tissue type in which the detectable cavitation thresholds were measured. The active and passive cavitation detection methods showed similar results to those observed in ex-vivo liver and kidney. This suggests that the phenomena of acoustic cavitation and boiling occur in living tissue and are not just due to the use of ex-vivo tissue. Histological studies were performed on the lesions generated from HIFU exposures which demonstrated acoustic cavitation, or acoustic cavitation and boiling. Damage from acoustic cavitation was sporadically located throughout the lesioned tissue, suggesting that cavitation activity occurs in regions where pre-existing nuclei are present.

The in-situ peak negative threshold pressures from the HIFU exposures in all of the different media used are shown in Table 12.1.

	Non-inertial Cavitation Threshold (-MPa)	Inertial Cavitation Threshold (-MPa)	Boiling Threshold (-MPa)	Chapter
Degassed water at 20^0C (n = 50)	≥1.80	≥ 2.10	N/A	6
Ex-vivo liver at 20^0C (n > 50)	≥1.52	≥ 1.77	≥ 1.86	7
Ex-vivo kidney at 20^oC (n = 77)	≥ 1.40	≥ 1.58	≥ 1.68	9
Ex-vivo kidney at 40^oC (n = 45)	≥ 1.31	≥ 1.40	≥ 1.98	9
Perfused liver at 38^0C (n ~ 100)	≥1.30	≥ 1.30	≥ 1.53*	10

Table 12.1. The *in situ* peak negative pressure thresholds required to generate cavitation activity in a number of different tissue types. Uncertainty in these measurements is ±17%. Refer to the relevant chapter for the specific value. *For HIFU exposures of 5 s duration, where all others were for 4 s.

12.2.2 Future work

Temperature monitoring would have provided clear indications of the peak temperatures required to generate boiling in tissue. However, invasive temperature monitoring has proved difficult, and so it should be possible to study temperature rises during exposures which cause boiling, using MRI temperature mapping. This could provide an indication of the peak temperatures that occur when audible emissions and power fluctuations are present. Use of this technique could make it possible to study the effect of rate of heating on the occurrence of boiling. Another benefit of MR temperature imaging would be the ability to identify 'hotspots' that could be due to acoustic cavitation enhanced heating. This could be limited by the spatial resolution of the MR temperature imaging.

In the studies undertaken here, the foci of the passive sensors were always aligned with the HIFU focal peak. It would be useful to investigate the positional variation in the pressure distribution on the HIFU field effect on the acoustic emissions. This could involve the use of an 'array' of passive sensors interrogating successive regions along the HIFU focal region. A study like this should provided useful spatial information about the cavitation activity from HIFU exposures, which could be related to lesion shapes. This technique could provide useful answers as to whether the occurrence of acoustic cavitation in specific locations in the tissue is affected more by the presence of nuclei or the peak negative pressure.

If the sonochemical measurements could be performed as a function of time during the HIFU exposure this could give valuable information for the quantification of the broadband emissions detected by the passive cavitation detection system in terms of the amount of bubble activity. This system would need to be more sensitive than the techniques used here as for the short exposures for which broadband emissions were detected no chemical change was measured.

Non-linear propagation of the HIFU field could cause uneven heating in the focal region, since the higher frequency components are focused over shorter distances in the tissue. It would be useful to identify whether these nonlinear components would interact with a bubble population, causing different acoustic cavitation activity from that seen when there are no superharmonics generated from non-linear propagation. This could be studied theoretically using a non-linear acoustic field model coupled with an appropriate bubble model (for example the Keller-Miksis equation). It should then be possible to investigate whether the number and relative amplitude of the non-linear harmonics generated from a HIFU transducer has any effect on the bubble activity and lesion formation.

The acoustic cavitation detection in this study was performed with at most 30 mm of attenuating tissue between the passive sensor and HIFU focal peak. In order for the system to be fully integrated for clinical applications, it would be necessary to detect the acoustic emissions at depths up to 120 mm (Visioli *et al*, 1999) and with the addition of different tissue path, for example a fat layer. This would need greater signal amplification than was used in this study (§4.2.2).

12.3 Cavitation enhancement

12.3.1 Lesion enhancement from cavitation

Two methods of enhancement of lesion formation from cavitation activity were investigated. The first of these was the use of preconditioning pulses which were designed to generate acoustic cavitation (using a short duration, and large peak negative pulse) immediately before a 4 or 8 s HIFU heating exposure. The rationale behind this approach was to generate acoustic cavitation, in a repeatable way, which would in turn give rise to enhanced heating from the bubbles generating larger lesions. A single HIFU transducer was used to provide both the preconditioning pulse and heating exposure. This configuration is the most suitable for clinical applications, since it was operated

from a single drive system (amplifier, matcher and transducer) with the addition of a second waveform generator and control hardware (FPGA card) to trigger the signal generators one after the other. Two frequencies of preconditioning pulse (0.8 and 1.7 MHz) were investigated, with the lower frequency pulse generating the largest increase in detected acoustic emissions during the HIFU exposure. The use of a preconditioning pulse resulted in a >100% increase in the total integrated emissions compared to an exposure without a preconditioning pulse. Unfortunately, this increase in detected acoustic emissions did not correlate with a significant increase in the lesion size. However, the use of preconditioning resulted in hyperechogenicity seen on a B-mode ultrasound scan, in the absence of boiling. This was not seen for unpre-conditioned exposures, but could be of clinical use for localisation of the possible locations of cavitation nuclei.

Investigation showed that the number of acoustic cycles (5-1000) in the preconditioning pulse had little effect on the amplitude of acoustic emissions and lesions sizes. However, the preconditioning did cause the lesions to have irregular shapes which were not seen without preconditioning. Clear 'hotspot' regions could be seen within the focal zone of the 1.7 MHz HIFU heating pulse in the lesioned tissue. In some cases, boiling was achieved, this was never seen in the absence of a preconditioning pulse for these exposure conditions. This suggested that there was enhanced heating in areas of increased bubble activity, but it was not a uniform effect, suggesting that a lack of cavitation nuclei in soft tissue could limit the use of acoustic cavitation to enhance lesion formation, without the introduction of contrast agents or other nuclei.

In a second study, the aim was to cause greater energy deposition in the target region during a cavitation free exposure (i.e. at acoustic pressures below the acoustic cavitation threshold), which should result in larger volumes of lesion ablation. This was achieved by generating a reflective region generated (between 10-20 mm) behind the target treatment area, using a 0.5 s boiling exposure. Boiling regions were targeted at a depth of 35 mm. Acoustic emissions (2-20 kHz) and drive voltage fluctuations detected from these exposures confirmed that boiling had occurred. The cavitation activity during these boiling exposures generated acoustic emissions of sufficient amplitude that they were detected by the passive cavitation detection system whose focal region was located approximately 10 mm away (at the lesioning focal depth 35 mm). Placement of a single boiling region behind the HIFU heating exposure was shown to have a

statistically significant enhancement effect on the lesion dimensions (~8%) when compared with the combined dimensions of the boiling and cavitation free exposures assessed using separate tissue samples. This technique may provide a useful way of exploiting cavitation induced optimisation of clinical HIFU treatments. In addition to the lesion size enhancement, the hyperechogenicity from the boiling region could be used as part of a confirmation to identify the outer edge of the targeted volume.

12.3.2 Future work

The enhanced heating observed in the acoustic cavitation preconditioning study seemed to be limited to specific regions of the tissue of less than 20% of the total lesion volume, where, it was hypothesised, cavitation nuclei were present. A useful study would be to investigate the availability of cavitation nuclei in soft tissue. In water, for example, the source of cavitation nuclei is well understood, but such information is not available for tissue.

Numerous mathematical models allow study of the behaviour of pre-existing bubbles exposed to a linear ultrasound field. However, it would be useful for a preconditioning study to be able to model the likelihood of cavitation inception in a target medium exposed to specific frequencies and peak pressures of a known HIFU field. This could first be done and tested in degassed water then applied to ex-vivo or in-vivo tissues. In connection with the modelling, it could be possible to use a preconditioning exposure only to generate hyperechogenic regions and use this to map out the area of possible concentrations of cavitation nuclei without causing any irreversible tissue damage. From a clinical prospective, this could be useful for the treatment planning process as is could indicate where acoustic cavitation enhanced heating could be achieved and thus the treatment time could be adjusted accordingly.

12.4 Final conclusion

The broad aim of this thesis was the investigation of whether cavitation could be used to optimise HIFU treatments. This has been tackled by the design and construction of a combine active and passive cavitation detection system which can be incorporated into a clinical device. This could be modified to provide real-time feedback on cavitation activity during HIFU exposures, and would be able to tell if boiling occurred. Feedback of this nature could be invaluable for avoiding the over-treatment of specific regions, and for interactively planning treatments. By avoiding over-treatment it should be

possible to speed up the delivery of HIFU exposure. The detection system used here has been successful in differentiating between acoustic cavitation and thermal ex-solution of gas vapour (boiling), two very different mechanisms of cavitation. This knowledge again provides information about exposure parameters that could be used for clinical HIFU treatments, which should give repeatable tissue ablation. For example, it would be a simple task to incorporate the monitoring of the electrical drive power and to identify when power fluctuations occur, in order to avoid generation of asymmetrical lesions due to boiling.

Enhanced heating from acoustic cavitation has been observed in ex-vivo tissue in this study. Unfortunately, the preconditioning technique seemed to be limited by the availability of cavitation nuclei. However, if this lack of cavitation nuclei could be overcome then it might be possible to increase tissue ablation rates by using acoustic cavitation combined with the thermal effect from HIFU exposures in soft tissue.

A number of different techniques for the identification of boiling have been demonstrated in this study and could be incorporated into a clinical system. In addition to the power fluctuations that were mentioned above, B-mode image subtraction could give an indication of where boiling occurred in the tissue, and audible emissions proved to be a reliable technique for the identification of the onset of boiling during a HIFU exposure. The increase in acoustic interference observed in B-mode images from boiling was used to approximately identity the location (in the axial plane) in the tissue that the boiling event occurred. The use of a boiling preconditioning exposure to increase the energy deposition in a subsequent exposure was shown to cause a statistically significant increase in the lesion dimensions (~8%). This technique would be very easy to implement in the clinical environment, and could also be used as part of the treatment planning process.

This thesis expands existing knowledge of cavitation activity and studies these phenomena in a number of different soft tissue types, thus increasing understanding of cavitation activity arising from HIFU exposures in soft tissue, and the pressure thresholds above which they occurred. This in turn leads to a greater understanding of these processes, and how they could affect clinical treatments.

Publications related to this thesis

McLaughlan J.R., Rivens I.H., Leighton T.G. , Humphrey V. , ter Haar G. , *A Study of bubble activity generated in Ex-Vivo Tissue by High Intensity Focused Ultrasound (HIFU),* – Under peer review for submission to UMB.

McLaughlan J.R., Rivens I.H., ter Haar G., (**2007**). *Cavitation detection in ex vivo bovine liver tissue exposed to high intensity focused ultrasound (HIFU),* 2007 IEEE International Symposium on Biomedical Imaging: From Nano to Macro, 1124-1127.

McLaughlan J.R., Rivens I.H., ter Haar G., (**2007**) *A study of cavitation activity in ex vivo tissue exposed to high intensity focused ultrasound,* 6th International Symposium on Therapeutic Ultrasound, 178-184.

McLaughlan J.R., Rivens I.H., ter Haar G., (**2006**). *A passive cavitation detection system for the monitoring of acoustic emissions for use in the optimisation of FUS treatments,* Proceedings of the Institute of Acoustics 28[Pt 1].

McLaughlan J.R., Rivens I.H., Shaw A., Leighton T.G., Humphrey V., Birkin P., Vain C., ter Haar G., (**2006**). *The design and implementation of a passive cavitation detection system for use with ex vivo tissue,* 5th International Symposium on Therapeutic Ultrasound, 338-342.

References

Aktins,P. (**1995**). *Concepts in Physical Chemistry*. Oxford Unviversity Press.

Apfel,R.E. (**1981**). *Acoustic cavitation prediction*. Journal of Acoustic Society of America 69[6] 1618-1623.

Apfel,R.E. (**1970**). *The role of impurities in cavitation-threshold determination*. Journal of Acoustic Society of America 48[5] 1179-1186.

Apfel,R.E. (**1984**). *Acoustic cavitation series: part four, Acoustic cavitation inception*. Ultrasonics 22[4] 167-173.

Apfel,R.E. (**1986**). *Possibility of Microscitation from Diagnostic Ultrasound*. IEEE Trans.Ultrason.Ferroelec.Freq.Contr. 32[2] 139-142.

Apfel,R.E., Holland,C.K. (**1991**). *Gauging the likelihood of cavitation from short-pulse, low-duty cycle diagnostic ultrasound*. Ultrasound in Medicine and Biology 17[2] 179-185.

Atchley,A., Prosperetti,A. (**1989**). *The crevice model of bubble nucleation*. Journal of Acoustic Society of America 86[3] 1065-1084.

Bailey,M.R., Couret,L.N., Sapozhnikov,O.A., Khokhlova,V.A., ter Haar,G., Vaezy,S., Shi,X., Martin,R., Crum,L.A. (**2001**). *Use of overpressure to assess the role of bubbles in focused ultrasound lesion shape in vitro*. Ultrasound in Medicine and Biology 27[5] 695-708.

Bailey,M.R., Pishchalnikov,Y.A., Sapozhnikov,O.A., Cleveland,R.O., McAteer,J.A., Miller,N.A., Pishchalnikova,I.V., Connors,B.A., Crum,L.A., Evan,A.P. (**2005**). *Cavitation detection during shock-wave lithotripsy*. Ultrasound in Medicine and Biology 31[9] 1245-1256.

Barnaby,S.W., Thornycroft,J. (**1895**). *Torpedo boat destroyers*. Proc.Inst.Civ.Engrs. 122 57.

Basude,R., Wheatley,M.A. (**2001**). *Generation of ultraharmonics in surfactant based ultrasound contrast agents: use and advantages*. Ultrasonics 39[6] 437-444.

Bihrle,R., Foster,R.S., Sanghvi,N.T., Donohue,J.P., Hood,P.J. (**1994**). *High Intensity focused ultrasound for the treatment of benign prostatic hyperplasia: Early United States clinical trials*. Journal of Urology 151 1271-1275.

Birchenhall,C. (**1994**). *Numerical Recipes in C - the Art of Scientific Computing*. Economic Journal 104[424] 725-726.

Birkin,P.R., Power,J.F., Leighton,T.G., Vincotte,A.M. (**2002**). *Cathodic electrochemical detection of sonochemical radical products*. Anal.Chem. 74[11] 2584-2590.

Birkin,P.R., Power,J.F., Abdelsalam,M.E., Leighton,T.G. (**2003**). *Electrochemical, luminescent and photographic characterisation of cavitation*. Ultrason.Sonochem. 10[4-5] 203-208.

Chapelon,J.Y., Margonari,J., Theillere,Y., Gorry,F., Vernier,F., Blanc,E., Gelet,A. (**1992**). *Effects of high-energy focused ultrasound on kidney tissue in the rat and the dog*. European Urology 22[2] 147-152.

Chappell,M.A., Payne,S.J. (**2006**). *A physiological model of the release of gas bubbles from crevices under decompression*. Respir.Physiol.Neurobiol. 153[2] 166-180.

Chappell,M.A., Payne,S.J. (**2006**). *A physiological model of gas pockets in crevices and their behavior under compression*. Respir.Physiol.Neurobiol. 152[1] 100-114.

Chaussy,C., Thuroff,S., Rebillard,X., Gelet,A. (**2005**). *Technology insight: High-intensity focused ultrasound for urologic cancers*. Nat.Clin.Pract.Urol. 2[4] 191-198.

Chen,W.S., Lafon,C., Matula,T.J., Vaezy,S., Crum,L.A. (**2003**). *Mechansims of lesion formation in high intesity focused ultrasound therapy*. ARLO 4[2] 41-46.

Chen,W.S., Brayman,A.A., Matula,T.J., Crum,L.A. (**2003**). *Inertial cavitation dose and hemolysis produced in vitro with or without Optison*. Ultrasound in Medicine and Biology 29[5] 725-737.

Chitnis,P.V., Cleveland,R.O. (**2006**). *Quantitative measurements of acoustic emissions from cavitation at the surface of a stone in response to a lithotripter shock wave*. Journal of Acoustic Society of America 119[4] 1929-1932.

Church,C.C. (**1989**). *A theoretical study of cavitation generated by an extracorporeal shock wave lithotripter*. Journal of Acoustic Society of America 86[1] 215-227.

Civale,J. (**2008)**. *Aspects of High Intensity Focused Ultrasound Treatment Planning:Rib Sparing, Attenuation, Thermometry and Exposure Determination*. University of London.

Clarke,R.L., ter Haar,G.R. (**1997**). *Temperature rise recorded during lesion formation by high-intensity focused ultrasound*. Ultrasound in Medicine and Biology 23[2] 299-306.

Clement,G.T., White,J., Hynynen,K. (**2000**). *Investigation of a large-area phased array for focused ultrasound surgery through the skull*. Physics Med.Biol. 45[4] 1071-1083.

Cleveland,R.O., Sapozhnikov,O.A., Bailey,M.R., Crum,L.A. (**2000**). *A dual passive cavitation detector for localized detection of lithotripsy-induced cavitation in vitro*. Journal of Acoustic Society of America 107[3] 1745-1758.

Coakley,W.T. (**1971**). *Acoustical detection of single cavitation events in a focused field in water at 1 MHz*. Journal of Acoustic Society of America 49[3B] 792-801.

Coleman,A.J., Choi,M.J., Saunders,J.E., Leighton,T.G. (**1992**). *Acoustic emission and sonoluminescence due to cavitation at the beam focus of an electrohydraulic shock wave lithotripter*. Ultrasound in Medicine and Biology 18[3] 267-281.

Coleman,A.J., Kodama,T., Choi,M.J., Adams,T., Saunders,J.E. (**1995**). *The cavitation threshold of human tissue exposed to 0.2-MHz pulsed ultrasound: preliminary measurements based on a study of clinical lithotripsy*. Ultrasound in Medicine and Biology 21[3] 405-417.

Coleman,A.J., Choi,M.J., Saunders,J.E. (**1996**). *Detection of acoustic emission from cavitation in tissue during clinical extracorporeal lithotripsy*. Ultrasound in Medicine and Biology 22[8] 1079-1087.

Cooper,C.M. (2000). The Cell: A Molecular Approach, Second Edition. The American Society for Microbiology, Washington DC, USA: Sinauer Associates Inc, Sunderland, MA, USA.

Coussios,C.C., Collin,J.R.T., and Muckle,A.P. (**2007)**. *Non-invasive Monitoring and Control of Inertial Cavitation Dynamics during HIFU Exposure In Vitro*. Coussious,C.C. and ter Haar,G. 6th International Symposium on Therapeutic Ultrasound[1st], 164-170. Melville, New York, AIP.

Coussios,C.C., Farny,C.H., Haar,G.T., Roy,R.A. (**2007**). *Role of acoustic cavitation in the delivery and monitoring of cancer treatment by high-intensity focused ultrasound (HIFU)*. International Journal of Hyperthermia 23[2] 105-120.

Crum,L.A. (**1979**). *Tensile strength of water*. Nature 278 148-278.

Crum,L.A. and Law,W. (**1995)**. *The relative roles of thermal and nonthermal effects in the use of high intensity focused ultrasound for the treatment of benign prostatic hyperplasia*. [3], 315-318. Trondheim, Norway, ICA 95 committee. Proceedings of the 15th International Congress on Acoustics.

Datta,S., Coussios,C.C., McAdory,L.E., Tan,J., Porter,T., De Court, Holland,C.K. (**2006**). *Correlation of cavitation with ultrasound enhancement of thrombolysis*. Ultrasound Med.Biol 32[8] 1257-1267.

Davidson,F. (**1991**). Ultrasonic Power Balances. In: Output Measurements for Medical Ultrasound, ed. R.C.PrestonLondon: Springer-Verlag, 75-90.

Deng,C.X., Xu,Q., Apfel,R.E., Holland,C.K. (**1996**). *In vitro measurements of inertial cavitation thresholds in human blood*. Ultrasound in Medicine and Biology 22[7] 939-948.

Devin,C. (**1959**). *Survey of Thermal, Radiation and Viscous Damping of Pulsating Air Bubbles in Water*. Journal of Acoustic Society of America 31[12] 1654-1667.

Duck,F.A. (**1990**). Acoustic Properties of Tissues at Ultrasonic Frequencies. In: Physical properties of tissuesLondon: Academic Press Ltd., 73-124.

Edmonds,P.D., Ross,P. (**1986**). *Acoustic-Emission As A Measure of Exposure of Suspended Cells-Invitro*. Ultrasound in Medicine and Biology 12[4] 297-305.

Eller,A., Flynn,H.G. (**1969**). *Generation of subharmonics of order one-half by bubbles in a sound field*. Journal of Acoustic Society of America 46[3] 722-727.

Eller,A.I. (**1970**). *Damping constants of pulsating bubbles*. Journal of Acoustic Society of America 47[5] 1469-1470.

Everbach,E.C., Makin,I.R., Azadniv,M., Meltzer,R.S. (**1997**). *Correlation of ultrasound-induced hemolysis with cavitation detector output in vitro*. Ultrasound in Medicine and Biology 23[4] 619-624.

Faraday,M. (**1831**). *On a peculiar class of acoustical figures; and on certain forms assumed by groups of particles upon vibrating elastic surfaces*. Phil.Trans.Roy.Soc. 121[] 299-340.

Farny,C.H. (**2007**). *Identifying and Monitoring the Roles of Cavitation in heating from High-Intensity Focused Ultrasound*. Boston University College of Engineering.

Flynn,H.G. (**1964**). Physics of Acoustic Cavitation in Liquids. In: Physical AcousticsNew York: Academic Press, 57-172.

Foster,R.S., Bihrle,R., Sanghvi,N.T., Fry,F.J., Donohue,J.P. (**1993**). *High-Intensity Focused Ultrasound in the Treatment of Prostatic Disease*. European Urology 23 S1 29-33.

Fox,F.E., Herzfeld,K.F. (**1954**). *Gas Bubbles with Organic Skin as Cavitation Nuclei*. Journal of Acoustic Society of America 26[6] 984-989.

Fry,F.J., Ades,H.W., Fry,W.J. (**1958**). *Production of reversible changes in the central nervous system by ultrasound*. Science 127 83-84.

Fry,F.J., Kossoff,G., Eggleton,R.C., Dunn,F. (**1970**). *Threshold ultrasound dosages for structural changes in the mammalian brain*. Journal of Acoustic Society of America 48[6] 1413-1417.

Fry,W.J., Fry,R.B. (**1953**). *Temperature Changes Produced in Tissue during Ultrasonic Irradiation*. Journal of Acoustic Society of America 25[1] 6-11.

Fry,W.J., Wulff,V.J., Tucker,D., Fry,F.J. (**1950**). *Physical Factors Involved in Ultrasonically Induced Changes in Living Systems: I. Identification of Non-Temperature Effects*. Journal of Acoustic Society of America 22[6] 867-876.

Fry,W.J., Tucker,D., Fry,F.J., Wulff,V.J. (**1951**). *Physical Factors Involved in Ultrasonically Induced Changes in Living Systems: II. Amplitude Duration Relations and the Effect of Hydrostatic Pressure for Nerve Tissue*. Journal of Acoustic Society of America 23[3] 364-368.

Fry,W.J., Barnard,J.W., Fry,F.J., Krumins,R.F., Brennan,J.F. (**1955**). *Ultrasonic lesions in the mammalian central nervous system*. Science 122[3168] 517-518.

Fry,W.J. (**1958**). *Use of Intense Ultrasound in Neurological Research*. American Journal of Physical Medicine 37[3] 143-147.

Fry,W.J. (**1958**). Intense Ultrasound in Investigations of the Central Nervous System. In: Advances in Biological and Medical Physics Volume IV, ed. J.H.Lawrence, T.A.CorneliusNew York: Academic Press Inc., 281-347.

Gaitan,D.F. and Crum,L.A. (**1990)**. *Observation of sonoluminescence from a single cavitation bubble in a water/glycerine mixture*. Hamilton,M.F. and Blackstock,D.T. 459. New York, Elsevier. Frontiers of Nonlinear Acoustics, 12th ISNA.

Gelet,A., Chapelon,J.Y., Poissonnier,L., Bouvier,R., Rouviere,O., Curiel,L., Janier,M., Vallancien,G. (**2004**). *Local recurrence of prostate cancer after external beam radiotherapy: early experience of salvage therapy using high-intensity focused ultrasonography*. Urology 63[4] 625-629.

Gooberman,G.L. (**1968**). *Ultrasonics: Therory and Application*. London: The English Universities Press Ltd.

Harvey,E.N., Barnes,D.K., McElroy,W.D., Whiteley,A.H., Pease,D.C., Cooper,K.W. (**1944**). *Bubble formation in animals*. J.Cell.Comp.Physiol. 24[1] 1-22.

Hilgenfeldt,S., Lohse,D., Zomack,M. (**2000**). *Sound scattering and localized heat deposition of pulse-driven microbubbles*. Journal of Acoustic Society of America 107[6] 3530-3539.

Hill,C.R., Rivens,I., Vaughan,M.G., terHaar,G.R. (**1994**). *Lesion Development in Focused Ultrasound Surgery - A General-Model*. Ultrasound in Medicine and Biology 20[3] 259-269.

Hill,C.R., Bamber,J.C., ter Haar,G.R. (**2004**). Attenuation and Absorption. In: Physical Principles of Medical UltrasonicsChichester: John Wiley & Sons Ltd, 93-166.

Hindley,J., Gedroyc,W.M., Regan,L., Stewart,E., Tempany,C., Hynnen,K., Macdanold,N., Inbar,Y., Itzchak,Y., Rabinovici,J., Kim,K., Geschwind,J.F., Hesley,G., Gostout,B., Ehrenstein,T., Hengst,S., Sklair-Levy,M., Shushan,A., Jolesz,F. (**2004**). *MRI guidance of focused ultrasound therapy of uterine fibroids: Early results*. American Journal of Roentgenology 183[6] 1713-1719.

Holland,C.K., Deng,C.X., Apfel,R.E., Alderman,J.L., Fernandez,L.A., Taylor,K.J. (**1996**). *Direct evidence of cavitation in vivo from diagnostic ultrasound*. Ultrasound in Medicine and Biology 22[7] 917-925.

Holt,R.G., Roy,R.A. (**2001**). *Measurements of bubble-enhanced heating from focused, MHz-frequency ultrasound in a tissue-mimicking material*. Ultrasound in Medicine and Biology 27[10] 1399-1412.

Hwang,J.H., Tu,J., Brayman,A.A., Matula,T.J., Crum,L.A. (**2006**). *Correlation between inertial cavitation dose and endothelial cell damage in vivo*. Ultrasound in Medicine and Biology 32[10] 1611-1619.

Hynynen,K. (**1991**). *The threshold for thermally significant cavitiation in dog's thigh muscle in vivo*. Ultrasound in Medicine and Biology 17[2] 157-169.

Ikeda,T., Yoshizawa,S., Tosaki,M., Allen,J.S., Takagi,S., Ohta,N., Kitamura,T., Matsumoto,Y. (**2006**). *Cloud cavitation control for lithotripsy using high intensity focused ultrasound*. Ultrasound in Medicine and Biology 32[9] 1383-1397.

Illing,R., Chapman,A. (**2007**). *The clinical applications of high intensity focused ultrasound in the prostate*. International Journal of Hyperthermia 23[2] 183-191.

Illing,R.O., Kennedy,J.E., Wu,F., ter Haar,G.R., Phillips,R.R., Protheroe,A.S., Middleton,M.R., and Cranston,D.W. (**2005)**. *Preliminary experience using extracorporeal high-intensity focused ultrasound for the treatment of kidney and liver tumours*. 754, 13-16. Kyoto. 4th International Symposium on Therapeutic Ultrasound. 2004.

Illing,R.O., Kennedy,J.E., Wu,F., ter Haar,G.R., Protheroe,A.S., Friend,P.J., Gleeson,F.V., Cranston,D.W., Phillips,R.R., Middleton,M.R. (**2005**). *The safety and feasibility of extracorporeal high-intensity focused ultrasound (HIFU) for the treatment of liver and kidney tumours in a Western population*. Br.J.Cancer 93[8] 890-895.

Ishikawa,T., Okai,T., Sasaki,K., Umemura,S., Fujiwara,R., Kushima,M., Ichihara,M., Ichizuka,K. (**2003**). *Functional and histological changes in rat femoral arteries by HIFU exposure*. Ultrasound in Medicine and Biology 29[10] 1471-1477.

Kanthale,P., Ashokkumar,M., Grieser,F. (**2008**). *Sonoluminescence, sonochemistry (H2O2 yield) and bubble dynamics: frequency and power effects*. Ultrason.Sonochem. 15[2] 143-150.

Keller,J.B., Miksis,M. (**1980**). *Bubble oscillations of large amplitude*. Journal of Acoustic Society of America 68[2] 628-633.

Kennedy,J.E. (**2004)**. *An Assessment of the Capacity of High Intensity Focused Ultrasound to Treat Tumours of the Liver and Kidney*. Wolfson College, University of Oxford.

Kennedy,J.E. (**2005**). *High-intensity focused ultrasound in the treatment of solid tumours*. Nat Rev Cancer 5[4] 321-327.

Khokhlova,V.A., Bailey,M.R., Reed,J.A., Cunitz,B.W., Kaczkowski,P.J., Crum,L.A. (**2006**). *Effects of nonlinear propagation, cavitation, and boiling in lesion formation by high intensity focused ultrasound in a gel phantom*. Journal of Acoustic Society of America 119[3] 1834-1848.

Kwak,H.Y., Panton,R.L. (**1985**). *Tensile strength of simple liquids predicted by a model of molecular interactions*. J.Phys.D:Appl.Phys. 18[4] 647-659.

Lauterborn,W. (**1976**). *Numerical investigation of nonlinear oscillations of gas bubbles in liquids*. Journal of Acoustic Society of America 59[2] 283-293.

Lauterborn,W. (**1980**). Cavitation and Inhomogeneities in Underwater Acoustics. Berlin: Springer.

Leeman,S., Vaughan,P.W. (**1980**). *On the use of the impedance bridge technique for monitoring transducer loading*. Journal of Sound and Vibration 70 306-307.

Leighton,T.G., Pickworth,M.J.W., Walton,A.J., Dendy,P.P. (**1988**). *Studies of the Cavitational Effects of Clinical Ultrasound by Sonoluminescence .1. Correlation of Sonoluminescence with the Standing Wave Pattern in An Acoustic Field Produced by A Therapeutic Unit*. Physics Med.Biol. 33[11] 1239-1248.

Leighton,T.G., Pickworth,M.J., Tudor,J., Dendy,P.P. (**1990**). *A search for sonoluminescence in vivo in the human cheek*. Ultrasonics 28[3] 181-184.

Leighton,T.G., Lingard,R.J., Walton,A.J., Field,J.E. (**1992**). *Bubble sizing by the non-linear scattering of two acoustic frequencies*. Natural Physical Sources of Underwater Sound 453-466.

Leighton,T.G. (**1994**). *The Acoustic Bubble*. London: Academic Press.

Leighton,T.G., Phelps,A.D., Ramble,D.G., Sharpe,D.A. (**1996**). *Comparison of the abilities of eight acoustic techniques to detect and size a single bubble*. Ultrasonics 34 661-667.

Leighton,T.G., Birkin,P.R., Hodnett,M., Zeqiri,B., Power,J.F., Price,G.J., Mason,T., Plattes,M., Dezhkunov,N., Coleman,A.J. (2005). *Characterisation of Measures of Reference Acoustic Cavitation (COMORAC): An Experimental Feasibility Trial. In: Bubble and Particle Dynamics in Acoustic Fields: Modern Trents and Applications*, ed. A.A.DoinikovKerala, India: Research Signpost, 37-94.

Leighton,T.G. (**2007**). *What is ultrasound?* Prog Biophys Mol Biol 93[1-3] 3-83.

Liu,H.L., Chen,W.S., Chen,J.S., Shih,T.C., Chen,Y.Y., Lin,W.L. (**2006**). *Cavitation-enhanced ultrasound thermal therapy by combined low- and high-frequency ultrasound exposure*. Ultrasound in Medicine and Biology 32[5] 759-767.

Lizzi,F.L., Coleman,D.J., Driller,J., Franzen,L.A., Leopold,M. (**1981**). *Effects of pulsed ultrasound on ocular tissue*. Ultrasound in Medicine and Biology 7[3] 245-252.

Luther,S., Mettin,R., Koch,P., Lauterborn,W. (**2001**). *Observation of acoustic cavitation bubbles at 2250 frames per second*. Ultrason.Sonochem. 8[3] 159-162.

Lynn,J.G., Zwemer,R.L., Chick,A.J., Miller,A.E. (**1942**). *A new method for the generation and use of focused ultrasound in experimental biology*. Journal of General Physiology 26 179-192.

Ma,Y., Symonds-Tayler,R., Rivens,I.H., and ter Haar,G.R. (**2007)**. *A new Clinical HIFU System (Teleson II)*. Coussios,C.C. and ter Haar,G.R. 87-91. Melville, New York, AIP Conference Proceedings. 6th International Symposium on Therapeutic Ultrasound. 6 A.D.

Mackay,R.S., Rubissow,G. (**1978**). *Decompression studies using ultrasonic imaging of bubbles*. IEEE Trans.Bio.Eng. 25[6] 537-544.

Madersbacher,S., Schatzl,G., Djavan,B., Stulnig,T., Marberger,M. (**2000**). *Long-term outcome of transrectal high- intensity focused ultrasound therapy for benign prostatic hyperplasia*. European Urology 37[6] 687-694.

Malcolm,A.L., ter Haar,G.R. (**1996**). *Ablation of tissue volumes using high intensity focused ultrasound*. Ultrasound in Medicine and Biology 22[5] 659-669.

McLaughlan,J.R., Rivens,I., ter Haar,G. (2007). *A Study of Cavitation Acitivity in Ex-Vivo Tissue Exposed to High Intensity Focused Ultrasound*. In: 6th Internation Symposium on Therapeutic Ultrasound, Melville, New York: AIP, 178-184.

Meaney,P.M., Clarke,R.L., ter Haar,G.R., Rivens,I.H. (**1998**). *A 3-D finite-element model for computation of temperature profiles and regions of thermal damage during focused ultrasound surgery exposures*. Ultrasound in Medicine & Biology 24[9] (pp 1489-1499).

Meaney,P.M., Cahill,M.D., ter Haar,G.R. (**2000**). *The intensity dependence of lesion position shift during focused ultrasound surgery*. Ultrasound in Medicine and Biology 26[3] 441-450.

Medwin,H. (**1977**). *Counting bubbles acoustically: a review*. Ultrasonics 15[1] 7-13.

Melodelima,D., Chapelon,J.Y., Theillere,Y., Cathignol,D. (**2004**). *Combination of thermal and cavitation effects to generate deep lesions with an endocavitary applicator using a plane transducer: ex vivo studies*. Ultrasound in Medicine and Biology 30[1] 103-111.

Miller,D.L. (**1981**). *Ultrasonic detection of resonant cavitation bubbles in a flow tube by their second-harmonic emissions*. Ultrasonics 19[5] 217-224.

Miller,D.L., Thomas,R.M. (**1995**). *Thresholds for hemorrhages in mouse skin and intestine induced by lithotripter shock waves*. Ultrasound in Medicine and Biology 21[2] 249-257.

Miller,D.L., Gies,R.A. (**1998**). *The interaction of ultrasonic heating and cavitation in vascular bioeffects on mouse intestine*. Ultrasound in Medicine and Biology 24[1] 123-128.

Miller,D.L., Creim,J.A., Gies,R.A. (**1999**). *Heating vs. cavitation in the induction of mouse hindlimb paralysis by ultrasound*. Ultrasound in Medicine and Biology 25[7] 1145-1150.

Morse,P.M., Ingard,K.V. (**1968**). *Theoretical Acoustics*. New York: McGraw Hill.

Neppiras,E.A., Noltingk,B.E. (**1951**). *Cavitation produced by ultrasonics: theoretical conditions for the onset of cavitation*. Proc.Phys.Soc. B64 1032-1038.

Neppiras,E.A., Fill,E.E. (**1969**). *A cyclic cavitation process*. Journal of Acoustic Society of America 46[5] 1264-1271.

Neppiras,E.A. (**1969**). *Subharmonic and other low-frequency emission from bubbles in sound-iradiated liquids*. Journal of Acoustic Society of America 46[3] 587-601.

Neppiras,E.A. (**1969**). *Subharmonic and other low-frequency signals from sound-irradiated liquids*. J.Sound Vib. 10[2] 176-186.

Neppiras,E.A., Coakley,W.T. (**1979**). *Acoustical cavitation in a focused field in water at 1 MHz*. J Sound Vib 45[3] 341-373.

Neppiras,E.A. (**1980**). *Acoustic Cavitation*. Physics Reports-Review Section of Physics Letters 61[3] 159-251.

Neppiras,E.A. (**1984**). *Acoustic cavitation series: part one, Acoustic cavitation: an introduction*. Ultrasonics 22[1] 25-28.

Noltingk,B.E., Neppiras,E.A. (**1950**). *Cavitation produced by ultrasonics*. Proc.Phys.Soc. B63 674-685.

Nyborg,W. (**2002**). *"Bubble Detection and Cavitation Monitoring"* ANSI S1.24 TR-2002. 80.

Parlitz,U., Englisch,V., Scheffczyk,C., Lauterborn,W. (**1990**). *Bifurcation structure of bubble oscillators*. Journal of Acoustic Society of America 88[2] 1063-1077.

Pennes,H.H. (**1948**). *Analysis of tissue and arterial blood temperatures in the resting human forearm 1*. Journal of Applied Physiology 1 93-122.

Plesset,M.S. (**1949**). *The dynamics of cavitation bubbles*. J.Appl.Mech. 16 277-282.

Poliachik,S.L., Chandler,W.L., Ollos,R.J., Bailey,M.R., Crum,L.A. (**2004**). *The relation between cavitation and platelet aggregation during exposure to high-intensity focused ultrasound*. Ultrasound in Medicine and Biology 30[2] 261-269.

Poritsky,H. (**1952**). *The collapse or growth of a spherical bubble or cavity in a viscous fluid*. Proceedings of the first U.S.national congress on applied mechanics] 813-821.

Preston,R.C., Chivers,R.C., Zeqiri,B., Robinson,S.P., Davidson,F., Bacon,D.R., Shaw,A. (**2008**). Output Measurments for Medical Ultrasound. London: Springer-Verlag.

Prosperetti,A., Crum,L.A., Commander,K.W. (**1988**). *Nonlinear bubble dynamics*. Journal of Acoustic Society of America 83[2] 502-514.

Prosperetti,A. (**1975**). *Nonlinear oscillations of gas bubbles in liquids: transient solutions and the connection between subharmonic signal and cavitation*. Journal of Acoustic Society of America 57[4] 810-821.

Prosperetti,A. (**1976**). *Subharmonics and ultraharmonics in the forced oscillations of weakly nonlinear systems*. American Journal of Physics 44[6] 548-554.

Prosperetti,A. (**1977**). *Application of the subharmonic threshold to the measurement of the damping of oscillating gas bubbles*. Journal of Acoustic Society of America 61[1] 11-16.

Prosperetti,A. (**1984**). *Acoustic cavitation series: part two, Bubble phenomena in sound fields: part one*. Ultrasonics 22[2] 69-77.

Rabkin,B.A., Zderic,V., and Vaezy,S. (**2005)**. *HIFU-induced hyperecho in ultrasound images, cavitation activity and thermal behavior*. 754, 43-46. Kyoto. 4th International Symposium on Therapeutic Ultrasound. 2004.

Rabkin,B.A., Zderic,V., Vaezy,S. (**2005**). *Hyperecho in ultrasound images of HIFU therapy: involvement of cavitation*. Ultrasound in Medicine and Biology 31[7] 947-956.

Rabkin,B.A., Zderic,V., Crum,L.A., Vaezy,S. (**2006**). *Biological and physical mechanisms of HIFU-induced hyperecho in ultrasound images*. Ultrasound in Medicine and Biology 32[11] 1721-1729.

Rayleigh Lord (**1917**). *On the pressure developed in a liquid during the collapse of a spherical cavity*. Phil.Mag. 34 94-98.

Rivens,I.H., Rowland,I.J., Denbow,M., Fisk,N.M., ter Haar,G.R., Leach,M.O. (**1999**). *Vascular occlusion using focused ultrasound surgery for use in fetal medicine*. Eur.J.Ultrasound 9[1] 89-97.

Roberts,W.W., Hall,T.L., Ives,K., Wolf,J.S., Jr., Fowlkes,J.B., Cain,C.A. (**2006**). *Pulsed cavitational ultrasound: a noninvasive technology for controlled tissue ablation (histotripsy) in the rabbit kidney*. Journal of Urology 175[2] 734-738.

Rota,C., Raeman,C.H., Child,S.Z., Dalecki,D. (**2006**). *Detection of acoustic cavitation in the heart with microbubble contrast agents in vivo: a mechanism for ultrasound-induced arrhythmias*. Journal of Acoustic Society of America 120[5 Pt 1] 2958-2964.

Roy,R.A., Madanshetty,S.I., Apfel,R.E. (**1990**). *An acoustic backscattering technique for the detection of transient cavitation produced by microsecond pulses of ultrasound*. Journal of Acoustic Society of America 87[6] 2451-2458.

Smith,S.W. (**1997**). *The Scientist and Engineer's Guide to Digital Signal Processing*. San Diego, CA: California Technical Publishing.

Sokka,S.D., King,R., Hynynen,K. (**2003**). *MRI-guided gas bubble enhanced ultrasound heating in in vivo rabbit thigh*. Physics Med.Biol. 48[2] 223-241.

Starritt,H.C., Duck,F.A., Humphrey,V.F. (**1989**). *An experimental investigation of streaming in pulsed diagnostic ultrasound beams*. Ultrasound in Medicine and Biology 15[4] 363-373.

Strasberg,M. (**1956**). *Gas bubbles as sources of sound in liquids*. Journal of Acoustic Society of America 28[1] 20-26.

Suslick,K.S., Doktycz,S.J., Flint,E.B. (**1990**). *On the origin of sonoluminescence and sonochemistry*. Ultrasonics 28[5] 280-290.

Suslick,K.S., Mdleleni,M.M., Ries,J.T. (**1997**). *Chemistry induced by hydrodynamic cavitation*. Journal of the American Chemical Society 119[39] 9303-9304.

Tanter,M., Pernot,M., Aubry,J.F., Montaldo,G., Marquet,F., Fink,M. (**2007**). *Compensating for bone interfaces and respiratory motion in high-intensity focused ultrasound*. International Journal of Hyperthermia 23[2] 141-151.

ter Haar,G. (**1995**). *Ultrasound focal beam surgery*. Ultrasound in Medicine and Biology 21[9] 1089-1100.

ter Haar,G.R., Rivens,I.H., Moskovic,E., Huddart,R., and Visioli,A. (**1998)**. *Phase 1 clinical trial of the use of focused ultrasound surgery for the tratment of soft tissue tumours.* SPIE proceedings .

Thomas,C.R., Farny,C.H., Wu,T., Holt,R.G., Roy,R.A. (**2006**). Monitoring HIFU Lesion Formation In Vitro Via The Driving Voltage. In: 5th International Symposium on Therapeutic Ultrasound, ed. G.T.Clement, N.J.McDannold, K.HynynenMelville, New York: AIP, 293-297.

Tu,J., Matula,T.J., Brayman,A.A., Crum,L.A. (**2006**). *Inertial cavitation dose produced in ex vivo rabbit ear arteries with Optison by 1-MHz pulsed ultrasound*. Ultrasound in Medicine and Biology 32[2] 281-288.

Vaezy,S., Shi,X., Martin,R.W., Chi,E., Nelson,P.I., Bailey,M.R., Crum,L.A. (**2001**). *Real-time visualization of high-intensity focused ultrasound treatment using ultrasound imaging*. Ultrasound in Medicine and Biology 27[1] 33-42.

Vallancien,G., Chartier-Kastler,E., Bataille,N., Chopin,D., Harouni,M., Bougaran,J. (**1993**). *Focused extracorporeal pyrotherapy*. European Urology 23 (Suppl. 1) 48-52.

Vaughan,M.G., ter Haar,G.R., Hill,C.R., Clarke,R.L., Hopewell,J.W. (**1994**). *Minimally invasive cancer surgery using focused ultrasound: a pre-clinical, normal tissue study*. British Journal of Radiology 67 267-274.

Vaughan,P.W. (**1968**). *Investigation of acoustic cavitation thresholds by observation of the first subharmonic*. J.Sound Vib. 7[2] 236-246.

Visioli,A.G., Rivens,I., ter Haar,G.R., Horwich,A., Huddart,R.A., Moskovic,E., Padhani,A., Glees,J. (**1999**). *Preliminary results of a phase I dose escalation clinical trial using focused ultrasound in the treatment of localised tumours*. European Journal of Ultrasound 9[1] 11-18.

Wall,P.D., Tucker,D., Fry,F.J., Mosberg,W.H. (**1953**). *The Use of High Intensity Ultrasound in Experimental Neurology*. Journal of Acoustic Society of America 25[2] 281-285.

Walton,A.J., Reynolds,G.T. (**1984**). *Sonoluminescence*. Adv Phys 33 595-660.

Watkin,N.A., Rivens,I.H., ter Haar,G.R. (**1996**). *The intensity dependence of the site of maximal energy deposition in focused ultrasound surgery*. Ultrasound in Medicine and Biology 22[4] 483-491.

Watkin,N.A., Morris,S.B., Rivens,I.H., ter Haar,G.R. (**1997**). *High Intensity focused ultrasound ablation of the kidney in a large animal model*. Journal of Endourology 11[3] 191-196.

Watmough,D.J., Davies,H.M., Quan,K.M., Wytch,R., Williams,A.R. (**1991**). *Imaging Microbubbles and Tissues Using A Linear Focused Scanner Operating at 20 MHz - Possible Implications for the Detection of Cavitation Thresholds*. Ultrasonics 29[4] 312-318.

Weissler,A. (**1959**). *Formation of Hydrogen Peroxide by Ultrasonic Waves: Free Radicals*. J.Chem.Soc. 81 1077-1081.

Winterton,R.H.S. (**1977**). *Nucleation of boiling and cavitation*. J.Phys.D:Appl.Phys. 10[15] 2041-2056.

Wu,F., Wang,Z.B., Chen,W.Z., Bai,J., Zhu,H., Qiao,T.Y. (**2003**). *Preliminary experience using high intensity focused ultrasound for the treatment of patients with advanced stage renal malignancy*. Journal of Urology 170[6 Pt 1] 2237-2240.

Wu,F., Wang,Z.B., Chen,W.Z., Zou,J.Z., Bai,J., Zhu,H., Li,K.Q., Xie,F.L., Jin,C.B., Su,H.B., Gao,G.W. (**2004**). *Extracorporeal focused ultrasound surgery for treatment of human solid carcinomas: early Chinese clinical experience*. Ultrasound in Medicine and Biology 30[2] 245-260.

Wu,F., Wang,Z.B., Zhu,H., Chen,W.Z., Zou,J.Z., Bai,J., Li,K.Q., Jin,C.B., Xie,F.L., Su,H.B. (**2005**). *Extracorporeal high intensity focused ultrasound treatment for patients with breast cancer*. Breast Cancer Res.Treat. 92[1] 51-60.

Wu,F. (**2006**). *Extracorporeal high intensity focused ultrasound in the treatment of patients with solid malignancy*. Minim.Invasive.Ther.Allied Technol. 15[1] 26-35.

Young,F.R. (**1989**). Cavitation. London: Imperial College Press.

Zderic,V., Keshavarzi,A., Andrew,M.A., Vaezy,S., Martin,R.W. (**2004**). *Attenuation of porcine tissues in vivo after high-intensity ultrasound treatment*. Ultrasound in Medicine and Biology 30[1] 61-66.

Zeqiri,B., Gelat,P.N., Hodnett,M., Lee,N.D. (**2003a**). *A novel sensor for monitoring acoustic cavitation. Part I: Concept, theory, and prototype development*. IEEE Trans.Ultrason.Ferroelectr.Freq.Control 50[10] 1342-1350.

Zeqiri,B., Lee,N.D., Hodnett,M., Gelat,P.N. (**2003b**). *A novel sensor for monitoring acoustic cavitation. Part II: Prototype performance evaluation*. IEEE Trans.Ultrason.Ferroelectr.Freq.Control 50[10] 1351-1362.

Zhong,P., Cioanta,I., Cocks,F.H., Preminger,G.M. (**1997**). *Inertial cavitation and associated acoustic emission produced during electrohydraulic shock wave lithotripsy*. Journal of Acoustic Society of America 101[5 Pt 1] 2940-2950.

Zhu,S., Dreyer,T., Liebler,M., Riedlinger,R., Preminger,G.M., Zhong,P. (**2004**). *Reduction of tissue injury in shock-wave lithotripsy by using an acoustic diode*. Ultrasound in Medicine and Biology 30[5] 675-682.